9th International Conference on

Fundamental and applied MHD, Thermo acoustic and Space technologies

SEVENTH FRAMEWORK PROGRAMME

Theme 9: SPACE

Riga – Latvia
June 16-20 , 2 0 1 4

Chairmen A. Alemany France, J. Freibergs, Latvia

Co-chairmen :

J.P. Chopart, France – C. Latge, France – M. Francois, France - E. Gaia, Italy

Secretaries : B. Collovati, France - M. Broka, Latvia
pamir@simap.grenoble-inp.fr

University of Latvia Institute of Physics

LISM Laboratoire d'Ingénierie et Sciences des Matériaux

Grenoble INP

Latvijas Universitāte Anno 1919

Université Joseph Fourier Sciences Technologie Médecine

Supporting Organisation

CNRS :	Centre National de la Recherche Scientifique
INP :	Institut Polytechnique de Grenoble
UJF :	Université Joseph Fourier Grenoble
CEA :	Commissariat à l'Energie Atomique

Ministère de l'Enseignement Supérieur et de la Recherche
Ambassade de France à Alger
Ambassade de France à Riga

Organising committee

A. Alemany, M. Broka, J.P. Chopart, B. Collovati , A.L. Daltin, J. Freibergs. M. Francois E. Gaia, C. Latge, S. Schanicina,

Scientific committee

Alemany A., France

Alradi M., Syria

Aogaki R., Japan

Balbaud F CEA France

Blums E., Latvia

Bouabdallah A., Algeria

Buligins L., Latvia

Cebers A., Latvia

Chopart J.P., France

Cuevas S., Mexico

Ellappan R.K., India

Etay J. , France

Francois M. France

Freibergs J., Latvia

Frick P., Russia

Gailitis A., Latvia

Gaia E. Italy

Gerbeth G., Germany

Jakovics A., Latvia

Latgé C., France

Li Puma A., France

Mogi I., Japan

Molokov S., UK

Mond M. Israel

Odenbach S.,Germany

Proctor M.R.E., UK

Skorvanek I Slovakia

Thess A., Germany

Uhlemann M., Germany

Zabinski P Poland

Montici A. Italy

Poli G. France

Roux J.P. France

Sellier A. France

Preface.

The pamir conference is organised for the 9th time and for the second time in Latvia. As in the past, pamir is a generalist conference on magneto hydro dynamics (MHD) and more generally in magneto sciences. It is focussed on basic MHD problems as for example turbulence and dynamo effect but considering also energetic and electro processing of material as well as the technology of liquid metal which is of a first importance in the concept of large power plant as I.T.E.R and the new recent development of the fast breeder reactors represented by generation 4.

The main relevant fluids considered by the topics of the conference are liquid metals which have high electrical conductivity but an important aspect of the magneto science is devoted to poorly conducting fluids as electrolytes submitted to the influence of magnetic fields offering large possibilities to control and improve the mass transfer in such media. In this field of research a new project in course of elaboration, **MACE** as **MA**gnetic **C**ontrol of **E**lectro chemistry, will be proposed in the frame of the **COST** program of the EU, under the leading of Professor **Piotr Zabinski** from the University of Krakov, Poland. A MACE meeting will be organised during the pamir conference.

Thus the conference is focussed on fundamental and applied researches combining several disciplines as hydrodynamics, mass and heat transfers, electromagnetism... Both theoretical and experimental aspects are considered as well as analytical and numerical methods. The participation of engineers from industrial companies and researchers from universities are particularly important in the objective of Research and Development activities.

As in the last pamir 2011, the present edition is coupled with a summer school centred on the activity of the European project "Space Thermo acoustic Radio-Isotopic Power System"

"**Space TRIPS"**.

Space TRIPS aims to demonstrate the feasibility of a highly efficient and reliable electrical generator for space, using radio isotopic heat source. The project is based on the modelling, design, construction and experimentation of a prototype of MHD electrical generator driven by a thermo acoustic engine. A design implementing this technology will be completed to asses the performance of a space system.

The project takes advantages of the complementary competences of 6 partners from 4 European countries.

They are

- HEKYOM start up company, French, develops Thermo acoustics applications
- CNRS (Centre National de la Recherche Scientifique) French research organisation
- IPUL Institute of Physics of the University of Latvia
- AREVA TA French company about nuclear activity
- Thales Alenia Space Italy specialised in Space Technology
- HZDR Germany , Research specialized in MHD activities

As it is usual in the EU project the dissemination of knowledge is an important aspect of space TRIPS especially in direction of young scientists and engineers. This is the reason why a summer school is organised in parallel with the conference and why two specific sessions of the conference are devoted for one at the thermo acoustic process and for the other to the space technology.

Space TRIPS is largely represented in the board of the two events, as chairmen

A. Alemany, France. J. Freibergs, Latvia.

and co chairmen:

J.P. Chopart, France – C. Latge, France – M. François, France - E. Gaia, Italy.

Foreword

These two volumes are the proceedings of the communication of the 9th pamir international conference held in Riga, Latvia, June 16 – 20, 2014.

The present edition of pamir benefits of the support of the EU by the way of the project Space Trips (Space Thermo acoustic Radio-Isotopic Power System) at the origin of the summer school that welcomes students of many European countries. The organizers of these two events express their gratitude to the University of Latvia which host the sessions of the conference, The French embassy in Latvia and the "Institut Francais en Lettonie" to host the Space Trips summer school. The papers are indexed according to the topics and the numerotation accorded to each of them.

The volume 1 contains the papers of:

A-Basic MHD
B-Thermo acoustic
C- Space: stress on technologies

The volume 2 contains the papers of:

D - Liquid metal technologies for coolant applications
E - Applied MHD for material application
F - Ferro fluid

For further information please contact the secretaries of the conference:

Beatrice Collovati	Tél: 0000 33 4 56 52 96 20
Pamir	e-mail: pamir@simap.grenoble-inp.fr
Maja Broka	Tél: 00 371 67944700
IPUL	e-mail: mbroka@sal.lv
Sveta Schanicina	Tél: 00 371 67944700
IPUL	e-mail: sveta@sal.lv

CONTENTS

VOLUME 2

D. LIQUID METAL TECHNOLOGIES FOR COOLANT APPLICATIONS
D.1. Power generation

D.2. MHD pumps and flow control

D.3. Measuring techniques for liquid metal coolants

D.5. Liquid metal mixing

E. APPLIED MHD FOR MATERIAL APPLICATION
E.1. Metallurgical applications

E.2. Magneto-electrolysis

E.3. MHD in crystal growth

E.4. Electromagnetic processing of material

E.5. Electromagnetic levitation

E.6. Magneto static

F. FERRO FLUID
F.1. Magnetic liquids

F.2. Electrohydrodynamics

F.3. Magnetorheological suspensions

ROLE OF THERMOELECTROMAGNETIC FORCES IN CAPILLARY POROUS SYSTEMS PROPOSED FOR LIQUID METAL COOLING OF FUSION REACTOR COMPONENTS

KALDRE I., LIELAUSIS O.
Institute of Physics, University of Latvia, 32 Miera str., LV-2169, Salaspils, Latvia
E-mail: kaldre@gmail.com

Abstract: Protection of plasma facing components against thermal and corpuscular overloads remains as one of the most important tasks in fusion related research. The interest in liquid metals is connected with the opportunity to create movable and renewable contact surface with plasma. Today as one of the most promising solutions is the Capillary Porous System (CPS). In this work SS/Li CPS has been analyzed focusing on positive and negative aspects caused by thermoelectromagnetic (TEM) forces. The absolute thermoelectric power of liquid Li is extremely high compared to other metals (20 μV/K). Thermoelectric current, interacting with the strong, plasma confining magnetic field (up to 5T) creates force on liquid metal, which might have a significant impact on device performance.

1. Introduction

Thermoelectromagnetic convection (TEMC) recently is of a particular interest in the field of crystal growth and solidification of metallic alloys [1]. This convection emerges as a result of thermoelectric current and applied magnetic field interaction, and may play significant role in solute and mass transport near solidification interface and in the mushy zone [2]. A high TE current density is defined by a high differential thermoelectric power, good electrical conductivity and high temperature gradient. Ability for a pair of materials to generate TE current is characterized by figure of merit which has dimension of [A/W]

$$Z_{TE} = \frac{\sigma \cdot \Delta S}{\lambda} \tag{1}$$

Electric potential and current distribution in continuous media is governed by Ohm's law eq. (2). In some circumstances thermoelectric term can be dominant source of electric current in the material.

$$\vec{\nabla} V = -S(T)\vec{\nabla} T - \vec{j} / \sigma \tag{2}$$

The computing technique developed for metallurgical applications is applied to a quite different field, to fusion technologies in this work. In liquid lithium cooling system thermoelectric current may create force which may drive a liquid convection or alter pressure distribution in the liquid lithium. Low density of Li allows TEM forces to induce significant liquid lithium flow easily. Idea to use thermoelectric pumping effect to remove heat from a divertor has been explored in last few years by Ruzic [3]. It has been shown that in such a way an intense enough free surface flow can be generated in a system of parallel grooves. No outer power source is needed and flow is driven conditionally by the heat flux itself.

2. Presentation of the problem

We are considering another version of divertor design when the thermoelectric flow is generated in a capillary porous system containing of stainless steel mesh surrounded by liquid lithium. As a base for the calculation of TEM forces a traditional schematic CPS version [4] has been chosen. As an outer coolant instead of water liquid Ga is proposed, which is more effective and can sustain higher temperature. The behaviour of a CPS (Liquid lithium/Stainless steel mesh) subjected to homogeneous and inhomogeneous heat flux from plasma has been analyzed numerically. It is demonstrated that local heat pulse from plasma may cause forces which pushes lithium into plasma and away from hottest place. These forces may exceed gravity and capillarity and be dominant force to determine lithium flow in the divertor. Order of magnitude estimations has been carried out to compare different physical effects.

Table 1. Properties of liquid lithium, stainless steel and 2/3 SS+1/3 Li by volume porous media used in numerical simulations and force density estimations.

Property	**Symbol**	**Lithium**	**Stainless steel**	**Porous media**	**Unit**
Thermal conductivity	λ	44	16	26	W/m*K
Heat capacity	C	4350	500	1800	J/kg*K
Electrical conductivity	σ	$3.6\cdot10^6$	$1.3\cdot10^6$	$2\cdot10^6$	Sim/m
Absolute thermoelectric power	S	20	0	7	μV/K
Density	ρ	500	7500	5000	Kg/m^3
Surface tension	γ	0.32			N/m
Viscosity	μ	$6\cdot10^{-4}$			Pa*s
Thermoelectric figure of merit	Z_{TE}	1.64	0	0.54	

The CPS under consideration contains a of 7 mm thick SS mesh layer with characteristic structure size of 0.5 mm. Inside this layer 2/3 of the volume is SS mesh and 1/3 is liquid Li. Liquid lithium is fed from the thin layer at the bottom of the CPS and brought to the contacting surface by capillary forces and pressure difference. Li flow in the device is shown in Fig.1. The deposited power is removed from the bottom of CPS layer by a liquid gallium flow contained between 4 mm stainless steel walls. The application of Ga allows to increase a maximum working temperature to 400^0C. At temperatures over 400^0C the SS walls would loss their corrosion- resistance with regard to Ga which may lead to other problems during prolonged exploitation of the system. TE current is generated at the interface between two media with different absolute thermoelectric powers if temperature gradient is parallel to interface, but TE current is also generated in the volume of the material if S is function of temperature. Macroscale TE current circulation is generated at the surface between CPS and SS wall, while small scale TE current flow is generated within the CPS. In CPS current path length is comparable to mesh structure size and magnitude can vary depending on CPS geometry, temperature gradient and other parameters. In this work we analyze only on large scale TE current. Principal scheme of the 200x200 mm divertor panel is given in Fig.2.

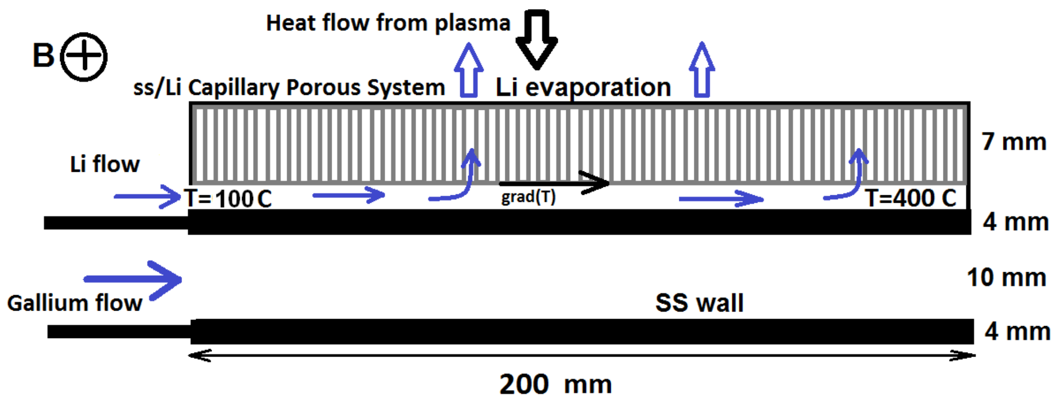

Figure 1: Li flow in the divertor. CPS here is depicted as array of the vertical stainless steel capillaries.

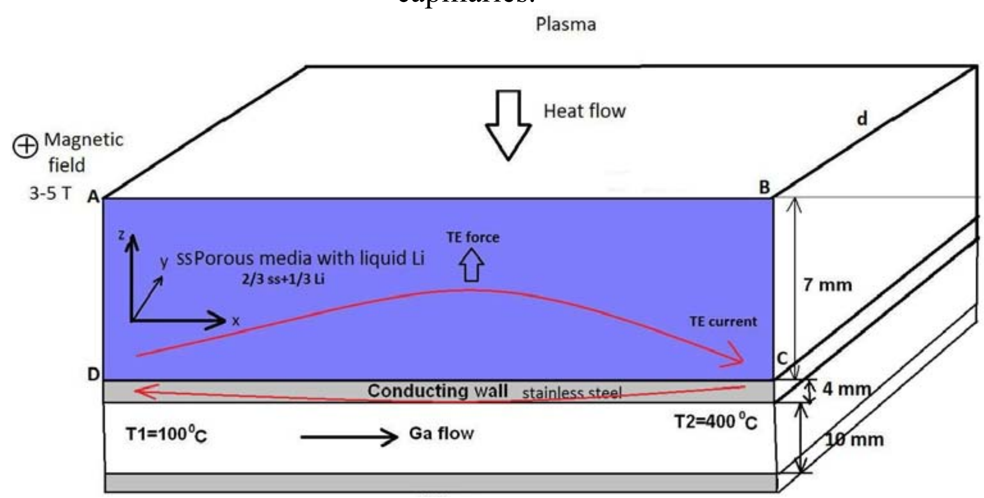

Figure 2: Schematic picture of 200x200 mm divertor plate. Thermoelectric current flow and Lorentz force are indicated with arrows.

Numerical models have been developed to calculate TE current density and TEM force if constant and inhomogeneous heat flux is applied perpendicular to the plasma/CPS surface. If homogeneous heat flux is applied to divertor plate depicted in Fig.2, then TE current flows in one direction through the CPS and in opposite through SS wall. Direction of the current is defined by the direction of temperature gradient and sign of differential thermoelectric power. Calculated TE current density in the case when a constant heat flux is applied and temperature gradient is perpendicular to CPS/SS surface is shown in Fig.3. In this case if heat flow is inhomogeneous, then situation is more complicated and current density and force distribution is difficult to predict. If Gaussian shape heat pulse is applied to plasma/CPS surface is numerically analyzed and results are shown and compared to homogeneous case in Fig.4. Temperature and current distribution are calculated Fig. 4b,c. Fig. 4d and Fig.4e compare TE force densities acting on CPS. Homogeneous heat flow creates almost uniform force perpendicular to plasma/CPS surface, while force density caused by inhomogeneous heat flow also creates force component parallel to CPS/plasma surface, thus may cause surface deformation and push Li out of the SS mesh in some places.

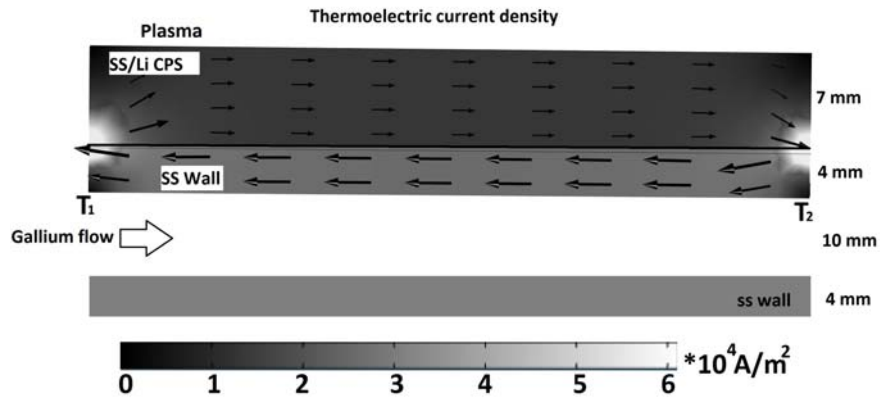

Figure 3. Thermoelectric current density in CPS region and in SS wall if constant heat flow is applied from the plasma zone.

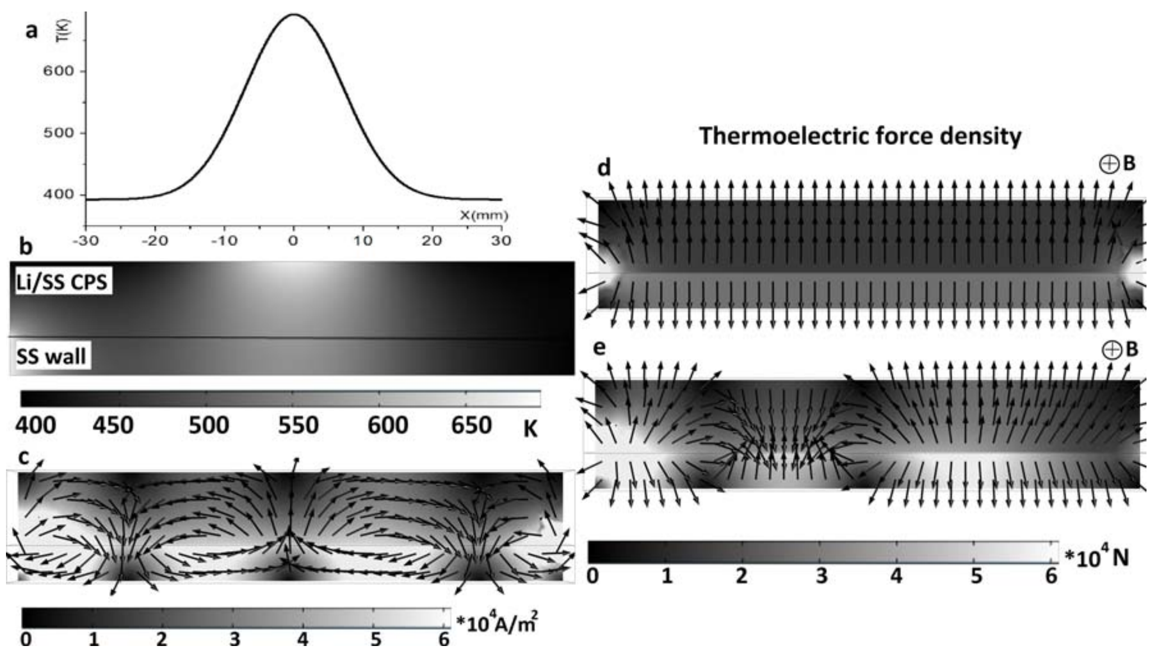

Figure 4. Thermoelectric current density if a non-homogeneous heat flux is applied.
a - temperature profile along plasma/CPS surface, b - temperature distribution in the divertor plate, c - calculated thermoelectric current density. Thermoelectric force distribution in case of: d - homogeneous, e - inhomogeneous heat flow. Only CPS and SS wall are shown in this picture.

The following quantities are used in numerical models and force estimations: d = 0.5 mm- capillary characteristic length, L = 7 mm - CPS layer thickness, θ = 15 K/cm - temperature gradient along the CPS/SS interface, B = 1 T - magnetic field induction, u = 2 cm/s - characteristic Li flow velocity. Force order of magnitude estimations is given in Table 2.

Table 2. Force density estimation acting on CPS in macroscale

Force	Equation	Characteristic force density
Capillary force	$F_c = 4\frac{\gamma}{dL}$	55 kN/m^3
Gravity force	$F_g = \rho g$	70 kN/m^3
Viscosity	$F_v = \frac{32\mu u}{d^2}$	31 kN/m^3
MHD braking force [7]	$F_e = \sigma u B^2$	40 kN/m^3
TEM force [8]	$F_{TE} = \sigma \Delta S \theta B$	50 kN/m^3

3. Conclusion

It is demonstrated that TE current may create force which has significant effect on the liquid Li flow within CPS. It is found that liquid metal surface can be deformed and liquid metal can be pushed away from the hot zone by TEM forces. This force has to be taken into account during design of the system. If an inhomogeneous heat flow is applied than temperature gradient in the CPS has all three components and TEM force is present in CPS regardless of magnetic field orientation. In case of Gaussian shape heat impulse from plasma zone and constant magnetic field along the surface, liquid Lithium is pushed away from hot zone as demonstrated by numerical models. Force density estimations indicate that TEM force can exceed all other forces under certain conditions, thus the influence of thermoelectric phenomena in Li CPS has to be carefully analyzed and taken into account during design of divertor for fusion reactors. This phenomena needs to be deeper evaluated and understood for better usage of it and to avoid negative effects of TEMC.

4. References

[1] Li, X.; Fautrelle, Y.: Influence of thermoelectric effects on the solid-liquid interface shape and cellular morphology in the mushy zone during the directional solidification of Al-Cu alloys under a magnetic field. Acta Materialia, vol. 55 (2007), iss. 11, pp. 690-704.

[2] Kaldre, I; Fautrelle, Y; Etay, J; Bojarevics, A; Buligins, L: Thermoelectric current and magnetic field interaction influence on the structure of directionally solidified Sn-10%wt.Pb alloy. Journal of Alloys and Compounds, vol. 571 (2013), pp. 50-55.

[3] Ruzic, D.N.: Lithium Walls: The Ultimate Technology. Illinois: Center for Plasma-Material Interactions, 2010.

[4] Mironov, S.V.; Evtikhin V.A.: The tests of liquid metals (Ga, Li) as plasma facing components in T-3M and T-11M tokamaks. Fusion Engineering and Design, vol. 81 (2006), p. 113-119.

[5] Shercliff, J. Thermoelectric magnetohydrodynamics. J. Fluid Mechanics, vol. 91 (1979), part 2, pp. 231-251.

[6] S.J. Zinkle. Summary of physical properties for lithium, Pb-17Li, and (LiF)n*BeF2 coolants. APEX Study Meeting Sandia National Lab, July 27-28, (1998).

[7] Davoust, L., Bertrand, F., Moreau, R., Tanguy, P., & Bolcato, R. Recent results on MHD damped convection in the horizontal Brigman configuration. Magnetohydrodynamics, vol.33 (1997), no. 4, pp. 319-327.

[8] Wang, J., Fautrelle, Y., Ren, Z., Li,X., Nguyen-Thi, H., Mangelinck-Noel, N., Salloum Abou Jaoude, G., Zhong, Y., Kaldre, I., Bojarevics, A., Buligins, L.: Thermoelectric magnetic force acting on the solid during directional solidification under static magnetic field. Applied Physics Letters, vol. 101 (2012), iss. 25, 251904.

DUAL-COOLANT LEAD-LITHIUM (DCLL) BLANKET: STATUS AND R&D IN THE AREA OF MHD THERMOFLUIDS

SMOLENTSEV S., ABDOU M.
University of California, Los Angeles, USA
E-mail: sergey@fusion.ucla.edu

Abstract : The DCLL is an attractive breeding blanket concept that leads to a high-temperature (T ~ 700°C), high thermal efficiency (η > 40%) blanket system. The key element of the concept is a flow channel insert (FCI) that serves as an electrical and thermal insulator to reduce the magnetohydrodynamic (MHD) pressure drop and to decouple the temperature-limited RAFM (reduced-activation ferritic/martensitic) steel wall from the flowing hot PbLi. The paper introduces the concept, reviews history of the development of the DCLL in the US and worldwide and then reviews the most important R&D results obtained in the US in the ITER DCLL TBM program (2005-2011) and more recently, including experimental and computational studies of MHD PbLi flows and corrosion of RAFM steel in PbLi in the presence of a magnetic field.

1. Introduction.

The DCLL blanket of a fusion power reactor promises a solution towards a high-temperature, high-efficiency blanket system while using temperature-limited reduced-activation ferritic/martensitic (RAFM) steel as structural material. In this concept, a high-temperature lead-lithium (PbLi) alloy flows slowly (V ~ 10 cm/s) in large poloidal rectangular ducts (D ~ 20 cm) to remove the volumetric heat generated by neutrons and produce tritium, while a pressurized (typically to 8 MPa) helium gas (He) is used to remove the surface heat flux and to cool the ferritic first wall (FW) and other blanket structures in the self-cooled region, and a low-conductivity flow channel insert (FCI), which is typically a few mm thick, with silicon carbide (SiC) as a suitable candidate material, is used for electrical and thermal insulation (Fig. 1).

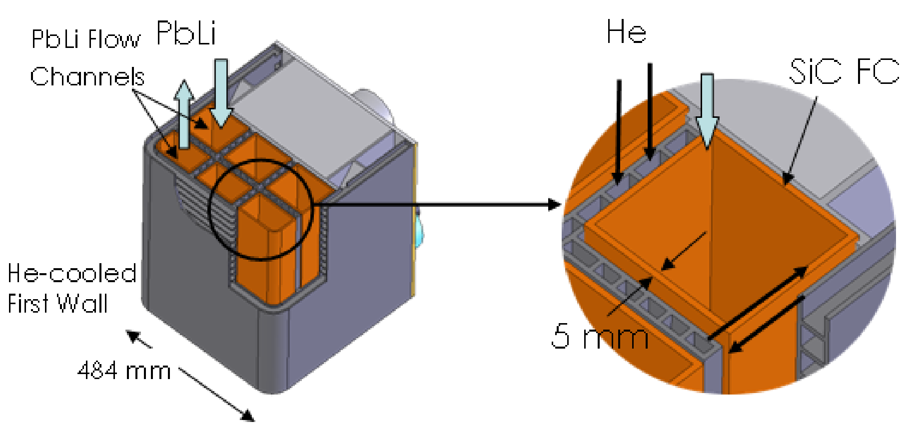

Figure 1: Schematic of DCLL blanket with poloidal PbLi channels, He-cooling channels and insulating SiC FCI.

Several designs of the DCLL blanket have been considered in Europe, the US and China. Historically, the first DCLL version, known as a low-temperature (LT) DCLL blanket [1], relies on qualified materials and existing fabrication technologies. A key component of this design is a sandwich-type FCI composed of steel/alumina/steel layers or a thin alumina layer on the wall to be used as electrical insulator for decoupling electrically conducting structural walls from the flowing PbLi. In the high-temperature (HT) DCLL blanket, first introduced in [2], an FCI made of SiC, either composite or foam, was further proposed as a means for electrical and also thermal insulation to provide acceptable MHD pressure drops, to achieve a high PbLi exit temperature of ~700°C and, ultimately, to provide high thermal efficiency of about 45% (as opposed to about 470°C and 34% in the LT design).

The unique features of the DCLL blanket associated with the flows of PbLi in a strong magnetic field suggest special R&D tasks that run into four basic areas, such as: (1) PbLi MHD thermofluids, (2) fluid materials interaction, (3) tritium transport, and (4) FCI development and characterization. In the rest of the paper, we summarize the most important R&D results obtained over the last ten years, including the US ITER TBM program (2005-2011) and more recent blanket studies in the US in the MHD thermofluids area. The particular topics reviewed in this paper are related to: (a) theoretical studies of MHD instabilities in poloidal flows, (b) experimental studies of PbLi MHD flows, (c) 3D computations of MHD flows with FCI, and (d) corrosion studies for the PbLi/RAFM system.

2. MHD instabilities in poloidal flows.

Two recent studies [3, 4] address quasi-two-dimensional (Q2D) MHD flows to elucidate possible MHD instability mechanisms in conditions relevant to DCLL. In the first one [3], direct numerical simulations (DNS) and a linear stability analysis are performed for a family of Q2D MHD flows with inflectional velocity profiles. The generic basic velocity profile with points of inflection is produced by imposing an external flow-opposing force. By varying this force, various instability modes and transition scenarios are reproduced. First, a linear stability analysis is performed and then nonlinear effects are studied using DNS. Special attention is paid to the location of the inflection point with respect to the duct wall. Complex non-linear flow dynamics, including various vortex-wall and vortex-vortex interactions, and even negative turbulence production are observed and analyzed as the inflection point approaches the wall. The analysis lends insight into what is typically called “jet instability” suggesting that instability and transition to Q2D turbulence in blanket flows occurs as a two-step process. First bulk vortices appear at the vicinity of the inflection point. Then, the bulk vortices interact with the side-wall boundary layer (at the wall parallel to the magnetic field) causing its destabilization and eventually turbulence.

The second study [4] considers MHD rectangular duct flows with volumetric heating (mixed-convection flows). The flows are upward, subject to a strong transverse magnetic field perpendicular to the temperature gradient, such that the flow is Q2D. Studies of this mixed-convection flow include analysis for the basic (undisturbed) flow, linear stability analysis and DNS-type computations. The parameter range covers the Hartmann number (*Ha*) up to 500, the Reynolds number (*Re*) from 1000 to 10,000 and the Grashof number (*Gr*) from 10^5 to 10^9. The linear stability analysis predicts two primary instability modes: (i) bulk instability associated with the inflection point in the velocity profile near the “hot” wall and (ii) side-wall boundary layer instability. A mixed instability mode is also predicted.

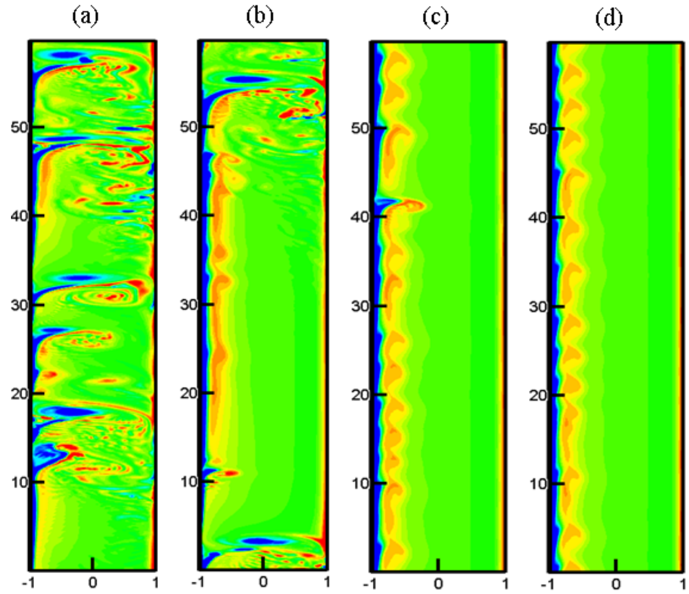

Figure 2: Vorticity snapshots in a turbulent mixed-convection flow at *Re* = 5000 and *Gr* = 10^8. *Strong turbulence*: (a) *Ha* = 50, and (b) *Ha* = 60. *Weak turbulence*: (c) *Ha* = 100, and (d) *Ha* = 120.

Effects of *Ha*, *Re* and *Gr* on turbulent mixed-convection flows are addressed via non-linear computations that demonstrate two characteristic turbulence regimes (Fig.2). In the "weak" turbulence regime, the induced vortices are localized near the inflection point of the basic velocity profile, while the boundary layer at the wall parallel to the magnetic field is slightly disturbed. In the "strong" turbulence regime, the bulk vortices interact with the boundary layer causing its destabilization and formation of secondary vortices that may travel across the flow, even reaching the opposite wall. In this regime, similar to observations in [3], the key phenomena are vortex-wall and vortex-vortex interactions.

3. Experimental studies of MHD PbLi flows.

A new MHD PbLi facility called MaPLE (Magnetohydrodynamic PbLi Experiment) has recently been constructed and successfully operated at UCLA [5]. The loop operation parameters are: maximum magnetic field 1.8 T, PbLi temperature up to 350°C, maximum PbLi flow rate with/without a magnetic field 15/50 l/min, maximum pressure head 0.15 MPa.

Ongoing work on development and testing of flow diagnostics needed for high temperature PbLi flows includes ultrasonic velocimetry (HT UDV) and an indirect technique of differential pressure measurements as described in detail in Refs. [5] and [6]. Intensive studies have been started to address MHD pressure drop reduction in PbLi flows using two different insulation techniques: (1) laminated walls [7] and (2) a SiC foam-based FCI [5]. Initial studies were also performed to address material compatibility between SiC and PbLi. These include static testing at high temperature of 700°C in a specially designed static chamber and dynamic testing of various FCI samples (see also Section 4).

4. 3D computations of MHD flows with FCI.

Prior to experimental studies on MHD pressure drop reduction in PbLi flows with an insulating FCI, computer simulations were performed using a 3D MHD, unstructured mesh, parallel code HIMAG [8]. In the ongoing experiments, a 30 cm SiC foam-based FCI segment manufactured by ULTRAMET, USA is tested first. The FCI is filled with either silica or carbon aerogel and then coated with a thin (~1 mm) CVD layer to prevent PbLi ingress into pores. In the next experiments, testing is planned on two coupled segments resulting in a total length of 60 cm. These two segments are separated with a small 1-mm slit.

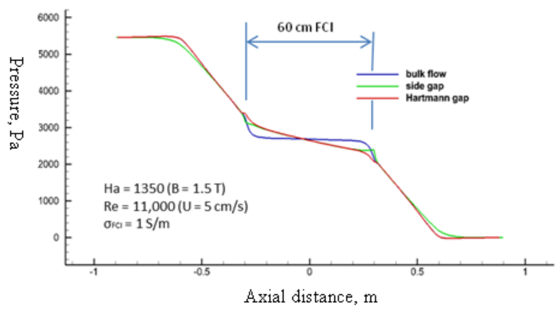

Figure 3: Typical pressure distribution in MHD flow with the FCI.

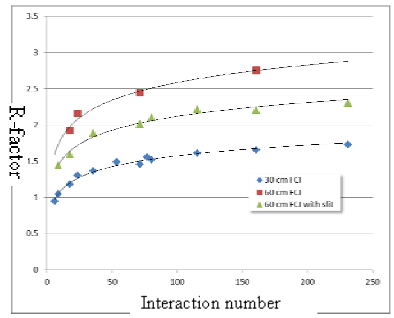

Figure 4: Simulations of the MHD pressure drop reduction in the FCI flows.

A pressure profile calculated for a 60-cm FCI is shown in Fig. 3. Figure 4 shows a trend found for the pressure drop reduction R-factor (the pressure drop without the FCI divided by the pressure drop with the FCI). Regardless of the *Re* and *Ha* values used in the computations, the R-factor is always described well as a function of the interaction number $N=Ha^2/Re$ only. It is noticeable that the R-factor is typically around 2. Such modest MHD pressure drop reductions in the experiment are related to the significant increase in the MHD pressure drop due to 3D MHD effects at the FCI entry/exit and also due to electrical current leakages from the bulk flow into the gap in the junction region between the two segments. However, extrapolation to real blanket conditions, where FCIs are continuously spaced inside the RAFM duct suggests much higher pressure drop reductions with the R-factor in the range 50-100.

5. MHD corrosion studies for PbLi/RAFM steel.

Implementation of RAFM steels and PbLi in blanket applications still requires material compatibility studies as many questions related to physical/chemical interactions in the RAFM/PbLi system remain unanswered. First of all, the mass loss caused by the flow-induced corrosion of the steel walls at temperatures in the range 450°C -550°C needs to be better characterized. Second, another serious concern is the transport of activated corrosion products and their precipitation in the cold section of the loop. Third, an important modeling parameter, the saturation concentration of iron in PbLi, needs further evaluations as the existing correlations demonstrate scattering of several orders of magnitude [9].

To address these issues, a computational suite called TRANSMAG (Transport Phenomena in Magnetohydrodynamic Flows) has recently been developed [9]. The computational approach is based on simultaneous solution of flow, energy and mass transfer equations, assuming mass transfer controlled corrosion and uniform dissolution of iron in the flowing PbLi. First, the new tool was applied to solve an inverse mass transfer problem, where the saturation concentration of iron in PbLi at temperatures up to 550°C was reconstructed from the earlier experimental data on corrosion in turbulent flows without a magnetic field in the form: $C^S = e^{13.604-12975/T}$, where T is the temperature of PbLi in K and C^S is in wppm.

Second, the new correlation was used in the computations of corrosion in laminar flows in a rectangular duct in the presence of a strong transverse magnetic field. It was found that the corrosion behavior is different between the side wall of the duct (parallel to the magnetic field) and the Hartmann wall (perpendicular to the magnetic field) due to formation of high-velocity jets at the side walls. The side walls experience a stronger corrosion attack demonstrating a mass loss up to 2-3 times higher compared to the Hartmann walls. This analysis suggests scaling laws for the mass loss in rectangular ducts: $ML \sim e^{pT} U_m^q B_0^s$ for the side wall, and $ML \sim e^{pT} U_m^q$ for the Hartmann wall, where q, $s \sim 0.5$.

6. References

[1] Malang, S; Schleisiek, K. (Editors): Dual Coolant Blanket Concept. Kernforschugszentrum Karlsruhe, Karlsruhe, KfK 5424, 1994.

[2] Tillack, M.S.; Malang, S.: High performance PbLi blanket. Proc.17th IEE/NPSS Symposium on Fusion Engineering, Vol. 2, 1000-1004, San Diego, California, Oct.6-10, 1997.

[3] Smolentsev, S.; Vetcha, N.; Moreau, R.: Study of instabilities and transitions for a family of quasi-two-dimensional magnetohydrodynamic flows based on a parametric model. Phys. Fluids 24 (2012) 024101.

[4] Vetcha, N.; S. Smolentsev, S.; Abdou, M.; Moreau, R.: Study of instabilities and quasi-two-dimensional turbulence in volumetrically heated MHD flows in a vertical rectangular duct. Phys. Fluids 25 (2013) 024102.

[5] Smolentsev, S.; Li, F.-C.; Morley, N.; Ueki, Y.; Abdou, M.; Sketchley, T.: Construction and initial operation of MHD PbLi facility at UCLA. Fusion Eng. Des. 88 (2013) 317-326.

[6] Smolentsev, S.; Kunugi, T.; Messadek, K.; Yokomine, T.; Young, J.; Yuki, K.; Ueki, Y.; Sketchley, T.; Li, F.-C.; Morley, N.; Abdou, M.: Status of TITAN Task 1–3 flow control and thermofluid modeling. Fusion Eng. Des. 87 (2012) 777-781.

[7] Aoyagi, M.; Inage, Y.; Ito, S.; Ebara, S.; Ueki, Y.; Yuki, K.; Li, F.-C.; Smolentsev, S.; Yokomine, T.; Kunugi, T.; Sketchley, T.; Abdou, M.; Hashizume, H.: Verification test of a three-surface-multi-layered channel to reduce MHD pressure drop. Proc. 8th Japan-Korea Symp. Nuclear Thermal Hydraulics and Safety (NTHAS8), Dec. 9-12, Beppu, Japan, N8P1089, 2012.

[8] Smolentsev, S.; Morley, N.B.; Abdou, M.; Munipalli, R.; Moreau, R.: Current approaches to modeling MHD flows in the Dual Coolant Lead Lithium Blanket. Magnetohydrodynamics 42 (2006) 225-236.

[9] Smolentsev, S.; Saeidi, S.; Malang, S.; Abdou, M.: Numerical study of corrosion of ferritic/martensitic steels in the flowing PbLi with and without a magnetic field. J. Nuclear Materials 432 (2013) 294-304.

AMTEC CLUSTERS AS ADD-ON SYSTEM FOR POWER GENERATION IN A CONCENTRATED SOLAR POWER PLANT

ONEA[1] A., DIEZ de los RIOS RAMOS[1] N., PALACIOS, J. L.[2], HERING[1] W.
[1] Karlsruhe Institute of Technology, Institute for Neutron Physics and Reactor Technology, Hermann-von-Helmholtz Platz 1, 76344 Eggenstein-Leopoldshafen, Germany
[2] University of Oldenburg, Ammerländer Heerstraße 114-118, 26129 Oldenburg
E-mail: alexandru.onea@kit.edu

Abstract: The present study reports a first estimation of the number of Alkali Metal Thermal Energy Converter (AMTEC) cells required for an AMTEC-Concentrated Solar Power (CSP) hybrid power plant in the 100 MWth class envisaged in [3]. Furthermore, numerical results obtained for the structural analysis of an experimental AMTEC cell developed at the Karlsruhe Institute of Technology (KIT) are reported.

1. Introduction

Due to the changes in the German energy policy, a shortfall can possibly appear in the energy coverage when the availability of the fossil resources will decrease to the extent that they cannot be used to deliver the electrical demand. This scenario is further aggravated by the worldwide increased energy demand and motivates the search for other environmental-friendly energy sources. In parallel, it is also essential to increase the efficiency of the present “green” energy technologies, such as wind power and solar power.

In this context, the Alkali Metal Thermal Energy Converter technology together with a thermal storage device represents a promising solution for the extension of the global efficiency and of the total electrical output of a thermal power plant. AMTEC devices are based on the unique property of β-alumina ceramics, such as β”-alumina solid electrolyte (BASE), to allow the transport of alkaline (sodium) ions, while having a high electric resistivity. On the anode side of an AMTEC cell, characterized by high temperature (~800 °C) and relative high pressure (~1 bar), the sodium ionizes, with ions being transported through the BASE and electrons directed towards an electric load to produce electricity. On the cathode side of the cell, characterized by low temperature (250 – 500 °C) and low pressure (10 – 100 Pa), the ions recombine with the electrons to form neutral sodium molecules in vapor state that is further condensed and circulated back to the anode side, so that the cycle can be repeated. For a detailed description of the AMTEC operating principle we refer to the paper of Heinzel et al. [1].

The use of liquid metals such as sodium for thermal power plants has been recently identified as the best heat transfer fluid, delivering the largest electrical energy to the grid and achieving the largest efficiency of the ideal delivered electricity, according to Liu et al. [2]. At the same heat capacity rate, liquid sodium has the highest average heat transfer rate compared with air, compressed air at 10 bar, super critical CO_2 at 100 bar, steam at 10 bar and molten salt. This is due to its extremely high heat conduction coefficient and hence the best heat transfer value.

Recently a concept of using liquid metals such as sodium for a hybrid thermal solar plant using AMTEC technology has been proposed by Hering et al. [3].

As an alternative for delivering the electrical base load, this new concept envisage the use of a heat storage tank that will allow the continuous operation of the facility during night and will also compensate the heat fluctuations that can occur during day operation. Further, the peaks in the thermal energy that can appear during day operation can be used by employing the AMTEC technology as an add-on system for direct generation of electricity. The low temperature side of the AMTEC devices operates at temperatures < 500 ^{0}C and it is connected to the storage tank. By this solution the "cold" sodium from the storage tank at ~200 °C is heated by the "waste" heat generated by the AMTEC devices. A concept design for a compact, small size solar thermal receiver using AMTEC converters generating has been proposed by Tanaka [4]. It is reported that the system conversion efficiency in maximum mode can reach 20 % at 1050 K and generate ~12 kWe, while in maximum output mode reaches 18 % and generates almost 23 kWe.

2. Preliminary layout of the AMTEC system for CSP

For the hybrid system AMTEC and Concentrating Solar Power (A&CP), the AMTEC system envisaged should be dimensioned in the range 1-10 MW, for a total system thermal output of about 100 MWth. The ratio can be optimized to meet the needs of the projected power plant. The yearly averaged thermal energy potentially available for AMTEC system, which is location dependent, should be correlated with the size of the base plant, receiver and of the thermal storage tank in order to properly dimension the AMTEC system.

For an AMTEC cell, the power vs. amperage curve has an inverted U-shape, defining therefore the voltage and amperage at the peak of the profile for maximal electrical power. Typically the maximum power density has been compared in literature. Underwood et al [5] proposed that the comparison should be made in terms of the AMTEC figure of merit Z_A, defined as the ratio of the measured maximum power density:

$$P_m = V_m I_m / A_e \ , \qquad (1)$$

where V_m is the applied voltage at maximum power, I_m is the total measured current at maximum power and A_e is the area of the electrode, to the theoretical maximum power density P_t:

$$Z_A = P_m / P_t \qquad (2)$$

The theoretical maximum power is the maximum power density produced minus the ohmic power losses occurring in the electrolyte, the resistances occurring in the current lead, BASE/electrode contact and sheet resistance. For the preliminary layout of the AMTEC system, the focus is on the maximum power density P_m that can be achieved by different configurations. Consideration of the figure of merit for a preliminary layout is still premature at this stage. A rough estimation of the number of BASE elements coated with electrodes for the output power required is performed in this study.

For this purpose it is considered as a reference configuration an AMTEC cell consisting of a single cylinder with one end closed and a surface of 30 × 200 mm^2 (diameter × length) covered by a structured electrode.

In order to determine the total electric power delivered, the experimental data reported by Fang and Knödler [6] for titanium diboride (TiB_2) electrodes at 700 °C and 800 °C and by Fletcher and Schwank [7] for titanium nitride (TiN) electrodes at the same temperatures have been extrapolated for the AMTEC geometry considered. For all sets of data, the area of the electrode was kept constant, while the current density varies due to the change in operating temperature and electrode material, as displayed in Table 1.

For long time operation of the AMTEC system the power degradation has to be taken into account, in order to eliminate it from the design phase by appropriately setting the AMTEC operating parameters. Richman and Tennenhouse [8] report critical values for the current density below which no power degradation occurs, e.g. a BASE containing 0.25 wt. % LiO_2 should be charged below a current density of 1 A/cm^2 in order to avoid the power degradation. Therefore, for the present calculation are considered only current densities below or slightly above this critical value.

Table 1 Current density and voltage extrapolated on a reference configuration

Electrode	TiB_2	TiB_2	TiN	TiN
Temperature (°C)	700	800	700	800
Current density (A/cm^2)	0.5	0.6	0.81	1.12
Voltage (V)	0.33	0.40	0.27	0.32
Electrode area (m^2) for P_m = 1 MW	612	421	462	278
Nr. BASE elements for P_m = 1 MW	32480	22337	24498	14750
P_m / A_e (W/m^2)	1633	2375	2166	3597
Data source	[6]	[6]	[7]	[7]

The power dependency on the electrode area is displayed in Figure 1. The output electrical power determined is very sensitive to the operating characteristics of the cell. Beside current density and operating temperature, many other issues such as BASE and electrode thicknesses, resistances of the current collector, current lead etc. have to be taken into account and correlated to achieve a robust AMTEC performance able to deliver a large amount of electrical energy without power degradation. The highest power can be obtained at the largest current density of 1.12 A/cm^2 and a temperature of 800 °C. For this system configuration an electric output in the range of 1 MW can be realized with approximately 14750 BASE elements coated with electrodes (total electrode area A_e = 278 m^2). A larger electrical output would impose significant raise in costs due to the increase in the number of BASE elements and is at least for the moment not realistic. In parallel, the task of increasing the critical current density above which power degradation can occur has to be further pursued.

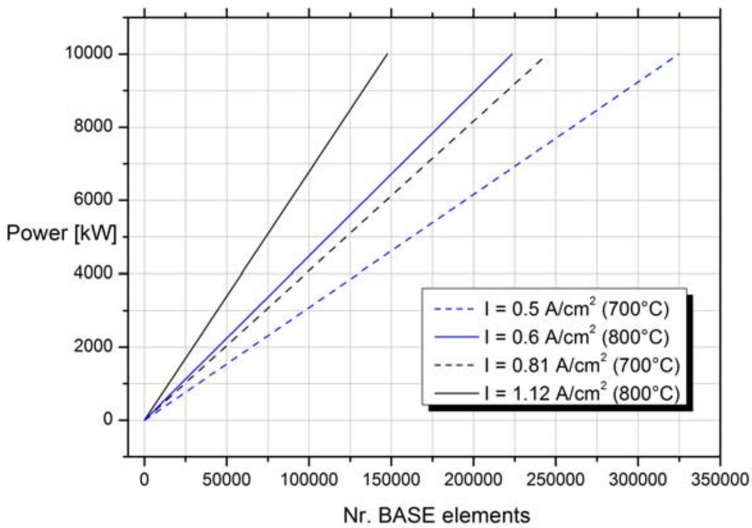

Figure 1: Total electric power versus required BASE elements.

The ratio of the maximum power to the total electrode area P_m/A_e is presented in Table 1. The above calculation is in good agreement with the data reported by Tanaka [4] for the AMTEC-solar receiver, for which in maximum power mode a ratio of $P_m/A_e \sim 3183$ W/m^2 at 1000 K can be calculated. To obtain the balanced optimum between the maximum electric power delivered and constant performances during long-time usage further studies have to be performed for a better estimation of the electrical power, taking into consideration also other AMTEC specific issues such as the small electrode effect.

3. AMTEC test facilities at KIT

The experimental investigation and development of AMTEC cells has been recently restarted at KIT in the frame of two research projects, the Helmholtz alliance on LIquid Metal TECHnology (LIMTECH) and Helmholtz Energy Materials Characterization Platform (HEMCP). The experimental program is focused on short term tests and long term tests of AMTEC cells, as well as tests of innovative materials for AMTEC cells in hot sodium environment. The short term tests are planned to start mid 2014 in the Amtec TEst FAcility (ATEFA) at KIT. For a detailed description of the facility and of the research projects we refer to the paper of Onea et al. [9]. The long term tests are planned to be performed in the 1000 K SOdium Loop to TEst materials and Corrosion (SOLTEC) facility that is presently at the end of the design phase at KIT. The experimental test campaign planned in the ATEFA facility is focused on AMTEC key issues such as the tests of BASE ceramics, electrode materials, new technologies, and stability of ceramic-metal interfaces.

4. Structural analysis of the AMTEC test cell

One of the critical issues related to an AMTEC cell is the BASE-metal interface. During operation, the BASE expands due to a thermal gradient that can reach up to several hundreds of K. Since the BASE is connected to a metallic part, the BASE-metal interface is severely stressed by the thermal and mechanical stresses induced in this region. Many authors, including Heinzel et al. [1], report the crack of BASE occurring rather frequently, and suggest that the demanding operating conditions (high temperature, large temperature gradient across the BASE) induce severe stresses in the BASE that lead to its failure. Unfortunately limited studies can be found in literature regarding the stress distribution in an AMTEC cell. Recently, a structural analysis of the AMTEC test cell developed at KIT has been performed (Palacios et al. [10]) using ANSYS software.

For the AMTEC test cell developed at KIT, the BASE is brazed to a transition piece made of Niobium (Nb) that is brazed on the other side to a metallic tube made of Inconel 617. The choice of Niobium is motivated by the fact that it has a similar coefficient of thermal expansion ($\alpha_{Nb} = 8.5\times10^{-6}$ K^{-1} at 1093 °C) with the BASE ($\alpha_{BASE} = 8.1\times10^{-6}$ K^{-1} at 1000 °C). Since the metallic pipe made of Inconel has a larger coefficient of thermal expansion of ($\alpha_{pipe} = 16.3\times10^{-6}$ K^{-1} at 900 °C), it will expand more, pressing therefore the transition piece.

The numerical model of the one experimental test cell developed at KIT is presented in Figure 2 (a). The braze material for the transition piece was considered to be nickel.

The structural analysis in stationary state has been performed for the nominal operating conditions planned, nevertheless considering the relevant parameters at their extreme range, i.e. the temperature gradient between the hot side and the cold was set to 750 °C, while the pressure gradient on the BASE tube was set to 0.2 MPa. Under these conditions the maximum shear stress in the metal-Nb joint (upper braze) was estimated to reach 9.1 MPa, which corresponds to a safety factor of 4.3, while the maximum shear stress in the Nb-BASE interface (bottom braze) was estimated to be 4.8 MPa, corresponding to a safety factor of 8.2. The maximum von-Mises stress in the transition piece reaches 21.6 MPa (safety factor 6.4), while the maximum principal stresses in the BASE is determined to be 1.83 MPa (safety factor 15). For the stress distribution determined under these operating conditions no material failure should occur in the test cell. The upper brazing between the transition piece and the metallic tube is determined to be the weakest component in the cell.

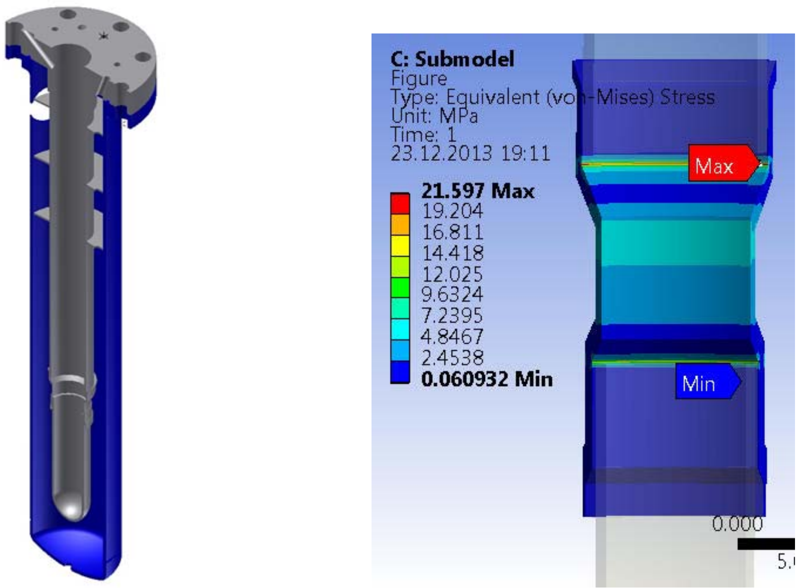

(a) (b)

Figure 2: a) ANSYS model of the experimental AMTEC test cell b) Stress distribution in the transition piece at ΔP = 0.2 MPa and ΔT = 750 ^{0}C.

5. Conclusions

The use of an AMTEC cluster with a reasonable number of elements as an add-on system for a CSP plant coupled with a thermal storage tank can be achieved for an electrical output in the range of about 1 MW if a robust AMTEC design can be attained, able to operate on a long time basis at a current density of ~1 A/cm^2 without power degradation.

Although in good agreement with the data reported in [4], further investigations should be made to appropriately estimate the real electric power delivered by a cluster of AMTEC cells, considering in parallel the long time power behaviour.

Furthermore, the stress distribution in the experimental AMTEC test cell developed at KIT has been numerically investigated and the location of the highest stresses has been identified.

References

[1] Heinzel, V., Huber, F., Peppler, W., Will, H. (1991) Technological tests with respect to the use of beta alumina in Alkali-Metal-Thermo-Electric converters (AMTEC), Key Engineering Materials 59 & 60, 38 –394.

[2] Liu, M., Belusko, M., Tay, S. N. H., Bruno, F. (2014) Impact of the heat transfer fluid in a flat plate phase change thermal storage unit for concentrated solar tower plants, Solar Energy 101, 220 – 231.

[3] Hering, W., Stieglitz, R., Wetzel, Th. (2012) Application of liquid metals for solar energy systems, 2nd European Energy Conference, Maastricht, Netherlands.

[4] Tanaka, K. (2010) Concept study of solar thermal receiver using alkali metal thermal to electric converter (AMTEC), Current Applied Physics 10, S254 – S256.

[5] Underwood, M. L., Williams R. M., Jeffries-Nakamura, B., Ryan, M. A. (1991) A figure of merit for AMTEC electrodes, Proc. of the 26th Intersociety Energy Conversion Engineering Conference IECEC '91, Vol. 5, Boston, 475 – 480.

[6] Fang, Q., Knödler, R. (1992) Porous TiB_2 electrodes for the alkali metal thermoelectric convertor, J. Materials Science 27, 6725 – 6729.

[7] Fletcher, R. W., Schwank, W. (2003) Recent developments in mixed ionic and electronic conducting electrodes for the Alkali Metal Thermal Electric Converter (AMTEC), Space Tech. Applic. Intern. Forum STAIF 2003, 722 – 729.

[8] Richman, R. H., Tennenhouse, G. J. (1975). A model for degradation of ceramic electrolytes in Na-S batteries, J. Am. Ceram. Soc. 58, 63-67.

[9] Onea, A., Diez de los Rios Ramos, N., Hering, W., Stieglitz R., Moster, P. (2013). Direct energy conversion using liquid metals, 3rd European Energy Conference E2C, Budapest, Hungary.

[10] Palacios, J. L., Onea, A., Diez de los Rios Ramos, N., Hering, W. – Structural and thermal analysis of an experimental AMTEC test cell. In preparation.

EXPERIMENTAL STUDIES OF LIQUID LITHIUM FILM FLOW IN MAGNETIC FIELD

PLATACIS[1] E., SOBOLEV[1] A., SHISHKO[1] A, MUKTEPAVELA[2] F.
[1]Institute of Physics, University of Latvia, Salaspils, LV-2169, Latvia
[2]Institute of Solid State Physics, University of Latvia, LV-1063, Riga, Latvia
E-mail: erik@sal.lv

Abstract. Possibility of practical realization of a super thin (h ≈ 0.1 mm) gravitational film flow of liquid lithium on a flat substrate exposed to a strong magnetic field oriented under some definite angle to the substrate surface is discussed. Results of the first experiment on the observation of such film flow formation performed at IPUL are reported.

1. Introduction.

A problem is considered related to the development of liquid metal (lithium) receiving contact devices for the divertor zone of small spherical tokamaks [1-3]. The latter might be used as an effective source of neutrons [4, 5]. It is assumed that in such devices the heat power of plasma flows concentrated at the separatrix of the poloidal magnetic field can be completely removed by the cooled solid divertor plates, but the liquid lithium film, slowly flowing over the surface, serves only to absorb the falling on it plasma particles.

It should be noted that in the experiments with a liquid lithium flow having a free surface, additionally to the stubborn technological problems of reliable wetting under the conditions of deep vacuum in the “hot” vacuum chamber (T ≈ 300-350 ^{0}C), there arise problems of reliable and long-term visualization of the objects under observation. These are determined by the high chemical activity of lithium vapours, the direct impact of which makes any optical system to malfunction.

All said above gives grounds to the use of pure lithium in experiment, so excluding its contamination with the materials adsorbed onto the inner surfaces of the liquid metal paths. Deep vacuum must prevent the possibility of adsorbed film formation of the free surface of liquid lithium. In fact, the presence of the adsorbed by the film substance on the lithium film surface can significantly alter the hydrodynamics of such a thin film flow and hence to crucially affect the physical realization of the super thin film flow.

2. Description of the experimental setup.

To perform experiments on the observation of the liquid lithium film flow, a setup has been developed at IPUL, which makes it possible to drive and visualize such flows in the solenoid of the super conducting magnet (SCM) “Magdalena”. In the central part of the cylindrical (D = 300 mm) working zone of the SCM (where the magnetic field is practically uniform), a cylindrical vacuum chamber was placed coaxially, with a plane substrate and a capillary system for liquid metal flow distribution (CSFD) situated inside the chamber. The setup cross-section by a vertical plane passing across the magnet axis is shown schematically in fig. 1. The substrate (3), 175 mm in length and 100 mm in width, was made from 8 mm thick copper sheet cladded with a 0.5 thick plate made of AISI 316L austenitic steel. Such choice of substrate materials agrees with the above-described concept of the divertor system of the spherical tokamak. The presence of stainless steel is needed to protect the heat and electrically conducting copper from the action of liquid lithium.

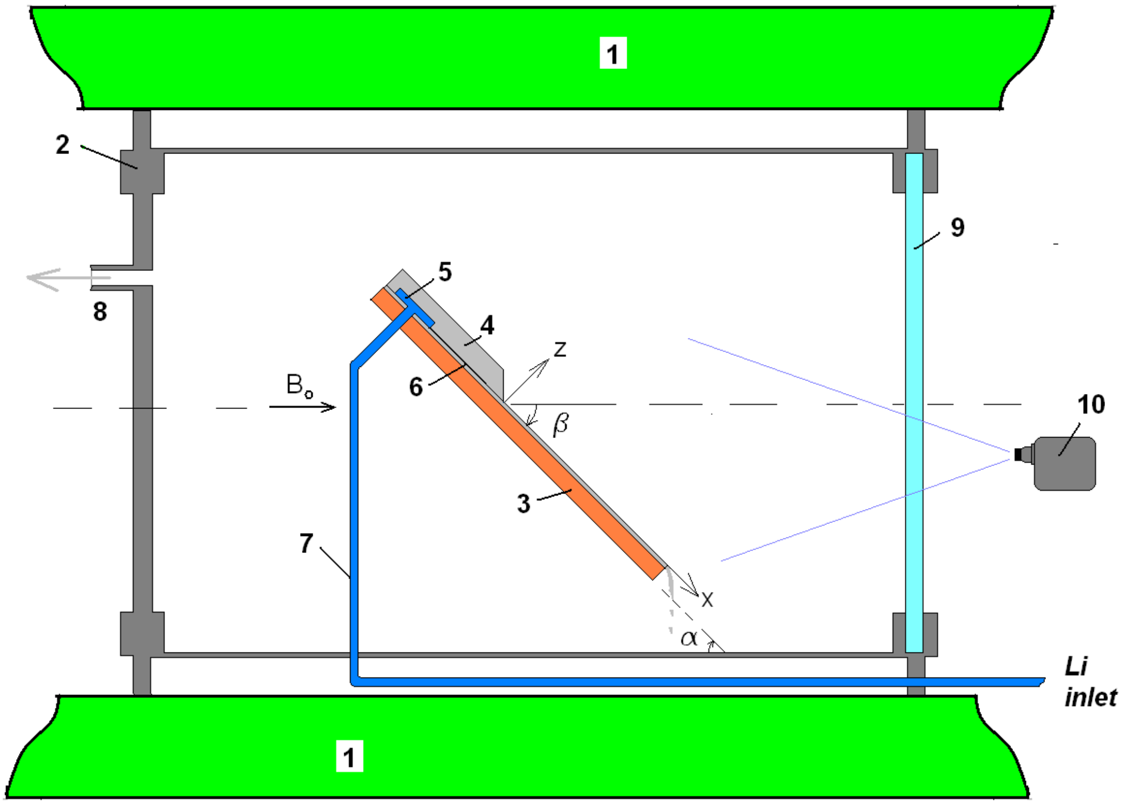

Fig.1: Schematic presentation of the experimental setup. 1 – superconducting magnet; 2 – vacuum chamber; 3 –substrate; 4 – stainless steel head; 5 – bath for liquid metal supply; 6 – zone of capillary channels; 7 – pipe for liquid metal supply; 8 – branch pipe of the vacuum system; 9 – quartz glass hole window; 10 – video camera.

The CSFD is a combination of a substrate and a head (4) made of the same stainless steel as thick as 6 mm. A reservoir (5), as deep as 3 mm, for liquid lithium supply to the capillary system was cut at the inlet end of the head. Paths, 2 mm wide and 0.2 mm deep, were engraved on the bottom surface of the head as far as 2 mm from each other. At a 10 mm distance from the outlet, all grooves between the paths were removed. In such a way, after the head was placed on the substrate, the reservoir (5) was connected to a slot nozzle (90 x 0.2 mm^2) by 22 capillary channels of 40 mm in length. The liquid metal was supplied to the CSFD through a stainless steel pipe (7), which passes through the substrate (3) near to the reservoir center.

As shown in fig. 1, the substrate with the CSFD was tilted at the angle $\beta = -45^o$ to the axis of the superconducting magnet such that the magnetic field $\mathbf{B}_0$ had both a normal to the substrate (B_z) and a tangential (B_x) component. Note that β is a sharp angle between the axial line of the magnet and the substrate measured from the axis in the anticlockwise direction.

The liquid lithium was supplied to the substrate as though a gas system as by using a special bellows device providing liquid lithium constant supply (cycle duration 320 sec) with the very small flowrate Q = 90 mm^3/sec. Observations were made using a video camera (10) through a quartz glass hole window (9).

Thus the above-described setup made it possible to observe a gravitational flow of liquid metal over the flat substrate tilted at $\beta = 45°$ to the horizon and at $\beta = -45^o$ to the force lines of the uniform magnetic field.

3. Estimation of the magnetic field influence on the CSFD operation.

The idea to use the proposed CSFD is based on an assumption that the main action on the distribution of the flow from the slot nozzle comes from the hydraulic resistance of the capillary channels. It is assumed that the pressure losses between the inlet and outlet of the capillary channels determined by the liquid lithium flow are much bigger in value than the pressure drops accompanying the liquid lithium flow in the separation reservoir.

If one assumes that the magnetic field, by significantly increasing the pressure drops in the capillary channels, does not so noticeably increase the pressure drops in the reservoir, the efficiency of the CSFD operation with the field increase will still enhance.

Detailed estimations of the efficiency the CSFD operation due to its orientation about the acting gravity and magnetic fields are presented in [6]. These estimates were obtained under the assumption that the capillary channels were enveloped by a solid well-conducting material. For the CSFD system under consideration, those estimations of the transverse magnetic field effect can be evaluated as a little higher.

Let us evaluate the magnitudes V_g and V_g^B calculated using the formulas in [6] for a situation realized in the experiment with β = 45°, β = -45°, B_0 = 1T:

$$V_g = 23.1 \text{ mm/s}, \; V_g^B = 1.65 \text{ mm/s}.$$

Since the value of V_g^B << 10 mm/s, one can expect a sufficient effectiveness of the used CSFD in the magnetic field B_0 = 1 T.

4. Estimation of the magnetic field action on the fully developed liquid lithium film flow.

Gravitational film flow in a uniform magnetic field is described in [6]. In Table 1 one can find parameters of the developed flows of liquid lithium calculated from the formulas in [6] under the experimental conditions (β = 45°, β = -45°), with the linear flowrate q = 1 mm^2/s and some values of the magnetic field B_0 of the solenoid.

Table 1. q = 1 mm^2/s, β = 45°, β = -45°

B_0, T	0	0.25	0.5	0.75	1.0
H, mm	0.076	0.091	0.16	0.306	0.522
⟨V⟩, mm/s	13.2	11.05	6.25	3.27	1.92
f_{em}^*	0	-0.509	-0.982	-1	-1
p_0	1	0.651	0.211	0.074	0.32

Along with the values of the film flow thickness h and mean film velocity ⟨V⟩ = q/h, f_{em}^* values are listed in the Table, which characterize the value of the normal to the substrate component of the electromagnetic force on the free surface related to the corresponding component of the gravity force $f_{gz} = -\rho g\cos\alpha$: $f_{em}^* = f_{emz}(h)/f_{gz}$. The dimensionless value p_0 characterizes the pressure of liquid lithium on the substrate related to the $\rho gh\cos\alpha$ value.

Table 1 gives evidences that in the situation realized in the experiment the normal to the substrate component of the electromagnetic force is directed opposite to the gravitational force that at B_0 = 1 T practically results in complete weight loss of the draining down molten lithium. All the above can significantly affect the very possibility of realization of a stable film flow.

5. Observation results on the Li film flow formation

In our experiments, the procedure described in [6] was applied. With the bellows device being switched on and supplying the liquid lithium with the flowrate Q = 90 mm^3/s, some liquid lithium was additionally supplied by the gas system for quicker filling of all delivering systems and the reservoir 5 as well as for liquid lithium supply onto the dry substrate. The appearance of lithium was registered by the video camera when numerous small drops of liquid lithium occurred practically over the entire width of the slot nozzle. This fact, to some extent, evidences of a sufficient enough effectiveness of the operation of the CSFD used in the experiment.

Due to the continuing supply of the liquid metal, these drops, enlarging in size, started to agglomerate that resulted in seven large drops distributed uniformly enough at the outlet nozzle. The gravitational forces made the drops to stream down the substrate, leaving behind glittery traces on the lithium-wetted surface. The further flow of lithium went on over these paths. Moreover, due to the action of surface tension [6], rather large agglomerations of liquid lithium were formed at the substrate bottom, in the zone where the surface bends. The lithium from the substrate drained in drops. In some moment of time, some of the above agglomerations combined with the neighbouring ones at the substrate bottom.

Then the video camera registered an unexpected phenomenon, i.e. the non-wetted surface between two paths was being covered with the liquid lithium and the process was going from the bottom upwards (opposite to the gravitational forces) and completed when the liquid lithium came up to the slot nozzle. It can be suggested that such an unusual behaviour of the molten metal in this case could be determined by the action of electromagnetic forces.

Upon completion of the process, it was decided to supply additionally an amount of liquid lithium through the gas system. This melt portion, draining, gradually covered the most of the substrate surface.

Unfortunately, the experiment was terminated at that stage because of the lithium vapours affecting the hole windows and making them opaque, which drastically distorted the image under observation.

Acknowledgements. The work was made in the framework of ERAF project No. 2010/0262/2DP/2.1.1.1.0/APLA/VIAA/176.

4. References

[1] Zakharov, L.E., Gorelenkov, N.N. et al.: Ignited spherical Tokamak and plasma regimes with Li walls. Fusion Eng. and Des. 72 (2004) 149.
[2] Zakharov, L.E.: http://w3.pppl.gov/zakharov. Professional website „Lithium: The Key to Fusion Power“.
[3] Zakharov, L.E.: Li wall fusion – the new concept of magnetic fision. J. Nuclear Science and Technology 2 (2011) 29.
[4] Sergeev, V.Yu., Kuteev, B.V. et al.: Concept of the divertor of a fusion neutron source based on a spherical Tokamak. Plasma Physics Reports 38 (2012) 7 521-539.
[5] Kuteev, B.V., Bykov, A.S. et al: Key Physics issues of a compact Tokamak fusion neutron source. FEC-23, Daejeon, Korea, Oct. 11-17, 2010, FTP/P6-10.
[6] Platacis, E., Flerov, A. et al.: Gravitational flow of a thin film of liquid metal in a strong magnetic field. Fussion Eng. and Des. (2014) (in press).

LM JET AND FILM FLOWS OVER SOLID SUBSTRATES IN STRONG MAGNETIC FIELDS

LIELAUSIS O., PLATACIS E., KLUKINS A., PEINBERGS J.
Institute of Physics of University of Latvia, 32 Miera, Salaspils, LV-2169 Latvia
E-mail: alex@sal.lv

Abstract: Free surface liquid metal (LM) flows in the presence of a magnetic field remain attractive because of a single reason. The workability of such flows is essential for several challenging power transforming and transferring projects. Power load capability should be considered as one of the main parameters determining the usefulness of any of such systems. In this relation a fast moving free surface LM flow stays beyond comparison. However, quite from the beginning of the development attending remain doubts about the spatial stability of such flows. In the presence of up to 4T magnetic fields different versions have been considered how to stabilize a free surface flow by means of solid substrates.

1. Introduction.

Free surface LM flows have been proposed to the role of a working medium in rather specific technologies including exotic future plans. So, in [1] a situation is considered when a LM jet used as a target for a 4MW proton beam at the production of pions. To capture the generated particles a magnetic field is foreseen; also the jet has to penetrate an up to 20T field. However, essentially better investigated are systems proposed for the protection of plasma facing components in fusion devices. Power load capability should be considered as one of the main parameters determining the usefulness of all such systems. A fast moving free surface liquid metal (LM) flow stays here beyond comparison. In this relation enlightening are the results gained on the small scale tokamak ISTTOK [2]. A LM limiter formed by a thin 2.5 mm Ga jet at a rather moderate ($v \approx 2.0$m/s) velocity was able to exhaust 2.4 kW in a 14.5 kW (ohmic) discharge. The corresponding volumetric power extraction capacity reached 2.4 kW/cm^3. The parameters of the discharge remained practically unchanged. However, the discharge caused a small displacement of the free flying flow; as the source floating potential inside the plasma has been assumed [3]. Whatever the reason of the deflection, essentially more stable would be a flow is backed by a solid substrate. We are accentuating here fast flows. It should be remembered that interesting can be also MHD flows at close to zero velocities .So, in [4] an attempt is made to create a creeping ($v \leq$ 1cm/s; thickness$\leq$ 1mm) Li flow over a plate in a strong 4T field. Aim of such a motion in a fusion application – controlling of the tritium dynamics. Because of the small thickness the liquid film will be prevented from overheating and evaporation – the generated heat can be extracted through properly cooled substrate.

2. Flows supported by curved substrates

Intriguing are the results of our recent experiments on jets passing over curved substrates [5].In our superconducting solenoid (up to 5T in a D=30cm; L=100cm.bore) three d=2.14mm InGaSn jets were targeted towards a cylindrical (R=95 mm) wall. The angle of incidence, fixed at 30^0, was rather blunt. The nozzles were made of 40mm long medical needles issuing from a cylindrical Plexiglas container (Fig.1). In the initial version the jets were targeted towards a non- prepared SS wall, it means, practically towards a non-wetted badly contacting substrate. The result was somewhat striking - in up to 4T fields the jets remained stable and well organized over the full length (~200 mm) of their path. The velocities reached 0.59 m/s (Fig.2a) In the next experiment the cylindrical SS wall was covered by a 4mm thick Cu insert, beforehand carefully treated. In this case the substrate should be considered as good wetted and electrically good contacting. As expected, without the field the jets tended to merge, to form a film-like flow. In this case we see a clear competition between the inertial and capillary forces. In the presence of a strong enough magnetic field the induced by the motion electromagnetic forces are dominating. The flow becomes unstable and fragmentary. The induced forces were able even to lift small volumes over the surface (Fig.2b).

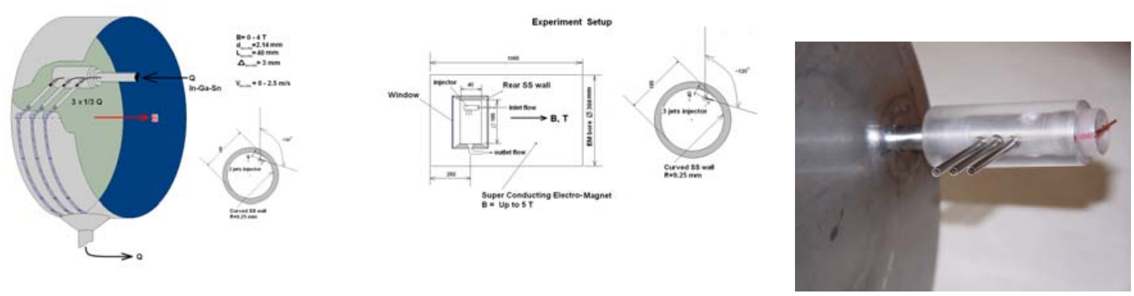

Figure 1: Scheme of the experiment with jets over curved substrates.

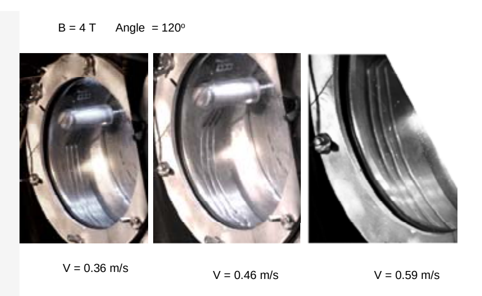

Figure 2a: Flow over non-wetted wall.

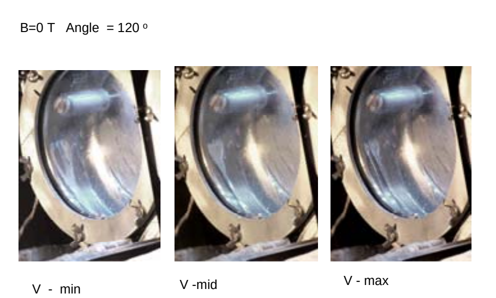

Figure 2b: Flow over a wetted wall.

3. Flows passing over flat plates

Let us start with a simple example. Fig.3 illustrates the situation when a single InGaSn jet is touching to a SS steel plate under small angle. The plate is glued on the surface of a permanent magnet which generates an orthogonal to the plate field with the intensity of order of 0.6 T. In addition to this, the plate is carefully vetted. In such a way a good electrical contact is ensured. Under such conditions the main actors are clearly defined - the inertial, the surface tension and the EM (Hartman) forces. It can be seen that after a definite distance the d=2.5 mm jet equally covers the full 3 cm width of the braking plate. It is a result which could be expected-a transfer of a jet flow into a film flow.

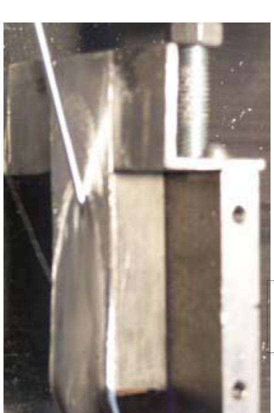

Figure 3: Spreading of a jet over a conducting plate.

In the main part of the experiments the principle scheme, compared with [4], remains unchanged (Fig.4).The magnet can be seen (a), the position of the working chamber inside the bore(b), also the chamber together with supplying lines(c). In Fig.5 an explanatory scheme is presented together with an experimental example. Worth mentioning, the typical to a fusion divertor field configuration was achieved. With regard to the axis of the magnet the container (together with the plate) was turned for 10 degrees. In such a way the typical to divertor topography of the field was approximately reproduced – 90% tangential, 10% orthogonal.

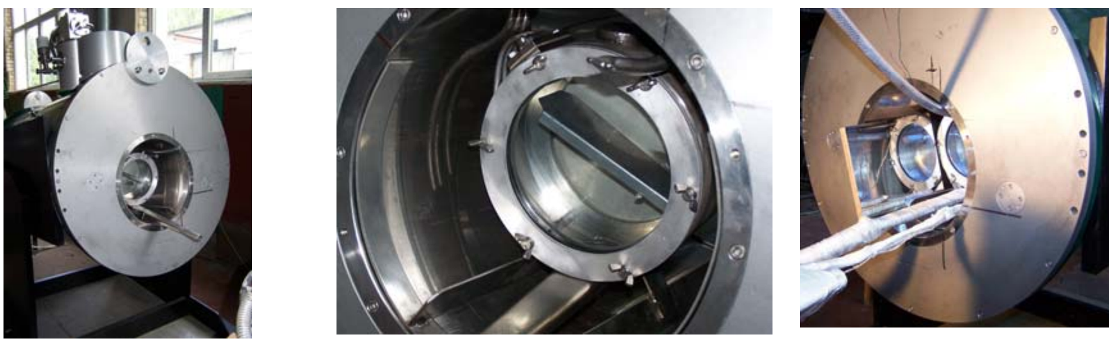

Figure 4: Arrangement of the experiments with flat substrates.

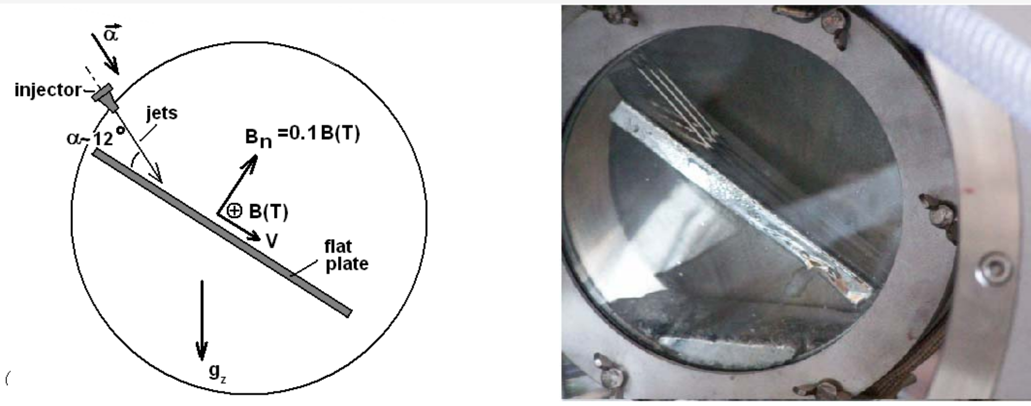

Figure 5: Geometry of the experiments and example of the flow at B = 1T; V = 2.1 m/s

Figure 6: Two running in parallel jets. B = 4T; V = 0.27 m/s.

During the experiments the magnetic field was increased up to 4T, the velocities varied in the range from 0.5 m/s to 2.5 m/s. There were some grounds to expect that the jets will be spread over surface of the plate. Here we can remind on the seemingly similar experiment presented in Fig.3. However, the jets clearly tended to a local compactness, instead of spreading (Fig.6). The conditions were changed -the SS surface could not be properly treated.

In Fig.7 an addition phenomenon can be seen. The jet is bent/deflected deeper into the magnet, even somewhat uphill, since the plate is inclined for approx. 10^0 with regard to the horizon. Attention should be paid to the boundary conditions typical to the described "strange" MHD process. First, the magnetic field was non-uniform.

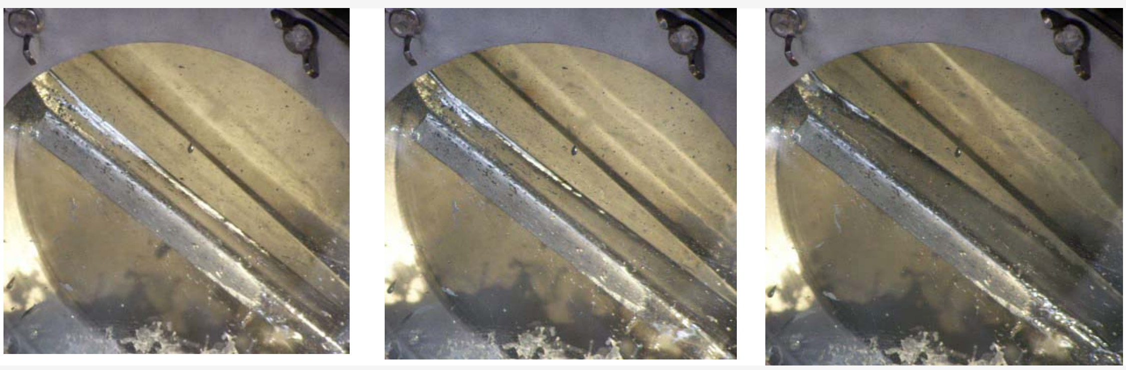

Figure 7: The behavior of a single jet at gradually decreasing velocities: B=4 T; velocity ():373;250;127 cm/s.(from left to right)

MHD experiments on free surface LM flows, it is not an easy task. How attractive and convincing the results will be, it depends on the quality of the photo and video records Objects of interest are the lustrous sharp reflecting liquid metal surfaces, deformed by the motion (characteristic length 10-15 cm, diameter or thickness 2-3 mm). They are located in a confined space inside the D=30 cm.bore of a superconducting solenoid, usually at a distance (~ 50 cm) from the edge of the solenoid. Liquid metal (InGaSn) communications covered by heaters and insulations are significantly overlapping the field of vision. The objects are placed inside a separate vacuum chamber with a window and internal lighting. Delicate handling is needed, particularly during metal injection into the chamber. Errors and carelessness in these moments lead to splashing of metallic droplets, jets; re- opening of the chamber connected with a de-pressurization, cleaning, etc. is inevitable. Another unpleasant moment, it is the presence of a strong magnetic field. This fact leads to the need to shoot objects from a considerable (≈1m) distance, at awkward angles, etc.

Conclusions.

The behavior of free surface liquid metal flows in the presence of a strong magnetic field is influenced not only by the well known boundary conditions (homogeneity of the field, wettability/contactability of the walls. Essential is also the role substrates curvature.

Acknowledgments.

The work was supported by EFDA in the framework of the EFDA Task: WP13-PEX03b-TO5 and ERAF Project No.2010/0262/2DP/2.1.1.1.0/10/APIA/VIAA

References

[1] McDonald, K.T.: Magnetohydrodynamics of a pulsed mercury jet entering a solenoid at an angle. A Targetry Scenario for Muon Collaider and a Neutrino Factory, Princeton/ December 1̃.
[2] R.B. Gomes, C. Silva, H. Fernandes, P. Duarte, O. Lielausis, A. Klyukin, E. Platacis. Dynamic behavior of a liquid gallium jet under the influence of the Tokamak ISTTOK plasmas; Proc. the 19 Intern. Conf. on Plasma Surface Interaction, P2-83, May 24-28 (2010) Sam Diego, USA.
[3] L.Benos, N. Pelekasis, R. Gomes: Interfacial stability of liquid metal flow in presence of an electromagnetic field, Proc the 3d International Symposium on Lithium applications for Fusion Devices, ISLA2013, October 9-11, 2013,C.R.ENEA Frascati.
[4] E. Platacis, A. Sobolevs, A. Shishko: Difficulties of creation of thin lithium film on the stainless steel substrate, Proc. the 3d International Symposium on Lithium applications for Fusion Devices, ISLA2013, October 9-11, 2013,C.R.ENEA Frascati.
[5] O.Lielausis, A.Klukins, E.Platacis.: MHD experiments on LM jets passing over curved substrates, Proc. the 3d International Symposium on Lithium applications for Fusion Devices, ISLA2013, October 9-11, 2013,C.R.ENEA Frascati.

LIQUID METAL IN NUCLEAR APPLICATIONS

PLATACIS E.
Institute of Physics, University of Latvia, Salaspils, Latvia
E-mail: erik@sal.lv

Abstract: For decades, the development of liquid metal technologies for nuclear applications is a main research topic in the research program of the Institute of Physics of the University of Latvia (IPUL).

1. Introduction

The recent 3–5 years can be characterized by a growing interest to liquid metals. Such interest is connected with the developing neutron spallation source facilities in some countries, ADS tasks, new generation of nuclear reactors, as well as with the building of an ITER facility in France.

The Institute of Physics, University of Latvia, is well known as a centre for Liquid Metal (LM) MHD research with a long year experience in different research fields, which have been involved in both theoretical and applied studies and experiments. Let us mention a few examples. The IPUL participated in the development of equipment for a setup, where the strong temperature dependence for corrosion in PbLi was discovered, including corrosion provoking conditions due to cavitation. The IPUL is involved also in the development of the LM target for the Neutron Spallation Source facilities, where one of the main problems is the protection of the container walls from pressure waves generated by the pulsing proton beam. Concerning the loop technique, a recently completed setup for PbBi should also be mentioned.

Effective international collaboration is crucial for the success here. In general, the IPUL cannot be directly involved in the design of the final full power installations. Its task is mainly the search for new approaches, along with physical preparations, prototyping, etc. In this regard, the IPUL activities are really diverse. The same could be said also about the on-going tasks. A hydraulic prototype of liquid metal PbBi version of the target for the European Spallation Source (ESS) is under investigation at the IPUL. The proposed by IPUL fast moving liquid gallium structures have been accepted as candidates for divertor protection in the potential fusion power plant, a next step project after ITER and DEMO. According to the Collaborative Project on European Sodium Fast Reactor (CP-ESFR), the IPUL must focus on high performance electromagnetic pumps and instrumentation for various electrically conducting liquids. As new and acute, the project SILER (Seismic-Initiated Events risk mitigation in Lead - cooled Reactors) should be emphasized. The IPUL is invited to analyze the situation with electromagnetic pump stability under the condition of seismic risk and to elaborate rules for optimal positioning of such pumps. The IPUL is interested to remain in the team developing later the EURISOL project. The aim is the design of a facility for the production of exotic radioactive ion beams. The IPUL must consider a version of the liquid metal proton/neutron converter, which is squeezed in a very limited space.

These and other questions related to LM will be presented in the report.

2. Fission related Liquid Metal researches

At the IPUL, the unique experience in different liquid metal technologies mainly associated with nuclear energy plants has been accumulated. The importance of this potential is confirmed by the fact that the IPUL participates in the coordinating SNEPT program (Sustainable Nuclear Energy Technology Platform) since the program very beginning. First, the problem of stability of powerful electromagnetic induction pumps for liquid metals has been chosen. At due time at the IPUL the warning has been stated that such pump can become unstable if its specific parameters are exceeded. The importance of these criteria has been proved practically.

This instability leads to the formation of counter flow, pressure losses and limited usage of EMP. The instability criterion has been theoretically derived in [1], the boundary between flow stability and instability has been determined experimentally. Experimental and numerical results are compared in [2]. Although qualitative agreement between theoretical predictions and experiment can be observed, a more detailed analytical study [3] and an experiment with controlled velocity/magnetic field perturbation implementation are necessary for a more profound understanding of the instability mechanisms in the EMP. Experimental investigations of this instability are planned with the newly installed 125 mm sodium loop.

The high productive pump has to be designed for the needs of the 4th generation nuclear reactor when all the assignments are achieved. Note that ready for use technical solutions preventing instability will be completely new for the design of reliable and efficient high productive pumps. The solutions described above will offer a long-term opportunity to develop liquid metal systems much faster and to satisfy the requirements for the 4th generation reactors with liquid metal systems and also their industrial applications.

3. Fusion related liquid metal researches

The concept of liquid metal use, especially liquid lithium, as the plasma-facing surface was raised many decades ago. Liquid metals have many advantages especially on the lifetime of the divertor components. Their surface is not subject to erosion, melting, craters and, in general, to surface damage. Also, the maintenance and the replacements of a liquid divertor is not so stringent as a solid material divertor. The liquid Li surface can also effectively lower the hydrogen isotopes' recycling and getter the impurities in fusion reactors. In addition, liquid Li surface has the ability to transfer heat out of the limiter/divertor region and continually provide a clean surface to plasma.

Suitable materials will be needed on DEMO to handle safely the high power loads in the divertor and beyond the limits of the current technology. In this framework, a possible solution has been found for the application of liquid metals as plasma facing materials (Li, Sn, Ga) realized in a capillary porous system (CPS) configuration in order to counteract the MHD forces on the liquid metal surface.

In contrast to CPS, a fast moving free surface flow is beyond comparison. To eliminate the intensity of the MHD interaction right from the beginning, preference was given to the fast moving jet or droplet screens. Promising are the results obtained on ISTTOK [4]. A limiter formed by a thin 2.5 mm Ga jet at velocities of 1.5-2.0 m/s was able to exhaust 2.4 kW in a 14.5 kW (Ohmic) discharge. The parameters of the discharge remained practically unchanged. With the IPUL superconducting solenoid (up to 5 T, D = 30 cm; L = 100 cm), three d = 2.14 mm InGaSn jets were targeted towards a cylindrical non-wetted SS wall. The result was somewhat striking: in up to 4 T fields the jets remained stable and well organized over the full length of their path.

The other aim of our works is focused on the understanding of the mechanism and features of the thin liquid metal film creation on the stainless steel matrix. For the successful use of lithium and other conductive liquid metals, it is necessary to investigate the influence of many technological factors on wetting and metal flow continuity. To conduct the experiments with pure surface of Li, a particular vacuum setup was designed and manufactured. A specially designed multi-channel distributor was installed into the setup. This enabled to drive a stable film flow of liquid metal on a steel SS 316L substrate at a temperature up to 450 °C.

The influence of a strong magnetic field on homogeneous distribution of the liquid metal along a stainless steel plate has been experimentally proved. Theoretical and practical research of the MHD effect, taking place inside the multi-channel distributor device, shows the applicability of this method to improve the distribution of liquid metal on the stainless gradient plate and could be considered as a theoretically promising divertor prototype.

It should be noted that the choice of construction materials for the blanket of the fusion reactor has not fully resolved. Still undecided is the problem of material corrosion in the liquid metal, under the radiation conditions and at relatively high temperatures. At present, the lead–lithium (Pb-17Li) eutectic is considered as the most suitable tritium breeder material. As an optimum version, EUROFER 97 steel is proposed, the corrosion rate of which in the liquid Pb-17Li eutectic is the least. However, these results have been obtained without taking into account the influence of a strong magnetic field. At the same time, this influence must be essential because of the variation of liquid metal flow hydrodynamics and because of the interaction of the magnetic field with ferromagnetic steel. Our task was to assess the magnetic field action on the corrosion process of EUROFER steel in the liquid PbLi at a temperature up to 550 °C. For the solution of this task, a special setup has been developed.

Some experiments carried out at the IPUL have shown that the magnetic field greatly affects the corrosion processes for austenitic and martensitic steels [5].

4. Neutron Spallation related liquid metal researches

Neutron scattering provides basic microscopic information on the structure and dynamics of materials, which add to our understanding of condensed matter in such fields as biology, material science, chemistry, earth science and physics. Europe is pre-eminent in this field, and the present proposal for the next generation neutron source, for the European Spallation Source will ensure the availability of highest quality neutron beams to a wide range of users from academic studies and industrial applications.

In the case of the European Spallation neutron Sources, the Lead Bismuth eutectic (LBE) target as a comparative solution has been chosen. Within the framework of the ESS Design Study, the liquid metal spallation target loaded with power of several megawatts is a critical component and needs a new advanced technology [6].

In order to develop a liquid metal (LM) target, it is necessary to test and investigate the thermo-hydrodynamics of LM flow, the hydraulic and structural behavior of the target for various inlet flow conditions (i.e. mass flow rates) and, in particular, for nominal operating flow rates and pressure in the system, as well as to determine the heat transfer conditions between the proton beam window and the coolant-liquid LBE.

The LBE neutron converter target, named METAL:LIC and developed by KIT and IPUL as a comparative solution for ESS, has been chosen for tests on LBE loop at the IPUL. The complete test campaign was carried out in two sessions:

- in the first session, all measuring and control systems, including the heating of the loop and target mock-up, were checked;
- in the second session, the distribution velocity and temperature of the liquid metal (PbBi) in the target module depend on the window temperature, and the liquid metal flow rate in the loop was investigated.

We consider the heat transfer in the Pb-Bi loop with an inductive heat source as a model for the proton beam caused heat deposition. The results of the first session experiments showed the following:

- The inductive heating can be successfully used for modelling of the integral heat deposition in the spallation target.

- By adjusting the frequency, it is possible to achieve different depth of heat deposition.

Nevertheless, reliable determination of the total power might require some additional measurements of the temperature upstream and downstream the heated zone.

In the ESS project with beam power up to 5 MW, a gas-cooled solid tungsten rotating target was used. The cooled rotating target concepts provide a larger proton beam facing window surface and thus the lower heat loads on the target window in comparison with the classical coaxial target window. An LM cooled rotating target is also under consideration at the IPUL. The LM cooled rotating target has several advantages if compared with the rotating gas cooled target. The advantages are the following: better heat transfer conditions, much smaller pressure and fluid flow velocity in the target, no necessity to synchronize the movement of the proton beam charges, as well as, smaller weight.

References

[1] Gailitis A.; Lielausis, O.: Instability of homogeneous velocity distribution in an induction-type MHD machine. Magnetohydrodynamics. (1975), No. 1, pp. 87 – 101.

[2] Araseki, H., Kirillov, I., Prelistsky, G., Ogorodnikov, A.:. Magnetohydrodynamic instability in annular linear induction pump. Part I. Experiment and numerical analysis. Nuclear Engineering and Design 227 (2004), pp. 29 – 50.

[3] Goldsteins, L., Gailitis, A., Buligins, L., Fautrelle, Y., Biscarrat, C.: Analytical investigation of MHD instability in annular linear electromagnetic induction pump. Proc. the 9th PAMIR International Conference June 16 – 20, 2014, Riga, Latvia, 5 p.

[4] Gomes, R.B., at all. Interaction of a liquid gallium jet with the tokamak ISTTOK edge plasma. Fusion Engineering and Design 83 (2008), 102-111.

[5] Platacis, E., at all: Corrosion phenomena of FMS steel in PbLi flow in magnetic field. Magnetohydrodynamics 48, 2 (2012).

[6] Buligins, L., Thomsen, K., Lielausis, O., Platacis, E. Poznyaks, A.: Integral geometry and coolant choices for high power neutron spallation target. Nucl. Instrum.. Methods Phys. Res. A, (Accepted, 2014).

FERROUS YOKE CONSTRUCTION INFLUENCE ON PERMANENT MAGNETS PUMP EFFICIENCY

BUCENIEKS I. KRAVALIS K., NIKOLUSKINS R.
Institute of Physics, University of Latvia, 32 Miera 32, LV-2169 Salaspils, Latvia
E-mail: imants@sal.lv

Abstract. The influence of outer passive ferrous yoke construction on the efficiency of the cylindrical electromagnetic induction permanent magnets pump has been investigated with a pump experimental model. The main goal for such studies is to simplify the ferrous yoke as its construction and as the possibility of its assembling/reassembling taking into account rather strong magnetic attraction forces between the ferrous yoke and the magnetic rotor of the pump, especially for more powerful pumps and, correspondingly, at its larger bigger dimensions and very strong integral magnetic attraction forces.

1. Introduction.

Electromagnetic induction permanent magnets pumps (PMP) during last 15 years have been successfully used in practice and seem rather perspective for future power plants, where liquid metals will be used as coolants [1, 2], as such pumps have simpler design and higher efficiency in comparison with traditional linear inductors pumps. There are different design concepts of PMP, but more perspective if compared with the disc-type PMP are the cylindrical PMPs ensuring a wider range of productivity both for developed output discharge pressure and, in particular, for provided much higher flow rates [3]. To increase the efficiency of the cylindrical PMP, at its construction usually an outer passive laminated ferrous yoke (which is optional) is used. A ferrous yoke essentially increases the magnetic field strength in the liquid metal layer in the pump channel and the pump efficiency [4] as EM forces induced in liquid metal are proportional to the magnetic field strength in the second power.

Four types of ferrous yoke design have been investigated. The first ferrous yoke was made from the stator of a used AC motor of laminated construction, ensuring minimum heat losses. The second design type of the ferrous yoke was made with cuts in the solid ferrous plate. The third ferrous yoke design, having the same geometry, was made just from a solid ferrous plate when heat losses in the ferrous yoke were maximum. The fourth ferrous yoke construction from compounded carbonyl iron powder (depending on the allowable maximum operating temperature of the bounding component) can be used for liquid metals with low operating temperatures (such as mercury and liquid metals eutectics having low melting temperatures). Experimental investigations were carried out in a range of frequencies up to 75 Hz of the induced alternating magnetic field in a liquid metal layer in the pump channel.

2. Experimental results.

Experiments were carried out in a liquid metal (In-Ga-Sn) circulation loop using a cylindrical PMP model (fig. 1). Four different ferrous removable yokes (fig. 2) after their sequent changing were installed in the pump model and the total active power consumed by the motor for pump driving was measured at different rotation speeds of the motor adjusted by using a frequency converter. The first ferrous yoke was made from the stator of a used AC motor. The second ferrous yoke was made (by bending) from a flat ferrous steel sheet, with 1 mm cuts previously made in it 3 mm distanced from each other. The third ferrous yoke was made of solid ferrous steel. The forth ferrous yoke was made from a carbonyl iron powder mixture with epoxy. The experimental results, demonstrating total heat losses in the pump (in the liquid metal layer, in the pump channel electrically conducting stainless steel walls and in the outer ferrous yoke) are illustrated in the graphs (fig. 3).

Figure 1: Experimental In-Ga-Sn loop with an EM induction cylindrical permanent magnets pump model.

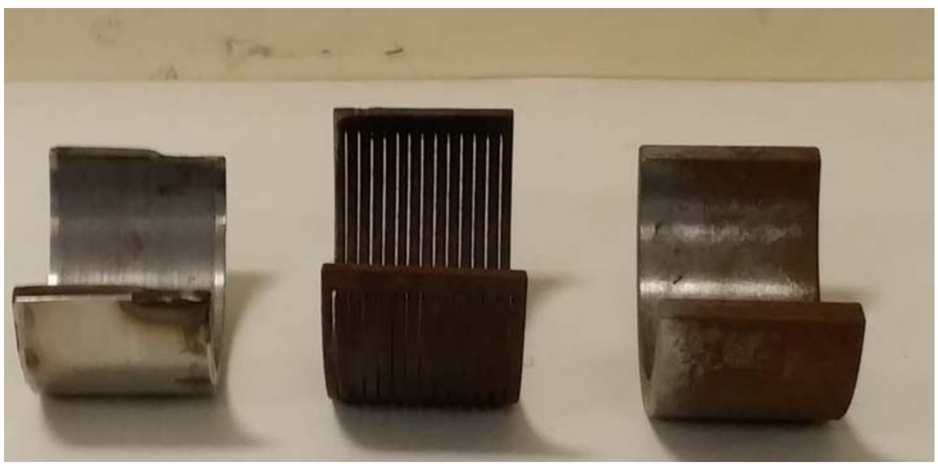

Figure 2: Different tested outer passive ferrous yokes: a) laminated; b) ferrous plate with cuts, and 3) solid ferrous yoke.

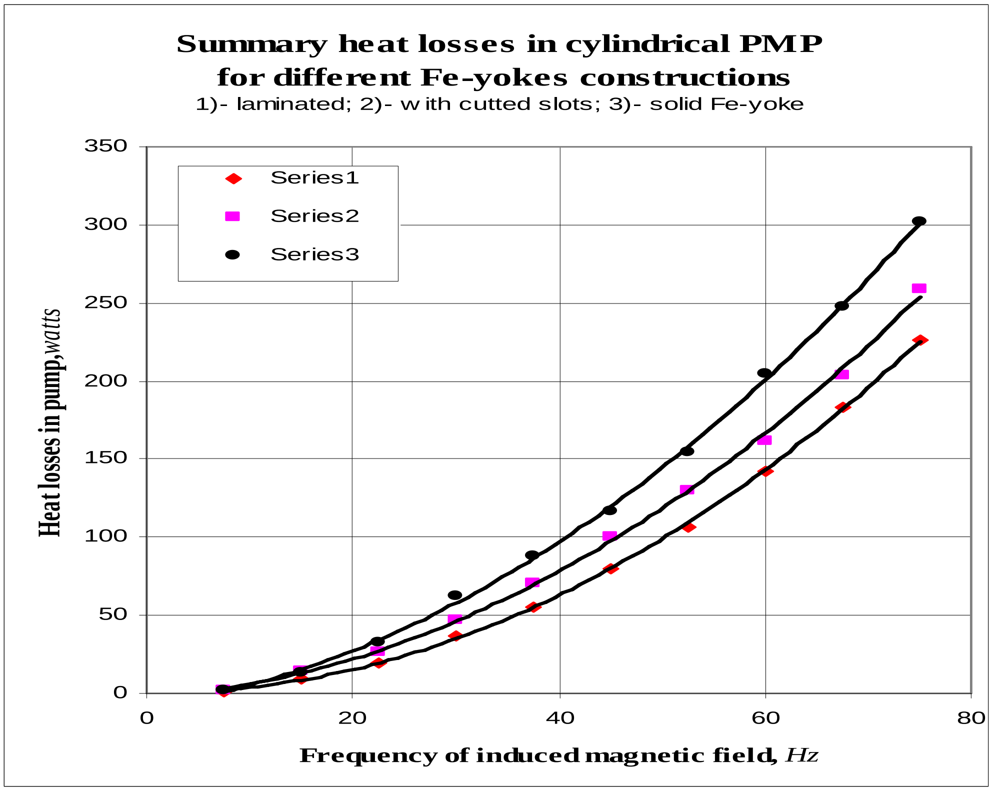

Figure 3: Comparison of heat losses in the pump model for different outer ferrous yoke designs.

As experimental results demonstrate, the difference in heat losses in the pump for different ferrous yoke constructions is not so dramatic. It is natural that with the solid ferrous yoke the pump efficiency is essentially lower, approximately by 25% at 75 Hz frequency in comparison with a pump with a laminated ferrous yoke (as used in standard electrical AC machines). In its turn, with the second ferrous yoke construction (with cuts in the ferrous plate), the pump efficiency is only by 12% lower. Experimental data extrapolation for higher frequencies of the induced alternating magnetic field in the pump (up to 150 Hz) demonstrate that the above-mentioned values of the pump efficiency drop by about 25% for the solid ferrous yoke and by about 12% for the ferrous yoke with cuts decrease, correspondingly, to 17% for the solid ferrous yoke and to 7% for the ferrous yoke with cuts.

3. Conclusion.

With the solid ferrous yoke design, the efficiency of the pump is essentially lower in comparison with a pump with a laminated ferrous yoke (as used in standard electrical AC machines). In its turn, with the second ferrous yoke construction (with cuts in the ferrous plate), the pump efficiency is higher in comparison with the solid ferrous yoke but a little lower in contrast to the accordingly laminated ferrous yoke. With the forth ferrous yoke construction (compounded carbonyl iron powder), the pump practically has the same pump efficiency (even a little higher) as a pump with a standard laminated ferrous yoke. So in many cases, at design and construction of more powerful pumps, the ferrous yoke may be produced from a solid ferrous material or from ferrous plates with cuts that essentially simplifies both the ferrous yoke production and its assembling/reassembling. In practice, for the EM pump installed in liquid metal circulations loop the efficiency of the pump may be so not crucial as, due to the higher heat losses in the pump, the power of the external loop heaters (for keeping a constant temperature in the loop) may be lower and, as a result, the lower pump efficiency practically has no influence on the efficiency of the whole integral liquid metal circulation loop.

4. References

[1] Bucenieks, I.: Perspectives of using rotating permanent magnets for electromagnetic induction pump design. Magnetohydrodynamics, vol. 36 (2000), no. 2, pp. 181-187.

[2] Bucenieks, I.: High pressure and high flow rate induction pumps with permanent magnets. Magnetohydrodynamics, vol. 39 (2003), no.4, pp. 411-417.

[3] Bucenieks, I.: Perspectives of increasing efficiency and productivity of electromagnetic induction pumps for mercury basing on permanent magnets, Proc. The 14th International Conference of Nuclear Engineering, Miami, Florida, USA, July 17-20, 2006, paper 14-89193.

[4] Bucenieks, I., Kravalis, K.: Efficiency of EM induction permanent magnets pumps, Magnetohydrodynamics, vol. 47 (2011), no.1, pp. 89-96.

A SIMPLIFIED MODEL OF CENTRIFUGAL ELECTROMAGNETIC INDUCTION PUMP WITH ROTATING PERMANENT MAGNETS

GOLDSTEINS[1] Linards, BUCENIEKS[2] Imants, BULIGINS[1] Leonids.

[1]UNIVERSITY OF LATVIA / Zellu 8, Riga, Latvia, LV-1002,
[2]INSTITUTE OF PHYSICS OF UNIVERSITY OF LATVIA / Miera 32, Salaspils, Latvia, LV-2169
E-mail address of corresponding author: Linards6@gmail.com

Abstract: In this work authors discuss main physical phenomena and present simplified axisymmetric analytical model of centrifugal electromagnetic induction pump (CEMIP). Obtained results are slightly modified for real geometry of CEMIP and compared with experimental data. In the end the comparison with linear electromagnetic induction pump (LEMIP) is performed. Possible advantages and optimization of CEMIP are discussed.

Introduction

Investigations of centrifugal electromagnetic pumps for liquid metal applications have been performed already in 1980ies [1]. Due to rather complicated construction and no significant superiority shown over traditional methods of liquid metal transport, such design has not gained wide appreciation and more common linear pumps are used.

The advantages electromagnetic induction pumps (EMIP) with rotating permanent magnets over inductor based ones have been demonstrated in [2]. Centrifugal EMIP or CEMIP with rotating permanent magnets was investigated analytically in regime of zero flowrate also providing experimental data in [3], but leaving some questions unanswered. The lack of analytical models, which could be used for integral characteristic estimation, does not allow correctly analyze CEMIP and compare with linear EMIP or LEMIP.

1. Presentation of the problem

We consider conducting cylinder (fig. 1), the height of cylinder b is relatively small compared to radius in cylindrical coordinate system. Rotating permanent magnet system creates a magnetic field in form of travelling wave moving over azimuth and interacts with conductive cylinder from radius R_1 to R_2. For simplicity, in this radial region external magnetic field is considered constant over height and has only z component:

$$B_e(\varphi,t) = Re\left[B_0 e^{iM(\omega_B t-\varphi)}\right] e_z \quad (1)$$

Such travelling field will induce EM forces and generate azimuthal motion of conductive media in direction of travelling field. By neglecting effects over height, it is convenient to use 2D polar coordinate system. Schematic of CEMIP is shown in fig. 2. One can divide the flow volume into two regions:

1. $R_i < \rho < R_1$ - inactive or radial transition region, where flow is determined by radial velocity component v_ρ and in case of non-zero flowrate azimuthal component v_φ is neglected.

2. $R_1 < \rho < R_2$ - active or magnetic field interaction and pressure development region, where flow is mainly determined by azimuthal velocity component v_φ, but radial component v_ρ also has significant impact because of inertial braking force, which appears due to radial (transverse) motion of fluid.

Developed pressure is determined by processes in active or magnetic field interaction region $R_1 < \rho < R_2$, therefore only this region is mainly considered in the simplified analytical model.

Several assumptions have been made to simplify the model. First of all, azimuthal and radial velocities have axi-symmetric forms to satisfy continuity:

$$v_\varphi(\rho) = \omega_\varphi \rho \quad (2); \quad v_\rho = \frac{Q}{2\pi\rho b} \quad (3)$$

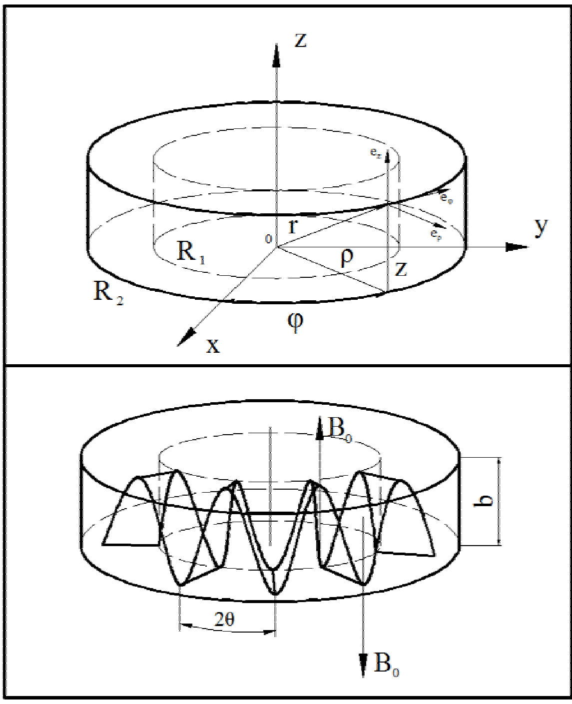

Fig. 1. Cylindrical coordinate system with conductive liquid and travelling magnetic field.

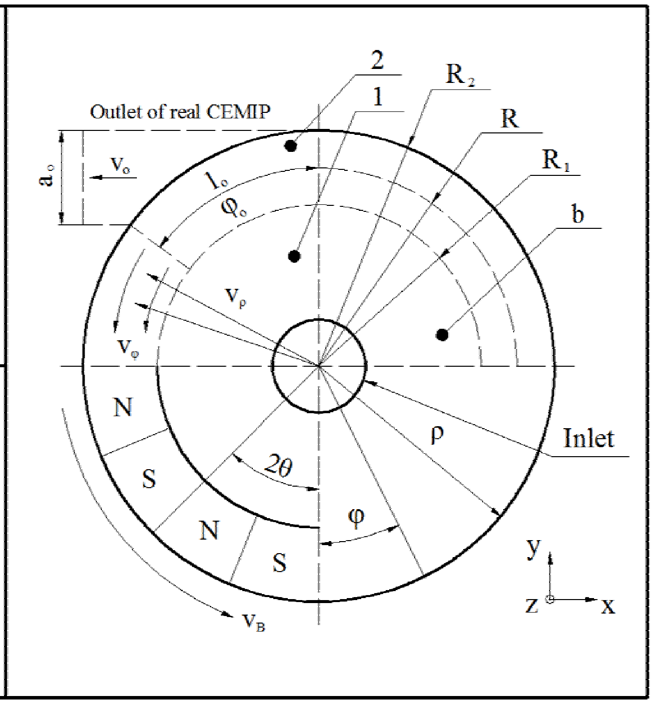

Fig. 2. Principal schematic of CEMIP. 1 – inactive region, 2 – active region.

Secondly, active parts mean radius is big enough to neglect curvature of cylindrical system and magnetic Reynolds number multiplied by slip is significantly less than unity:

$$R_2 - R_1 = \Delta R \ll R \quad (4); \quad Rm_s = \frac{\mu_0 \sigma (v_B - v_\varphi)\tau b}{\pi d_m} \ll 1 \quad (5)$$

In case of (5), the averaged EM force can be expressed in rather simple form (6). Frictional losses are taken into account by semi-empirical formulation [4] of friction factor λ.

$$f_{EM} = \frac{\sigma B_0^2 k_v}{2}(v_B - v_\varphi)e_\varphi - \frac{\sigma B_0^2}{2} v_\rho e_\rho \quad (6); \quad f_{Loss} = -\frac{\lambda}{D_h}\cdot\frac{\rho_m v_\varphi^2}{2} e_\varphi \quad (7)$$

As λ is function of velocity solution method requires initial guess and iterative approach. After inserting (6, 7) in Navier - Stokes equation we have 2 equation system of 2 unknown parameters v_φ and p:

$$\begin{cases} \rho_m\left(\frac{v_\rho^2}{\rho} + \frac{v_\varphi^2}{\rho}\right) - \frac{\sigma B_0^2}{2} v_\rho = \frac{\partial p}{\partial \rho} & (8) \\ \frac{\lambda}{D_h}\cdot\frac{\rho_m v_\varphi^2}{2} + 2\rho_m \frac{v_\varphi v_\rho}{\rho} - \frac{\sigma B_0^2 k_v}{2}(v_B - v_\varphi) = 0 & (9) \end{cases}$$

After radially averaging second term in (9) with (10) and introducing rations of forces K - inertial friction; N_λ - electromagnetic friction (11, 12):

Equation (9) is transformed to quadratic algebraic equation solution of which is:

$$v_\varphi = \frac{v_B}{2}(K + N_\lambda)\left[\sqrt{1 + \frac{4N_\lambda}{(K + N_\lambda)^2}} - 1\right] \quad (13)$$

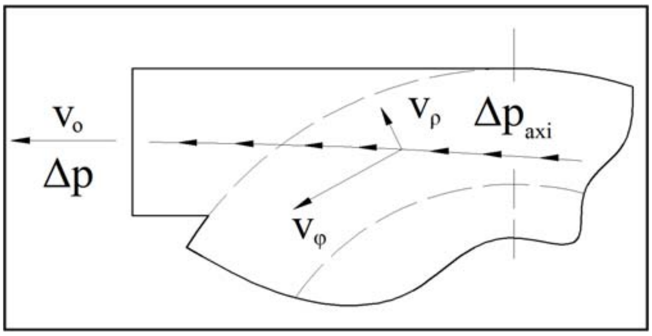

Fig. 3. Some mean streamline in the outlet.

Using (3, 13) in integration of (8) solution for axi-symmetric case is obtained. However, for real geometry (fig. 3) Bernoulli's law is used on some mean streamline by coefficients (14, 15) and using axi-symmetric solution. Finally, using (4) and introducing (16) developed pressure of CEMIP can be calculated (17) or in case of zero flowrate Q using (18).

$$k_\varphi = \left(\frac{1}{\varphi_o}\int_0^{\varphi_o}\cos(\varphi)\,d\varphi\right)^2 \quad (14); \quad k_\rho = \left(\frac{1}{\varphi_o}\int_0^{\varphi_o}\sin(\varphi)\,d\varphi\right)^2 \quad (15); \quad v_R = \frac{Q}{2\pi R b} \quad (16)$$

$$\Delta p = \rho_m \cdot \frac{\Delta R}{R}\cdot\left(v_\varphi^2 + v_R^2\right) - \frac{\sigma B_0^2 v_R R}{2}\cdot\ln\left(\frac{R_2}{R_1}\right) + \frac{\rho_m}{2}\cdot\left(k_\varphi v_\varphi^2 + k_\rho v_R^2 - v_o^2\right) + \delta p_t \quad (17)$$

$$\Delta p\Big|_{Q=0} = \frac{\rho_m v_\varphi^2}{2}\cdot\left[2\frac{\Delta R}{R} + k_\varphi\right] \quad (18);$$

2. Comparison with experimental results

Experimental loop (fig. 4) consisted of electromotor (1.) and rotor of magnetic system (2.). It was possible to change air gap (*d*) using bolt mechanism. Channel of pump with liquid metal (4) was placed into open vessel (3.) externally cooled by the water. In-Ga-Sn eutectic was used to be able operate in room temperature and without external heating. Valve (5.) and EM conduction flow meter (6.) were used to regulate and measure flowrate of CEMIP. Single differential gas-liquid manometer (7.) was used to estimate developed pressure difference between inlet and outlet. It was possible due to the fact that diameter of expansion tank (9.) was much larger than diameter of manometer and changes of base level were so minor that they could be neglected. Before filling the loop from supply tank (10.) it was for-vacuumed with mechanical vacuum pump (8.). Experimental loop parameters are collected in (table. 1).

Table. 1. Parameters and their values of experimental setup.

CEMIP dimensions				Other parameters		B field parameters	
Radius, m		Dimensions, m				d, mm	B_0,T
R_2	0.15	b	0.01	σ, S/m	3. 46 e6	5	0.27
R	0.125	a_o	0.06	ρ_m, kg/m^3	6.44 e3	10	0.18
R_1	0.1			μ, Pa/s	2.4 e-3	15	0.13
R_i	0.02			Poles	16	20	0.09

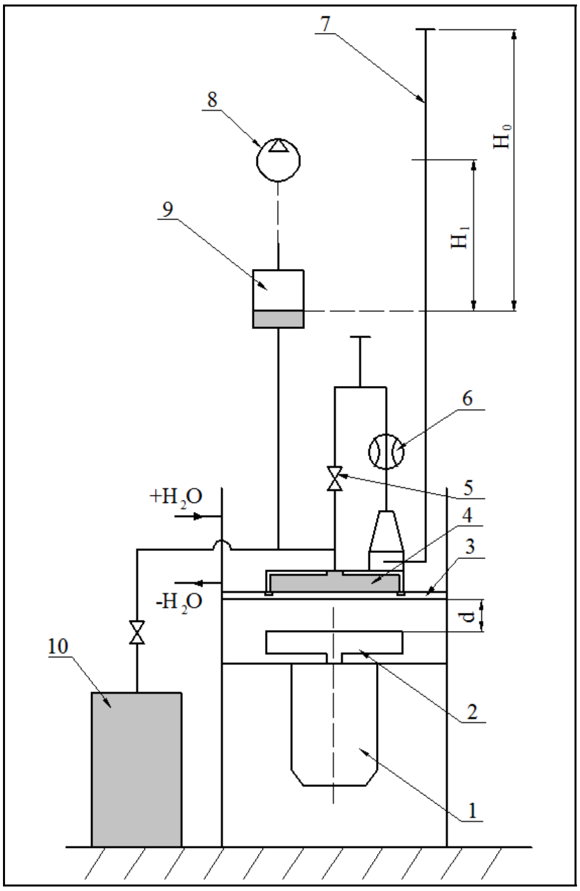

Fig. 4. Experimental loop of CEMIP.

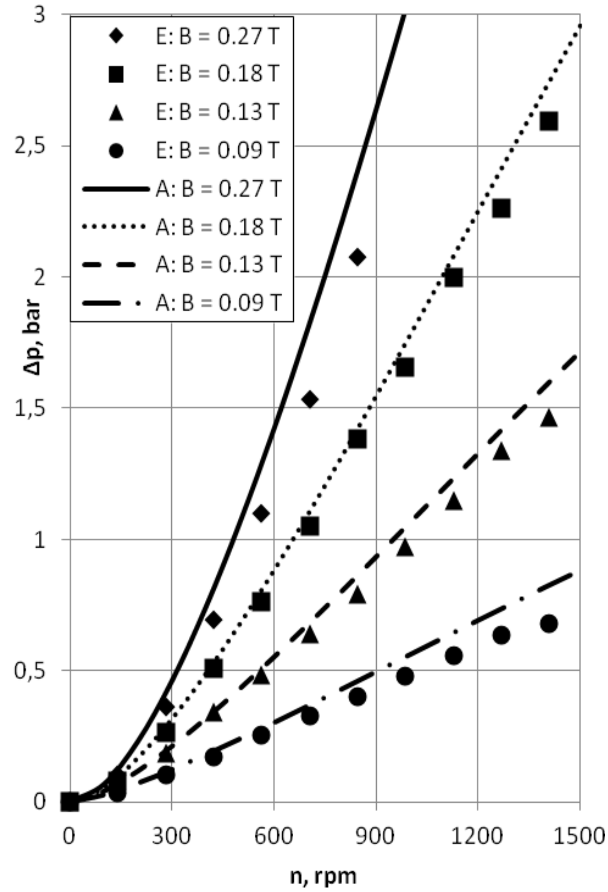

Fig. 5. Developed pressure as function of magnetic systems rotation speed. Q = 0 [l/s].

Comparison of maximum developed pressure with different amplitude of magnetic field B_0 is shown in (fig. 5), where E – experimental data and A – analytical solution (18). It can be observed, that in all cases analytical results correspond to experiment fairly well. In the case of high N_λ (high B_0 and low v_B), developed pressure increases as quadratic function of rotation, while for smaller values it increases almost linearly.

In (Fig. 6 -- 9.) E - experimental data and A – analytical solution (17) of $\Delta p - Q$ curves with fixed rotation speed n and magnetic field amplitude B_0 are compared. Theoretical model qualitatively corresponds to experimental data. However, better agreement is achieved with lower B_0 (N_λ) (fig. 8, 9). It could be explained by smaller influence of friction factor λ, which is estimated approximately, in calculation of v_φ and therefore developed pressure.

3. Conclusion

The simplified estimations (17, 18) derived in this work shows qualitative agreement with experimental data (fig. 5 – 9) and can be used for estimation of integral parameters of CEMIP. Due to principally different physical mechanism of pressure development from LEMIP, such device might have advantage in application where mixing of conductive media is required and low N_λ. Expanded and detailed version of this study can be found in [5].

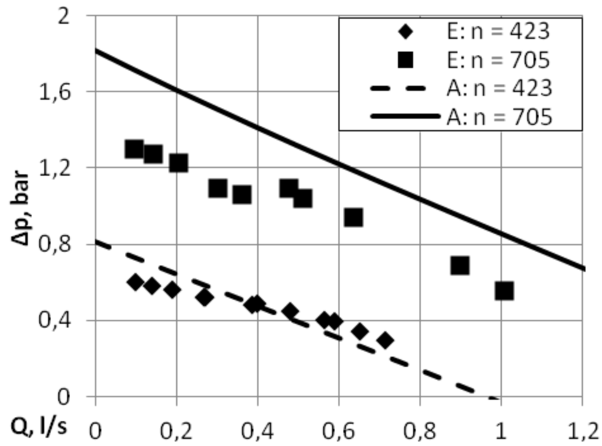

Fig. 6. $\Delta p - Q$ curves, $B_0 = 0.27$ [T].

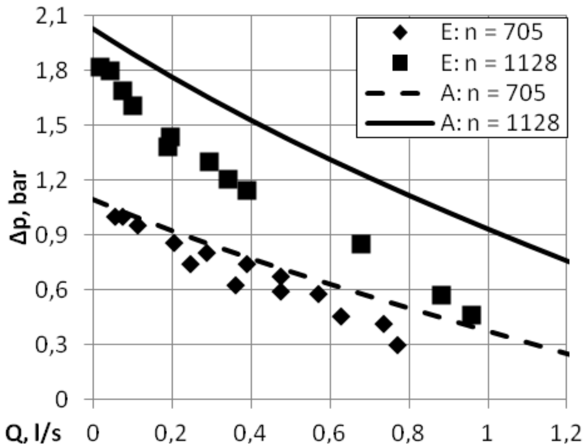

Fig. 7. $\Delta p - Q$ curves, $B_0 = 0.18$ [T].

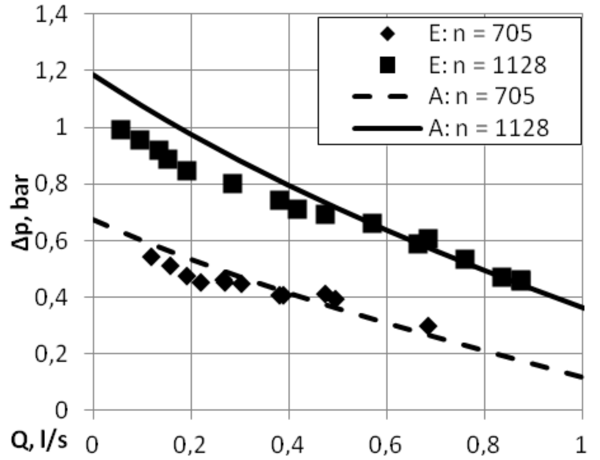

Fig. 8. $\Delta p - Q$ curves, $B_0 = 0.13$ [T].

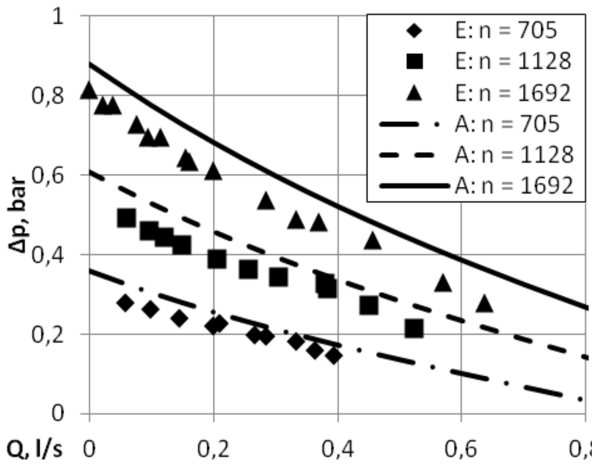

Fig. 9. $\Delta p - Q$ curves, $B_0 = 0.09$ [T].

4. References

[1] MUIZNIEKS A., PLATONOV V. et al.: Method of approximate calculation of the characteristics of a centrifugal conduction pump in a nonzero discharge regime. Magnetohydrodynamics, (1986), pp. 102 – 105.

[2] BUCENIEKS I.: Perspectives of using rotating permanent magnets for electromagnetic induction pump design. Magnetohydrodynamics, 36 (2000), pp. 181 – 188.

[3] BUCENIEKS I., SUKHOVICH E. et al.: Centrifugal pump basing on rotating permanent magnets. Magnetohydrodynamics, 36 (2000), pp. 189 – 196.

[4] IDELCHIK I.: Texbook of hydraulic resistances, *„Mashinostrojenie”,* Moscow (1975) (in Russian).

[5] GOLDSTEINS L., BUCENIEKS I. et al.: A simplified model of centrifugal electromagnetic induction pump (CEMIP) with rotating permanent magnets, 50(2), (2014), *Accepted for publication.*

ANALYTICAL INVESTIGATION OF MHD INSTABILITY IN ANNULAR LINEAR ELECTROMAGNETIC INDUCTION PUMP

GOLDSTEINS[1,2,3] Linards, GAILITIS[4] Agris, BULIGINS[1] Leonids, FAUTRELLE[2] Yves, BISCARRAT[3] Christine.

Affiliation: [1]UNIVERSITY OF LATVIA / Zellu 8, Riga, Latvia, LV-1002,
[2]SIMAP / Domaine Universitaire, BP 75 – 38402 Saint Martin d'Hères, France
[3]CEA CADARACHE / Saint Paul lez Durance, 13108, France
[4]INSTITUTE OF PHYSICS OF UNIVERSITY OF LATVIA / Miera 32, Salaspils, Latvia, LV-2169

E-mail address of corresponding author: Linards6@gmail.com

Abstract: In this work model of spatially and temporally developing azimuthal perturbations is analyzed in an infinitely long radially averaged geometry of an annular linear induction pump (ALIP). Using linear stability analysis, it is shown that in convective type instability process these perturbations can be significantly amplified before leaving the system. Perturbation development rates and its transient nature are analyzed to be used for estimations of unhomogeneity amplification in a system of finite length.

1. Introduction

It has been reported (theoretically, experimentally and numerically) [1, 2, 3] that high power induction pumps operating with liquid sodium exhibit instable operating modes, which are characterized by non-axisymmetric distribution of velocity and magnetic field, vibrations, low frequency pressure fluctuations and undesirable energy and pressure losses.

A theoretical base of this phenomenon is established by A. Gailitis and O. Lielausis [1] where a fundamental instability threshold of infinite induction machine is derived – magnetic Reynolds number > 1. Since then, there are only few authors like F. Werkhoff [4] who have tried to study similar or more sophisticated models, however significant improvements over the base theory has not been reported.

2. Presentation of the problem

Let us analyze case of ALIP identical to [1]. It is simplified from real ALIP by infinite geometry, neglecting influence of channel walls and using current sheet formulation only for main harmonic of the field (fig. 1.).

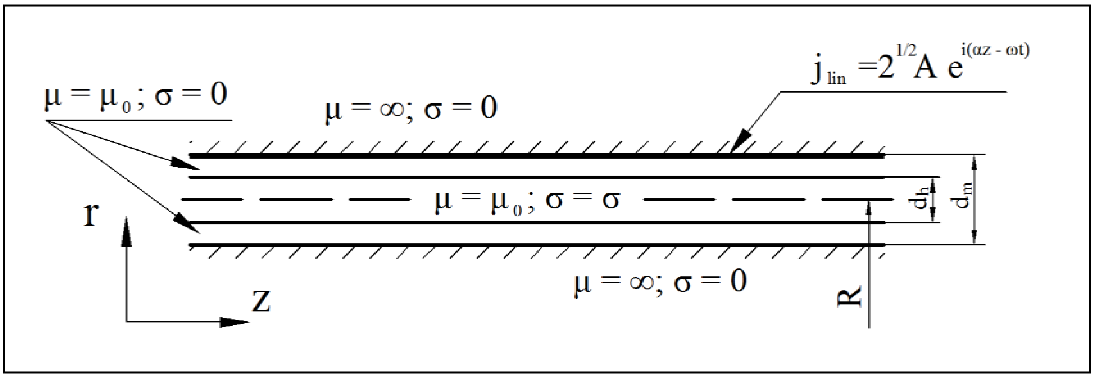

Fig. 1.A simplified model of infinite EMIP.

Moreover, consider that (where τ – pole pitch and l – length of system):

$$d_h < d_m \ll R, \tau \quad (1); \qquad \tau \ll l \quad (2)$$

From condition (1) it can be rather correctly assumed that linear current density j_{lin} is evenly spread over height of non-magnetic gap d_m, significant is only radial component of magnetic field and all other effects are averaged over radius. Condition (2) declares that longitude end effects are negligible – therefore geometry can be considered as infinitely long.

Consider only r component of magnetic field and z, φ velocity components in form:

$$B = B_0(\varphi, z, t)e^{i(\alpha z - \omega t)}e_r \quad (3); \qquad v = v_z(\varphi, z, t)e_z + v_\varphi(\varphi, z, t)e_\varphi \quad (4)$$

Then induction equation for r component of magnetic field is:

$$\Delta B - \mu_0 \sigma \left(\frac{d_h}{d_m}\right)\left[\frac{\partial B}{\partial t} + (\nabla v)B\right] = \frac{i\mu_0 \alpha \sqrt{2} A}{d_m} e^{i(\alpha z - \omega t)} \quad (5)$$

Choosing characteristic space and time scales as:

$$L = \frac{2\tau}{2\pi} = \frac{1}{\alpha} \quad (6); \qquad T = \frac{1}{2\pi f} = \frac{1}{\omega} \quad (7)$$

Defining magnetic Reynolds number ε and magnetic field dimensionless amplitude b:

$$\varepsilon = \frac{\mu_0 \sigma v_B}{\alpha}\left(\frac{d_h}{d_m}\right) \quad (8); \qquad b = \frac{B_0 d_m \alpha}{\sqrt{2}\mu_0 A} \quad (9)$$

Induction equation can be rewritten in dimensionless form:

$$\left[\frac{\partial^2}{\tilde{R}^2 \partial \varphi^2} - 1 + i\varepsilon(1 - \tilde{v}_z)\right]b + \left[\frac{\partial^2}{\partial \tilde{z}^2} + 2i\frac{\partial}{\partial \tilde{z}} - \varepsilon\left(\frac{\partial}{\partial \tilde{t}} + \frac{\tilde{v}_z \partial}{\partial \tilde{z}} + \frac{\tilde{v}_\varphi \partial}{\tilde{R}\partial \varphi}\right)\right]b = i \quad (10)$$

In order to analyze the balance of momentum in flow it is necessary to calculate distribution of electromagnetic force density:

$$f_{EM} = \left(\frac{d_m}{d_h}\right)\left[\frac{\nabla \times B}{\mu_0} - j\right] \times B \quad (11)$$

From which dimensionless form of quasi – stationary electromagnetic force:

$$\tilde{f}_{EM} = \sigma v_B \left(\frac{\mu_0 A}{d_m \alpha}\right)^2 \varepsilon^{-1}\left[Re(b)e_z - \tilde{\nabla}\left(\frac{bb^*}{2}\right)\right] \quad (12)$$

In order to simplify solution, it is more convenient to solve vorticity equation, therefore gradients become zeros and single equation for radial vorticity component is:

$$\beta\left(\frac{\partial}{\partial \tilde{t}} + \frac{\tilde{v}_z \partial}{\partial \tilde{z}} + \frac{\tilde{v}_\varphi \partial}{\tilde{R}\partial \varphi}\right)\tilde{\omega} = -(\tilde{\nabla} \times (\tilde{v}|\tilde{v}|))_r + j^2 \varepsilon^{-1} Re\left(\frac{\partial b}{\tilde{R}\partial \varphi}\right) \quad (13)$$

j^2 is modified interaction parameter (ratio of electromagnetic and friction forces) and β is modified Reynolds number (ratio of inertial and friction forces), $k_m{}'$ - geometric parameter:

$$j^2 = \frac{2\sigma d_h}{\lambda \rho v_B}\left(\frac{\mu_0 A}{d_m \alpha}\right)^2 \quad (14); \qquad \beta = \frac{2 d_h \alpha}{\lambda} \quad (15); \qquad \kappa_m' = 1 + \left(\frac{1}{\alpha R}\right)^2 \quad (16)$$

(10), (13) and continuity equation (16) closes the system of described problem:

$$\frac{1}{R}\frac{\partial V_\varphi}{\partial \varphi} = -\frac{\partial V_z}{\partial z} \quad (16)$$

We look for solution with perturbations that have spatial and temporal dependency:

$$V_z = q + \delta V_z\left[e^{(nz-\gamma t)}\cos(m\varphi)\right] \quad (17); \qquad b = b_c + \delta b_m\left[e^{(nz-\gamma t)}\cos(m\varphi)\right] \quad (18)$$

n and γ are spatial and temporal development rates of perturbation:

$$n = \frac{k}{\alpha} \quad (19); \qquad \gamma = \frac{\Omega}{\omega} \quad (20)$$

q and b_c are unperturbed solutions of system as described in [1].

Considering only real n and γ, after linearization system becomes:

$$\varepsilon_q = \varepsilon(1-q) \quad (23); \qquad \varepsilon_\gamma = \varepsilon(\gamma - q) \quad (24)$$

The determinant of system (21, 22) considering only linear (with respect to n, γ) terms:

$$2|q| - \frac{\beta}{\varepsilon}\varepsilon_\gamma = \frac{f^2}{(1+\varepsilon_q^2)} \cdot \frac{\varepsilon_\gamma - \kappa_m' + \varepsilon_q^2 + 2n\varepsilon_q}{\kappa_m'^2 - 2\kappa_m'\varepsilon_\gamma + \varepsilon_q^2 + 4n\varepsilon_q} \quad (25)$$

By expanding last term of (25) in Taylor series we transform identity that n and γ can be easily expressed:

$$A = \left[2|q|\left(\frac{4\varepsilon_q + 2\varepsilon q\kappa_m'}{\kappa_m'^2 + \varepsilon_q^2} - \frac{2\varepsilon_q - \varepsilon q}{\varepsilon_q^2 - \kappa_m'}\right) + \beta q\right]\frac{(\kappa_m'^2 + \varepsilon_q^2)(1-q)}{\varepsilon_q^2 - \kappa_m'} \quad (27)$$

$$B = \left[2|q|\left(\frac{2\varepsilon\kappa_m'}{\kappa_m'^2 + \varepsilon_q^2} + \frac{\varepsilon}{\varepsilon_q^2 - \kappa_m'}\right) + \beta\right]\frac{(\kappa_m'^2 + \varepsilon_q^2)(1-q)}{\varepsilon_q^2 - \kappa_m'} \quad (28)$$

Now using equation for dimensionless developed pressure (29) [1]:

$$p = \frac{f^2(1-q)}{(1+\varepsilon_q^2)} - q|q| \quad (29)$$

And inserting (26) into (29) we have:

$$p = An - B\gamma + \frac{2|q|(\kappa_m'^2 + \varepsilon_q^2)(1-q)}{\varepsilon_q^2 - \kappa_m'} - q|q| \quad (30)$$

Last two terms of (30) are solution for stability threshold derived in [1] (31). Development rates n and γ are function of pressure difference from stability threshold (32):

$$p_0 = \frac{2|q|\left(\kappa_m'^2 + \varepsilon_q^2\right)(1-q)}{\varepsilon_q^2 - \kappa_m'} - q|q| \quad (31); \quad \Delta p = p - p_0 = An - B\gamma \quad (32)$$

By expressing γ from (32) and inserting it into exponent of perturbation development:

$$\delta v(z,t) = \delta v \cdot e^{\frac{\Delta p}{B}t} \cdot e^{n(z - v_g t)} \quad (33); \quad v_g = \frac{A}{B} = q + \Delta_g \quad (34)$$

$$\Delta_g = \frac{4|q|\varepsilon_q\left(\varepsilon_q^2 - 2\kappa_m' - \kappa_m'^2\right)}{\left(4|q|\varepsilon\kappa_m' + \beta\left(\kappa_m'^2 + \varepsilon_q^2\right)\right)\left(\varepsilon_q^2 - \kappa_m'\right) + 2|q|\varepsilon\left(\kappa_m'^2 + \varepsilon_q^2\right)} \quad (35)$$

Group velocity of perturbation (34) is not exactly equal to mean velocity of flow, but has correction (35). For $\beta >> 1$, $k_m' \approx 1$, $q > 0$ (case of real ALIP) Δ_g will be positive in stable regime ($0 < \varepsilon_q < 1$), near ($\varepsilon_q \approx 1$) it will have singularity and negative sign ($1 < \varepsilon_q < 3^{0.5}$), after ($\varepsilon_q = 3^{0.5}$) Δ_g is nonnegative. As singular behavior is not common in nature, pump can experience uncontrolled transient from stable to unstable regime, which is experimentally observed in [3]. Moreover, (33) is solution of first order partial differential (transport) equations' initial value problem (IVP) similar as discussed in [5]. Perturbation in the initial moment (t = 0) can be expressed in Fourier's series (36), then solution of this IVP is (37):

$$\delta v(z,0) = \sum_{h=-\infty}^{\infty} a_h e^{ihz} \quad (36); \quad \delta v(z,t) = e^{\frac{\Delta p}{B}t} \cdot \sum_{h=-\infty}^{\infty} a_h e^{ih(z - v_g t)} \quad (37)$$

Expression (37) captures the nature of perturbation development in a convective instability process. In (37) second term describes movement of perturbation with (34) while sustaining its shape, however, first term states that it will exponentially develop in time. Such behavior described above is illustrated in (fig. 2). Consider idealized pump with length L, and some randomly shaped perturbation in initial time moment t_0 in the inlet. If pump is stable, perturbation will move towards outlet while dying – out (t_4) and after leaving the system. Similarly, if pump is unstable (fig. 3) perturbation will also move towards outlet, but being amplified. Reaching some maximum in the outlet (t_4) it eventually leaves the system.

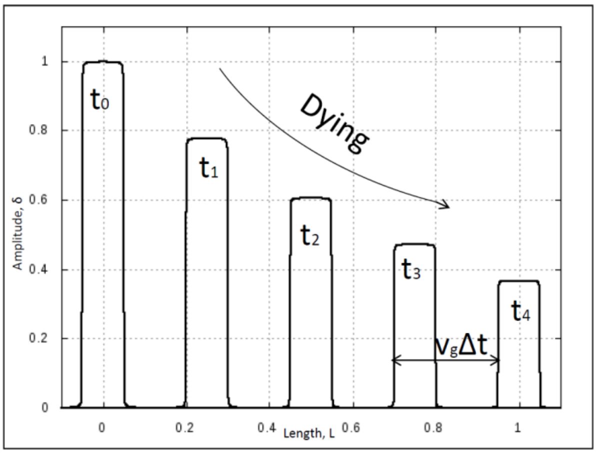

Fig. 2. Principal schematic of perturbation development in stable regime.

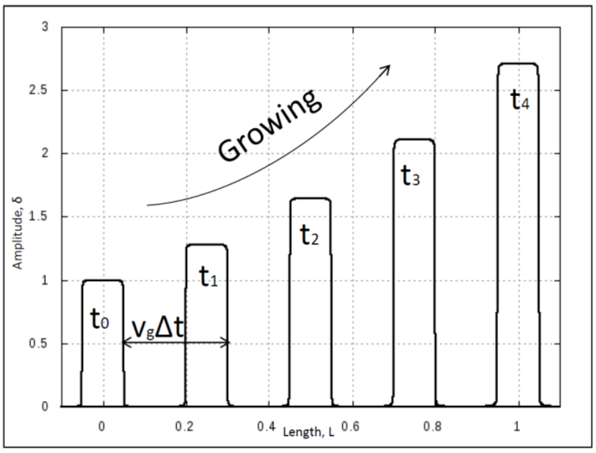

Fig. 3. Principal schematic of perturbation development in unstable regime.

Now consider (fig. 4) that pump is unstable and some perturbation always exist in the inlet (point B). In a static case ($\gamma = 0$), it will be amplified up to point E (Bold line B – E) by a exponential factor (38).

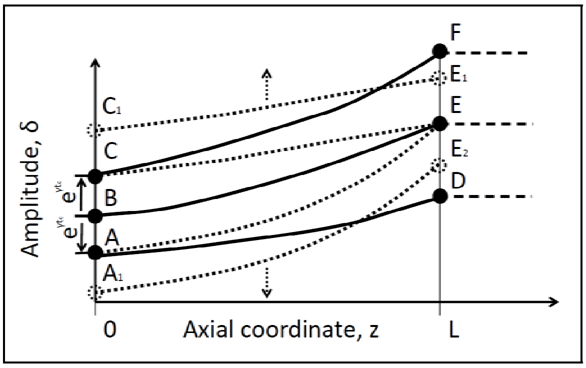

Fig. 4. Principal schematic of perturbation development in unstable regime.

Suppose that for some particular reason perturbation in the inlet starts to increase from B with $\gamma < 0$ for characteristic time interval - same as necessary for perturbation to travel from 0 to L - and stops at point C. Apparently, it results in lower spatial development rate n and it is described by dotted line C-E and (39).

$$n_{\gamma=0} = \frac{\Delta p}{A} \quad (38); \quad n_{\gamma\neq 0} = \frac{\Delta p + B\gamma}{A} \quad (39)$$

However, as $\gamma = 0$ again, after characteristic time interval it is described by bold line C – F and spatial development rate is (38). If it hadn't been stopped spatial development would remain as in (39), but amplitude would continue to increase in time, dotted line C_1 – E_1, and so forth. Similarly, if perturbation in inlet decreases from B with $\gamma > 0$ for and stops at point A, after characteristic time interval it can be described by dotted line A – E corresponding to (39) and afterwards with bold line A – D (38). Also if it hadn't been stopped amplitude would continue to decrease increase in time, dotted line A_1 – E_2, and so forth.

3. Conclusion

Preformed linear stability investigation reveals nature of convection type instability in ALIP. It is shown that some random perturbation will travel with group velocity (34) while sustaining its shape and develop (fig. 2 and 3) until it leaves the system. Development rates of perturbation can be calculated using (26 – 28).

If some mechanism exists that generates small static perturbation in the inlet of ALIP (e.g. geometrical imprecision) its amplification can lead to inhomogeneous flow in the outlet. Moreover, if transient behavior exists in the inlet (e.g. turbulent flow) perturbation will have different rates of amplification (fig. 4) which might lead to significant fluctuations of developed pressure.

4. References

[1] GAILITIS A.; LIELAUSIS O.:Instability of homogeneous velocity distribution in an induction-type MHD machine. Magnetohydrodynamics. (1975), No. 1, pp. 87 – 101.

[2] ARASEKI H.; KIRILLOV I. et al.: Magnetohydrodynamic instability in annular linear induction pump.Part I. Experiment and numerical analysis. Nuclear Engineering and Design. 227 (2004) pp. 29 – 50.

[3] OTA H.; KATSUKI K. et al.: Development of 160 m^3/min Large Capacity Sodium-Immersed Self-Colled Electromagnetic Pump. Journal of NUCLEAR SCIENCE and TECHNOLOGY. 41 (2004), pp. 511–523.

[4] WERKHOFF F.: Finite - length effects and stability of electromagnetic pumps. Experimental thermal and fluid science (1991), No. 4, pp. 166 – 170.

[5] EVANS L. C.: Partial Differential Equations, *„American Mathematical Society"*, (1998), pp. 18–20.

THE ASTRID PROJECT AND RELATED R&D ON NA TECHNOLOGY

LATGE C., LE COZ P., GASTALDI O., GAUCHE F., DEVICTOR N.
CEA Cadarache 13108 Saint Paul lez Durance, France
E-mail: christian.latge@cea.fr

Abstract: The pre-conceptual design of the ASTRID project has been launched in 2010 by CEA. The objectives of this first phase are to consider innovative options to improve the safety level with progress made in SFR-specific fields. A few examples of these innovations are: a core with an overall negative sodium void effect, specific features to prevent and mitigate severe accidents, power conversion system decreasing drastically the sodium-water reaction risk, improvements in In-Service Inspection and Repair, etc. ASTRID will also be designed to pursue the R&D on sodium fast reactors and demonstrate the feasibility of transmutation of minor actinides. The paper describes the current status of the project, the mains results obtained during the pre-conceptual design and address also the main R&D needs and results, focused on sodium technology. Main R&D tracks and dedicated technological platforms have been identified, particularly thanks to the European project ADRIANA, and some more recent up-date, and are described in this paper.

1. Introduction

The future of mankind is confronted with increasing energy demands, the gradual exhaustion of fossil fuels, and the pressure to reduce greenhouse gas emissions. This is why more and more countries are considering nuclear energy as a viable element of their energy mix. But, a policy to preserve uranium resources must therefore be developed to sustain this development. This is why a “fourth generation” approach has been initiated at the beginning of this century, focussed on fast reactors which are able converting a large amount of uranium-238 into plutonium-239 while producing electricity. In this way, it will become possible to exploit more than 90% of natural uranium to generate electricity, rather than only 0.5 to 1% in light water reactors. The large quantities of depleted and reprocessed uranium available in France could be used to maintain the current electricity production for several thousand years. The worldwide availability of primary fissile resources could thus be multiplied by more than 50. The construction of fast reactors will also open the door to unlimited plutonium recycling (multi-recycling) by taking advantage of its energy potential, and to minor actinides(americium, neptunium, curium, etc.). transmutation.

The Generation IV Technology Roadmap has identified six systems for their potential to meet the new technology goals to improve Safety, Sustainability, Economic competitiveness and Proliferation resistance. Within the frame of Generation IV International Forum (GIF), four main objectives have been defined to characterize the future reactor systems that must be sustainable, cost-effective, safe and reliable, proliferation resistant and protected against any external hazards.

In Europe, the Strategic Research Agenda (SRA) of the Sustainable Nuclear Energy Technology Platform (SNETP) has selected these three Fast Neutron Reactor systems as a key structure in the deployment of sustainable nuclear fission energy, mostly characterized by their primary coolant: sodium, pure lead and helium.

Among the Fast Neutron Reactor Systems, the SFR has the most comprehensive technological basis as result of the experience gained from worldwide operation of several experimental, prototype, and commercial size reactors since the 1940s. This experience corresponds to about 410 years of operation by end of 2012. Moreover, this concept is associated with the potential to meet the GEN IV criteria. This concept is currently considered as the Reference within the European Strategy. Six reactors are in operation: BOR60 and BN600 in Russia, Joyo and Monju in Japan, FBTR in India and CEFR in China. Two reactors are being built: PFBR (500MWe) in India and BN800 (800MWe) in Russia and several projects are currently developed: FBR1&2 in India, BN1200 in Russia, JSFR in Japan, PGSFR in Korea, CDFR in China…In France, ASTRID, Advanced Sodium Technological Reactor for Industrial Demonstration is currently designed, with the contribution of CEA and several partners. It is an industrial prototype and an irradiation tool [1].

2. Specifications for ASTRID

To meet the above-mentioned objectives, Generation IV sodium fast reactor (SFR) concepts must be significantly improved, particularly in the following fields:

– Further reducing the probability of a core meltdown accident through improved preventive measures,
– Integrating the impact of a mechanical energy release accident as early as the design phase if the demonstration of its 'practical elimination' is not sufficiently robust,
– Taking into account feedback from the Fukushima accident,
– Improving the capacity to inspect structures in sodium, with efforts especially focusing on structures ensuring a safety function.
– Reducing the risks associated with the affinity between sodium and oxygen: sodium fires and sodium/water reactions.
– Achieving a better availability factor than previous reactors, while aiming for the performance levels required by current commercial reactor operators.
– Ensuring the transmutation of minor actinides if this radioactive waste management option is chosen by the French government.
– Being competitive in relation to other energy sources with equivalent performance levels.

As an integrated technology demonstrator, ASTRID has the main objective of demonstrating advances on an industrial scale by qualifying innovative options in the above-mentioned fields. It must be possible to extrapolate its characteristics to future industrial high-power SFRs, particularly in terms of safety and operability [2].

ASTRID will nevertheless differ from future commercial reactors for the following reasons:

– ASTRID will be a 1500 MWth reactor, i.e. generating about 600 MWe, which is required to guarantee the representativeness of the reactor core and main components. This level will also compensate for the operational costs by generating a significant amount of electricity. A sensitivity study will be conducted on this power level.
– It will be equipped for experiments. Its design must therefore be flexible enough to be able to eventually test innovative options that were not chosen for the initial design. Novel instrumentation technologies or new fuels will be tested in ASTRID.
– It will be commissioned at approximately the same time as Generation III power plants, which means that its level of safety must be at least equivalent to these reactors, while taking into account lthe lessons from the Fukushima accident. Focus will nevertheless be placed on validating safety measures enabling the future reactors to ensure an even more robust safety level. This means taking into account core meltdown accident conditions from the design phase [1].
– ASTRID's availability objective is below that of a commercial power plant due to its experimental capacity. However, the options chosen must demonstrate that a higher level of availability can be reached when extrapolated.
– Without being a material testing reactor (MTR), ASTRID will be available for irradiation experiments like those conducted in PHENIX in the past. These experiments will help to improve the performance of the core and absorbers, as well as to test new fuels and structural materials, such as carbide fuel and oxide dispersion steel (ODS) cladding. ASTRID will be equipped with a hot cell for examining irradiation objects, built either in the plant or nearby.
– ASTRID will be able to transmute radioactive waste so as to go on with the demonstration of this technique at larger scales for reducing the volume and lifespan of final radwaste.

- Though future fast reactor plants intend to be breeders, ASTRID will be a self-breeder considering the current nuclear material situation, while being able to demonstrate its breeding potential.
- ASTRID must also integrate feedback from past reactors, especially PHENIX and SUPERPHENIX, while being clearly improved and belonging to Generation IV. It must take into account current safety requirements, especially in terms of protection against both internal and external acts of malevolence, as well as the protection of nuclear materials, while meeting the latest requirements in terms of proliferation resistance, and controlling its costs by following a value analysis approach from design.

3. Project organisation

- The CEA has been appointed by the French Government to manage the ASTRID Project. This involves:
  - Operational management by a project team which is also responsible for the industrial architecture, i.e. it defines the different engineering work packages.
  - Managing most of the R&D work and qualification of the options that will be chosen for ASTRID.
  - Assessment of studies carried out by its industrial partners in charge of technical work packages, or external engineering companies.
  - Direct responsibility of the core work package.
- The CEA has set up partnerships with French and foreign industry players who are providing both technical and financial support. These partnerships are based on bilateral contracts between the CEA and the relevant industrialist. To date, agreements have been signed with: EDF, AREVA NP, ALSTOM, COMEX Nucléaire, BOUYGUES, TOSHIBA, JACOBS Nucléaire, ROLLS ROYCE, ASTRIUM.

About 550 people are currently working on the ASTRID project, half of them are provided by the industrial partners. The project remains open to other partnerships, whether French or foreign.

Suck partnerships enable the CEA to concentrate on the ASTRID pre-conceptual design by implicating key industrial players whose experience and skills in their respective fields will guarantee the project's success. The association of different industrial partners offers a number of advantages: it fosters innovation, ensures that the industrial issues are covered (operability, manufacturability, etc.) as early as the design phase, while providing a source of funding for the pre-conceptual design phases 1 and 2 since the partners have partially financed the project [2].

As the project owner, the CEA ensures the strategic and operational management of the project. It is also responsible for drafting the safety reports and maintaining dialogue with the French Nuclear Safety Authority (ASN).

The ASTRID project aims at integrating a number of innovative options to meet the objectives of the Generation IV reactors while fulfilling its specifications. It is therefore relying on an important R&D programme at the CEA – SFR R&D. This was launched in 2006 as part of the three-party framework agreement with EDF and AREVA, to provide in due time the data required to qualify the ASTRID options.

Since 2007, the CEA has also been setting up a series of international partnerships to consolidate and develop its R&D efforts. These partnerships make it possible to share the development costs and the use of heavy experimental infrastructures.

4. Current status and general schedule

The R&D actions performed within the scope of the three-party CEA-EDF-AREVA framework between 2007 and 2009 made it possible to establish the preliminary project orientations and to finalize a number of structuring concepts, e.g. the pool-type primary system and the UO_2-PuO_2 fuel. These actions provided the foundation for the project orientations file issued in September 2010, which lists the finalized structuring options and the remaining open options. By leaving some options open, this gives the project enough time to study a number of innovative solutions that could be integrated into the design with the aim at clearly positioning ASTRID as a Gen IV reactor.

The pre-conceptual design phase was launched in October 2010 and involved 3 phases:

- A preparatory phase which served to structure the project, formalize the project requirements, and define the main milestones and lead-times. It ended with an official review which launched the following phase in March 2011.
- The pre-conceptual design (dubbed AVP1 in French) aims at analyzing the open options – particularly the most innovative – so as to choose the reference design by the end of 2012, at last at the beginning of 2013.
- The conceptual design (dubbed in AVP2 in French) started in January 2013 and aims at consolidating the project data to obtain a final and consistent conceptual design by late 2015. It will include a cost estimate and a more detailed schedule, facilitating the decision-making process for the next phases of the project.
- The basic design phase is planned from 2016 to 2018.

Several options were investigated in parallel during the pre-conceptual design ([2], [3]). This involved examining a number of innovations with the potential to provide significant improvements compared with previous reactors. This phase was concluded with several design option reviews to finalize the project as much as possible before launching the second phase of the pre-conceptual design.

Main options have been selected by the end of 2012. The conceptual design – lasting until late 2015 – will consolidate the first phase, allowing to optimize the design, confirm or question some options, and providing more information and greater consistency.

Dialogue has been instigated with the French Nuclear Safety Authority (ASN) during the first phase of the pre-conceptual design, which resulted in a "safety orientations report" submitted in June 2012. The safety options report will be written and submitted to ASN at the end of the conceptual design (AVP2)

5. Examples of options studied and decided during the pre-conceptual design

***Low void effect core*.** The CFV[1] core concept is based on a low sodium void effect. This core concept involves heterogeneous axial $UPuO_2$ fuel with a thick fertile plate in the inner core and is characterised by an asymmetrical, crucible-shaped core with a sodium plenum above the fissile area.

The CFV core concept is focusing on optimising the core neutron feedback parameters (reactivity coefficients) so as to obtain improved natural core behaviour during accident conditions leading to the overall core heating. The CFV concept also retains a low reactivity loss thanks to the fuel pins with a larger diameter. Generally speaking, the CFV core retains a number of key advantages in terms of longer cycles and fuel residence times, as well improved behaviour during an accidental control rod ejection transient with respect to conventional core designs.The CFV core has been chosen as the reference option for the conceptual design studies.

Malevolent hazards. Hazards of both internal and external (aeroplane impact) origin are taken into account from design.

Decay heat removal. The objective is to design decay heat removal systems that are sufficiently redundant and diversified so that the practical elimination of their total failure

[1] French abbreviation for "*Cœur à Faible effet de Vide sodium", meaning low void effect core*

over a long period of time can be supported by a robust demonstration. To meet this goal, both water and air will be used as cold sources. Furthermore we will take advantage of the favourable characteristics of sodium reactors in terms of their high thermal inertia, large safety margins before sodium boiling and their capability to cope with natural convection flows. Different systems have been studied during the pre-conceptual design and selected for further studies.

Mitigation of potential core meltdown/ mechanical energy release accident: To provide defence in depth against scenarios such as the melting of the core, the ASTRID reactor will be equipped with a core catcher. It will be designed to recover the entire core, maintain the corium in a sub-critical state while ensuring its long-term cooling. As other equipments important for safety, it must be inspectable. Several options have being investigated in terms of the possible core-catcher technologies, locations (in-vessel or outside the vessel) and attainable performance levels. A sustained R&D effort will remain necessary in parallel on such subject, to help for the selection of the more promising technical solutions. The choice of in-vessel option for the conceptual design studies has been done by the end of 2013.

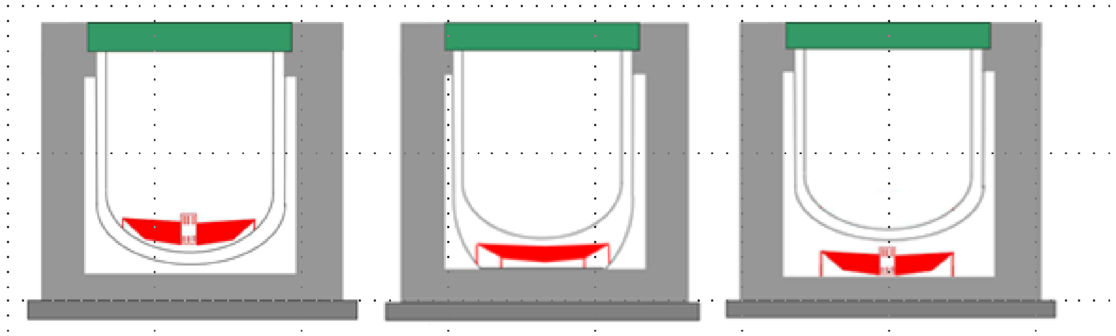

Figure 1: Three options for core catcher location.

Containment. The containment will be designed to resist the release of mechanical energy caused by an hypothetical core accident or large sodium fires, to make sure that no countermeasures are necessary outside the site in the event of an accident.

***Capability to inspect structures in sodium*.** Contrary to the PHENIX and SUPERPHENIX reactors, the periodic inspection of the reactor block internal structures has been integrated at the early stage of the design. The design of these structures, and particularly those contributing to the core support, were conceived to make easier their inspection. Technologies now exist that enable this inspection either from outside or inside the vessel. They mainly use optical and ultrasonic methods.

Architecture of primary and secondary circuits During the pre-conceptual design phase, a pool-type reactor with conical '*redan*' (inner vessel) has been early selected: a solution extrapolated from previous reactors and the EFR project. This solution has the advantage of being well-known; simplications have been made to allow for extended ISIR access. In terms of the reactor block, it has been decided to use three primary pumps together with four intermediate heat exchangers, each one associated with a secondary sodium loop which includes modular stream generators or sodium-gas heat exchangers.

The choice is currently focusing on electromagnetic pumps to equip the secondary loops, on the basis of one pump per loop.

***Steam or gas power conversion system (PCS)*.** In order to reduce the risks associated with the affinity between sodium and water, studies have been carried out on 2 power conversion systems:

– To improve the safety and acceptability of the reactor with the *de facto* elimination of the risks associated with sodium-water reactions, an innovative energy conversion system is being considered that uses gas (nitrogen) for the thermodynamic transformations (Brayton cycle). This type of system has never been built for the pressure and power ranges required in ASTRID so it will first be necessary to make sure of its feasibility, cost and compatibility with SFR constraints. In any case, this concept would be coupled to the reactor through an intermediate sodium system, in order to exclude any risk of gas entrainment into the core.

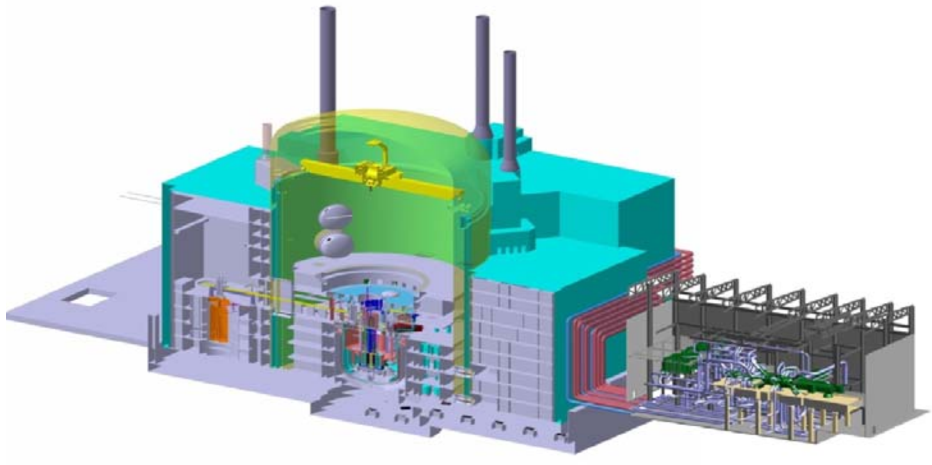

Figure 2: ASTRID lay-out.

– For the water-steam PCS option, the following improvements were investigated: Modular steam generators (heat exchange power of each module about 150 MWth), Steam generator concepts ensuring better protection against wastage, and finally reinforcement of the redundancy and performance of the leak detection systems. The monolythic helical steam generator has been chosen for the water-steam PCS option, mostly on the basis of its reliability and cost.

The very innovative gas PCS option has been selected to be deeply investigated during the conceptual design phase, the water-steam PCS being the back-up option.

Fuel handling. At the beginning of the ASTRID project, it was decided use a sodium environment in which to load and unload the fuel sub-assemblies. This implied a sodium external vessel storage tank (EVST) whose capacity depended on whether a whole core unloads is deemed necessary or not. During a cost killing phase, every choice made in the AVP1 phase has been reviewed and, for economic reasons, it was decided to suppress the ex-vessel storage tank for the conceptual phase and to move a gas route for fuel handling.

Transmutation capabilities. The transmutation of minor actinides is part of the ASTRID specifications. Only americium and neptunium are considered. With a percentage of 2% of minor actinides in a homogeneous core or 10% in dedicated blankets, there is no major impact on the plant design.

6. Main R&D needs in support to ASTRID

Deriving from the feedback of experience, very high levels of requirements have been set for the ASTRID reactor. Innovations are needed to further enhance safety, reduce capital cost and improve efficiency, reliability and operability, making the Generation IV SFR an attractive option for electricity production. Within the frame of the 6^{th} PCRD and the ADRIANA Project, a first review of the R&D needs has been done [4]. It was consolidated through the evolution of the ASTRID project. The main R&D developments are driven by some major topics [4][5]:

- Thermal-hydraulic behavior (operation and safety). This large topic covers many subjects to be studied. Of course it relies on the use of several specific codes, like TRIO-U… But some complementary experimental validation and qualification are needed such as the internal thermal-hydraulics of the fuel bundle, pressure drop, cavitation… These tests can be performed in water. Tests in Na have to be performed for testing their behaviour in transient conditions, and characterizing the fluid behaviour at the outlet for the FA due to sodium flow in the inter assemblies space for example.

- Improvement of system reliability and operation (availability, safety, investment protection,…). This objective mainly relies on the performance of instrumentation for continuous monitoring but also ISIR (In-Service Inspection and Repair). First, continuous monitoring acts during normal operation phase and is based on the control of operating parameters and on measurements which give structure and component health state. Moreover, this instrumentation allows detecting any initiator of incidents and accidents or the first consequences of the discrepancies with nominal operational conditions.
- Improvement of decay heat removal (safety). Decay heat removal is a major challenge for all types of nuclear reactors. For sodium cooled fast reactors, passive decay heat removal based on Na natural convection is possible. This is one of the important advantages of these reactors. The behaviour of these systems operating in natural convection is a key point to demonstrate its reliability in case of total plant black out for example. The CATHARE and TRIO-U codes, developed in France, are the key tool for system calculations and simulations. A qualification study of these systems has to be carried out based on some experimental validation.
- Improvement of the reactivity control (safety). At first, the arrangement of the SFR could be optimized in order limit the sodium void effect, but in complement a very deterministic approach could likely be used. For example, hydraulically sustained control rods and a 3rd level of emergency shutdown system could be used. And then their qualification in representative conditions is needed (hydraulic tests (vibrations, risks of up-loading, pressure drop, cavitation, …), and mechanical tests in order to demonstrate the feasibility of shut-down (rod gripping system) and insertion in relevant normal or abnormal conditions.
- Optimization of the handling route (availability, economics). The main goals are to reduce of investments costs with improvement of the In Vessel Fuel Handling System compactness and duration of FA loading/unloading operations. As there is no external fuel storage in the current ASTRID design, the reliability of the different steps of the fuel handling route is a major issue. Then two main constraints have to be considered: the handling of assemblies with high residual power and the requirement to treat on-line the fuel assemblies form the sodium internal storage to the in used fuel assemblies' pool. They induce the necessity to develop innovative handling systems, in comparison with the previous ones and more efficient fuel assemblies cleaning processes (to be defined and qualified).
- Design simplification (economics, performances, periodical inspection). This topic covers very different actions. It can concern the primary vessel and its internals design (for example to be able to address all the periodical inspection), but also the development of electromagnetical pumps for the secondary circuit (components requiring few maintenance actions and presenting the advantage of having almost no halving time).
- Elimination of the occurrence of a large sodium/water reaction (economics, availability and safety). Risk of sodium-water interaction concerns sodium of the secondary circuit and water of the ternary circuit in the steam generator. This interaction can be accompanied by relatively complex phenomena (such as wastage and multiple tubes rupture). Sodium-water-air reaction is also envisaged when two leaks water and sodium intervene in the same premise due to external accident event. This reaction could occur during operation (including cleaning of components). The risk of explosions has to be deeply considered for two cases: explosion of hydrogen in presence of air and also thermal explosion (fast vaporisation) of water in contact with hot sodium. There is a need of validated model for such phenomena, and validations.
- Some cross-cutting topics like material studies, improvement of system reliability. The SFR system raises a number of material issues due its environment i.e. corrosion phenomena

among them generalized corrosion (limited for stainless steel in contact with high quality sodium (low impurities level – few ppm of O)) and related mass transfer, mechanical behaviour of structures for vessels, pipes and internal components, and a special focus on cladding material used for the fuel assemblies. The main goal is to confirm performances of new structural materials of e.g. cladding (ODS), reactor vessel, internals, heat exchangers, coatings, with regards to the expected operating conditions (high burn-up, temperature, dose, stress), new potential intermediate coolant, new innovative Energy Conversion System (ECS).

- Improvement of behaviour in severe accident conditions. The development and qualification of severe accident codes and mitigation devices for ASTRID require a comprehensive experimental programme. It encompasses in-pile experiments, prototypic corium experiments and simulant material tests. In particular, in-pile experiments are necessary to study the behaviour of large pins, of the ASTRID CFV heterogeneous subassemblies during severe accident transients and of in-core mitigation devices. Corium experiments are required at small medium scale and large scale (mainly for Fluid Corium Interaction, corium relocation and core catcher issues).

7. R&D platforms dedicated to ASTRID

The number of facilities identified to support the ASTRID program is quite large (around 40 facilities or specific programs). Therefore for sake of simplicity and to rationalize the renovation and design works, this amount of facilities was shared into four technological platforms covering the entire R&D and component qualification domains. These four platforms are [6]:

- PAPIRUS platform: It is a set of small or medium size sodium loops for in sodium experimental tests. These facilities can be devoted for modelling code validation, in sodium instrumentation studies and validation, specific technological validation of mechanical concepts or components mock-up, or determination of dissolution & corrosion laws in sodium for core or structure materials. This platform is currently 90 % achieved. Some new facilities are under construction.

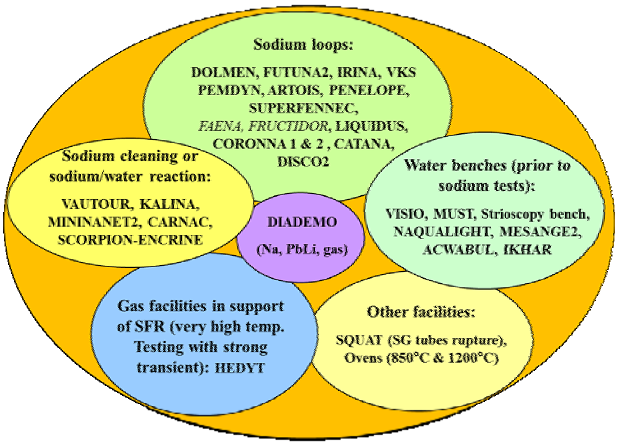

Figure 3: Overall perimeter of the PAPIRUS platform.

Figure 4: Overall view of the DIADEMO-Na facility.

- GISEH platform: It is a set of loops and mock ups used with simulant fluid (water and air) allowing the qualification of thermo-hydraulic codes or validating hydraulic data of the primary vessel (hot/cold plenum), or some complex part of specific SFR components (water collector in Steam Generator, or Compact Heat Excahngers mock ups), hydraulic in Fuel Assemblies). This platform is under construction. Some facilities already exist.

- CHEOPS platform: This platform is a group of large sodium facilities devoted to run R&D requiring large scale conditions. It allows to realize some qualification of mock-up of ASTRID components at significant and representative scale (Sodium/Gas heat exchanger (in case of selection of a gas Brayton cycle [13]).
- PLINIUS 2 platform: PLINIUS is an existing platform. It is a set of facilities dedicated to studies linked to severe accident for GEN 2/ GEN 3 reactors. PLINIUS 2 will be a new set of facilities completing the existing platform and insuring the future R&D program in this field. One of its first specificity is to take into account the possibility to study sodium corium interaction.

In some specific cases, CEA identified that some technological gaps that could be covered by a foreign facility. This has led to identify some international collaborative works. One significant example is the wastage tests performed at O Arai research centre (Japan) by JAEA in 2011 or the aerosol carbonation tests carried out in Indian ATF sodium facility belonging to IGCAR. New possibilities of collaborations are under investigation, with organizations involved in SFR design or European organizations through ARDECO bilateral collaborative projects.

Conclusion

By pursuing R&D and launching the ASTRID programme, France is clearly on the path to developing a concept of Generation IV reactors based on the sodium-cooled fast reactor technology, which could become operational at the industrial level, if necessary, in the middle of the 21st century to offer a sustainable use of the uranium and plutonium resources, based on the demonstration ensured by the erection, commissioning and operation of ASTRID in the mid term. The ASTRID reactor would also contribute to the R&D effort on the transmutation of minor actinides. This paper has also underlined the needs in term of experimental testing, for development, validation and qualification of systems devoted to SFRs and recalled the development strategy of experimental platforms in support of ASTRID program.

References

[1] Gauche, F.: Generation IV approach - The development of Sodium Fast Reactors. Proc. the 8th PAMIR Conference, Borgo, France, Sept 5-9 2011.

[2] Le Coz, P. et al.: The ASTRID Project : Status and Prospects. Proc. ICAPP’13, Jeju Island, Korea, 14-18 April 2013.

[3] Abonneau, E. et al.: The ASTRID Project: Status and Prospects towards the Conceptual Phase. Proc. ICAPP’14, Charlotte NC USA, April 6-9, 2014.

[4] Devictor, N. et al.: R&D challenges for SFR design and safety analysis – opportunities for international cooperation. Proc. IAEA FR13 conference, Paris, France, March 4-7, 2013.

[5] Latge, C et al.: ADRIANA Project: identification of research infrastructure for the SFR, within the frame of European Industrial Initiative for Sustainable Nuclear Fission. Proc. ICAPP 2012, Chicago (2012).

[6] Gastaldi, O. et al.: Experimental platforms in support of the ASTRID program: existing and planned facilities. Proc. ICAPP’14, Charlotte NC USA, April 6-9, 2014.

ACOUSTIC MHD GENERATOR

GAILITIS A.
Institute of Physics University of Latvia, Salaspils-1, LV-2169, Miera 32,Latvia
E-mail: gailitis@sal.lv

Abstract : Acoustic MHD generator is a part in a Thermo-acoustic Radio-Isotopic Power System project SPACETRIPS for space application. The radio-isotopic source produces heat. The thermo-acoustic generator converts it into sound. The MHD generator further converts sound into electricity. For decades our Institute developed conductive MHD generators working in DC mode. Now we have to adopt our experience [1] to AC mode.

1. Structure of the MHD generator

For specificity we assume MHD unit made from ferromagnetic insulator (e.g. laminated steel or SOMALOY) with configuration and sizes given on Fig.1. As working fluid there serves molten sodium filled in a through-going channel. In a middle of the channel its cross-section is a narrow (high= h , radius= r) annular gap surrounded by a secondary coil and a radially magnetized permanent ring magnet. Conical inlet/outlet parts of the channel are azimuthally separated into $n = 32$ insulated sub-channels. Separating walls there are ferromagnetic insulators, while short continuations in the gap are nonmagnetic insulators. The gap division size is $d = 2\pi r / n$.

Sound from thermo-acoustic generator forces gap sodium to oscillate in axial direction with velocity u in radial DC field B creating closed azimuthal AC current loop. An AC magnetic field pattern adds to the permanent field and induces voltage $V = 2\pi r E_V$ in both the secondary coil and a gap sodium.

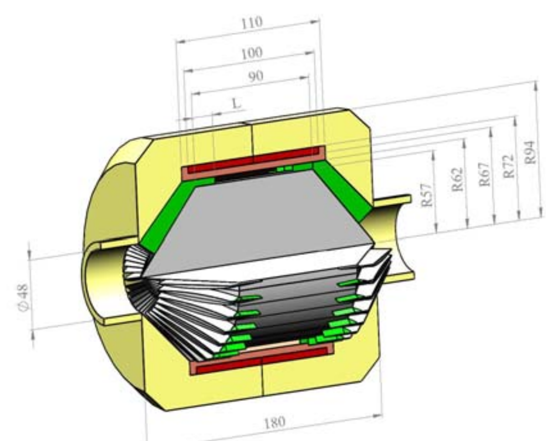

Figure1: Generator
R57—R62 sodium channel (gap)
R62—R67 x 110 secondary coil
R62—R72 x 100 permanent magnet
L — insulator

2. Computation

The small size of the device means low magnetic Reynolds. This allows us to combine free access simulation code FEMM4.2 with an equivalent circuit approach in a following way:

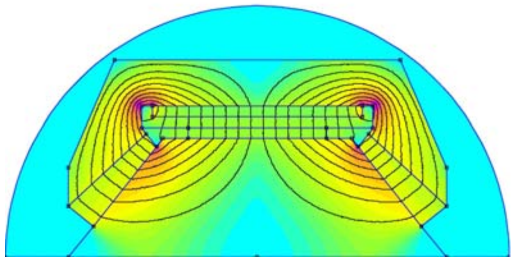

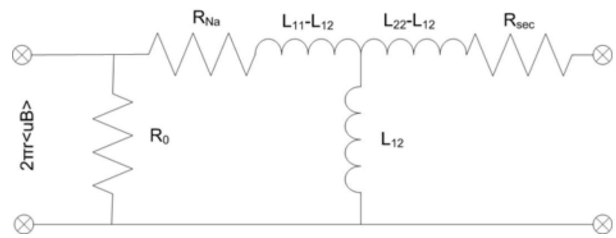

Figure 2: Magnetic field pattern. Figure 3: Equivalent circuit.

i. We define problems geometry for FEMM4.2 according to Fig.1. The inlet/outlet areas we declare as radially laminated ferromagnetic with a reduced filling factor.
ii. Operating in an axisymmetric DC mode the FEMM4.2 computes magnetic field pattern (Fig.2), as well as a single turn inductances for active part of the channel (L_{11}), for the secondary coil L_{22} and their mutual inductance L_{12}.
iii. All other properties of MHD generator we get using FEMM4.2 output as an input in a simple FORTRAN code based on AC equivalent circuit approach.

3. Formulation of equivalent circuit approach

An acoustic MHD generator combines two electrical machines - a conductive MHD generator converting Na flow energy into electrical current with a transformer transforming it into voltage applied to the consumer. Transformer part of effective circuit (Fig.3.) contain three inductances. Measured from left transformer shows L_{11}, from right L_{22}. If test current is applied on one side the others side voltage shows L_{12}.

Definition of generator part is much longer [1]. Azimuthal current in sodium

$$j = \sigma(uB(x) - E_u(x) - E_V(x))$$

contains electrical field in two terms: E_V set by transformer input voltage V and an insulators response to uB

$$E_u(x) = u\int B(x_1)g_3(x,x_1)d^3x_1 = ub(x)$$

with a formal 3D Green function $g_3(x,x_1)$. Total power generation in Na reads

$$Q = \sigma u^2 \int B(x)(B(x)-b(x))d^3x - \sigma u \int_{\Omega} E_V(x)B(x)d^3x$$

In generating part of equivalent circuit (Fig.3) three numerical values R_{Na}, V_0 and R_0 should be set:

i. Sodium resistance for induced current. The whole our approach is valid only for large $n >> 1$ when axial size of an active volume $\Omega = 2\pi r h l_{active}$ slightly exceeds insulator-free part of the gap: $l_{active} = l_{free} + 2\times 0.22d$ $\{0.22 \approx \ln(2)/\pi$, see [1]$\}$:

$$R_{Na} = 2\pi r / \sigma h l_{active}$$

In equivalent circuit $I_{Na} = (V_0 - V)/R_{Na}$. Power generation there

$$Q_{circuit} = V_0^2/R_0 + (V_0 - V)I_{Na} + VI_{Na} = V_0^2(1/R_0 + 1/R_{Na}) - V_0V/R_{Na}$$

should correspond to Q.

ii. For V_0 we assume $E_V(x) = V/2\pi r$ working in a volume Ω only and compare last term in Q with one in $Q_{circuit}$:

$$V_0 = \sigma u R_{Na} \int_{\Omega} (E_V(x)/V) B(x) d^3x = 2\pi r u < B >_{\Omega},$$

where $< B >_{\Omega}$ means B average in Ω.

iii. For R_0 we compare first term in Q with one in $Q_{circuit}$

$$1/R_0 = \sigma \int_{whole} (B(x) - b(x)) B(x) d^3x / < B >_{\Omega}^2 - 1/R_{Na}$$

Integration there is over the whole channel. Azimuthal integration leads to 1D formula

$$b(z) = \int_{subchannel} B(z_1) g_1(z, z_1) dz_1$$

$$1/R_0 = \left(\int_{whole} (B(z) - b(z)) B(z) dz / (< B >_{\Omega}^2 \, l_{active}) - 1 \right) / R_{Na}$$

For real computation we use two approximations:

$$g_1(z, z_1) \approx 2G(2|z - z_1|/d)/d$$

$$\int_{whole} (B(z) - b(z)) B(z) dz \approx \int_{free} B^2(z) dz + \int_{subchannels} (B(z) - b(z)) B(z) dz + 0.085 d (B_R + B_L)$$

In correction term $0.085 \approx \ln(2)/\pi - 0.5 \sum_{k=1,\ldots\infty} 1/((k - 0.5)\pi)^3$; B_R, B_L are field values at right and left insulator tips. With such assumption in uniform field $R_0 = \infty$ as it should be.

$$G(z) = \frac{1}{\pi} \sum_{k=1}^{\infty} \exp(-(k - 0.5)\pi |z|)/(k - 0.5) = \frac{1}{2} \int_{-1}^{1} f(x, z) dx$$

$$f(x, z) = \sum_{k=1}^{\infty} \exp(-(k - 0.5)\pi |z|) \cos((k - .5)\pi x)$$

The $G(z)$ is a Green function because $f(x, z)$ satisfies the Laplace equation. A proper normalization of $G(z)$ and a smoothness $\partial f(x, z)/\partial z|_{z=0} = 0$ both are due to the identity $\sum_{k=1,\ldots\infty} \sin(k - 0.5)x/(k - 0.5) = \pi/2$ for $0 < x < \pi$ [2].

4. Results

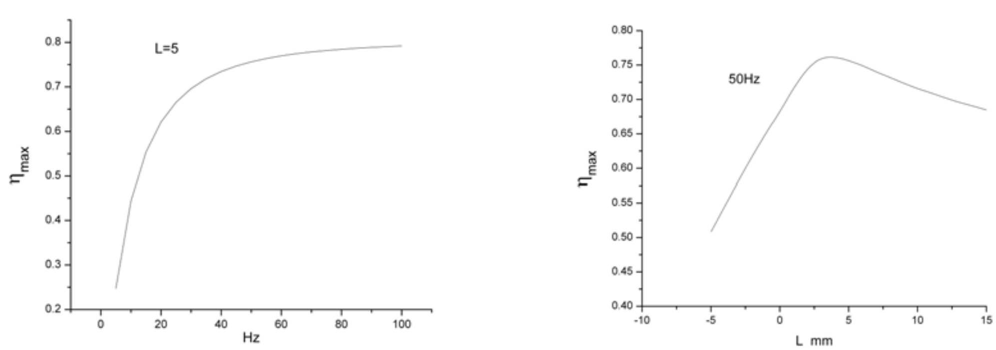

Figure 4: Efficiency dependence on the sound frequency and insulator length.

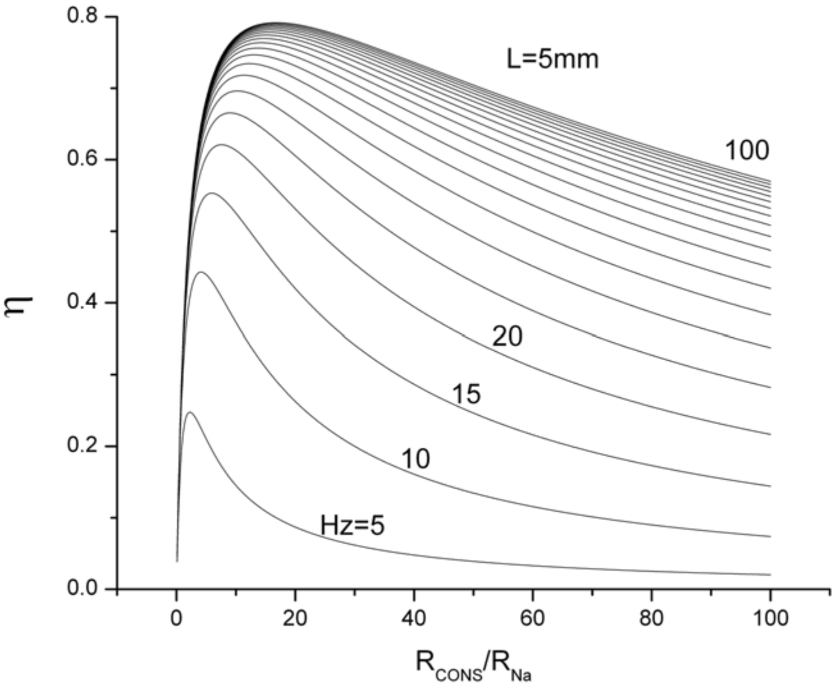

Figure 5: Efficiency vs. load and frequency.

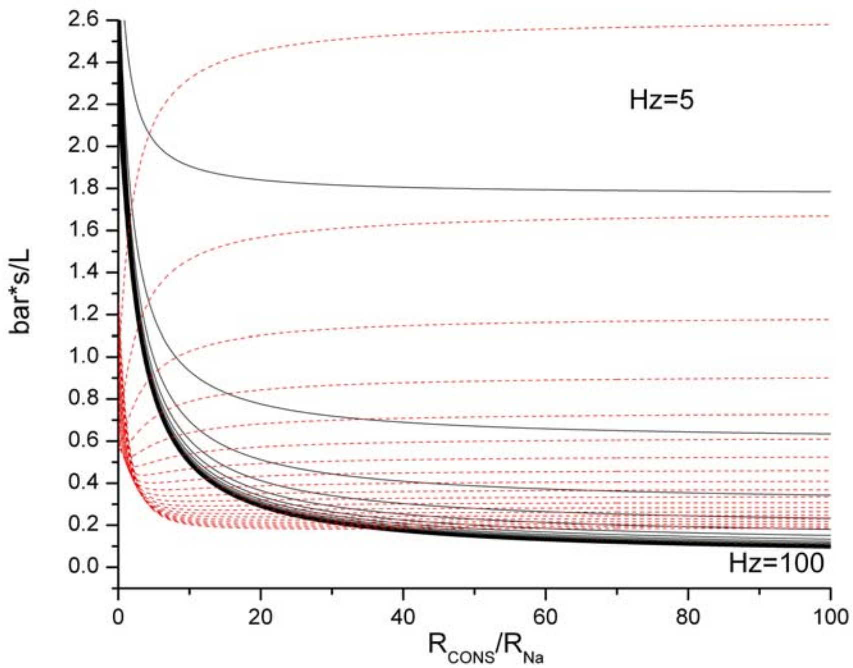

Figure 6: Acoustic impedance. Active part – solid line, reactive – dash.

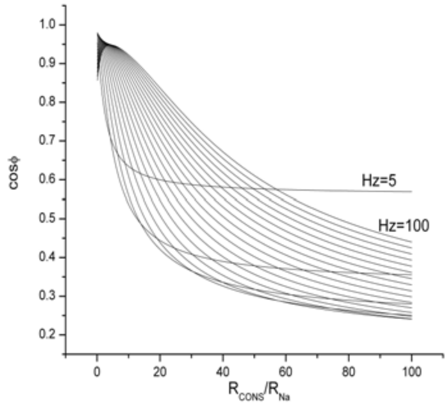

Figure 7: Acoustic cosϕ.

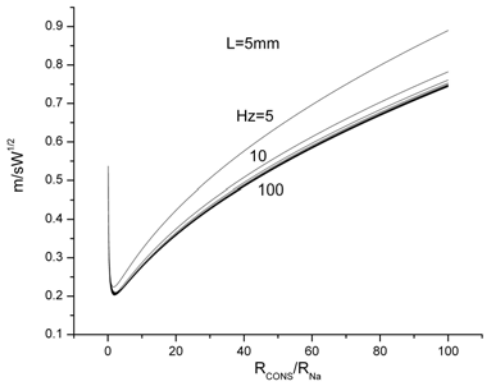

Figure 8: Na velocity for 1W output.

5. Conclusions

Effective circuit is fast and useful tool to analyze different generator aspects. In this paper only ideal generator was considered. Practical things such as sodium inertia, viscosity, loses in constructive materials etc. were omitted. No problem to include most of them into effective circuit and rerun the code.

References

[1] Birzvalks Y.A. Basics of theory and calculation for conductive DC MHD pumps. Zinatne. Riga. 1968 (In Russ).

[2] Gradshteyn and Ryzhik's Table of Integrals, Series, and Products Alan Jeffrey (ed.) Fifth edition (January 1994) 1, 204 p. ISBN number: 0-12-294755-X.

DESIGN OF ANNULAR LINEAR INDUCTION PUMP FOR HIGH TEMPERATURE LIQUID LEAD TRANSPORTATION

JAE SIK KWAK*, HEE REYOUNG KIM
Ulsan National Institute of Science and Technology, UNIST-gil 50, Ulsan, Republic of Korea
*Corresponding author: sikjae10@unist.ac.kr

Abstract :The annular linear induction pump (ALIP) with the flowrate of 30 L/min and the developing pressure of 1 bar was designed for transportation of liquid lead which is used for neutron target. The characteristics of design variables are analysed by electrical equivalent circuit method taking into account hydraulic head loss in the narrow annular channel of the ALIP. The pump was divided into two parts, which consisted of the primary one with electromagnetic core and exciting coils, and secondary one with liquid lead flow. The design program, which was composed by using MATLAB language, was developed to draw pump design variables according to input requirements.

1. Introduction

Electromagnetic (EM) pumps have been employed to transport heavy liquid metals such as mercury, lead, and so on. That arise at their application in liquid metals cooled reactors and other plants, for example, neutron target or neutron spallation sources. Using of mechanical pumps for heavy liquid metals for these purposes are associated with problems of providing reliable mechanical propellers and seals operating at rather high loads and heavyduty mentioned above operation conditions. As an alternative solution, the EM pumps (Figure 1), which are thought to effectively overcome the disadvantages of mechanical pumps [1], are considered. The characteristics of design variables are analyzed by electrical equivalent circuit method taking into account hydraulic head loss in the narrow annular channel of the ALIP. The design program, which is composed by using MATLAB language, is developed to draw pump design variables according to input requirements of the flowrate, developing pressure and operation temperature.

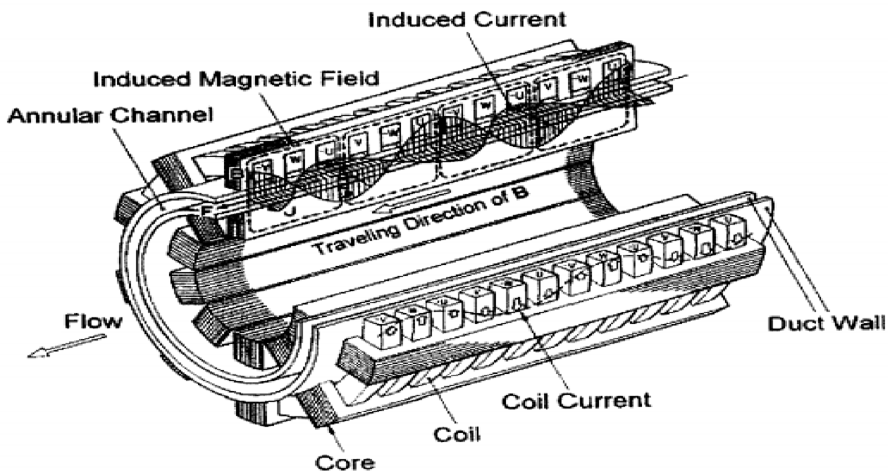

Figure 1: Schematic diagram of ALIP.

2. Structure of ALIP

2.1 Electromagnetic core

Structure of ALIP is shown in Figure 2. In this illustration, electromagnetic core can be divided into two parts, inner core and outer core which induce magnetic field to axial direction and radial direction. So material for core must be ferromagnetic body which has high permeability. It also maintains magnetic characteristics and mechanical strength in high temperature and fast neutrons. For blocking loss of magnetic field and heat generation caused by eddy current in core inside, stacking isolated ferromagnetic plane is recommended. Especially, inner core have to be placed radial form in the duct for considering direction of magnetic field.

Outer core is manufactured by stacking chain of E type core. And use a material silicon steel plate coated by insulation organic matter. Outer core bunch is fixed by stainless steel square pipe and bolts with nuts. Inner core is manufactured by stacking I type core, be placed in the inner duct and sealed by cone for preventing contact with liquid lead [2,3].

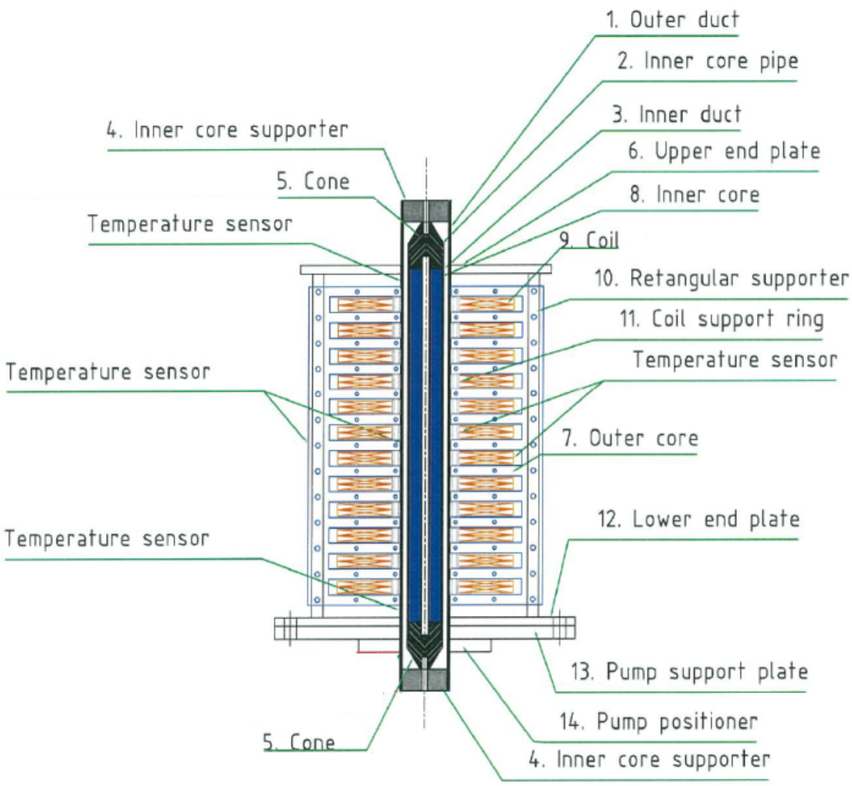

Figure 2: Structure of ALIP.

2.2 Electromagnetic coil

Materials for electromagnetic coil must have heat-resisting and low electrical resisting properties in the environment of high temperature and neutron irradiation. In the case of ALIP, electromagnetic coils are twined circularly and flowing electric current directly. So insulation between coils is essential.

2.3 Insulating material

Insulating materials must block electrical contact not only gap of coils but also between coil and outer cores. Because of filling factor, thin insulating materials are better as electrical insulation is allowed. It must be twined circularly with electromagnetic coil, have flexibility and heat-resisting properties.

2.4 Structural material

Structural material means components of pump except core, coil, and insulating material. These fix components (plates and supporters), protect from high temperature liquid lead (duct), helps flow of liquid lead (cone) and so on. Structural material must protect pump from high temperature lead in the aspects of heat and chemical reactivity. And it should not distort magnetic field. So austenite stainless steel is recommended because which is nonmagnetic material.

3. Analysis on the design parameters of ALIP

Basically ALIP changes driving power and efficiency by geometrical shape, size, and operating variables. The driving power and efficiency function can be derived by electrical equivalent circuit method. The pump was divided into two parts, which consisted of the primary one with electromagnetic core and exciting coils, and secondary one with liquid lead flow. The main geometrical variables of the pump included core length, inner diameter, flow gap, and so on while the electromagnetic ones covered turns of coil, number of pole pairs, input current, input frequency, and so on.

3.1 Electrical equivalent circuit method

The ALIP can be illustrated like Figure 3as electrical equivalent circuit. In the Primary one,R_1 is wire wound resistance in the coil, X_1 is leakage reactance from the core, X_m is magnetization reactance from the core, andR_2 is equivalent resistance of liquid metal. And function between developed pressure ΔP and average flow rate Q express like below [4, 5].

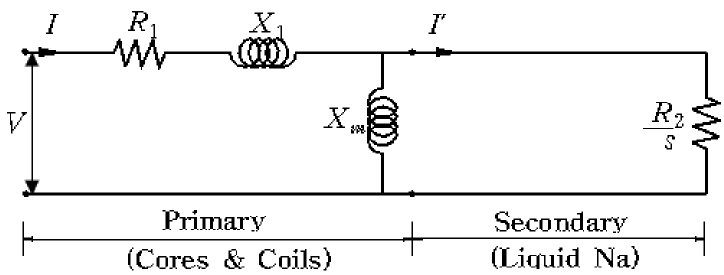

Figure 3: Electrical equivalent circuit of ALIP.

$$\Delta P = \frac{3I^2}{Q}\frac{R_2(1-s)}{s\left(\frac{R_2^2}{X_m s^2}+1\right)} \tag{1}$$

Equivalent resistance and equivalent reactance are knownfrom Laithwaite standard design formula calculated by magnetic circuit composed of geometrical and operational variables.As a result, below formula can be derived.

$$\Delta P = (3\,6\sigma s f \tau^{2}\,([(\mu_0\,k_w\,NI)]^{2})/(p g_e^{2}\,\{\pi^{2} + (2\mu_0\,\sigma s f \tau^{2})^{2}\,) \tag{2}$$

From the formula (2), correlation between developed pressure and pump design variables which are frequency, pole pairs flow gap, pole pitch, and so on can be known. Like above, efficiency formula can be also derived.

3.2 Characteristics of design parameters

From the developed pressure and efficiency formula by electrical equivalent circuit method, derive relations of design parameters. These are simplified in Table 1.

Table 1: Characteristic of structure elements [3]

Structural Elements		Action Characteristics
Size of Outer Core	Increase	• Leakage reactance increase • Allowed Turns of coil increase
	Decrease	• By the decrease of leakage reactance, efficiency increase • Allowed turns of coil decrease
Duct Width	Increase	• For same output, need more current and efficiency decrease • Flow gap decrease
	Decrease	• output and efficiency increase • Flow gap increase
Pole Pitch	Increase	• Synchronous speed increase • Length of Inner core and weight, size of pump increase
	Decrease	• Size of pump decrease • Body force increase in same input
Number of Pole	Increase	• Dispersion of fluid thrust • Pump size increase
	Decrease	• Leakage reactance increase (in secondary part)
Size of Inner Core	Increase	• Pump weight increase • Area of duct increase (in same duct width)
	Decrease	• Pump weight decrease • Area of duct decrease (in same duct width)
Number of Coil	Increase	• Input current decrease in same output
	Decrease	• Input current increase in same output

4. Design program based on MATLAB

In the MATLAB code, sections for calculation are divided into 10 sections which are 'Required specification', Electromagnetic variables', Geometrical variables', Electro-geometrical variables', 'Hydro dynamical variables', 'Equivalent impedance', 'Power factor and goodness factor', 'Developed pressure', 'Electrical input and efficiency', 'Design Specification'.

In the Required specification section, input 3 main outputs of pump,pressure, temperature, and flow rate. And the code calculates other outputs for reaching to goal of 3 main outputs. In the electromagnetic variables section, input current, turns of coils, frequency, pole pairs, electrical resistivity of materials based on temperature, and so on. In the geometrical variables section, input basic size of pump like core length, flow gap, thickness of ducts, ratio of slot width to slot pitch, and so on. Then the equipped formulas calculate the detailed sizes of pump components. So I don't have to do detail design for each components of pump.In the other sections except last section, the code calculates outputs based on equipped formulas which are derived by equivalent circuit method. Also, hydrodynamics factors are considered. The pump input and output variables by using the code were represented in table 2.

5. Conclusions

The analysis on the design of ALIP for high temperature liquid lead transportation was carried out by using the electrical equivalent circuit method and taking the hydraulic loss into account. The design variables for the pump with the required flow rate and developed pressure were analyzed from the induced formulae. The computer code based on the present analysis was developed for the design of the small ALIP and applied to the design of pump for transportation of liquid leads with the flow rate of 30 L/min, the developed pressure of 1 bar and operation temperature of 500 . The material of the pump core, coil and structure was determined taking into consideration of the operation environment of the high temperature of 500 . The design analysis of the pump and developed computer code was thought to be effectively employed to design and manufacture the small ALIP.

Table 2: Pump variables using the MATLAB design code

	Design variables	Values
Hydrodynamic	Flow rate [L/min]	30
	Developed pressure [bar]	1.01
	Temperature [ ]	500
	Velocity [m/sec]	0.535
	Slip [%]	96.3
	Reynolds number	19218
	Head loss [Pa]	17471.959
Geometrical	Core length [mm]	480.0
	Outer core diameter [mm]	524.5
	Inner core diameter [mm]	37.1
	Inter core gap [mm]	12.70
	Flow gap [mm]	6.10
	Inner duct thickness [mm]	2.80
	Outer duct thickness [mm]	2.80
	Slot width [mm]	19.20
	Slot depth [mm]	206.00
	Core depth [mm]	231.00
	Core thickness [mm]	25.00
	Stacked coil think [mm]	186.00
	Coil support ring [mm]	10.00
	Space in slot depth [mm]	10.00
	Tooth width [mm]	19.20
	Slot pitch [mm]	38.40
	Conductor width [mm]	12.00
	Conductor thickness [mm]	6.00
	Insulator thickness [mm]	0.20
Electrical	Input current [A]	38.0
	Input voltage [V]	427
	Impedance [Ohm]	11.2
	Input VA [kVA]	28.1
	Input power [kW]	8.5
	Power factor [%]	30.1
	Goodness factor	0.3
	Pole pitch [cm]	12.00
	Number of slot [#]	12
	Turns/slot [#]	60
	Number of pole pairs [#]	2
	Slot/phase/pole [#]	1
	Hydraulic efficiency [%]	5.70

REFERENCES

[1] I.Bucenieks, J.Freibergs, E.Platacis.:Evaluation of Parameters of Powerful Electromagnetic Induction Pumpson Permanent Magnets for Heavy Liquid Metals, IV International Workshopon Materials for HLM-cooled Reactors and Related TechnologiesROMA, ITALY, May 21-23, (2007).

[2] Hee-Reyoung. K.:MHD Dynamic Analysis and Development of Design Method of an Annular Linear Induction Electromagnetic Pump, Ph. D. Dissertation, Seoul National University, (1998).

[3] Tae-Bong. P.:A Study on the Magnetic Fluid Flat Distribution in MHD Field, MSc. Dissertation, Changwon National University, (2003).

[4] Borghi, C. A.:Cristofolini, A.;Fabbri, M.;Study of the Design Model of a Liquid Metal Induction Pump, IEEE Trans. Magn., vol.34, no.5, (1999), pp.2956-295.

[5] Naser, S. A.: Linear motion electromagnetic systems, John Wiley &Sons, (1998), 131-263.

NUMERICAL MODEL OF INDUCTION PUMPS ON ROTATING PERMANENT MAGNETS

KOROTEEVA[1] E.Yu., SCEPANSKIS[2] M., BUCENIEKS[1] I.
[1]Institute of Physics, University of Latvia, Miera iela 32, LV-2169, Salaspils, LV-2169, Latvia
[2]Laboratory for Mathematical Modelling of Environmental and Technological Processes, University of Latvia, 8 Zeļļu str., LV-1002 Riga, Latvia
E-mail: forsp@mail.ru

Abstract: A disks type electromagnetic induction pump based on permanent rotating magnets is studied numerically. The theoretical analysis of such pumps is cumbersome since the magnetic field and, hence, the induced electromagnetic forces are distributed non-uniformly in both radial and transverse directions. In this work, the 3D numerical model of a liquid metal flow in a semi-circular duct between two rotating disks is being developed. A finite element analysis is performed using ANSYS software.

1. Introduction

Electromagnetic (EM) pumping technology is being extensively used nowadays in a variety of industrial and research applications, including liquid metal flow control in cooling circuits. Different types of EM pumps are being designed to generate the molten metal movement. In EM induction pumps on permanent magnets (PMP) [1] an alternating travelling magnetic field which induces electromagnetic driving forces in liquid metal is generated by the system of rotating magnetic poles of alternating polarity. Theoretical analysis and experimental tests demonstrated the significant advantages of PMPs in comparison with traditional EM pumps based on 3-phase linear inductors, such as: simpler construction due to the absence of windings, smaller dimensions and size, and much higher efficiency [2-4].

One of the possible modifications of the PMP is the disk-type design concept shown in fig. 1. The active magnetic system consists of two solid ferrous disks with permanent magnets fastened on them in the radial direction. The flat bent channel of the pump with liquid metal, having a rectangular cross-section, is located between the disks. The main parameters defining the efficiency of the disk-type PMP is the magnetic field strength and its distribution in the liquid metal layer in the pump channel.

The design of reliable and more powerful EM pumps requires increasing their efficiency and improving the output parameters (developed pressure and flowrate). However, the experimental investigations of EM induction pumps and the disks-type PMPs in particular, are associated with technical and economical difficulties. The theoretical prediction of disk-type PMP parameters is also complicated since the problem is highly three-dimensional, and the magnetic field, and consequently the electromagnetic forces are non-uniformly distributed both in radial direction and also across liquid metal layer in the channel of the pump and in electrically conducting walls of the channel. In this regard, the numerical simulations of the problem seem to be an appealing alternative from both practical and financial point of view.

In this work, the numerical model of the disk-type induction pump based on rotating permanent magnets is developed. ANSYS software is used to conduct the EM simulations of the pump performance.

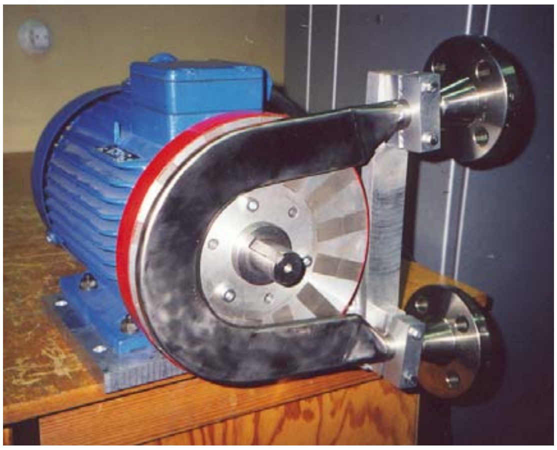

Figure 1: Photo of a typical disk-type the EM induction pump with permanent magnets (the second disk is removed).

2. Disk-type PMP design

The disk-type PMP 3D model created in ANSYS is illustrated in fig. 2. The pump consists of two basic parts: rotor (two rotating disks with installed permanent magnets) and stator (C-shape stainless steel channel carrying liquid metal).

The outer radius of magnetic system is 230 mm. The solid ferrous yoke has a thickness of 12 mm. The permanent magnets are located in the radial direction around the disk and fastened on the aluminium base. Each magnet has a rectangular form (60x30x20 mm^3) and the residual magnetization of Br = 1.1 T. The total of 16 magnets with sequentially altering polarities is placed on each disk with poles facing the channel side walls (i.e. the magnetic polarities are oriented along the rotation axis).

The pump channel with Wood's metal has a rectangular cross-section (with the liquid metal layer of 11 mm thickness and 70 mm height), and the mean radius of the C-shape part of the channel is 114 mm. The inner and outer steel channel walls are 3 mm thick, and the side walls are 2.5 mm thick. The distance between the magnetic disks ranges from d = 20 mm up to its maximal value d = 48 mm, with the air gap between both sides of the pump channel and a disk surface changing from 2 mm up to 16 mm.

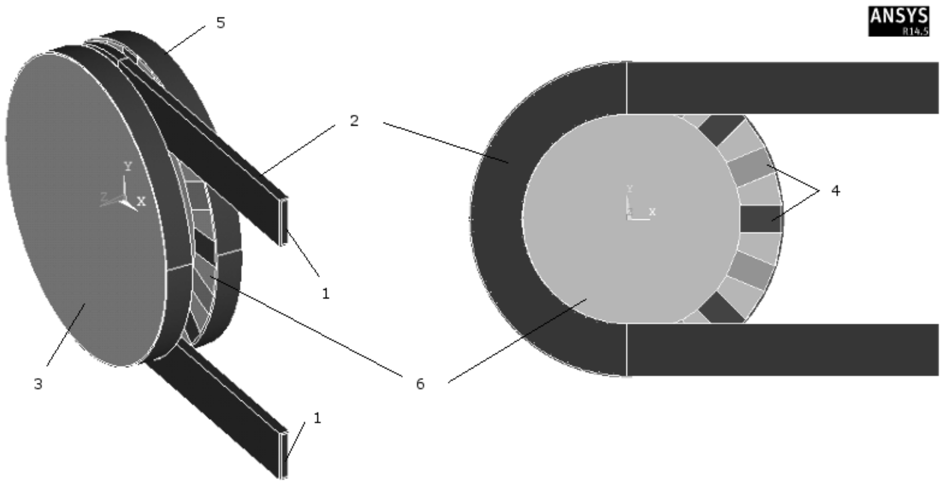

Figure 2: 3D model of disk-type PMP: 1 – liquid metal; 2 – pump channel (steel); 3 – ferrous yoke; 4 – permanent magnets; 5 – steel ring; 6 – aluminium base. The air volume and the second disk (on right image) are not shown.

The two magnetic disks rotate simultaneously with the frequency *f* (rev/s) generating an altering magnetic field, *B*, in the volume of the pump channel. The cross product of the current density field, *j*, induced in the conducting media (both liquid metal and the steel wall), and the magnetic field intensity, *B*, is a three-dimensional field of electromagnetic volumetric forces distributed along the pump channel, *Fmag*:

$$\vec{F}mag = \vec{j} \times \vec{B} \tag{1}$$

3. Simulation procedure and results

The simulation of an EM pump requires solving both electromagnetic and fluid dynamic equations. In most of industrial processes involving liquid metals (such as pumping) the low magnetic Reynolds number assumption can be used. This means that the electrical current generated by the fluid flow does not significantly affect the magnetic flux, whereas the flow itself is strongly governed by the magnetic field [5]. Since both fields are uncoupled, the numerical analysis and computations are significantly simplified. The Lorenz force (1) resulting from the solution of the electromagnetic problem introduced as a source force for the fluid-dynamic simulations.

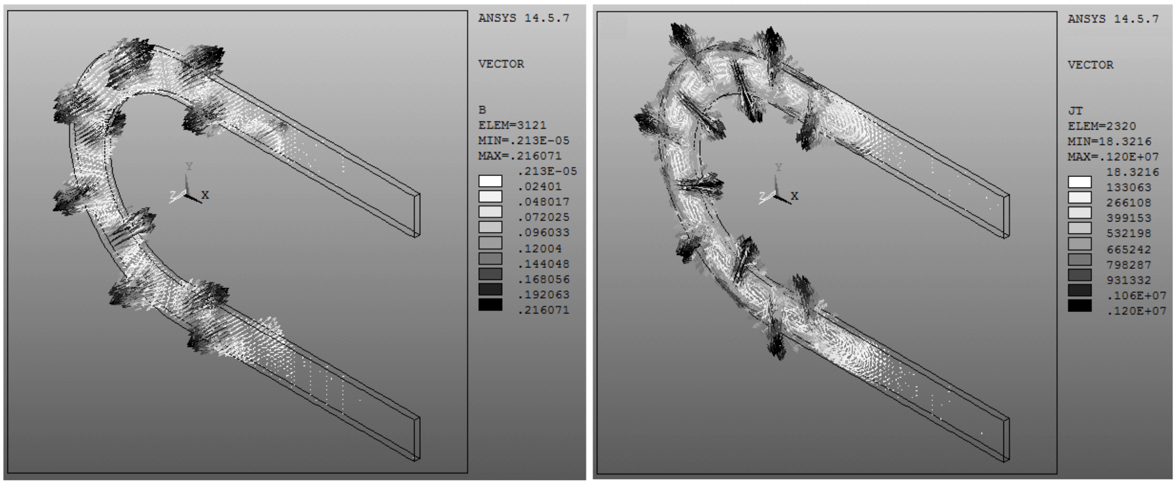

Figure 3: Distribution of (left) magnetic field intensity, *B* (T), and (right) total current flux density, *jt* (A/m3), in the liquid metal layer; *d* = 40 mm, *f* = 8 rev/s.

This paper presents the work concerning the first step of the numerical analysis - electromagnetic simulations and their experimental validation. The finite element method (FEM) analysis is conducted using ANSYS 14.0 commercial software. The transient dynamic calculations are performed simulating one full cycle (T=1/f) of the 3D magnetic system rotating at the speed of up to f =24 rev/s. The total number of elements exceeds $1.1\text{x}10^5$, with about $4\text{x}10^3$ liquid metal elements in the pump channel.

The parameters of interest, provided by the ANSYS solutions, are: the electromagnetic force field, magnetic field, electrical current density both in the liquid metal layer and the steel channel wall, as well as the total Joule heat produced in them.

Fig. 3 and fig. 4 show the vector fields of magnetic intensity, *B*, and the total current density, *jt*, both in liquid metal layer and the pump channel wall, respectively. The results are obtained for f=8 rev/s (T=0.125 s) after one full turn of the disks separated by d = 40 mm. The magnetic field distribution corresponds with the experimental data [4].

The operating principal of the disk-type PMP can be seen in fig. 5 where the distribution of the driving electromagnetic force, *Fmag* (N), in the central plane of the liquid metal layer is shown. The disks are rotating counter-clockwise from the view point generating the counter-clockwise motion of the fluid in the C-shape channel.

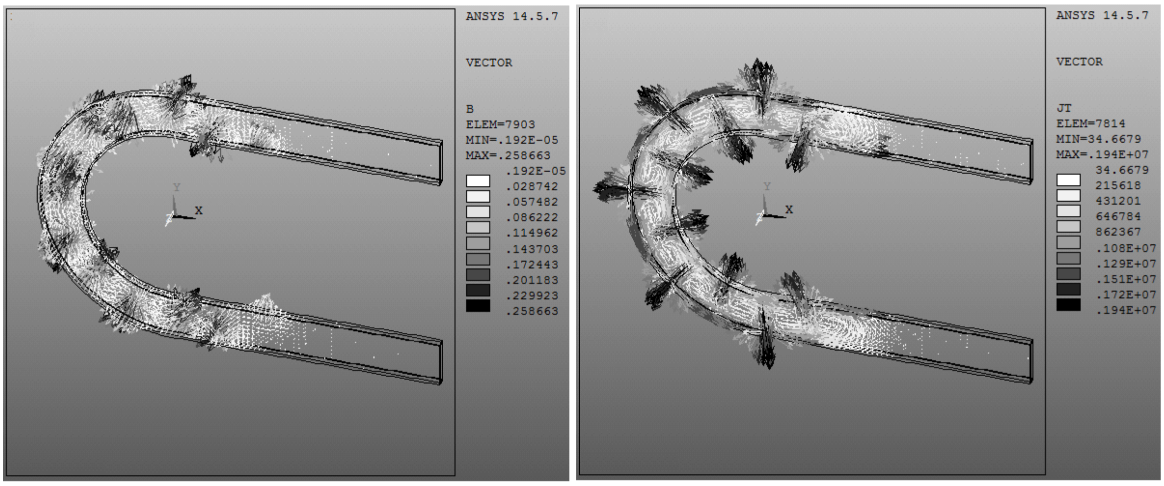

Figure 4: Distribution of (left) magnetic field intensity, *B* (T), and (right) total current flux density, *jt* (A/m3), in the channel steel wall; *d* = 40 mm, *f* = 8 rev/s.

The total Joule heat dissipated in the conducting materials during one period of rotation *T* is calculated by summing up the Joule heats produced in all the elements though all the time steps. In the first approximation (no fluid motion) the value for both the liquid metal layer and the steel channel wall is estimated to be of the order of $3x10^2$ W.

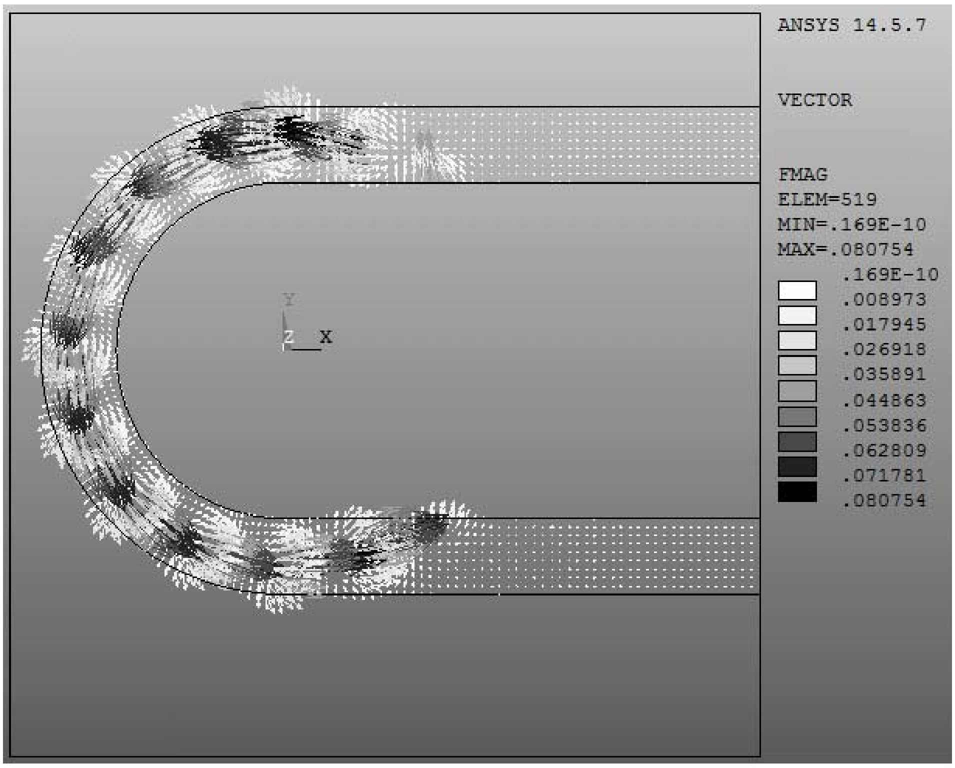

Figure 5: Distribution of magnetic vector force field, *Fmag* (N), in the central plane of the liquid metal layer; *d* = 40 mm, *f* = 8 rev/s.

4. Conclusion

Numerical modelling is an essential and effective tool in electromagnetic induction pump analysis, involving the design of more powerful pumps and optimization of their parameters. In this work, the 3D numerical model of the disk-type pump on rotating permanent magnets is developed. The finite element analysis based on using ANSYS software is employed to simulate the dynamics of the rotating magnetic system and to calculate the induced pumping forces. The results are consistent with the existing experimental data.

Since the problem is highly three-dimensional (due to the disk-type pump design), the simulations are complicated and computationally expensive. Extending the numerical analysis taking into account the fluid dynamic effects of moving liquid metal is the main goal of the future research.

5. Acknowledgements.

The research, which is the contribution of Dr. E.Yu. Koroteeva and Dr. M. Ščepanskis, was financially supported by European Social Fund (project no. 2013/0018/1DP/1.1.1.2.0/13/APIA/VIAA/061).

The authors also acknowledge V.Geža for indispensable technical consultation concerning the performance the simulation using ANSYS software and Dr. K.Kravalis for consultations in design of the pump.

6. References

[1] Bucenieks, I.: Perspectives of using rotating permanent magnets for electromagnetic induction pump design. Magnetohydrodynamics. 36 (2000) 181-187.
[2] Bucenieks, I.: High pressure and high flow rate induction pumps with permanents magnets. Magnetohydrodynamics. 39 (2003) 409-416.
[3] I. Bucenieks, K. Kravalis: Efficiency of EM induction pumps with permanent magnets. Magnetohydrodynamics 47 (2011) 89 – 97.
[4] I. Bucenieks, K. Kravalis R. Krishbergs: Pressure – flow rate characteristics of the pumps with permanent magnets. Magnetohydrodynamics 47 (2011) 97 – 105.
[5] Davidson, P.A.: An Introduction to Magnetohydrodynamics. Cambridge University Press (2001).

THE VISCOUS EFFECTS ON A SMALL MHD PUMP

HEE REYOUNG KIM
Ulsan National Institute of Science and Technology, 50 UNIST-gil Ulju-gun
Ulsan, KOREA
Corresponding author: kimhr@unist.ac.kr

Abstract : A one-dimensional MHD analysis has been performed for the viscous and end effects on a magnetohydrodynamic pump. The calculations show that the developed pressure difference resulted from electromagnetic and viscous forces in the liquid metal is expressed in terms of the slip, and that the viscous loss effects are negligible compared with electromagnetic driving forces except in the low-slip region where the pumps operate with very high flow velocities comparable with the synchronous velocity of the electromagnetic fields, which is not applicable to the practical MHD pumps.

1. Introduction

The linear induction MHD pumps have been employed for circulating the sodium coolant in Liquid-Metal Reactors. The MHD pumps have the advantage over the mechanical pumps due to the fact that they have no rotating parts, which results in simplicity and convenience of maintenance and repair. The basic operational experiments on pilot linear induction MHD pumps with various geometrical shapes have been carried out, and the practical applications have been made for the other areas of research like liquid metal chemistry. The linear induction MHD pump gets the driving power from Lorentz's forces generated by the time-varying magnetic fields and the current induced in the electrically conductive liquid metal. Mathematical solutions for the driving forces are obtained by solving MHD equations of incompressible viscous flow coupled with Maxwell's equations under appropriate assumptions. It is found that the mechanical pressure gradients developed in the pump duct are given as a function of the slip including other pump variables. Since the pumping pressures are developed by Lorentz's forces experiencing viscous drag forces, viscous loss effects on the electromagnetically-developed liquid metal flow need to be investigated. Generally, the Hartmann number given by the system scale length and magnetic field with viscosity and electrical conductivity is used as a measurement of viscous effect [1]. In the present work, direct comparison of the electromagnetic force with viscous force is carried out by analytical solutions obtained from related equations. The calculated results show, at the nominal conditions, that the pump performance can be analyzed by electromagnetic treatment due to negligible viscous effects. In this paper, MHD flow and electromagnetic analyses on the annular linear induction MHD pumps with flowrates of 60 L/min are carried out by solving MHD and Maxwell's equations.

2. Analysis of viscous losses by MHD laminar flow analysis

The MHD pump is driven by Lorentz's force given by products of induced current ($\mathbf{J}$) and magnetic field ($\mathbf{B}$) perpendicular to it. Electrically conductive liquid fluid also experiences viscous forces while it is developed by Lorentz's force. In this respect, an attempt has been made to obtain the expression for the pressure gradient mathematically by analyzing MHD equations coupled with Maxwell's field equation. As shown in figure 1, a typical annular linear induction MHD pump has sloted external cores in which exciting coils are inserted to generate $\boldsymbol{J} \times \boldsymbol{B}$ force in the liquid metal flowing in the annular duct [2-4].

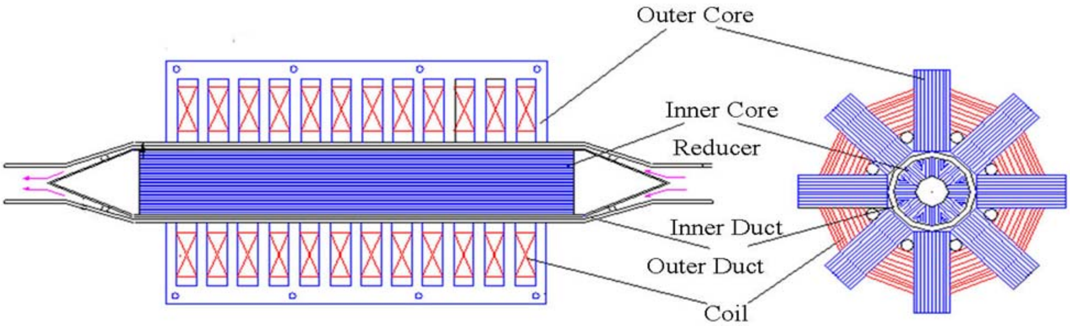

Figure 1: Cross-sectional view of an MHD pump.

But, to simplify the problem, the real pump core shape of is turned into a smooth core face replacing exciting coils by an equivalent current sheet to real coil arrangement as depicted in figure 2 [5].

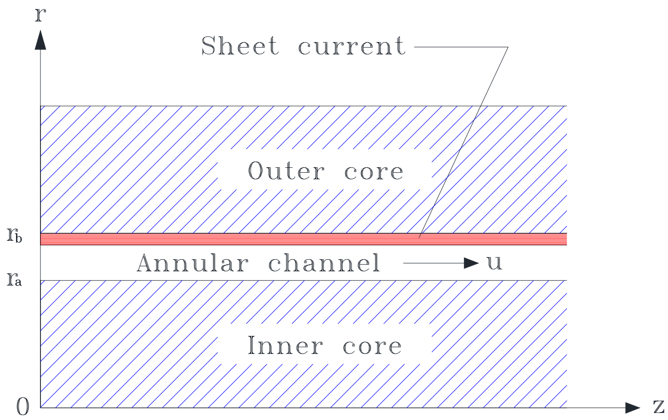

Figure 2: Simplified laminar model with equivalent current sheet .

A few more assumptions are introduced as follows [5].

(1) The pump has an infinitely-long annular channel with an equivalent current sheet replaced by discrete primary windings slotted in the outer core.

(2) All fields in the pump are axisymmetric ($\frac{\partial}{\partial\theta} = 0$) in view of cylindrical arrangement of the pump system.

(3) The equivalent current sheet representing the three-phase currents (I) of continuous primary windings of N turns having pole pairs of p and pole pitch of $\tau$is given by $J_a(r_2, z, t) = J_m e^{i(\omega t - kz)}\vec{\theta}$ where $J_m = 3\sqrt{2}k_w NI/p\tau$.

(4) The sheet current produces traveling sinusoidal fields in the same form of J_a with angular frequency of ω and wave number of k for ***B*, *E*** and ***J***.

(5) Radial magnetic field (B_r) is uniform due to negligible skin effect in a narrow liquid metal gap.

(6) The liquid metal flow is incompressible.

To analyze the system, first of all, MHD equations are needed for expressing conservations of fluid and momentum. The pressure gradient (∇P) arouses from the combined action of electromagnetic driving and hydrodynamic drag forces in the conducting fluid of density ρ, viscosity η, and fluid velocity $\boldsymbol{u}$. Electromagnetic term by Lorentz's force is related with Maxwell's equations. Besides, induced current density (***J***) in the Lorentz's force is represented from Ohm's law given by electrical conductivity (σ) and fields ($\boldsymbol{E}+\boldsymbol{u}\times\boldsymbol{B}$) induced both by traveling sinusoidal magnetic fields and conductive flow movement across them. Then governing equations are given as :

- MHD equations

$$\nabla \cdot \boldsymbol{u} = 0 \tag{1}$$

$$\rho\left\{\frac{\partial \boldsymbol{u}}{\partial t} + (\boldsymbol{u} \cdot \nabla)\boldsymbol{u}\right\} = -\nabla P + \eta \nabla^2 \boldsymbol{u} + \boldsymbol{J} \times \boldsymbol{B} \tag{2}$$

In the MHD equations, in practical sense, when velocity and flowrate are indicated, they generally mean the averaged values over time. Therefore, we will try to analyze the system in the time-averaged point of view. The time-averaged MHD equations are resulted in two reduced equations for flow velocity and magnetic field.

$$\frac{d^2\bar{u}}{dr^2} + \frac{1}{r}\frac{d\bar{u}}{dr} - \alpha^2 \bar{u} = \frac{1}{\eta}\frac{dP}{dz} - \alpha^2 U_s \tag{3}$$

$$\frac{dB_z}{dr} = \{\mu_0 \sigma(-U_s + u) + f\} B_r \tag{4}$$

where $\alpha^2 = \frac{\sigma B_r^2}{2\eta}$, $U_s = \frac{\omega}{k}$ (synchronous speed).

B_r can be treated as a constant since radial magnetic field does rarely change at a narrow inter-core gap in induction machines having negligible skin effects. In general, magnetic core materials have very large permeabilities compared with those of liquid metals, and the differences of tangential magnetic fields between core ($\boldsymbol{H_1}$) and liquid metal ($\boldsymbol{H_2}$) regions are given by sheet current density ($\boldsymbol{K}$) as $\boldsymbol{n} \times (\boldsymbol{H_1} - \boldsymbol{H_2}) = \boldsymbol{K}$. Thus for the present pump model, magnetic fields at inner and outer radius give $B_z(r_2) = \mu_0 J_m$, $B_z(r_1) = 0$. Applying no-slip boundary conditions for velocity ($\bar{u}$) at the cylindrical walls (r_1, r_2), i.e., $\bar{u}(r_1) = \bar{u}(r_2) = 0$, The solutions were expressed for the time-averaged velocity expressed in terms of the modified Bessel functions, I_0 and K_0, of zeroth order as

$$u(r) = \{A I_0(\alpha r) + B K_0(\alpha r) - 1\}\left\{\frac{1}{\alpha^2 \eta}\frac{dP}{dz} - U_s\right\} \tag{5}$$

where

$$A = \frac{K_0(\alpha a) - K_0(\alpha b)}{K_0(\alpha a) I_0(\alpha b) - K_0(\alpha b) I_0(\alpha a)}$$

$$B = \frac{I_0(\alpha b) - K I_0(\alpha a)}{K_0(\alpha a) I_0(\alpha b) - K_0(\alpha b) I_0(\alpha a)}$$

If an average slip (s) over the channel gap is defined by $s = \frac{1}{r_2 - r_1}\int_{r_1}^{r_2}\left(1 - \frac{\bar{u}}{U_s}\right) dr$, the radial magnetic field (B_r) and axial pressure gradient ($\frac{dP}{dz}$) are obtained as function of s together with other pump parameters.

$$B_r = \frac{\mu_0 J_m}{(-\mu_0 \sigma s U_s + fk)(r_2 - r_1)} \tag{6}$$

$$\frac{dP}{dz} = \frac{1}{2}\sigma U_s B_r^2 \left\{ s + (1-s)\left(1 + \frac{1}{\frac{1}{r_2 - r_1}\int_{r_1}^{r_2}(AI_0(\alpha r) + BK_0(\alpha r) - 1)\,dr}\right)\right\} \tag{7}$$

The axial pressure gradient has been developed by two components, Lorentz's force and viscous term. The first term of right-hand side, $\frac{1}{2}\sigma U_s B_r^2$ is originated from the electromagnetic force density which is simply obtained by direct calculation of $\boldsymbol{J} \times \boldsymbol{B}$. The other terms of right-hand side correspond to viscous force density. To compare the viscous force density with electromagnetic force density, as an example, numerical values of pressure differences versus slip (or flowrate) are represented graphically in figure 3 for a pump system with flowrate of 40,000 L/min under a pressure difference of 15 atm. Figure 3 indicates that viscous force density is negligible compared with electromagnetic force density through all flowrate values except for near synchronous speed (s = 0). Practically induction pumps are not operated at near the synchronous speed with very low slip. Due to real hydraulic load like valve or piping system, such low slip value needs to be avoided so that the system can generate quite realistic developing force. Since MHD pumps are generally operated at sufficiently high slip region to generate a considerable developing force overcoming heavy hydraulic pressure load (more than a few atms), the pump system analyses can be treated by electromagnetic analysis alone neglecting viscous effects. After all, it is thought that mechanical pressure gradient in the system can be replaced by electromagnetic force density ($\boldsymbol{J} \times \boldsymbol{B}$) alone.

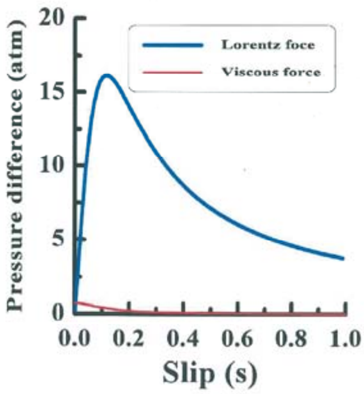

Figure 3: Comparison of viscous force effects with Lorentz's ones on producing the pressure difference between the inlet and the outlet.

Conclusion

Calculated results of the MHD flow analysis shows that the viscous loss effects on producing pressure differences are negligible compared with electromagnetic driving forces except in the low slip region where the pumps operate with very high flow velocities comparable with the field synchronous speed.

References

[1] Branover, H.: Magnetohydrodynamic flow in ducts, A John Wiley & Sons, New York (1978).
[2] Nasar, S.: Linear motion electromagnetic systems, A John Wiley & Sons, New York (1985).
[3] Nasar, S.: Linear motion electric machines, A John Wiley & Sons, New York (1976).
[4] Hee Reyoung, K and Yong Bum, L: Design and Characteristic Experiment of the Small Annular Linear Induction Electromagnetic Pump, Annals of Nuclear Energy, 38(2011) 1046-1052.
[5] Lawson, P.: Hydromagnetic channel flows: A John Wiley & Sons, New York (1960).

Self-calibrating phase-shift flowmeter for liquid metals

LOONEY, R. and PRIEDE, J.
Applied Mathematics Research Centre, Coventry University, United Kingdom
looneyr@uni.coventry.ac.uk; j.priede@coventry.ac.uk

Abstract: We present an improved phase-shift flowmeter that has a significantly reduced sensitivity to the variation of the electrical conductivity of the liquid metal. Two simple theoretical models of flowmeter are considered where the flow is approximated by a solid body motion of finite-thickness conducting layer. In the first model, the applied magnetic field is represented by a harmonic standing wave. In the second model, the sending coil is approximated by a couple of straight wires placed above the layer. We show that the effect of electrical conductivity can strongly be reduced by using the phase shift between the sending coil and the upstream receiving coil to rescale the measured phase shift between two receiving coils.

1 Introduction

This paper is concerned with further development of a recently invented AC induction flowmeter for liquid metal flows based on phase shift measurements [1, 2]. The flowmeter operates by measuring the phase disturbance caused by the flow of liquid metal in an applied ac magnetic field. The main advantage of the phase-shift flowmeter is the robustness to external perturbations compared to measurements of the amplitude used by conventional eddy-current flowmeters. However, the phase disturbance depends not only on the velocity of liquid but also on its electrical conductivity.

The aim of this work is to reduce the dependence of the flow-induced phase shift measurements on the electrical conductivity of liquid. The basic idea is that not only the liquid flow but also the alternation of the magnetic field itself gives rise to the phase shift in the induced magnetic field. The current version of the flowmeter employs only the former effect. The latter effect, which gives rise to phase shifts between the sending and receiving coils, is dependant on the conductivity of the liquid. Therefore it may be used to compensate for the effect of conductivity on the flow-induced phase shift. The feasibility of such an approach is investigated using two simple theoretical models of the phase-shift flowmeter, where the flow is approximated by a solid body motion of a finite-thickness conducting layer. In the first model, the applied magnetic field is represented by a harmonic standing wave. In the second model, the sending coil is approximated by a couple of straight wires placed above the layer.

2 Basic Equations

Consider a medium of electrical conductivity σ moving with the velocity $\vec{v} = \vec{e}_x V$ in an ac magnetic field with the induction $\vec{B}$ alternating harmonically with the angular frequency ω. The induced electric field follows from the Maxwell-Faraday equation as $\vec{E} = -\vec{\nabla}\Phi - \partial_t \vec{A}$, where Φ is the electric potential, $\vec{A}$ is the vector potential and $\vec{B} = \vec{\nabla} \times \vec{A}$. The density of the electric current induced in the moving medium is given by Ohm's law

$$\vec{j} = \sigma(\vec{E} + \vec{v} \times \vec{B}) = \sigma(-\vec{\nabla}\Phi - \partial_t \vec{A} + \vec{v} \times \vec{\nabla} \times \vec{A}).$$

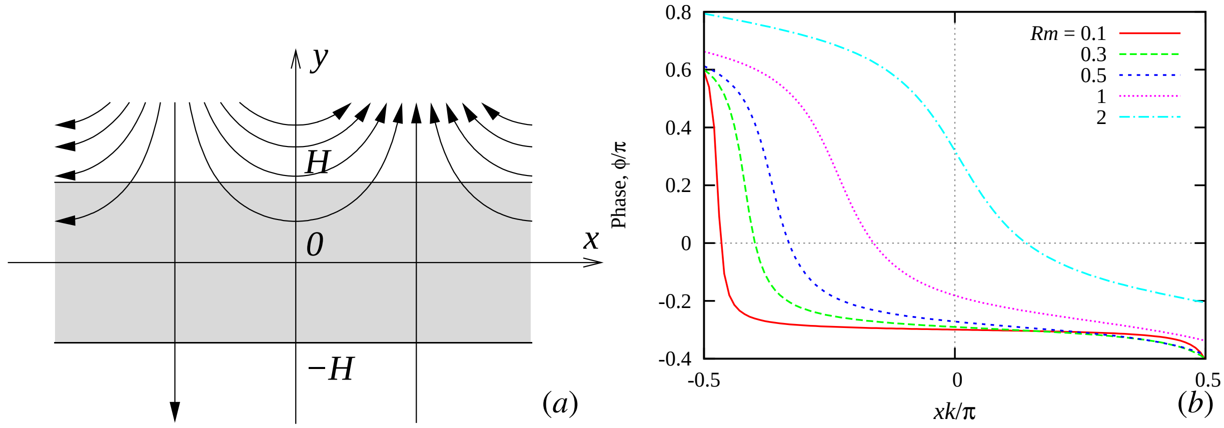

Figure 1: Model of a conducting layer of thickness $2H$ in the external magnetic field represented by a standing harmonic wave (a). Phase distribution over a half-wavelength of the applied magnetic field at various dimensionless velocities defined by Rm (b).

Assuming the ac frequency to be sufficiently low to neglect the displacement current, Ampere's law $\vec{j} = \frac{1}{\mu_0}\vec{\nabla} \times \vec{B}$ leads to the following advection-diffusion equation for the vector potential

$$\partial_t \vec{A} + (\vec{v} \cdot \vec{\nabla})\vec{A} = \frac{1}{\mu_0 \sigma} \nabla^2 \vec{A}, \tag{1}$$

where the gauge invariance of $\vec{A}$ has been used to specify the scalar potential as $\Phi = \vec{v} \cdot \vec{A} - \frac{1}{\mu_0 \sigma} \vec{\nabla} \cdot \vec{A}$. We now consider an applied magnetic field varying in time harmonically as $\vec{A}_0(\vec{r},t) = \vec{A}_0(\vec{r})\cos(\omega t)$, which allows us to search for a solution in the complex form $\vec{A}(\vec{r},t) = \Re\left[\vec{A}(\vec{r})e^{i\omega t}\right]$. Equation (1) for the amplitude distribution of the vector potential takes the form

$$i\omega \vec{A} + (\vec{v} \cdot \vec{\nabla})\vec{A} = \frac{1}{\mu_0 \sigma} \nabla^2 \vec{A}. \tag{2}$$

We focus now on a simple 2D externally applied magnetic field, which is invariant along the unit vector $\vec{\varepsilon}$. Such a magnetic field can be specified by a single component of the vector potential $\vec{A} = \vec{\varepsilon} A$ which leads to the boundary conditions $[A]_S = [\partial_n A]_S = 0$, where $[f]_S$ denotes the jump of quantity f across the boundary S where$\partial_n \equiv (\vec{n} \cdot \vec{\nabla})$ is the derivative normal to the boundary.

We start with a simple model where the conducting medium is a layer of thickness $2H$ shown in Fig. 1(a), and the applied magnetic field is a harmonic standing wave with the vector potential amplitude given by

$$\vec{A}_0(\vec{r},t) = \vec{e}_z A_0(\vec{r},t) = \vec{e}_z \hat{A}_0(y)\cos(kx)\cos(\omega t),$$

where k is the wave number in the x-direction. We choose the half-thickness H as the length scale and introduce a dimensionless ac frequency $\bar{\omega} = \mu_0 \sigma \omega H^2$ and the magnetic Reynolds number $Rm = \mu_0 \sigma V H$. The latter represents a dimensionless velocity. It is important to note that this key parameter depends on the product of the physical velocity and electrical conductivity. The full derivation of a solution based on the above and its continuation to a external field generated by a couple of straight wires is to be found in [2].

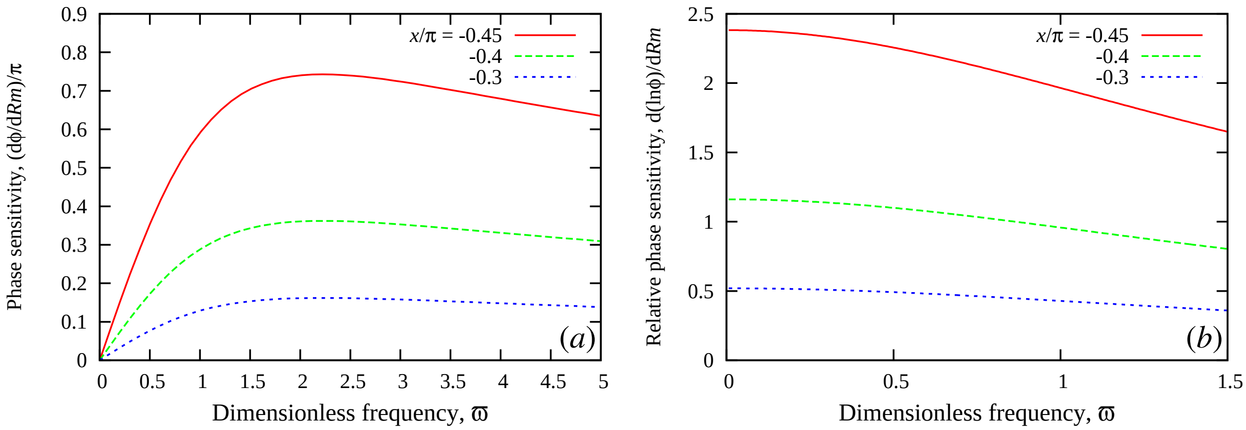

Figure 2: The phase sensitivity (a) and the relative phase sensitivity (b) versus the dimensionless frequency $\bar{\omega}$ at various horizontal observation positions below the layer for $k = 1$

3 Numerical Results

Single Harmonic of the magnetic field

Let us start with the original phase-shift flowmeter as a basis for the following development. Figure 1(b) shows the distribution of the phase between two nodes of the applied magnetic field along the bottom of the layer. For the layer at rest, the phase distribution is piecewise continuous with jumps in value at the wave nodes. These discontinuities are smoothed out by the motion of the layer and shifted further downstream as Rm is increased. Figure 1(b) also shows an important feature of the phase variation, that the strongest variation occurs at the right, immediately downstream of a node whereas the variation to the left, upstream of a node, is relatively weak, especially at lower values of Rm.

The variation of phase φ with Rm at low velocities can be characterized by the phase sensitivity $K = \pi^{-1} \partial_{Rm}\varphi|_{Rm=0}$. The dependence of this quantity on the dimensionless frequency $\bar{\omega}$ is plotted in Fig. 2(a) for several observation points. As $\bar{\omega}$ has a similar effect to Rm the reduction can be achieved by scaling the phase variation with the phase itself, which leads to the relative phase sensitivity

$$K_r = \pi K/\varphi. \tag{3}$$

As seen in Fig. 2(b) with small $\bar{\omega}$ this quantity tends to constant for given observation point. Although the relative phase sensitivity is not completely independent of $\bar{\omega}$ it can be seen that at lower values of $\bar{\omega}$ it varies much less than the unscaled phase sensitivity shown in 2(a). Following this idea the effect of conductivity can be reduced by scaling the phase shift between the voltages measured by the two receiving coils with the phase shift between the sending and receiving coils. Since, as shown above, the phase shift upstream of a node is less affected by the motion of the layer then downstream of a node, the upstream measurement shall be used to scale the phase shift between the receiving coils. Rescaling the phase shift directly with the reference phase, as done for sensitivity, is not sufficient as according to equation (3) the result still remains proportional to Rm. Since at small $\bar{\omega}$ the reference phase varies directly with $\bar{\omega}$ which, similar to Rm, is proportional to

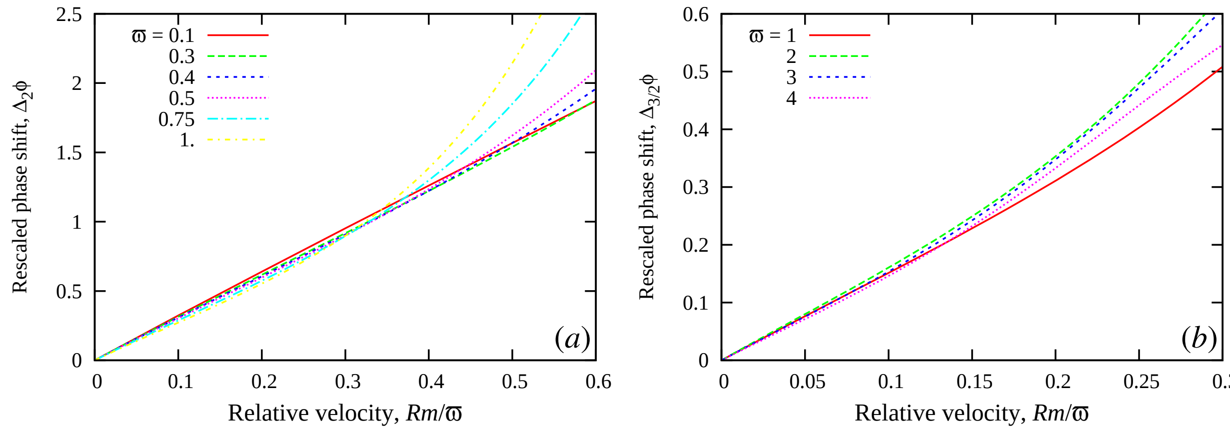

Figure 3: Rescaled phase shift $\Delta_2\varphi$(a) and $\Delta_{3/2}\varphi$ (b) between two observation points placed below the layer at $\pm x = 0.3$ versus the relative velocity $Rm/\bar{\omega}$ for $k = 1$ and various dimensionless frequencies $\bar{\omega}$.

conductivity. The following scaling by the square of the reference phase will eliminate conductivity

$$\Delta_2\varphi = \frac{\Delta_0\varphi}{\varphi^2}, \tag{4}$$

where $\Delta_0\varphi = \varphi_+ - \varphi_-$is the difference between the downstream and upstream phases which are denoted by φ_+ and φ_- respectively.

For the rescaled phase shift to be insensitive to σ it cannot be dependent directly on $\bar{\omega}$ or Rm, but must be a function of these control parameters such that σ is eliminated. We choose this to be $Rm/\bar{\omega} = V/(\omega H)$. Henceforth this ratio shall be referred to as the relative velocity.

Figure 3(a) shows that, when plotted against the relative velocity, the rescaled phase shift given by Eq. (4) has a weak dependence on $\bar{\omega}$ as long as $\bar{\omega}$ is low. For sufficiently low relative velocities, the variation of the rescaled phase shift with $\bar{\omega}$ is weak up to $\bar{\omega} \approx 1$. This range of low relative velocities depends on the locations of the observation points. The closer the observation point to the nodes ($x = \pm 0.5$) the shorter the range of relative velocities for which the rescaled phase difference remains invariant with $\bar{\omega}$. Figure 3(a) shows that far enough from the nodes the relationship between rescaled phase difference and relative velocity is invariant for a range of dimensionless frequency from 0.1 to 1, which corresponds to a change of an order of magnitude to the conductivity.

The scaling given in Eq. (4) only holds for low $\bar{\omega}$ where shielding effect causes the reference phase to vary non-linearly as $\sim \bar{\omega}^{1/2}$. This non-linearity is compensated for by taking the reference phase to the power of 3/2 instead of the square. It results in a second rescaled phase difference $\Delta_{3/2}\varphi = \Delta_0\varphi/\varphi^{3/2}$ which is plotted against the relative velocity in Fig. 3(b). It can been seen that the proportionality of the relative velocity and this rescaled phase difference is invariant for a greater range of $\bar{\omega}$.

Sending coil modelled by two straight wires

In this section we consider the case of an external magnetic field generated by a couple of straight wires. Figure 4(a) shows that the range of $\bar{\omega}$ where the phase sensitivity varies linearly is rather

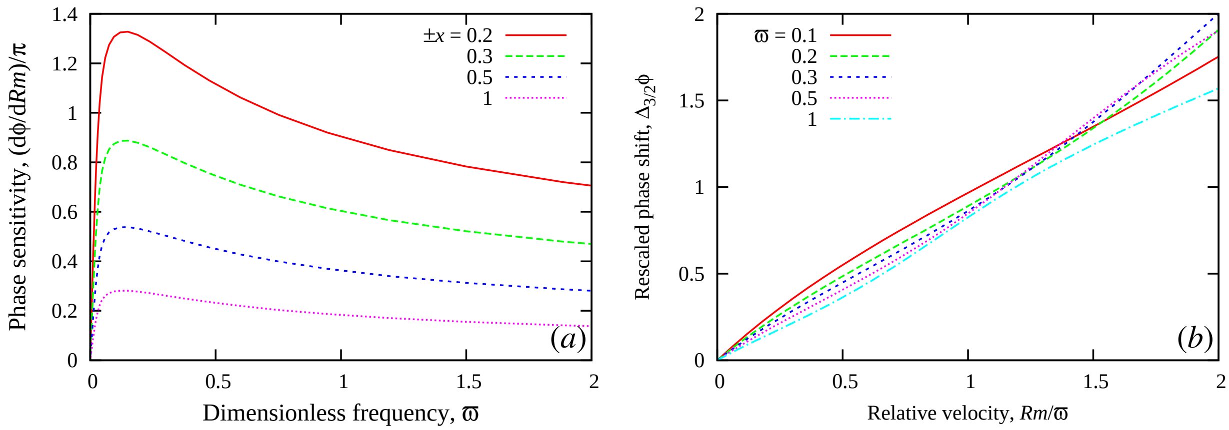

Figure 4: The phase sensitivity versus the dimensionless frequency $\bar{\omega}$ at various horizontal observation positions at below the layer (a) and rescaled phase shift $\Delta_{3/2}\varphi$ between two observation points placed below the layer at $\pm x = 1$ versus the relative velocity $Rm/\bar{\omega}$ for various dimensionless frequencies $\bar{\omega}$(b) for a sending coil modelled by two straight wires.

short As above this non-linearity is compensated by the rescaled phase shift $\Delta_{3/2}\varphi$ which is plotted in Fig. 4(b) with observation points placed symmetrically at $x = \pm 1$ As seen the rescaled phase shift depends essentially on the relative velocity whilst the variation with $\bar{\omega}$ is relatively weak.

4 Conclusions

We have demonstrated that the dependence of the flow induced phase shift measurements on the electrical conductivity of the liquid can be reduced by including the phase shift between the sending and receiving coils into the measurement scheme. It was shown that a strong reduction in the effect of conductivity is attainable by rescaling the measured phase difference by the reference phase shift between the sending coil and the upstream receiving coil. This rescaling is dependent on the nature of the variation of the phase shift with the frequency. At low frequencies, where this variation is linear, the reduction is achieved by rescaling with the square of the reference phase. At higher frequencies, the shielding effect results in non-linear variation of the reference phase with the frequency. This non-linearity can be compensated by a rescaling with the reference phase shift to the power of $3/2$ instead of the square.

References

[1] Priede, J.; Gerbeth, G.; Buchenau, D.; Eckert, S.: German patent DE 102006018623B4 (2008).

[2] Priede, J.; Buchenau, D.; Gerbeth, G.: Contactless Electromagnetic Induction Flowmeter For Liquid Metals. Meas. Sci. Technol. 22 (2011) 055402.

MHD PbLi LOOP AT IPUL

IVANOV S.,SHISHKO A., FLEROV A., PLATACIS E., ROMANCHUKS A., ZIK A.
Institute of Physics of University of Latvia, 32 Miera iela, Salaspils, LV-2169 LATVIA
E-mail: ivanov@sal.lv

Abstract: The report describes the MHD PbLi loop at IPUL, the equipment and operations. The loop operation parameters are the maximum magnetic field 5 T, the magnet bore 30 cm, PbLi temperature up to 400°C, the maximum PbLi flowrate with/without magnetic field 0.5/2 l/s, the maximum pressure head 0.48 MPa.

1. Introduction

Eutectic lead–lithium (PbLi) alloy has been proposed as a tritium breeder and coolant fluid in several liquid metal blanket concepts for future fusion power plants [1],[2],[3], including self-cooled lead–lithium (SCLL), dual-coolant lead–lithium (DCLL), helium-cooled lead–lithium (HCLL), water-cooled lead–lithium (WCLL), and Lead-Lithium Ceramic Breeder (LLCB) blankets. Various studies, both experimental and theoretical, were performed focusing on various aspects of PbLi flows [4],[5],[6],[7] and associated heat and mass transfer phenomena with and without magnetic field.

There are only a few magnetohydrodynamic (MHD) PbLi facilities currently in operation: a loop at the Institute of Physics in Latvia, several MHD PbLi loops DRAGON I–IV at the Institute of Plasma Physics of the Chinese Academy of Sciences, an ELLI loop at the Korea Atomic Energy Research Institute, and an MHD PbLi facility at UCLA (USA).

Some loop modifications were used in experiments with models of LLCB channel units (blanket concepts for DEMO of India) performed with Indian colleagues from the Institute of Plasma Research, Bhabha Atomic Research Center, Veermata Jijabai Technological Institute. [8, 9, 10].

Below we are described the special feature of the MHD facilities at IPUL such as the loop; the magnet; the pump and the flowmeter; pressure gauges; a system for measuring pressure drops in the channel; probes to register electric potential variations on the channel walls; loop heating and insulation; heat shielding of the magnet; a system of thermal stabilization; a system of melting and oxide removal; the procedure of the loop filling and pouring out; a sampling system and sampling data processing to minimize measuring errors; supplement devices – a system of vacuuming, inert gas supply and pressure release.

2. Magnet

For an experimental study of the flows of the conducting liquids in the strong magnetic field to order of IPUL is created the Cryogen-Free magnet system (Fig.1). The 5 Tesla Cryogen-Free magnet system (CFM) is one of a range of cryogen-free magnet systems produced by Cryogenic Ltd [11]. The system utilizes a single two stage cryocooler to produce temperatures of around 4.2Kelvin at the magnet. This magnet comprises a single winding designed to generate a homogeneous field up to 5 Tesla. The CFM has an 300 mm room temperature bore. The whole cryostat can also be rotated through 90 degrees in 10 degree intervals from the horizontal to the vertical position. The outer case of the CFM is manufactured from aluminium alloy. The room temperature bore is manufactured from stainless steel. The cryostat vacuum jacket has ports for the cryocooler, magnet current leads, magnet protection

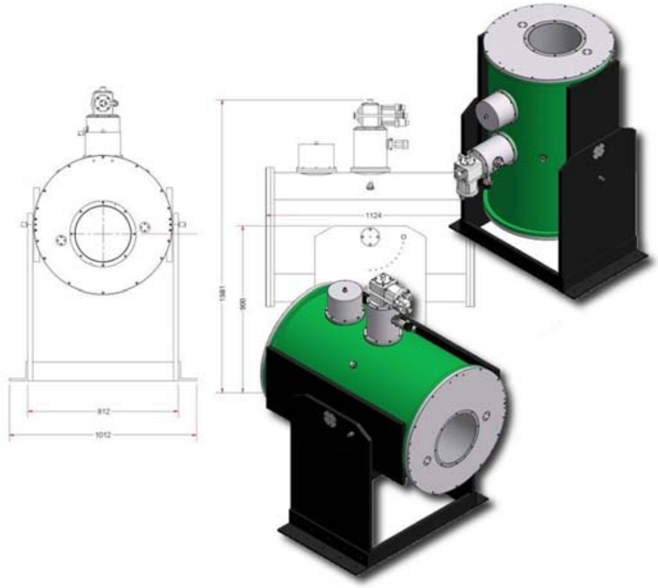

Figure 1: Cryogen-Free magnet system (CFM) produced by Cryogenic Ltd.

leads, instrumentation and evacuation. Radiation heat load to the magnet is minimized by means of a high purity aluminium radiation shield connected to the first stage of the cryocooler used in conjunction with multilayer super insulation between the room temperature outer wall and the shield. The radiation shield is attached to the first stage of the cryocooler and in operation cools to approximately 35-40K. The second stage is attached directly to the magnet and has a base temperature of <4.2K. High Temperature Superconductor (HTS) current leads are located and thermally linked (whilst electrically isolated) between the first and second stages of the cryocooler. Electrically resistive current leads extend from room temperature to the HTS lead sat the 1st stage. Temperature sensors are located throughout the system to monitor various internal components during the cooldown and subsequent operation of the system. Data from the thermometers may be displayed on a computer graphically and stored in data files for further analysis. Carbon ceramic sensors are used throughout the system as they are robust and have exhibit low magneto-resistance. The thermometers are wired to an 1l pin and 16 pin Fischer connectors located on the cryocooler turret. An overpressure valve for the cryostat is on the cryocooler turret.

3. Loop

The PbLi MHD experimental loop is a closed loop system and consists of a dump tank of capacity ~10 l, seven expansion tanks, one electromagnetic pump for circulation of liquid metal in the loop and one solenoidal super conducting magnet (SCM). A schematic of the loop is shown in Fig.2. The loop is made with circular pipe of 27.3 mm ID and has a total flow length of ~6.5 m (both way).The SCM produces an axial magnetic field within its central hole, which is ~1000 mm long and has a diameter ~300 mm. This puts restriction on the flow length of liquid metal in transverse magnetic field direction and hence the test section is accordingly designed to get maximum possible flow length perpendicular to magnetic field. The argon gas is used as a covered gas on all expansion tanks and is used to estimate the total liquid metal pressure drops in the loop. It is also used to initially fill the loop by pressuring the dump tank. The isothermal (T = 350^{o}C) PBLi loop was equipped with a rotational magnetic pump with permanent magnets [12], which is allowed to vary by wide range of the

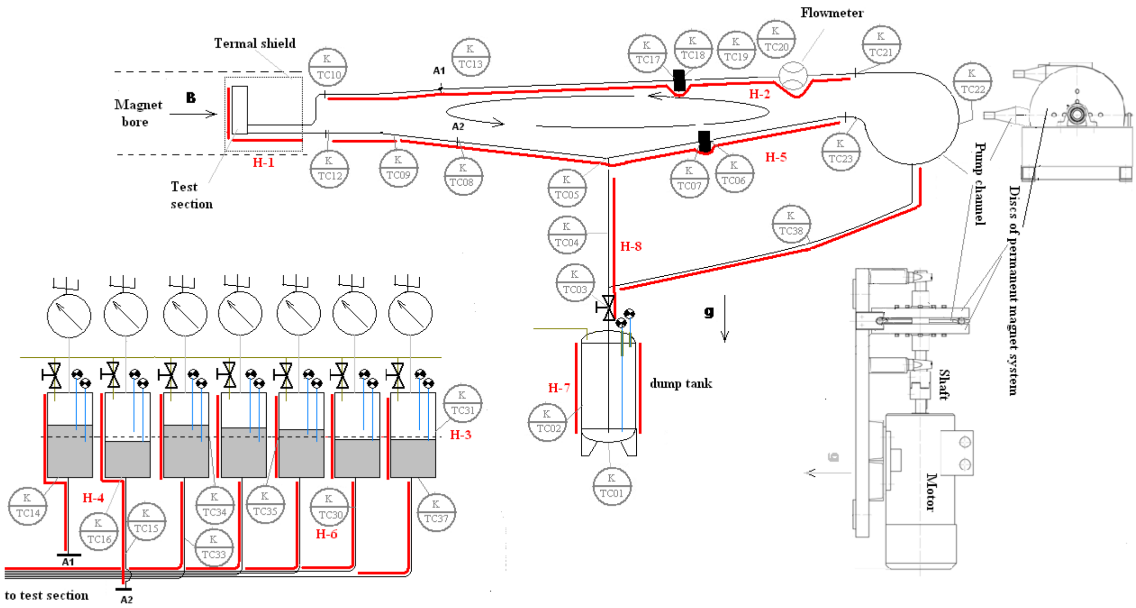

Figure 2: PbLi loop.

liquid metal flow rates (in both directions of the Pb17Li flow). A simplest Faraday flow meter gauge (probe) was installed in the loop. The prism-shaped duct of the probe (its cross-section of about 5 x 42 mm^2, length 65 mm) was formed by tapering the central part of the tube of D_{inner} = 28 mm of thickness 2 mm. The magnetic field B ~ 0.5 T in the probe duct was induced by an imposed symmetric C-shaped magnetic system with permanent magnets, the active surface of which was 60 x 60 mm^2. Pins for electric potential measuring were welded to the end walls in the middle of the prism-shaped duct.

The calibration of flowmeter is carried out on potential measurements on the walls of channel of the test section [13].

On the system of measurement of pressure drop. Local static pressures in the PbLi loop by the tubes of the selection of pressure are transferred to the expansion tanks, where in each tank is located its level of the free surface of PbLi. Above the free surface of PbLi is located inert gas argon, whose pressure is measured through the thin tubes cooled to room temperature by gas manometers GDH of 14 AN. Identical expansion tanks are fixed at one height, they have the identical *level of filling* (LF), are equipped with *indicators of level of fillings* (ILF). LF is located approximately in the middle of tanks. Expansion tanks are selected so as to in entire range of the measurements of pressures the level of free surface is located inside them. ILF has two contact devices that switch on with contact from PbLi. The level of the free surface of PbLi, with which operate the contact device is used for calculation the *initial gas volume* above PbLi, pressure in which is measured by pressure sensor. Two contact sensors make possible to determine the position of the free surface of PbLi within the limits of their levels. For achievement accuracy are necessary the following operations:

1) All valves connecting expansion tanks with the general gas-vacuum main are opened with the filling of PbLi loop. Entire system including loop, expansion tanks and pressure sensors is thoroughly heated to 600÷620 K and is evacuated.

2) By the pressure of inert gas by that supplied to the melting tank PbLi is rises into the loop and the expansion tanks to the contact only with the lower contact device of the ILF of each tank (with the turned-off electromagnetic pump);

3) After establishing the level of the free surface of liquid metal in the tank to the LF we know *the initial volume* V_{ig} of gas, utilized for calculating the correction for a difference in columns in the tanks. The effective height of the initial gas column is $h_{ig} = V_{ig}/(\pi R^2)$, where R - inside radius of tanks.

4) After the establishment of the level in all tanks at the LF overlaps the circuit leading to the melting tank, the identical pressure of inert gas of argon simultaneously into all measuring tanks will be given.

5) After the warming up of added argon in the expansion tanks they are disconnected from the general gas-vacuum main, are recorded the *initial pressures* P_{ig}, pump for the warming up of the badly heat-insulated parts of the loop (channels of pump and flow meter) is switched on and begin steps in the measurement of losses of pressure in the test section. After the installation of with the aid of the pump of the value the requisite flowrate, a pause for stabilization of regime are making, whereupon all values are recorded.

6) With data processing for determining the losses of pressure in test section the formula is used

$$\Delta p = p_{1fg} - p_{2fg} + \rho g \cdot 10^5 \cdot \left\{ h_{2ig} \cdot \frac{p_{2ig}}{p_{2fg}} - h_{1ig} \cdot \frac{p_{1ig}}{p_{1fg}} \right\}$$

To a gas pressure difference (from pressure sensors) the correction for columns difference in expansion tanks is added. This difference is of calculated from the pressures of gas (pressure of sensors). The value of this correction is less than 10%.

On the accuracy of the method of measurement of pressure drop. The gas volume above LF approximately 1 liter, 94% of volume of gas - in the expansion tank with stabilized temperature of 600±6 K, 6% - in the thin tube leading from the expansion tank (with temperature 600 K) to the pressure sensor (300±6 K). The accuracy of temperature stabilization in the tanks gives an error in measuring the correction of pressure on a change in the columns of PbLi connected with a change of the volume of gas in the tanks less than 1%. The conditions of heating expansion tanks and cooling of tubes are identical. Assuming that the free surface of PbLi after the correct operate ILF exactly in the middle between them we obtain the error in determination of the initial volume of gas connected with the accuracy ILF - 3%. Thus the error in determination of the volume of gas from the deviation of temperature and error in determination of initial volume in each tank is 4%. For a difference in the levels error is 8%. Since the correction of pressure connected with the difference of levels is less than 10% of the difference of gas pressures, then error connected with the computable correction is less than 0.8%. Error of the gas manometer (GDH of 14 AN) is 0.01 bar. With drop measurement into 1 bar the error of manometers is 2%. Accumulated error is less than 2.8%. With a pressure drop in 2 bars the error is less than 1.8%. With drop measurements of 0.2 bars the error is less than 10.8%.

4. Conclusion

The experience of the IPUL team in the design and manufacturing of EM pumps, in the production of eutectic lead–lithium alloy as well as the skills of mechanical, electrical and technological works makes it possible to quickly produce optimal equipment for the loops and systems for experiments. These skills allow to properly adjusting the loop for various tasks of the lead–lithium blankets.

In the near future, we plan to model the processes in the channels of a blanket with ceramic inserts and prepare experiments on heat/mass transfer in the PbLi flow channel in a strong magnetic field.

References

1. Overview of liquid metal TBM concepts and programs by C.P.C. Wong, J.-F. Salavy, Y. Kim, I. Kirillov, E. Rajendra Kumar, N.B. Morley, S. preprint of an invited paper to be presented at the 8th Int.Symp. on Fusion Nucl. Technology, in Heidelberg, Germany, September 30, 2007
2. Ellappan, R.; Jayakumar, T.; Suri, A.K..: Overview of TBM R&D activities in India.
3. Malang, S. ; Tillack, M., Wong, C.P.C.; Morley, N.; Smolentsev, S.: Development of the lead lithium (DCLL) blanket concept, Fusion Science and Technology 60 (2011) 249–256.
4. Smolentsev, S.; Moreau, R.; Abdou, M. : Characterization of key magnetohydrodynamic phenomena in PbLi flows for the US DCLL blanket, Fusion Engineering and Design 83 (2008) 771–783.
5. Buhler,L.: Three dimensional liquid metal flows in strong magnetic fields, Institut für Kern und Energietechnik Programm Kernfusion, FZKA-7412, September 2008.
6. Muller, U.; Buhler, L. : Magnetofluiddynamics in channels and containers, Springer-Verlag Berlin Heidelberg, 2001, ISBN 3-540-41253.
7. Hunt, J.C.R.: Magnetohydrodynamics flow in rectangular duct, Journal of Fluid Mechanics 21 (1965) 577–590.
8. Bhattacharyaya, R.; Patel, A.; Ellappan, R.; Swain, P. K.; Kumar, S. ; Ivanov, S.; Shishko, A.; Platacis, E. ; Ziks A. : Liquid metal MHD experimental activities for LLCB TBM development. Fusion Engineering and Design 88 (2013) 2244–2250.
9. Swain, P.K.; Satyamurthy, P.; Bhattacharyay, R.; Patel, A.; Shishko, A.; Platacis, E; Ziks, A.; Ivanov, S.; Despande, A.V. : 3D MHD lead–lithium liquid metal flow analysis and experiments in a test-section of multiple rectangular bends at moderate to high Hartmann numbers. Fusion Engineering and Design 88 (2013) 2848-2859.

10. Patel, A.; Bhattacharyay, R.; Swain, P.K.; Satyamurthy, P. ; Sahu, S.; Rajendrakumara, E.; Ivanov, S.; Shishko, A.; Platacis, E. ; Ziks, A.: Liquid metal MHD studies with non-magnetic and ferro-magnetic structural material. Fusion Engineering and Design 88 (2013) 2244–2250.

11. 5 Tesla Cryogen Free Magnet Job Number 2455. Manual.
12. Bucenieks, I.;Kravalis, K. : Characteristics of disk type electromagnetic induction permanent magnet pump. 7th International PAMIR Conference. France 2008.Vol.1 pp. 93-96.

13. Ivanov, S.; Shishko, A.; Patel, A.; Swain, P.K.; Bhattacharyay, R.; Sushil, K.; Satyamurthy, P. : Calibration of MHD flow meter in PbLi loop from the measurement of electric potentials on walls of the rectangular channel in a strong magnetic field, in: 8th PAMIR International Conference on Fundamental and Applied MHD, Borgo– Corsica – France, September 5–9, 2011.

NOVEL INDUCTION COIL SENSOR SYSTEM FOR CONTACTLESS INDUCTIVE FLOW TOMOGRAPHY

RATAJCZAK M., WONDRAK T., TIMMEL K., STEFANI F., ECKERT S.
Helmholtz-Zentrum Dresden-Rossendorf, P.O. Box 510119, D-01314 Dresden, Germany
E-mail: m.ratajczak@hzdr.de

Abstract: We present preliminary results of flow measurements for two different models of continuous casters using the contactless inductive flow tomography. In the first experiment we used a rectangular slab caster with a dominating two-dimensional flow structure under the influence of an electromagnetic brake. For the second experiment a round caster was used in which a magnetic stirrer around the submerged entry nozzle should create an unstable three-dimensional swirling flow.

1. Introduction

More than 95% of the world's steel is produced by means of continuous casting [1]. The steel flows from a tundish through a submerged entry nozzle (SEN) into the copper mould. The mould is cooled from the outside, so that the steel starts to solidify. A strand of steel with a liquid core is pulled continuously out of bottom of the mould. The flow structures in the mould are subject to many investigations, since they have a huge impact on the quality of the steel. The flow pattern in the melt can be influenced, e.g. by DC electromagnetic brakes (EMBr). The opaqueness and high temperature of the melt pose a huge problem to existing techniques for flow measurement. It is desirable to have a contactless method for measuring the structure of the velocity field of the melt. Contactless inductive flow tomography (CIFT) achieves this by reconstructing the flow in the mould from measurements outside the mould of the flow induced perturbations to an applied magnetic field [2].
In section 2 we give a short overview of the mathematical background for CIFT. After presenting the experimental setup in section 3 we show preliminary results for CIFT-reconstructed flows in the presence of a DC-magnetic braking field for a model of a slab caster in section 4. In part 5 we present preliminary results from experiments with a 3D-flow in a round caster.

2. Mathematical Background

A magnetic excitation field $\mathbf{B_0}$ is applied to the melt. From Ohm's law for moving conductors with the velocity **v** and electrical conductivity σ, one can calculate the induced magnetic field **b** at positions outside of the container using Biot-Savart's law. [2]

$$\mathbf{b}(\mathbf{r}) = \frac{\mu_0\sigma}{4\pi}\iiint_V \frac{[\mathbf{v}(\mathbf{r}')\times\mathbf{B}(\mathbf{r}')]\times(\mathbf{r}-\mathbf{r}')}{|\mathbf{r}-\mathbf{r}'|^3}dV' - \frac{\mu_0\sigma}{4\pi}\oiint_S \varphi(\mathbf{s}')\frac{\mathbf{n}(\mathbf{s}')\times(\mathbf{r}-\mathbf{s}')}{|\mathbf{r}-\mathbf{s}'|^3}dS' \tag{1}$$

The measurement of the electric potential φ would require a direct electrical contact with the melt. This can be overcome by calculation of the potential from Poisson's law for divergence free current distributions.

$$\varphi(\mathbf{s}) = \frac{1}{2\pi}\iiint_V \frac{[\mathbf{v}(\mathbf{r}')\times\mathbf{B}(\mathbf{r}')]\cdot(\mathbf{s}-\mathbf{r}')}{|\mathbf{s}-\mathbf{r}'|^3}dV' - \frac{1}{2\pi}\oiint_S \varphi(\mathbf{s}')\frac{\mathbf{n}(\mathbf{s}')\cdot(\mathbf{s}-\mathbf{s}')}{|\mathbf{s}-\mathbf{s}'|^3}dS' \tag{2}$$

In the integral equations (1) and (2), **B** is the superposition of the induced magnetic field **b** and the applied magnetic field $\mathbf{B_0}$. In metallurgical applications the magnetic Reynolds number Rm is much smaller than one, therefore the influence of **b** on $\mathbf{B}$ is negligible and we get a linear relation between **v** and **b**. The calculation of **v** from **b** is an ill-posed linear inverse problem, which can be solved using Tikhonov's regularization [2]. In our applications, the excitation field $\mathbf{B_0}$ is typically in the order of 2 mT at the position of the mould. The induced magnetic field **b** is in the order of 100 nT, but can be as small as a few Nanotesla. For the reconstruction of a mainly two-dimensional flow, like in a slab-caster, a single magnetic field is sufficient. For the reconstruction of a three-dimensional flow two magnetic fields in different directions need to be applied.

3. Experimental setup

0At the Helmholtz-Zentrum Dresden-Rossendorf a model of a continuous caster was created, called Mini-LIMMCAST (Mini Liquid Metal Model of Continuous Casting), see Figure 1 [3]. The eutectic alloy GaInSn is used instead of liquid steel. The GaInSn is pumped from a stainless steel catchment tank to the tundish. The stopper in the tundish is lifted and the GaInSn flows through an SEN into the mould. After passing a weir, which controls the position of the meniscus in the mould, the liquid metal flows back into the catchment tank. The flow rate can be adjusted by the position of the stopper rod. The mould and the SEN can be exchanged easily. We conducted experiments with rectangular slab caster and a round caster.

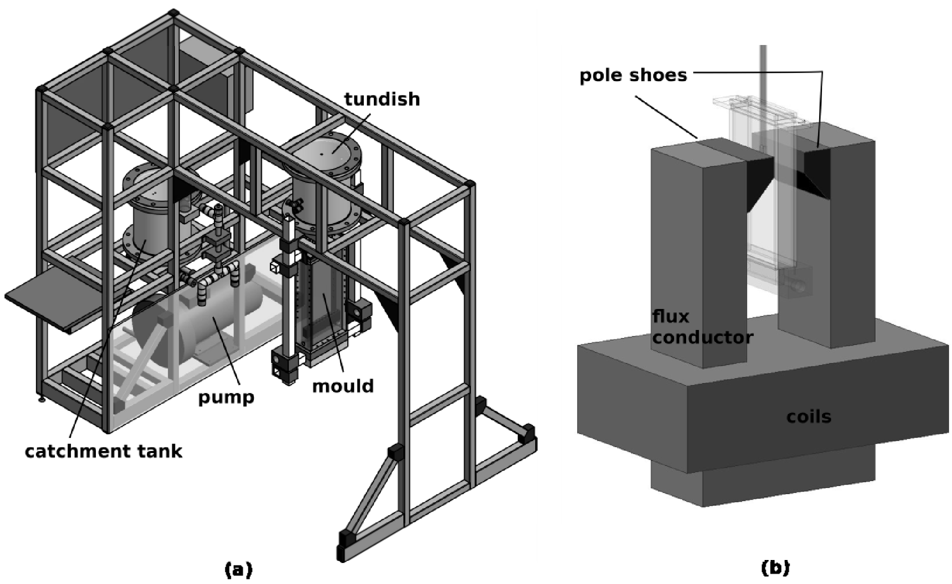

4. CIFT for a rectangular slab caster under the influence of an electromagnetic brake

Experiments were conducted with a slab caster mould with a rectangular cross section of 140 × 35 mm² and a height of 350 mm. The SEN had two oval shaped ports, pointing to the narrow faces of the mould [4]. In contrast to the previous measurements with Fluxgate probes, the induced magnetic field was measured with 2 × 7 cylindrical induction coils positioned to the narrow sides of the caster. Each induction coil has 340,000 windings with a conductor diameter of 25 µm. The signals from the coils were amplified between by 20 dB by differential amplifiers made by FEMTO before being digitalized by an AdWin 18-bit-Analog-Digital-

Converter system (ADC). Since the induction coils pick up the superposition of the excitation field and the induced field, it is crucial to have a highly linear signal processing system.
A ruler-type brake as depicted in Figure 0 (b) was used to generate a DC magnetic field with a field strength of up to 300 mT perpendicular to the wide faces of the mould and hence to the main flow direction. In this configuration the ferromagnetic parts (pole shoes) of the EMBr modify the applied and the induced magnetic field. Therefore, we measured the induced magnetic field in the presence of the pole shoes and reconstructed the velocity, before we switched on the DC magnetic field of the brake, as seen in Figure 1(b). It shows a typical double roll in accordance to previous measurements [4]. From UDV measurements [5], it is known that under influence of the brake the jet is moved upward and flows horizontally towards the narrow face of the mould. This can also be seen in the measurement of the induced magnetic field. The next task will be the reconstruction of the velocity for an active brake.

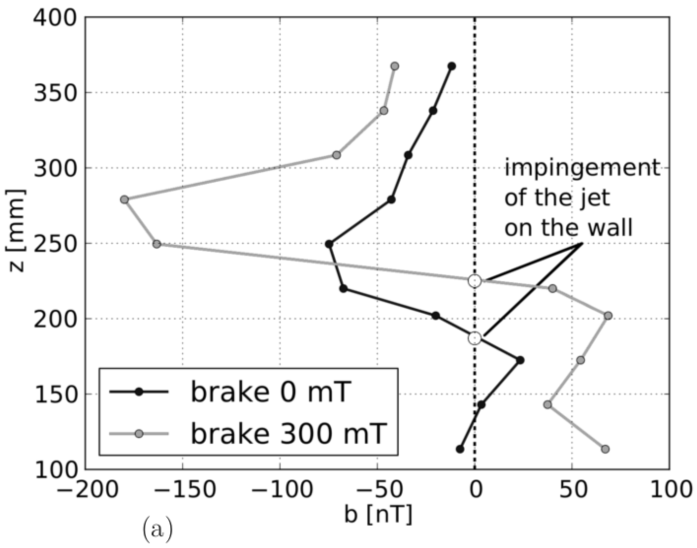

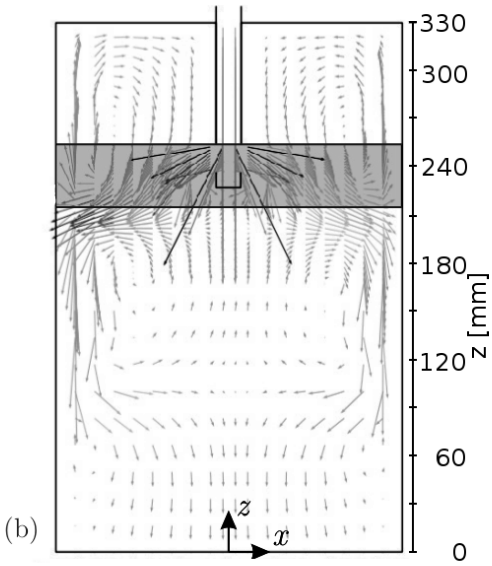

Figure 1: (a) Comparison of **b** along the left narrow face for active and non-active EMBr. (b) Reconstructed velocity field for non-active EMBr, showing a clear double-roll structure. The grey bar shows the position of the pole shoes.

5. CIFT for a round caster under the influence of a magnetic SEN-stirrer

In our cylindrical mould with a height of 800 mm and diameter of 80 mm, combined with a SEN with a downward faced outlet, a widening of the downstream and a poloidal upstream is expected. To influence the flow pattern we used a magnetic stirrer with two permanent magnets rotating around the SEN with a variable rotation rate of up to 50 Hz. The rotating magnetic field in the order of 500 mT gives rise to azimuthal velocity components in the SEN, which should create an unstable helical flow in the mould.

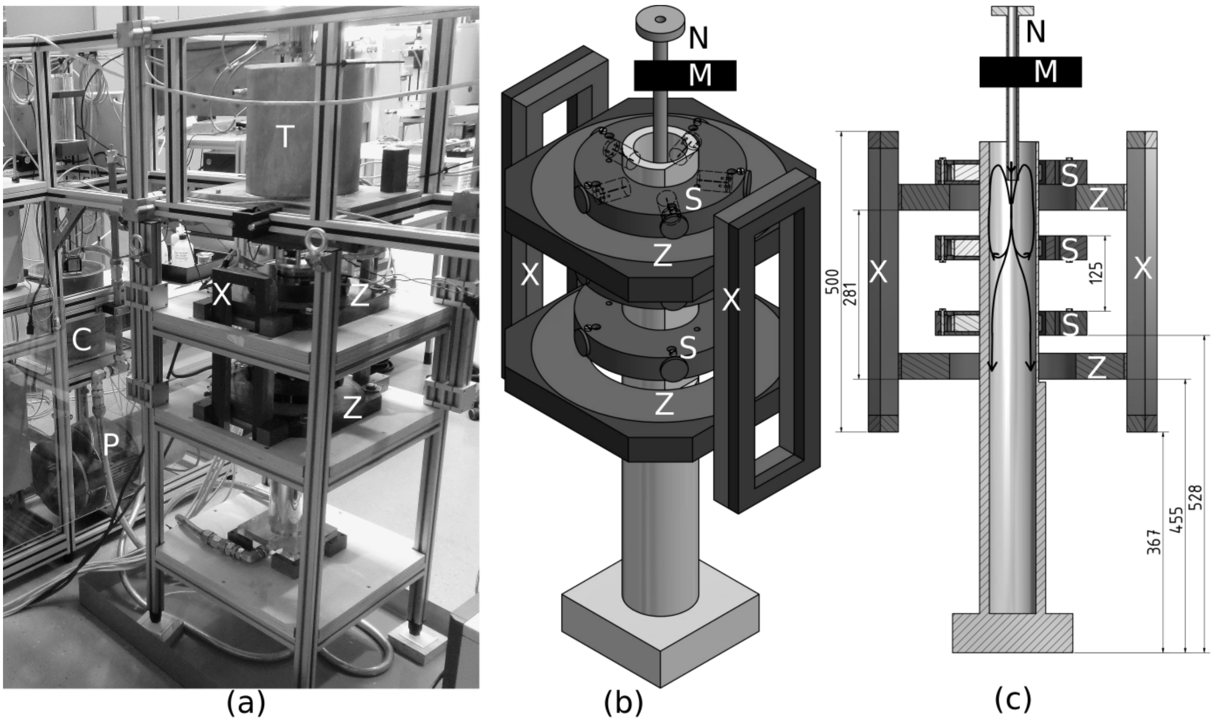

0
To reconstruct a three-dimensional flow, two magnetic fields in different directions are needed [2]. For a cylindrical mould, these can be a transversal and an axial field, $\mathbf{B_x}$ and $\mathbf{B_z}$, respectively. In contrast to the previous measurements on the demonstration facility [2], we are now able to measure the induced magnetic field for both applied magnetic fields simultaneously by choosing two different AC frequencies. For an adequate separation we used for $\mathbf{B_x}$ 7 Hz, and for $\mathbf{B_z}$ 3 Hz, thus avoiding the undesirable skin effect.
0We used 15 induction coils to measure the magnetic field. The induction coils were facing

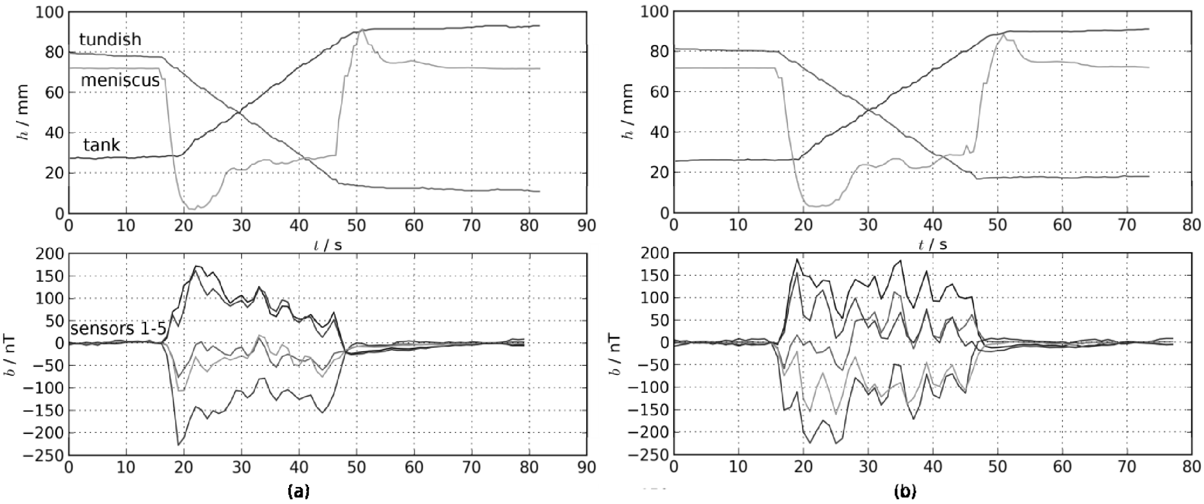

the surface of the mould and are placed in three 12.5 cm spaced z-positions close to the mould at the imaginary corners of a pentagon (see Figure 1). In addition to the induction coils used in the experiments with the EMBr, we are now able to use gradiometric coils which are measuring the radial gradient of the induced magnetic field due to the new 24-bit ADC system from LTT Tasler. As expected, gradiometric coils are much more robust to distortions of the environmental magnetic field, e.g. generated by the magnetic stirrer around the SEN.
Nevertheless, after digitizing the induced voltage from the pickup coils with 10 kS/s, digital filtering was needed if the stirrer was switched on. In this case a Chebyshev-inverse low pass filter of degree 5 was applied, before the amplitude of the sinusoidal signal was extracted using the quadrature demodulation (QDT). If the rotation rate of the stirrer was close to the frequency of the applied magnetic field, additional filtering in form of a moving Gaussian filter was required.
In order to evaluate the new measurement system for a cylindrical mould, we applied only $\mathbf{B_x}$ and measured the induced magnetic field for the experiments with active and non-active stirrer around the SEN. The recorded magnetic field at the uppermost sensor array is shown in Figure 4 for those experiments. In comparison to the measurement without stirrer (Figure 4a), the induced magnetic field in the case of an active stirrer is much more fluctuating which can be attributed to a more unstable flow in the mould (Figure 4b). The next task will be the implementation of the inversion algorithm for calculation of **v**.

6. Discussion and outlook

In this paper, we showed that CIFT is able to measure the induced magnetic field **b** of 100 nT in the presence of a 300 mT DC-magnetic braking field and ferromagnetic materials at a liquid metal model of a slab caster. Significant differences in **b** can be measured if the EMBr is used, indicating a changed flow pattern.
In addition we showed that measurement of **b** is possible when the flow in a round caster is influenced by a magnetic SEN stirrer. When the stirrer is switched on, the measured magnetic field shows increased variations, indicating fluctuations in the flow. The reconstruction of the velocity field and data analysis for two applied magnetic fields, needed for a full 3D-reconstruction, are yet to be done.

7. Acknowledgements. The research is supported by the German Helmholtz Association in frame of the Helmholtz-Alliance LIMTECH.

8. References

[1] World Steel Association: World Steel in Figures 2013.
[2] Stefani, F.; Gundrum, T.; Gerbeth, G.: Contactless Inductive Flow Tomography. Phys. Rev. E 70 (2004), 056306.
[3] Timmel, K.; Eckert, S.; Gerbeth, G.; Stefani, F.; Wondrak, T.: Experimental modelling of the continuous casting process of steel using low melting point metal alloys – the LIMMCAST program. ISIJ Int. 50 (2010), 1134-1141
[4] Wondrak, T.; Galindo, V.; Gerbeth, G.; Gundrum, T.; Stefani, F.; Timmel, K.: Contactless inductive flow tomography for a model of continuous steel casting. Meas. Sci. Techn. 21 (2010), 045402.
[5] Timmel, K.; Eckert, S.; Gerbeth, G.: Experimental and numerical modelling of the fluid flow in the continuous casting of steel. Eur. Phys. J.-Spec. Top. 220 (2013), 151-166

LIQUID METAL STIRRING BY ROTATING LOCALIZED MAGNETIC FIELD IN A CYLINDRICAL CONTAINER

RIVERO[1,2] Michel, CUEVAS[1] Sergio and RAMOS[1] Eduardo
[1]Instituto de Energías Renovables, Universidad Nacional Autónoma de México, 62580 Morelos, México
[2]Institut für Prozessmess- und Sensortechnik, Technische Universität Ilmenau, 98693 Ilmenau, Germany,
e-mail address of corresponding author: michel.rivero@tu-ilmenau.de

Abstract: Within the context of the Electromagnetic Processing of Materials, this paper addresses experimentally the electromagnetic stirring of a liquid metal. The analyzed problem consists in the flow of a shallow liquid metal layer (GaInSn) driven by an array of small rotating permanent magnets located at the bottom of a cylindrical Plexiglas container. The explored magnet arrays vary from one single magnet up to five magnets eccentrically located at a distance of 42.2 mm from the rotation axis. The radial velocity component was recorded using Ultrasound Doppler Velocimetry (UDV).

1. Introduction

The main idea behind electromagnetic stirring is to create a rotational Lorentz force in a conducting fluid by the interaction of electric currents with an external magnetic field [1, 2]. Electric currents can be produced by applying a potential difference between electrodes in contact with the fluid or can be induced in the fluid by time-varying magnetic fields. In metallurgical applications the use of AC magnetic fields at frequencies smaller than 60 Hz is more common. These fields can be produced by applying an AC current through specially located arrays of coils that result in different magnetic field distributions. Depending on the position in which coils are arranged and/or the way in which current is injected, we may obtain a Traveling Magnetic Field (TMF) [3], a Rotating Magnetic Field (RMF) [4] or a combination of both. The possibility of creating a Lorentz force that stirs the fluid in a nonintrusive way is very important for many technological applications. For instance, the quality of the ingots in the metallurgical industry greatly depends on the solidification process. The homogeneity in the distribution of elements in the melt plays an important role in the physical and chemical properties of the alloy. During solidification, segregation of elements occurs, that is, conglomeration of elements at the interfaces, namely, the free surfaces or the walls. Segregation can be avoided by using pulsed magnetic fields [5] where the understanding of spin-up flows is very important. We refer as spin-up flow to the transient flow produced by an increment in the velocity of a fluid initially at rest or in steady state. In this case, the increment in velocity is induced by an AC magnetic field. Experimental and numerical results [6, 7] show that these fields are able to generate vortices that avoid segregation at the boundary layers by throwing elements from the interfaces to the center of the container, enhancing the mixing process.

The principal disadvantage of magnetic fields produced through AC or DC current in coils is the high consumption of electric energy. An interesting alternative is the use of magnetic fields generated by compact and efficient magnet arrays requiring no continuous energy expenditure [8]. Permanent magnets can be fully competitive with electromagnets for applications in which magnetic fields are up to 2 T [9]. Although magnet arrays can give rise to static or variable, and uniform or non-uniform magnetic fields, fields with rapid spatial variation cannot be achieved using permanent magnets. Their limited operation temperature is also a drawback; however, advances in material science have produced magnets that can work up to 500 °C [10, 11] and cryogenic technology could be used to increase this operating temperature limit as well as the magnetic field within a cryogenic temperature range [12]. The use of magnet arrays for electromagnetic stirring applications has been barely investigated [13, 14] and, in part, this is one of the motivations of the present work. We experimentally analyze the stirring of a liquid metal (eutectic alloy GaInSn) in a cylindrical container, achieved through the rotation of permanent magnets that are small compared with radius of the container, and located close to its bottom.

2. Experimental setup

An experimental device, whose detailed description can be found in Ref. [15], was designed to investigate the influence of different magnet arrays on the electromagnetic stirring of a liquid metal in a cylindrical configuration. The setup consists in an acrylic cylindrical container with an inner diameter of 197.2 mm filled with the ternary alloy GaInSn up to a height 13 mm. At the bottom of the cylinder, different arrays that vary from one single magnet up to five Neodymium magnets (12.7 mm diameter) are placed in a rotating external acrylic disc driven by an electrical motor. The magnets are located equidistantly from each other on a circumference of a fixed radius (42.2 mm) centered on the rotation axis. The supporting base is attached to a synchronous pulley and mounted over a bearing. This subsystem is coupled by a timing belt to a smaller synchronous pulley mounted in a motor. Figure 1 shows a sketch of the electromagnetic stirrer. The rotation frequencies of the magnets vary from 0.4 to 7.3 Hz and in all cases presented here the rotation is in clockwise direction. The strength of the magnetic field at the bottom of the GaInSn layer is 0.065 T. In order to diminish the oxidation rate of the liquid metal, a 4 mm layer of hydrochloric acid solution was poured above it. The experiment consists in rotating a given array of small permanent magnets so that the time-varying magnetic field induces Lorentz forces that are able to stir the liquid metal. It is of particular interest to determine if small disturbances produced by the rotation of localized magnets originate a global stirring of the liquid metal. The flow was characterized using the UDV technique, placing the ultrasound transducer outside the cylinder perpendicular to the container's wall so that the transducer axis points radially to the center of the cylinder at a height of 5 mm from the bottom of the GaInSn layer, and allows to measure the radial velocity component as function of space and time.

Figure 1: Sketch of the electromagnetic stirrer in cylindrical configuration.

3. Results

The measured signal of velocity shows repetitive patterns and, under certain conditions (i.e. characteristic rotation frequencies) oscillations of the free surface appear. In order to determine the characteristic frequencies of such phenomena, the Fast Fourier Transform

(FFT) analysis was applied to the velocity signal at every measured point. With these results we were able to find not only the characteristic frequencies, but also to discern approximately the global flow patterns. Although not presented here, the observed patterns indicate that during some time intervals the flow goes to the center of the cylinder and in a later time interval the fluid is driven to the cylinder walls [15]. Figure 2 shows the maximum value of the power spectra for all the analyzed penetration depths (i.e. positions along the ultrasound beam) corresponding to the flow generated by two magnets located at 42.2 mm from the cylinder axis, rotating at a frequency of 1.75 Hz. In this figure, the results of five different experiments are superposed so we can assure experimental reproducibility. A similar behavior was observed for the different magnet arrays and rotation frequencies explored. It is important to mention that experiments 4 and 5 in Figure 2 were performed without the hydrochloric acid solution layer. We observe that this layer does not affect significantly the dynamics of the flow. The experiments for all the explored magnet configurations and rotation frequencies show velocity patterns whose characteristic frequencies are always smaller than 0.6 Hz. In addition, it was observed that under certain experimental conditions the system resonates and its surface begins to oscillate at frequencies higher than 1 Hz. In order to distinguish all the characteristic frequencies of the flow, the plots were divided in two sections: one from 0 to 0.65 Hz approximately, where the bulk flow frequency (BFF) and its harmonics appear, and from 0.65 to 7 Hz, corresponding to the free surface oscillation (FSO) frequency. In Figure 2, the first peak corresponds to the bulk flow frequency while the second one represents its first harmonic. In turn, the peak in the second section of the plot (frequencies > 0.5 Hz) corresponds to the free surface oscillation frequency (FSOF). As we are only showing the maximum of the power spectrum along the whole penetration depth, it must be pointed out that the bulk flow frequency is not observed nor in the central region of the container (80 - 120 mm) neither close to the cylinder walls (0-30 mm and 170-200 mm); while the FSOF is observed all along the measured line since a backward and forward movement is produced.

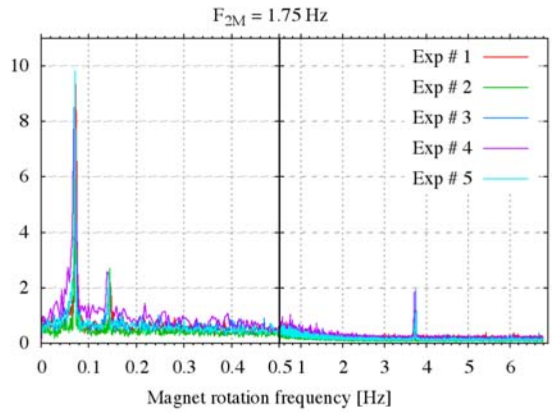

Figure 2: Maximum values of power spectra for the experiments performed with two magnets rotating at a frequency of 1.75 Hz. Note that the frequency axis was shrunk in order to show the peak at 3.8 Hz.

Figure 3 shows the bulk flow frequency and free surface oscillation frequency as a function of the magnet rotation frequency for all experiments with all magnet arrays when magnets are placed at 42.2 mm from axis. We observe an increase in the characteristic bulk flow frequencies as the magnet rotation speed is increased. We notice that as we increase the number of magnets the BFF does not grow linearly. This can be seen by defining the normalized frequency as the BFF divided by the number of magnets. For a magnet rotation frequency (MRF) of 6.06 Hz and one magnet, the normalized frequency is 0.115 Hz, and it decrease for two magnets to 0.093 Hz. This value increases to 0.136 Hz when three magnets are used and diminishes up to 0.105 Hz for five magnets. Then for an array of two magnets, we have a local minimum and for three magnets a maximum. The latter can be considered as a global maximum due to the fact that if we increase the number of magnets and all of them have the same orientation, the distribution of the total magnetic field will tend to diminish the inhomogeneities in the direction of rotation of the array (the resulting magnetic field will tend to that produced by a ring shaped magnet) and eventually a more homogeneous and less intense motion will be produced. We should remember that the maximum number of magnets that we can use is limited by the shape, size and arrangement of the magnets, as well as the rotation radius. Finally, if we use a disordered array of magnets (that is, with not equidistant location and unsorted magnetic pole orientation), the resulting bulk flow frequencies will be smaller than the corresponding values obtained with an ordered array. In addition, if the magnets are close to each other the resulting effect will be similar to the produced by a smaller number of magnets. When we look at the FSO frequencies produced by this disordered array, we observe that depending on the MRF the free surface oscillates at frequencies that follow the tendency lines of other ordered arrays, in this case arrays of 1, 2 or 4 magnets (see Figure 3).

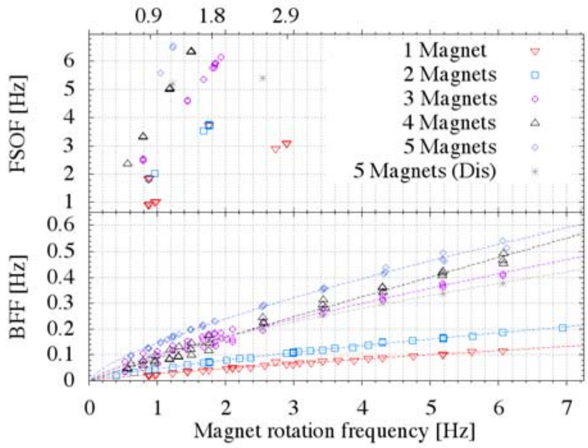

Figure 3: Bulk flow frequency (BFF) and free surface oscillation frequency (FSOF) as a function of magnet rotation frequency for all magnets arrays rotating at 42.2 mm from the axis. The notation (Dis) corresponds to the disordered array of 5 magnets.

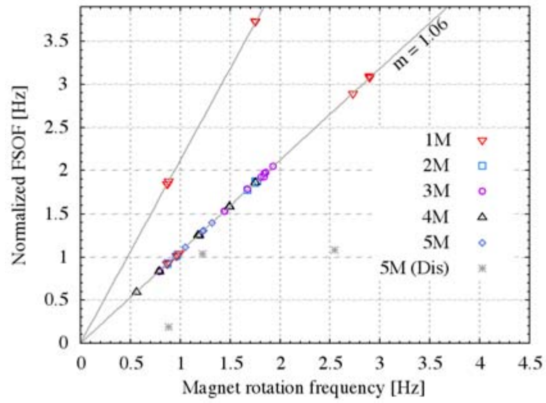

Figure 4: Normalized free surface oscillation (FSO) as function of magnet rotation frequency. Linear fitting lines correspond to $y = mx$, and $y = 2mx$, where $m = 1.06$ is the slope of the fitted line.

Figure 4 shows the normalized FSOF as a function of the magnet rotation frequency. We observe that the majority of the normalized frequencies corresponding to ordered arrays, adjust to a linear fitting with a slope $m = 1.06$. Additionally, it is found that for the explored rotation radius of 42.2 mm only one harmonic appears when one magnet is used. It is important to notice that as the number of magnets is increased the maximum MRF at which

FSO occurs decrease. So, in general we can say that as MRF is increased, the characteristic bulk frequencies also grow. But bulk frequencies do not grow linearly as the majority of the FSOFs do. From Fig. 4, we may conclude that most of the experiments in which oscillations of the free surface occur have a linear behavior in the sense that when we plot the normalized FSOF of all experiments, if exist, they fit to the same tendency line.

4. Conclusion

The experimental analysis of an electromagnetic stirring device based on a rotating localized magnetic field was carried out. The flow takes place in a cylindrical container where a shallow liquid metal layer is driven by Lorentz forces induced in the fluid by the rotation of different arrays of small permanent magnets. The goal of this study was, on the one hand, to explore if small perturbations produced by the rotation of localized magnetic fields can produce a global stirring of the liquid metal and, on the other, to characterize the flow quantitatively. Fast Fourier Transform analysis of the velocity signals obtained with the UDV along a diameter of the cylindrical container was used to determine characteristic frequencies of the flow structures. These experiments showed that the motion of localized magnetic fields in different configurations is able to produce a global perturbation on the bulk and free surface of the liquid metal. Future work will be focused on the characterization of the flow patterns produced by the different arrays of magnets and to determine the characteristic flow regions where energy is mainly transferred.

Financial support from CONACYT, Mexico, through Project 131399 is acknowledged.

5. References

[1] Davidson, P. A. : An introduction to magnetohydrodynamics. UK, Cambridge University Press (2001).
[2] Moffatt, H. K.: Electromagnetic stirring. Phys. Fluids A, 3 (1991), 1336-1343
[3] Lantzsch, R.; Galindo, V.; Grants, I.; Zhang, C.; Pätzold, O.; Gerbeth, G.; Stelter M.: Experimental and numerical results on the fluid flow driven by a traveling magnetic field. J. Crystal Growth, 305 (2007), 249-256.
[4] Grants, I.; Gerbeth, G.: Experimental study of non-normal nonlinear transition to turbulence in a rotating magnetic field driven flow. Phys. Fluids, 15 (2003), 2803-2809.
[5] Eckert, S.; Nikrityuk, P.A.; Rabiger, D.; Eckert, K.; Gerbeth, G.: Efficient melt stirring using pulse sequences of a rotating magnetic field: Part I. Flow field in a liquid metal column. Metall. Mat. Trans. B, vol. 38 (2007), 977-988.
[6] Ungarish, M.; The spin-up of liquid metal driven by a rotating magnetic field. J. Fluid Mech., 347 (1997), 105-118.
[7] Nikrityuk, P. A.; Eckert, S.; Eckert, K.: Spin-up and spin-down dynamics of a liquid metal driven by a single rotating magnetic field pulse. European J. Mech. B/Fluids, 27 (2008), 177-201.
[8] Müller, K.-H.; Krabbes, G.; Fink, J.; Gruss, S.; Kirchner, A.; Fuchs, G.; Schultz, L.: New permanent magnets. J. Magnetism Magnetic Mat., 226-230 Part 2 (2001), 1370-1376.
[9] Coey, J.M.D.: Permanent magnet applications. J. Magnetism Magnetic Mat., 248 (2002), 441-456.
[10] Liu, J. F.; Ding, Y.; Zhang, Y.; Dimitar, D.; Zhang, F.; Hadjipanayis, G. C.: New rare-earth permanent magnets with an intrinsic coercivity of 10 kOe at 500 °C. J. Appl. Phys., 85 (1999), 5660-5662.
[11] Peng, L.; Yeng, Q.; Zhang, H.; Xu, G.; Zhang, M.; Wang J.: Rare earth permanent magnets Sm_2 (Co, Fe, Cu, $Zr)_{17}$ for high temperature applications. J. Rare Earths, 26 (2008), 378 382.
[12] Benabderrahmane, C. et al: Development of a 2 m $Pr_2Fe_{14}B$ Cryogenic Permanent Magnet Undulator at SOLEIL, Journal of Physics: Conference Series 425 (2013)
[13] Wang, X.D.; Li, T.J.; Fautrelle, Y.; Dupouy, M.D.; Jin, J.Z.: Two kinds of magnetic fields induced by one pair of rotating permanent magnets and their application in stirring and controlling molten metal flows. J. Crystal Growth, 275 (2005), e1473 e1479.
[14] Bojarevics, A.; Beinerts, T.: Experiments on liquid metal flow induced by a rotating magnetic dipole. Magnetohydrodynamics, 46 (2012), 333-338.
[15] Rivero, M.: Experimental study of flows in electromagnetic stirring and pumping devices. PhD Thesis, National Autonomous University of Mexico, 2012.

APPLICATION OF MAGNETICALLY DRIVEN TORNADO-LIKE VORTEX FOR STIRRING FLOATING PARTICLES INTO LIQUID METAL

GRANTS Ilmārs, RAEBIGER Dirk, VOGT Tobias, ECKERT Sven, GERBETH Gunter
Helmholtz-Zentrum Dresden-Rossendorf, PO Box 510119, 01314 Dresden, Germany
E-mail address of the corresponding author: i.grants@hzdr.de

Abstract: A tornado-like vortex is driven by magnetic body forces. A continuously applied rotating magnetic field provides source of the angular momentum. A pulse of a much stronger travelling magnetic field drives a converging flow that temporarily focuses this angular momentum towards the axis of the container. A highly concentrated vortex forms that produces a funnel-shaped surface depression. The ability of this vortex to entrain floating unwetted particles in liquid metal is investigated experimentally.

1 Introduction

The magnetic bar stirrer is a useful piece of standard laboratory equipment. It creates a whirlpool that somewhat resembles a tornado [1] and efficiently entrains floating powder into the liquid. The mechanics of such a flow is largely based on a simple principle. Due to angular momentum conservation the circular motion of a fluid accelerates towards the center of a converging flow. Such converging and spinning liquid metal flow may be generated by alternating magnetic fields in a fully contact-less way. A converging flow may be created by the travelling magnetic field (TMF). The angular momentum, in turn, can be injected by the rotating magnetic field (RMF). To avoid interference of both fields their frequencies should be considerably different [2]. At certain conditions when the TMF induced magnetic force is about 100 times stronger than the RMF force, this combination produces a quasi-steady concentrated vortex [2] that somewhat resembles atmospheric vortices. This vortex, however, remains blurred and does not develop a pronounced funnel on the surface. It appears not nearly as effective in entraining floating particles as the magnetic bar stirrer vortex. During the spin-up phase, however, a reproducible sharp deep vortex funnel is observed. The difference from the established flow is explained by a relatively low level of turbulence during the spin-up [3] that enables a much higher degree of vortex concentration.

Aim of the current experiment is to assess suitability of such transient flow for the purpose of stirring floating particles into the melt. If successful, such approach may be used in the technology of metal matrix composite casting.

2 Background

2.1 Magnetic forces

Let us consider a cylinder of liquid metal with constant electric conductivity σ, kinematic viscosity ν and density ρ inserted in uniform rotating and traveling magnetic fields with flux densities $B_{R,T}$ and angular frequencies $\omega_{R,T}$, respectively. The axial wave number of TMF is κ. Under the common low-frequency and low-induction conditions the RMF and

TMF induce magnetic body forces with well-known distribution [2]. The RMF induces a purely azimuthal force whose time-averaged value is given by

$$F_\phi = \sigma\omega_R B_R^2 r f(r,z), \tag{1}$$

where $f(r,z)$ is a dimensionless shape function. This force drives a rotating flow with secondary meridional circulation [4]. The dimensionless force magnitude is given by the magnetic Taylor number $Ta = \sigma\omega_R B_R^2 R_0^4/(\rho\nu^2)$. The TMF creates an axially directed force whose time averaged value is given by [2]

$$F_z = 0.25\sigma\omega_T B_T^2 \kappa r^2. \tag{2}$$

Depending on the direction of the TMF wave vector, the liquid metal at the outer part of the container is pushed up- or downwards that drives an axi-symmetric flow torus. The dimensionless magnitude of this force is $F = \sigma\omega_T B_T^2 \kappa R_0^5/(2\rho\nu^2)$. The magnetic flux density of both magnetic fields B_R and B_T in equation (1) and (2), respectively, is given in terms of the root mean square value. The magnetic force expressions (1,2) assume a low frequency of the respective alternating magnetic field. This is true if the shielding factor $S = \mu_0\sigma\omega_T R_0^2 < 3$, where μ_0 is the magnetic permeability [4]. This is fulfilled in our experiment.

2.2 Properties of transient tornado-like vortex

A pulse of a strong upwards directed TMF initiates a converging flow at the top surface. Because of the angular momentum conservation the azimuthal velocity attains a $\propto 1/r$ profile in the outer inviscid part of this converging flow. Being strong enough the flow produces a surface deformation on the metal surface. Depending on the RMF strength the deformation has the shape of a single sharp funnel or multiple smaller depressions rotating about a common centre (Fig. 1). This flow pattern is robust and reproducible during the initial spin-up only. As flow matures, the funnel breaks down. The initial spin-up typically lasts a few seconds [3]. There are two distinct regimes controlled by the strength of the RMF. For a weak RMF the peak swirl is much weaker than the TMF driven meridional flow and it increases with Ta while the vortex width stays invariant. For a strong RMF the peak swirl intensity stays nearly constant approaching that of the meridional flow velocity while the vortex diameter increases with Ta. The maximum swirl concentration is, thus, reached on the border between those regimes at a certain "optimum" RMF strength Ta_{tr}. This threshold value is a function of the TMF intensity F and it depends strongly on the type of boundary conditions at the top surface. For a free top surface $Ta_{tr}/F \propto F^{-0.625}$ while for a solid cover $Ta_{tr}/F \propto F^{-0.4}$ (Fig. 12b in [3]).

3 Experiment

3.1 Magnetic system

The inductor of combined magnetic fields KOMMA [5] has been used. At the bottom of the inductor bore there is a built-in cooling plate for directional solidification. The inductor is designed for the generation of rotating magnetic fields (RMF) and axially travelling magnetic fields (TMF) whereby the field parameters B_R, B_T, ω_R and ω_T can be controlled independently. The generation of the RMF is realized by a radial arrangement of six coils, whereby opposing coils are connected as pole-pairs. The TMF is generated

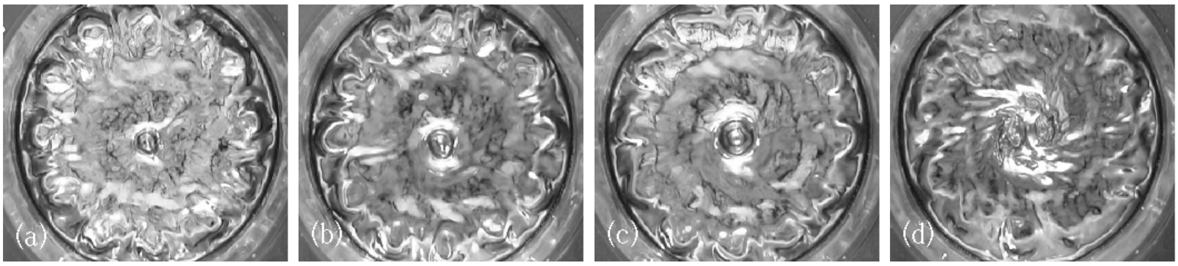

Figure 1: Snapshot of the free surface of GaInSn in a 170 mm container with a magnetically driven tornado-like vortex at $t = 1.5$ s [3]. The TMF strength is $F = 6.6 \times 10^9$; the relative RMF strength is $Ta/F = 10, 14, 25$ and 50×10^{-4} for (*a–d*), respectively.

inside a line-up of six coils at an equal distance of $h = 0.035$ m, yielding a wave number of $\kappa = 2\pi/6h = 30$ m^{-1}. The frequency of the RMF is fixed to $\omega_R/2\pi = 50$ Hz and the TMF frequency is $\omega_T/2\pi = 100$ Hz in this study. Diameter of the inductor's bore is 70 mm. The TMF coils are fed by three-phase alternating current from three power amplifiers coupled to high current transformers. That allows to minimize the ramp-up time of the TMF pulse.

3.2 Particle insertion procedure

Tin is molten and overheated to 320 °C in a stainless steel mould of 50 mm diameter. Height of the molten metal is about 50 mm. Oxides and other impurities are mechanically removed from the surface. The mould is then inserted in the inductor with the RMF continuously running. After about 30 s the TMF pulse is applied and simultaneously the particles (45 μm diameter Al_2O_3 spheres) are dropped on the surface. Duration of the TMF pulse is 10 s. After the pulse the TMF induction is reduced by a factor of 1/3. The metal is then solidified under continuous RMF and TMF.

3.3 Estimates of the magnetic field strength

Formation of a sharp surface depression has been observed [3] for a value of the dimensionless parameter

$$\mathcal{F} = \frac{\sigma\omega_T B_T^2 R_0^2}{2(\rho g s)^{1/2}}\kappa R_0 = F\frac{\nu^2}{g h_c R_0^2} > 3, \tag{3}$$

where $h_c = (\gamma/\rho g)^{1/2} \approx 2.5$ mm is the capillary length, g is the gravity acceleration and γ is the surface tension. To be on the safe side, let us require $\mathcal{F} = 10$ that produces $F \approx 1.6 \times 10^8$ for tin. The magnetic field induction can now be estimated as $B_T = 75$ mT at $\omega_T/2\pi = 100$ Hz for a $2R_0 = 50$ mm mould. The following physical properties of liquid tin are assumed: $\rho = 7 \times 10^3$ kg/m^3, $\sigma = 2 \times 10^6$ S/m, $\nu = 10^{-6}$ m^2/s and $\gamma = 0.5$ N/m. Depending on the boundary conditions on the top surface, the calculated optimum RMF strength Ta_{tr} varies between 0.7×10^5 ($B_R \approx 1.4$ mT) for free-slip and 0.53×10^6 ($B_R \approx 3.9$ mT) for no-slip [3].

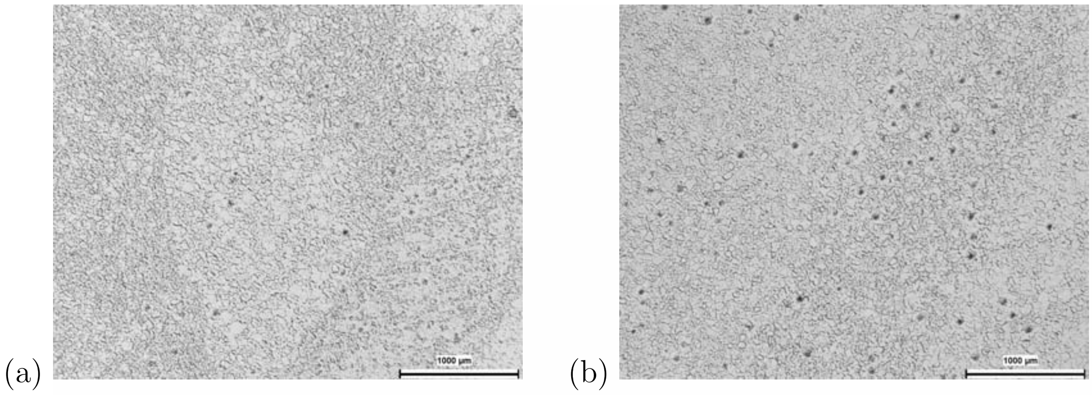

Figure 2: Microscopic views of polished tin samples with Al_2O_3 inclusions. Frame area is 12.5 mm^2.

4 Results and discussion

The oxide layer quickly formed on the surface of the molten tin creating an uncertainty in the boundary conditions, which strongly influence the optimum RMF induction. Therefore, we first observed the surface deformation without adding particles. The oxide layer turned out to be rigid enough to resist the initial RMF driven flow. Though, the layer was broken by the spin-up vortex shortly after the beginning of the TMF pulse. The pulse only caused a significant surface deformation, when the RMF strength was at the upper limit of estimates $B_R \approx 4$ mT corresponding to the “optimum” for the no-slip boundary conditions. That shows that the boundary conditions influence the spin-up vortex basically through the initial conditions. In case of free-slip the upper layer of the initial flow caries considerably more angular momentum than in case of no-slip. Role of the boundary conditions appears limited to the initial state, since the shift to nearly free-slip conditions during the spin-up phase did not reduce the “optimum” RMF.

The spin-up funnel had an estimated depth of 2 to 3 cm and a duration of about two seconds. That was enough to entrain a volume of about 3 ml of particles dropped on the surface at the beginning of the pulse. This volume, however, survived the submergence and popped out of the metal immediately after the TMF pulse. This behavior may have been caused by an oxide film that enwraps the particles. Another cause could be relatively small size of the mould resulting in an insufficient level of turbulence and a too bulky funnel tip as compared to the entire flow. A better dispersion may be expected in a larger mould.

The oxide film may be prevented by an appropriate flux. The flux, however, will wet the particles and, thus, hold them trapped. This may be avoided by the following approach. In another attempt to stir the particles into the melt we alloyed them mechanically with tin into pellets. For this purpose we mixed one part of aluminum oxide particles with five parts by mass of tin powder (45μm). The powder mixture was then mechanically pressed into 8 mm thick discs. Density of these disks was 5.2 kg/m^3 that implies porosity of about 20%. The disks were cut into pieces of a characteristic size 4 mm. The pellets (30 g) were dropped on the surface of the melt at the beginning of the TMF pulse. The spin-up vortex entrained and kept them submerged for the entire duration of the pulse. A lesser part of the pellets appeared on the surface after the pulse. The sample was solidified under a continuous TMF of $B_T = 25$ mT and an RMF of $B_R = 6$ mT. Some of the submerged pellets were found at the side edge of the solidified ingot.

Apparently, they have been held attached to the mould wall by surface tension forces. Figure 2 shows two microscopic views of a section of the obtained ingot. By counting individual particles in these figures the average inter-particle distance is estimated as 0.45 mm. That corresponds to a particle volume fraction of 0.05%, at most. Thus, no more than 5% of the particles initially in the pellets were mixed into the metal. This poor performance is likely connected to the persistence of pellets even when continuously submerged. The melting time of a pellet with radius r_p is estimated as $r_p^2\rho\Lambda/(\Delta T\lambda) \ll 10$ s, where $\Lambda = 59$ kJ/kg is the heat of fusion and $\lambda \approx 50$ W/Km the heat conductivity of tin. Thus, the metal contained in pellets should have been molten during the TMF pulse. Apparently, the pellets were held together by capillary forces forming a mixture of microscopic liquid tin droplets, aluminium oxide particles and gas voids. That would not happen if each separate particle was fully enveloped by metal. Thus, a reduced porosity and increased metal volume fraction in pellets may facilitate their disintegration.

5 Summary

Floating oxide particles are submerged into liquid metal by a spin-up vortex. Though, the particle pocket survives the high velocity flow in our experiment with a relatively small melt volume. Initial mechanical alloying with the metal facilitates particle dispersion which still remains poor in the current test. It is suggested that surface protection by flux and use of denser pellets with a lower oxide particle content may improve the efficiency of their dispersion.

Acknowledgement

Samples were kindly prepared by Mrs. M. Rossner from Division of Structural Materials at Helmholtz-Zentrum Dresden-Rossendorf. Financial support from the Helmholtz Association in form of the Alliance “Liquid Metal Technologies” is gratefully acknowledged.

References

[1] Halász, G., Gyüre, B., Jánosi, I. M., Szabó, K.G., & Tél, T. : Vortex flow generated by a magnetic stirrer. American J. Phys. 75 (2007) 1092–1098.

[2] Grants, I., Zhang, C., Eckert, S. & Gerbeth, G. : Experimental observation of swirl accumulation in a magnetically driven flow. J. Fluid Mech. 616 (2008) 135–152.

[3] Vogt, T., Grants, I., Eckert, S. & Gerbeth, G. : Spin-up of a magnetically driven tornado-like vortex. J. Fluid Mech. (2013) 641–662.

[4] Davidson, P. A. : Swirling flow in an axisymmteric cavity of arbitrary profile, driven by a rotating magnetic field. J. Fluid Mech. 254 (1992) 669–699.

[5] Willers, B., Eckert, S., Nikrityuk P. A., Rabiger,D., Dong, J., Eckert, K., Gerbeth, G. : Efficient Melt Stirring Using Pulse Sequences of a Rotating Magnetic Field: Part II. Application to Solidification of Al-Si Alloys. Metall. and Mat. Trans. B 39B (2008) 304–316.

SOME METHODS FOR ELECTROVORTEX FLOWS CONTROL IN DC ARC FURNACES WITH BOTTOM ELECTRODE

KAZAK O.
Department of Physics and Technology, Donetsk National University
24 University str., Donetsk, Ukraine
E-mail address of corresponding author: olegkazak@yandex.ru

Abstract: The paper is devoted to simulation of vortex flows in the DC electric arc furnaces with different temperature and positions of the bottom electrode. The electromagnetic, temperature and hydrodynamic distribution parameters are obtained. The shear stress on the fettle area is offered as a criterion for the estimation of vortex flows influence on the increased wearing of the fettle. It is shown that the bottom electrode lifting above the surface at the electrode radius leads to the decrease of shear stress on the fettle area by 30% and cooling down the bottom electrode to the melting metal temperature – by 15%.

1. Introduction

The DC electric arc furnaces (EAFs) with the bottom electrode in the industrial practice has shown higher efficiency, low heat loss, lower components wear and higher quality of steel produced [1]. The exploitation of these furnaces has shown a high rate of fettle wear near the bottom electrode that connected with electrovortex flow [2]. Electrically vortical flows (EVF), appearing under electromagnetic forces as a result of non-homogeneous distribution of the current density through the liquid conductor, can be observed in many technological processes: electro slag remelting process (including DC and AC EAFs, electrolysis cells and submerged-resistor induction furnaces), arc welding, processes of semiconductor crystals growing, electro vortex engines etc [3]. The present paper deals with the electrically vortical flows in numerous model tasks for DC EAFs with different parameters of bottom electrode.

2. Presentation of the problem

The operation period of DC EAFs with the bottom electrode can be divided into the following stages: melting of the burden; liquid period when steel is produced; tapping. The time of liquid period ranges from 15 % to 60 % of all operation period depending on the steel type that is produced and on the quality of starting raw material [1]. It is essential that the processes in DC EAFs during the liquid period should be estimated.

In this type of furnaces the vortex flow of liquid metal is the result of spatial unevenness of the current with the absence of outer magnetic field. The current in the liquid creates a magnetic field of its own, which causes vortex movement of the liquid.

Convection flows make its own contribution to the vortex flow and appear under uneven distribution of the temperature throughout the liquid volume. It is shown in the work [3] that heat convection in electrovortex flow with axial symmetry appears when the radial gradient exists ($\partial T/\partial r \neq 0$). The direction of convection depends on increase or decrease of temperature value with the increase of the distance from the axis of symmetry.

To build the mathematical model of EVF the magneto hydrodynamic model is adopted with the following assumptions: the medium is considered non-magnetic and a good conductor, convective current can be neglected, physical characteristics of the medium are assumed to be homogeneous and isotropic and depend on temperature.

During the liquid period the temperature difference throughout the metal volume can range depending on the mode of furnace operation. Thus, when the arc works at full power the temperature ranges from 3773 K in the arc area at the cathode to 1923 K in the bottom electrode area and along the fettle surface. At the low power of the arc the temperature difference throughout the metal volume does not exceed 50 K. It should be noted that the metal at this period is liquid.

The velocity of the liquid that appears under electromagnetic force can be estimated as $u_0 = j_0 L\sqrt{\mu_0/\rho} \approx 0.3 m/s$ [3]. The Grashof number that defines the ratio of relative intensity of convection depending on the temperature range and electrovortex flow in the furnace is ranged in different periods from $Gr = 0.5 < 1$ (with the low power of the arc) to $Gr = \beta\Delta TgL/u_0{}^2 \approx 18.5 > 1$ (with the full power of the arc), that corresponds to the insignificant or essential contribution of the convection to the general vortex flow [3]. According to the preliminary estimation during the full arc power period it is necessary to take convection into account, but convection can be neglected at the period of low arc power.

The relative power of Joule heating as compared with another heat source (heat from the arc) is low $Q = \dfrac{j_0^2 L}{\sigma\rho c u_0 \Delta T} \approx 10^{-3} << 1$. This means the arc heat is more intense than joule heating [3]. Peclet heat number that defines the ratio of the free heat convection transfer to the molecule heat conduction equals $Pe = u_0 L/\chi \approx 10^{-5} << 1$ that means the domination of molecule heat conduction over free heat convection [3].

The magnetic Reynolds number is a part of the magnetic induction equation. The magnetic Reynolds number is low in this problem ($Re_m = \mu_0 \sigma u_0 L \approx 0.4 < 1$), meaning that the movement of liquid conductor does not change the magnetic field and the calculation can be carried out in non-induction approximation [3].

The processes in the DC EAFs during metal smelting are not steady. However, they are rather slow and can be described in quasisteady or just steady formulation. For steady statement the molten metal movement in the furnace can be described by the system of equations for magnetic, heat transfer and hydrodynamic processes.

The electromagnetic processes in liquid metal can be described by Maxwell's equations

$$\nabla \times \vec{B} = \mu_0 \vec{j}\,, \nabla \cdot \vec{B} = 0\,, \tag{1}$$

$$\nabla \times \vec{E} = 0\,,\ \nabla \cdot \vec{E} = \frac{\rho_e}{\varepsilon_0}\,, \tag{2}$$

Ohm's law for fluid in motion

$$\vec{j} = \sigma\left(\vec{E} + \vec{u} \times \vec{B}\right) \tag{3}$$

and charge conservation law

$$\nabla \cdot \vec{j} = 0\,, \tag{4}$$

where $\vec{j}$ – current density, ρ_e – charge density, $\vec{B}$ – magnetic induction intensity vector, $\vec{E}$ – electrical field intensity, σ – specific conductance, μ_0 – permeability of free apace, ε_0 – permittivity of free space, $\vec{u}$ – liquid velocity.

The heat parameters are calculated by heat transfer equation

$$\rho C_p u \cdot \nabla T = \nabla \cdot ((a + a_T)\nabla T) + j^2/\sigma\,, \tag{5}$$

where ρ – density, C_p – specific heat , T – temperature, a – heat conduction coefficient, a_T – turbulent heat conduction coefficient, j^2/σ – Joule heats source.

The hydrodynamic processes in the liquid can be described by Navier-Stokes equation

$$\rho\vec{u}\cdot\nabla\vec{u} = \nabla\cdot(-pI + (\eta+\eta_T)(\nabla\vec{u} + (\nabla\vec{u})^T) - (2/3)(\nabla\cdot\vec{u})I) + \rho\vec{g} + \vec{j}\times\vec{B}\,; \qquad (6)$$

and equation of continuity

$$\nabla\cdot(\rho\vec{u}) = 0\,, \qquad (7)$$

where p – pressure, $\vec{g}$ – gravitation, υ – dynamic-viscosity coefficient, $\eta = \upsilon/\rho$ – coefficient of kinematics viscosity, $\vec{I}$ – identity operator for points on the boundary. The following forces are considered in the equation (6): $-\nabla\cdot p$ – pressure force; $\nabla\cdot(\eta+\eta_T)(\nabla\vec{u} + (\nabla\vec{u})^T)$ – force of viscous friction; $\vec{j}\times\vec{B}$ – Lorentz electromagnetic force.

According to the preliminary estimation the Reynolds number under the movement in DC EAF is $Re = u_0 L/\nu \approx 10^6$, which is equivalent to the developed turbulent flow that can be described within $k-\varepsilon$ turbulence model.

To build a model of the processes in liquid metal the parameters of the industrial DC EAF with the bottom electrode are taken into account [4]. The geometrical arrangement of the furnace has been shown in Fig. 1

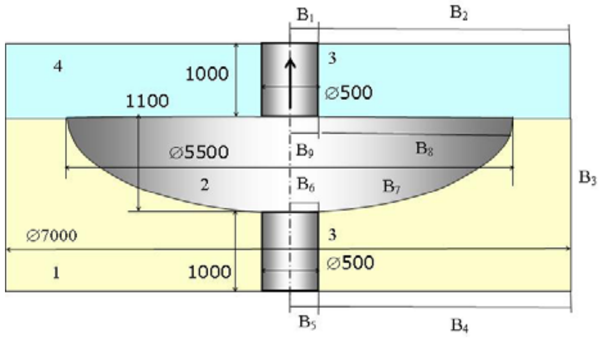

Figure 1: 1 The arrangement of cylindrical DC EAF
(1 – fettle, 2 – liquid metal, 3 – electrodes, 4 – slag).

The main parts of the configuration in Fig. 1 are 1 – fettle, 2 – liquid metal, 3 – top and bottom electrodes, 4 – slag. The axial symmetry allows calculating the half of the cross-section area. Its main parameters are: furnace capacity – 100 t, direct current load 80-100 kA, the mainlines voltage is 500-1000 V, power of current consumption 40-100 MW, polarity – «+» on bottom electrode.

The formulated problem was solved with the corresponding boundary conditions that are defined in fig. 3 as B_1-B_9. Electromagnetic conditions: B_1, B_5, B_6, B_9 current density on the boundary with normal cross-section of electrode $j_n = j_0 = I/S$, where S - cross section of electrode; B_8, B_7 current insulation j_n=0; B_6, B_7, B_8, B_9 the conditions of continuity of electric and magnetic fields $E_{\tau_1} = E_{\tau_2}$, $D_{n_1} = D_{n_2}$ and $B_{n_1} = B_{n_2}$, $B_{\tau_1} = B_{\tau_2}$. Heat conditions: B_9 – constant temperature of electric arc T_1 = 3300 K; B_6 – constant temperature on bottom electrode T_2 = 1980 K; B_8 – constant temperature on boundary with slag T_3 = 1900 K; B_7 – constant temperature on boundary with fettle T_3 = 1900 K. Hydrodynamic conditions: B_6, B_7, B_8, B_9 the no-slip boundary condition on all boundaries of liquid was used, both on the boundary of the liquid with the fettle and the boundary of liquid with slag. The last approximation is based on the fact that slag viscosity is much higher than liquid viscosity and it can be considered as no-slip condition.

Some results of simulation the processes proceeding in liquid steel are given below. Fig. 2a demonstrates the vector and contour fields of the Lorentz force near the bottom electrode (anode) and Fig. 2b hydrodynamic fields of velocity vector, contour and streamlines, where 1 – fettle, 2 – liquid metal, 3 – bottom electrode. The value of Lorentz force ranged and comprised about 30 % of volumetric gravity force. The figure demonstrates that the higher intensity of vortex flows appears in liquid metal volume. The convection flows are in the line with electrovortex flows and vortex flows increases. The maximum value of the vortex flow velocity was located on the axis of symmetry and reaches 0.5 m/s. The vortex flow velocity value in close to the bottom electrode and the fettle comprises about 0.3 m/s

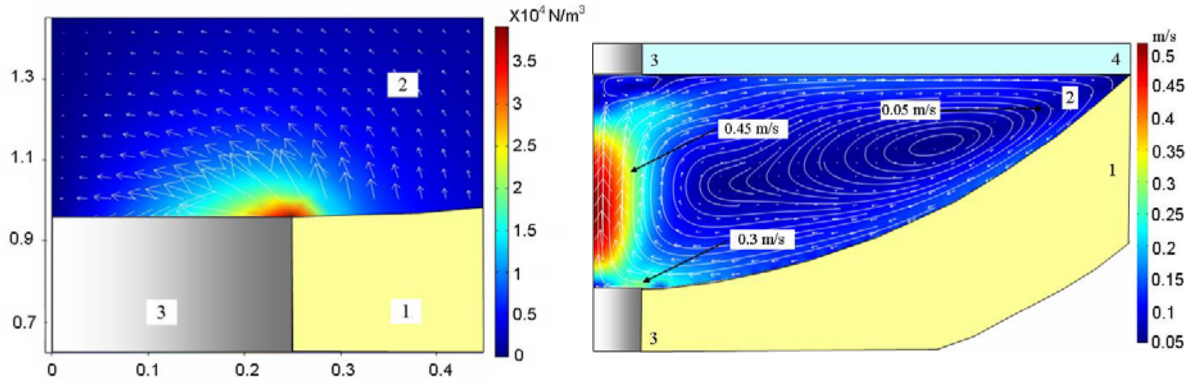

a) b)

Figure 2: a) the vector and contour field of Lorentz force near the bottom electrode; b) the vector, contour field and streamlines of velocity with convection.

The change of the bottom electrode position and temperature are two of the possible ways to reduce the negative influence of the liquid metal vortex flow on the increased fettle wearing. To estimate this effect some simulation of hydrodynamic processes at different positions and temperature of bottom electrode has been done.

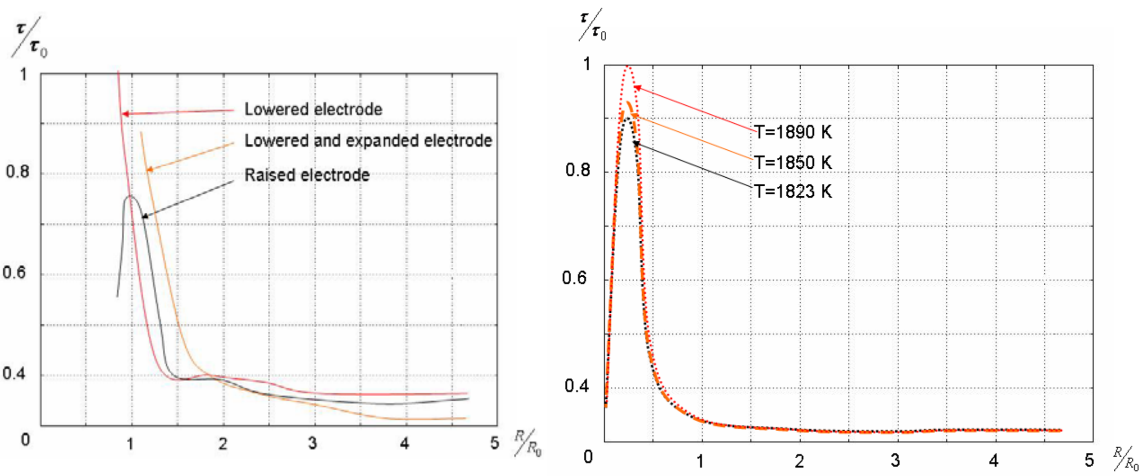

a) b)

Figure 3: Comparison of the shear stress on fettle surface at different bottom position and temperatures on the distance to the axis of symmetry ($\tau_0 = 120$ Pa, $R_0 = 0.25$ m).

Fig. 3 are shown comparison graphs of the values of the shear stress as a function of distance from the axis of symmetry for different bottom electrode position and temperature. Graph shows the magnitude of the shear stress in dimensionless coordinates. As the scale of the shear stress is taken the characteristic value of this quantity for the standard electrode ($\tau_0 = 120$ Pa) on the distance, expressed in electrode radius ($R_0 = 0.25$ m).

It is shown that lifting the bottom electrode above the surface of the fettle by the electrode radius value leads to the decrease of the shear stress on the fettle area by 30 %, while putting the bottom electrode lower than the fettle surface by the electrode radius value and expending the bottom electrode to the electrode radius value reduce the stress by 10 % [5].

To reduce the negative impact of the melt vortex movement to the bottom electrode and fettle near it, a series of numerical experiments with different bottom electrode temperature are carry out. The decrease of temperature bottom electrode has little effect on the general character and speed of the melt, but significantly affects to the velocity of the melt near the bottom electrode. Thus, when the temperature of bottom electrode comes to the melting point the metal velocity at shear sublayer is reduced by 20 %, while the value of the shear stress – by 15 % [6].

To verify the obtained results all calculations were done in ANSYS and COMSOL. At every stage the obtained results were compared with the known theoretical and experimental data and calculations received with the help of other software packages. The coincidence of the calculations done by different methods with analytical assumptions and experimental data in terms of all EVF characteristics under different conditions and with different installations proves the reliability of the methods and significance of the results [5-6].

3. Conclusion

The magnetohydrodynamic model for modelling EVF in different technological installations was adopted in the work. The research is carried out by computer modelling methods and software packages.

The processes in numerous laboratory and industrial installations, such as a laboratory installation with hemispherical volume filled with eutectic liquid and a DC EAFs with the bottom electrode, were simulated numerically. The specific features and laws of EVFs occurrence and course in these installations are determined.

The new criteria for the estimation of EVFs influence on the increased wearing of the bottom electrode and the fettle near it are offered: a rotor of the Lorenz force and shear stress on the fettle area. These criteria allow estimating the influence of the moving liquid on the fettle area. The criteria adequacy is confirmed by the theoretical researches and the good correlation with a number of experimental data.

The work offers the ways of EVFs control in the DC arc furnace with the bottom electrode by changing the bottom electrode position and temperature decrease at the bottom electrode of the furnace bath in order to increase the stability of the fettle wearing near the bottom electrode.

It is shown that the bottom electrode lifting above the surface at the electrode radius leads to decrease of shear stress on the fettle area by 30 % and cooling down the bottom electrode to the melting metal temperature – by 15 %.

The technique of EVFs control in the DC arc furnace with the bottom electrode is developed, allowing to reduce the fettle wearing and to optimize the furnace work.

4. References

[1] Nekhamin, S.M., Lunin, A.G., Krutyanskii, M.M., Filippov, A.K.: DC arc melting furnaces. Refractories and Industrial Ceramics, vol. 46 (2005), no. 1, 37-39.

[2] Zaycev, V.A., Medovar, L.B.: Bottom electrodes of DC arc furnace, SEM, 2009, No 2, pp. 3-8 (in Russ.).

[3] Bojarevics, V., Freibergs, J., Shilova, E., Shcherbinin, E.V.: Electrically Induced Vortical Flows, Riga: Zinatne, 1985, 315 p. (in Russ.).

[4] Michielan, A, Lavaroni, G, Fior, A: The Danieli Danarc TM furnace, ABS Rev. Met., France, 2000, no. 6, pp 745-752.

[5] Kazak, O.: Modelling of vortex flows in DC electric arc furnace with different bottom electrode positions, Metallurgical and Materials Transactions B, vol. 44 (2013), no 5, p. 1243-1250.

[6] Kazak, O.: Numerical modelling of electrovortex and heat flows in DC electric arc furnace with cooling bottom electrode, Heat and Mass Transfer 2013, DOI: 10.1007/s00231-013-1265-1.

APPLICATION OF MHD TECHNOLOGY IN NON-FERROUS METALLURGY IN SIBERIA

TIMOFEEV[1,2] V., KHATSAYUK[1,2] M., LYBZIKOV[1,2] G., AVDULOV[1,2] A.
[1]LLC "RPC Magnetohydrodynamics", 26A Akademika Kirenskogo str., Room 302, 660074, Krasnoyarsk, Russia
[2]Department of Electrotechnology and Electrotechnics, Siberian Federal University, 79/10 Svobodny pr., Room P7-04, 660041 Krasnoyarsk, Russia
E-mail address of corresponding author: viktortim0807@mail.ru , maxhac@ya.ru

Abstract: The present article reviews a number of the research works carried out by the staff of the specialized department "Electrotechnology and Electrotechnics" of the SFU in cooperation with a scientific and engineering company "NPC Magnetohydrodynamics" LLC, which aim is to solve the problems of MHD stirring of melts in furnaces and stirrers for melting-casting production of aluminum alloys.

1. Introduction.

Production of primary aluminum is a very energy-consuming process. Therefore electrolytic plants are usually built in the areas rich in energy resources. Eastern Siberia possesses good sources of power supply including the hydropower electric stations of Kans-Achinsk coal basin. Cheap energy in the region has contributed greatly to appearance of powerful production facilities both for primary aluminum and aluminum-based alloys. While preparing multi-component alloys it is essential to mix the melt in furnaces and stirrers in order to even its chemical composition and the temperature along the bath volume.

The present article describes the results of our team's research work connected with the problems of the location, form of the electric current and character of the inductor magnetic flux aimed to solve the problems of MGD stirring of a melt in furnaces and stirrers.

2. Stirring of a melt in furnaces and stirrers.

Magnetohydrodynamic (MHD) stirring technologies have lately become quite widespread. Stirring is considered to be effective if it leads to elimination of all the inhomogeneities in a melt and creates a homogenous structure along the bath volume. Inhomogeneities are divided into macroscopic and microscopic. In order to eliminate those inhomogeneities, MHD-stirrers should induce excitement of large-scale laminar and coherent vortex movements combined with small-scale pulsations in order to form associative formations in the melt [1].

The peculiarity of metal heating in gas or electric furnaces and stirrers is that the energy is normally transferred to the melt by radiating. Therefore, the temperature drop between the upper and lower melt layers reaches 100° C when heated for a long time. The upper layer high temperature helps increase the oxidation speed and saturation of the melt with hydrogen. When MHD-stirrers are turned on, the temperature between the layers is evened [2].

Let us consider two ways of installation of an MHD stirrer regarding the melt bath. The first way is as follows: the source of the running magnetic field is installed from the bath side wall. The second way: the inductor is placed under the bath bottom. Fig. 1 shows a sketch of the furnace with an MHD-stirrer inductor placed from the furnace side wall. Such an installation is more preferable in case when the installation of the inductor under the bottom will cause additional works to change the furnace foundation. However, recently metallurgical and aluminum factories have started using tilting furnaces.

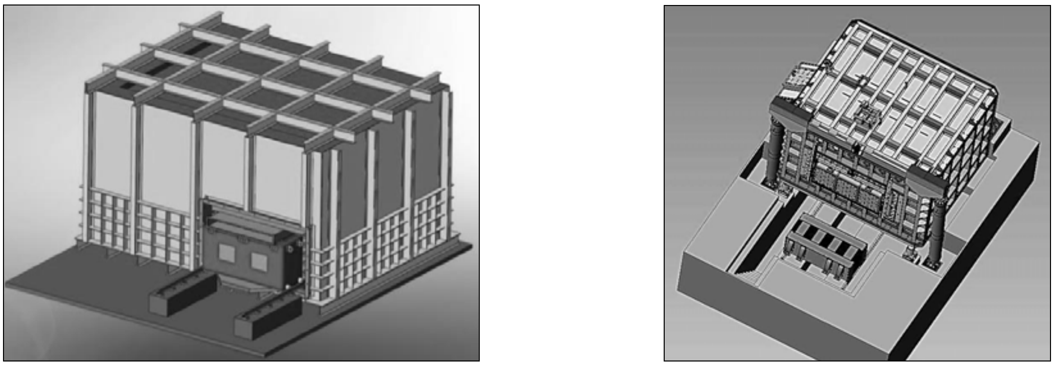

Figure 1: Sketches of static and tilting furnaces with MHD stirrers.

Fig. 1 shows the static and tilting furnaces with an inductor installed at the side wall of the furnace and under the bottom correspondingly.

To solve a problem of electromagnetic stirring of the melt in the furnace, a numerical model has been developed which has enabled to carry out the correct computation of the electromagnetic and thermal and hydrodynamic fields in a three-dimension setting taking into account the main peculiarities of the furnace and MHD-stirrer inductor [3, 4]. A mathematical model consists of two main parts: a mathematical model to analyze the electromagnetic field based on a Maxwell equation, which enables to define the distribution of the bulk force in the aluminum melt; and a mathematical model based on the Navier-Stokes equations, which enables to define the velocity field in the melt and the distribution of temperatures in the melt, the refractory lining and on the furnace surface both with and without the application of an MHD stirrer.

As a result of the numerical analysis of the hydrodynamic field on the melt, the pictures of the velocity field and motion trajectory have been received, an estimation of the turbulent movement has been made and the integral parameters of the system "inductor-melt" have been defined.

The distribution of the velocity field with the established melt movement (t = 180 s) with the inductor installed under the bath bottom is shown in Fig. 2a.

A significant factor influencing the kinetics of the alloy solution is the presence of the developed turbulent movement in the area of the distribution of the alloying elements. The area with the significant turbulent movement and the dynamics of its change can be presented with a change of the iso-volume with the kinetic energy of the turbulent pulsations $k > 0.001$ m^2/s^2 at the moments of time 20 s and 90 s in Fig. 5. From the figure, it is clear that the increase of the turbulent movement happens rather slowly and the main area with the

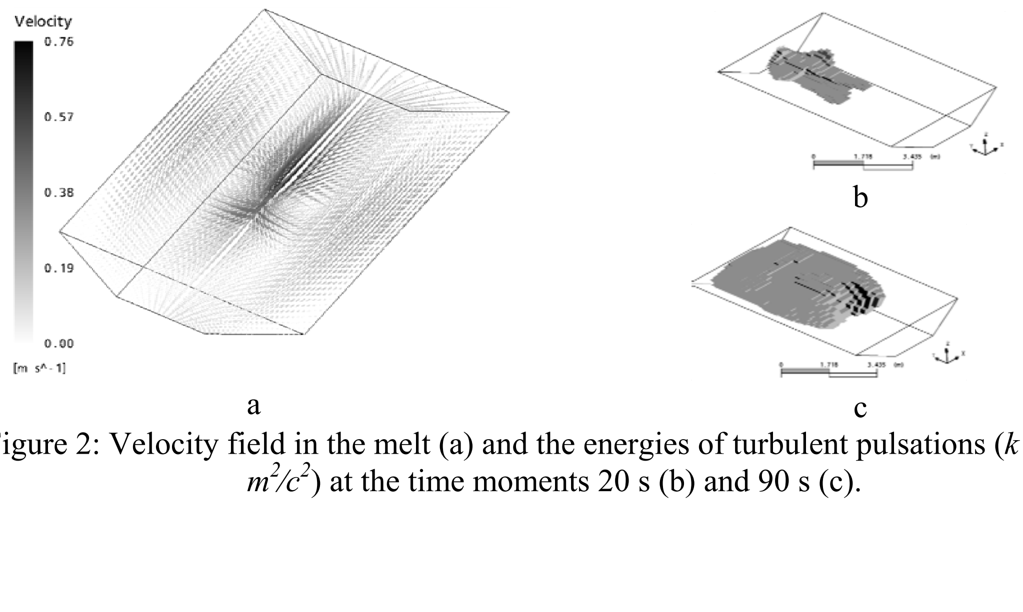

Figure 2: Velocity field in the melt (a) and the energies of turbulent pulsations ($k > 0.001$ m^2/c^2) at the time moments 20 s (b) and 90 s (c).

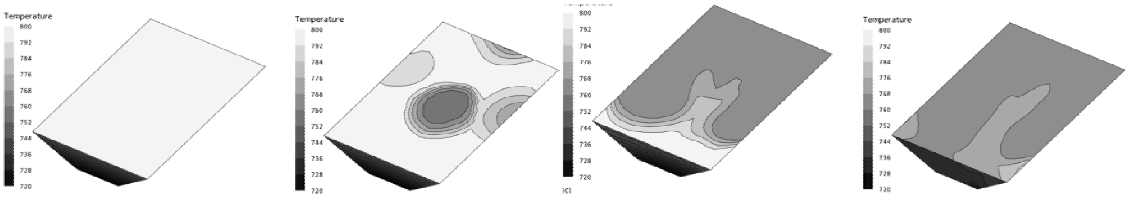

Figure 3: The dynamics of the temperature distribution of the melt surface.

developed turbulence is only observed at the outlet of the inductor (Fig. 2b). The developed turbulent movement at the moment of time 90 s nearly coincides with the area of the main motion trajectories (Fig. 2c) and takes 2/3 of the melt bath volume.

Apart from accelerated solution of the alloys, MHD-stirring leads to evening the temperature in the melt. The temperature distribution on the melt surface at different moments of time is shown in Fig. 3.

The temperature analysis shows that in the central part of the bath there is a significant heat-and-mass transfer thanks to the ascending currents leading to quick evening of the temperature above the inductor. Besides, it follows from the temperature distributions that in the area in front of the inductor (inlet of the inductor) there is a zone of the melt stagnation which is stirred badly. The presence of the area with the melt stagnation speaks for the necessity to reverse the running magnetic field.

MHD stirrers used at the present time are normally fed with sinusoidal currents, have low efficiency and the power coefficients. An MHD-stirrer, fed with non-sinusoidal periodical currents, having certain inductor parameters and power source operation modes, has a distinct advantage over MHD-stirrers with sinusoidal feeding, while presence of pulsing electromagnetic forces leads to elimination of micro-inhomogeneities in multi-component melts [5]. Let us suppose, that for each phase of the inductor winding there is a periodic strain of a rectangular shape *u(t)* (Fig. 4). As each phase has an active resistance *R* and inductivity *L*, there is a transition process whenever the voltage polarity changes. The length of the transition processes t_n depends on the parameters of the inductor *R* and *L*, and is defined with the time constant $\tau_в$. Taking into account the law of commutation and the character of the transition processes the electric current form i*(t)* will also have the form shown in Fig. 4. Upon the completion of the transition process there is a stage in the winding with the length t_y, during which the current does not change. The electromagnetic field will repeat the form of the currents.

Provisionally the process of the interaction of such fields shape with the bath liquid metal can be divided into two stages. The first one – when the field does not change (time t_y), and has a maximally deep penetration into the metal thickness, and the second one when the

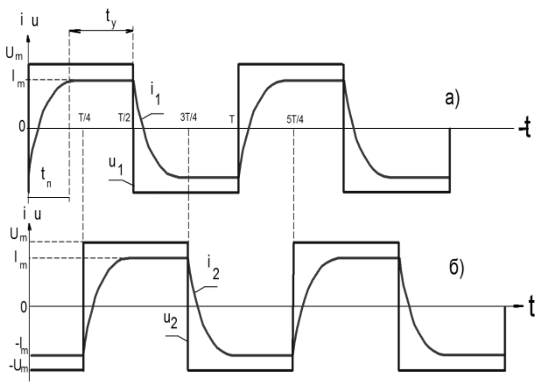

Figure 4: Voltage and current in the inductor phases.

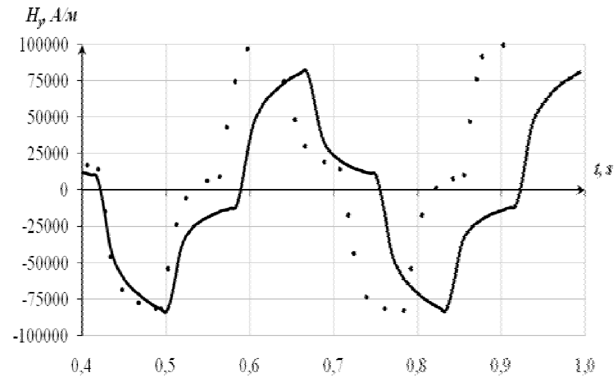

Figure 5: Comparison of the computational and experimental data (on the right).

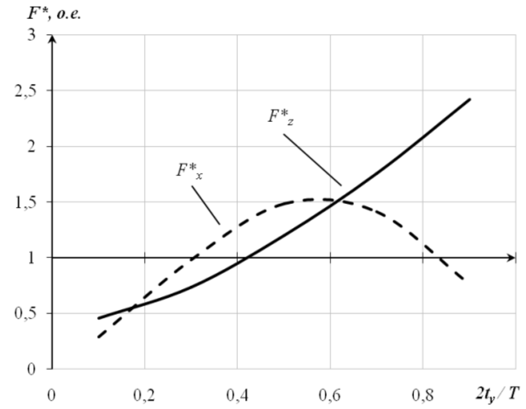

Figure 6: Components of the electromagnetic force with different parameters of the impulse relative the sinusoidal feeding.

field changes with the course of time with a high speed (time t_n), and there are ring (vortex) currents appearing in the metal thickness. The currents interact with the field and create a force that brings metal into motion. For effective stirring of liquid metal in the bath, it is reasonable to influence the melt with the running electromagnetic field. For this there are two and more windings installed in the inductor that are fed with the source with the voltage equal in form and frequency but with the voltages shifted in phase. For example, for a two-phase inductor the phase shift between the voltages can be *T/4* (Fig. 4).

In order to determine the electromagnetic characteristics of MHD-stirring with non-sinusoidal periodical feeding with different values of a relative parameter $t_y^* = 2t_y/T$, a mathematical model of transition electromagnetic processes was developed. To check the developed mathematical model an experimental device consisting of a two-phase inductor with impulse power supply source was developed and constructed. The frequency of inductor supply is 3±0.3 *Hz*. The similar parameters were used to carry out the numerical modeling with the application of the developed mathematical model [6], as a result of which the dynamics of the electromagnetic field was obtained. The comparison chart for the data obtained is shown in Fig. 5. The mentioned charts show that the mathematical model correctly simulates the character of the magnetic field shape and can be used to analyze electromagnetic process in MHD-stirrers with non-sinusoidal periodical currents.

Fig. 6 shows computational dependencies of the electromagnetic force components on the relative parameter $2t_y/T$. The values of the electromagnetic forces are shown relatively to the force with non-sinusoidal feeding of the similar frequency.

As it follows from the charts shown, with $2t_y/T \geq 0.4$ the values of the both tangential and normal components of the electromagnetic force with non-sinusoidal feeding of the inductor winding exceed the similar values of the inductor windings fed with sinusoidal currents. In addition, the computations and measuring taken at the physical modeling have shown that in general the consumption of the reacting power decreases in comparison with an option when the inductor winding is fed with a sinusoidal current.

One of the problems of MHD-stirrers, installed from the bath side, is their low operational efficiency when the metal level in the bath is less than 0.3m. To solve this problem, it is proposed to use a stirrer with a transversal magnetic flux (Fig. 7b) [7].

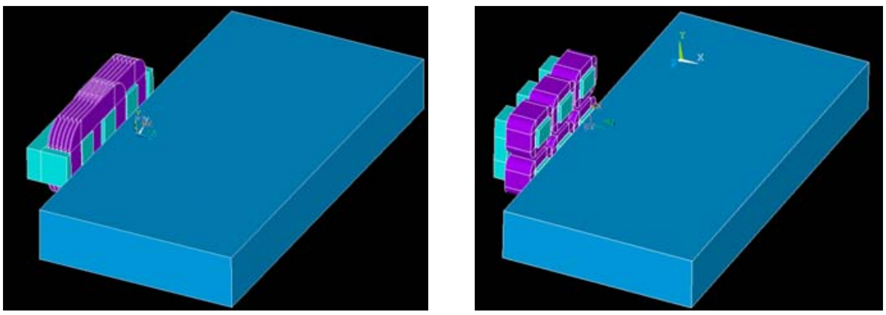

a b

Figure 7: MHD stirrer with longitudinal and transversal magnetic fluxes.

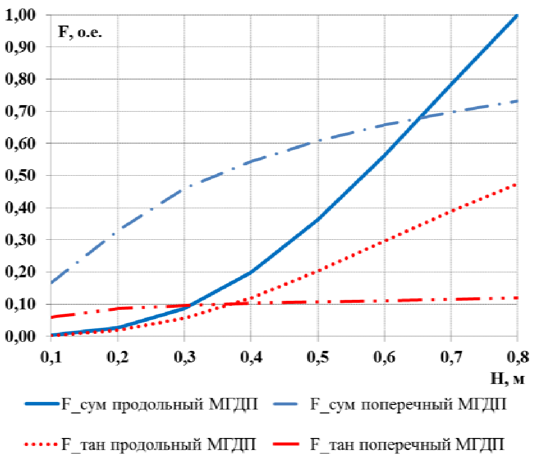

Figure 8: integral force values created by the electromagnetic field in the melt

To evaluate the operational efficiency of a MHD-stirrer with a transversal magnetic flux (Fig. 7b), numerical modeling of electromagnetic processes was made. For comparison, a MHD-stirrer with a longitudinal magnetic flux was chosen (Fig. 7a). Size, weight and power parameters of the stirrer with a transversal magnetic flux were similar to a MHD stirrer with a longitudinal magnetic flux.

Fig. 8 shows the obtained integral force values, created by the operation of the MHD-stirrer with longitudinal and transversal magnetic fluxes. There is a metal level in the bath along the axis of abscissas. There are force values in relative units along the axis of ordinates; the effort developed by the MHD stirrer with a longitudinal magnetic flux in the melt with the level of 0.8 m is taken as 100%.

As we see from the charts, when the furnace is fully filled with the melt, the stirrer with a longitudinal magnetic flux creates a great effort. However starting from the metal level of 0.6 meters the stirrer with a transversal flux is more efficient. When the metal level is less than 0.2 meters from the rated value, the stirrer with a transversal magnetic flux has a better operational efficiency. MHD-stirrers with a transversal magnetic flux installed on the furnace side wall are better to be used to provide efficient stirring in static melting furnaces with a low melt level (less than 0.3 m). In this case, the size, weight and power parameters will be similar to the existing devices.

3. Conclusion

1. In order to obtain the homogenizing melt in the whole volume of the furnace-stirrer bath it is necessary to carry out MHD stirring with reversing of the melt motion trajectory.
2. An MHD-stirrer with non-sinusoidal periodical currents carries out stirring of liquid metals in a more efficient way, at that the power coefficient increases and stirring time decreases.
3. For efficient stirring in static furnaces and stirrers with the melt level less than 0.3 meters it is reasonable to use MHD-stirrers with a transversal magnetic flux, installed from the side wall.

4. References

[1] Timofeev, V.; Korchagin, A.; Pavlov, E.; Timofeev, N.: Control of convective flows in liquid metal influenced by electromagnetic forces. Journal of Siberian Federal University 1 (2012) 28-37.

[2] Timofeev, V.; Khatsayuk, M.: Control of convective melt flows in the channel part of the induction furnace. Izvestiya RAN. Energetika. 3 (2013) 130-136.

[3] Pavlov, E.; Bogovalov, S.; Timofeev, V.; Nadtochyi, D.: Magnetohydrodynamic stirrers of aluminum melts in resistance furnaces. Reporter of SibGAU. 3 (2006) 199-204.

[4] Timofeev, V.; Khatsayuk, M.; Pervukhin, M.: MHD technology in melting-casting industry of aluminum alloys. Induction heating. 4 (2012) 15–21.

[5] Timofeev, V.; Lybzikov, G.; Khatsayuk, M.; Eremin, M.; Timofeev, S.: Magnetohydrodynamic stirrer liquid metal with a non-sinusoidal currents. Journal of Siberian Federal University. Engineering and Technologies. 6 (2013) 166-177.

[6] Pervukhin, M.; Minakov, A.; Khatsayuk, M.; Sergeev, N.: Mathematic simulation of electromagnetic and thermal-hydrodynamic processes of the system “inductor-ingot” of an electromagnetic mould. Magnetohydrodynamics, 1 (2011) 79-88.

[7] Timofeev, V.; Avdulov, A.; Avdulova, Yu.; Boyakov, S.; Gudkov, I.: MHD-stirrer for works with low level of aluminum melt in bath of furnace. Induction Heating. 26 (2013) 16-20

FREE SURFACE DEFORMATION AND FORMATION OF ELECTRICAL DISCHARGES UNDER CURRENT CARRYING FLUIDS IN MAGNETIC FIELDS

KLEMENTYEVA[1] I.B., PINCHUK[2] M.E., TEPLYAKOV[1] I.O., ABDELLAH KHARICHA[3]
[1]JIHT, 13/2 Izhorskaya str., 125412 Moscow, Russia
[2]IEE, 18 Dvortsovaya nab., 191186 St.-Petersburg, Russia
[3] University of Leoben, Franz-Josef-Straße 18, 8700 Leoben, Austria
E-mail: ira.klementyeva@mail.ru

Abstract: Results of investigations of high current discharges formation under liquid metal free surface deforming due to interaction of passing through it electric current with current's own magnetic field are described in the paper. Discharge characteristics and parameters of its ignition are presented here. Visualization pictures of free surface deformation and electrical discharge formation are shown in the paper. Processes taking place in the system are considered. Mechanism of formation of the discharge over the liquid metal surface is discussed.

1. Introduction

The significance of these investigations is in solving of the fundamental problems of magneto-hydrodynamics and discharge physics and also in solving of the application problems related to improving the performance of technical devices in power engineering and industry. The investigations are relevant and caused by the need to create energy-efficient technologies. The electrical discharge under the liquid metal surface appears in different technological processes. One of the applications of research results is in metallurgy. With the use of magneto-hydrodynamics methods of control [1, 2] of electrical discharges and electro-vortex flows it is possible to successfully improve many electrometallurgical processes – welding, melting, melt purification. Another important application of the received results is in nuclear and thermonuclear power engineering for intencification of mixing of plumbum and lithium for creation of eutectic alloy [3] planed to be used as a heat transfer agent. The investigations of processes in current-carrying fluids with high current electrical discharges under free surface of liquid metals are of fundamental interest.

Two types of liquids were use for experiments in the work – plumbum (Pb) and eutectic alloy indium-gallium-tin (In-Ga-Sn) (weight content: Ga – 67%, In – 20.55%, Sn – 12.5%, +10.5C). Pb and eutectic alloy plumbum-lithium are planned to be the heat transfer agent in modern reactors on fast neutrons. Whereas In-Ga-Sn are sutable for modeling of the system under interest due to low melting point and no hazard to health. The investigated processes are complex and comprise deformation of the free surface of the liquid metall, electrical discharge ignition and electro-vortex flows formation. Deformation of the free surface and formation of electro-vortex flows are caused by interaction of electric current running through the electro-conductive liquid with current's own magnetic field. Then the electrical discharge ignites influencing hydrodynamics and heat-exchange processes in the system.

Tasks of current work are: to reveal causes and conditions of electrical discharge ignition; to determine parameters of the electrical discharge.

2. Presentation of the problem

The base element of the experimental setup is a test section (fig 1) that is a steel or copper rod electrode with hemispherical edge (diameter – 20mm or 5mm) and a cylindrical or hemispherical [4] container (diameter – 10cm and height – 5cm or diameter – 18.8cm) filled with the melted metal (plumbum Pb or eutectic alloy In-Ga-Sn) playing role of another electrode. The rode electrode is dipped initially into the melted metal. Electric current in the circuit is organized by accumulator power source or three phase power source with open circuit voltage U_{oc} up to 13V or 20V correspondingly.

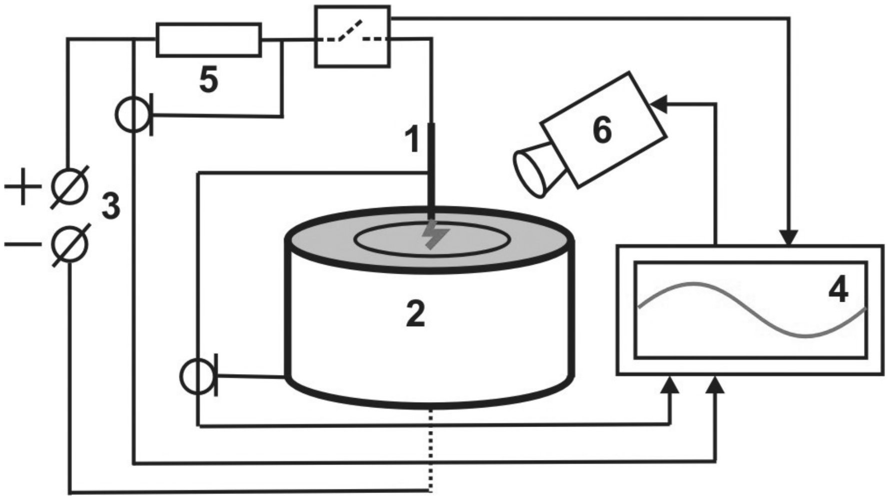

Figure 1. Scheme of the experimental setup. 1 – rod electrode, 2 – cylindrical or hemispherical container, 3 – accumulator power source or three phase power source, 4 – oscillograph, 5 – electric current shunt, 6 – high speed digital photo camera.

Synchronization scheme gives required time sequence and time intervals between switching on of electric current and triggering of recording equipment. Electric current runs an oscillograph generating pulse signal to trigger video camera. The oscillograph and camera record processes before and after electric current switching on.
Electrical parameters, circuit current I and voltage U measured between the electrode and the free surface of the liquid metal, are registered with four-channel digital recording ocsillograph Tektronix TDS 2014.
Electric current is defined through voltage drop on current shunt (0.2mOhm or 0.05 mOhm).
Processes visualization is performed with high speed digital photo camera Citius Imaging C10 of following specification: maximum matrix resolution – 652×496, pixel size – 10mkm, maximum registration rate – 10000 frames per second, time of exposure – from 6mks, synchronization accuracy – 1mks.
Experiments were carried out in air and argon at P – 1Atm.

3. Results and discussion

Fig 2 and fig 3 represent processes in the system through voltage U measured between the electrode and the liquid metal and voltage drop measured on the current shunt that reflects electric current I in the circuit in experiments with melted Pb [5].
It is seen that at initial stage after switching on of electric current U ~ 2V and I ~ 500A and there is no any discharge in the system. Then U and I start to rise and falls correspondingly due to free surface deformation under action of electro-motive body force that is a result of

interaction of passing through the liquid metal electric current with its own magnetic field. After that there is rapid increase of U getting its maximal value in the experiment that reflects reduction of contact area between the electrode and the liquid metal. Following oscillogram ranges demonstrate ignition and evolution of the electrical discharge in the system with parameters: $U_{arc} \sim 10V$, $I_{arc} \sim 100 - 200A$ (fig 4).

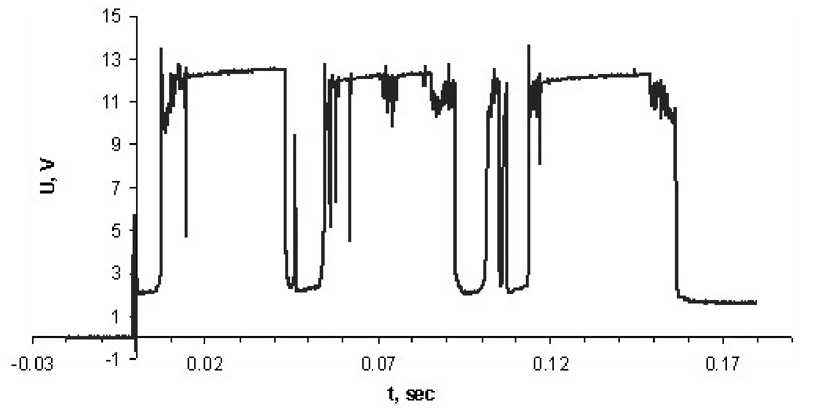

Figure 2. Voltage U measured between the electrode and the cylindrical container with melted Pb

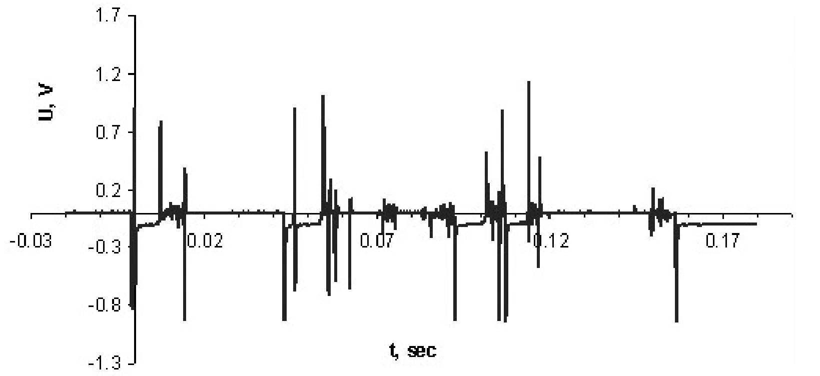

Figure 3. Voltage drop measured on the current shunt that reflects electric current I in the circuit in the experiments with melted Pb.

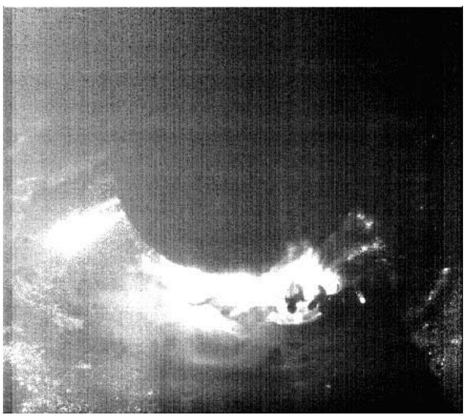

Figure 4. Image of the electrical discharge in the experiments with Pb.

High-speed videos confirm the picture of processes development described above. Free surface deformation and discharge ignition repeat during the run of the experiment with following parameters: frequency of discharge ignition due to deformation of the free surface ~ 30Hz, time of discharge evolution ~ 7ms, and frequency of discharge pulsations ~ 0.5ms. As the rod electrode is an anode the pulsations of the discharge reflects movement of a discharge attachment point to the electrode along it [6, 7].
Estimations of breakdown voltages approve that the cause of discharge ignition is deformation of the free surface due to action of electro-motive body force.
High-speed video frames of the experiments with In-Ga-Sn demonstrate deformation of the contact surface, its detachment from the rod electrode (fig 5 a) and ignition of the electrical discharge (fig 5 b).

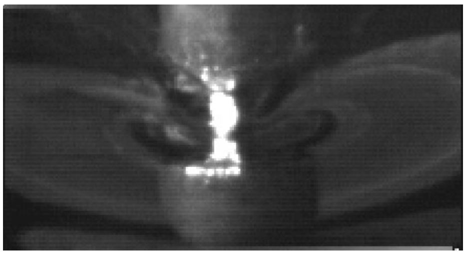

a

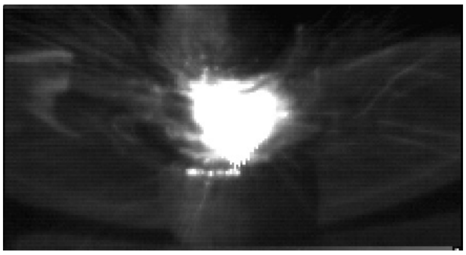

b

Figure 5. a) Deformation of the contact surface, its detachment from the rod electrode, b) ignition of the electrical discharge in the experiments with In-Ga-Sn.

Character of the processes in the experiments with Pb and In-Ga-Sn are the same qualitatively. Fig 6 represents voltage drop measured on the current shunt that reflects electric current I in the circuit in the experiments with In-Ga-Sn. Electrical discharge paramrters for the case are: U_{arc} ~ 0.24V, I_{arc} ~ 520A.

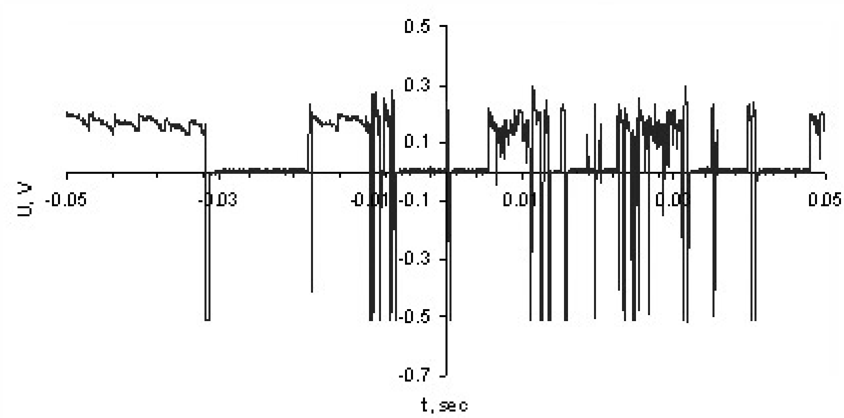

Figure 6. Voltage drop measured on the current shunt that reflects electric current I in the circuit in the experiments with In-Ga-Sn.

4. Conclusion

Experimental studies of formation of the electrical discharges over the surface of the liquid metal were carried out. Discharge characteristics and parameters of its ignition were determined. Wave form, free surface deformation and discharge evolution were visualized. It was confirmed that the cause of discharge ignition is deformation of the free surface due to action of electro-motive body force. The results will be used for investigations and estimations of influence of pinch-effect on vortex structure and velocity field in liquid metals at MHD method application for intensification of mixing and heat transfer in technical devices.

5. Acknowledgements.

The work is supported by RFBR N 14-08-31078 and N 13-08-90444.

6. References

[1] Klementyeva I.B., et al.: Interaction of electrical discharge with gas medium in external magnetic field and influence of the interaction on flow structure and mixing. High Temperature. V.48 No.1 (appl.) (2010) 132-137.
[2] Klementyeva I.B., et al.: Peculiarities of interaction of electrical discharge with gas flow in external magnetic field. Letter Journal of Technical Physics. V.33 No.22 (2007) 16-22.
[3] Freibergs J., Klavins J., Lielausis O., Mikelsons A., Zandarts J. MHD technology for the production of Pb-Li eutactic alloys. The 15th and 6th PAMIR conference on fundamental and applied MHD fusion. 259-262.
[4] Ivochkin Yu.P., et al.: Investigation of deformation of free surface and its influence on intensity of electro-vortex flows of liquid metal. Thermal Processes in Engineering. V.4 No.11 (2012) 487-496.
[5] Klementyeva I.B., Pinchuk M.E.: Formation of electrical discharges under free surface of current carrying fluids. Physics of extreme states of matter. (2014) 192 – 193.
[6] Klementyeva I., Moralev I.: Electrical discharge interaction with gas flows in external magnetic field. IEEE Transactions on Plasma Science, Special Issue – Images in Plasma Science. (2011) 2144-2145.
[7] Klementyeva I.B., et al.: Experimental investigation of electrical discharges in gas flows in external magnetic field. High Temperature. V.49 No.6. (2011) 816-825.

INFLUENCE OF MHD-PROCESSES IN WORKING AREA OF MAGNETODYNAMIC INSTALLATIONS FOR ALUMINIUM ALLOYS ON THEIR OPERATING CHARACTERISTICS

DUBODELOV[1] V.I., SLAZHNIEV[1] M.A., MOYSEEV[1] Yu.V., BOGDAN[1] K.S., PODOLTSEV[2] A.D., GORYUK[1] M.S.
[1] Physico-Technological Institute of Metals and Alloys NAS of Ukraine, Kyiv, Ukraine, Vernadsky Ave. 34/1, Kyiv-142, MSP, 03680, Ukraine
[2] Institute of Electrodynamics NAS of Ukraine, Kyiv, Ukraine, Peremogy Ave. 56, Kyiv-57, MSP, 03680, Ukraine
E-mail: mgd@ptima.kiev.ua , slazhnev@ptima.kiev.ua

Abstract: There are determined the factors, which affecting the work efficiency of casting magnetodynamic installations (MDI) for aluminium alloys. It is shown, that basic reserve for rise of technical parameters of MDI is related with reduction of magnetic fields dispersion and raises its concentration in T-shaped working area (WA) of MDI, and also with the decreasing of negative influence of vortex structures on borders of working area. It is developed the (3D) measuring method of magnetic fields distribution. It is defined the ways for optimization of systems for generating of electromagnetic fields and its superposition in working area of MDI.

1. Introduction

The magnetodynamic installation for aluminium alloys a long time and successfully is used in foundry for alloys treatment and making of castings. Presently for used in casting technologies melting-dosaging equipment the requirements about providing of energy-saving (according to useful mass on an aluminium no more than 0.08 kW*h/kg) and rising of range of technical descriptions became tougher. Its related to development of technologies and expansion of nomenclature of products on the brands of alloys, size of casting, its weights and geometry, for example, for the processes of casting under pressure, semicontinuous and continuous pouring. In particular, its necessary to provide more wide possibilities of magnetodynamic equipment on the value of the created pressure (from 30 kPa to 50 kPa), realization of the modes of the intensive heating (from 3°C/min to 10°C/min) and stirring of melt (with speed from 1 to 10 m/sec), and also expansion of range of realized at pouring mass flow rate – both toward the increase (from 3 kg/sec to 10 kg/sec), and reductions (from 0.3 to 0.05 kg/sec).

Analysis of results of performed before researches of MHD-processes on boards and in the working area MDI, and also estimation of factors lowering efficiency of work of MDI for aluminium alloys [1] showed that basic reserve of the pressure rise and expense descriptions are related to reduction of dispersion and concentration rise in working area (WA) lines of magnetic field created by an electromagnet, by the decline of the negative influencing of vortical structures, appearing on the boards of WA as a result of slump of the magnetic field, and also neutralization of effect of intaking of liquid metal in WA, the conditioned by co-interaction of magnetic field of current in a liquid-metal explorer with the magnetic field of electromagnet.

2. Presentation of the problem

For expansion of views of machineries of origin of magnetohydrodynamic effects in channels and working area MDI, which negatively affecting on hydraulic and operating descriptions of such installation, electromagnetic processes in T-shaped WA were researched at different working modes of MDI.

On the first stage of researches studied influencing of construction elements (metallic casing of channel) MDI (fig.1) on distributing (distortion, dispersion, absorption) of the magnetic field created by the external electromagnet. On the second stage the features of distributing of the magnetic fields in T-shaped WA were researched, at imitation of presence metal by location on the horizontal cavity of the W-shaped channel aluminium plate (fig 1), which are repeating rounding the environs T-shaped WA, at the passing of alternating currents was provided by the own electromagnetic systems (inductors). For systematization of experimental data of distributing of magnetic induction and construction of its topographies a vertical coordinate matrix is used a point measuring of induction of the magnetic field in T-shaped WA of MDI (fig 1).

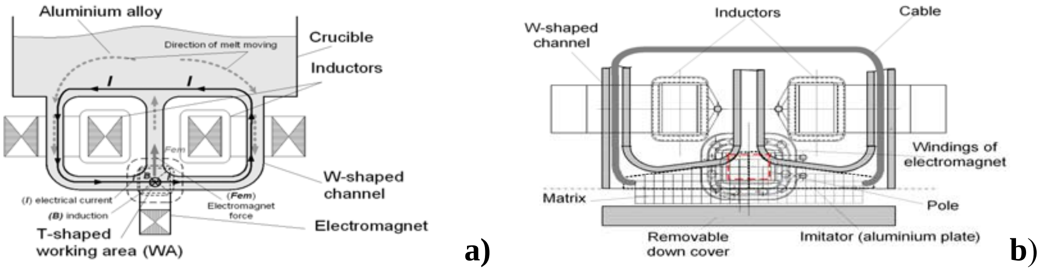

Figure 1: Scheme of MDI (a) and W-shaped channel of MDI (b) and method of magnetic induction distributing researching in the imitation mode.

With the purpose of the detailed study of the «spatial distributing» of the magnetic field (induction is to 1.0 T) in T-shaped WA of MDI and record of instantaneous values of the vectoral component of magnetic induction by 3D-sensor allowing to realize the continuous measuring of normal (Z) and two tangential components (X, Y) of induction was developed. The dispersions of fields (distributing of normal and tangential components of magnetic field) not far from T-shaped WA was determined by apparatus, which providing the simultaneous three-vectoral measuring of parameters of the magnetic field in the set point of space. 3D induction sensor consists of six sensors of Hall, mounted as a cube with a rib 6 mm, three output signals (U_x, U_y, U_z) giving out, variable voltage on which proportionally intensity of the magnetic field in the three mutually perpendicular directions in the point of sensor location.

Researches of distributing of magnetic induction, dispersions and influencing of elements of construction of channel in WA and systems of electric currents inductions and its intercommunication, was produced in three stages: at the switched electromagnet MDI; at the switched electromagnet and set in a channel aluminium plate; at the switched electromagnet, set in a channel to the aluminium plate with passing the electric current, inducted by the inductors. The results of experimental researches showed that in areas (fig. 2a) proper 1 and 2 of plane in relation to the pole of electromagnet, there is distortion of distributing of lines of the magnetic field as a result of interaction with material of channel casing. The area of maximal normal values of magnetic induction is found in neighbouring of projection of pole of electromagnet, and in relation to the plane T-shaped WA of MDI closeness of induction (by the value not below 0.05 T), is distributed on 35÷40% to its area, where and electromagnetic pressure is created. The maximal value of magnetic induction corresponds to the center of pole of electromagnet.

The analysis of the distribution of the magnetic induction topographies at presence of «imitator» (fig. 2b) (imitator – aluminium the plate from the aluminium alloy with thickness 8 mm, the form of which corresponded to geometry of horizontal area of the W-shaped channel of MDI) showed characteristic for the mode of imitation «deflection» of normal component of magnetic induction for vertical lines and narrowing on a horizontal line (a white line corresponds to the size equal 20% from the basic value of magnetic induction). This phenomenon is caused by the interaction of the external magnetic field with appearing in current conductive aluminium the vortical electrical currents and its contours, which raise the reactive resistance to magnetic field.

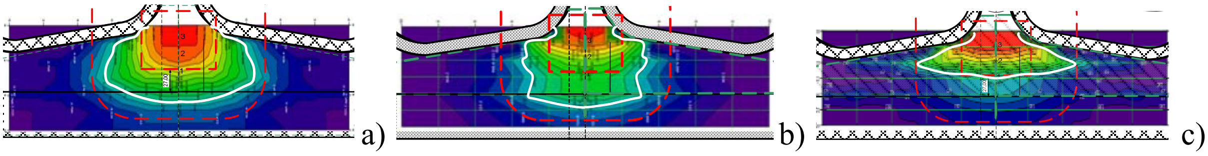

Figure 2: Distributing of normal components of induction in T-shaped WA MDI in the imitation mode: a) at the electromagnet switched ($\boldsymbol{B \neq 0; I = 0}$); b) with “imitator” ($\boldsymbol{B \neq 0; I = 0}$); c) at placed on the horizontal area T-shaped WA “imitator” with the current ($\boldsymbol{B \neq 0; I \neq 0}$).

At research of influencing of MHD-processes in the working area MDI on operating descriptions in the imitation mode at passing through the aluminium plate the inducted current and superposition of the external magnetic field, was it is shown, that concentration of normal component of magnetic induction in area of the discharge to pipe of WA to increases on 25%, and in down part of WA to decrease on 15% (fig. 2c). Thus the effective square of WA, where are the electromagnetic forces are created, makes no more than 60% its actual value.

The graphic image of algebraic difference of redistribution of the normal component magnetic induction, conditioned by influencing of the magnetic field of current, passed on a metallic conductor in WA, is shown in fig. 3.

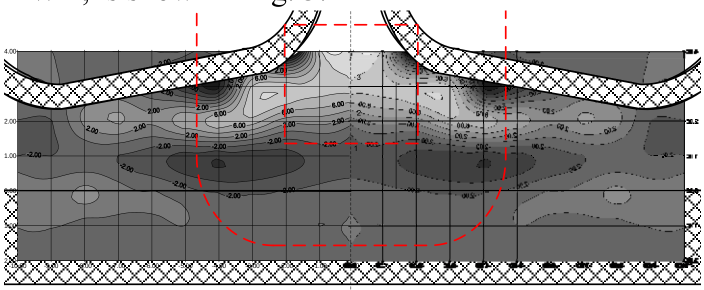

Figure 3: Topography of redistribution of normal component of induction of the magnetic field in T-shaped WA of MDI in the imitation mode.

Determinate MHD-effect (fig. 2c and fig. 3) is classified as a reaction of “anchor” in WA of MDI [3], as a result of interaction between the external alternating magnetic field, generated by an electromagnet and alternating magnetic field, created in liquid-metal conductor by the horizontal area of the W-shaped channel, which having meeting direction in relation to the external magnetic field in lower part of WA and accordant direction in overhead part.
Influencing of «anchor» reaction increases with the increase of current density $\boldsymbol{j}$ in WA and stipulates the unevenness of distributing of induction, that results to decline of electromagnetic interaction efficiency and appearing the areas of the differentiated distributing, both by a electromagnetic forces ***Fem*** and electromagnetic pressure ***Pem***.

In the applied sense, at the analysis of the pressure descriptions MDI, in depending from parameters of inductors work and electromagnet [4, 5] (fig. 4a), its shown, that with the increase of the voltage on inductors, the angle of slope of pressure descriptions decreasing and dependence of coefficient of pressure loses linear.

By other important aspect, which determining influence of MHD-processes on operating descriptions of the MDI, there is influencing of electromagnetic processes of co-operation of the magnetic fields of currents in a liquid-metal conductor in channel with the core (yoke) of electromagnet. This influence is characterized by the appearing of «involvement» effect as a result of negative vector of electromagnetic pressure in WA, the size of which makes 20÷25% from pressure descriptions MDI (fig. 4b). Thus, the electromagnetic pressure created in MDU, corresponds 30÷35 kPa, and the loss of pressure due to inducing in the disconnected coils of electromagnet makes from 6.0 to 8.75 kPa.

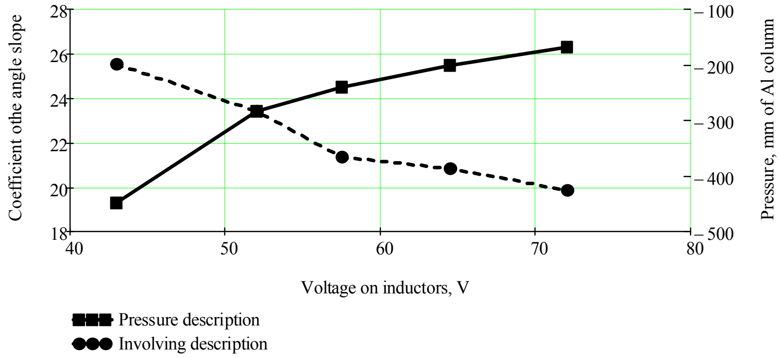

Figure 4: Dependence pressure descriptions and negative component of the electromagnetic force from voltage on inductors.

Along with this, research tangential component induction in this case (fig. 1) on the Y-axis corresponding to the component of the magnetic field induced in a T-shaped WA by alternating current, which passing through the aluminum plate has demonstrated the existence density of the maximum concentration induction in the lower parts of WA (fig. 4), and presence of the phase angle between alternating magnetic fields from 23º÷43º (0.18π÷0.28π), which reduces the electromagnetic pressure on 1.5÷4.5 kPa (70÷180 mm pressure by liquid aluminum alloy column).

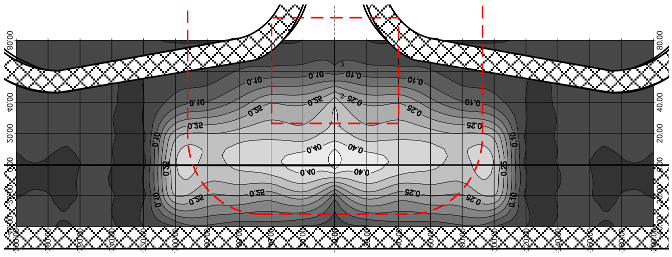
Figure 5: Frontal topography and distribution graph of the tangential (axial) component of the magnetic field induced in the T-shaped WA by AC passing through the aluminum plate.

Distribution represented by the magnetic field created by the alternating electric current (fig.5) obtained experimentally in simulated work MDI mostly its mode "pump", the picture quality predetermines the redistribution component of the current density ***j*** in the WA and its surroundings as a result of interaction with an external magnetic field of the electromagnet and is characterized by displacement (pushing) the flow lines in the area remote from the projection of the poles of an electromagnet. A characteristic feature of the effect on the performance of education MDI is significant differential values of the normal component of the magnetic induction in the WA, resulting in the formation of pressure fluctuations and the magnitude of the electromagnetic volume electromagnetic forces therein. Analysis of topography (fig. 3c) shows that at a distance of 50-60 mm from the edge of the vertical projection on the horizontal pole of the electromagnet takes place decrease the absolute value of the normal component of the magnetic induction of up to 50%, and up to 80 mm - 80%. Recession induction vertically in WA from bottom edge electromagnet pole distance of 50 mm is over 85%. The result of this differential induction in two-dimensional plane WA determines the difference value and the volume of the electromagnetic forces of the electromagnetic pressure in T-shaped WA, in which there is rotate on 90º the melt flow and dynamic vortex structures formation.

These vortex structures have a wide range of impacts on the hydraulic characteristics of the MDI and hydrodynamic processes in channels and the working area installation, and at speeds of melt channels MDI (up to 1 m/sec) and high current densities in the channels has been increasing dynamic pressure oscillations and electromagnetic pressure (10÷20% from its nominal value at a frequency from 1 Hz up to 3Hz), and at the transition to the metal with medium speeds (over 1 m/sec) at high current densities , due to the turbulence of flow in WA and the output therefrom is stabilized oscillation pressure characteristics, which do not to exceed 10-15 %. However, the oscillation frequency becomes one or two additional (2nd and 3rd) harmonics - 0.4÷0.8 Hz, 2.5÷3 Hz, 3.4÷4 Hz [6].

Among the most promising areas for further research is to optimize the processes of redistribution of the normal component of the magnetic induction in the WA and its surroundings, with a view to a more rational use of working volume WA to create volumetric electromagnetic forces, optimization of magnetohydrodynamic processes in it, stabilize and improve the operational and technical characteristics of magnetohydrodynamic systems.

To eliminate the harmful influence of the "anchor effect" pole electromagnet geometry and its projection on the working area can be transformed from a parallelepiped with width 100% for width of WA and height 70 % from height of WA, to trapezoidal form with the width of the upper base of the trapezoid - 40÷50 %, the lower base - of 120÷200% and 90-100% about height of WA. This will ensure a forced change (rotate on 90º angle) direction of the streamlines in the flow of melt moving through T-shaped WA, reduce friction loss, prevent the formation of stable vortex structures.

Increasing pressure characteristics MDI can be achieved by increasing the depth of the base WA by 50÷60% by performing indentations in the bottom part of the W-shaped channel. Estimated growth promoted by electromagnetic pressure, while maintaining constant values of the current density and the magnetic flow is up to $\approx$ 50÷60%. To eliminate the effect of retracting melt by creating a negative vector of the electromagnetic force in the working area, a special design of the electromagnetic system MDI as two U-shaped electromagnets, not connected to a common yoke, with two windings, which is included in the counter mode. The proposed solution avoids interaction of magnetic core of an electromagnet with induced in the liquid metal coil electrical current and increase the pressure and flow characteristics by 15÷25%.

3. Conclusion

The factors that reduce the efficiency of the operating magnetohydrodynamic units (MDI) for aluminum alloys its shown, that the main reserve increased performance MDI associated with reduced dispersion and increase in the concentration of magnetic fields in T-shaped WA, as well as reducing the negative influencing of vortex structures on its borders. Experimental studies aimed at researching the magnetohydrodynamic processes in MDI allowed to specify the representation of the role of the particular geometry of WA, the location and geometry of the C-shaped poles of an electromagnet, and the redistribution component of the current density $\boldsymbol{j}$ and the normal component of the external magnetic field in the projection of T-shaped WA. An assessment of the impact of MHD-effects in T-shaped WA on efficiency, technical and operational characteristics of MDI.

4. References

[1] Polishchuk V.P.; Tsin M.R.; Horn R.K. et al: Magnetohydrodynamic pumps for liquid metals. Kyiv, Naukova Dumka (1989) 256.

[2] Slazhnev N.A.: System of flow characteristics stabilization in magnetoweighting installation at variable level of the melt in the crucible. Metal casting and Ukraine (2011) 8 34-40.

[3] Afanasiev U.V.: Fluxgate devices. Leningrad, Energoatomizdat 1986.

[4] Verte L.A.: Magnetohydrodynamics in metallurgy. Moscow, Metallurgy 1975.

[5] Fikssen V.N.; Dubodelov V.I.; Gorshkov A.O.; Slazhnev N.A.; Shcherba A.A.; Shnurko V.K.: The study of the influence of the amplitude and frequency of the supply current to the hydraulic pressure in magnetodynamic installation. Tehnichna Elektrodinamika. (2001) 2 15-19.

[6] Fikssen V.N.; Dubodelov V.I.; Slazhnev N.A.; Gorshkov A.O., Musienko V.G.: Stabilization of the set level of melt in magnetohydrodynamic installations, Casting Process (2002) 1, 33-38.

THE INFLUENCE OF PROCESSING PARAMETERS ON FLUID FLOW IN CONTINUOUS CASTING OF MOULD WITH VERTICAL ELECTROMAGNETIC BRAKE

WANG ENGANG, LI FEI
Northeastern University, China
Email: egwang@mail.neu.edu.cn

Abstract: Some traditional kinds of the electromagnetic brake (EMBr) such as EMBr Ruler and FC-Mould are widely used in the continuous casting process, which generally have the patterns of level magnetic poles in the wide side of the mould. However, these magnetic poles are fixed in a certain height level of the mould, which generally could not fit the intermittently change of the depth and angle of submerged entry nozzle (SEN) during the casting process. That will reduce the effect of EMBr and even bring some negative effect such as impeding bubble floating.

In this papers, a new pattern of EMBr was proposed, which magnetic poles are vertically installed on the narrow sides of the mould from the meniscus to the impinge point of melt from the outlet of SEN, it is named as vertical EMBr (V-EMBr). The remarkable characteristic of V-EMBr is that their control effect is not affected by the change of melt surface level, the outlet position and angle of SEN. Moreover, the covered region of V-EMBr is the key region of initial solidifying shell in the mould, which generally brings subsurface defects in slab owing to the bubbles and inclusions are captured by initial solidifying shell.

The numerical simulation and physical experiment on the control of fluid flow, bubbles and inclusions under V-EMBr was investigated according to casting speed, immersion depth of nozzle and magnetic flux density. The results show that the impinging velocity of melts from SEN on the narrow sides of mold is obviously reduced. Meanwhile, the free surface velocity and turbulence energy are also obviously decreased, so that it is helpful to reduce the capture of the non-metal inclusions and bubbles by the initial solidifying shell and the meniscus near the narrow side of the mould. The magnetic flux density of 0.3~0.4T with the V-EMBr is enough to control the fluctuation of meniscus and the impinging of melt from SEN to the narrow sides of mould. It prove the V-EMBr could control the fluctuation of free surface and the impinging on the narrow sides of mold with the reasonable magnetic field parameters, and it especially can satisfy the change of immersion depth and outlet angle of the SEN during a long time continuous casting process.

THERMO-ELECTRIC MAGNETIC EFFECT DURING SOLIDIFICATION: IN SITU OBSERVATION AND THEORETICAL INTERPRETATION

FAUTRELLE[1] Y., REINHART[2] G., BUDENKOVA[1] O., NGUYEN THI[2] H., WANG[1] J.
[1] SIMAP laboratory, Grenoble Institute of Technology, France
[2] IM2NP, Marseille, France

Abstract: In the case of application of permanent magnetic field on liquid metals, some recent results revealed a dual effect on the liquid metal flow. Firstly, the magnetic field has a selective damping action on the flow at the scale of the crucible, due to the breaking part of the Lorentz forces. Secondly, the interaction of thermo-electro-electric currents near the solid-liquid interface (planar or dendritic front) with the applied magnetic field leads to the generation of electromagnetic forces (Thermo-Electric Magnetic effect), which act both on the liquid and on the solid at the scale of the meso-microstructures. We have investigated the TEM effect both theoretically, numerically and experimentally. The TEM forces may generate significant liquid motions, both in the bulk as well as in the mushy zone. This has been clearly shown by some theoretical investigations and numerical modeling using COMSOL software. It is also shown that TEM forces exist in the solid phase. We have been able also to calculate analytically the TEM forces acting on solid particles, e.g., sphere, cylinders. More complex shapes were dealt with numerical modeling. We have performed experimental investigation of the influence of a permanent magnetic field applied during the columnar and equiaxed solidification of Al-4wt%Cu. In situ visualization was carried out by means of synchrotron X-ray radiography. The TE forces when they are not curl-free, generate fluid flows both in the liquid bulk and in the mushy region. The latter effect was confirmed by the in situ experiments. Significant segregations and channeling effects were observed in the mushy zone. The experimental results also show that the TEM forces on the solid may lead to dendrite fragmentation as well as grain motions. It is shown that the TEM forces are responsible for a motion of dendritic/equiaxed particles, perpendicular to the direction of gravity. A heuristic analysis allowed us to estimate the fluid velocities and the velocities of the solid particles. A good agreement was found with the experimental data. Similar observations were also made during equiaxed growth in a temperature gradient. The in situ observation of the grain trajectories for various values of the temperature gradient demonstrated that gravity and TEM forces were the driving forces which controlled the grain motion (see figure below).

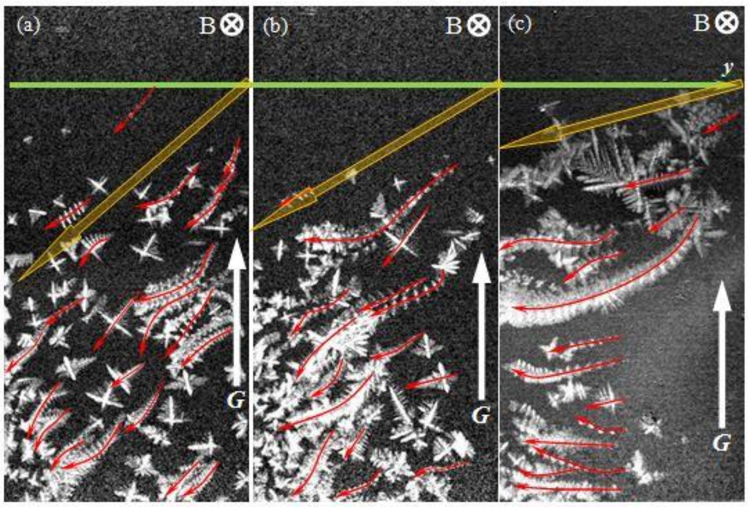

Figure: Successive - time overlaying images of equiaxed grain movements showing their deflections with different magnitude thermal gradients. (a) G = 500 K/m; (b) G = 1000K/m; (c) G = 2000K/m. (B = - 0.08 T; cooling rates are 2 K/min).

APPLICATIONS OF LORENTZ FORCE TECHNIQUES FOR FLOW RATE CONTROL IN LIQUID METALS

DUBOVIKOVA Nataliia, KARCHER Christian, KOLESNIKOV Yuri
Technische Universität Ilmenau
Institute of Thermodynamics and Fluid Mechanics
P.O.Box 100565, D-98684 Ilmenau, Germany
corresponding author: nataliia.dubovikova@tu-ilmenau.de

Abstract: Lorentz force velocimetry (LFV) is based on the electromagnetic induction of braking force acting on an electrically conductive fluid, which moves through a static magnetic field. Two such methods are presented here. First, time-of-flight LFV allows determining the flow rate of liquid metal by two flow meters placed at a predetermined distance by finding the time delay between their signals. Secondly, Lorentz torque velocimetry is a technique, which uses an electromagnetic pump with a torque sensor connected to the pump's shaft. Simultaneous pumping and measurement of the torque allows controlling the flow rate.

1. Introduction

Flow rate measurements in aggressive and hot fluids like liquid metals is a complicated task. Liquid metals are not transparent to allow usage of optical methods and chemical corrosion makes it impossible to employ mechanical probes. Therefore the most promising methods for liquid metal flow rate control are contactless techniques, a big branch of which is based on principles of magnetohydrodynamics [1]. Lorentz force velocimetry (fig 1) is such non-contact method based on electromagnetic principles.

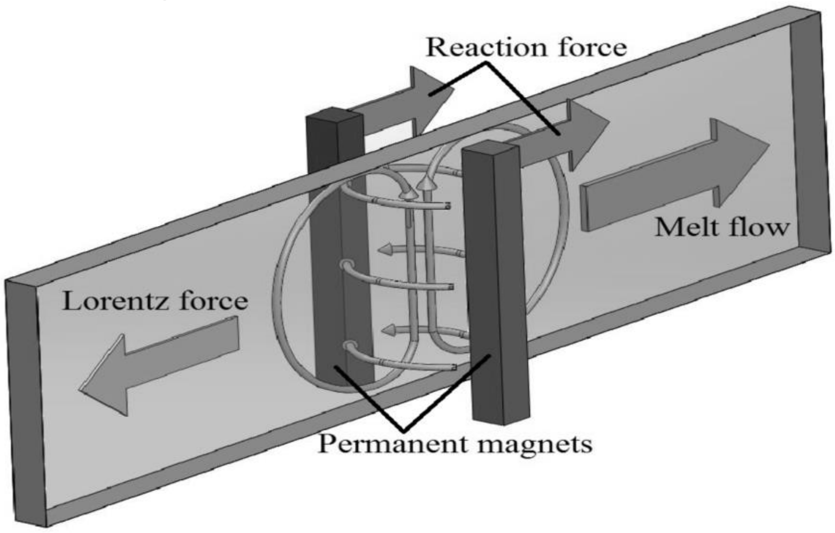

Figure 1: Electrically conductive liquid moves with velocity v through magnetic field of permanent magnets; magnetic field penetrates moving liquid and their interaction creates eddy currents inside the liquid, which give rise to Lorentz force F_L ("braking force"); resulting force of reaction F_R=-F_L acts on permanent magnets and can be measured

When an electrically conducting fluid moves across magnetic field lines, which are created by a permanent magnet, the induced eddy currents lead to a Lorentz force, which brakes the flow. The Lorentz force density is roughly [2]:

$$F_L \sim \sigma v L^3 B^2, \quad (1)$$

where σ is the electrical conductivity of the fluid, B is the magnitude of the magnetic field and L is the characteristic length of system. Magnetic field B and the moving, conducting medium interact in such a way as to restrain the relative motion of the field and the medium [3]. Magnet system and force sensor form a so-called Lorentz force flow meter. Because the force depends on velocity, it provides a velocity dependent signal for flow meter applications.

When Lorentz force appears within the liquid, according to Newton's third law, reaction force appears, which acts on the source of flow disturbance – the permanent magnet. For measuring of the value of force $F_{R,}$ which is equal to Lorentz force and opposite in direction, different ways are used. The devices that are applied to measure the Lorentz force can be constructed in two ways [2]. They can be designed as static flow meters where the magnet system is at rest and one measures the force acting on it. Alternatively, they can be designed as rotary flow meters where the magnets are arranged on a rotating wheel and the torque is a measure of the flow velocity [4]. We present examples of both methods here - Time-of-flight LFV [5] and Lorentz torque velocimetry (LTV) – flow control by the system of electromagnetic pump and torque sensor.

2. Experimental setup and results

Time-of-flight LFV (fig 2a,b) allows measurement of the flow rate in liquid metal and is unaffected by physical properties of fluid or by outer conditions. As the time-of-flight principle is based on cross-correlation measurements, two flow meters are mounted on a channel at a certain distance D to each other.

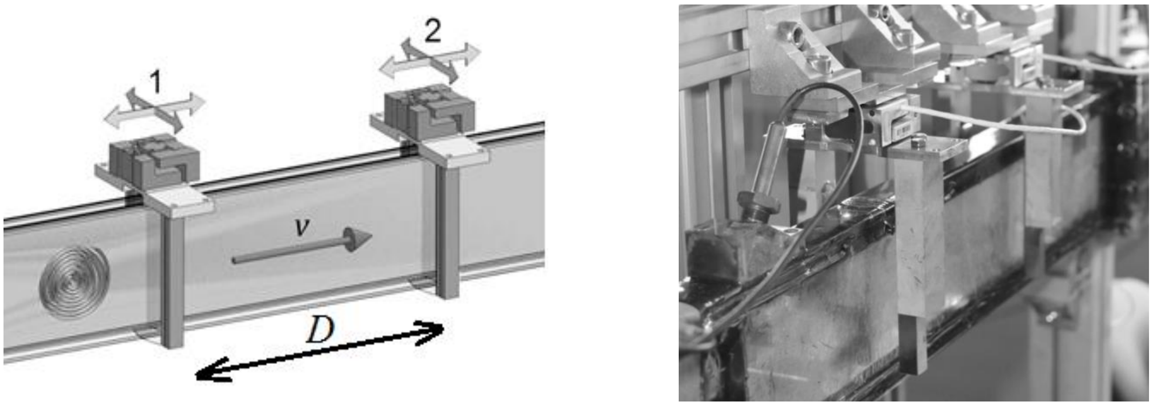

a b

Figure 2: Principle scheme of time-of-flight LFV (a) and the photo of the device (b)

A closed rectangular channel is used for the experiment. The channel with cross-section 80 mm x 10 mm is filled with the alloy GaInSn in eutectic composition. This allows conducting of model experiment at room temperature. The magnet system consists of permanent magnets with magnetic induction of 450 mT at the surface and two-component strain gauge sensors, which are mounted to record the force that the fluid exerts on the magnet system. Experiment procedure results in evaluating the transit time τ (time-of-flight) of any vortex structure that is present in the flow needed to pass through the distance D to obtain the volumetric flow rate Q_V is then given by the relation:

$$Q_V=vA=kD/\tau, \quad (2)$$

where A – cross-section area of the channel, k – experimental coefficient of proportionality. To increase both the rate and the intensity of such vortex structures and likewise the rate of usable signals, vortices can be generated by two different methods: mechanically – by immersing a solid body in the channel, or electromagnetically – by formation of magnetic obstacles [6] within the fluid as a result of static or time-dependent magnetic field. In other words according to time-of-flight LFV, velocity is estimated by measuring the traveling time τ for the vortex to cross a predefined distance *D* between flow meters.

Measurements of time shift τ are based on obtaining a cross-correlation function of two force signals (fig 3a,b), which are registered by magnetic measurement systems as a result of disturbance by the passing vortex (in fluid experiment) or copper plate (in dry experiment).

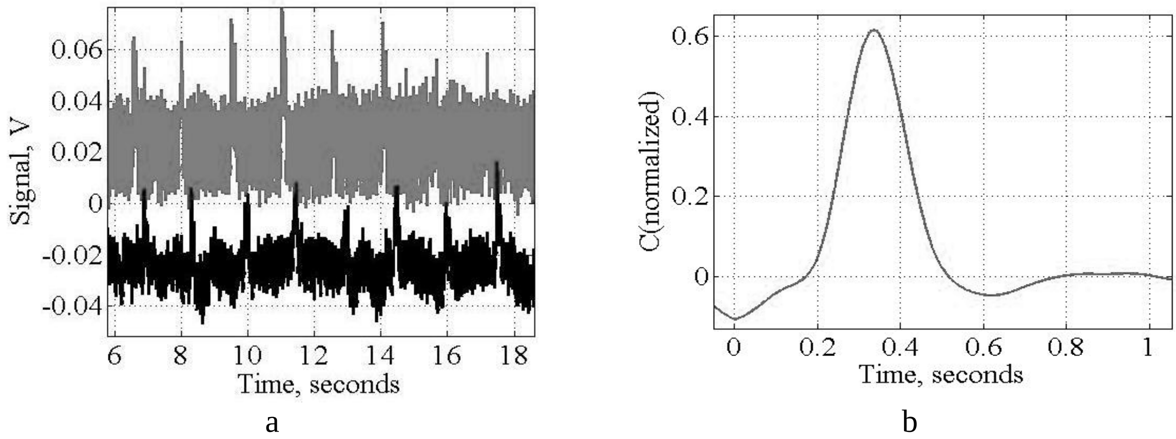

Figure 3: Raw signal of time-of-flight LFV (dry tests) with several peaks, caused by serial copper plate movement through magnetic field of first flow meter (grey curve) and second flow meter (black curve) (a) and normalized cross-correlation coefficient C of the signals (b)

To ensure correct working of flow meters it is necessary to provide dry tests in which solid material – copper plate – was used instead of moving vortex. Because σ of solid conductor is about twenty times higher than σ of the melt, the Lorentz force induced by its movement is likewise twenty times higher (according to (1)) and it is possible to observe clear peaks on both signals even without additional filtering. The main goal of dry tests is to register signals that prove operating performance of measurement scheme. When plate is moved serially through the magnetic field of both flow meters with a known velocity and two peaks are observed in each trial.

Another method – LTV [7] – includes applying electromagnetic pump as flow-controlling and as flow-measurement device simultaneously.

Figure 4a shows the principal scheme of such a pump. The pump consists of a pair of metal disks, on each of which a total of 20 finger-type permanent magnets are mounted. The disks are arranged on a shaft that is connected to an electrical motor. By controlling the motor power, we can control the rotation frequency n of the shaft. The rotation of permanent magnets generates a time-dependent magnetic field acting on liquid within the gap between the two rotating disks. In turn, the rotary field gives rise to Lorentz force that pumps the liquid and acts on the pump shaft as a back reaction. A strain gauge torque sensor is mounted on the shaft to measure the torque that is exerted on liquid.

Using such an arrangement, the volumetric flow rate Q_V can be estimated by the relation:

$$Q_V = kT/(\sigma B^2 Ll) \tag{3}$$

where *T* is the measured torque, *l* its lever, and *k* is the device factor. This factor depends on a number of specific experimental parameters like the aspect ratio of the flow channel, the actual geometric arrangement of the permanent magnets, among others. Hence, the specific value of *k* has to be obtained for each experimental setup by a calibration procedure. Within our experiment, two methods – ultrasonic Doppler velocimetry and local velocimetry by Vives-probe [8] – were used as standards to measure velocity value; the results show strong temperature-dependent behaviour of *k*, which indicates necessity of qualitative temperature control of liquid in the experiment.

For obtaining specific value of l, one needs to conduct simultaneous measurement of Lorentz force F_L and torque T for various rotation frequencies in order to find the functional relation $T/F_{L.}$ However, calibration of the device using liquid metal is complicated, time-consuming and expensive. Therefore we perform a dry calibration procedure. The main idea of dry calibration is to model the liquid by a solid electrically conducting non-magnetic material like solid aluminium bars. In this case F_L can be measured by commercial strain gauge force sensors and the ratio of torque to force could be easily calculated.

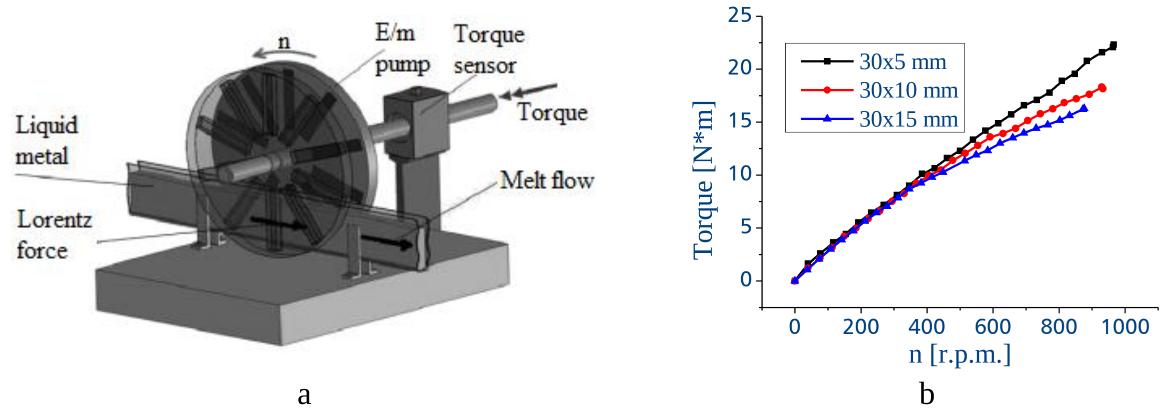

Figure 4: Working principle (a) and Lorentz torque measurement result of dry calibration (b) of LTV flow control. Electromagnetic pump pushes liquid and, hence is a subject to a reaction torque (b) that was measured by torque sensor.

Figure 4b shows the resulting torque acting on the shaft as measured by the torque sensor. In the graph we use a scaled representation of the measured value. The re-scaling has been performed to eliminate the inherent dependence of the data on the width of the aluminium bars. In detail we use the scaling:

$$T_{SC}=T(H/W), \qquad (4)$$

where H and W denote the distance between wheels and the width of the aluminium bar, respectively. The motivation for this re-scaling stems is explained below.

As a rule Lorentz force and produced by it torque increase with increasing of cross-section of the conductive material because with a change of a plate's width as a consequence two parameters are changing: the volume of a conductive material that is influenced by magnetic field, and its electric resistance to induced eddy current, as well as the gap between wheels of e/m pump. Besides, magnetic field distribution in between of wheels is not homogeneous: it decreases from walls to the middle of gap. Hence magnetic field, which passes through thick plate, has higher value than through thin one.

The difference between scaled values of measured torque under high rotation frequency of the e/m pump is caused mainly by change of magnetic Reynolds number Re_m (fig 5a) for aluminium bars. An increase of width results in an increase of the magnetic Reynolds number Re_m given by the relation by $Re_m=\mu\sigma vL$, where μ is the magnetic field constant. This increase is due to the increase of the electromagnetic interaction length L. As it is known from MHD, larger values of Re_m result in stronger induced magnetic fields that fight against the applied primary field [9]. This give rise to a weakening of the overall magnetic field that contributes to the Lorentz force. Therefore lower values for T are observed in cases of thicker plates. For liquid experiment the obtained values of Re_m are ten times less than dry calibration results because of difference between σ of aluminium ($3{,}5\cdot10^7$ S/m) and GaInSn ($3{,}5\cdot10^6$ S/m). Hence the dependence between Re_m and the scaled pump power in case of liquid is linear, while for aluminium the ratio has curvilinear contour [9].

According to fig 5b, the lowest reachable value of *Re* is proportional to $5 \cdot 10^3$. The experimentally registered *Re* is higher than its critical value for channels, hence only turbulent flow can be provided within the experiment.

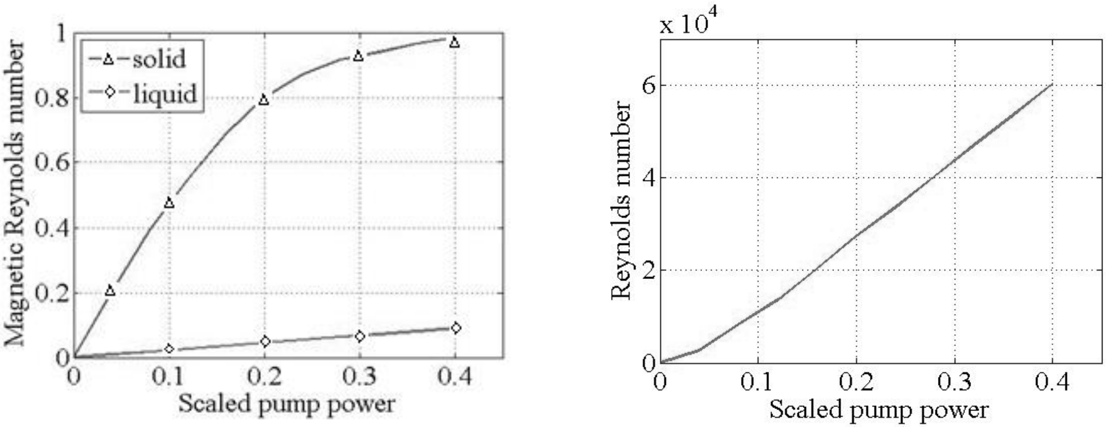

a b

Figure 5: Obtained by LTV values of the magnetic Reynolds number Re_m for solid (aluminium bars) and liquid (GaInSn) materials (a), and reachable values of Reynolds number *Re* (b) in the experimental channel

3. Conclusion

The model experiments described here demonstrate that time-of-flight LFV and LTV are feasible non-contact electromagnetic techniques for measuring and control of volumetric flow rates in turbulent liquid metal flow. The first technique is based on cross-correlating the force data registered by the two flow meters. Due to this it is independent of any fluid properties and the magnetic field distribution. The second method allows complete control of the flow rate of the fluid.

The experiment shows that both methods must be properly calibrated by applying additional measurement techniques and controlled temperature regime. The ratio between time shift and characteristic flow time strongly depends on the separation distance of the flow meters and presumably, on the geometry of the obstacle, which is submerged into the flow or created in contactless way in order to produce detectable vortex structures. In addition an optimal data processing technique for fluid time-of-flight results is necessary to obtain precise value of volumetric flow rate within the channel.

4. References

[1] Shercliff, J. A. The Theory of Electromagnetic Flow-Measurement, Cambridge, UK, Cambridge University Press, 1962.

[2] Thess, A.,Votyakov, E., Knaepen, B., Zikanov, O. Theory of the Lorentz force flowmeter. - New Journal of Physics, 9, (2007), 299.

[3] Priede, J., Buchenau, D., and Gerbeth, G. 'Single-magnet rotary flowmeter for liquid metals'. Journal of Applied Physics 110 (3), (2011), 034512.

[4] Davidson, P.A. An introduction to Magnetohydrodynamics. Cambridge, UK, Cambridge University Press, 2001.

[5] Jian, D., Karcher, Ch. Electromagnetic flow measurements in liquid metals using time-of-flight Lorentz force velocimetry. Meas. Sci. Technol. (2012), 23.

[6] Votyakov, E. V., Kolesnikov, Y., Andreev, O. and others Structure of the Wake of a Magnetic Obstacle. Phys. Rew. Letters 98, (2007), 144504.

[7] Dubovikova, N., Kolesnikov, Y., Karcher, C. Flow rate measurement in aggressive conductive fluids. European Physical Journal (EPJ) Web of Conferences, 67 (2014), 02022.

[8] Ricou, R., Vives, C. Local velocity and mass transfer measurements in molten metals using an incorporated probe. Int J Heat Mass Transfer 25 (1982), 1579–1588.

[9] Moffatt, H. Keith Reflections on Magnetohydrodynamics. Cambridge, UK, Cambridge University Press, 2000.

INFLUENCE OF MHD PLASMA ACTIONS IN CASTING MAGNETODYNAMIC INSTALLATION ON HOMOGENEITY OF LIQUID ALUMINIUM ALLOYS AND THEIR PROPERTIES IN SOLID STATE

DUBODELOV[1] S., SIDOROV[2] V., SKOROBOGATKO[1] J., GORYUK[1] M., FIKSSEN[1] V., POPEL[2] P., NARIVSKY[1] A.
[1] Physico-Technological Institute of Metals and Alloys of Ukraine NAS, Kyiv, Ukraine
[2] Ural State Pedagogical University, Ekaterinburg, Russia
E-mail: mgd@i.kiev.ua

When studying the liquid state of the metallic systems, many researches prove that preparation of alloys (for example, on aluminium base) goes with the formation of micro-inhomogeneities in the melt. They are caused by metallurgical heredity of charge. At solidifying of alloys, such micro-inhomogeneities provoke substantial declining of structure and properties. Therefore, it is necessary to provide destruction of such formations. For decision of this problem, a new method of complex treatment of aluminium melts has been developed. It is based on combination of homogenizing influence on liquid metal both electromagnetic and high-power plasma effects. Plasma action is concentrated in the local area of aluminium melt being found into macrovolume of liquid metal. At that, liquid aluminium alloy is contained in a bath of specialized magnetodynamic installation (MDI). The melt is heated by induction currents and thermostated at a set temperature (no more than 800 ^{0}C). Such temperature is substantially lower than the temperature of transition of melt from the metastable micro-inhomogeneity state to micro-homogeneity equilibrium state. So, as a result, two areas of thermal and forced actions are formed in liquid metal: 1) via submerged plasmatron in the melt volume; 2) via crossed electromagnetic fields in a region of direct MHD action on the melt.

The feature of the first area consists is the following. At the nozzle exit section of the submerged plasmatron, the temperature of liquid alloy can be ca. 3000-5000 ^{0}C (it is substantially more than the average temperature of the melt). It causes a considerable temperature gradient. There is evaporation of alloy components in this area, and then, as moving off the area of plasma stream action, there is condensation of components. So, it is a specific type of thermal-time processing, combining alternation of evaporation and condensation. At that, there is realized the thermal destruction of microgroups of clusters with negative hereditary structure.

To provide the processing of all melt volume in the MDI by direct action of plasma, it is used the frequent moving of liquid aluminium alloy under the action of electromagnetic forces generated in the second above-mentioned processing area. That is the feature of the MDI.

Liquid metal in its working area is processed by electromagnetic actions: alternating electric current with density to 20×10^6 A/m^2; alternating magnetic field by induction to 0.3 T (it is created on the definite area of the induction channel, the so called working area of MDU). As a result of superposition of current and field, it is generated volume electromagnetic force (to 60×10^5 N/m3). It provides melt motion. Also, because of MHD-effects there are vortexes originated. Due to frequent passing of the melt through the working area, the indicated factors substantially affect the thermal and forced processing of liquid metal. As result, complex MHD-plasma action on liquid metal realizes disintegration existed regions of micro-inhomogeneities. So, at relatively low overheating of all aluminium melt volume in MDI, this melt repeatedly moves through the local area of the plasma heating (to 5000 ^{0}C) and at one time processed by power MHD and hydrodynamic actions. It causes disintegration regions of microinhomogeneities, removes negative metallurgical heredity, and promotes liquid alloy homogeneity. As result, it is achieved the improvement of structure and rise of properties of solid alloys and castings.

LORENTZ FORCE SIGMOMETRY: A NOVEL TECHNIQUE FOR MEASURING THERMO-PHYSICAL PROPERTIES OF MOLTEN METALS

ALKHALIL[1] S., THESS[1] A., FROHLICH[2] T., KOLESNIKOV[1] YU.
[1] Ilmenau University of Technology / Institut für Thermo - und Fluiddynamik, Germany
[2] Ilmenau University of Technology, Institute for Process Measurement and Sensor Technology, Germany
E-mail: shatha.alkhalil@tu-ilmenau.de

The precise measurement of the thermo-physical properties of molten metals such as electrical conductivity, density, and viscosity are of great importance for industrial applications, in particular, for MHD flow control in high-tech production processes. We term the technique "Lorentz force sigmometry" as deriving from the Greek letter sigma often used to denote the electrical conductivity. In previous measurements techniques a resistance of vessel with two electrodes for measuring electrical conductivity of molten metal has been used [1]. For chemically aggressive hot liquids, there is no suitable material for electrodes. In our technique, we apply non-homogeneous magnetic field acting on a moving conducting fluid in which according to Ohm's law the eddy currents are induced. These eddy currents produce a secondary magnetic field. In consequence, the interaction of the applied magnetic field with induced eddy currents generates a Lorentz force that breaks the motion of the fluid. At the interaction of secondary and applied magnetic fields, the same force acts on magnet system [2]. By measured this force and the mass of fluid flowing through the magnetic system we calculate the electrical conductivity of the fluid. The results of two series of measurements are presented, one with solid bars made of copper and aluminum to find the calibration factor of the setup then we use this calibration factor to calculate the electrical conductivity of a third solid bar made of brass. Our results compared with working of a commercial device, called by SigmaTest, give the error less than 0.5%. The other measurements are with liquid metal alloy in the composition of Ga67In20.5Sn12.5 at room temperature in order to find the calibration factor which will be used to measure the electrical conductivity of ferrous and non-ferrous molten metals at high temperature in industrial conditions.

References

[1] S. Schiefelbein, N. Fried, K. Rhoads, and D. Sadoway: A high-accuracy, calibration-free technique for measuring the electrical conductivity of liquids. American Institute of Physics, 07/1998; 69(9).
[2] A. Thess, E. Votyakov, B. Knaepen and O. Zikanov: Theory of the Lorentz force flowmeter. New Journal of Physics 9/299, 08/2007.

EFFECT OF A SUPERIMPOSED DC MAGNETIC FIELD ON AN AC INDUCTION SEMI-LEVITATED MOLTEN COPPER DROPLET

BOJAREVIČS[1] A., BEINERTS[1] T., GRANTS[2] I., KALDRE[1] I., ŠIVARS[1] A., GERBETH[2] G., GELFGATS[1] G.
[1] Institute of Physics University of Latvia, Miera str. 32, LV-2169, Salaspils, Latvia
[2] Helmholtz-Zentrum Dresden-Rossendorf
E-mai: andrisb@sal.lv

Abstract: While a piece of pure Copper on a ceramic substrate was inductively melted by 9 to 18 kHz AC magnetic field with axial magnetic DC field superimposed, the liquid metal stably semi-levitated in the expected "conical" free surface shape. The diameter of the liquid metal at the basis was 30 mm, the volume – more than 20 cm^3. Replacing the ceramic substrate with a Glassy Carbon, which was not wetted by the molten Copper, caused instability of the semi-levitated Copper droplet. In the absence of the DC field severe chaotic instabilities of the liquid metal shape occurred, causing splashes and uncontrolled contact with crucible walls. When axial DC magnetic field with induction 0.35 T was superimposed the liquid metal droplet exhibited harmonic azimuthal wave deformation of the free surface. Higher frequencies lead to smaller characteristic wavelength. Transverse DC magnetic field direction suppressed the travelling wave deformations of the droplet shape. Stabilizing effect of the DC magnetic field during induction melting has been shown for axial, transverse and 45 degree direction magnetic field. These results experimentally demonstrate the possibilities to improve the stability of levitated metal volumes by superimposed DC magnetic field.

High frequency magnetic field induction melting of metals is a well-known technique in crystal growth and advanced metallurgy. An overview of the technologies was given by A. Mühlbauer [1]. One of the techniques is the cold crucible semi-levitation induction melting, while liquid metal is supported by a water cooled substrate from below [2]. Here we report some curious observations while developing a small scale experimental setup for high melting point liquid metal electromagnetic processing during HF AC semi-levitation with superimposed DC magnetic field. A schematic of the initial experimental setup and the stably semi-levitated pure liquid Copper region are shown on the Figure 1. The AC field frequency range was from 9 to 18 kHz, maximum induction up to 0.09 Tesla. The DC magnetic field with maximum induction 0.35 Tesla was delivered by a permanent magnet assembly, permitting to apply quite uniform field over the sample region in the direction range from axial to horizontal. Under the impact of the axial DC field the semi-levitated liquid Copper free surface was very stable up to the overheat level when the boiling of the Copper in vacuum happened at approximately 1650 ^{o}C. The magnitude of the DC field was not sufficient to considerably damp the flow in the liquid metal, but was sufficient to suppress turbulence in the semi-levitated liquid metal. In the absence of the DC field and sufficiently high dimensionless frequency Ω the magnitude of the flow velocity U_0 may be estimated from the balance of the electromagnetic forcing in the skin-layer and the inertia force and the balance of magnetic and hydrostatic pressure on the surface of the melt:

$$\rho \frac{U_0^2}{\delta} = \sigma\omega\delta B^2 \qquad \frac{B^2}{\mu_0} = \rho g H$$

$$\delta = \sqrt{\frac{1}{\sigma\omega\mu_0}} \qquad \Omega = \sigma\omega\mu_0 R^2 \gg 1$$

$$U_0 = \sqrt{gH} = \frac{B}{\sqrt{\rho\mu_0}}$$

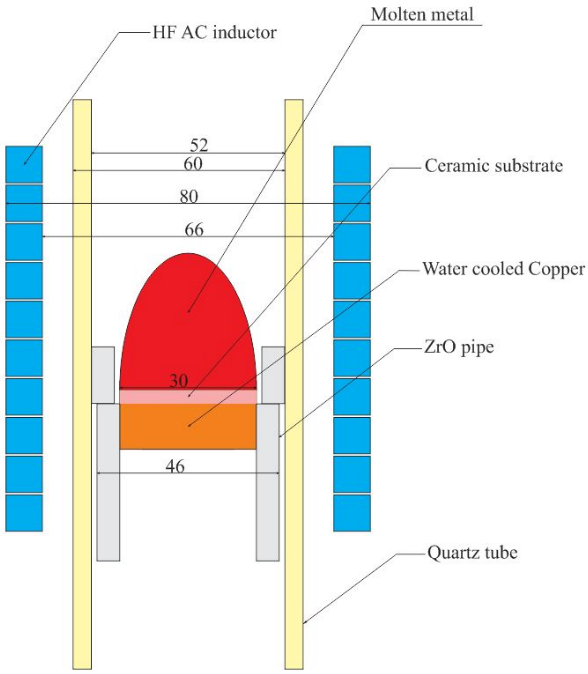

Figure 1. A schematic of the setup on the left and the semi-levitated Copper in axial 10 kHz AC field and DC field on the right.

where is the density of the liquid metal, – conductivity, – angular frequency of the

AC field, B – the induction of the AC field at the bottom rim of the semi-levitated region, δ – the skin-depth, R – the radius of the substrate, H – the height of the semi-levitated region. The dimensionless frequency magnitude was **Ω** = 160 in liquid Copper at 18 kHz AC field. When DC field is superimposed, the flow in the core region inside the skin-depth would be damped to U, if MHD interaction parameter N >> 1:

$$U = \frac{U_0}{N} \qquad N = \frac{\sigma}{\rho}\frac{B_D{}^2 R}{U_0} = \frac{\sigma}{\rho}\frac{B_D{}^2 R}{\sqrt{gH}}$$

where B_D is the induction of the DC magnetic field. During the reported experimental tests, assuming liquid Copper physical properties, N ≈ 2 at maximum AC and DC field inductions.

Obviously the direction of the DC field would be important, how the flow and turbulence is damped. What type of conducting fluid flow would be damped? The flow interacting with the DC field should induce the electrical current circulation; otherwise there would not be any damping impact. Applying a curl operation on Ohm’s law delivers necessary condition for electrical current circulation, assuming zero divergence of magnetic field and velocity:

$$\nabla \times \frac{j}{\sigma} = (B_D \nabla)U - (U\nabla)B_D \quad \text{or} \quad \nabla \times \frac{j}{\sigma} = B_D \frac{\partial U}{\partial l_B} - U\frac{\partial B_D}{\partial l_U}$$

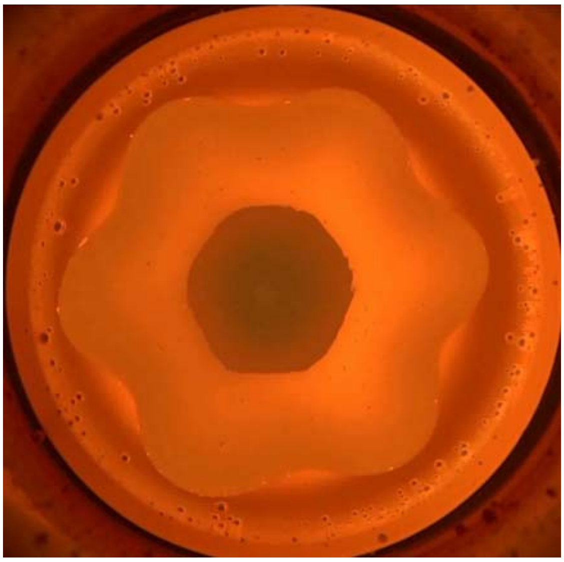
Figure 2. 18 kHz AC field, axial DC field.
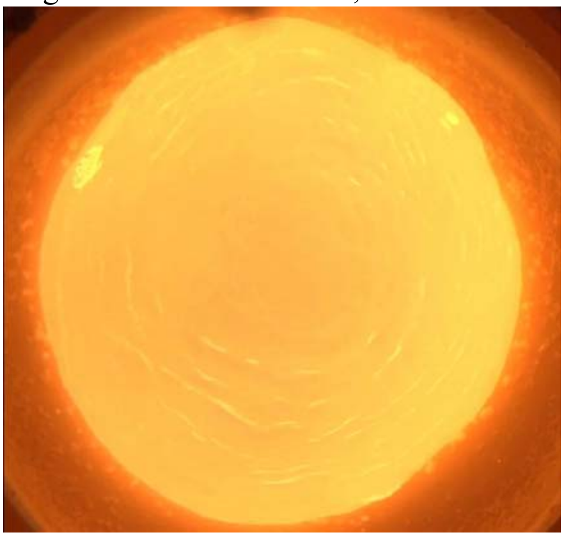
Figure 3. 18 kHz AC field, transverse DC field.
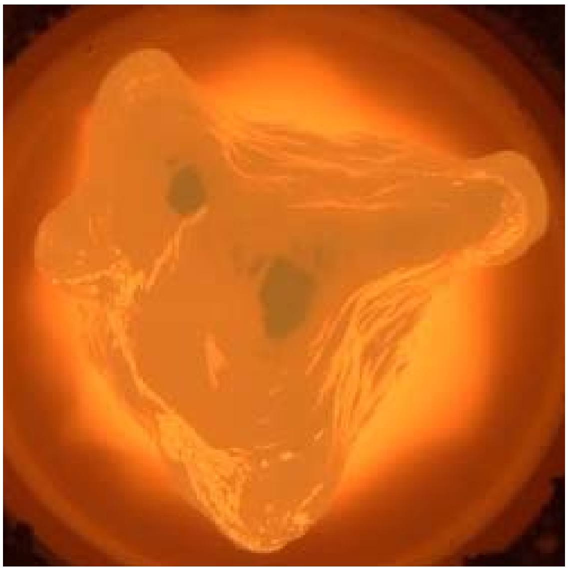
Figure 4. 18 kHz AC field, no DC field.

where j is the current density. The former equation may be interpreted, that the motion of a conductor in magnetic field produces electrical current only, if the magnetic field varies along the direction of the velocity and/or if there is a variation of velocity along the direction of the magnetic field. Or, if DC field is uniform, there is no induced current, if velocity of the melt does not vary in in the direction of the field and no interaction with the flow.

The unexpected happened when the ceramics support was replaced by a Glassy Carbon. During impact by the superimposed axial AC and DC fields a highly organized azimuthal wave pattern of the molten Copper droplet shape were observed. If the melt has zero velocity at the interface with the substrate, nothing like observed should ever happen! The only obvious experimental observation was that above the temperature 1200 C^{o} the Glassy Carbon was not wetted by the Copper melt. It was obvious that the phenomenon resembles well known behavior of the fully levitated liquid droplets [3, 4]. In the current experiment there was no full levitation, the droplet was supported by the Glassy Carbon substrate. Similar behavior is known, the historical priority being the unstable droplet of the water on a well heated substrate due to Leidenfrost effect, when similar azimuthal waves are also observed. Experimental observations of such type of instability has been reported [5, 6], but the former cases include substantial difference from the current one – during cited experiments there have been a layer of an encapsulating, substrate wetting, nonconducting fluid between the oscillating fluid and the substrate. In our case the vacuum surrounding pressure eliminates any vapor cushion beneath the semi-levitated molten metal. The only questionable suspect regarding the fluid interface may be the Copper oxide, which becomes liquid at temperature above 1200 C^{o}. But, on the other hand, Copper oxide decomposes in vacuum at the temperature above the 1200 C^{o}. It was obvious that no-slip boundary condition on the bottom was not valid.

The axial DC magnetic field did not suppress any waves with fluid motion not varying in the field direction, but the flow became highly ordered, with 6-mode azimuthal wave travelling anticlockwise. The axial DC field has damped most of the azimuthal flow produced turbulence due to the AC field induced flow in the core of the melt region, which has a pronounced variation along axial magnetic field, but did not suppress the wavy motion, which has no variation along the DC field.

The transverse DC magnetic field eliminated azimuthal wave motion, but did not suppress the flow in the core of the droplet as efficiently as the axial direction. The free surface deformations of the droplet were quite chaotic and fast. The general shape of the droplet became slightly extended along the direction of DC magnetic field – from top to bottom on the Figure 3. The free surface is rippled by a capillary waves with a wavelength comparable with skin-depth, approximately 2 mm. It may be suggested that higher induction of the DC field at N >> 1 would achieve damping of the flow and surface deformations.

The Copper droplet became extremely unstable, when DC magnetic field was removed. The chaotic shape of the droplet was changing very fastly, video recording with 50 frames per second deliver evidence, that during the period of 20 ms the shape was completely transformed. Turbulent flow in the core of the droplet, azimuthal wave instability and capillary surface rippling add up to unstable state of the droplet, saved from complete destruction only by the walls of the Glassy Carbon crucible, from which the droplet bounces back.

Reduction of the frequency of the AC magnetic field two times to 9 kHz, increased the skin-depth. In general the droplet behaved similarly as described above, but became considerably more unstable. In axial DC field the azimuthal wave exhibited 5 and 6 mode numbers, the amplitude of the wave was higher. Without DC field small diameter jets were splashed out quite often, as may be seen on the right side of Figure 7.

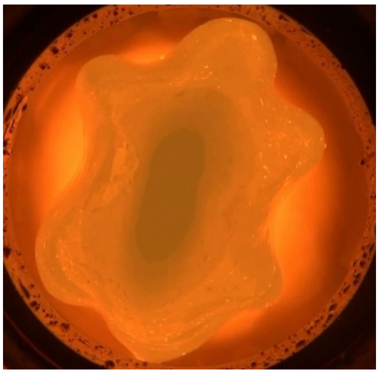

Figure 5. 9 kHz AC field, axial DC field.

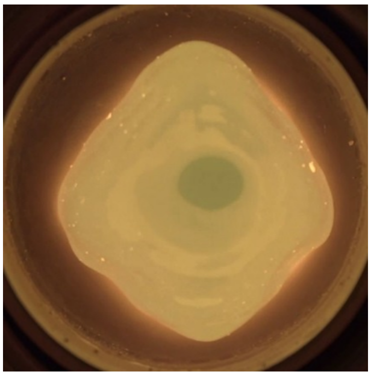

Figure 6. 9 kHz AC field, transverse DC field.

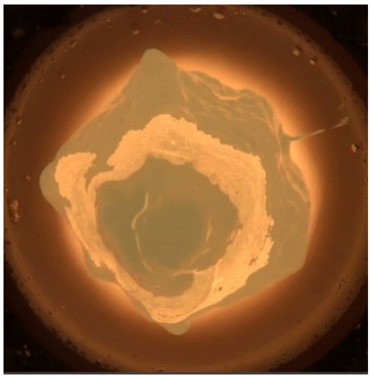

Figure 2. 9 kHz AC field, no DC field.

The orientation of the DC magnetic field at 45 degree angle to the axis was also aplied during melting, displaying similar stabilizing effect as the transverse direction field.

Conclusion

The reported unstable behavior of the semi-levitated droplet crucially depends on the wetting of the substrate. Only if there is no wetting and probably the no-slip boundary condition the behavior becomes acceptable. The azimuthal wave type instability is observed both in absence of the DC magnetic field and in axial magnetic field. The DC field delivers substantial stabilization of the droplet, even if the MHD-interaction parameter is not too large. The direction of a DC field with a considerable transverse component seems most promising for stabilization. It may be suggested that in AC field configuration for full levitation of the molten metal, the correct choice of the magnitude and direction of the DC magnetic field may allow stable levitation of the large drops of liquid metal even during very high magnitude of the high frequency AC magnetic field.

References

[1] A. Mühlbauer. Innovative Induction Melting Technologies: A Historical Review. Modelling for Material Processing, Riga, June 8-9 (2006).

[2] A. Umbrasko, E. Baake and B. Nacke, A. Jakovics. Numerical studies of the melting process in the induction furnace with cold crucible. The International Journal for Computation and Mathematics in Electrical and Electronic Engineering,Vol. 27 No. 2, 2008, pp. 359-368.

[3] Gailitis, A: Oscillations of a conducting drop in a magnetic field. Magnetohydrodynamics. Vol. 2, No. 2, pp. 79-90 (1966).

[4] Priede, J: Oscillations of weakly viscous conducting liquid drops in a strong magnetic field. Journal of Fluid Mechanics. Vol. 671, pp. 399-416 (2011).

[5] Spragg, K; Sneyd, A; Fautrelle, Y: Mathematical analysis of the oscillations of a liquid metal drop submitted to low frequency magnetic fields. International Scientific Colloquium. Modelling for electromagnetic processing, Hannover, October 27-29 (2008).

[6] V. Kocourek, Ch. Karcher, M. Conrath, and D. Schulze. Stability of liquid metal drops affected by a high-frequency magnetic field. PHYSICAL REVIEW E **74**, 026303, 7 p, 2006.

SOLIDIFICATION PROCESS IN A BENCHMARK EXPERIMENT

ZAIDAT K., FAUTRELLE Y., HACHANI L.
Grenoble - INP/SIMAP, France
E-mail: kader.zaidat@simap.grenoble-inp.fr

Abstract: The introduction of magnetic field in the solidification process is one of the effective methods to improve the microstructure and mechanical performance of alloys (by controlling the defects as freckles or segregated channels). At SIMaP-EPM laboratory, we have proposed to control the fluid flow with a travelling magnetic field (TMF). With this kind of electromagnetic field the control of the intensity and the direction of Lorentz force are easy (by changing the order of electric phases). Since ten years, EPM team developed some experiments and models around the TMF. The present work deals with a experimental and numerical studies of solidification process under forced convection induced by a travelling magnetic field (TMF). The impact of TMF and gravity on segregations of a Tin-Lead alloy has been examined.

SEGREGATION CONTROL DURING DIRECTIONAL SOLIDIFICATION USING MAGNETIC FIELD AND ELECTRIC CURRENT

KALDRE[1] I., FAUTRELLE[2] Y., ETAY[2] J., BOJAREVICS[1] A., BULIGINS[3] L.
[1]Institute of Physics University of Latvia, Miera str. 32, LV-2169, Salaspils, Latvia
[2]SIMAP-EPM, PHELMA-Campus, BP75, 38402 St Martin d'Hères Cedex, France
[3]University of Latvia, Faculty of Physics and Mathematics, 8 Zellu str., LV-1002 Riga, Latvia
E-mail: imants.kaldre@gmail.com

Abstract: Component segregation during solidification of a multicomponent alloy is an important practical problem. Segregation can be caused by gravity field or melt flow in the crucible. Applied magnetic field during solidification creates thermoelectromagnetic convection (TEMC). Magnetic field creates Lorentz force if electric current is applied. Secondly, magnetic field damps large scale melt convection thus limiting heat and solute exchange. These two mechanisms allow us to modify net melt convection and segregation in the crucible by applying electric current and magnetic field during solidification of a metallic alloys.

1. Introduction

Electric current may appear near solidification front due to thermoelectric effect between solid and liquid phases, caused by temperature gradient and differential thermoelectric power between solid and liquid phases [1, 2]. However direction and magnitude of this current is mainly defined by the material properties and interface morphology, and temperature gradient at the interface, which are difficult to control and maximum intensity of this current is limited. If transverse magnetic field is applied to directionally solidifying alloy, then macrosegregation in the crucible scale perpendicular to magnetic field direction is observed as a consequence of thermoelectromagnetic convection (TEMC) [3]. Electric current may also be applied externally, thus creating Lorentz force and convection flow of the liquid melt. Directional solidification under applied electric current and magnetic field has been studied by several authors [4, 5]. If direct electric current is applied through the solidification front, then current component which is perpendicular to the magnetic field interacts with it and melt convection is caused by this force.

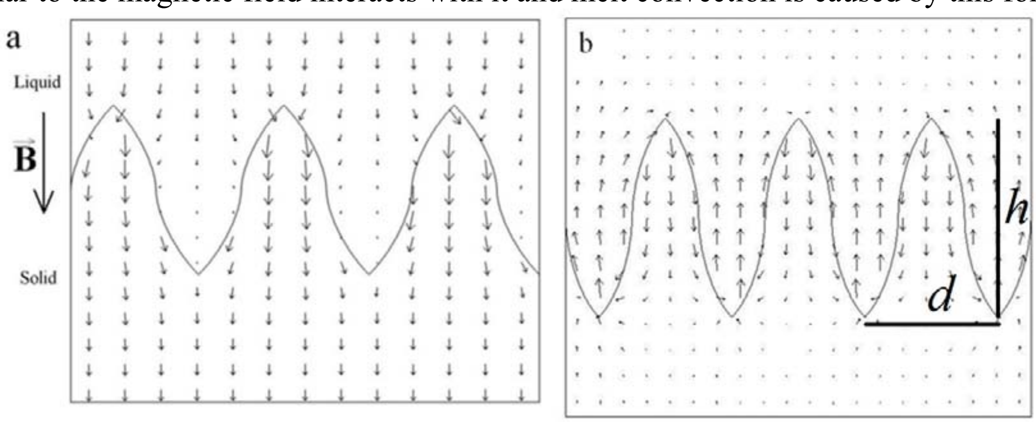

Figure 1: Conduction current redistribution at the dendritic interface due to different conductivities of solid and liquid phases: a) current distribution at the interface between two media with different conductivities; b) current component when axial current in the bulk of the liquid is subtracted.

Electrical conductivities of solid and liquid phases can differ several times for metals and metallic alloys, thus at the dendritic solidification interface electric current redistribution takes place. In the bulk of the solid and liquid domains current density is uniform and Lorentz force caused by homogeneous magnetic field is irrotational. If this current component is neglected then we obtain current pattern at the interface similar to TE current as shown in Fig. 1.

In this work Sn-Pb alloy is directionally solidified under 0.5 T static transverse magnetic field and applied electric current through the solidification interface. Macrosegregation caused by current and magnetic field interaction caused electromagnetic convection is experimentally investigated in this work. Study has been focused on investigation of simultaneous action of electromagnetic convection and thermoelectromagnetic convection. Possibilities to control macrosegregation by applied electric current and magnetic field during directional solidification has been experimentally and theoretically analyzed and possibilities to eliminate or enhance effect on the solidified structure caused by TEMC has been verified.

2. Presentation of the problem

High purity tin and lead (99.99%) was used to prepare Sn-10%wt.Pb alloy, which was then casted into the alumina799 crucible (L=110mm, ID=6mm, OD=10mm). Samples were then remelted and solidified under intense electromagnetic stirring to ensure good homogeneity of initial samples, which are later directionally solidified in a Bridgman setup at controlled growth velocity and temperature gradient. In these experiments growth velocities from 2 μm/s to 10 μm/s was used. Temperature gradient at the interface was θ=8 K/mm in all experimental sessions of this work. Upper part of the sample is melted by the resistive furnace around the crucible while bottom part is kept solid by water cooled copper ring. Furnace and water cooled ring are stationary while crucible is lowered by a programmable pulling system. Solidification front is always located between heater and cooler at the same location. Thus, the actual solidification velocity was assumed to be equal to the pulling velocity of the crucible. Transverse magnetic field of 0.5 T was created by a permanent magnet system. For optical microscopy analysis samples were polished to 1 μm surface roughness and then chemically etched with 4% nitric acid ethanol solution, which darkened the lead-rich fraction. Electric current is introduced in liquid part through 4 mm diameter stainless steel electrode as shown in Fig.2.

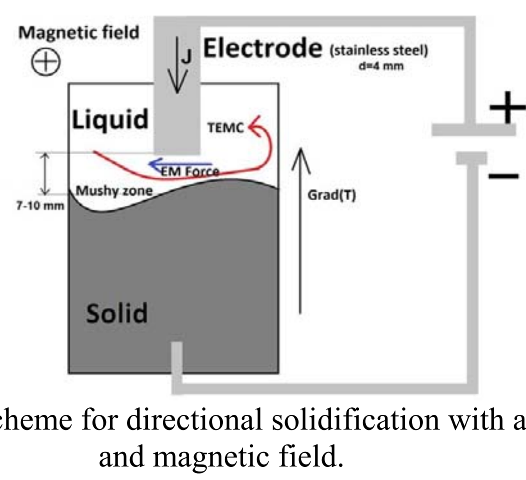

Figure 2. Experimental scheme for directional solidification with an applied electric current and magnetic field.

Estimation of TEMC magnitude is given in Ref.[3, 6] by solving simplified Navier-Stokes equation. According to these estimations for given materials and solidification conditions characteristic velocity is about 0.25 mm/s. Electric current density which would allow to achieve same convection velocity can be estimated. Electric current density component, which is perpendicular to magnetic field, depends on ratio of electric conductivities of alloy at solid and liquid states, and ratio between vertical and horizontal structure lengths as illustrated in Fig.1. Expression relating these quantities is given by Equation 1, which is only valid if conductivities and sizes are of the same order of magnitudes.

$$j_{\perp} = j\left(1 - \frac{\sigma}{\sigma_s}\right)\frac{h}{d} \tag{1}$$

The order of magnitude of TE current can be estimated as given in Ref [3].

$$j_{TE} = c\sigma\theta(S_l\text{-}S_s) = 1.1\cdot10^4 \text{ A/m}^2 \tag{2}$$

If $h \approx d$, then $j \approx 2j_{TE}$ and necessary electric current to achieve similar convection as TEMC is approximately $2\cdot10^4$ A/m^2 or 0.5 A current through 6 mm diameter sample.

Table 1: Physical properties of Sn-10%wt.Pb alloy used in estimations. Physical properties are given for melting temperature (Tm = 220 ^{o}C)

Quantity	**Symbol**	**Value**	**Unit**
Density	ρ	6974	kg/m^3
Electric conductivity	σ	$2\cdot10^6$	sim/m
Dynamic viscosity	μ	0.0021	Pa·s
Absolute thermoelectric power (s)	S_s	$-2\cdot10^{-6}$	V/K
Absolute thermoelectric power (l)	S	$-1\cdot10^{-6}$	V/K
Differential thermoelectric power	P	$1\cdot10^{-6}$	V/K
Temperature gradient at the front	θ	3	K/mm
Crucible radius	R	3	mm
Volumetric thermal expansion	β	$6.8\cdot10^{-5}$	1/K
Free fall acceleration	g	9.81	m/s^2
Form constant	c	0.5	

In our case, the temperature gradient is directed along the axis of the crucible from bottom to the top. This means that applied current from bottom of the sample enhances TEMC, while the current from the top creates convection opposite to TEMC. Several solidification experiments were performed to verify this hypothesis. Experimental results are summarized in Fig.3 and Fig.4. Fig. 3 shows directionally solidified 6 mm-diameter Sn-10%wt.Pb sample at velocity 3 μm/s with different electric current values. Fig. 3(b) shows solidified sample without magnetic field and electric current. Fig.3a shows solidification structure with applied transverse magnetic field of 0.5 T, segregation in this case is caused solely by TEMC. Note that in the latter case the TEM force produces a transverse flow in the direction perpendicular to the magnetic field from right to left in Fig. 3(a). Accordingly, a large segregation normally appears on the left part of the ingot as confirmed by Fig. 3(a). Fig.3(c) shows how segregation can be enhanced by the application of electric current from the bottom of the sample. Fig.3d shows structure of solidified sample if current is applied from the top of the sample. In this case according to the estimations electromagnetic convection acts opposite to TEMC with the same magnitude. As can be seen in this case segregation is significantly weaker. Fig.3(e) shows the case when electromagnetic convection is two times stronger than TEMC and acts opposite to it, it is observed that segregation direction is reversed compared to Fig.3(a) where TEMC only is present.Fig.4 shows solidification structure of Sn-10%wt.Pb alloy solidified at 10 μm/s. It can be seen that in this case macrosegregation is less distinct which agrees to our expectations, because in all works describing TEMC it is concluded that TEMC effects can be better observed if solidification velocity is low. Indeed, segregation formation requires a certain time which is linked to the amplitude of TEMC. Conversely, the latter case indicates that TEM velocities are less or equal at most to 10 μm/s, what is consistent with the theoretical estimates.

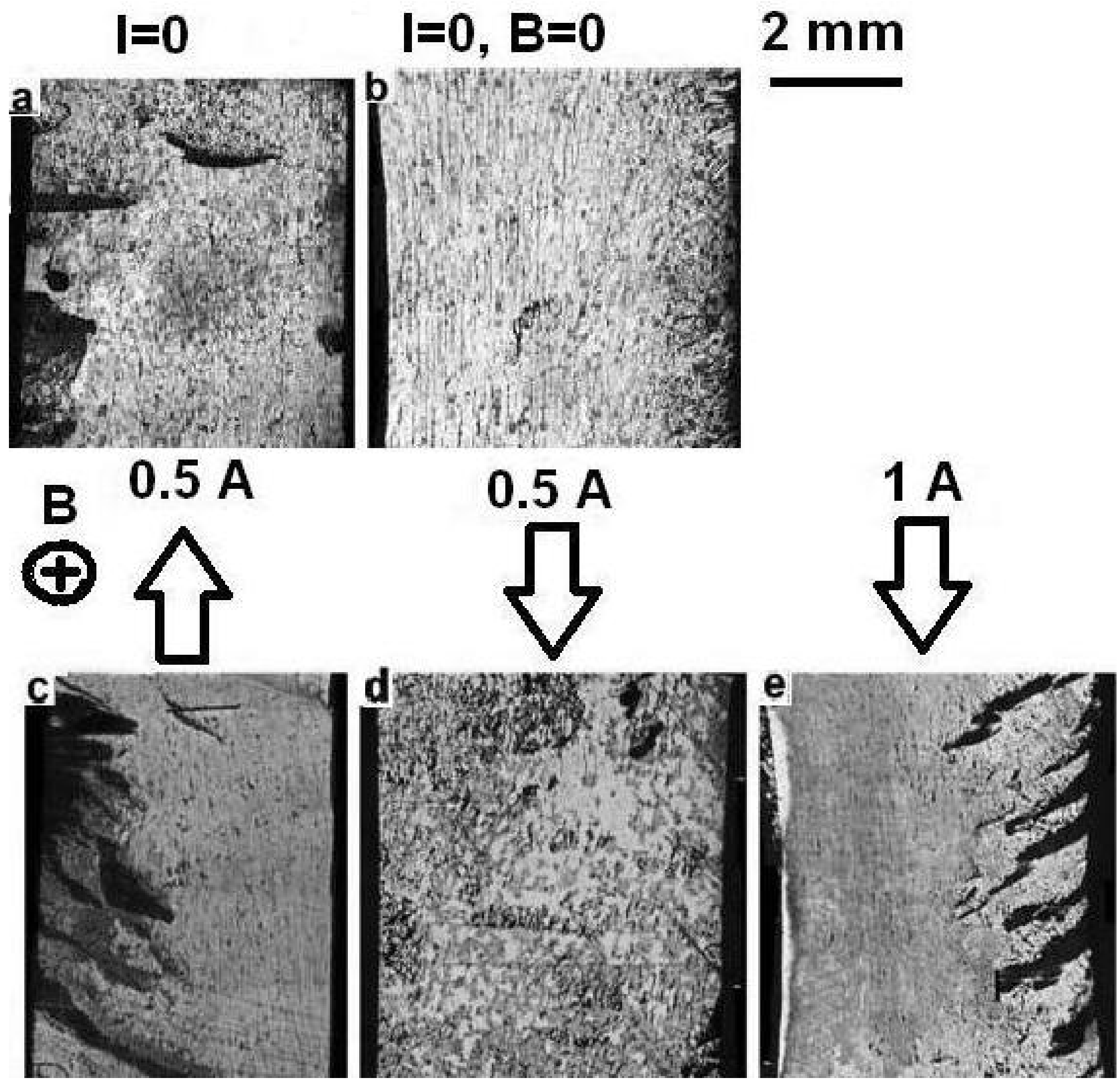

Figure 3: Directionally solidified Sn-10%wt.Pb alloy at v =3 μm/s under static transverse magnetic field 0.5 T and electric current: a) I = 0, B = 0.5 T; b) I = 0, B = 0; c) I = 0.5 A, B = 0.5T; d) I = -0.5 A, B = 0.5 T; e) I = -1 A, B = 0.5 T.

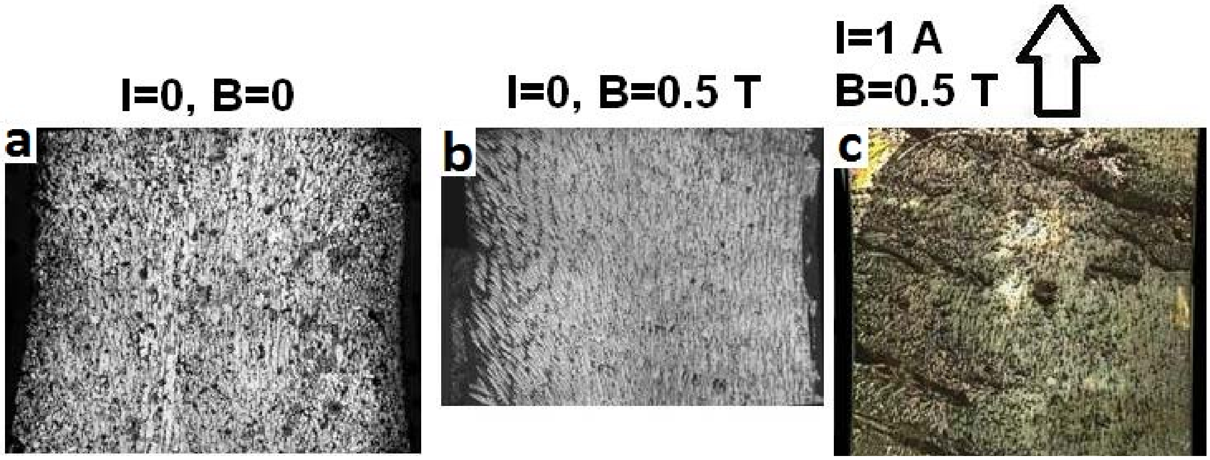

Figure 4: Directionally solidified Sn-10%wt.Pb alloy at v =10 μm/s under static transverse magnetic field 0.5 T and electric current: a) I = 0, B = 0; b) I = 0, B = 0.5 T; c) I = 1 A, B = 0.5 T.

3. Conclusion

It is experimentally demonstrated that direct current through the sample can be used to control macrosegregation during directional solidification of the metallic alloy. Theoretical analysis and numerical simulation show that transverse magnetic field and applied electric current produce force distribution similar to thermoelectric force density. Thus this method allows enhancing or suppressing the macrosegregation caused by thermoelectromagnetic convection. Experimental work presented in this paper confirms this hypothesis that by choosing appropriate electric current value, segregation caused by thermoelectromagnetic convection can be fully compensated, enhanced or reversed by electromagnetic convection.

4. References

[1] Shercliff, J.A: Thermoelectric magnetohydrodynamics. J. Fluid Mechanics, vol. 91 (1979), part 2, pp. 231-251.
[2] Li, X; Fautrelle, Y; Rn, Z.M: Influence of thermoelectric effects on the solid-liquid interface shape and cellular morphology in the mushy zone during the directional solidification of Al-Cu alloys under a magnetic field. Acta Materialia, vol. 55 (2007), Iss. 11, pp. 3803-3813.
[3] Kaldre, I; Fautrelle, Y; Etay, J; Bojarevics, A; Buligins, L: Thermoelectric current and magnetic field interaction influence on the structure of directionally solidified Sn-10%wt.Pb alloy. Journal of Alloys and Compounds, vol. 571 (2013), pp. 50-55.
[4] Usui, M, K Iwai, and S Asai. "Crystal Alignment of Sn–Pb Alloy by Controlled Imposition of a static magnetic field and alternating electric current during solidification." ISIJ international, vol. 46 (2006), pp. 859-863.
[5] Vives, C: Solidification of tin in the presence of electric and magnetic fields. J. Crystal Growth, vol.76 (1986), Iss.1, pp. 170-184.
[6] Kaldre, I; Fautrelle, Y; Etay, J; Bojarevics, A; Buligins, L: Thermoelectric current and magnetic field interaction influence in the motion of liquid metal. PAMIR 2011 Proceedings, Borgo, France, September 2011.
[7] Kaldre, I; Fautrelle, Y; Etay, J; Bojarevics, A; Buligins, L: Absolute thermoelectric power of Pb-Sn alloys. Modern Physics letters B, vol. 25 (2011), Iss. 10, pp. 731-738.

STUDY OF TURBULENCE THE IN PRESENCE OF STRONG ELECTROMAGNETIC NOISE IN THE MHD STIRRER WITH TRAVELLING AND ROTATING MAGNETIC FIELD

PAVLINOV[1] A., KOLESNICHENKO[1] I., FRICK[1] P., GOLBRAICH[2] E.
[1]Institute of Continuous Media Mechanics, Perm, Russia
[2]Physics Department, Ben-Gurion University, Beer-Sheva, Israel
E-mail: pam@ icmm.ru

Abstract : We discuss the problem of spectral analysis of signals from electromagnetic probes operating in turbulent MHD flow, provided by strong magnetic field. Using a wavelet based technique for cross-correlation signal analysis and filtrating we show that at frequencies lower than the frequency of applied magnetic field the spectral properties of the velocity field can be clearly seen in spite of the fact that the measured fields are much weaker than the driving rotating (or travelling) magnetic field.

1. Introduction

External alternating electromagnetic fields (for example rotating or/and travelling magnetic fields) are widely used in various areas of science and technology for liquid metal flow generation. Arising flows are characterized by sufficiently strong turbulence. Turbulence affects the processes of heat and mass transfer in liquid metals, and its study is an important applied (and scientific) problem.

However, direct measurement of turbulent fluctuations in the considered flows is problematic. This is due to the fact that the measurement of the turbulent flow characteristics are made by sensors which are located in the metal forced by the external alternating electromagnetic field. In this case, weak currents and their fluctuations measured by sensors contain information not only about the turbulent flow characteristics, but also about fluctuations of the external electromagnetic fields. Hence, there is a problem of separation of the useful signal in such experiments from interference caused by external fields.

We study the possibility to separate the pulsations caused by the liquid metal flow from the direct and indirect influence of the applied magnetic field. In our studies, we used one of the most common methods for measuring velocity in MHD flows based on the conductive probes. For processing the obtained data, we have developed a method based on the wavelet analysis.

2. Presentation of the problem

We study the liquid metal flow generated in a cylindrical vessel by the electromagnetic stirrer (fig. 1). The stirrer is a set of a ferromagnetic core (magnetic circuit) and copper coils which generate variable magnetic field inside the cylinder volume. A cooling system of tubes, in which water is circulating, prevents the coils overheating. The stirrer includes two independent coil systems which allow to generate the rotating flow (by rotating magnetic field, RMF) and the poloidal flow (by travelling magnetic field, TMF) [1, 2].

The velocity measurement were carried out using 2 conductive probes, mounted on the side wall of the vessel on the distance of 10 mm from the wall (fig.1). We use 2-axis local probes designed to provide a good dynamical resolution of rotating and poloidal motions. A small permanent magnet imposes locally a strong magnetic field and nearby electrodes are used to measure the induced difference of electric potentials, linked to the local velocity of the fluid. Each conductive probe consists of two pairs of electrodes 1 placed around the magnet 2 (the sizes of the magnets are 10 x 2 x 2 mm), magnetic field induction on the magnet is ~20mT on the distance of 3 mm. Diameter of the sensor housing 3 is 6 mm. The probe measures the axial and azimuthal velocity components. The instrumentation preamplifier 4 is INA128 (Texas Instruments, bandwidth 20 KGz, common-mode rejection ratio above 120dB with gain 30dB). The data acquisition system comprises an 24-bit analog-to-digital converter (ADC) NI 9227 with a sampling rate of 5 kHz. Also, we are recording the signal from the current loop, located on one of the phases of the power supply and the signal from the Hall sensor PM placed outside the vessel inside the stirrer (fig.1).

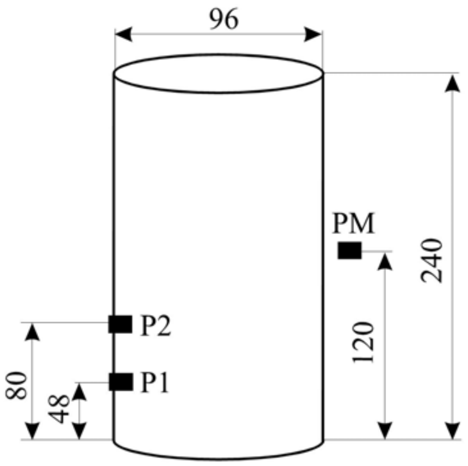

Figure 1: Scheme of sensors position.

Analyzing signals, we have recognized a strong dominance of harmonic (and nonharmonic) oscillations caused by the applied magnetic fields. This dominance makes questionable even the possibility to recover some reliable information concerning the properties of small-scale (turbulent) velocity oscillations. The signal show that the vertical (as well as the azimuthal) component of the velocity oscillates (and change directions) together with the magnetic field. The measured signals are well correlated and we cannot determine what do sensors measure: fluctuations of the velocity, magnetic fields or both.
To separate the useful signal against external noises, we developed a scale-by-scale correlations analysis filtering method, created on the base of wavelet analysis. The method allows us to define the range of frequencies for which the signal oscillations are strongly provided by the turbulence and not by the electromagnetic noise.
In the frame of the problem under discussion of special interest is the wavelet cross-correlation, which allows us to look for the scale-by-scale (or frequency-by frequency) cross-correlation of two signals [3]. The choice of the analyzing wavelet is very important. In the case of signals which contain a number of isolated events (pulses) of different duration (scale) and one would like to analyze the correlation of this events in both signals scale-by-scale, the wavelet with a good space resolution is required.

3. Results

The modulus of the wavelet cross-correlation function between vertical component of velocity from probe P2 and the magnetic field, measured by the Hall probe at position PM (see fig.1), is shown in fig.2 for the case of applied RMF with different value of frequency. The strong correlated interval shifts to higher frequencies. It is related with the fact that the influence of the magnetic field occurs on the carrier frequency and multiples thereof. Hence, at frequencies below the carrier one the cross-correlation becomes small. Then, the measured spectrum should be determined in this frequency range by the flow fluctuations and not by the RMF. Thus, below the carrier frequency of RMF the potential probe is weakly affected by the strong external magnetic field and can be used for analysis of turbulence in the flow.

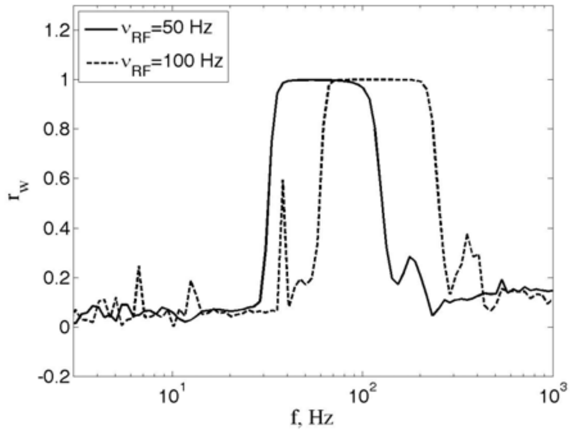

Figure 2: Cross-correlations for different frequency of applied magnetic field.

Rotating magnetic field leads to the formation of helical Taylor–Gertler vortices in the wall region. The size of the vortices depends on the velocity (Hartmann). Since different vortices have different direction of rotation, the traveling magnetic field acts on neighboring vortexes differently. Some vortices must be amplified, while others weaken. Sensors in the experiment located at a distance 10mm from the wall. As shown in [4], just as the sensors are located in vortex area. Therefore, we can assess the impact of both fields on the flow from the measured data. The figure **N** shows the change in the turbulence intensity measured by the probe P2. Clearly seen that the injection energy on the main scale (and therefore the entire spectrum) decreases with increasing amplitude of the traveling field. In addition, from the behavior of the spectra we can see, that structure of a turbulent field is changed too. Thus, we arrive at the possibility to control the intensity of turbulence near the wall, which is very important in many metallurgical applications.

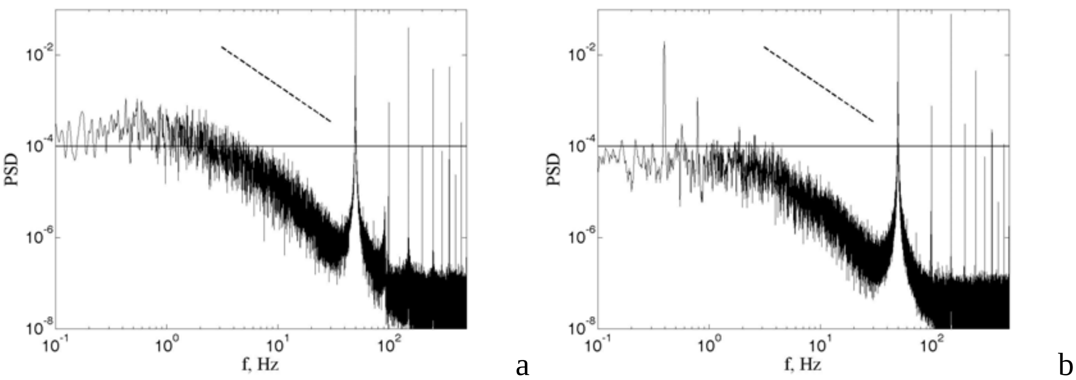

Figure 3: Spectra of azimuthal component of velocity; (a) - I_{TMF} = 7A, (b)
(I_{RMF} = 1.6 A, 50 Hz, probe P2, dotted line is the Kolmogorov's spectra -5/3).

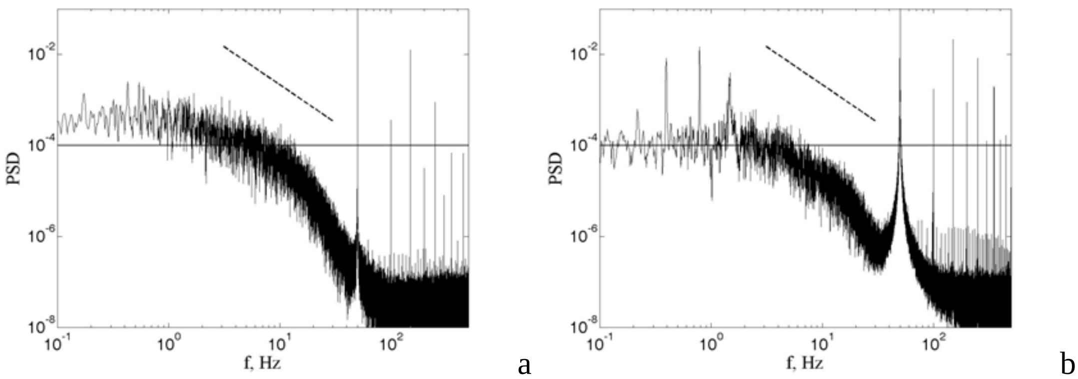

Figure 4: Spectra of axial component of velocity; (a) - I_{TMF} = 7 A, (b)
(I_{RMF} = 1.6 A, 50 Hz, probe P2, dotted line is the Kolmogorov's spectra -5/3).

3. Conclusion

Thus, we propose a method of purification and analysis of turbulent MHD experimental data. The developed method of processing these data, based on the study of scale-by-scale wavelet cross - correlations. We studied the possibility of separation between the signals from MHD turbulent flow pulsations and the direct or/and indirect influence of an external magnetic field. On the basis of wavelet cross-correlation analysis we show that it is possible to allocate a range of frequency in the measured spectra which characterizes the pulsations of the velocity field. Further development of this method will allow us to analyze the turbulence in the flow under the study and obtain its performance in different conditions of exposure to electromagnetic fields.

Acknowledgements. Financial support from the International Research Group Program supported by Perm region Government and RFBR project 13-01-96042_r_ural_a is gratefully acknowledged.

4. References

[1] Denisov, S.; Mann, M.; Khripchenko, S.: MHD stirring of liquid metal in cylindrical mould with free surface. Magnetohydrodynamics, 33 (1997), 365-374.

[2] Kolesnichenko, I.; Khalilov, R.; Khripchenko, S.; Pavlinov, A.: MHD stirrer for cylindrical molds of continuous casting machines fabricated aluminium alloy. Magnetohydrodynamics, 48 (2012), 221-233.

[3] Nesme-Ribes, E.; Frick, P; Sokoloff, D.; Zakharov, V.; Ribes, J.-C.; Vigouroux, A.; Laclare, F.: Wavelet analysis of the Maunder minimum as recorded in solar diameter data. Academie des Sciences Paris Comptes Rendus Serie B Sciences Physiques, 321 (1995), 525-532.

[4] Golbraikh, E.; Kapusta, A.; Tilman, B.: Helical properties of MHD flows arising under the action of rotating magnetic field. Magnetohydrodynamics, 46 (2010), 1, 79–83.

TRAVELLING MAGNETIC FIELD MIXING FOR PARTICLE DISPERSION IN LIQUID METAL

BOJAREVICS[1] V., PERICLEOUS[1] K., GARRIDO[2] M., FAUTRELLE[2] Y., DAVOUST[2] L.
[1]University of Greenwich, Park Row, London, SE10 9LS, UK
[2]SIMAP-EPM. BP 75, 38402 Saint Martin d'Héres, France
E-mail: v.bojarevics@gre.ac.uk

Abstract: The experimental Bridgman type furnace combined with travelling magnetic field Bitter coil mixing arrangement is used to investigate the solidification structure and the additive particle distribution dynamics. Supporting numerical models combine time dependent fields, developing turbulent flow fields, moving free surface, solidification front and the Lagrangian dynamic particle tracking.

1. Introduction

In order to enhance the mechanical properties of the material the transition from columnar to equiaxed grains should be promoted and the grain size reduced. For this purpose, the use of inoculants such as TiB_2 microparticles as grain refiners is very efficient [1-3]. The introduction and distribution of the particles inside the material represents always a challenge especially when the particle size is decreased. Different methods have been developed such as mechanical stirring, pulse magnetic fields or ultrasound. The advantage of using magnetic field is the completely contactless influence on the liquid metal. In the case of a traveling magnetic field (TMF) the flow direction and its intensity can be easily controlled to produce required distribution of the inoculant particles within the matrix material. The TMF can be used to increase the number of nucleation points which will enhance the reduction of grain size in the alloy [4,5] and to homogenize the temperature of the melt. The electromagnetic mixing helps to produce equiaxed dendrites and prevent the growth of cellular dendrites [6,7]. Melting light metal alloys (Al, Mg, etc) in the presence of electromagnetic (EM) field can help to diffuse inclusions of various sizes in the liquid volume or oppositely concentrate these on the surface of the solidified melt. Barnard et al. [8] demonstrated experimentally that melting in a high frequency AC field indeed brings particles to selected locations on the surface of consequently solidified metallic sample. Bubbles and inclusions are observed to move selectively in the presence of EM field during the steel casting [9]. Materials of special properties, like an increased concentration of additive particles near the surface, are produced in the presence of the imposed electromagnetic field [10]. Numerically the particle paths can be predicted [11,12] accounting for the added electromagnetic force effects. The electromagnetic force acts directly only on electrically conducting inclusions, however the electromagnetic force in the surrounding fluid creates a gradient of pressure giving additional integral force even on the non-conducting inclusions of various sizes and composition. The gravity induced buoyancy acts vertically, but the EM 'buoyancy' acts in the direction opposite to the EM force. In addition to this, the large scale electromagnetically driven flow circulation exerts a drag force, torque and shear, which contribute to the particulate transport. The paper presents results obtained using a TMF of low intensity during the melting of aluminum alloy 357 with TiB_2 microparticles added with the purpose of grain refining.

2. Experimental procedures

Experiments were carried out using a Bridgman furnace equipped with a bitter coil. The furnace VB2 (Vertical Bridgman 2 inches) manufactured by Cybestar is characterized by a

zone of a controlled temperature gradient. The hot and cold end zones are equipped with graphite resistors for heating. This bitter coil provides a traveling magnetic field of 10 mT and frequency of 50 Hz. The phase shift is set as 60 degrees between the coil sections.
The material used as matrix material was Aluminum 357. This alloy is commonly used in casting of aerospace structures. TiB_2 microparticles were selected to be mixed with aluminum 357. The diameter of the particles was 8.6μm and its density 4.52 g/cm^3 .The percentage in weight added to the aluminum alloy was 0.85 %. The final weight of the specimen is 730 g. The material is introduced in the furnace inside a crucible made of quartz which is supported by a graphite container. Microparticles and aluminium are introduced at the same time in the furnace. A block of the filling material was made using a stack of the plates filled with the TiB_2 microparticles (Figure 1). The amount of material of the specified weight permits to obtain a final specimen 15 cm high and 5 cm in diameter.

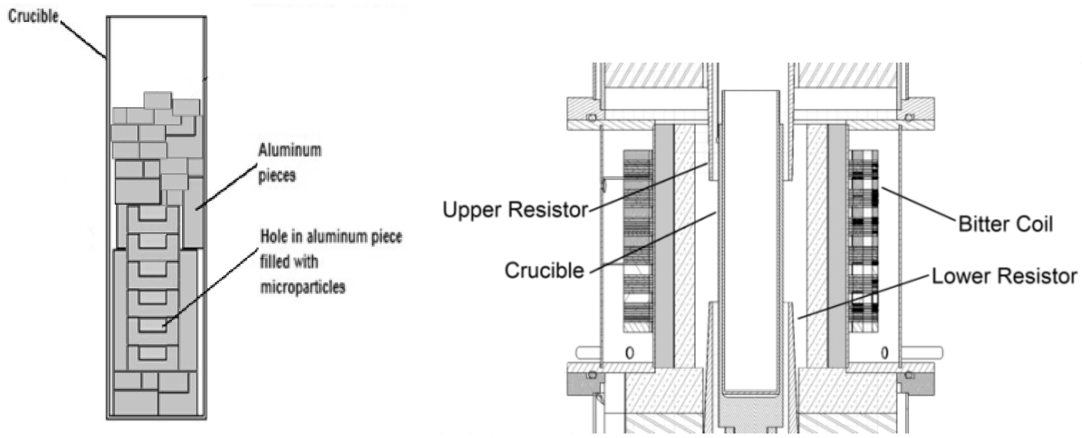

Figure 1: Crucible filling and the furnace cross-section of the experimental device with the Bitter coil at SIMAP, Grenoble.

The aluminum has a very high reactivity with the oxygen and forms aluminum oxide in milliseconds. In order to avoid an oxide layer over the surface of the crucible, the furnace is subjected to vacuum conditions, of 10^{-3} mbar at the beginning of the experiment. Afterwards, an open cycle of argon flow of 2.3 l / min is maintained during the totality of the experiment. The pressure inside the furnace is maintained in this way at 1200 mbar.
The aluminum alloy was heated to a temperature of 800°C imposed in upper and lower resistors. This temperature was maintained during 1.5 hours. Electromagnetic stirring started when this temperature was attained. Upwards and downwards TMF was alternated every 10 minutes and set to upwards direction during the cooling period until the solidification of the material. The temperature of the lower resistor was brought to 700 °C creating a gradient of 660 K/m which was kept until the end of the cooling. The rapid cooling would enhance the reduction of the grain size, therefore, the cooling rate selected was 0.25 K/s.

3. The mathematical model and results
The mathematical basis of the present model is the time-dependent Navier-Stokes and continuity equations for an incompressible fluid, and the thermal energy conservation equations with the Joule heating term for the fluid and solid zones of the metal charge [14]. The turbulent viscosity and the effective thermal diffusivity is the subject of the turbulence model accounting for the EM effects. The numerical solution of the coupled problem is obtained using the pseudo-spectral collocation method, employing the continuous co-ordinate transformation for the shape tracking. The time-dependent fluid flow problem is set with appropriate boundary conditions: at the free surface of the liquid the normal hydrodynamic stress is compensated by the surface tension, whilst at the solid walls the no-slip condition is

applied to the velocity wherever there is a contact at any given time. The free surface contact position moves as determined by the force balance and the kinematic conditions. During the melting or solidification, the solid-liquid interface is traced automatically as the solidus temperature surface $T = T_S$ moves with the coupled effects of the solid fraction-modified specific heat function. The temperature field corresponds to the thermally insulating side wall and the linearly decreasing in time hot top/cold bottom condition. The EM mixing and the additive particle distribution is investigated using the numerical models combining the time dependent EM fields, developing flow fields, the moving free surface and solidification front. The EM mixing is achieved by the Bitter type coil arranged in separate sections with a prescribed phase shift. The device schematic is shown in the Figure 1 and the numerical model with a computed velocity field - in the Figure 3.

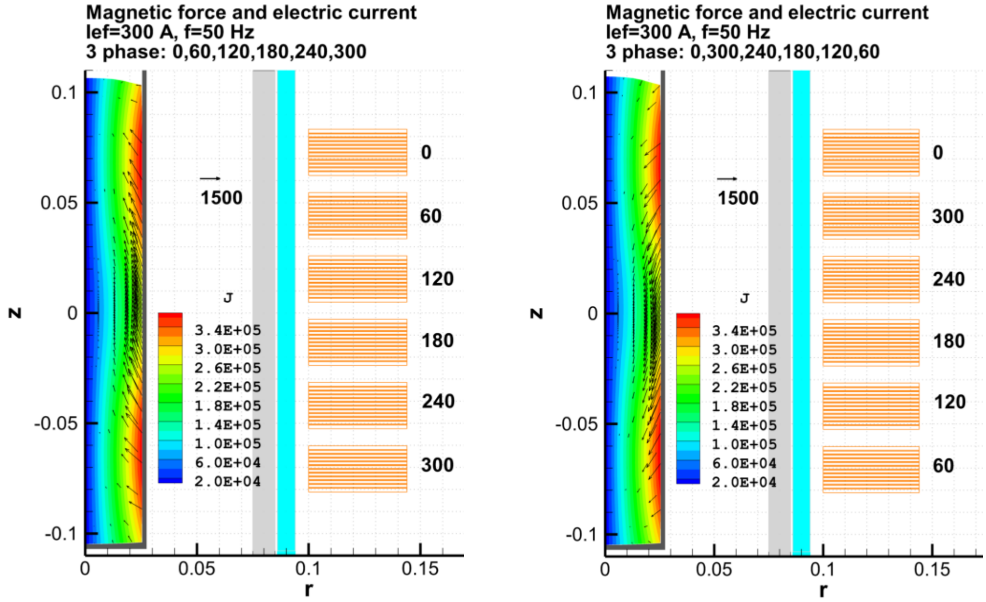

Figure 2: Upwards (left) and downwards (right) travelling magnetic field electric current and force distribution in the aluminium sample.

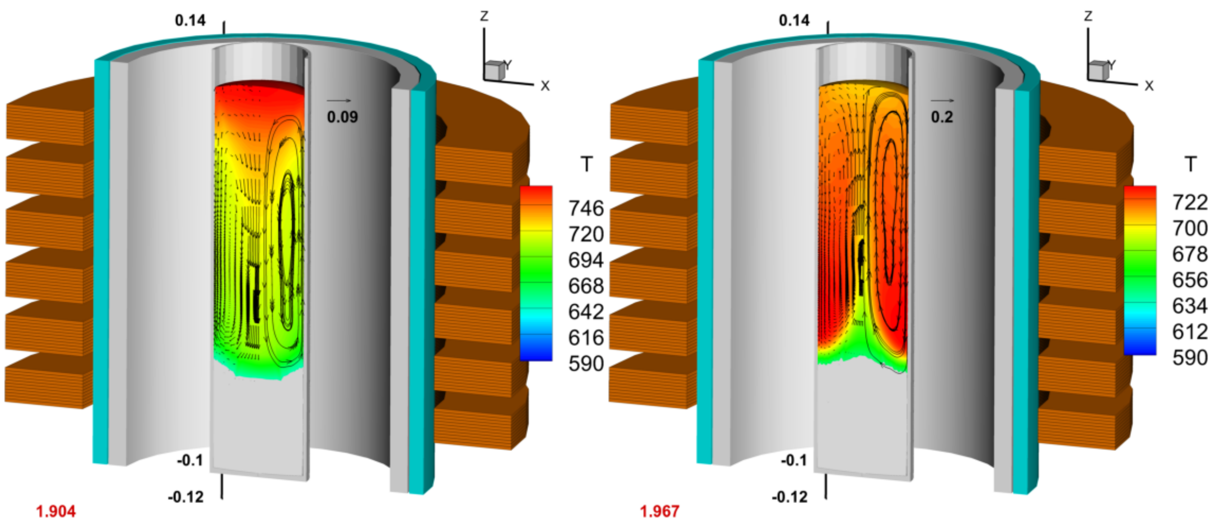

Figure 3: The velocity field in aluminium samples due to the upward (left) and downward (right) travelling magnetic field.

The AC phase shift permits to create the travelling magnetic field either upward or downward (Figure 2 shows the time average EM force distribution), which permits a variety of the mixing patterns affecting the solidification front and various scenarios of the particle motion.

The particles of micro to nano-size are added at desired locations in order to follow their paths and concentration, following their distribution in the gradually solidified metal ingot. Larger particles (> 10 µm) are the most sensitive to the buoyancy and the EM force effects, while smaller size particles follow closely the fluid flow pattern, only deviating in the regions of the higher EM force density and being entrapped when reaching the solidification front. The choice of flow pattern ensures the desired distribution of the particles. The upward EM field favors the fast entrapment of the particles at the bottom solidification front (Figure 4, left). On the contrary, the downward traveling field creates the flow, shown in the right of the Figure 3, leads to enhanced particle concentration at the top part of the melt (Figure 4, right), thus delaying or even preventing the additive supply to the solidification front.

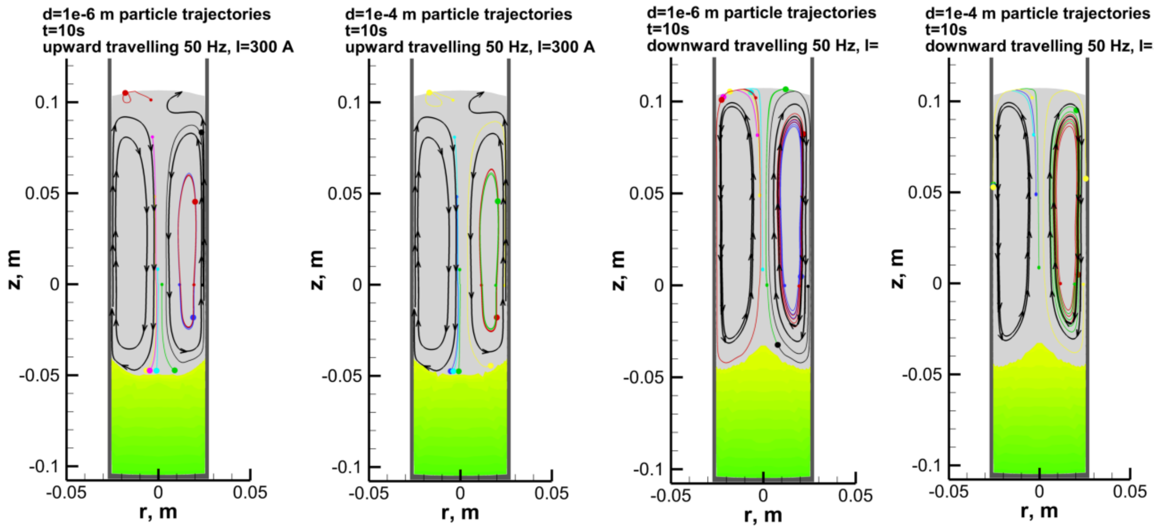

Figure 4: Various size particle trajectories in **aluminium** melt for the upward (left) and the downward (right) travelling magnetic field.

The results presented are preliminary and a full experimental verification is expected. The numerical model show areas in which the magnetic field is more intense and the optimum flow direction for the particle dispersion to the solidified metal matrix. The highest intensity of the magnetic field is located at the middle of the bitter coil area. In consequence, the particles would be more effectively dispersed if they are positioned there at the beginning of the experiment.

4. Experimental results and discussion

The microscopic study of the solidified specimens revealed an apparently good dispersion of the particles. Agglomeration and settling can easily occur due to the difference in density between aluminum and TiB2. The images obtained from the analysis of material from the lower part of the crucible showed no signs of agglomeration. The extraction of the particles could have been the result of the polishing performed on the samples. The upper part of the specimen showed different results. The number of particles found during the optical inspection was higher than on the lower part. Signs of possible TiB_2 agglomerates were found. The characterization of the specimens is still in process and the number of particles will be determined accurately in future work. The following images were taken from samples of the lower part of the specimen. The images show equiaxial grains at distances of less than 1 cm from the wall of the crucible. There are clear signs of refining the aluminum 357 stirred with the TiB additive (Figure 5, left) and the aluminum 357 solidified without refining (right).

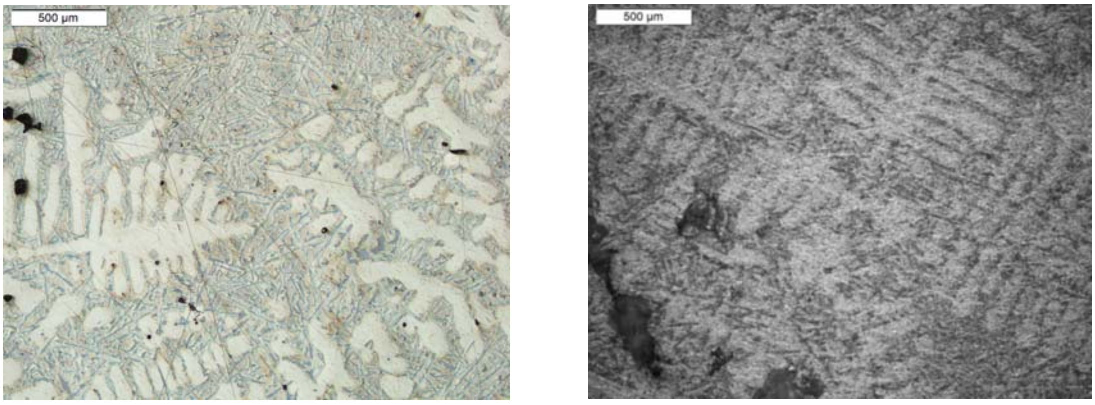

Figure 5: Micrographs of the solidified samples: (left) aluminum 357 stirred with the TiB additive. (Right) Equiaxial dendrites and signs of porosity without refining.

5. Conclusions

Intense mixing can be achieved using both upwards and downward travelling magnetic field. The melt front shape is strongly affected by the flow direction and the type of side wall thermal conditions. The particle paths and the concentration can be optimised to the desired outcome manipulating the EM field. The combined use of grain refiner and low intensity traveling magnetic field has shown positive results in the refining of the material.

Acknowledgments. The authors acknowledge financial support from the ExoMet Project (co-funded by the European Commission (contract FP7-NMP3-LA-2012-280421), by the European Space Agency and by the individual partner organizations)

6. References

[1] Grain refining of Pure Aluminium. Light Metals 2012, Edited by: Carlos E.Suarez. TMS, The Minerals & Materials Society, 2012.

[2] Greer AL, Bunn AM, Tronche A, Evans PV, Bristow DJ. Acta Mater (2000), 48, 2823.

[3] Spittle JA, Int J. Cast Metal Res (2006), 19, 210.

[4] D.G McCartney ‘’Grain Refining of Aluminium and Its Alloys using Inoculants’’, International Materials Reviews , (1989), vol. 34, no.5, pp. 247-260.

[5] Alcoa Report, ‘’New Process for Grain Refinement of Aluminium,’’ DOE Project Final Report, Contract No. DE-FC07-98ID13665, September 22, 2000.

[6] C. Vives, 1990, Hydrodynamic, thermal and crystallographical effects of an electromagnetically driven rotating flow in solidifying aluminium alloys. Int. J. Heat Mass Transfer, Vol. 33, 2585-2598.

[7] J.K. Roplekar, J.A. Dantzig, 2001, A study of solidification with a rotating magnetic field. Int. J. Cast Metals Res., Vol. 14, 79-95.

[8] L. Barnard, R.F. Brooks, P.N. Quested and K.C. Mills, Ironmaking and Steelmaking, 20, N 5, 344-349 (1993).

[9] J.W.Haverkort, T.W.J. Peeters. Magnetohydrodynamic effects on insulating bubbles and inclusions in the continuous casting of steel. *Metallurgical and Materials Transactions*, 41B (2010), pp. 1240-1246.

[10] S. Taniguchi, A. Kikuchi, Proc. 3rd Int. Symp. Electromagn. Proc. Materials, ISIJ, Nagoya, 315-320 (2000).

[11] T. Toh, H. Yamamura, H. Kondo, M. Wakoh, Sh. Shimasaki, S. Taniguchi. Kinetics Evaluation of Inclusions Removal During Levitation Melting of Steel in Cold Crucible. *ISIJ Internat.*, 47, No 11 (2007), p. 1625-1632.

[12] V. Bojarevics, K. Pericleous and R. Brooks. Dynamic Model for Metal Cleanness Evaluation by Melting in Cold Crucible, Metallurgical and Materials Transactions, B, 2009, v. 40, N 3, 328 – 336.

[13] D. Leenov and A. Kolin, Journ. Chem. Phys., 22, N 4, 683-688 (1954).

[14] V. Bojarevics, R.A. Harding, K. Pericleous and M. Wickins, Metallurgical and Materials Transactions, 35B, 785-803 (2004).

MAGNETIC FIELD EFFECT ON PROPERTIES OF GALVANOSTATICALLY DEPOSITED Co–Pd ALLOYS

ŻABIŃSKI[1] P., SOKÓŁ[1] A., MECH[1] K., TOKARSKI[2] T., KOWALIK[1] R.

[1]AGH University of Science and Technology, Faculty of Non-Ferrous Metals, Department of Physical Chemistry and Metallurgy of Non–Ferrous Metals
al. A. Mickiewicza 30, 30-059 Krakow
[2] AGH University of Science and Technology, Faculty of Non-Ferrous Metals, Department of Structure and Mechanics of Solids
al. A. Mickiewicza 30, 30-059 Krakow
E-mail: zabinski@agh.edu.pl

Abstract : The results of studies on the influence of magnetohydrodynamic effect (MHD), paramagnetic and magnetic field gradient force on properties of an electrochemically synthesized Co-Pd alloys. The electrolysis was performed at constant current conditions. An attention was mainly dedicated to the influence of the magnetic field on the process efficiency, composition, structure and morphology of the synthesized Co-Pd alloys.

1. Introduction

External magnetic field during deposition of an alloy causes additional convection at the electrode surface coming from magnetohydrodynamic effect (MHD), paramagnetic force and magnetic field gradient force. The additional convection results in changes of the alloy composition, structure and morphology and by this way on the further properties of obtained alloys. In the literature there can be found that Pd-Co alloys are characterized by better electrocatalytic properties for ORR than pure palladium [1]. In catalysers composed of two metals, of which one has poorly occupied (Co) and the second (Pd) completely occupied d orbitals, the result of their interactions might be lowering of Gibbs free energy for the process of electrons transport [2].

The properties of Co – Pd alloys deposited in the magnetic field of parallel and perpendicular orientation of the magnetic field forces lines vs working electrode were described. Particular attention was focused on the influence of current density, direction and value of magnetic field induction vector on composition, structure and morphology of Co – Pd alloys.

2. Results

The composition of electrodeposited alloys depends on many factors, including the concentration of individual components of electrolyte, presence of complexing agents, pH, temperature, a substrate material as well as the WE potential or the value of applied cathodic current density. The first step of the tests was performed to determine the value of cathodic current density enabling deposition of coatings well adhesive to the substrate. The electrolysis was performed in different times depending on applied current density. Coatings were deposited for 120 min for i = 10, 20 [mA/cm^2], and 60 min for i = 50, 100, 250 [mA/cm^2] from the electrolyte containing 0.01 M $Pd(NH_3)_4Cl_2$ and 0.005 M $CoCl_2$ $6H_2O$. Significant differences were noticed in the composition of alloy coatings and in cathodic current efficiency depending on the applied current intensity (Fig. 1). The lowest content of Co (28 at. %) was featured by an alloy obtained at i = 50 [mA/cm^2], for which the highest current efficiency (6.4 %) was achieved simultaneously. However, the coating was characterized by high internal stresses manifested by micro cracks and lack of cohesion of deposits with the material of substrate. Therefore, the further alloys deposition was performed at current intensity of 10 [mA/cm^2].

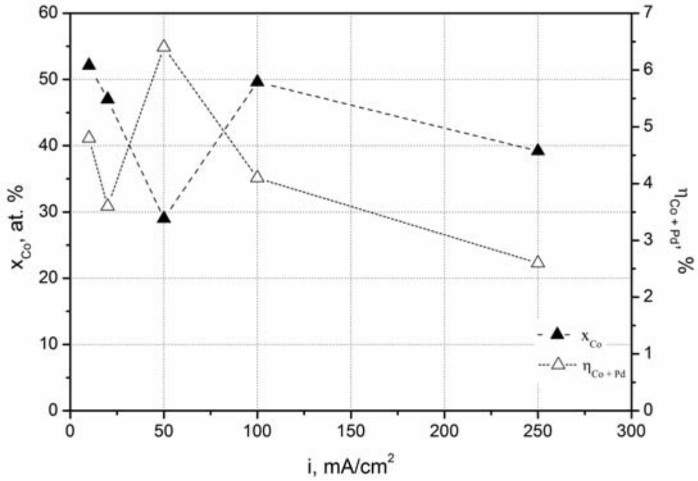

Figure 1: Influence of cathodic current density on Co content in alloys (x_{Co}) and current efficiency (η_{Co+Pd}) (0.01 M $Pd(NH_3)_4Cl_2$, 0.005 M $CoCl_2$ $6H_2O$, 1.68 M NH_4Cl, pH = 9.5, T = 25 °C).

Electrolysis performed at different concentrations of $Pd(NH_3)_4Cl_2$ allowed determination of the bath composition effect on Pd content in the obtained alloys (Tab). The highest current efficiency was achieved for 0.1 M $Pd(NH_3)_4Cl_2$ and it is connected with an increase of rate of the $[Pd(NH_3)_4]^{2+}$ complex reduction reaction. The electrolyte of such concentration of $Pd(NH_3)_4Cl_2$ was used for tests on the MF influence. The increase of $Pd(NH_3)_4Cl_2$ concentration from 0.01M to 0.1M caused an increase of current efficiency from 4.8 % to 75.2 % as it can be seen in Table 1.

Table 1. Alloys composition and cathodic current efficiency depending on the content of $Pd(NH_3)_4Cl_2$ in electrolyte (0.005 M $CoCl_2$ $6H_2O$, 1.68 M NH_4Cl, pH = 9.5, T = 25 °C).

$Pd(NH_3)_4Cl_2$ [mol/dm^3]	x_{Co} [% at.]	x_{Pd} [% at].	η_{Co} [%]	η_{Pd} [%]	η_{Co+Pd}, [%]
0.001	94.9	5.1	6.3	0.2	6.5
0.01	52.1	47.9	3.2	1.6	4.8
0.1	2.5	97.5	3.3	71.9	75.2

Further studies were performed at different orientation of MF lines: parallel and perpendicular. Parallel orientation was applied to induce additional convection following the Lorentz force action. Whereas, perpendicular orientation aimed to generate paramagnetic force action and magnetic field gradient force. As it is visible in Fig. 2, the applied MF, regardless of its configuration, caused significant lowering of current efficiency in relation to alloys deposited without a MF and an increase of cobalt content in the obtained coatings.

The diffraction patterns registered for the obtained alloy coatings are visible in Figs. 3a–d. An increase of grain size with an increase of cathodic current density was noticed. The XRD diffraction pattern in Fig. 3a, shows, regardless of current intensity, three repetitive peaks indicating the presence of phase $CoPd_x$ with FCC structure whose location changes with the relation of content of Co and Pd in alloys (Fig. 3) [3-5].

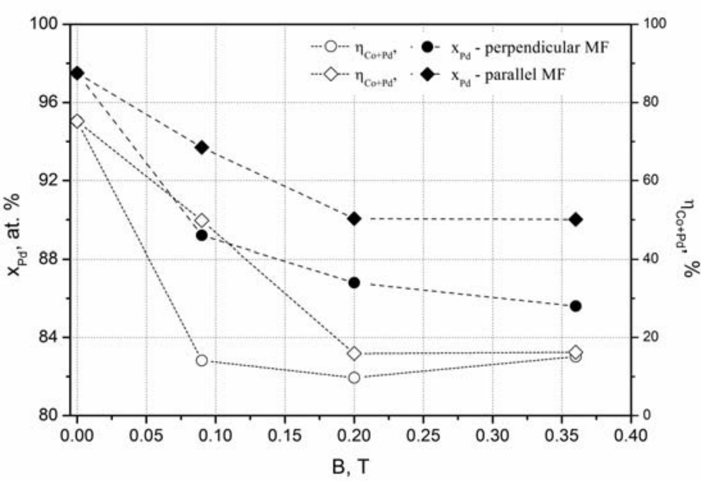

Figure 2: Influence of magnetic field induction vector on Pd content in deposited alloys and cathodic current efficiency (0.1 M $Pd(NH_3)_4Cl_2$, 0.005 M $CoCl_2$ $6H_2O$, 1.68 M NH_4Cl, pH = 9.5, T = 25 °C).

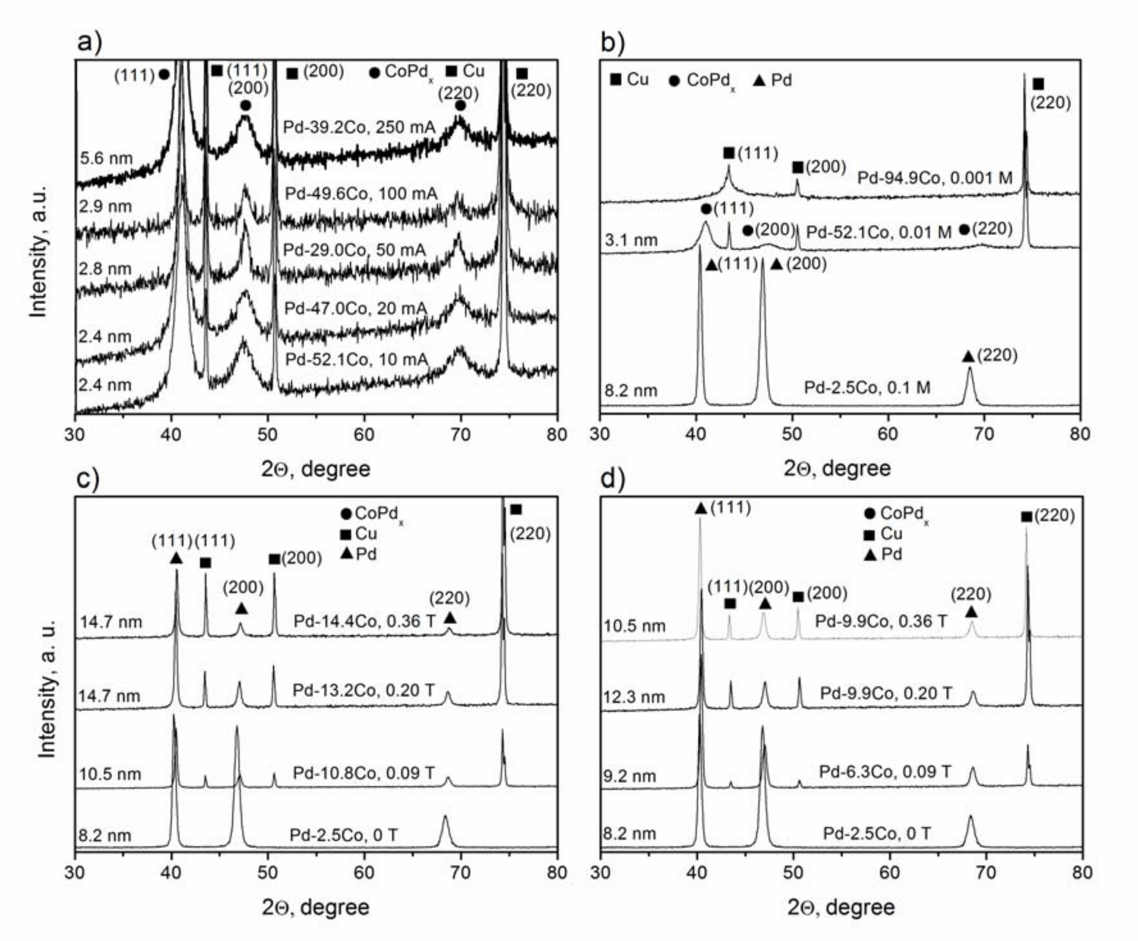

Figure 3: XRD diffraction patterns of alloys deposited at different current density (a), $Pd(NH_3)_4Cl_2$ concentration (b) and in MF of different magnetic field induction vector value and orientation: perpendicular (c) and parallel (d).

The influences of Pd salt concentration on structural changes in the obtained alloys are visible in Fig. 3b. XRD diffraction pattern of an alloy deposited from electrolyte containing

0.001 M $Pd(NH_3)_4Cl_2$ shows three peaks coming from the Cu substrate. After increasing the concentration of $Pd(NH_3)_4Cl_2$ from 0.01 M to 0.1 M, there are a visible shifts of peaks coming from planes (111), (220) and (200) of the phase $CoPd_x$ to a location typical for the FCC structure of pure Pd (2Θ = 40.12°, 2Θ = 46.66° and 2Θ = 68.12°).

The applied MF regardless of configuration did not cause, apart from an increase of grain size with an increase of the value of magnetic induction vector, changes in the deposit structure (Figs. 3c,d). It was observed that regardless of the orientation, an increase of the value of magnetic induction vector resulted in an increase of the grain size. The perpendicular MF also caused higher than for parallel one decrease of current efficiency which is manifested by increased intensity of peaks coming from the substrate material with an increase of MF intensity (Fig. 3c,d).

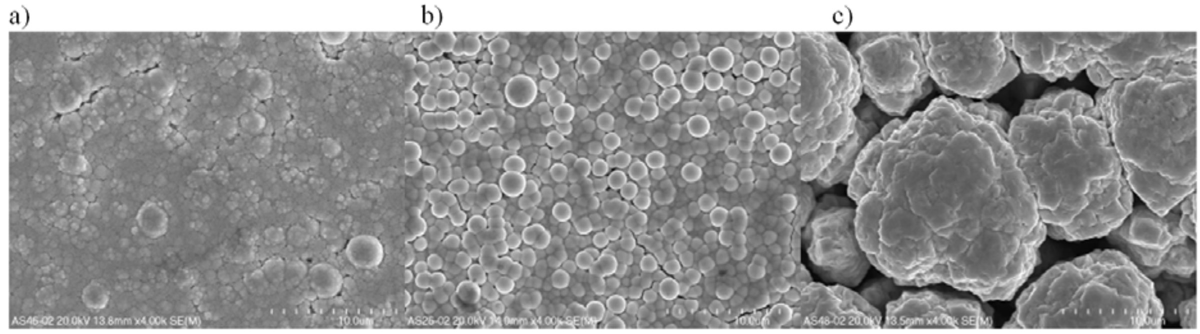

Figure 4: Microphotographs of alloys deposited form electrolytes of different $Pd(NH_3)_4Cl_2$ concentration: a) 0.001 M, b) 0.01 M, c) 0.1 M (0.005 M $CoCl_2$ $6H_2O$, 1.68 M NH_4Cl, pH = 9.5, T = 25 °C, res. 4000 X).

Observations of alloys morphology with the use of SEM microscope showed, similarly to XRD analysis, that the size of cathodic deposit grain increased remarkably with an increase of $Pd(NH_3)_4Cl_2$ concentration which can be seen in Fig. 4.

3. Conclusion

The best adherent coatings were deposited from electrolyte containing 0.1 M $Pd(NH_3)_4Cl_2$ at cathodic current intensity at i = 10 [mA/cm^2]. The magnetic field, regardless of configuration, caused a decrease of current efficiency of the electrolysis process. It can be also concluded, based on XRD measurements that MF influencing crystallisation process. An increase of the value of magnetic induction vector independently on MF orientation increased the deposits grain size.

4. References

[1] Suo Y.; Zhuang L.; Lu J.: First-principles considerations in the design of Pd-alloy catalysts for oxygen reduction. Angewante Chemie - International Edition. 46 (2007) 2862-2864.

[2]. Wang Y. X.; Balbuena P. B.: Design of Oxygen Reduction Bimetallic Catalysts: Ab initio-Derived Thermodynamic Guidelines. Journal of the Physical Chemistry B. 109 (2005) 18902-18906.

[3]. Heibel M.; Kumar G.; Wyse C.; Bukovec P.; Bocarsly A. B.: Use of sol-gel chemistry for the preparation of cyanogels as ceramic and alloy precursors. Chemistry of Materials. 8(7) (1996) 1504-1511.

[4]. Matsuo Y.: Ordered Alloys in Cobalt-Palladium System. Journal of Physical Society Japan. 32(4) (1972) 972.

[5]. Buschow K. H. J.; Vanengen P. G.; Jongebreur R.: Magneto-Optical Properties of Metallic Ferromagnetic Materials. Journal of Magnetism and Magnetic Materials. 38(1) (1983) 1-22.

CHIRAL CATALYTIC ACTIVITIES IN MAGNETOELECTROCHEMICAL ETCHING

AOGAKI[1,8] R., MORIMOTO[2] R., ASANUMA[3] M., MOGI[4] I., SUGIYAMA[5] A., MIURA[6] M., OSHIKIRI[7] Y., YAMAUCHI[8] Y.
[1] Polytechnic University / 2-20-12-1304, Ryogoku, Sumida-ku, Tokyo 130-0026 Japan, [2] Saitama Prefectural Showa Water Filtration Plant / 100 Shinjukushinden Kasukabe, Saitama 344-0113 Japan, [3] Yokohama Harbour Polytechnic College / 1 Honmokufuto Naka-ku Yokohama 231-0811 Japan, [4] Institute for Materials Research, Tohoku University / 2-1-1 Katahira Aoba-ku Sendai Miyagi 980-8577 Japan, [5] Institute for Nanoscience and Nanotechnology, Waseda University / 513 Waseda-tsurumaki-cho Shinjuku-ku Tokyo 162-0041 Japan, [6] Hokkaido Polytechnic College / 3-190 Zenibako Otaru Hokkaido 047-0292 Japan, [7] Yamagata College of Industry and Technology / 2-2-1 Matsuei Yamagata-shi Yamagata 990-2473 Japan, [8] National Institute for Materials Science / 1-1 Namiki Tsukuba Ibaraki 305-0044 Japan.
E-mail address of corresponding author: AOGAKI.Ryoichi@nims.go.jp

Abstract: Chiral catalytic activities of electrode surfaces fabricated by magneto-electrochemical etching have been theoretically examined for the two cases of macroscopic rotation; in the first case, a tornado-like stream called vertical magnetohydrodynamic (MHD) flow rotates the solution over the electrode, and in the second case, the whole electrode system uniformly rotates. As a result, the following three points were clarified; 1) In the absence of oxide layer such as passive film, the activities arise from screw dislocations of 2D pits. 2) For the vertical MHD flow, under upward and downward magnetic fields, D- and L-activities appear, respectively. 3) For the system rotation, only L-activity is obtained.

1. Introduction

The chemical reactivity of catalyst for some fundamental aspects such as stereoselectivity and chirality are issues of paramount importance. Chirality is a fundamental concept in chemistry and life science, and chiral catalysts play the most important scientific and technological roles in modern industry with intense economic impact. In this sense, how to fabricate chiral catalysts is still an open question with important fundamental and technical interest.

Mogi has first found the appearance of the enantiomorphic activities of electrodes deposited in vertical magnetic fields [1,2]. Then, the following studies clarified that the chiral activities are attributed to numerous chiral screw dislocations on 2D and 3D nuclei, which are created with minute vortexes called micro- and nano-MHD flows arising from magnetic field and macroscopic rotation [3,4]. The most important theoretical result concerning the catalytic activity for enantiomorphic reagents was that the chiral symmetry is broken to L-activity side. The fabrication process of this type catalyst under magnetic field and rotation is universal. In view of the fact that stars and nebulae are also evolved under magnetic field and rotation, whether such type catalysts had contributed to the molecular evolution of amino acids in the cosmic space would be a quite interesting problem for the origin of homochirality.

Furthermore, is anodic etching also possible to bestow the same kind of catalytic activity to electrode surfaces? According to this question, in the present paper, with regard to anodic etching, two cases of macroscopic rotation under a magnetic field are theoretically examined; the first case is that a tornado-like stream called vertical MHD flow rotates over the electrode surface, and the second case is that the whole electrode system uniformly rotates.

2. Theory

2.1 Electrochemical instabilities of 3D and 2D pits

In anodic etching, two types of pit are possible to grow; one is 3D pit with an about 1 μm diameter, forming a deep hole. The other is 2D pit with an about 100 μm diameter, forming a shallow hole. Due to a localized large amount of metallic ions dissolved, the growth of 3D pit is controlled by nonequilibrium fluctuation of concentration overpotential. Since a positive overpotential is applied to a metal surface, for the pit to unstably develop with time, the overpotential fluctuation is required negative. However, metallic dissolution always provides a positive overpotential fluctuation, so that 3D pits are stable and cannot grow [5].

On the other hand, 2D pit formation is also under a control of concentration overpotential, i. e., a negative fluctuation of it is inevitable for unstable growth. In this case, since 2D pits arise from electric double layer, the overpotential fluctuations of the electric double layer are newly joined, making the pitting process unstable under the following condition,

$$\left(\partial\langle\Phi_1\rangle/\partial\langle\Phi\rangle\right)_\mu \langle\Phi_2\rangle > 0 \tag{1}$$

where, $\langle\Phi_1\rangle$ and $\langle\Phi_2\rangle$ are the average potential fluctuations of the Helmholtz and diffuse layers, respectively, and $\left(\partial\langle\Phi_1\rangle/\partial\langle\Phi\rangle\right)_\mu$ is the differential potential coefficient, and the subscript μ implies that all other quantities are kept constant. From these discussions, it is concluded that in anodic dissolution without passive films, only 2D pit can develop with time. In Fig. 1a and 1b, Eq. (1) is represented by the potential distributions in the electric doublw layer, which correspond to the cases of the absence and presence of specific adsorption of anion. On the contrary to cathodic deposition [6], anodic etching can always develop in the form of 2D pits. In addition, it shoud be noted that because of the disturbance of concentration overpotential, fluid motion makes the pit formation less active.

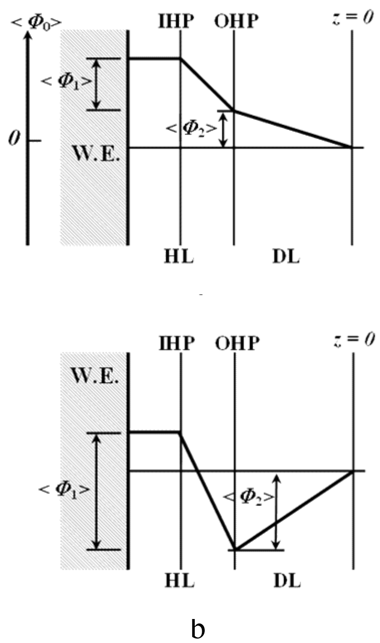

b

Figure 1: Potential distributions in electric double layers in unstable 2D pitting. a, without specific adsorption; b, with specific anionic adsorption.

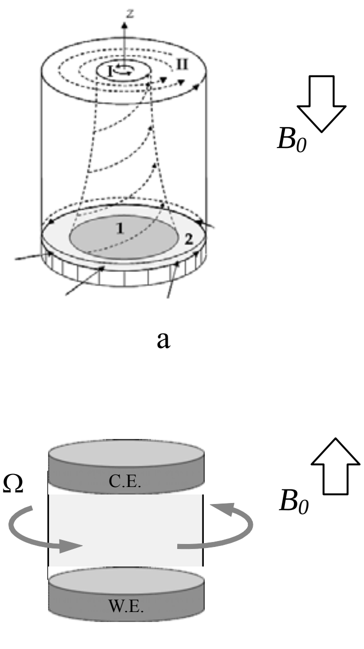

b

Figure 2: Macroscopic rotations. a, vertical MHD flow; b, system rotation. B_0, the magnetic flux density; Ω, the angular velocity.

2.2 Chiral activity induced by vertical MHD flow

2D pits unstably growing on an electrode surface acquire chirality from microscopic vortexes called micro-MHD flows under magnetic field and macroscopic rotation. Two types of macroscopic rotations in magnetic field are represented in Fig. 2, i.e., a tornado-like rotation over an electrode surface called vertical MHD flow and an electrode system rotation.

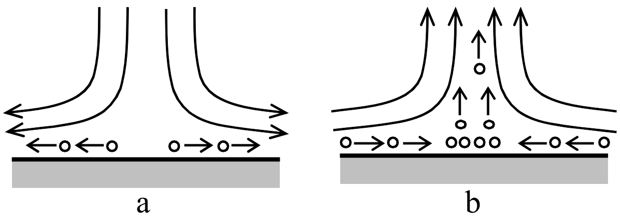

Figure 3: Rigid and free surface formations. a, rigid surface; b, free surface; ○, vacancy.

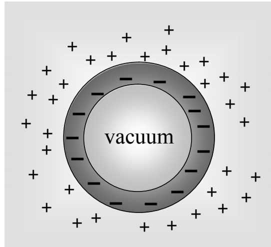

Figure 4 : Ionic vacancy.

In accordance with ionic vacancies gathered and spread out, as shown in Fig. 3, upward and downward micro-MHD flows yield free surface without friction and rigid surface with friction, respectively. Here, ionic vacancy created during electrode reaction works as an atomic-scale lubricant, which is shown in Fig. 4, i. e., a free vacuum space with an about 0.1 nm diameter surrounded by ionic cloud [7]. On the rigid surface, due to friction, micro-MHD flow disappears, and the solution is kept stationary, whereas it can rotate on the free surface without friction. As elucidated above, the stationary solution on the rigid surface assists the unstable growth of 2D pit, whereas the solution flow on the free surface rather suppresses it, so that as indicated in Fig. 5, the current lines are distorted inside and outside on the rigid and free surfaces, respectively. In an upward vertical magnetic field, Lorentz force thus induces clockwise (CW) and anticlockwise (ACW) rotations on the rigid and free surfaces, respectively. Here, on the rigid surfaces with friction, the solution is kept stationary, the vortex rotation is not transcribed to a pit surface. Only on the free surfaces without friction, such a transcription is possible, i. e., under an upward magnetic field, micro-MHD flows with ACW rotation contribute the fabrication of chiral screw dislocations.

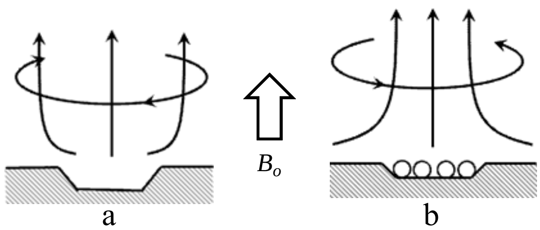

Figure 5: Current lines and activated rotations. a, rigid surface; b, free surface; ○, vacancy.

2.2.1. Positive reinforcement by Coriolis force

In the absence of energy supply, micro-MHD flows once activated by magnetic field dwindle with time. Coriolis force by the vertical MHD flow makes special contribution to sustain them. In Fig. 6, the positive reinforcement by the Coriolis force is exhibited; on the electrode surface, two layers are formed. The micro-MHD flows mentioned above are activated in the lower layer by the magnetic field, whereas the Coriolis force yields other vortexes in the

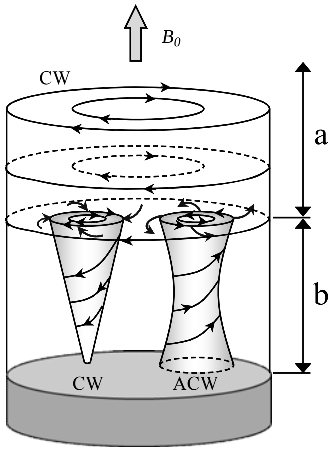

Figure 6: Reinforcement process by the vertical MHD flow. a, rotating layer; b, stationary layer.

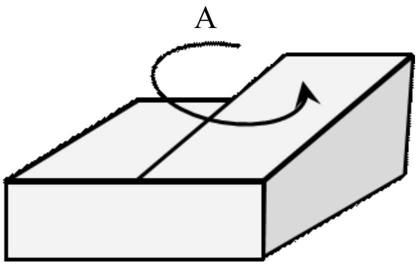

Figure 7: Formation of a screw dislocation. A, the rotational direction of micro-MHD flow.

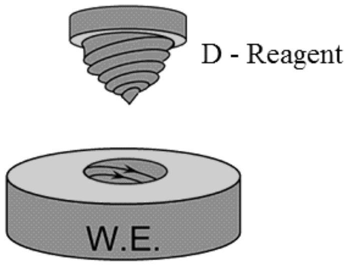

Figure 8: Mirror-image relationship between reagent and dislocation.

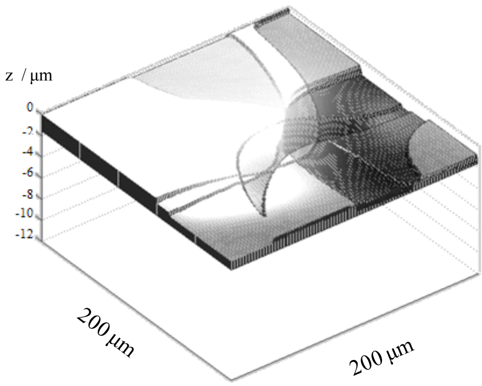

Figure 9: ACW screw dislocations calculated after 10 times pitting.

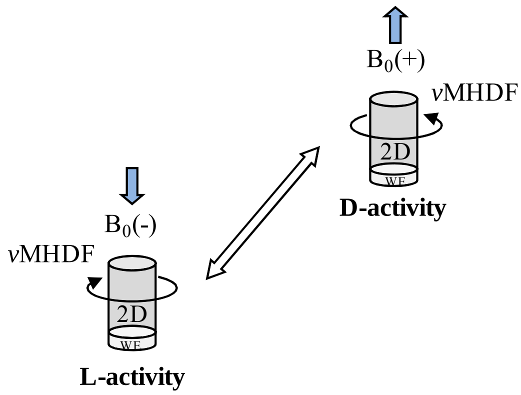

Figure 10: Chiral activity by vertical MHD flow.

upper layer rotating with the vertical MHD flow. As a result, through the vortexes in the rotating upper layer, the kinetic energy of the vertical MHD flow is supplied to the vortexes in the lower layer.

2.2.2. Enantiomorphic activity of screw dislocation

Figure 7 illustrates a screw dislocation formed by a micro-MHF flow. Since dissolution takes place in the same direction as that of the vortex flow, ACW screw dislocation is created from ACW micro-MHD flow. Because enantiomorphic catalysis has a mirror-image relationship with reagent, as shown in Fig. 8, the ACW screw dislocation is active for a D-type (CW) reagent, i. e., having D-activity. Figure 9 shows ACW pits formed on a free surface, which is theoretically calculated after 10 times repeated pitting. The catalytic activities in all cases of magnetic field directions are put in order in Fig. 10, i. e., in an upward magnetic field, D-activity emerges, whereas in a downward magnetic field, L-activity arises.

2.3. Chiral activity induced by system rotation

When an electrode system rotates under a vertical magnetic field, as shown in Fig. 11, Coriolis force is directly imposed to the micro-MHD flows activated by magnetic field, inducing precession of the vortexes. As a result, a cooperative effect arises between Lorentz force and Coriolis force, so that the product of the magnetic flux density and the angular velocity of the system rotation $B_0\Omega$ determines the chirality of the micro-MHD flows. The theoretical calculation indicates that only the case of positive $B_0\Omega$ is allowed for vortexes on free surfaces, and that the following physical parameter called Coriolis vorticity determines the rotational direction of the vortexes.

$$\tilde{\omega}_z = -AB_0\Omega\,\tilde{j}_z \qquad (2)$$

where A is a positive constant, and $\tilde{j}_z$ is the extended current density, which is positive in case of anodic etching. Therefore, for a positive $B_0\Omega$, the Coriolis vorticity $\tilde{\omega}_z$ becomes negative, i. e., CW rotation emerges. In accordance with the case of vertical MHD flow, this implies L-activity for enantiomorphic reagents. For a negative $B_0\Omega$, rotational motion on a free surface is not permitted, so that as shown in Fig. 12, chiral activity is not obtained.

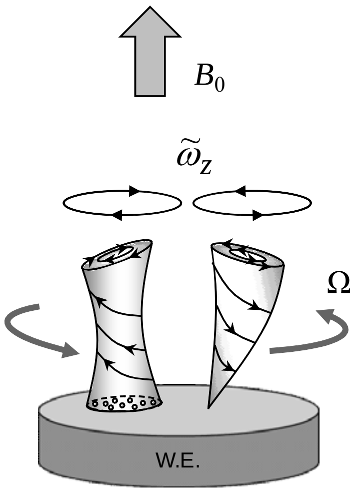

Figure 11: Precession of micro-MHD flow.

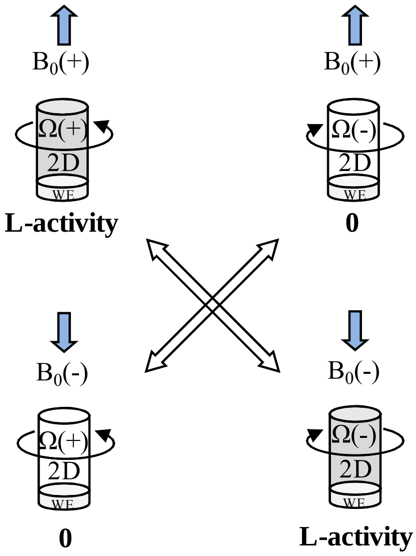

Figure 12: Chiral activity by system rotation.

3. Conclusion

The following three points were concluded; in the absence of passive film, chiral activity arises from screw dislocation of 2D pit. For vertical MHD flow, under upward and downward magnetic fields, D- and L-activities appear, respectively. On the other hand, for system rotation, only L-activity arises. Namely, in anodic etching also, chiral symmetry is broken to L-activity side.

4. References

[1] Mogi, I.; Watanabe, K.: Chiral electrode behavior of magneto-electrodeposited silver films. ISIJ Int. 47 (2007) 585-587.

[2] Mogi, I.; Morimoto, R.; Aogaki, R.; Watanabe, K.: Surface chirality induced by rotational electrodeposition in magnetic fields. Scientific Reports. 3 (2013) 2574.

[3] Aogaki, R.: Micro-MHD effect on electrodeposition in the vertical magnetic field. Magnetohydrodynamics. 39 (2003) 453-460.

[4] Aogaki, R.; Morimoto, R.: Nonequilibrium fluctuations in micro-MHD effects on electrodeposition. Heat and Mass Transfer: Modeling and Simulation (ed. Hossain, M. : InTech, Croatia) (2011) 189-216.

[5] Aogaki, R.: Instability of Nonequilibrium Fluctuation on Pitting Dissolution (I). J. Electrochem. Soc. 142 (1995) 2954-2966.

[6] Aogaki, R.: Instability of Nonequilibrium Fluctuation in Electrochemical Nucleation I. Occurrence of Instability. J. Chem. Phys. 103 (1995) 8602-8615.

[7] Aogaki, R.: Theory of Stable Formation of Ionic Vacancy in a Liquid Solution. Electrochemistry. 76 (2008) 458-465.

CHIRAL SURFACE FORMATION BY MAGNETOELECTROCHEMICAL ETCHING

MOGI[1] Iwao, AOGAKI[2] Ryoichi, WATANABE[1] Kazuo
[1] Institute for Materials Research, Tohoku University, Katahira, Sendai 980-8577, Japan
[2] Polytechnic University, Sagamihara, Kanagawa 252-5196, Japan
E-mail address of corresponding author: mogi@imr.tohoku.ac.jp

Abstract: Chiral surface formation was found in magnetoelectrochemical etching (MEE) as well as magnetoelectrodeposition. The MEE of copper films was conducted in galvanostatic conditions with various etching currents under a magnetic field of 5 T perpendicular to the electrode surfaces. The MEE film electrodes exhibited current difference in voltammograms between alanine enantiomers, and such chiral behavior depended on the etching current and the polarity of the magnetic field at the MEE processes.

1. Introduction

Chirality induction is one of the most attractive functionality in magnetoelectrolysis (electrolysis under magnetic fields). Chiral surfaces of metals and minerals have potentials as chiral catalysts, which could play wide roles in organic syntheses, pharmaceutical industry and molecular evolution of biochemical systems. Thus, studies on chiral surface formation are of great significance, and magnetoelectrolysis can be expected to contribute to the development of novel technique for the preparation of chiral surfaces.

We have reported that magnetoelectrodeposition (MED) is able to produce chiral surfaces of metal films of silver and copper [1-5]. This surface chirality could be induced by the MHD and micro-MHD vortices arising from the Lorentz force acting on faradaic currents [6,7]. The MED films showed chiral recognition for the enantiomers of several amino acids, glucose and tartaric acid [1-3,8].

The micro-MHD effect was also observed in magnetoelectrochemical etching (MEE) [9] as well as in MED. Figure 1 shows a schematic of the micro-MHD and vertical MHD vortices excited in the MEE processes under magnetic fields perpendicular to electrode

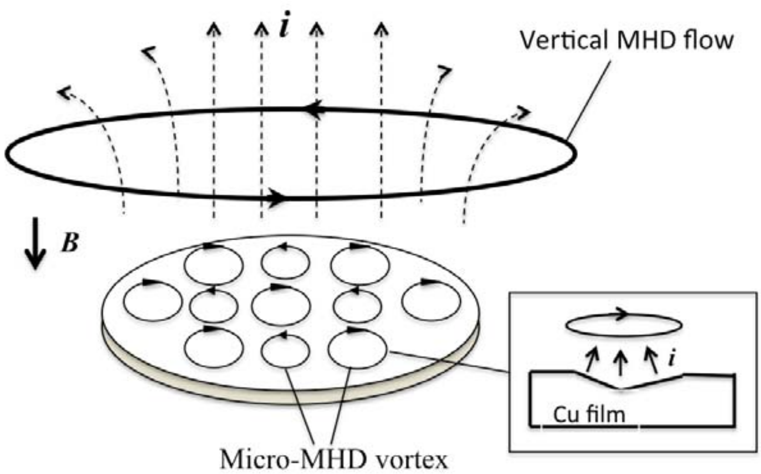

Figure 1: Schematic of the MHD effects in magnetoelectrochemical etching. The magnetic field ***B*** is imposed antiparallel to the faradaic current ***i*** and perpendicularly to the electrode surface.

surfaces. Electrochemical etching is a non-equilibrium process, and non-equilibrium fluctuation produces a number of pits on the etching surfaces. The micro-MHD vortices emerge around such pits (see an inset in Figure 1), and then they form self-organized states on the film surface. The vertical MHD flow is excited around the electrode edge and make interference on the micro-MHD vortices. Thus MEE processes are expected to produce chiral surfaces. In this paper, we report the experiments of MEE of Cu films with galvanostatic conditions and the dependence of chirality of the MEE films on the etching currents and the polarity of magnetic field.

2. Experimental of magnetoelectrochemical etching

In the electrochemical experiments, a conventional three-electrode system was employed: a polycrystalline Pt disc working electrode with a diameter of 1.6 mm, a Cu plate counter electrode, and a Ag | AgCl | 3 M (M = mol dm^{-3}) NaCl reference electrode. Before the etching processes, Cu films with a thickness of approximately 300 nm were prepared by electrodeposition on the working electrode in the absence of magnetic field. The etching of the Cu films was conducted in galvanostatic conditions with various constant currents of 15 – 30 mA cm^{-2} in a 50 mM $CuSO_4$ + 0.5 M H_2SO_4 aqueous solution until the film thickness decreased to approximately 150 nm. The passing charges were 0.8 C cm^{-2} at the electrodeposition and 0.4 C cm^{-2} at the etching. In the MEE process, the electrochemical cell was placed at the bore center in a cryocooled superconducting magnet, and a magnetic field of 5 T was imposed perpendicularly to the electrode surface. Here, the MEE films prepared in the magnetic field parallel and antiparallel to the faradaic currents are called +5T-film and –5T-film, respectively.

The MEE Cu films were used as electrodes after the pretreatment of surface oxidization from Cu to CuO, as described in our previous paper [3]. The chiral behaviors of the MEE film electrodes were examined using the voltammetric measurements of the enantiomers of alanine (an amino acid). The voltammograms were measured in a 20 mM alanine + 0.1 M NaOH aqueous solution with a potential sweep rate of 10 mV s^{-1}.

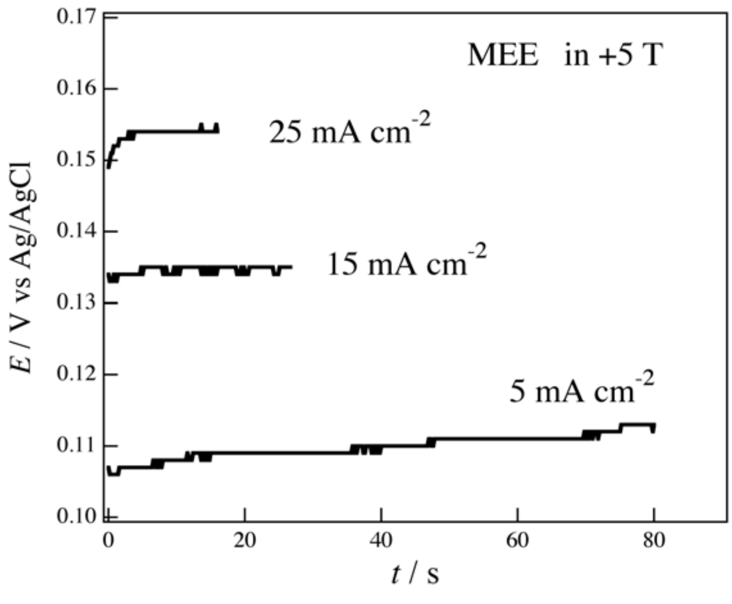

Figure 2: Electrode potential vs time during the MEE processes in +5 T at the etching current of 5, 15 and 25 mA cm^{-2}. The passing charge was 0.4 C cm^{-2}.

3. Results and discussion

Figure 2 shows the time dependence of working electrode potential during the MEE process in +5 T at the etching currents of 5, 15 and 25 mA cm^{-2}. The electrode potentials rise by ~ 5 mV for initial several seconds and then reach constant values at any etching currents. In such steady states, the micro-MHD vortices and the vertical MHD flow could form a self-organized state [7,10]. The steady potential increased almost linearly with increasing etching current in the region of 5 to 30 mA cm^{-2}.

Figure 3 shows voltammograms of L- and D-alanines on the (a) 0T-film, (b) –5T-film and (c) +5T-film electrodes, where all the MEE films were prepared at an etching current of 20 mA cm^{-2}. Alanine molecules are oxidized on the Cu electrodes around 0.7 V [11], where the voltammogram has a current peak. The voltammograms of the alanine enantiomers are coincident each other on the 0T-film electrode, meaning achirality of the film surface. On the other hand, the –5T-film electrode exhibits L-active chirality for the enantiomers; namely, the peak current of L-alanine is greater than that of D-alanine. This fact demonstrates that the MEE process induces the surface chirality on the Cu films.

The chiral sign of the MEE films should depend on the polarity of magnetic field at the MEE process. The reversal of the magnetic field direction is expected to lead to the mirror-image chirality of the MEE films. However, Figure 3(c) shows that the +5T-film electrode exhibit achirality, even though the –5T-film electrode exhibits L-active chirality. On the contrary, when the etching current was 25 mA cm^{-2}, the +5T-film electrode exhibited D-active chirality, and the –5T-film electrode exhibited achirality.

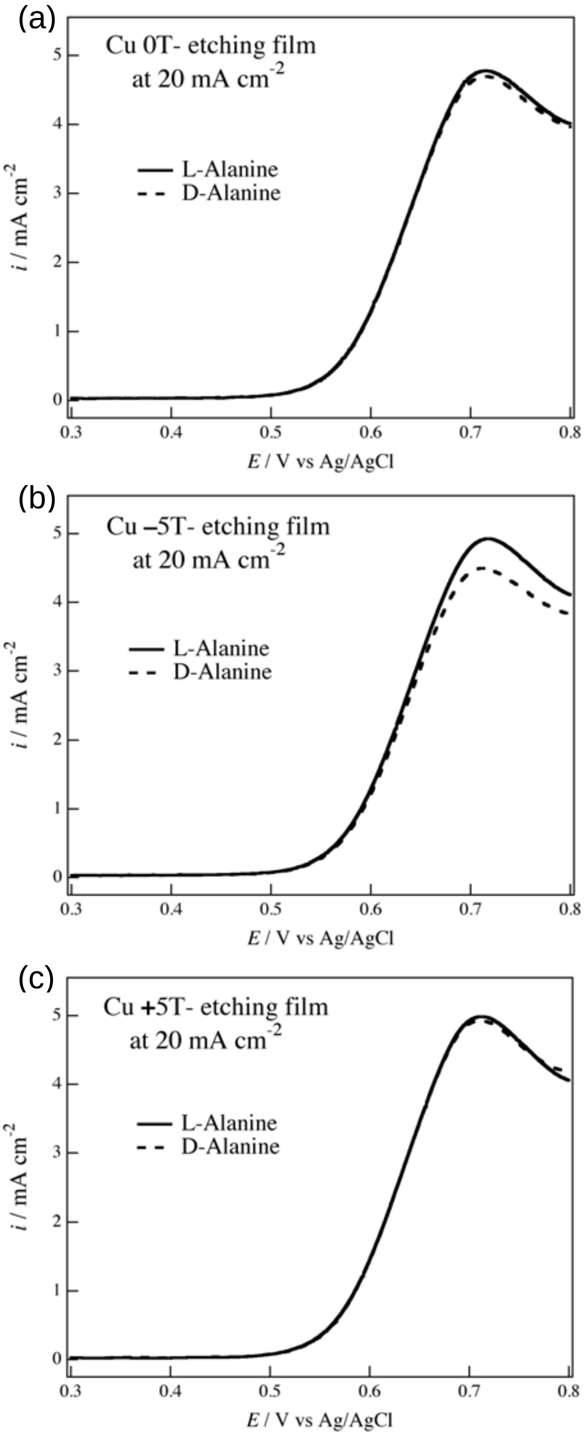

Figure 3: Voltammograms of L- and D-alanines on (a) the 0T-film electrode, (b) the MEE –5T-film and (c) the +5T-film electrodes, where the films were prepared at the etching current of 20 mA cm^{-2}.

In the case of magnetoelectrodeposition (MED) of Ag and Cu films, the reversal of the magnetic field direction induces the mirror-image chirality of the MED films [1-4]. For example, Cu MED +5T-films exhibit L-active chirality, and the –5T-films exhibit D-active one. This is why the direction of vertical MHD flow is determined by the magnetic field direction and the interference of the vertical

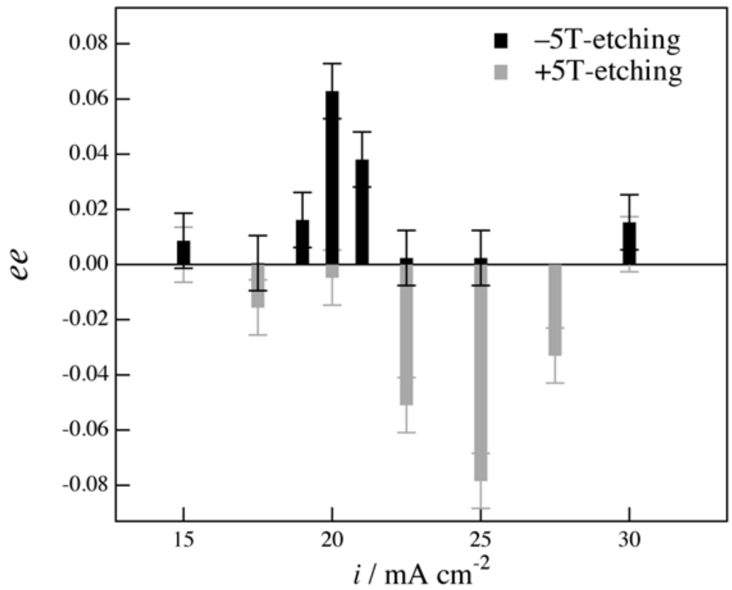

Figure 4: The ee ratios of +5T-film and –5T-film electrodes for alanine enantiomers versus the etching currents at the MEE processes.

MHD flow breaks the symmetry of the micro-MHD vortices [7]. However, the results in these MEE experiments suggest that the reversal of the magnetic field direction at the same etching current does not lead to the mirror-image chirality but lead to achirality.

We examined the etching current dependence of the chirality of the MEE 5T-films, and the result is shown in Figure 4, where enantiomeric excess (*ee*) ratios are plotted against the etching current for both polarities of magnetic field. The *ee* ratio in the voltammograms of enantiomers can be defined as $ee = (i_p^L - i_p^D) / (i_p^L + i_p^D)$, where i_p^L and i_p^D represent the peak currents of L- and D-alanines, respectively. The positive sign of ee ratio represents the L-activity, the negative sign represents the D-activity. While the –5T-film exhibits the maximum L-activity at 20 mA cm^{-2}, the +5T-film exhibits the maximum D-activity around 25 mA cm^{-2}. These results indicate that the optimal electrochemical condition for the L-active film formation is not the same as that for the D-active film formation. As a result, the chirality of the MEE films disappears in the films prepared in the opposite magnetic field at the same etching current, as shown in Figures 3(b) and 3(c). The asymmetric feature in the optimal conditions for L and D active surfaces implies symmetry breaking in the chiral surface formation, being of great interest in connection with the homochirality in molecular evolution.

Acknowledgements. This research was partially supported by JSPS KAKENHI Grant-in-Aid for Scientific Research (C) No.25390040. The authors thank the staff members of the High Field Laboratory for Superconducting Materials of IMR Tohoku University for the use of the cryocooled superconducting magnet.

4. References

[1] Mogi, I.; Watanabe, K.: Chiral electrode behavior of magneto-electrodeposited silver films. ISIJ Int. 47 (2007) 585-587.
[2] Mogi, I.; Watanabe, K.: Magnetoelectrochemical chirality in Ag electrodeposition. J. Chem. Chem. Eng. 4(11) (2010) 16-22.
[3] Mogi, I.; Watanabe, K.: Chiral recognition of amino acids by magnetoelectrodeposited Cu film electrodes, Int. J. Electrochem., 2011 (2011) 239637
[4] Mogi, I.; Watanabe, K.: Chirality of magnetoelectrodeposited Cu films, Magnetohydrodynamics, 48 (2) (2012) 251-259.

[5] Mogi, I.; Morimoto, R.; Aogaki, R.; Watanabe, K.: Surface chirality induced by rotational electrodeposition in magnetic fields, Scientific Reports 3 (2013) 2574.
[6] Aogaki, R.: Micro-MHD effect on electrodeposition in the vertical magnetic field. Magnetohydrodynamics 39 (2003) 453-460.
[7] Aogaki, R.; Morimoto, R.: Nonequilibrium fluctuations in micro-MHD effects on electrodeposition. Heat and Mass Transfer: Modeling and Simulation (ed. Hossain, M. : InTech, Croatia) (2011) 189-216.
[8] Mogi, I.; Watanabe, K.: Enantioselective recognition of tartaric acid on magnetoelectrodeposited copper film electrodes, Chem. Lett. 41 (2012) 1439-1441.
[9] Shinohara K.; Hashimoto K.; Aogaki R.: Magnetic field effect on copper corrosion in nitric acid, Chem. Lett., 31(2002) 778-779.
[10] Mogi, I.; Aogaki, R.; Morimoto, R.; Watanabe, K.: Magnetoelectrodeposition for the chiral surface formation of Cu films, ECS Trans. 45 (12) (2013) 1-8.
[11] Luo, P.; Zhang, F.; Baldwin, R.P.: Constant potential amperometric detection of underivatized amino acids and peptides at a copper electrode, Anal. Chem., 63 (1991) 1702-1707.

DEMIXING OF AN INITIALLY HOMOGENEOUS SOLUTION OF PARAMAGNETIC IONS IN INHOMOGENEOUS MAGNETIC FIELDS

YANG[1] X., TSCHULIK[2] K., UHLEMANN[3] M., ODENBACH[1] S., ECKERT[1] K.
[1] Institute of Fluid Mechanics, Chair of Magnetouiddynamics, Measuring and Automation Technology, TU Dresden, D-01069 Dresden, Germany
[2] Department of Chemistry, Oxford University, Oxford OX1 3QZ, UK
[3] Institute for Complex Materials, IFW Dresden, P.O. 270116, 01171 Dresden, Germany
Email: xuegeng.yang@tu-dresden.de

Abstract: Applying interferometry to an aqueous solution of paramagnetic manganese ions, subjected to an inhomogeneous magnetic field, we observe an unexpected but highly reproducible change in the refractive index. This change occurs in the top layer of the solution, closest to the magnet. The shape of the layer is in accord with the spatial distribution of the largest component of the magnetic field gradient force. It turns out that this layer is heavier than the underlying solution because it undergoes a Rayleigh-Taylor instability upon removal of the magnet.

1 Introduction

Magnetic fields were proved to be a useful tool to manipulate objects according to their magnetic properties on macroscale, microscale and occasionally on nanoscale (1)(2). An increasing interest is noticeable in the application of magnetic fields to manipulate of objects according to their magnetic properties. These applications are based on the magnetic field gradient force $\vec{f_m}$. However, the control of superparamagnetic nanoparticles in magnetic field gradients is a formidable task because the large mean-squared displacement due to Brownian motion makes it difficult for the magnetic field gradient force to track such small particles at all(3)(4). Thus, with a view to the atomic scale, corresponding to paramagnetic ions, any impact of $\vec{f_m}$ was considered even less likely. However, recent study on molecular scale also showed results unexpected from established physical models, for example, the manipulation of single molecular spin or phase separation in dispersion of nanorods, see references in (5).
In the present contribution, we show the opposite of what was stated above: we demonstrate that magnetic ions in a homogeneous aqueous solution can be locally enriched by means of a superimposed magnetic gradient field. This finding is not only of high interest from the theoretical point of view, but is of great importance for a variety of applications, for example, for recycling of rare-earth metals from industrial waste water.

2 Experimental

Paramagnetic $MnSO_4$ solutions with different concentrations were prepared using analytical grade reagents and deionized water. The total magnetic susceptibility of the solution is given by

$$\chi_{sol} = \sum_k \chi_{mol,k} \cdot C_k \tag{1}$$

where $\chi_{mol,\ k}$ and C_k refers to the molar susceptibility of the molecules and concentration of sort k. Taking $\chi_{mol,\ H_2O} \cdot C_{H_2O} = -9 \cdot 10^{-6}$ into account along with the molar susceptibility of

$MnSO_4$, $\chi_{mol,\ MnSO_4} = 1.678 \times 10^{-7}\ m^3/mol$ we can derive the susceptibilities of the solutions used. In this way, we find e.g. 1.588×10^{-4} for an 1 M $MnSO_4$ solution. The homogeneous $MnSO_4$ solution was injected into the cuboid glass cuvette with an inner side length of 10.0 mm, which was covered by a thin glass cover slip. A cylindrical NdFeB permanent magnet with a diameter of 10.0 mm and a height of 5.0 mm was placed 0.5 mm above the cover slip, see Fig. 1a.

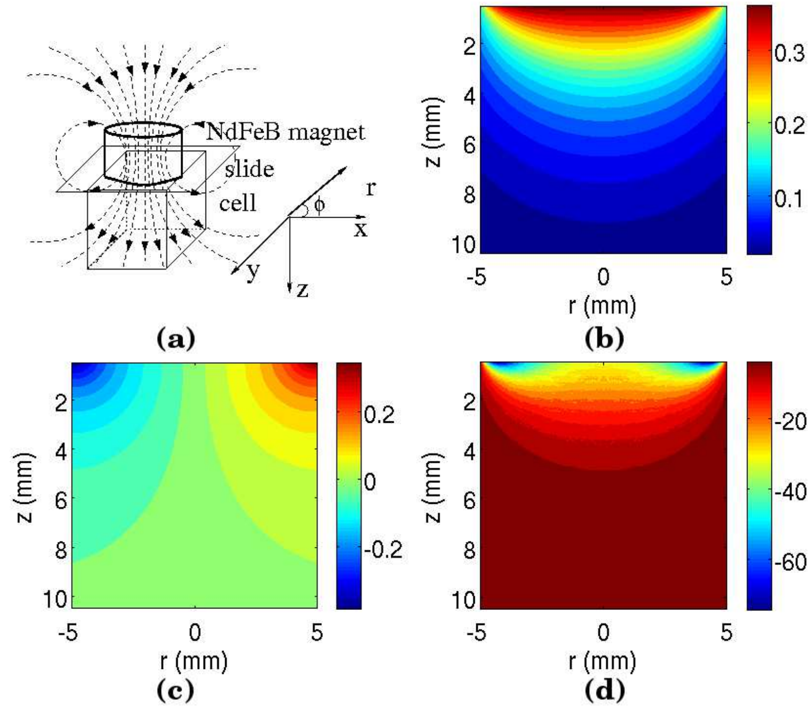

Figure 1: (a) Sketch of magnet and cell setup. (b) and (c) represent B_z and B_r in Tesla. (d) shows the dominant part, $B_z\frac{\partial B_z}{\partial z}$ in T^2/m, of the axial field gradient component according to Eq. 3.

The resulting spatial distribution of the magnetic induction $\vec{B}$ around the magnet was simulated by means of a Finite Element Solver (Amperes 9.0) and is axisymmetric by definition. Hence, the azimuthal component B_ϕ and the respective derivative, $\partial/\partial\phi$ cancel out in the azimuthal direction. As a result, the following components in r and z direction remain in the field gradient force density $\vec{f_m}$:

$$[(\vec{B} \cdot \nabla)\vec{B}]_r = B_r\frac{\partial B_r}{\partial r} + B_z\frac{\partial B_r}{\partial z} \tag{2}$$

$$[(\vec{B} \cdot \nabla)\vec{B}]_z = B_r\frac{\partial B_z}{\partial r} + B_z\frac{\partial B_z}{\partial z} \tag{3}$$

To intuitively understand the plots in Fig. 1b-d, imagine the magnetic dipole, Fig. 1a. The field lines exit at the magnet's north pole, which immediately faces the solution. Hence, in the upper central part of the solution, B_z is the dominating component (Fig. 1b). By contrast, because of the bending of the field lines towards the opposite south pole, B_r becomes noticable along the perimeter of the magnet, i.e. at the upper sidewalls of the cuvette, see Fig. 1c. Significant gradients, $\partial B_r/\partial r$, appear only in the corners, while $\partial B_z/\partial z$ also penetrates the upper bulk solution. Thus, one can show that the dominant component in (Eq.2-Eq.3) is $B_z\frac{\partial B_z}{\partial z}$, as plotted

in Fig. 1d.
A Mach-Zehnder interferometer was used to study the evolving concentration distribution of $C_{Mn^{2+}}$ in the cell under the action of $\vec{f}_m$. The velocity distribution was measured using Particle Image Velocimetry (PIV). The setup and details of both techniques were the same as in our previous work (6). The recording was carried out for 10 seconds at a time interval of 60 seconds for 20 minutes. All results in this paper were time-averaged over one second, i.e. 10 frames.

3 Results and discussions

The key result of this work is the observation of a highly reproducible bending of the fringes in the interferograms directly below the magnet after the magnet is applied to the paramagnetic solution, which is directly caused by a change of concentration in this region. This clearly indicates a change in the refractive index Δn of the solution, which may be caused by a change in either the concentration or the temperature of the solution. However, no physical reason is identifiable for the latter because the solution was safely prevented from being heated by the laser or from cooling through evaporation. Thus, we processed the interferogram packages under the assumption, that Δn is entirely caused by a change in the concentration, $C_{Mn^{2+}}$, of the Mn^{2+} ions.

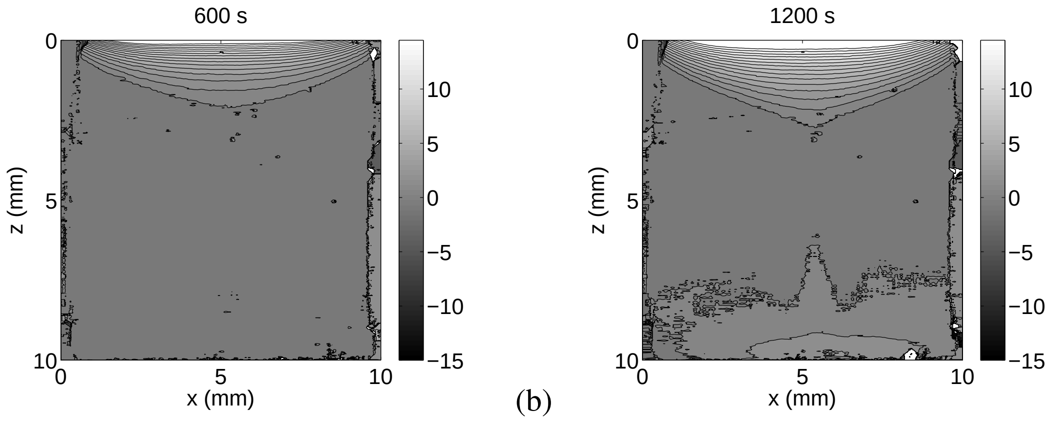

(a) (b)

Figure 2: Iso-concentration contour plots of the 1 M $MnSO_4$ solution (a)600 s and (b) 1200 s after the magnet was applied on top of the cell. The unit in the legends is the concentration change in mM.

Fig. 2 shows the resulting contour plots representing the change in $C_{Mn^{2+}}$ for 1M $MnSO_4$ solutions at t = 600 and 1200 seconds after the magnet was applied. We observed the formation of a convex layer close to the magnet in which $C_{Mn^{2+}}$ is higher than in the bulk. The enrichment increases with time, cf. Fig. 2(a) and (b), to reach a steady state at t $\sim$ 1200 s(Fig 2b). The larger the amount of C_0, the stronger the concentration increase at the top, which is found to reach 2% of C_0. The convex shape of the optical inhomogeneous layer below the magnet reproduces the convex shape of the spatial distribution of the dominant component of the magnetic field gradient force (Fig. 1d).
The origin of this increase can be understood by zooming into the concentration contour plots and applying PIV in parallel. Fig. 3a proves that there is a drainage from the enrichment layer down to the bottom center of the cell. This drainage, which feeds the increase at the bottom as visible in Fig. 2b, is associated with a downward flow visualized by the PIV measurement in Fig. 3b. The downward flow occurs in the center of the cell, i.e. at the position of maximum

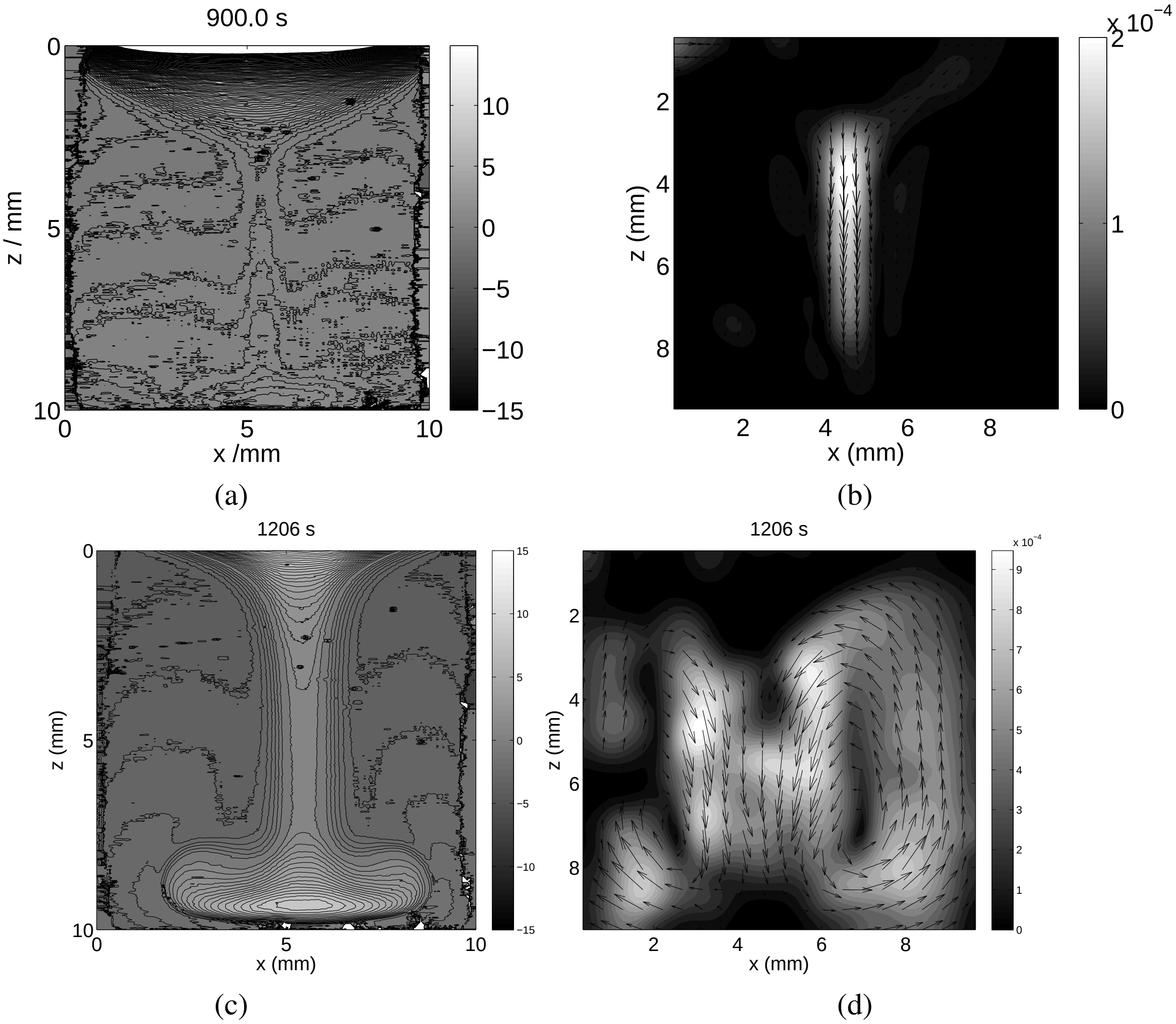

Figure 3: Iso-concentration contours (a, c) and velocity vector plots (b, d) of the solution 900 seconds after the magnet was applied on top of the cell (a and b) and 6 seconds after the magnet was removed (c and d) for the 1 M $MnSO_4$.

bending of the concentration iso-contours in Fig. 3a. Thus we can infer that the steady state results from a balance between an attraction of Mn^{2+} ions towards the magnet and their depletion due to a drainage by means of a downward flow.

The next important question to be answered is that of what happens when the magnet is removed. Fig. 3 c and d show that the enriched layer on top of the cell immediately drops down to the bottom in a few seconds. This closely resembles a Rayleigh-Taylor instability which occurs when a layer of higher density is imposed on another one of lower density. The falling plume, entraining the content of the enrichment layer, can be seen well in Fig. 3c. This plume creates a downward flow in the center which is clearly visible in the PIV, Fig. 3d. By continuity, an upward flow occurs in the outer parts of the cell which replaces the fluid dragged from the enrichment layer.

This observed demixing of an initially homogeneous solution is a highly reproducible but unexpected phenomenon. Indeed, for the present case of a $MnSO_4$ solution in a closed system with concentrations significantly below the solubility product, one would not expect a demixing even in the presence of the applied magnetic field. Therefore, we first speculated about a parasitic thermal effect. However, with the precautions explained above, both heating by the laser and evaporative cooling of the solution are excluded, and hence also any kind of magnetocaloric pumping. Also, no nanoparticle formation was detected using dynamic light scattering within one hour of the solution being stored under experimental conditions.

4 Conclusions

The concentration enrichment which we report above is restricted neither to the paramagnetic Mn^{2+} ions nor to SO_4^{2-} as anions. We found that similar phenomena also occur for the stronger paramagnetic Gd^{3+} or for Cl^- as an anion. By contrast, no significant effect was found for the $CuSO_4$ solution because χ_{sol}, and correspondingly $\vec{f}_m$, are much smaller than in $MnSO_4$. We believe that this possibility to separate paramagnetic metal ions from aqueous solutions might be of significant interests for recycling purposes.

Acknowledgements

Financial support from Deutsche Forschungsgemeinschaft (DFG) in frame of the Collaborative Research Center (SFB) 609 and by DLR (50 WM 1350) are gratefully acknowledged.

References

[1] Pamme N.: Magnetism and microfluidics. Lab. Chip, 6 (2006) 24–38
[2] Rosensweig R. E.: Ferrohydrodynamics. Mineola, NY: Dover Publications 1997
[3] Monzon L.; Coey J.M.D. : Magnetic fields in electrochemistry: The Kelvin force. a mini-review. Electrochem. Commun. 42 (2014) 42–45
[4] Coey J.M.D.; Aogaki R.; Byrne F.; Stamenov P: Magnetic stabilization and vorticity in submillimeter paramagnetic liquid tubes. Proc. Natl. Acad. Sci. U.S.A. 106 (2009) 8811–8817
[5] Yang X.; Tschulik K.; Uhlemann M.; Odenbach S.; Eckert K.: Enrichment of paramagnetic ions from homogeneous solutions in inhomogeneous magnetic fields. J.Phys. Chem. Lett. 3 (2012) 3559–3564
[6] Yang X.; Eckert K.; Muehlenhoff S.; Odenbach S.: On the decay of the lorentz-force-driven convection in vertical concentration stratification during magnetoelectrolysis. Electrochim. Acta 54 (2009) 7056–7065

HOW TO IMPROVE THE UNIFORMITY OF METAL DEPOSITION AT VERTICAL ELECTRODES BY ELECTROMAGNETIC FORCES

MUTSCHKE[1,2] G., MÜHLENHOFF[3] S., SELENT[2] R., YANG[2] X., UHLEMANN[3] M., FRÖHLICH[2] J., ODENBACH[2] S., ECKERT[2] K.
[1]Helmholtz-Zentrum Dresden-Rossendorf, Institute of Fluid Dynamics, PO Box 510119, 01314 Dresden, Germany
[2]Technische Universität Dresden, Institute of Fluid Mechanics, 01062 Dresden, Germany
[3]Leibniz Institute for Solid State and Materials Research IFW Dresden, Helmholtzstraße 20, 01069 Dresden, Germany
E-mail address of corresponding author: g.mutschke@hzdr.de

Abstract : In electrochemical plating often a uniform deposition is desirable allowing to reduce both energy and material costs. Magnetic fields are well known to influence the mass transfer during electrolysis and offer easy control of the deposition process. In this paper, first, time-constant Lorentz forces are considered which, if properly designed, may considerably im-prove the uniformity of the deposit. Second, time-dependent Lorentz forces are investigated. It is demonstrated that pulsed deposition offers a comparable enhancement of the uniformity.

1. Introduction

Both pulse plating and magnetoelectrolysis are convenient techniques capable of improving the quality of electrochemically deposited layers. Pulse plating is based on the modification of the concentration boundary layers at the electrodes by periodic charging and discharging of the electric double layer. Magnetoelectrolysis, on the other hand, employs a Lorentz force density, $\mathbf{f} = \mathbf{j} \times \mathbf{B}$, resulting from the coupling between the electric current density $\mathbf{j}$ in the electrolyte and the external magnetic field $\mathbf{B}$, to force or to modify the convection of the electrolyte. Despite the different underlying mechanisms, similar effects can be achieved. One of the aims of this work is to ask whether a combination of both techniques leads to synergies when aiming at superior homogeneity of the metal deposits.

Indeed homogeneity of the deposit is one of the ultimate goals of any electrodeposition process. According to Faraday's law, inhomogeneities indicate an inhomogeneous current distribution. A main source of inhomogeneities is natural convection. The electrochemical reactions cause concentration and thus density changes near the electrodes which give rise to a buoyant fluid flow within the boundary layers [5]. Regarding a deposition at a vertical cathode in a large cell, the rising fluid flow is responsible for a thickness δ of the concentration boundary layers that increases in the upstream direction as $y^{1/4}$ [6] where $y = 0$ is the leading edge of the cathode. Since j is proportional to $\partial C/\partial x \approx \Delta C/\delta$, a $j \sim y^{-1/4}$ dependence follows. As a consequence, $\mathbf{j}$ is higher at the bottom of the cathode [7], inducing a bigger deposit thickness there. To improve the homogeneity of the deposit, thus saving time and material, homogenization of the concentration boundary layer is vital.

In the first part of this work we examine how this can be achieved by using static Lorentz forces which significantly affect buoyant fluid layers as they emerge [1,8–10]. The second part is devoted to time-dependent Lorentz forces arising from the combinations of modulated current densities j(t) with static magnetic fields [2-4].

2. Presentation of the problem

The setup considered in both experiment and simulation is shown in Fig. 1a. For the electrochemical deposition a cubic glass cell was used (inner side length H=10 mm) with plane vertical electrodes, the anode being a copper plate and the cathode a glass sheet with a 50 nm Au layer (PVD). The size of the electrodes was 10 mm×10 mm with a distance of 8 mm between them. The cell was placed between two identical pairs of NdFeB permanent magnets, each of them connected via an anchor (Fig. 1a). The two pairs were positioned such that their magnetic fields were horizontal but in opposing directions. This generates a magnetic field $\mathbf{B} = (B_0 \pm b \cdot x)\, \mathbf{e_z}$ with a constant gradient b over the whole cell with positive values at one electrode and negative values at the other, where the absolute values as well as the gradient depend on the distance between the two pairs of magnets [12]. A gap of Δx =20 mm provides a magnetic induction of ±125 mT at the electrodes with a gradient of b=±31 T/m, compared to ±175 mT and ±44 T/m at a distance of Δx = 15 mm.

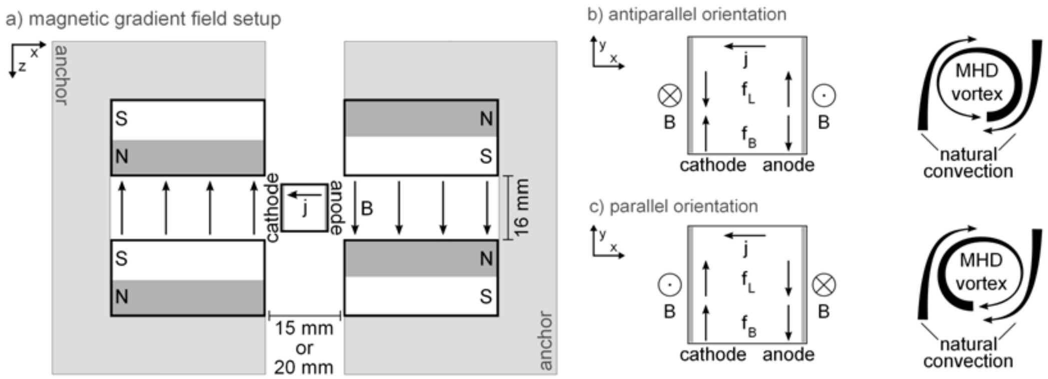

Figure 1: a) Sketch of the setup with magnetic gradient field (top view). (b–c) Scheme of the orientation between the Lorentz and buoyancy force, f and f_B, for antiparallel (b) and parallel (c) configurations along with the resulting convective flow regimes (side view).

Electrodeposition was carried out twice for each flow regime under galvanostatic conditions at 6 mA/cm^2 for 2 h in a 0.05M CuSO4-solution at pH3 (adjusted with H_2SO_4). Subsequently, the cathode was removed from the cell, rinsed with deionized water and EtOH and embedded in acrylic resin (Struers EpoFix). Cutting the specimen into two halves along the vertical centre line produces four samples for each flow regime to be analysed. After polishing and microscopy (TSO long range microscope, 20× magnification, Baumer TXG50 camera, resolution 3.4 px/µm) the thickness of the deposited Cu layer was determined and averaged over the four samples. For the deposition parameters given above, an average layer thickness of d = 16 µm can be predicted according to Faraday's law.

To support the experiments and to develop strategies for an efficient temporal modulation of the Lorentz force, two-dimensional numerical simulations were performed, representing the vertical center plane between the electrodes. For further details of the numerical method we refer to [11, 12, 4].

The relative orientation between the Lorentz force **f** and the buoyancy force $\mathbf{f_b}$ plays a crucial role for the interaction between MHD and natural convection. According to the experimental setup (Fig. 1a), **f** points downward along the y-direction at the cathode and upward at the anode. As a result, a convection roll is established; the axis of which is parallel to the z-axis. The flow of this MHD roll is directed counter-clockwise, i.e. antiparallel to the natural convection as sketched in Fig. 1b. For details, we refer to [13]. Inverting the magnetic field gradient switches the rotation direction of the MHD roll towards a clockwise one, because the Lorentz-force-driven convection is now oriented parallel to the natural convection (Fig. 1c).

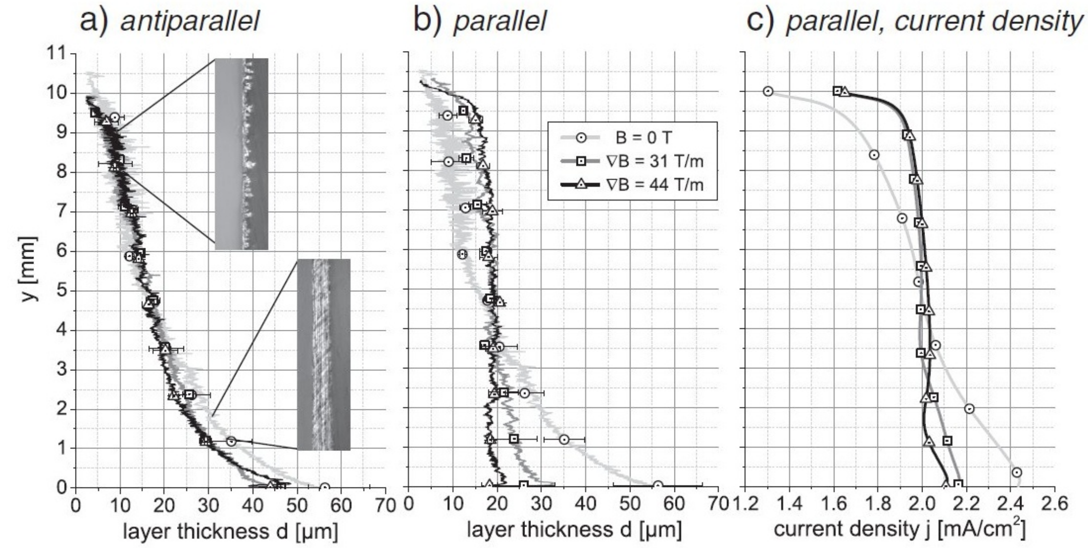

Figure 2: (a,b) Layer thickness measured along the cathode for different orientations of the Lorentz force after 120 min (j=6 mA/cm^2), c) Current density (computed) along the cathode for parallel orientation of Lorentz force and buoyancy force after t=10 min (j=2 mA/cm^2) [1].

Since own previous work showed that the relative orientation of the involved forces substantially affects the flow characteristics and hence the mass transport, the deposit thickness for both regimes is analyzed and compared with the case of pure natural convection.

3. Results for a time-constant Lorentz force

For the reference case without **B** (Fig. 2a, light grey line) it is obvious that the copper deposition is very inhomogeneous, ranging from a thickening at the bottom up to d=55µm toward a decrease to about 10 µm in the upper part. Additionally, dendritic growth structures can be observed within this region (insets in Fig. 2a). When the Lorentz and buoyancy forces are aligned in antiparallel mode (Fig. 1b), only marginal deviations in the shape of the resulting deposit are observed (Fig. 2a, dark-grey and black line). Only the thickening at the bottom is about 5 µm smaller for forced convection, and even a region of dendritic growth can be found between y = 7 and 10 mm.

In contrast to the antiparallel case, the layers deposited when Lorentz force and buoyancy force are oriented *parallel* to each other (Fig. 1c) exhibit a much more uniform shape, shown in Fig. 2b. In this case, the two effects support each other, and the strongly depleted fluid layer in front of the cathode is removed. Cu-ion rich electrolyte is advected from the anode and pushed upwards along the cathode where it serves as a reservoir for deposition. This in turn leads to uniform concentration boundary layers and hence to a homogeneous deposit thickness of about d = 20 µm in a large central part of the electrode.

The improved homogeneity of the deposit layer due to the Lorentz force is also supported by the numerical simulations (Fig. 2c). Qualitatively, the current density resembles the experimental results of deposit thickness discussed above even for this low value of **j**. For both values of the magnetic field gradient, the homogeneity of the current density distribution is improved considerably.

4. Results for pulsed deposition

The main part of the results presented here employs a temporal modulation of the current density with reversal as depicted in Fig. 3. Beside, although not shown, also time-periodic modulations of the current density without reversal and superimposed temporal modulations of the magnetic field amplitude were considered [4].

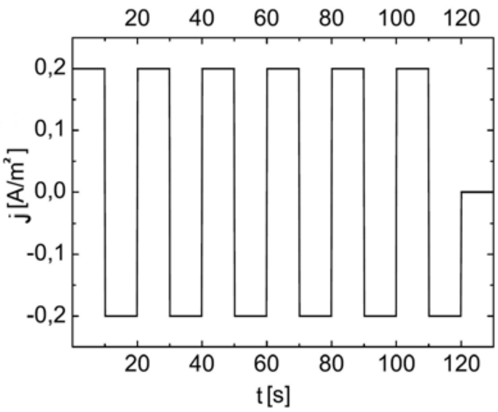

Figure 3: Temporal modulation of the current density j(t) with reversal.

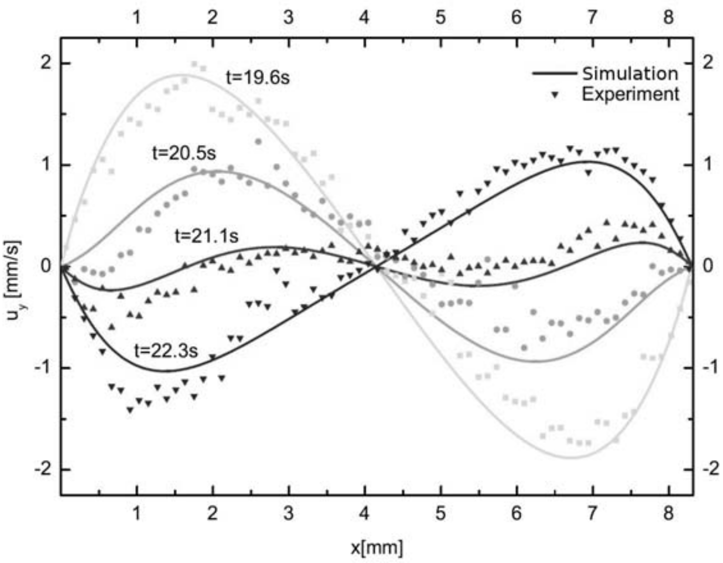

Figure 4: Comparison of measured velocity profiles from [3] with numerical simulations [4].

Fig. 4 shows snapshots of the vertical velocity profiles between the electrodes (placed at x=0 and x = 8.4 mm) near the instant t=20 s where the current density switches from j(t)=-0.2 A/m^2 (squares) to j(t)=+0.2 A/m^2 (triangles), equivalent to a reversal of the direction of **f** at both electrodes. The reversal process in the velocity profiles is nicely seen, and a good agreement between simulation and experiment can be stated. In order to define an electrode-averaged measure for the deviation from uniform deposition $\delta_{cu}(y)$ which locally depends on height y, a mean value and a standard deviation can be defined as

$$\bar{\delta}_{cu} = \frac{1}{L_y}\int_y \delta_{cu}(y)\,dy, \qquad \sigma_r = \int_y \frac{\sqrt{(\delta_{cu}(y) - \bar{\delta}_{cu})^2}}{\bar{\delta}_{cu}}\,dy \qquad (1)$$

Fig. 5 shows the temporal evolution of these quantities versus time. The insert highlights the temporal growth of the standard deviation which cannot be avoided in this configuration. The mean value follows a sawtooth behaviour as the net deposition periodically vanishes.

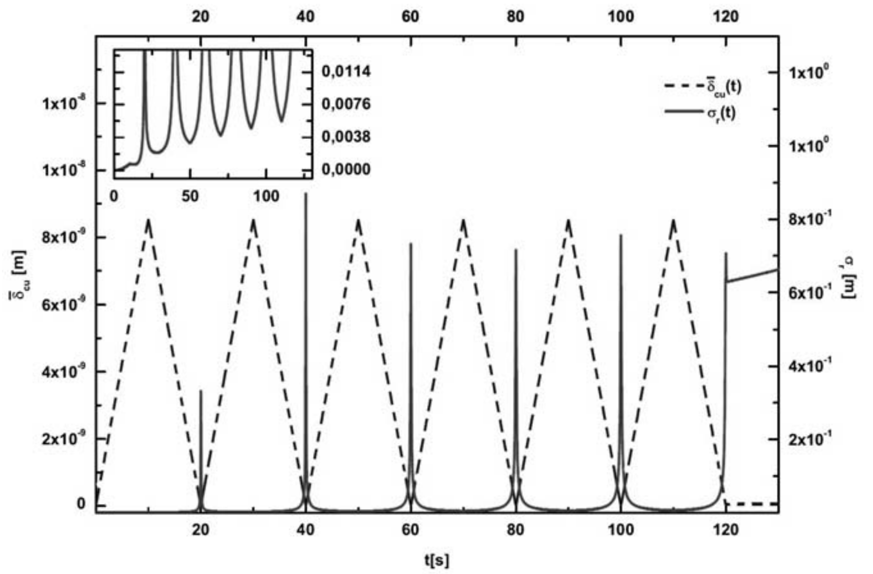

Figure 5: Temporal evolution of the deviation from uniform deposition [4].

5. Conclusion and Outlook

The results presented in this paper clearly show that a properly designed Lorentz force can considerably improve the homogeneity of a metal deposit at vertical electrodes in natural convection conditions. In the case of a nearly time-independent Lorentz force this effect is most pronounced when the latter is orientated in the same direction as the buoyancy force at the electrodes [1]. Furthermore, proper time-dependent Lorentz forces with periodic cell currents are proven to deliver comparable uniformity [2]. A further delay of the build-up of the vertical density stratification which prevents uniform deposition can be achieved when the magnetic field amplitude is used for control in addition. Further results of an advanced temporal management of the current density and of the magnetic field are described in [4] and will be published elsewhere.

6. References

[1] S. Mühlenhoff, G. Mutschke, M. Uhlemann, X. Yang, S. Odenbach, J. Fröhlich, K. Eckert; Electrochem. Comm. 36 (2013) 80–83.
[2] Mühlenhoff, S.: PhD thesis, TU Dresden, 2012.
[3] X. Yang, K. Eckert, S. Mühlenhoff, M. Uhlemann, S. Odenbach; Electrochem. Comm. 11 (2009) 318-322
[4] Selent, R.: Diploma Thesis, TU Dresden, 2011.
[5] C.R. Wilke, M. Eisenberg, C.W. Tobias, J. Electrochem. Soc. 100 (11) (1953) 513-523.
[6] N. Ibl, R.H. Müller, J. Electrochem. Soc. 105 (6) (1958) 346-353.
[7] C. Wagner, J. Electrochem. Soc. 104 (2) (1957) 129-131.
[8] T.Z. Fahidy, Chem. Eng. J. 72 (1) (1999) 79–82.
[9] X. Yang, K. Eckert, K. Seidel,M. Uhlemann, Electrochim. Acta 54 (2) (2008) 352–359.
[10] S. Mühlenhoff, G. Mutschke, D. Koschichow, X. Yang, A. Bund, J. Fröhlich, S. Odenbach, K. Eckert, Electrochim. Acta 69 (2012) 209–219.
[11] S. Mühlenhoff, G. Mutschke, D. Koschichow, X. Yang, A. Bund, J. Fröhlich, S. Odenbach, K. Eckert, Electrochim. Acta 69 (2012) 209–219.
[12] D. Koschichow, G. Mutschke, X. Yang, A. Bund, J. Fröhlich, Russ. J. Electrochem. 48 (2012) 682–691.
[13] X. Yang, S. Mühlenhoff, P. Nikrityuk, K. Eckert, Eur. Phys. J. Spec. Top. 220 (2013) 303–312.

NUMERICAL SIMULATION OF THE MASS TRANSFER OF MAGNETIC SPECIES AT ELECTRODES EXPOSED TO SMALL-SCALE GRADIENTS OF THE MAGNETIC FIELD

MUTSCHKE[1,2] G., TSCHULIK[3] K., UHLEMANN[4] M., FRÖHLICH[2] J.
[1]Helmholtz-Zentrum Dresden-Rossendorf, Institute of Fluid Dynamics, PO Box 510119, 01314 Dresden, Germany
[2]Technische Universität Dresden, Institute of Fluid Mechanics, 01062 Dresden, Germany
[3]Oxford University, Dept. Chemistry, Oxford OX1 3QZ, UK
[4]Leibniz Institute for Solid State and Materials Research IFW Dresden, Helmholtzstraße 20, 01069 Dresden, Germany
E-mail address of corresponding author: g.mutschke@hzdr.de

Abstract:
The mechanisms responsible for the spatially inhomogeneous thickness of metal layers obtained by electrochemical deposition in magnetic gradient fields at small scale are controversially discussed in the literature. The paper presents the results of numerical simulations which support the reasoning that local convection at the electrode, driven by the curl of the magnetic gradient force, is responsible for the effects observed. The deposition of paramagnetic and of diamagnetic ions is discussed, and the influence of electrically inert magnetic ions present in the electrolyte is enlighted.

1. Introduction

In the recent past, there has been a broad discussion in the community about the mechanisms responsible for the spatially inhomogeneous deposition of magnetic ions obtained in magnetic gradient fields. A variety of experimental studies reported on structured and inversely structured deposits in the milli- and micrometer range, thereby resembling the spatial distribution of the magnetic field at the electrode. For an up-to-date review, we refer to [1]. By order of magnitude estimations of the forces involved, the Lorentz force $\mathbf{f_L}$ and the magnetic gradient force $\mathbf{f_m}$, it was shown that the magnetic gradient force clearly dominates the Lorentz force if the length scale of the magnetic gradient is of the order of millimeter or below [2]. In the same reference it was shown that in case of simple deposition from paramagnetic ions like Cu^{2+} (no other magnetic ions are involved), local convection driven by the curl of the magnetic gradient force can explain the structuring effect observed.

In the following, experiments of the deposition of diamagnetic ions were performed as well, and cases where inert magnetic ions are additionally present in the electrolyte, were also considered, mentioning a set of different possible mechanisms [3]. In [4], two different explanations are given when obtaining either structured or inversely structured metal deposits.

Already at the PAMIR 2009 conference, a consistant and unique explanation of all experimental results of deposition in small-scale magnetic gradient fields was proposed by the present authors. A careful analysis of the influence of electrically inert magnetic ions added to the electrolyte allows to argue, that the action of the resulting local convection at the electrode can deliver a consistent explanation [5]. Recently, this reasoning was proven numerically [6]. Below, we present details of numerical simulations performed on this topic, covering the cases of deposition of paramagnetic and of diamagnetic ions.

2. Presentation of the problem

The magnetic gradient force for a number *i* of species of magnetic ions beside the diamagnetic water molecules can be written as

$$\mathbf{f_m} = \frac{1}{2\mu_0}\chi_{sol}\,\nabla B^2\ , \qquad \chi_{sol} = \chi_{H_2O} + \sum_i \chi_i^{mol} c_i\ . \tag{1}$$

Contrary to the reasoning in [4,7] it can be argued that the ("magnetic") pressure of that force cannot force convection in the deposition setups considered. Instead of this potential part, the rotational part of the force is responsible for the effect. Consider, for example two species of magnetic ions. The curl of the force in this case reads

$$\nabla\times\mathbf{f_m} = \frac{1}{2\mu_0}(\chi_1^{mol}\nabla c_1 + \chi_2^{mol}\nabla c_2)\times(\nabla B^2)\ . \tag{2}$$

As can be seen, the diamagnetic property of the water molecules does not play any role. Furthermore, inert magnetic ions may have a strong influence on the magnetic gradient force. When depositing from supporting electrolytes that contain a strongly paramagnetic but electrochemically inert cation (e.g., Mn^{2+}, Dy^{3+}), changes of concentration of this inert ion become important. Due to electroneutrality, its concentration usually increases at the cathode where its flux must vanish [8]. In case of depositing Cu^{2+} from an electrolyte that consists of, e.g., $c_{Cu2+} << c_{Mn2+} \approx c_{SO42-}$ it can be shown that $\nabla c_{Cu2+} / \nabla c_{Mn2+} \approx -2$.

For depositing paramagnetic Cu^{2+} (species 1) in a simple case without other magnetic cations in excess it is known that the curl of the force drives a flow which is resulting in local convection towards the magnet, thereby enriching the concentration boundary layer and thus enhancing mass transfer [2]. If, on the other hand, the supporting electrolyte contains strongly paramagnetic ions, species 2 is dominating the curl since, e.g., $\chi_{para}^{mol} / \chi_{Cu2+}^{mol} > -10$ for Mn^{2+}, Dy^{3+}. Therefore, the curl changes sign and the direction of convection is inverted compared to the case of simple copper deposition. Thus, a local flow is forced, which brings the depleted electrolyte inside the concentration boundary layer towards the magnet where it leaves the electrode. As a result, mass transfer is expected to decrease. The same is valid for the deposition of diamagnetic ions (e.g., Bi^{3+}, Zn^{2+}), for which $|\chi_{dia}^{mol}| << \chi_{Cu2+}^{mol}$. In order to prove this reasoning, numerical simulations have been performed in a vertical cylindrical cell of 8 mm diameter and 10 mm height. At the center of the cathode on top, a cylindrical NdFeB magnet (diameter 1 mm, height 3 mm, distance 70 μm) was placed, which is magnetized in the axial direction. The electrolyte consists of 0.01 M $CuSO_4$ and 0.1 M $MnSO_4$. A potentiostatic deposition at a cell voltage of 0.2 V (copper electrodes) was simulated for a duration of 300 s, leading to diffusion-limited mass transfer. More details will be published elsewhere. Fig. 1 (top part) shows the Cu^{2+} concentration and the velocity of the electrolyte near the magnet for the magnetically pure Cu^{2+} case (left) and the case with magnetic Mn^{2+} ions (right) at t = 10 s. Depositing Bi^{3+} in the presence of Mn^{2+} ions (not shown) looks very similar to the latter case. Clearly, the characteristic convection patterns expected from the above analysis are found which qualitatively persist during ongoing deposition. The evolution of the deposit thickness is shown below and corresponds to the experimental findings in Refs. [3, 4]. Recent measurements in Ref. [9] support the proposed convection model.

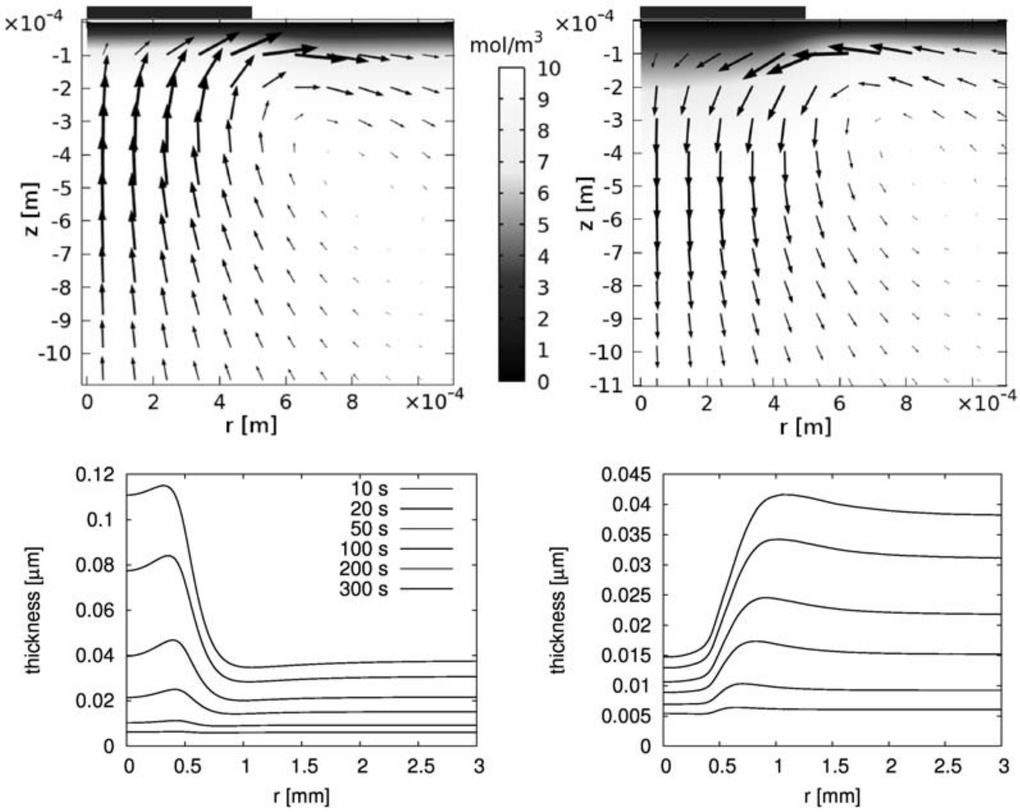

Figure 1: Top: Concentration of Cu^{2+} and normalized velocity vectors at t = 10 s in the domain part below the magnet (black bar on top: radial extent). Left: Cu-case (u_{max} = 0.03 mm/s), right: Cu-Mn case (u_{max} = 0.05 mm/s). Bottom: Corresponding temporal evolution of the thickness of the copper layer [6].

3. Conclusions

The structuring effect in small-scale magnetic gradient fields can be consistently explained by local convection forced by the rotational part of the magnetic gradient force. Numerical simulations clearly support this reasoning.

4. References

[1] M. Uhlemann, K. Tschulik, A. Gebert, G. Mutschke, J. Fröhlich, A. Bund, X. Yang, K. Eckert; Eur. Phys. J. Spec. Top. 220 (2013) 287-302.

[2] G. Mutschke, K. Tschulik, T. Weier, M. Uhlemann, A. Bund, J. Fröhlich ; Electrochim. Acta 55 (2010) 9060-9066.

[3] K. Tschulik, X. Yang, G. Mutschke, M. Uhlemann, K. Eckert, R. Sueptitz, L. Schultz, A. Gebert; Electrochem. Comm. 13 (2011) 946.

[4] P. Dunne, L. Mazza, and J. M. D. Coey, Phys. Rev. Lett. 107 (2011) 024501. P. Dunne, R. Soucaille, K. Ackland, J.M.D. Coey, Appl. Phys. Lett. 111 (2012) (07B915).

[5] G. Mutschke, K. Tschulik, T. Weier, M. Uhlemann, A. Bund, A. Alemany, J. Fröhlich; Magnetohydrodynamics 48 (2012) 299-304.

[6] G. Mutschke, G. K. Tschulik, M. Uhlemann, A. Bund, J. Fröhlich ; Phys. Rev. Lett. 109 (2012) 229401.

[7] L.M.A. Monzon, J.M.D. Coey, Electrochem. Comm. 42 (2014) 42-45.

[8] C. Wagner, J. Electrochem. Soc. 95, 161 (1949).

[9] K. Tschulik, C. Cierpka, G. Mutschke, A. Gebert, L. Schultz, M. Uhlemann, Anal. Chem. 84 (2012) 2328.

OXIDE SYNTHESIS BY MAGNETOELECTRODEPOSITON

DALTIN A.L., BENAISSA M., CHOPART J.P.
LISM, EA4695, URCA, B.P. 1039 - 51687 Reims Cedex 2 - France.
al.daltin@univ-reims.fr

Abstract : Electrodeposition under superimposition of uniform magnetic field is appearing as a new method for the synthesis of oxides and doped-oxides. In this study, copper-doped ZnO and manganese-doped Cu_2O deposits were prepared and magneto-induced effects on electrocrystallization have been investigated. Comparison was made with electrodeposition obtained without magnetic field. The electrochemical behaviour, the morphology, the chemical composition and the structure of the deposits were discussed. Modifying oxide growth and final morphology with magnetohydrodynamic effects were observed.

1. Introduction

Magnetoelectrodeposition, i.e., electrodeposition under the superimposition of a magnetic field on the electrochemical cell, is largely used in the case of metal or alloy thin films synthesis, but up to now, very few papers concerned oxide deposits [1-6]. The effects of magnetic field on electrodeposition have been underlined by several authors [7-9] and could generate very promising potential applications [10]. These effects include modifications of electrocrystallization kinetics [3], growth process [5], morphology [6], texture, composition and smoothness of the deposit [10 and references therein]. These modifications, due to magnetically induced convective effect called magnetohydrodynamic (MHD) effect, take place at the cathode-electrolyte interface and could modify electrochemical reactions. Also microscopic minute vortexes, called micro-MHD flow could undergo [11]. Depending on the orientation of the cathode relative to the magnetic field orientation and the species in presence, some forces can be created such as the Lorentz force (F_L), the magnetic gradient force (F_B) and the paramagnetic force (F_P) (this later force, if paramagnetic species are under mass transport control).
Cathodic electrolytic deposition has been used in the past until today for the synthesis of numerous oxides reviewed in different papers [12-15]. The interest of the electrochemical synthesis of oxides in a one-step process at low temperature lies in fast and low-cost production.
In this paper Mn-doped Cu_2O has been studied for the promising defect-induced ferromagnetism. Up to now, the origin of the high T_c ferromagnetism in Cu_2O base dilute semiconductors (DMSs) is not well understood. Defects and therefore synthesis modes are responsible for these magnetic properties. It has been shown that both the positions of the doping transition-metals (substitutional or interstitial Mn atoms) and the vacancies have strong influences on the ferromagnetism of the doped Cu_2O [16-17]. Previous results on $Cu_{2-x}Mn_xO$ electrodeposition have been reported [18], indicating that the ferromagnetic properties can be tuned simply by controlling electrochemical growth conditions. On the other hand, it has been shown that magnetic field brings modification on the electrocrystallization of Cu_2O [5-6]. Here the electrodeposition of copper oxide (with or without Mn doping) is reported with various Mn concentrations under 1T magnetic field superimposition. This paper reports also on the growth of Cu-doped ZnO nanostructures by magnetoelectrolysis. ZnO has been extensively studied because of its large band gap (3.2 eV) with large exciton binding energy (60 meV) at room temperature and its wide applicability in functional devices [19-21].

Among doped ZnO materials, some of them can provide dilute magnetic properties such as room temperature ferromagnetism observed in Cu- doped ZnO [22].

2. Experimental section

Here oxides and doped-oxide were electrodeposited on an indium tin oxide (ITO) covered glass using a three electrode set-up. The working electrodes (WE) of about 1 x 2 cm were cleaned before deposition by immersion in an ethanol solution, followed by drying in air. The counter electrode was a Pt wound wire and the reference electrode, the Ag/AgCl one. A glass double-wall cell was used to maintain a constant temperature for all experiments. This cell was put inside the gap of a Drusch EAM 20G electromagnet. A constant and homogeneous magnetic field with amplitude up to 1T, oriented parallel to the horizontal upward electrode surface was applied during experiments with superimposed magnetic field. The electrolytes of this study were prepared from deionised water and analytical grade chemicals. The cathodic depositions of the ZnO and copper-doped ZnO were performed at 80°C from chloride electrolytes with the compositions and conditions listed in table 1. The cathodic depositions of the Cu_20 and maganese-doped Cu_20 were performed at 60°C from sulfate electrolytes with the compositions and conditions listed in table 2. The depositions were carried out in a potentiostatic mode with a potentiostat-galvanostat PGZ 300 Radiometer Analytical.

Table 1 Electrolytes compositions and conditions of ZnO and Cu-doped ZnO depositions

	$[ZnCl_2]$ M	[KCl] M	$[CuCl_2]$ M	T °C	pH	-E $V_{/AgAgCl}$	t s	B T
ZnO	5.10^{-3}	0.1	0	80±2	5.7±0.3	1.05	9000	0-1
Cu-doped ZnO - A	5.10^{-3}	0.1	3.10^{-6}	80±2	5.7±0.3	1.05	9000	0-1
Cu-doped ZnO - B	5.10^{-3}	0.1	6.10^{-6}	80±2	5.7±0.3	1.05	9000	0-1

Table 2 Electrolytes compositions and conditions of Cu_20 and Mn-doped Cu_2O depositions

	$[CuSO_4]$ M	$[C_3H_6O_3]$ M	$[MnSO_4]$ M	T °C	pH	-E $mV_{/AgAgCl}$	-Q C	B T
Cu_20	0.4	3	0	60±2	10±0.3	200	1	0-1
Mn-doped Cu_2O - A	0.4	3	10^{-3}	60±2	10±0.3	200	1	0-1
Mn-doped Cu_2O - B	0.4	3	10^{-2}	60±2	10±0.3	200	1	0-1

The deposits were examined by employing a scanning electron microscope (SEM) JEOL JSM 6460LA and chemical compositions were determined by an EDS JEL 1300 Microprobe coupled with the SEM. The crystalline structure was determined by X-ray diffraction (XRD) using a BRUKER D8 ADVANCE X-ray diffractometer coupled with a copper anticathode ($\lambda_{CuK\alpha}$ = 1.5056 Å).

3. Results and discussion

Figure 1 A shows the variation of the current as a function of the deposition time recorded during the deposition of the deposits conducted with conditions of table 1. The steady-state current decreases with magnetic field superimposition. Under B = 1 T, the steady state current increases with $CuCl_2$ concentration. XRD diffractograms of ZnO and doped-ZnO in figure 1B confirm the ZnO zincite structures (ICDD 36-1451) of the deposits obtained under 1T magnetic field as for deposits electrodeposited without magnetic field superimposition. This phase belongs to hexagonal crystal system. The diffraction peaks intensities of ZnO (100) decrease with $CuCl_2$ concentration. The highest intensities are for planes (100) and (101) as it has already shown for ZnO flower-like structures [23]. Figures 2 present some SEM top views of the different deposits obtained with or without a 1 Tesla magnetic field amplitude superimposition for respectively 0, 3 µM and 6 µM of doping concentration of copper chloride in the solution at different magnifications. These micrographs show that when magnetic field is superimposed on the electrochemical cell during ZnO electrodeposition, the nanostructures arrange themselves into homocentric bundles, which is not the case without magnetic field superimposition. When copper is introduced in the electrolyte solution, the growth mechanism changes.

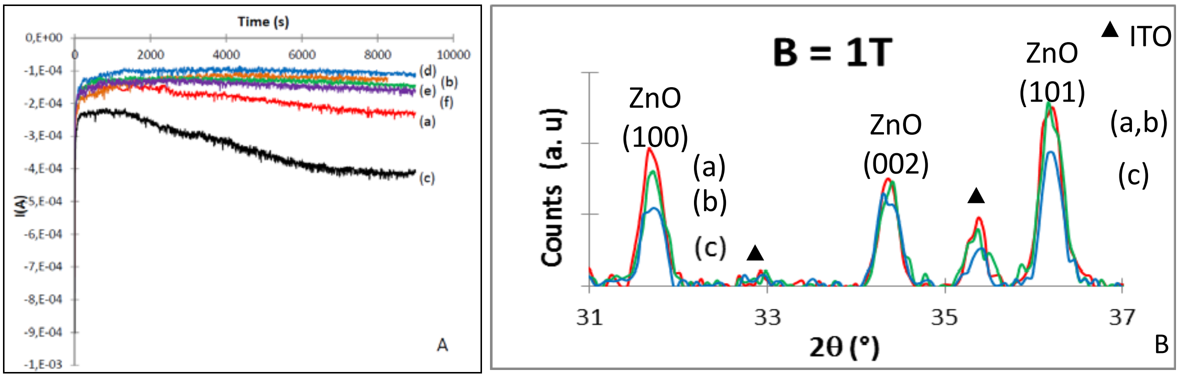

Figure 1: A: Current time (I-t) curve of ZnO deposits from electrolytes with 0 (a,d), 3µM (b,e) and 6µM [$CuCl_2$] (c,f) under 0T (a-c) or 1T (d-f). B. XRD diffractogram of ZnO deposits from electrolytes with (a) 0,(b) 3 and (c) 6 µM [$CuCl_2$] under 1T.

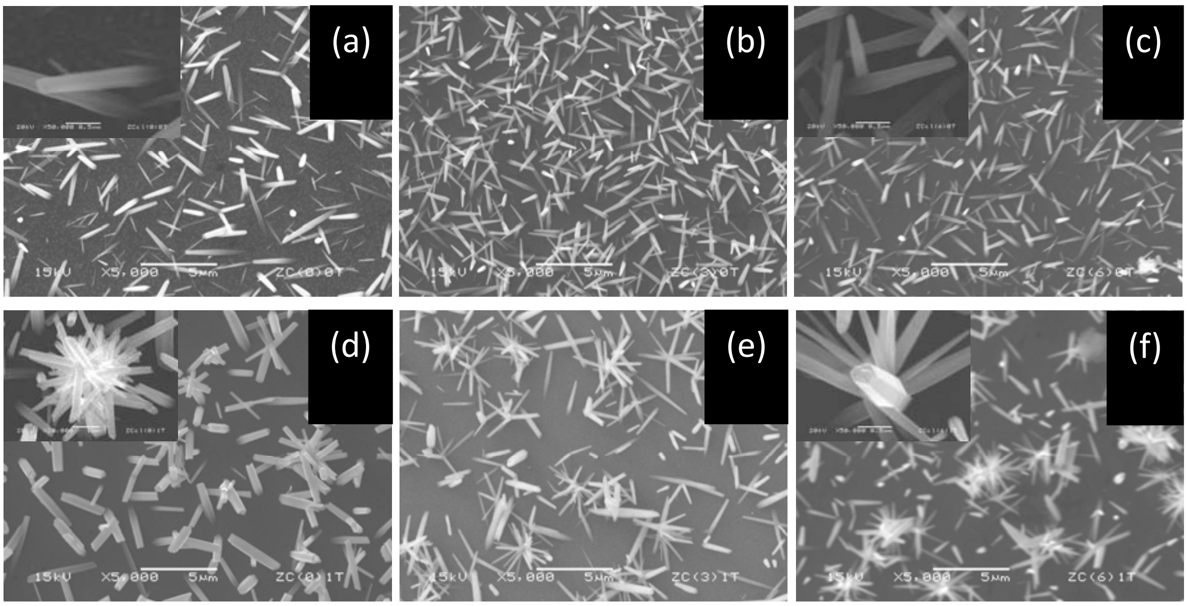

Figure 2: SEM images of Cu-doped ZnO nanostructures obtained by electrodeposition at a potential E = -1.05V/AgAgCl with different $CuCl_2$ electrolyte concentrations: (a,d) 0 µM, (b,e) 3µM, (c,f) 6µM, under magnetic field superimposition: (a-c) B = 0 T and (d-f) B = 1 T at a magnification of X 5000.

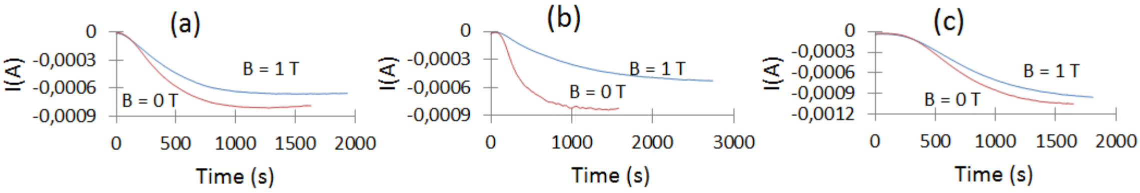

Figure 3: Current time (I-t) curve of Cu_2O deposits from electrolytes with 0 (a), 10^{-3} M (b) and 10^{-2} M [$MnSO_4$] (c) under 0T or 1T.

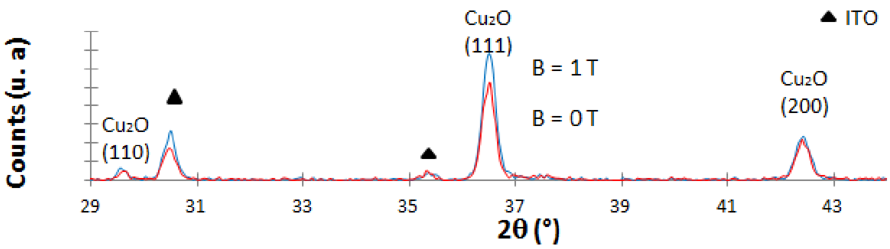

Figure 4. XRD diffractogram of Mn-doped Cu_2O deposits from electrolytes with 10^{-2} M [$MnSO_4$] for 0 and 1T magnetic field superimposition.

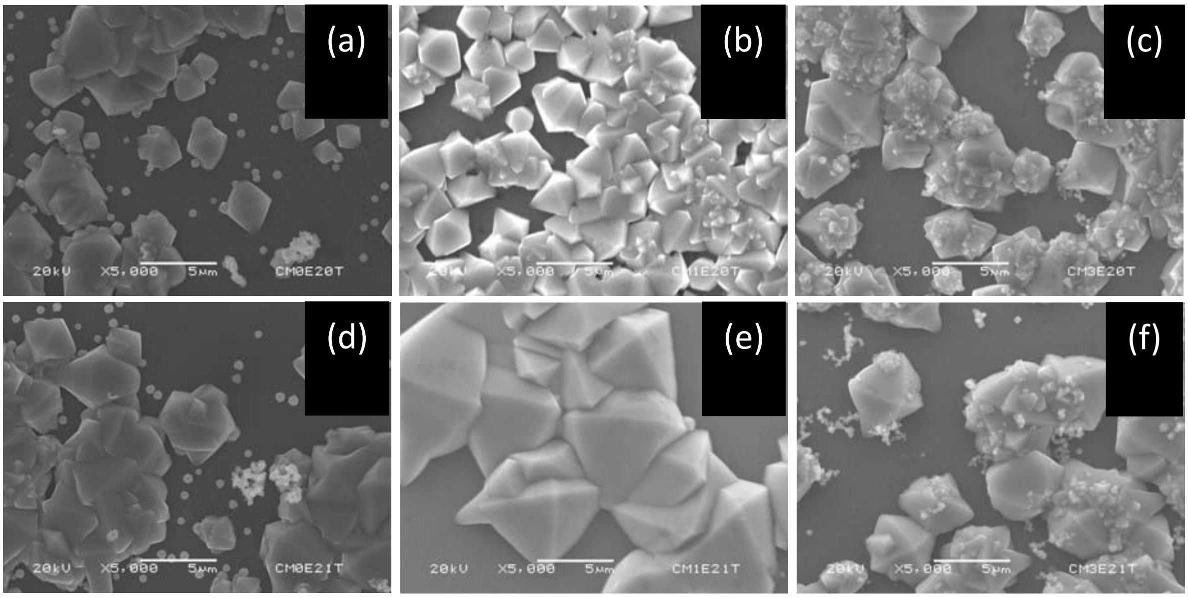

Figure 5: SEM images of Mn-doped Cu_2O electrodeposited at a potential E = -1.05V/AgAgCl with different $MnSO_4$ electrolyte concentrations: (a,d) 0 M, (b,e) 10^{-3} M, (c,f) 10^{-2} M, under magnetic field superimposition: (a-c) B = 0 T and (d-f) B = 1 T at a magnification of X 5000.

The mechanism for the electroprecipitation of the ZnO nanorods is given in the following equations

$$O_2 + 2\,H_2O + 4e^- \rightarrow 4\,OH^- \quad (1)$$

$$Zn^{2+} + 2\,OH^- \rightarrow ZnO + H_2O \quad (2)$$

Also the shape of ZnO deposited in baths of chloride could be hexagonal pillar or obelisk, due to the adsorption of Cl^- on the {0110} planes more easily than on (0001) plane [24]. The MHD convection promotes the growth of larger nanorods due to a higher concentration of Zn^{2+} near the external surface, and a higher aspect ratio due to the higher chloride concentration. Moreover, the shape of ZnO particles changes from needle to hexagonal obelisk nanorods with magnetic field superimposition. Homocentric bundles corresponding to multipod structures obtained under magnetic field result from initial nucleation followed by the growth of the obelisk shaped ZnO around these nuclei. The µMHD convection could be responsible for the growth of branches on the initial nuclei giving homocentric bundles. For deposits with high copper chloride concentration, these branches at the base of the central pillar are finer than the latter. Figure 3 shows chronoamperometric curves of Cu_2O (a) and Mn-doped Cu_2O (b-c). Also here the current intensities decrease with magnetic field superimposition for the three electrolyte compositions. As these deposits were obtained in the coulometric mode, the time is increased when the electrodeposition is made under magnetic field. XRD patterns (Figure 4) of the deposits indicate that the cuprite (ICDD 05-667) is the only phase present in all cases. (110) and (111) are more intense under magnetic field than without. Here, octahedral crystals, bigger under B = 1T, were synthesized and do not completely covered the ITO substrates (Figure 5). With Mn incorporation, smaller crystallites with higher Mn concentration under magnetic field appear.

4.Conclusion

The various studies presented in this paper illustrate the challenge of tuning morphology or composition by applying magnetic field on electrodeposition of oxide and doped-oxide. Both magnetohydrodynamic convection and micro-MHD effect induce modifications from the beginning of the growth process.

Acknowledgements : Authors thank the Champagne-Ardenne council for financial support.

4. References

[1] Lee, J. D. Kim, H. S., Jeong, S. Y. Kim, K. H., Lee, J. J., Ahn, B.Y., Kim, S. I., J. the Korean Phys. Soc. 51, 3 (2007) pp. 1109-1112.
[2] Morisue M., Nambu, M., Osaki, H., Fukunaka, Y., J. of Solid State Electrochem 11 (2007) pp. 719-726.
[3] Daltin, A. L., Bohr, F., Chopart, J. P., Electrochim. Acta 54, 24 (2009) pp. 5813-5817.
[4] Mogi, I., Watanabe, K. Journal of Physics: Conference Series 156 (2009) 012027.
[5] Daltin, A. L., Chopart, J. P. Crystal Growth and Design 10,5 (2010) pp. 2267-2271.
[6] Daltin, A. L., Addad, A., Baudart, P., Chopart, J. P., CrystEngComm 13, 10 (2011) pp. 3373-3377
[7] Fahidy, T. Z. Progress in Surface Science, 68, 4-6 (2001) pp. 155-188.
[8] Bund, A., Koehler, S., Kuehnlein, H.H., Plieth, W., Electrochemica Acta 49 (2003) pp.147-152.
[9] Monzon L. M. A., Coey J.M.D., Electrochem. Comm.42 (2014) 38-41.
[10] Alemany,A.; Chopart, J.P. In Fluid Mechanics and its Application; Molokov, S., Moreau, R., Moffatt, H. K., Eds.; Springer: Dordrecht, The Netherlands, 2007; Vol. 80, pp. 391-407.
[11] Aogaki, R., Morimoto, R., Asanuma, M., Journal of Magnetism and Magnetic Materials, 322, 9-12 (2010) pp. 1664-1668.
[12] Therese, G.H.A., Kamath, P.V., Chemistry of metals, 12,5(2000) pp1195-1204.
[13] Zitomirsky, Adv. In Colloïd and Interface Sc., 97,1-3 (2002)pp. 279-317.
[14] Pauporté, Th., Goux, A., Kahn-Harari, A., De Tacconi, N., Chenthamarakshan, C.R., Rajeshwar, K., Lincot, D., Journal of Physics and Chemistry of Solids, 64, 9-10 (2003) pp. 1737-1742.
[15] Lincot, D., Thin Solid Films, 487, 1-2 (2005) pp. 40-48.
[16] Liu Y.L., Harrington,S., Yates,K.A., Wei, M., Blamire,M.G., MacManus-Driscoll, J. L. and Liu, Y.C., Appl. Phys. Lett. 87, (22), art.no. 222108, 1-3, (2005).
[17] Chang, G.S., Kurmaev, E.Z., Boukhvalov, D.W., Moewes, A., Finkelstein,L.D., Wie, L., and MacManus-Driscoll, J.L., J. Phys. Codens. Matter 20, (21), art.no. 215216, (2008).
[18] Li, L., Cheng, Y., Wang, W., Ren, S., Yang, Y., Luo, X., Liu, H., Solid State Communications 151, 21(2011) pp. 1583-1587.
[19] Gao, D., Xu, Y., Zhang, Z., Gao, H., Xue,D., J. Appl. Phys. 105, 063903 (2009).
[20] Mouet, T., Devers,T., Applied Surface Science 256, 4114-4120 (2010).
[21] Xing, G.Z., Lu,Y.H., AIP ADVANCES 1, 022152 (2011).
[22] Jeong, Y.E., Park, S., Current Applied. Physics. V14.1 (2014).
[23] Frade, T., Melo Jorge, M.E., Gomes, A., Materials Letters 82 (2012) pp 13-15.
[24] Elias, J., Tena-Zaera, R., Lévy-Clément, C., J. Electroanal. Chem. 621, 2, (2008) pp 171-177.

MAGNETO-INDUCED EFFECT DURING MN-DOPED CU_2O ELECTROCRYSTALLIZATION

BENAISSA M., DALTIN A.-L., CHOPART J.-P.
LISM, EA4695, URCA, B.P. 1039, 51687 Reims Cedex 2, France.
E-mail: al.daltin@univ-reims.fr

In this paper, Mn-doped Cu_2O has been studied for the promising defect-induced ferromagnetism. Up to now, the origin of the high Tc ferromagnetism in Cu_2O base dilute semiconductors (DMSs) is not well understood. Defects and therefore synthesis modes are responsible for these magnetic properties. It has been shown that both the positions of the doping transition-metals (substitutional or interstitial Mn atoms) and the vacancies have strong influences on the ferromagnetism of the doped Cu_2O [1-2]. Previous results on $Cu_{2-x}Mn_xO$ electrodeposition have been reported [3], indicating that the ferromagnetic properties can be tuned simply by controlling electrochemical growth conditions. On the other hand, it has been shown that magnetic field brings modification on the electrocrystallization of Cu_2O [4-5]. Here the electrodeposition of copper oxide (with or without Mn doping) is reported with various Mn concentrations under 1T magnetic field superimposition. Comparison is made with electrodeposition obtained without magnetic field. Transient current curves can be drastically modified with Mn^{2+} electrolyte concentration and magnetic field superimposition [Fig]. In addition grain size and crystallite morphology are changed depending on the electrodeposition conditions.

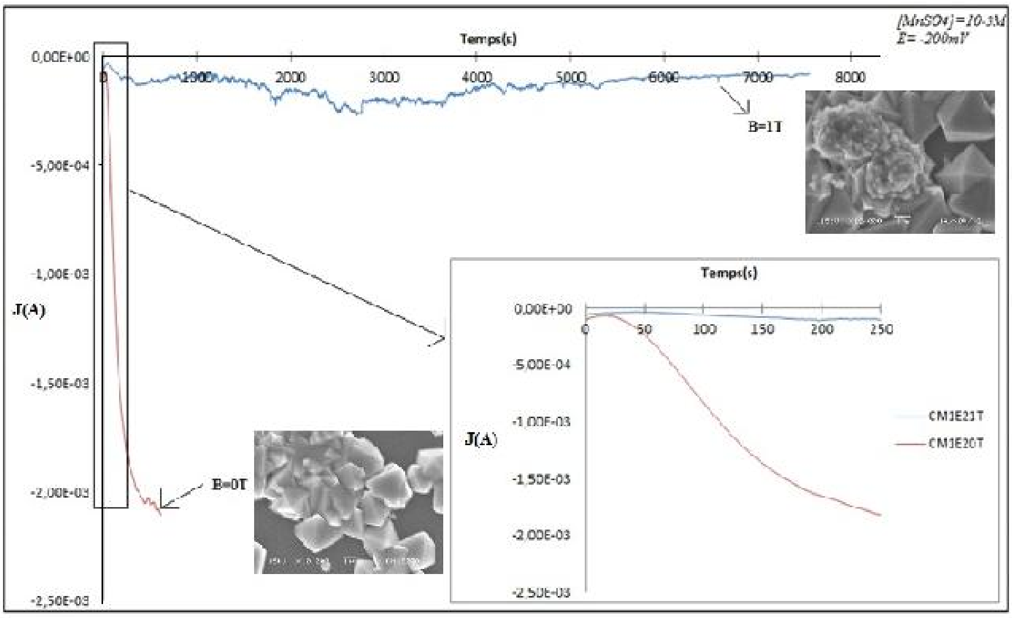

Figure: Current curve of Mn - doped Cu2O electrodeposition at - 200mV/ Ag _ AgCl and Q= - 1C with: [MnSO4] at 10 - 3 M, under magnetic field superposition B: (1) 0T and (2) 1T.

References

[1] Chang, G,S., Kurmaev, E.Z., Boukhvalov, D.W., Moewes, A., Finkelstein, L.D., Wei, M., MacManus-Driscoll, J,L.: Defect-induced ferromagnetism in Mn-doped Cu_2O. J. Phys. Codens. Matter 20, (21), art.no. 215216, (2008).

[2] Li, L., Cheng, Y., Wang, W., Ren, S., Yang, Y., Luo, X., Liu, H.: Effects of copper and oxygen vacancies on the ferromagnetism of Mn- and Co-doped Cu2O. Solid State Communications 151(21), 1583-1587, (2011).
[3] Liu, Y.L., Harrington, S., Yates, K.A., Wei, M., Blamire, M.G., MacManus-Driscoll, J.L. and Liu, Y.C.: Epitaxial ferromagnetic $Cu_{2-x}Mn_xO$ films on (001) Si by near-room-temperature electrodeposition. Appl. Phys. Lett. 87, (22), art.no. 222108, 1-3, (2005).
[4] Daltin, A.L., Addad, A., Baudart, P. and Chopart, J.P.: Morphology of magneto-electrodeposited Cu_2O microcrystals. CrysEngComm, 13 (10), 3373-3377 (2011).
[5] Daltin, A.L., Bohr, F., Chopart, J.P.: Kinetics of Cu_2O electrocrystallization under magnetic fields. Electrochimica Acta, volume 54 (24), 5813-5817 (2009).

MORPHOLOGY AND MICROSTRUCTURE EVOLUTION OF COBALT FERRITE THIN FILMS PREPARED BY ONE-STEP MAGNETO-ELECTRODEPOSITION

LI[1,2] D., DALTIN[2] A.-L., WANG[1] Q., CHOPART[2] J.-P., HE[1] J.
[1] Key Laboratory of Electromagnetic Processing of Materials (Ministry of Education), Northeastern University, Shenyang, 110004, China
[2] LISM, Université de Reims Champagne-Ardenne, B.P. 1039, 51687 Reims Cedex 2, France
314 Box, Northeastern University, No.3-11 Wenhua Road, Shenyang, 110004, P.R.China
Tel:+86-24-83681726, Fax:+86-24-83681758, E-mail address:
wangq@mail.neu.edu.cn, al.daltin@univ-reims.fr

Abstract: In this paper, we report a one-step pulse-electrodeposition method assisted by a magnetic filed for preparing $Co_xFe_{3-x}O_4$ films on a Ti substrate. Grain shape, grain size, Co:Fe ratio, and microstructure in the $Co_xFe_{3-x}O_4$ films were modified dramatically by controlling the deposition potential during the pulse-electrodeposition process. The dependence of the grain shape and grain size on the deposition potential is due to the change of microstructure and Co:Fe ratio in the films with the potential induced by the MHD effects.

Keywords: *Cobalt ferrite; Thin Film; Microstructure; Pulse-electrodeposition; Magnetic fields*

1. Introduction

Due to their excellent electrochemical performance, higher magnetic anisotropy and moderate saturation magnetization, iron-cobalt oxides with spinel structures have attracted considerable interests as promising candidates for modern innovative applications such as gas sensors[1], catalysts for various reactions[2], anodes for lithium ion batteries[3], magneto-optic recording media[4]. Up to now, a variety of methods of synthesizing $Co_xFe_{3-x}O_4$ thin films have been developed include sputtering, physical vapor deposition, chemical vapor deposition, pulsed laser deposition and electrochemical deposition [5-8]. Most of these techniques involve a two-step process, the CoFe alloy precursors first formation, and then followed by oxidation at high temperature [9]. However, the high temperature annealing can cause unwanted reactions between the substrate and the deposited film, which affect the grain size, morphology, chemical stability and the magnetic property [10-11]. It is widely accepted that the practical application of $Co_xFe_{3-x}O_4$ thin films will depend on the capability of precise controlling the composition, particle size and structure during the preparation process. Magneto-electrodeposition could be an alternative method to obtain $Co_xFe_{3-x}O_4$ thin films by single-step at low temperature, with precise controlling the ratio of Co:Fe, morphology, and microstructure, furthermore to tailor the chemical and physical properties of the films. Recently, magnetic fields are widely used to control the mass transfer processes in electrochemical cells[12], since under a magnetic fields a Lorenz force arises, and the magnetohydrodynamics (MHD) convection governs the hydrodynamic boundary layers. Krause et al. [13] found that electrodeposition under a 1T magnetic field, Co deposit shape changed into double sized hexagonal crystallites. The previous study of us [14] also shown that magnetic fields induced drastic morphological variations in the electrodeposited CoNi films from short-clavated grain shape to silk-like nanowires, and the applied magnetic fields led to an increase of the Co:Ni ratio in the deposits. In addition,because of the higher instantaneous current density in comparison to direct current plating, pulse electrodeposition has been found to be an effective means of perturbing the adsorption/desorption processes and hence offers an opportunity of controlling the microstructure of the electrodeposits. This work presents one-step pulse-electrodeposition of Cobalt-Ferrite thin film on the Ti substrate under a 1T magnetic fields. The aim of this work is to study the evolution of composition, surface morphology, and microstructure of cobalt ferrite thin films under the condition of magneto-pulse-electrodeposition.

2. Experimental

All electrodeposition experiments were performed in a conventional three-electrode cell without agitation. Polished titanium of 1cm diameter was used as the working electrode, the counter electrode was a quadrate Pt plate of $1 \times 1cm$, and Ag/AgCl/KNO_3(sat.) was used as a reference electrode. The electrolyte composed of 100mM Co^{2+} 50mM Fe^{3+} , 150mM triethanolamine (TEA), and 2M NaOH. Pulse-electrodeposition using a potentiostat-galvanostat VersaSTAT 4 was performed at 80 . The electrochemical cell was plunged into the gap of Drusch EAM 20G electromagnet that delivers a uniform horizontal magnetic field up to 1T parallel to the electrode surface. To deposit good quality films, various parameters such as deposition potential, magnetic flux density, deposition time and duty cycle etc., were optimized as shown in Table.1.

Table 1. Processing conditions of electrodeposition of the cobalt ferrite films

Pulse-potential $V1_{Ag/AgCl}$	Deposition time, t1	Pulse-potential $V2_{Ag/AgCl}$	Deposition time, t2	Cycles	Magnetic field
-1.17V~-1.19V	1s	-0.95V	4s	300	1T

The surface morphology and chemical composition of the deposited films were investigated by scanning electronic microscopy (SEM) appended with an energy-dispersive X-ray spectroscope (EDX, SUPRA 35) at three different positions on the films. The topography were investigated with atomic force microscopy (AFM). For the characterization of the microstructure of the films, X-Ray Diffraction (XRD, Bruker D8 Advance) measurements were performed using standard θ-2θ geometry with Cu $K\alpha$ radiation.

3. Results and discussion

Since in case of without magnetic field, the electrodeposited films obtained under the experimental condition in this work were not adherent and covered the substrates bad, all the electrodeposition were optimized by performing in a 1T magnetic field. Typical SEM and AFM morphologies of cobalt ferrite films pulse-electrodeposited with potential ranged from -1.17V to -1.19V$_{Ag/AgCl}$ are shown in Fig. 1.

The figure demonstrates drastic morphological variations with the pulse-potential during the electrodeposition process. The spherical grain linked together to form a coralliform morphology as shown in Fig.1(a). While in case of the potential up to -1.18V$_{Ag/AgCl}$, the top of the branches in coral seemed to split into many irregular small grains. With the increase of the applied potential to -1.19V$_{Ag/AgCl}$, the grains of this coralliform deposit is very similar to the structure of sea anemones, that is, every spherical grain consisted of many crystal whiskers in it. Since the difference in surface analysis between AFM (3D overview in perpendicular to the surface) and SEM (2D morphological structure in parallel to the surface), the AFM image could not answer the morphology evolution of the films, but shown the films are composed of fairly large number of round nanometer sized grains. The average values of lateral feature size, which can be used to characterize the grain size, were calculated according to AFM images in the following section.

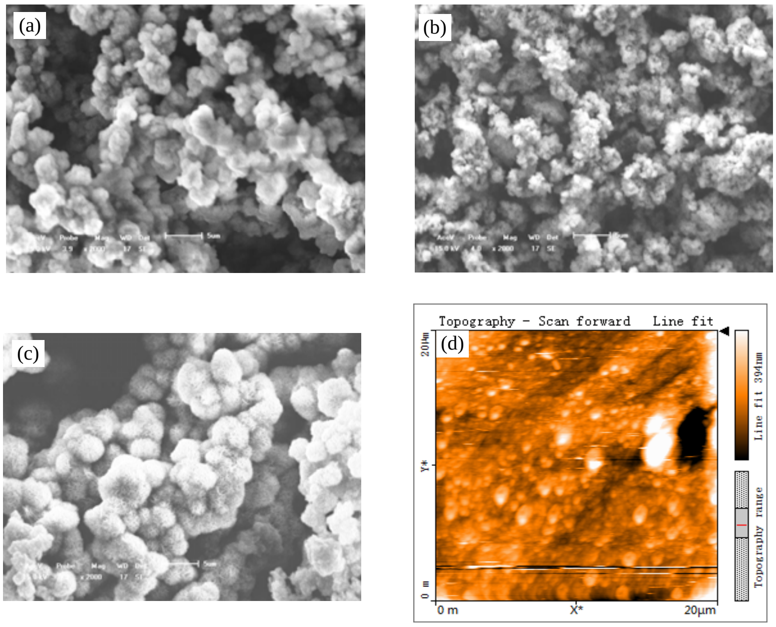

Figure 1: SEM images of $Co_xFe_{3-x}O_4$ thin films deposited at (a) -1.17V $_{Ag/AgCl}$; (b) -1.18V$_{Ag/AgCl}$; (c) -1.19V$_{Ag/AgCl}$ potentials assisted by 1T magnetic field; and the typical AFM image at (d) -1.18V$_{Ag/AgCl}$.

Corresponding to the evolution of the morphology, we use the EDX to measure the change of composition in the deposited films with different pulse-potentials. The results in Tab. 2 shown that the Co:Fe ratio depended on the deposition potential. The Co concentrations in the films were lower at less negative potentials and higher at more negative potentials. With the deposition potential went to more negative values, more Co^{2+} were reduced at the electrode surface, resulting in a increase of the Co:Fe ratio in the film. These phenomena may be attributed the MHD effect in a magnetic field, which yields significant convection, and in turn increases the current efficiency. However due to the different kinetic reaction rate between Fe^{3+} and Co^{2+} substitution, the deviation between the Co concentration and Fe concentration at the electrode surface was larger when the growth rate of the film was faster at more negative potentials caused by the MHD effect[15]. The deviation resulted in the Co:Fe ratio in the $Co_xFe_{3-x}O_4$ thin films a non-linear variation with the deposition potential. In case of -1.18V$_{Ag/AgCl}$, the x value was 0.97, which indicates that the film obtained under this condition was composed of almost $CoFe_2O_4$. This can be verified in the X-ray diffraction pattern.

Table 2. The dependence of the composition of $Co_xFe_{3-x}O_4$ 0 x 1 films on the deposition potentials: the x value in $Co_xFe_{3-x}O_4$ was calculated based on the Co:Fe ratio in the films.

Pulse-potential	Co (at%)	Fe (at%)	O (at%)	x
-1.17V $_{Ag/AgCl}$	8.6	31.1	60.3	0.65
-1.18V $_{Ag/AgCl}$	14.2	29.9	55.9	0.97
-1.19V $_{Ag/AgCl}$	12.1	30.5	57.4	0.85

The X-ray scan of the $Co_xFe_{3-x}O_4$ films pulse-electrodeposited on titanium were shown in Fig.2. Despite of the high peaks (marked with black dots) for the substrate (Ti), the films exhibited the diffraction peaks corresponding to both the transition metal oxides (Fe_2O_3) and the spinel cobalt ferrite ($CoFe_2O_4$). At less negative potential, the film was mostly composed of

Fe_2O_3, while at more negative potentials, the films was mostly composed of $CoFe_2O_4$. Especially at -1.18$V_{Ag/AgCl}$, the said planes as (111),(220),(311),(400),(511) corresponded to the $CoFe_2O_4$. The peaks shown in Fig 2 agree well with the Co:Fe ratio measured by EDX. For example, the x value in $Co_xFe_{3-x}O_4$ films was near unit at -1.18$V_{Ag/AgCl}$, which implied that by adjust the potential assisted by magnetic field, we could prepare spinel cobalt ferrite without other oxidations by one-step magneto-electrodeposition method.

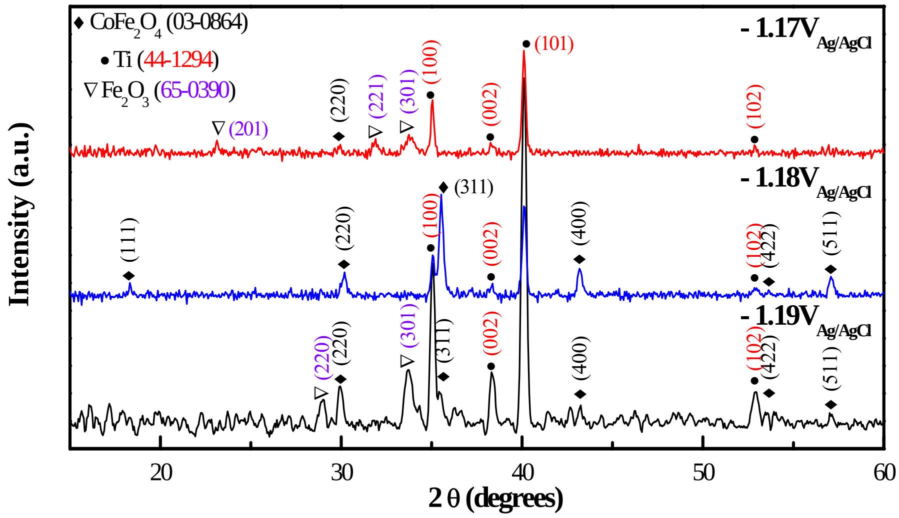

Figure 2: The X-ray diffraction pattern of cobalt ferrite films deposited at different potentials.

Table 3. Comparison of crystallites size of electrodeposited $Co_xFe_{3-x}O_4$ films obtained by calculations based on the Scherrer equation and AFM

Potential ($V_{Ag/AgCl}$)	Sherrer(nm)	AFM (nm)
-1.17	33	47±2
-1.18	25	38±2
-1.19	50	61±2

Since the morphology and microstructure of the films were dramatically depended on the potential during the electrodeposition, the grain size should also be affected by the MHD effect caused by the interaction between the pulse-current with the magnetic field. We have calculated the crystallites size by use of Scherrer's equation and AFM measurement (Table. 3). The particle size R_0 was estimated from AFM analysis by the following equation [16]: $R_0 = \left(\frac{A_0}{\pi N_0}\right)^{1/2}$, in which A_0 represents the AFM total image area and N_0 is the grain number. According to these two calculated methods the obtained films consisted different nuclei sizes due to the changing amplitude of pulse-potential. It should be mentioned that the calculated mean grain size by using Scherrer’s formula according to the X-ray diffraction share the same trend as that measured based on the AFM images. With the potential moving to more negative, the MHD effects [17] increase to bring more Co^{2+}(Fe^{3+} to the surface of the electrode, which results in the fast nucleation and is responsible for the small grain size at -1.18 $V_{Ag/AgCl}$. However, in case of -1.19 $V_{Ag/AgCl}$, the Co (Fe) deposition becomes to be diminished, since the hydrogen-ion reduction dominates the total reduction process resulting in the decrease of the current efficiencies of Co (Fe). This may be a reason for the formation of bigger grain by growth at more higher pulse-potential.

From the morphological viewpoint, the properties of the electro-deposited films depend not only on the chemical position, but also strongly on the morphology, grain size ,and microstructure [18-19]. Therefore, the in-situ application of magnetic field during the pulse-electrodeposition is exceptionally well suited for tailoring the properties of cobalt ferrite, by non-contact controlling Co:Fe ratio, grain shape, grain size and phase composition. The present work paves the way for optimized electroplated cobalt ferrite thin films by adjusting the potential during one-step magneto-electrodeposition.

4. Conclusions

The influence of the interaction between the pulse-potential and a magnetic field with a flux density up to 1T on the morphology and microstructure of electrodeposited $Co_xFe_{3-x}O_4$ film has been investigated. The SEM figures demonstrated that MHD effects induced drastic morphological variations from coral-like to sea-anemone-like. More negative potential led to an increase of the Co:Fe atomic ratio in the deposits. The XRD pattern further verified that at -1.18$V_{Ag/AgCl}$ we could obtain $CoFe_2O_4$ film with ultra-fine grains in it by one-step magneto-electrodeposition. The non-monotonic dependence of morphology, composition, and microstructure on pulse-potential may be attributed to the overlap effects of MHD on the current efficiency and on the hydrogen-ion reduction during the deposition process.

Acknowledgments. This work was financially supported by the National Natural Science Foundation of China (Grant No. 51101032), the Fundamental Research Funds for the Central Universities (Grant No. N130402002), Agence Nationale de la Recherche France (Programme COMAGNET, Grant No. 2010-INTB-903-01).

References

[1] Said A. A; El Salaam K, M. A.; Hassan E. A.; Elawad A. M.; Elwahab M. M. M. A.: J. Phys. IV, 7 (1997) 687-688.
[2] Chaudhari G. N.; Pawar M. J.; Optoelectron J.: Adv. Mater., 10 (2008) 2574-2577.
[3] Sharma Y.; Sharma N.; Rao, G. V. S.; Chowdari B. V. R.: Solid State Ionics., 179 (2008) 587-597.
[4] Giri A. K.; Kirkpatrick E. M.; Moongkhamklang P.; Majetich S. A.; Harris V. G.: Appl. Phys. Lett. 80 (2002) 2341-2343.
[5] Zhou J. P.; He H. C.; Nan C. W.: Appl. Surf. Sci., 253 (2007) 7456-7460.
[6] Sartale S. D.; Ganesan V.; Lokhande C. D.: Phys. Status Solidi A., 202 (2005) 85-94.
[7] Araujo C.; Almeida B. G.; Aguiar M.; Mendes J. A.: Vacuum, 82 (2008) 1437-1440.
[8] Lokhande C. D.; Kulkarni S. S.; Mane R. S.; Nandi K. C.; Han S. H.: Curr. Appl. Phys., 8 (2008) 612-615.
[9] Hua Z. H.; Chen R. S.; Li C. L.; Yang S. G.; Lu M.; Gu B. X.; Du Y. W.: J. Alloy. Compd., 427 (2007) 199-203.
[10] Castaldi L.; Giannakopoulos K.; Travlos A.; Niarchos D.: Appl. Phys. Lett. 85 (2004) 2854-2856.
[11] Li D. G.; Levesque A.; Wang Q.; Franczak A.; Wu C.; Chopart J. P.; He J. C.: CMC-Comput. Mater. Con., 670 (2012) 1-12.
[12] Koza J. A.; Karnbach F.; Uhlemann M.; McCord J.; Mickel C.; Gebert A.; Baunack S.; Schultz L.: Electrochim. Acta., 55 (2010) 819-831
[13] Krause A.; Hamann C.; Uhlemann M.; Gebert A.; Schultz L.: J. Magn. Magn. Mater. 290-291 (2005) 261-264.
[14] Li D. G.; Levesque A.; Franczak A.; Wang Q.; He J. C.; Chopart J. P.: Talanta 110 (2013) 66-70.
[15] He Z.; Koza J. A.; Mu G. J.; Miller A. S.; Bohannan E. W.; Switzer J. A.: Chem. Mater., 25 (2013) 223-232.
[16] Raoufi D.: App. Surf. Sci., 255 (2009) 3682-3686.
[17] Koza J. A.; Uhlemann M.; Gebert A.; Schultz L.: Electrochim. Acta., 53 (2008) 5344-5353.
[18] Armyanov S.: Electrochim. Acta. 45 (2000) 3323-3335.
[19] Ergeneman O.; Sivaraman K.M.; Pané S.; Pellicer E.; Teleki A.; Hirt A.M.; Baró M.D.; Nelson B.J.: Electrochim. Acta 56 (2011) 1399-1408

APPLIED TRAVELLING MAGNETIC FIELD DURING SILICON SOLIDIFICATION IN A BRIDGMAN CONFIGURATION

CABLEA[1] M., GAGNOUD[1] A., NOURI[2] A., DELANNOY[1] Y., ZAIDAT[1] K.
[1]SIMAP/EPM, 1340 rue de la piscine, F - 38402, Saint Martin dHeres Cedex, France
[2]Silicor Materials, 1 royal gate boulevard, Vaughan, Canada
E-mail: mircea.cablea@sima.grenoble-inp.fr

Silicon continues to be the most used material for the development of solar cells in the photovoltaic industry. Far from the performances of mono crystalline silicon obtained from expensive crystal growth methods like Czochralski method, the less expensive multi-crystalline silicon, obtained from a directional solidification process, is used as a base material for solar cells in order to keep a low production cost especially if the high performances of the cells are not the top priority. Metallurgical grade raw materials could provide an even lower production cost if the impurities distribution could be controlled during the process. In order to reach the best possible electrical performances for the cells, a reduced number of crystal defects as grain boundaries and dislocations is desired. The impurities are generally trapped at the grain boundaries, but they could also precipitate thus decreasing the quality of the solar cells. An option to overcome this problem without decreasing the growth rate is to induce a controlled fluid flow in the liquid. That could enhance the segregation and allows the imposing of a desired interface shape in a controlled manner.

A vertical Bridgman type furnace (VB2) equipped with an electromagnetic stirrer was developed in order to study the solidification process of Si under travelling magnetic field. The furnace was equipped with a Bitter type electromagnet that can provide a travelling magnetic field able to induce a convective flow in the liquid. As a result the axial segregation of metallic impurities is improved while controlling the interface deflection. A numerical model was developed in ANSYS Fluent commercial software to support and complete the experimental set-up. This paper presents experimental and numerical results of this approach.

YANG Y., LUO T., LI Y., FENG X.
Institute of Metal Research, Chinese Academy of Sciences, China
E-mail: ysyang@imr.ac.cn

The effects of a DC field on the orientation of Ni-based single crystal growth were researched in this report. A single crystal superalloy with different original orientations grows under the DC field. The orientation of the Ni-based single crystals was measured by the XRD method. It is found that the misorientation from [001] of the Ni-based single crystal superalloy becomes smaller which grows with the DC field. The misorientation of the single crystal superalloy is decreased from 18 degrees to 10 degrees, and then decreased to 3 degrees under the action of the DC field. The change of misorientation caused by the electric field is considered that is from the variation of asymmetric temperature and solute diffusion in front of the S/L interface. When growing the single crystal superalloy under the electric field, Joule heat and electromigration taking place in front the interface perturb the temperature and solute diffusion and change their asymmetric.

MODELLING OF THE INFLUENCE OF ELECTROMAGNETIC FORCE ON MELT CONVECTION AND DOPANT DISTRIBUTION DURING FLOATING ZONE GROWTH OF SILICON

SABANSKIS[1] A., SUROVOVS[1,2] K., KRAUZE[1] A., PLATE[1] M., VIRBULIS[1] J.
[1]Faculty of Physics and Mathematics, University of Latvia, 8 Zellu str., LV-1002, Riga, Latvia
[2]Institute of Solid State Physics, University of Latvia, 8 Kengaraga str., LV-1063, Riga, Latvia
E-mail address of corresponding author: andrejs.sabanskis@lu.lv

Abstract: Numerical modelling of floating zone process is considered. A local analysis of the electromagnetic (EM) field distribution near the external triple point (ETP) was carried out and the result was included in the calculation of phase boundaries, to improve the surface current formulation. 3D hydrodynamic calculations were performed using the open source code library *OpenFOAM*. The influence of high-frequency EM field is shown by comparing phase boundaries, convection in melt and radial resistivity variation profiles. The results are compared with experimental data.

1. Introduction

The floating zone (FZ) method is applied for growth of silicon (Si) single crystals appropriate for power electronics (high purity crystals), because molten silicon is not in contact with other materials. High-frequency (HF) inductor is used to melt silicon feed rod with induced currents. Molten silicon flows downwards and crystallizes due to radiative heat losses. Numerical modelling is used for process development due to its inexpensiveness and possibility to reveal aspects that cannot be observed directly, e.g. hydrodynamics (HD) in melt. It is crucial to describe EM field as precisely as possible, because it influences the shape of phase boundaries as well as convection and dopant transport in melt. From the dopant field it is possible to obtain radial resistivity variation (RRV) in grown single crystal [1]. The models can be validated using experimental RRV measurements.

In the present work the precision of calculation of EM field is improved introducing a correction near triple points and verified by comparison with experiment. The influence of the EM field on phase boundaries, melt convection and dopant distribution in melt is presented and discussed. Main physical fields in melt are analysed, the shape of crystallization interface and RRV profiles are compared to experimental data [2].

2. Mathematical models and software

2.1. *Phase boundaries*. 2D axisymmetric calculations of phase boundaries are carried out using a specialized program *FZone* [3]. Since the skin depth varies between 0.038 mm for the copper inductor and 1.3 mm for the solid silicon, much less than the characteristic dimensions of the FZ system (≈ 0.1 m), the EM field distribution is determined by surface current density. HF EM field is calculated considering the 3D HF inductor [4]. 3D induced surface power density values are azimuthally averaged and included in 2D axisymmetric phase boundary calculations as a heat source. From the temperature field and heat balance equations, the direction and magnitude of the movement of each interface point are obtained, and the quasi-stationary shape of phase boundaries is found iteratively [3].

2.2. *EM correction near electrical resistivity jump.* The HF approximation, which is described in [3], cannot be used when the exact distribution of volumetric EM field is important – for example, in the vicinity of solid-liquid interface, where skin depth changes 5 times. A local analysis of the EM field distribution in the vicinity of external triple point was carried out using the complex vector potential formulation. It was shown that in the first few millimetres near the ETP the actual induced power is significantly differs from the HF approach: more power is induced in the melt and less in the crystal, see Figure 1. The result of local analysis was included in *FZone* as correction to EM heat sources at free melt and crystal side surfaces. Because of changed EM heat sources in crystal and melt, inductor current needs to be adjusted to maintain the same zone height. The crystallization interface shape near the ETP changes due to local heat source changes; global shape changes occur because of different inductor current and integral induced power on free melt surface.

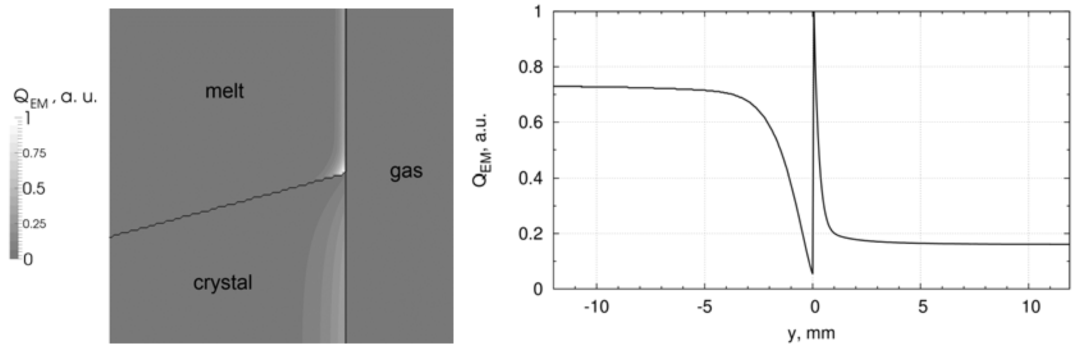

Figure 1: Left: induced EM power density distribution in the vicinity of ETP, arbitrary units. Right: linear induced EM power, arbitrary units. $y>0$ corresponds to melt, $y<0$ – to crystal.

2.3. *3D melt flow*. The unsteady 3D melt flow in the FZ process is modelled using the open source code library *OpenFOAM*. For the considered system Reynolds number is roughly 1500, therefore the melt flow is considered as laminar. The detailed description of the mathematical model is given in [1], only the details relevant to the present study are summarized.

For incompressible melt flow, Navier-Stokes equations are solved, and for description of buoyancy, Boussinesq approximation is used. The crystallization interface is considered as velocity outlet with the boundary conditions for velocity that include constant mass flow and rotation. The melting interface is considered as inlet. The Marangoni force distribution (obtained from temperature field) and tangential to surface EM force distribution acquired from the 3D HF EM calculations are used for boundary conditions for the melt velocity on the free melt surface: $f = \frac{1}{4}\mu_0 \delta \nabla_s j^2 + M \nabla_s T,$ where f is surface force, $\delta = \frac{1}{\sqrt{\pi f_{ind} \sigma \mu_0}}$ is skin depth, ∇_s is surface gradient, j is surface current density, $M = -1.3 \cdot 10^{-4}$ N/(m K) is Marangoni coefficient, T is temperature, f_{ind} is inductor current frequency and σ is conductivity of liquid silicon. Marangoni force is directed from higher to lower temperatures, EM force, F_{EM}, – typically in the opposite direction. Temperature field is governed by non-stationary convection-diffusion equation. Boundary conditions are: fixed temperature, equal to melting point of Si, on melting and crystallization interfaces; fixed heat flux density, equal to sum of radiative heat losses and EM induced power density, on melt free surface. For the dopant concentration field, C, the mass transport equation is solved. From the calculated C distribution at the crystallization interface the resistivity of grown crystal, ρ, can be obtained: $\rho = 1/k_0C$, where k_0 is the segregation coefficient.

3. Calculation results

Phase boundaries of the considered 4” FZ system (information about IKZ Berlin system parameters and geometry of inductor can be found in [2]) are calculated using program *FZone* and shown in Figure 2 on the left. When EM correction at ETP is included, higher inductor current is required to hold prescribed zone height (32.5 mm) and it leads to larger deflection of crystallization interface. This shape is closer to the experimental one. Induced EM power density and force density vectors for different inductor current frequency are in Figure 2 on the right. Heat sources are approximately the same, because calculation algorithm is maintaining fixed zone height. F_{EM} is slightly different: maximal values are 0.49 N/m^2 for 3 MHz and 0.57 N/m^2 for 2 MHz.

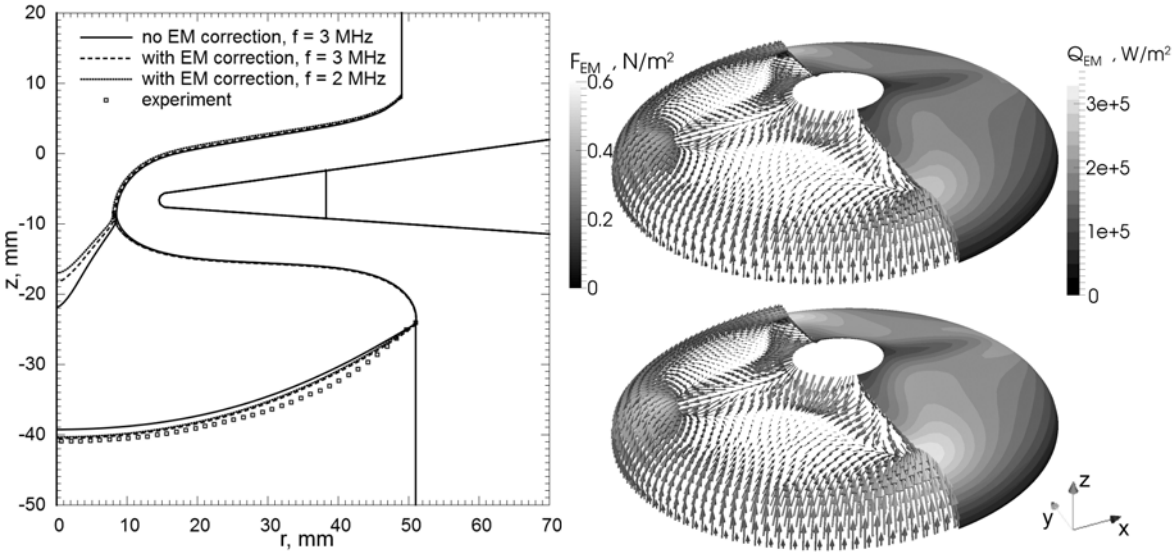

Figure 2: Left: phase boundaries of considered system for various EM fields. Right: EM heat sources and EM force on free melt surface for cases with EM correction for different inductor current frequency (top – 3 MHz, bottom – 2 MHz). Current suppliers are in +x direction.

Using the obtained axisymmetric shape of phase boundaries, 3D HD calculations were performed on a block-structured mesh consisting of 80000 hexahedral elements. A sample of calculated fields – melt velocity, temperature and dopant concentration – is shown in Figures 3 and 4. Characteristic temperature maxima are formed below the additional slits of inductor due to non-symmetric induced heat sources (see Figure 2). Velocity field shows that near the ETP EM forces are dominating and creating a distinct vortex directed upwards.

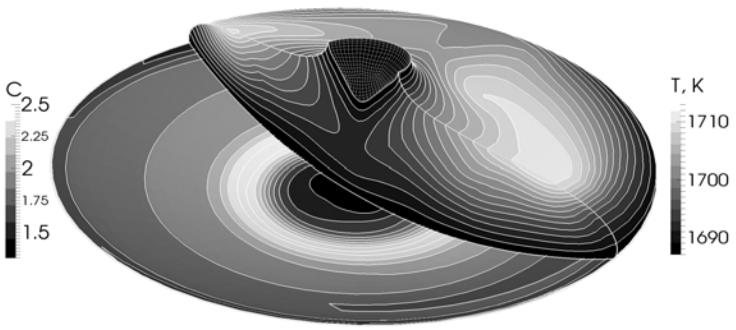

Figure 3: Crystallization interface and vertical cut of the melt. Melt temperature is shown in the right part of melt; dopant concentration is depicted on crystallization interface. Calculation example with EM correction and f_{ind} = 3 MHz.

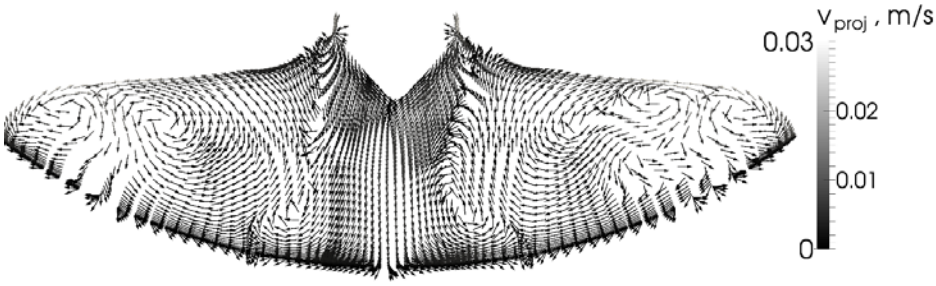

Figure 4: Time-averaged melt velocity projection on the vertical slice of the melt, perpendicular to inductor current suppliers, f_{ind} = 3 MHz.

To investigate the influence of EM forces on melt motion more precisely, distribution of tangential melt velocity component (projected on the plane of the slice) is shown in Figure 5. The case where EM force is not considered differs considerably from other cases which are very similar despite to different EM forces for frequency of 2 and 3 MHz. It can be explained with increased temperature gradients in 2 MHz case (maximum temperature increased from 1712 to 1720 K) causing larger Marangoni forces which are compensating the increased EM forces in this case (see temperature distribution in Figure 6), which compensate changes in EM force. Finally, from concentration distribution on crystallization interface RRV profiles are obtained (see Figure 7). The sum of squared differences between experimental and calculated RRV profiles in Table 1 shows that the case with EM correction and f_{ind} = 3 MHz describes experimental data more precisely than others. Experimental data was obtained using f_{ind} = 3 MHz, and the expected result that calculation with f_{ind} = 2 MHz has a worse agreement with experiment indicates that the used system of numerical models is sensitive to inductor current frequency.

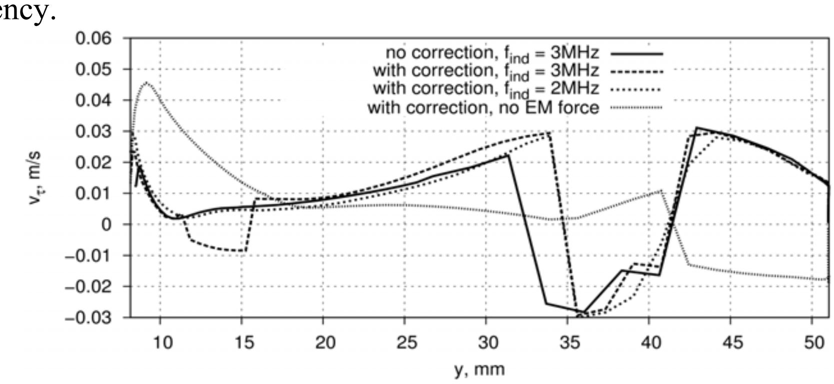

Figure 5: Distribution of in-plane velocity on melt free surface. *y* is horizontal coordinate perpendicular to inductor current suppliers, 51 mm corresponds to ETP.
v_τ is defined as positive if melt moves towards the crystal axis.

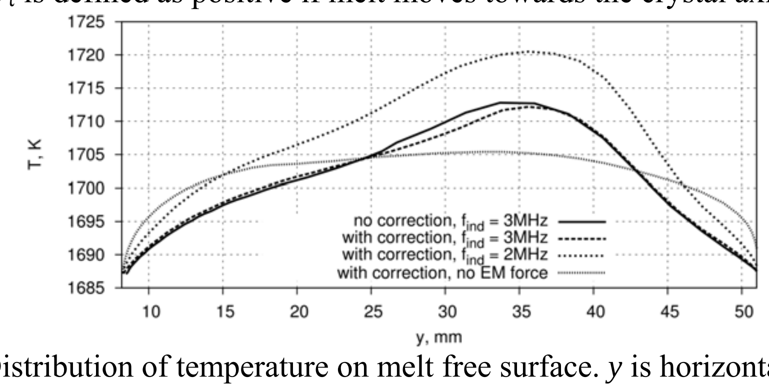

Figure 6: Distribution of temperature on melt free surface. *y* is horizontal coordinate perpendicular to inductor current suppliers, 51 mm corresponds to ETP.

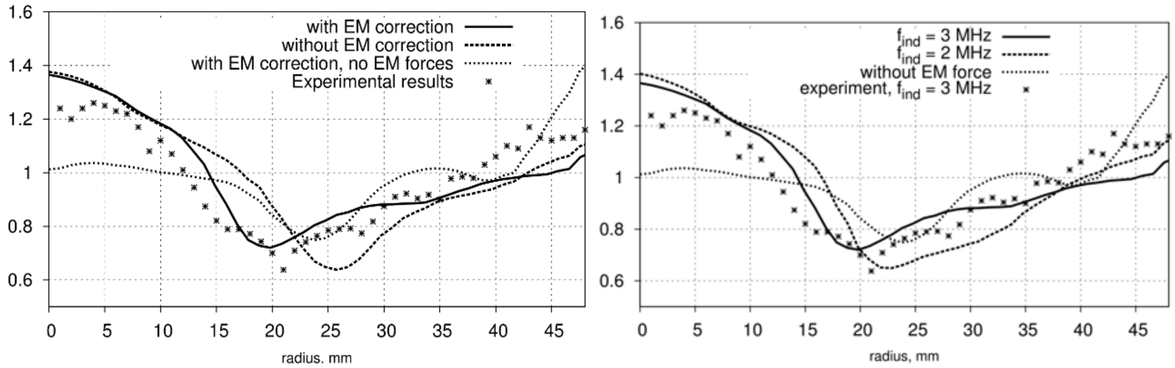

Figure 7: RRV profiles. Resistivity is normalised to its average and displayed in arbitrary units. Left: f_{ind} = 3 MHz, right: calculations on the mesh obtained with EM correction.

No EM correction, f_{ind} = 3 MHz	With EM correction, f_{ind} = 3 MHz	With EM correction, no EM forces	With EM correction, f_{ind} = 2 MHz
0.80	0.38	0.88	0.67

Table 1. Sum of squared differences between experimental and calculated RRV profiles, in arbitrary units.

4. Conclusions

It was shown that EM field has significant influence both on the shape of phase boundaries and on melt hydrodynamics. Introduced EM correction allows to describe phase boundaries more precisely, and it leads to changes in RRV profile, even although direct influence of correction on 3D HF EM field distribution is not taken into account. Position of resistivity minima became closer to experimentally observed and sum of squared differences diminished, therefore EM correction improved models' qualitative and quantitative correspondence to experiment. Experimental data for f_{ind} = 2 MHz would be valuable for further validation of the mathematical models.

When calculations are performed without EM forces, distribution of velocity on melt free surface shows that Marangoni force reverses vortices near ETP. Due to the complexity of flow pattern, clear influence of the lowering of inductor current frequency cannot be detected due to intense buoyancy and Marangoni forces, which partially compensate EM forces. The next aim of the study could be implementation of EM correction in 3D HF EM calculation program, which creates EM heat sources – boundary conditions for melt flow calculations, to observe direct influence of EM correction on the 3D melt flow and dopant distribution.

5. Acknowledgments

This work has been supported by the European Regional Development Fund, project Contract no. 2013/0051/2DP/2.1.1.1.0/13/APIA/VIAA/009.

5. References

[1] Lacis, K.; Muiznieks, A.; Rudevics, A.; Sabanskis, A.: Influence of DC and AC magnetic fields on melt motion in FZ large Si crystal growth. Magnetohydrodynamics. 46 (2010) 119-218.

[2] Rost, H.-J.; Menzel, R.; Luedge, A.; Riemann, H.: FZ silicon crystal growth at reduced RF frequencies. JCG. 360 (2012) 43-46.

[3] Ratnieks, G.; Muiznieks, A.; Muhlbauer, A: Modelling of phase boundaries for large industrial FZ silicon crystal growth with the needle-eye technique. JCG. 255 (2003) 227-240.

[4] Muiznieks, A.; Rudevics, A.; Riemann, H.; Lacis, U.: Comparison between 2D and 3D modelling of HF electromagnetic field in FZ silicon crystal growth process. International Scientific Colloquium Modelling for Material Processing, Riga. (2010) 61-65.

3D MODELING OF THE INFLUENCE OF THE INDUCTOR ON THE PHASE BOUNDARIES IN FZ CRYSTAL GROWTH

PLĀTE M., KRAUZE A., VIRBULIS J.
Department of Physics and Mathematics, University of Latvia
8 Zeļļu str., Rīga, Latvia
E-mail address of corresponding author: matiss.plate@lu.lv

Abstract: In a recent development, an improved mathematical model of the floating zone (FZ) silicon single crystal growth process takes into account main 3D aspects of the influence of a strongly asymmetric high frequency electromagnetic (HF EM) field. The model considers EM pressure acting on the free melt surface. 3D molten zone shape and the global heat exchange calculations are coupled. The influence of EM field asymmetry on the shape of phase boundaries and the meniscus angle is investigated for the FZ processes with 4” and 5” crystal diameter.

1. Introduction

In the FZ process, Fig. 1, a polycrystalline silicon feed rod is heated by a single-turn pancake-shaped HF induction coil. A molten zone is formed under the inductor, and a single crystal is pulled down from there at a constant rate.

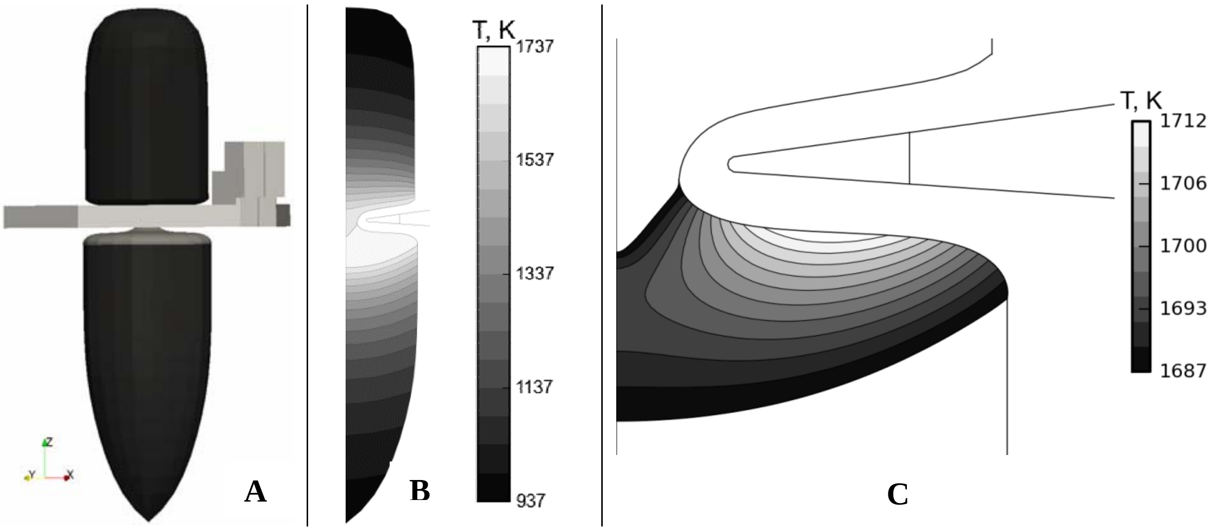

Figure 1: Mathematical modelling of the FZ process. Illustrative 3D scheme of the whole FZ system (panel A). The inductor (shown in grey) melts the feed rod, so that a molten zone develops below it. The crystal is pulled downwards from the bottom of the molten zone. Temperature field in the whole axisymmetric system (panel B) and in the melt (panel C).

Due to the crystal and feed rod rotation, FZ crystal growth systems are quite axisymmetric, and temperature distribution in the silicon, radiation exchange, and phase boundary shapes are usually modeled with 2D axisymmetric models, see [1] and Fig. 1-B, 1-C. For example, program FZone [1] uses this approach to obtain quasi-stationary states of FZ process via iteratively coupled calculations.

In FZone, 3D HF EM equations are solved to obtain 3D distributions of the EM pressure and power, which are azimuthally averaged and supplied to 2D axisymmetric models. Averaged EM pressure distribution is used to solve the equation for the 2D axisymmetric equilibrium shape of the free melt surface. The averaged EM power distribution together with the results from 2D radiation heat exchange calculations are used to formulate the boundary conditions for 2D heat transfer equations for the silicon. Finally, the calculated heat flow disbalances determine the rate of change of the solid-melt phase interfaces.

A significant drawback of this approach is the assumption that the shape of the free melt surface is axisymmetric. The shape of the free melt surface is affected by the distribution of the induced EM pressure, which has pronounced asymmetry because of the pancake-shaped form of the one-turn inductor and the presence of slits on it. Hence the shape of the free melt surface can also be expected to be asymmetric. The EM field distribution itself, however, is sensitive to the changes in the free melt surface shape, which means that modelling it as axisymmetric may introduce errors in the evaluation of the induced EM power.

To investigate the possible influence of asymmetry of the free surface shape, an improved model for the FZ process has been developed, based on the FZone program, in which modelling the 3D free surface shape is done explicitly and is iteratively coupled with calculations of the 3D HF EM field distribution. The improved model has been applied to a typical 4" FZ crystal growth process (data provided from IKZ, Berlin [2]) and a 5" process, and the calculation results have been compared with those from calculations with axisymmetric free surface shape.

2. Mathematical model

2.1. Model for 3D HF EM field. The EM field distribution in the FZ system is characterized by a distinct skin effect due to high field frequency (≈ 3MHz). The skin-layer depth varies between 0.038 mm for the Cu inductor and 1.30 mm for the solid silicon, much less than the characteristic dimensions of the FZ system (≈ 0.1 m). The EM field distribution is therefore determined by surface current density $\vec{i}$. Its distribution is obtained by solving an equation for the electric stream function Ψ , using a 3D boundary element method. See [2, 3] for details.

2.2. Model for 3D free melt surface. The model for the free surface shape is based on the model implemented by Surface Evolver program [4]. The free surface is discretized with linear triangular elements, identical to the one used in 3D HF EM field calculations. A hydrostatic approach is used, in which the free surface form corresponds to its equilibrium shape, at which the sum of the surface tension ($\vec{F}_\sigma$), gravitational ($\vec{F}_g$), and constant pressure ($\vec{F}_0$) forces is zero on each non-fixed surface mesh node. By analogy with $\vec{F}_0$, we also add the electromagnetic force $\vec{F}_{EM}$, exerted by the EM pressure on the surface:

$$\vec{F}_\sigma = \sigma\frac{\partial S}{\partial\vec{r}},\ \vec{F}_g = -\frac{\partial E_g}{\partial\vec{r}},$$
$$\vec{F}_0 = p_0\frac{\partial V}{\partial\vec{r}},\vec{F}_{EM} = -p_{EM}\frac{\partial V}{\partial\vec{r}},$$

where $\vec{r}$ is a radius vector of a node, S and V denote surface area and volume of the melt, E_g is gravitational energy expressed as a surface integral, σ is a surface tension coefficient, p_0 is a constant pressure term, and p_{EM} is EM pressure distribution.

An algorithm iterates an initial surface shape with fixed triple point line positions by shifting the surface nodes proportionally to the normal component of total force until the equilibrium shape is reached. An iterative procedure chooses such a p_0 value, that the averaged meniscus angle at the crystal triple point line were equal to the silicon growth angle of 11°.

After the free surface shape is obtained, the EM calculations with the new free surface shape are repeated and the EM pressure distribution is updated. This cycle of 3D EM and free surface calculations is repeated until a stable free surface shape is obtained.

2.3. Coupling 3D EM and free surface model with 2D heat transfer model of FZone. To couple the EM-free-surface calculations with 2D heat transfer model of FZone, the EM power values are azimuthally averaged and provided to the heat transfer model. The result of the FZone calculations are a new geometry of the FZ system, including new positions of the triple point lines, and new inductor current strength.

The coupled EM-free-surface and 2D heat transfer calculations are repeated iteratively until a stable, quasi-stationary solution for the whole FZ system is found, i.e., the geometry of the FZ system and its parameters stop changing.

3. Calculation results

4” and 5” FZ crystal growth systems were modeled both with axisymmetric and 3D free surface models. 4” process data were provided by IKZ, Berlin [2]. 5” system was obtained by simply increasing the crystal and feed rod radii by 25%.

Table 1: Inductor current strength and deflection of the crystallization interface for 4” and 5” processes obtained by both models.

Process	Free surface model	Inductor current I, A	Deflection H_C, mm
4”	Axisymmetric	884.5	16.2
4”	3D	886.5	16.2
5”	Axisymmetric	1060.4	24.5
5”	3D	1062.6	25.7

The target zone height, defined as a vertical distance between the triple point line at the crystal and the lower outer point of the feed rod, was set to 32.5 mm for all cases. The inductor frequency was 3 MHz. The inductor had a main slot (1.5 mm width) and three additional slots of 2.0 mm width. The material properties of silicon were taken from [1]. The pulling velocity of the crystal was 3.4 mm/min for the 4” system and 3.0 mm/min for the 5” system. The feed rod was pulled at a constant rate to ensure mass conservation.

The calculations show that the inductor current strength, the deflection of the crystallization interface, and the shapes of the FZ system parts in general are practically the same in the results for the 4” system (Tab. 1), i.e., the 3D asymmetry of the free surface shape played no role for this system. However, there are significant differences in the 5” inch results: the deflection is higher, and a part of the feed rod melted away in the calculations with 3D asymmetric melt surface, see Fig. 2. The reason for this is the changes in the distribution of the azimuthally averaged EM power on the free surface, see Fig. 3, where it is shown as a function of the free surface arc length. The EM power increases near the neck for 5” process, which explains higher melting of the feed rod. There are practically no changes in the power distribution between axisymmetric and 3D cases for the 4” system.

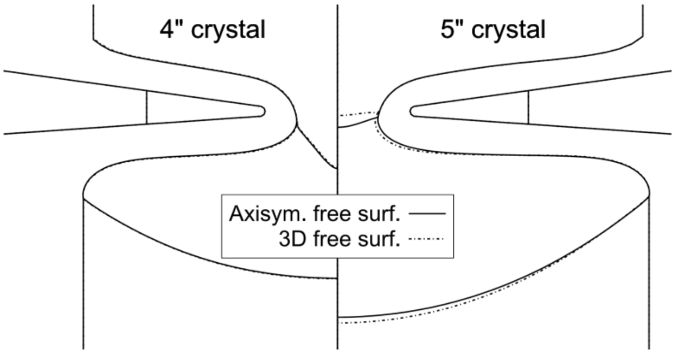

Figure 2: Shapes of the phase boundaries obtained by axisymmetric and 3D free surface models for 4” and 5” crystals.

Fig. 4 shows deviations of the 3D free surface shapes from the axisymmetric ones. The magnitude of the deviations is higher for 5” system, which explains the larger influence of these deviations. The free surface of the 5” system near the neck is, on average, elevated significantly above the axisymmetric surface. It is therefore closer to the inductor, which explains the increase of the received EM power at the neck. FZone uses azimuthally averaged pressure values internally to calculate phase boundary shapes, so its calculated axisymmetric free surface shape has actually a deflection near the neck, see Fig. 2, left, due to increased pressure. Increased EM power near the neck melts part of the feed rod and shifts upwards the triple point line at the feed rod rim. This leads to the free surface bending away from the inductor, thus counter-balancing the EM pressure influence.

Fig. 5 shows azimuthal distribution of the meniscus angle deviations from 11º at the crystal rim. One can see four distinct minima that are related to the EM pressure maximums on the free surface, created by the inductor slits. The main slit causes absolute minimum at 270º, and this minimum is lower for 5” system. The three side slit minima are higher, however, because the pressure maximums for 5” system lay at a greater distance from the crystal rim.

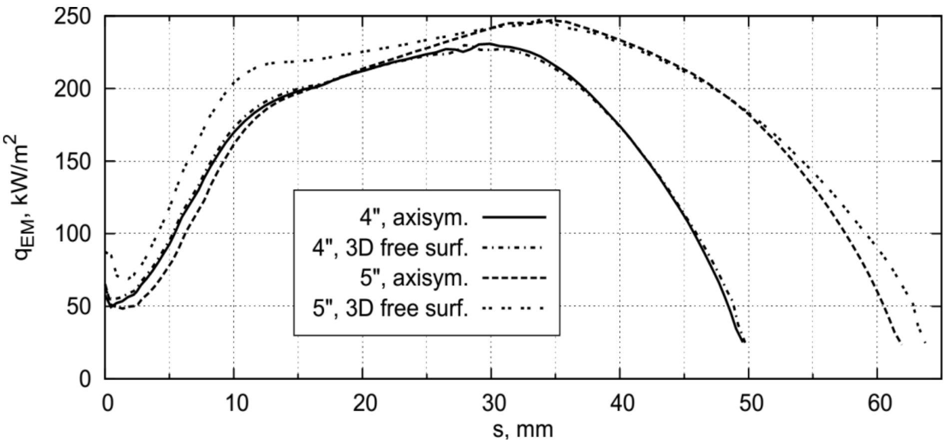

Figure 3: Azimuthally-averaged distributions of EM power density on the free melt surface as functions of arc length s along the free surface 2D profile for 4” and 5” processes. $s = 0$ corresponds to the triple point line at the feed rod (neck). Differences between axisymmetric and the 3D free surface models.

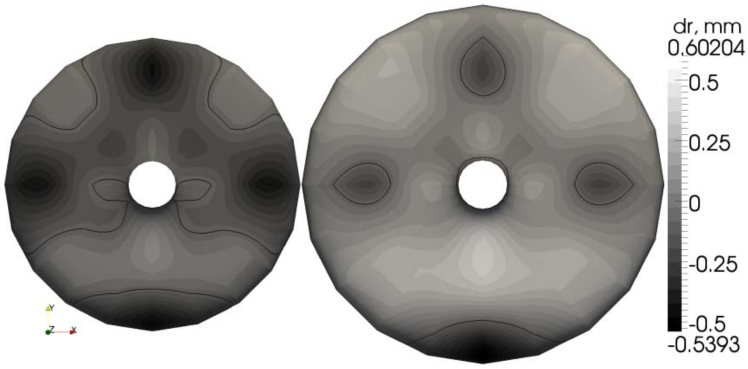

Figure 4: Deviation of the free surface in the normal direction from the axisymmetric free surface shape, 4” (left) and 5” (right) processes. Black line corresponds to dr = 0 mm.

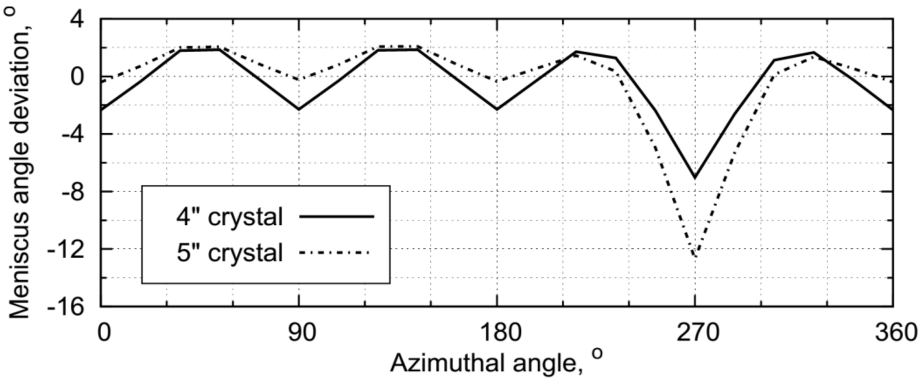

Figure 5: Azimuthal distribution of the meniscus angle deviation from the growth angle (11º).

4. Conclusions

The improved mathematical model with 3D free surface shape modeling has been successfully implemented in the program code for a quasi-stationary model of the FZ process. The calculations showed that the influence of 3D deformations in the free surface shape on the global heat transfer was negligible for the 4” crystal system, but significant for the 5” system. The EM power generation was increased in the area around the neck due to higher local elevation of the free surface. One can expect this effect to be more significant for FZ systems with larger crystal radii; therefore modeling full 3D shape of the free surface could be considered necessary for calculations of these systems.

5. Acknowledgements.

This work has been supported by the European Regional Development Fund, project contract No. 2013/0051/2DP/2.1.1.1.0/13/APIA/VIAA/009.

6. References

[1] G. Ratnieks; Muiznieks A.; Muhlbauer A.: Modelling of phase boundaries for large industrial FZ silicon crystal growth with the needle-eye technique. JCG. 255 (2003), 227-240

[2] Rost, H.-J.; Menzel, R.; Luedge, A.; Riemann, H.: FZ silicon crystal growth at reduced RF frequencies. JCG. 360 (2012), 43-46

[3] Muiznieks A.; Lacis K.; Rudevics A.; Lacis U.; Sabanskis A.; Plate M.: Development of numerical calculation of electromagnetic fields in FZ silicon crystal growth process. MHD. 46 (2010), 475-486

[4] Muhlbauer A.; Muiznieks A.; Lessmann H. J.: The calculation of 3D high-frequency electromagnetic fields during induction heating using the BEM. IEEE Trans. Magn. 29 (1993), 1566-1569

[5] Brakke, K. A.: The surface evolver. Exper. Math. 1 (1992), 141-165

ELECTROMAGNETIC FLOW CONTROL IN THE RIBBON GROWTH ON SUBSTRATE (RGS) PROCESS

BECKSTEIN P., GALINDO V., GERBETH G.
Helmholtz-Zentrum Dresden-Rossendorf (HZDR)
Bautzner Landstraße 400, 01328 Dresden, Germany
E-mail: p.beckstein@hzdr.de

The Ribbon Growth on Substrate (RGS) technology promises a very efficient approach for future photovoltaic (PV) silicon wafer production compared to the majority of commonly accepted processes. Although, for an eventual break-through of this RGS technology a number of remaining problems need to be addressed to increase process stability. We have therefore performed numerical investigations in order to study the influence of the involved AC magnetic fields on the silicon melt during the RGS process.

1. Introduction to the RGS process

Photovoltaic silicon is today mainly produced by directional solidification of multi-crystalline silicon or by the Czochralski growth method of silicon single crystals. Wafers are then obtained by sawing the ingots. The unavoidable sawing losses of prevalent processes are still in the range of 40…50% of the fed material. One very efficient way to avoid this deficit in terms of energy and material is the Ribbon Growth on Substrate (RGS) technology, which was suggested and developed during the last decade [1, 2].

The basic idea of this process is a continuous feeding of molten silicon into a casting frame without bottom, while a solidified silicon foil is extracted sidewise on a sub-cooled moving substrate underneath. Figure 1 shows a schematic of this principle. This brings both a close to perfect material yield by avoiding sawing losses, and a low energy consumption due to the continuous nature of the processing. Nearly all of the silicon melt is directly used to form the wafer itself. Another distinct advantage of the RGS process also comes from its fully decoupled solidification and casting velocity.

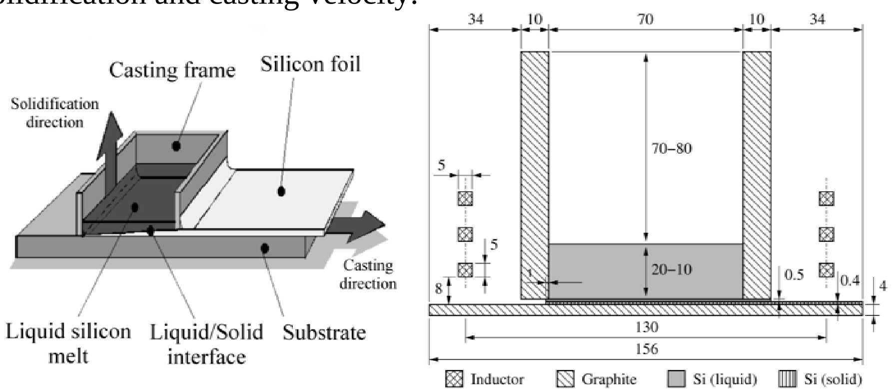

Figure 1: Scheme of the RGS process without excitation coils (left, [1]) and the simplified numerical model geometry (right, dimensions in mm). The drawing on the right represents both a central longitudinal section of the actual 3D-model and a derived 2D-version of the full model.

One challenging task in realizing this idea technically is the need to fully control the liquid silicon outflow. On this account, AC magnetic fields are applied to counter the gravitational forces acting on the melt, without contact. The excitation coil which is therefore utilized provides both a kind of magnetic valve and an inductive heating of the casting frame. The Former actively prevents leakage in the slit regions and reduces wave-like oscillations at the extraction front of the silicon foil through electromagnetic forces. This valve only works because of capillarity effects in the slit regions based on the strong surface tension of the melt.

Recent activities on electromagnetic retention for liquid silicon have been reported in [3]. A leading problem which still has to be addressed is the occurrence of flow instabilities and meniscus oscillations at the open slits where the moving substrate enters and leaves the casting frame.

We show in this paper that it is generally possible to selectively influence the process by means of tailored magnetic fields. Based on simplified numerical simulations we demonstrate the effect of the applied AC magnetic fields on the silicon melt in the RGS process, taking into account the strong time-dependent coupling to the flow in the melt. The model which was used for this analysis is shown in Figure 1 (right). Part of the numerical investigation is devoted to the effect of different coil system geometries on the stress balance along the slit. Moreover, as the induction coil frequency is sensitive to the circuit load, the induction's dependency on the filling level was of considerable interest for sensing purposes.

2. Modelling overview

A typical associated process parameter set, which evolved mainly from empirical analysis, is a RMS-current of $I_{RMS} = 1000\,\mathrm{A}$ at a frequency of $f = 10\,\mathrm{kHz}$ to feed the excitation coils, in combination with a substrate velocity of u_s = 1 m/s. The most important properties of involved materials, as shown in Figure 1 (right), are listed in Table 1.

Material	$\rho\ \left[\frac{\mathrm{kg}}{\mathrm{m}^3}\right]$	η [Pa · s]	$\sigma\ \left[\frac{\mathrm{S}}{\mathrm{m}}\right]$	$\gamma\ \left[\frac{\mathrm{N}}{\mathrm{m}}\right]$	δ [mm]
Liquid silicon	2580	0.86×10^{-3}	1.20×10^{6}	0.733	5.0
Solid silicon	2540	-	8.30×10^{4}	-	17.0
Graphite	1880	-	1.25×10^{5}	-	14.0
Copper	8960	-	6.00×10^{7}	-	0.7

Table 1: Material properties for different materials: Density ρ, kinematic viscosity η, electrical conductivity σ, surface tension coefficient γ and skin depth $\delta = \sqrt{\frac{1}{\pi f \mu_0 \sigma}}$ assuming a frequency of 10 kHz.

A comprehensive RGS-model has to correctly represent a fully three-dimensional and two-way-coupled system of AC magnetic fields and fluid flow with free surfaces at the slit and at top of the melt in the crucible for those material values presented above.

The magnetic fields may be described using the $\boldsymbol{A}$ -V -formulation of the Maxwell-Equations implying MHD approximations, a small Magnetic Reynolds Number and no magnetization as:

$$\boldsymbol{B} = \nabla \times \boldsymbol{A}; \quad \boldsymbol{E} = -(\partial_t \boldsymbol{A} + \nabla V); \quad \frac{\|\boldsymbol{u} \times \boldsymbol{B}\|}{\|\boldsymbol{E}\|} \ll 1 \tag{1}$$

Here the velocity field is denoted by $\boldsymbol{u}$, the time by t . Taking the magnetic vector potential $\boldsymbol{A}$ with applied Coulomb-Gauge and the electric scalar potential V instead of the magnetic $\boldsymbol{B}$ and electric field $\boldsymbol{E}$ allows us to explicitly introduce a source current density $\boldsymbol{j}_s(I_{RMS})$ term into the system which represents the effect of the excitation coil [4]. In case of a constant ($\nabla\sigma = 0$) or even zero ($\sigma \equiv 0$) electrical conductivity it can be shown [5], that the scalar potential may simply be neglected if $\boldsymbol{A}$ is conceptually substituted with a modified version: $\hat{\boldsymbol{A}} = \boldsymbol{A} - \int \nabla V \mathrm{d}t$. That is, if we imply constant σ for each material only $\boldsymbol{A}$ is required:

$$\nabla \times \nabla \times \boldsymbol{A} + \sigma\mu_0\partial_t \boldsymbol{A} = \mu_0 \boldsymbol{j}_s; \quad \nabla \cdot \boldsymbol{A} = 0 \tag{2}$$

$$\boldsymbol{j} = \boldsymbol{j}_i + \boldsymbol{j}_s,\ \boldsymbol{j}_i = -\sigma\partial_t \boldsymbol{A} \tag{3}$$

The field $\boldsymbol{j}_i$ represents the induced current density. To find suitable boundary conditions, the numerical domain is divided into several regions with constant σ . A detailed mathematical description of all the boundary conditions can also be found in [4]. By introducing complex-valued sinusoidal fields, equations **Error! Reference source not found.** to **Error! Reference source not found.** can be transformed into their frequency domain for an angular frequency of $\omega = 2\pi f$. This approach leads to a stationary problem since the time derivatives may then be substituted with a complex-valued angular frequency ($\frac{\partial}{\partial t} = i\omega$). For the momentum balance of the fluid, only the time-averaged Lorentz force $f = \frac{1}{\rho}\langle J \times B \rangle_t$ is important. The fluid dynamics describing the silicon melt flow is governed by the principle of conservation of mass and momentum. For the RGS-model this leads to the incompressible Navier-Stokes-Equation [6] with additional terms for gravity and the time-averaged Lorentz-Force as described above:

$$\rho[\partial_t u + (u \cdot \nabla)u] = \nabla \cdot \tau + \rho g + \langle J \times B \rangle_t ; \quad \nabla \cdot u = 0 \tag{4}$$

$$\tau = \eta[\nabla u + (\nabla u)^T] - pI \tag{5}$$

Here τ represents the total stress tensor including the diagonal fluid pressure p . Surface tension is only acting on free surface boundaries. It is thereby worth to mention that the viscosity of the external atmosphere, which is in contact with the liquid melt at the conductor boundary, is several orders of magnitude smaller than the viscosity of the melt itself. Thus, the fluid boundary condition at the free surface with its outward unit normal n and unit tangent vector t can be modeled using a simplified Young-Laplace-Equation (e.g. [7])

$$s = n \cdot \tau = -p_{\text{ext}} n - 2\gamma\kappa n \tag{6}$$

$$\kappa = -\frac{1}{2} \cdot (\nabla_\Gamma \cdot n); \quad \nabla_\Gamma = \nabla - n\partial_n = (I - nn^T)\nabla \tag{7}$$

for constant γ . Therein the stress vector is denoted by s and the external fluid only appears through its pressure p_{ext}. The surface gradient operator ∇_Γ defines the mean curvature κ of the free surface. For a planar surface ($\kappa = 0$) equation **Error! Reference source not found.** can be simplified to the free-slip boundary condition with fixed pressure if the wall is additionally claimed to be impermeable:

$$u \cdot n = 0; \quad s \cdot n = -p_{\text{ext}}; \quad s \cdot t = 0 \ . \tag{8}$$

For arbitrarily shaped interfaces the normal component of the velocity is not necessarily zero. Thus, the interface has to be moved accordingly while still ensuring its impermeable nature. In the scope of our work the Arbitrary Lagrangian-Eulerian (ALE) technique was chosen to realize the interface tracking [8]. In simplified terms, the essential idea of ALE for free surface flows is to allow the grid - which is used for discretization - to move independently from the fluid flow. Only the free surface is under constraint, such that the fluid velocity u equals the mesh velocity u_{m} there. For all other boundaries u_{m} is restricted accordingly. The independent mesh-movement away from the boundaries then allows a free and preferably smooth mesh point distribution. In our case a Laplace-smoothing for u_{m} was utilized [9]. Stationary walls were modelled with the no-slip boundary condition ($u = 0$), whereas for the moving substrate wall an inhomogeneous Dirichlet boundary condition was necessary ($u = u_{\text{g}} \cdot e_y$, process direction y). Along the wetted walls, the interface contact line may have the freedom to slide. Thus, the velocity must not be restricted there directly. To model this behavior, the generalized Navier-Slip boundary condition was consulted [10]:

$$u \cdot n = 0; \quad s \cdot t = -\frac{\eta}{\beta} u \cdot t \ . \tag{9}$$

The slip length β is present to relate a tangential boundary friction force to the current local slip velocity. For all of our calculations $\beta = 0.01 \cdot h$ was used, where h denotes a mean local mesh (element) size of the discretized numerical model.

3. Simulation results

The basis of our analysis was to gain detailed information of all involved fields. To reduce the computational effort, we thought of the melt domain to be fixed during this first step: The magnetic field calculations including the Lorentz force were performed using the finite element solver OPERA (Cobham plc). The results revealed high amplitudes for f in all regions close to edges and corners of the fluid domain as shown in Figure 2 (left).

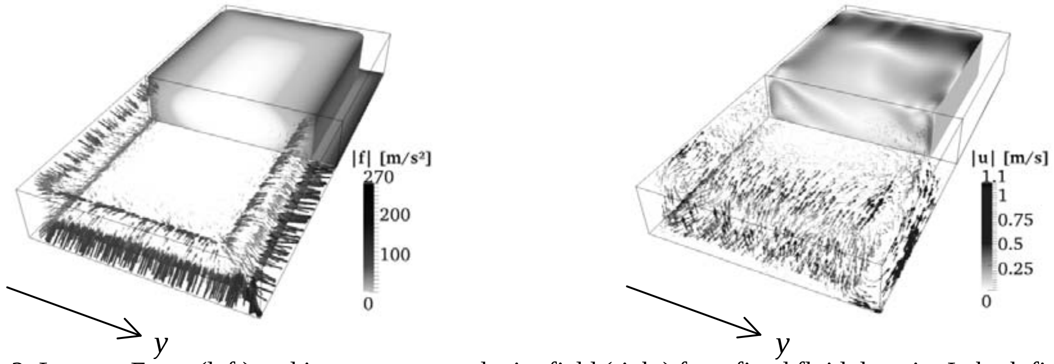

Figure 2: Lorentz-Force (left) and instantaneous velocity field (right) for a fixed fluid domain: In both figures all solid material domains are hidden. The front part shows the related vectors, the rear part the corresponding amplitudes for one half of the fluid domain, respectively. The process direction is indicated by *y*.

Given this, we concluded that the liquid silicon melt would actually be subject to a strong deformation if we had not restricted our model as a premise. The corresponding forced fluid flow was simulated with a finite volume solver of the openFOAM library suite. The resulting velocity field u is also illustrated in Figure 2 (right) for comparison. That the fluid flow is mainly influenced by the Lorentz force is one substantial finding here. A boundary driving effect of the moving substrate along the y-direction can barely be identified since the global maximum velocity magnitude is more than one order of magnitude higher then u_S. Hence we assume that the magnetic force is mainly responsible for exciting flow instabilities. As the strong Lorentz force is however crucial to balance the gravitational force, it cannot simply be reduced. This can be demonstrated with the help of the magnetic pressure $p_B = \dfrac{B^2}{2\mu_0}$.

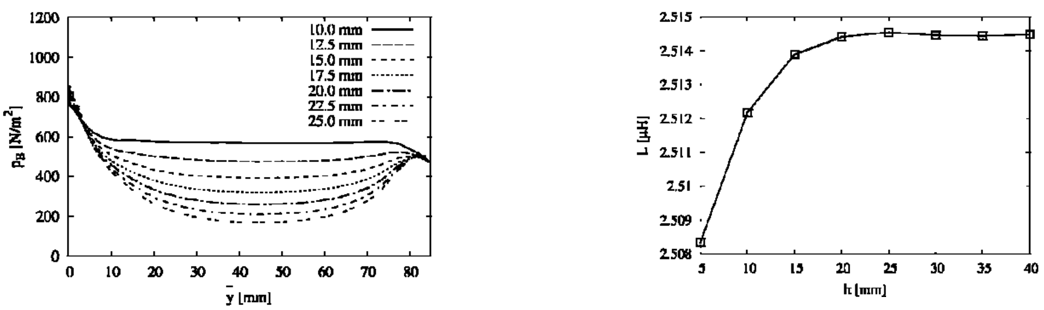

Figure 3: Magnetic pressure along a wafer side (left, arc length $\bar{y}$) for different casting frame side wall strengths (Front: $\bar{y} = 0\text{mm}$, Back: $\bar{y} \approx 78\text{mm}$) and magnetic inductivity (right) based on I_{RMS} for diff. melt heights.

Figure 3 (left) illustrates p_B along a wafer side for different casting frame side wall thicknesses as a result of an investigation on how the melt flow could be shielded in order to reduce the magnetic forcing on the bulk region. The hydrostatic pressure at the bottom of the casting frame results in $p_g = \rho g h \approx 506 \frac{\mathrm{N}}{\mathrm{m}^2}$ for a typical fixed melt level height of $h = 20\mathrm{mm}$. Comparing p_B with the trends in Figure 3 (left) clearly shows that a properly working magnetic valve is very sensitive to small geometric changes. Figure 3 (right) moreover shows the total magnetic inductivity $L = \frac{W}{I_{\mathrm{RMS}}^2}$ of the system against different melt level heights, where W denotes the time-averaged magnetic field energy $W = \frac{1}{2\int \langle H \cdot B \rangle_t \, \mathrm{d}V}$. The total system inductivity proved not to be as sensitive as expected for measuring the melt level height based on phase or frequency shifts in the power supply of the excitation coil. There is only a small change of just about 0.3% for L in the range of $h = 5\,\mathrm{mm}$ and $h = 40\,\mathrm{mm}$. Further investigations will show if this is enough to produce a significant influence on the driving oscillating circuit. Recent development engaged in revising our model to account for surface deformation at the top of the fluid domain. Latest results for a successful 2D-simulation with COMSOL Multiphysics are presented in Figure 4.

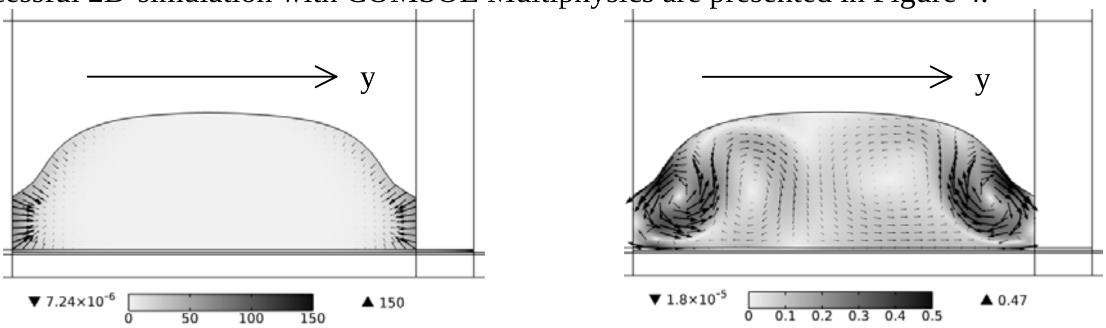

Figure 4: Dome shaping of the fluid domain for a simplified 2D-model (central longitudinal section of the 3D-model): Time-averaged Lorentz force (left) and fluid velocity (right) at the simulation time of $t = 3$ s after applying the magnetic field.

The magnitudes of the Lorentz force (left) and the velocity field (right) are in quite good agreement with central longitudinal section of the 3D-model. From the shape of the dome and based on the maximum field magnitudes, this shows a manifold flow character and that none of the momentum source terms in equation **Error! Reference source not found.** is clearly dominating. This is one major reason which makes the whole modeling challenging and simulations require high computational costs, especially in 3D. But it also shows the dominance of the magnetic forcing compared to the driving effect of the moving substrate.

4. Conclusion

The RGS process is a promising technology for future silicon wafer production, but the involved physics make high demands on numerical investigations which are necessary for improving process controllability and stability. We have successfully performed 3D-simulations to numerically confirm the functioning melt retention based on tailored magnetic fields. A parameter study revealed the total system inductivity as a function of the melt level. Finally, we demonstrated that the surface deformation is substantially important for a satisfactory model. Further investigations will mainly concern an improved contact line modelling, expected surface oscillations and the surface deformation in 3D.

Acknowledgements. Financial support for this research from the German Helmholtz Association in frame of the Alliance "Liquid Metal Technologies (LIMTECH)" is gratefully acknowledged.

References

[1] Schönecker, A., Geerligs, L. J., and Müller, A. Solid State Phenomena, 95-96 (2004), 149-158.
[2] Hahn, G. and Schönecker, A. Journal of Physics: Condensed Matter, 16 (2004), R1615-R1648.
[3] Santara, F., Delannoy, Y., and Autruffe, A. Journal of Crystal Growth, 340 (2012), 41-46.
[4] Binns, K. J., Lawrenson, P. J., and Trowbridge, C. W. The Analytical and Numerical Solution of Electric and Magnetic Fields. Wiley, 1992.
[5] Morisue, T. IEEE Transactions on Magnetics, 18 (1982), 531-535.
[6] Ferziger, J. H. and Peric, M. Computational Methods for Fluid Dynamics. Springer-Verlag, 2002.
[7] Scardovell, R. and Zalesk, S. Annual Review of Fluid Mechanics, 31 (1999), 567-603.
[8] Hughes, T. J.R., Liu, W. K., and Zimmermann, T. K. Computer Methods in Applied Mechanics and Engineering, 29 (1981), 329–349.
[9] COMSOL 4.4 Multiphysics Reference Manual. 2014.
[10] Bruus, H. Theoretical Microfluidics. Oxford University Press, 2008.

THERMOELECTRICALLY DRIVEN MHD FLOW FIELD IN UNDERCOOLED CRYSTAL GROWTH

KAO A., PERICLEOUS K.
University of Greewich, UK
E-mail: a.kao@gre.ac.uk

This paper investigates the complex fluid structures that may form during the undercooled growth of a single equiaxed dendrite placed in an externally applied magnetic field. Due to variations in surface temperature along the solidification front, thermoelectric currents form, which interacting with an external magnetic field result in a Lorentz force that drives microscopic fluid flow. The phenomenon was named Thermoelectric Magnetohydrodynamics (TEMHD) by Shercliff . Depending on the alloy's thermoelectric properties TEMHD can be a dominant mechanism in interdendritic spaces and consequently have a significant impact on crystal morphology . Such a situation arises during electromagnetic levitation experiments, where the application of an external DC magnetic field is commonly used to dampen macroscopic flow [1].

A fully coupled 3-dimensional time-dependent numerical model incorporating solidification, thermoelectrics and fluid flow has been developed to analyzed the evolution of both the solidification front and the fluid structure for various orientations of the magnetic field. The results of the simulations have been presented in previous publications [2].

The situation is complex both physically and computationally and difficult to interpret. By topographically representing the dendrite as a sphere and mapping the surface energy on its surface, a closed analytic solution can be obtained. Furthermore, in a low magnetic field limit, the solution becomes linear. Due to the cubic symmetry of the surface energy and the inter-changeability of the Cartesian axes, it is only necessary to solve for a single orientation of the magnetic field. Combined with linear superposition, the fluid structure can determined for any orientation of the magnetic field.

A comparison to the numerical simulations for a small crystal at an early growth stage (fig.1), gives good agreement for both the direction and magnitude of fluid flow, which develops a complex vortical structure.

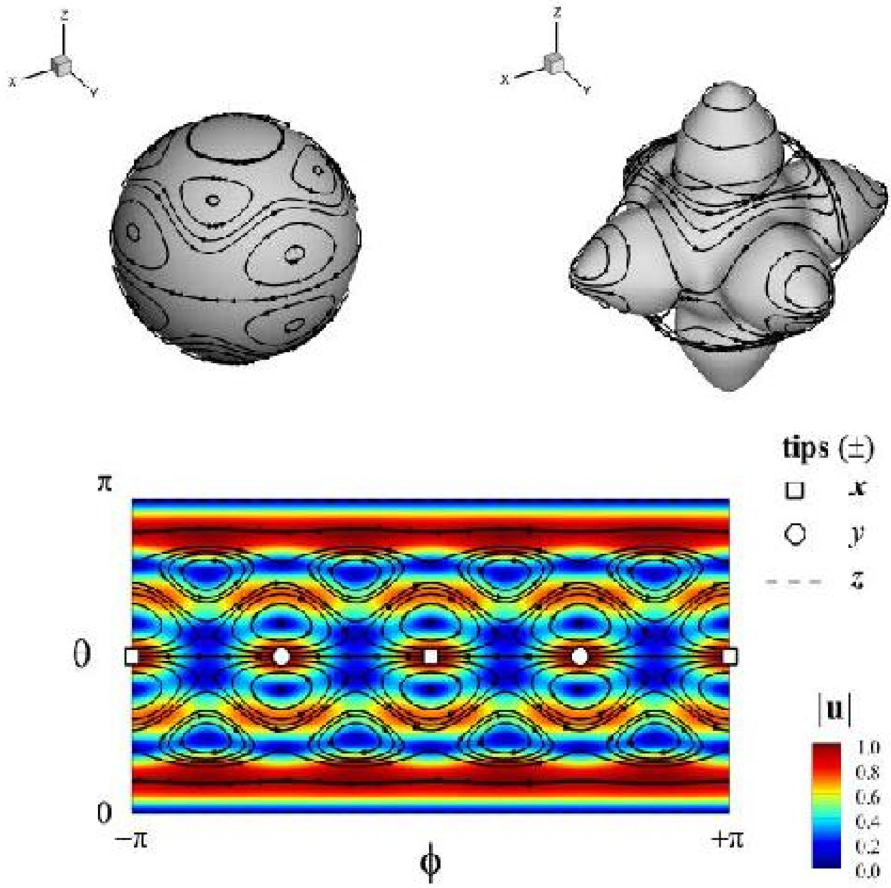

Figure 1: Fluid flow for a z-orientated magnetic field. Top left: analytic solution. Top right: numerical solution. Bottom: Mercator projection.

References

[1] H. Kotabate, H. Fukuyama, T. Tsukada, S. Awaji, Measurement Science and technology, vol. 1, no.2, 2009.
[2] A. Kao and K. Pericleous, Magnetohydrodynamics, vol. 48, no. 2, 361-370 (2012).

CONTROL OF CONVECTIVE FLOWS IN A RECTANGULAR CRUCIBLE BY A SPECIAL TYPE OF ELECTROMAGNETICAL STIRRING

NEGRILA R.A., POPESCU A., PAULESCU M., VIZMAN D.
Faculty of Physics, West University of Timisoara, Bd. V. Parvan 4, 300223 Timisoara, Romania
e-mail address of corresponding author: negrila.andrei.radu@gmail.com

Abstract : One of the key issues in the technology development of directional solidification (DS) of silicon for photovoltaic applications is to control the interface shape and impurities distribution through tailoring the melt convection. In this view a new type of melt flow control through electromagnetic stirring (EMS) for the DS of silicon is proposed. To show the potential of the EMS method both numerical and experimental investigations were performed in a model experiment for a GaInSn melt. The computed velocities were studied and compared to experimental Doppler ultrasound velocity profiles.

1. Introduction

In directional solidification (DS), which is the main method for growing photovoltaic silicon, accounting for over 50% of the world market share, a major role in heat and species transport is played by the melt convection. Some previous contributions [1-7] show that melt convection plays a crucial role for the heat transfer, solid-liquid interface shape (and thus for thermal stress and dislocations) and for the distribution of impurities and dopants. In DS the buoyant (or natural) convection, has positive effects on the crystalline quality of the ingot by reducing the segregated impurity diffusion boundary layer in front of the growth interface and thus homogenizing the impurity distribution inside the melt. Therefore, the impurity concentration incorporated into the crystal is reduced and unwanted effects such as morphological destabilization of the crystalline growth interface or impurity precipitate formation in the melt are usually avoided.

However, there are some limitations to the effectiveness of buoyant convection. Precipitates tend to be formed and incorporated into the growing silicon lattice between buoyant convection loops [8,9]. Another limitation is the formation of a poorly mixed area in the center of the melt, separating natural convection structures from the melt surface and crystal interface [7], which favors precipitate formation there. Also, with the increase of crucible dimensions, the control of melt flow in a beneficial way becomes a very challenging task. In recent years, some techniques have been proposed in order to tailor melt flow in a DS process. Some of them are based on travelling [10-12] or rotating [13-15] magnetic fields; others on a mix between vertical magnetic field and electrical current [16, 17] and another on mechanical stirring [18].

Based on the idea of melt stirring from Electromagnetic Czochralski method developed by Watanabe et al [19], numerical modeling was carried out in the case of DS, for a similar configuration with one electrode placed in a vertical magnetic field [16]. Due to practical crystal growth reasons, a new configuration for melt flow control (EMS), with two electrodes in contact with the melt placed in a vertical magnetic field, was investigated by numerical simulation in [17] and found to be very effective.

2. Numerical model and experimental set-up

In order to validate the numerical modeling for this method of electromagnetic stirring, both numerical and experimental investigations have been carried out on a model experiment in an isothermal square-shaped crucible, where a room temperature liquid alloy mimics a silicon melt inside a DS set-up. Two types of electrodes configurations were considered:

- a symmetric configuration (SC) with the two electrodes placed along a diagonal, symmetric from the central point, at a third diagonal length from the corner point (fig 1b)
- an asymmetric configuration (AC) with one electrode placed in the center of the free melt surface and the second one placed on a diagonal closer to the corner point at the third distance between the center and the corner point (fig 1c)

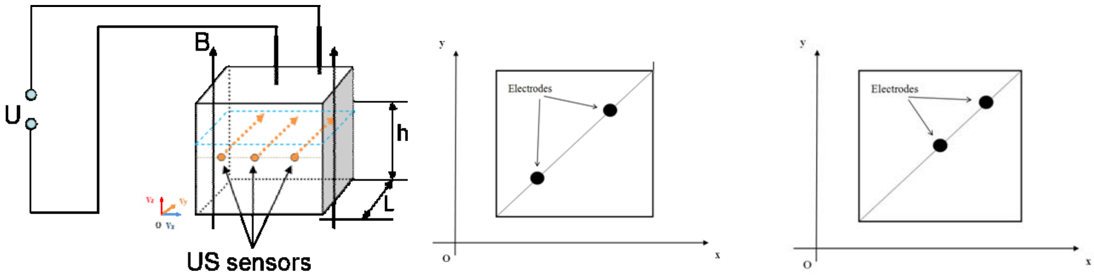

(a) (b) (c)

Figure 1: (a) Crucible geometry for 3D modeling of GaInSn melt stirring, using a vertical magnetic field combined with an electrical DC current, induced into the melt by: (b) 2 symmetrical electrodes, (c) 2 asymmetrical electrodes.

The melt flow is described by the three-dimensional time-dependent equations of mass and momentum conservation:

$$\nabla u = 0 \quad (1)$$

$$\rho\frac{\partial u}{\partial t} + \rho(u\nabla)u - \mu\nabla^2 u = -\nabla p + f_L, \quad (2)$$

where ρ is the density, u the melt velocity, p is the pressure, j is the electric current density, B is the magnetic field induction. The influence of the steady magnetic field on the melt flow is considered by the Lorentz force density $f_L = j \times B$ in the Navier-Stokes equations. For the calculation of the Lorentz force, the electric current density $\boldsymbol{j} = \sigma(-\nabla\Phi + \boldsymbol{v} \times \boldsymbol{B})$ induced in the melt is taken into account, where σ is the electric conductivity, $\boldsymbol{v}$ is the melt velocity and Φ the scalar electrical potential. Φ is calculated by an additional differential equation obtained from the electrical current continuity equation:

$$\nabla j = 0 \rightarrow \Delta(= \nabla(v \times B) \quad (3)$$

The crucible walls and melt free surface are considered to be electrical isolated. Therefore $[\nabla|\square_{\downarrow}n \,(= 0$ on all boundaries except the surface elements, where the electrodes touch the melt, where $\square\nabla|\square_{\downarrow}n \,(= -j_{\downarrow}n/\sigma$, with j_n the density of the electrical current. The magnetic field imposed is vertical and constant, independent of the melt rotation. The auto-induced magnetic field generated by the electrical current is not taken into account in the numerical model, as its influence is very small for the modeled values of I and B. The melt flow velocities along the boundaries at the crucible and at the crystal are set to $v = 0$ (no-slip). Along the free surface of the melt, „no shear stress" condition is considered. The simulation has been performed using the STHAMAS3D software. The computational domain is 70 x 70 x 50 mm^3 in size consisting of a block with a non-orthogonal grid that has a local refinement at the walls in order to resolve the boundary layers. The mesh in the melt consists typically of 180000 control volumes, which is assumed to be sufficient to resolve the main features of the flow. In order to obtain a realistic solution starting from an arbitrary initial solution at least 900 sec real time were computed with a time step of 0.1 sec.

In order to validate the numerical simulation, an experimental model was developed (fig 2), consisting of a square-shaped plexiglas crucible (70 x 70 x 70 mm^3) placed in a vertical magnetic field. The crucible contains a 50 mm high GaInSn room temperature liquid alloy, which has similar material properties to molten Silicon. Two electrodes are in contact with the alloy melt surface, through which a direct current passes. Velocity profiles are measured by Ultrasound Doppler Velocimetry (UDV) with ultrasonic transducers being placed perpendicular on the plexiglas crucible surface at 3 different positions for one flow plane at a time (fig 1 a, fig 2). The experimental velocity profiles are then compared to numerical ones extracted from the simulations, which correspond to the same position.

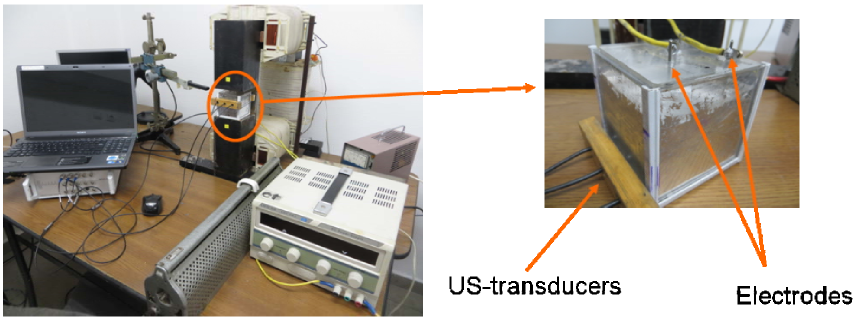

Figure 2: EMS model experiment set-up with a GaInSn melt in a plexiglas crucible connected through electrodes to a DC source and placed inside an electromagnet's vertical magnetic field.

3. Results and discussions

The combination of a vertical magnetic field and radial components of the electrical current generates a Lorentz force distribution inside the melt, which gives rise to different flow structures, depending on electrical current intensity, magnetic field induction and electrode positioning.

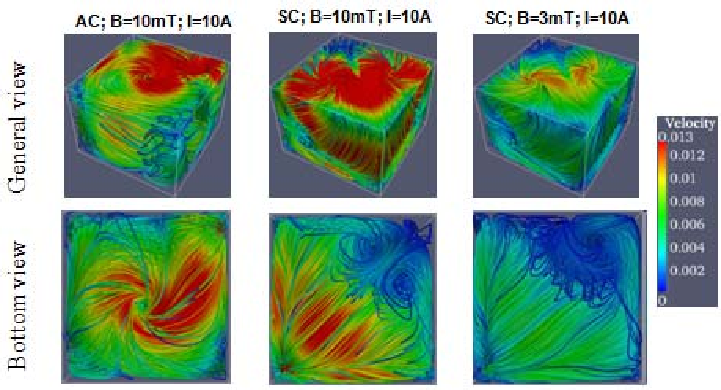

(a) (b) (c)

Figure 4: Flow structures particle tracking for: (a) asymmetrical electrodes position at I = 10 A, B= 10 mT; (b) symmetrical electrodes position for I = 10 A, B = 10 mT; (c) symmetrical electrodes position for I = 10 A, B = 3 mT.

The flow structure depends on the electrodes positioning. It can be seen from fig 4a that, in the case of an asymmetrical electrode positioning, the flow structure is dominated by an azimuthal rotation around the central electrode, while in the case of the electrodes symmetrical positioning (fig 4b,c), the flow structure changes from a spiraling rotation around the two electrodes at the top to a meridional recirculation at the bottom. It is also a notable fact that the melt stirring is also strong for a magnetic field of just 3 mT (fig 4c).

Using the experimental set-up described in section 2, velocity profiles have been obtained through the ultrasound Doppler velocity profile method, in order to validate the numerical model. The main area of interest presented here is the region close to the bottom of the crucible, which is chosen because it is important to see if the flow is strong enough at the melt-crystal growth interface to avoid impurity accumulation in the boundary layer in front of it.

In fig 5, the velocity field from the 45 mm height plane is represented. At this plane velocity profiles taken from 7 mm, 35 mm and 63 mm from the edge are compared with the ones measured in the experiment at the same position. The experimental values represent the flow velocity projection on the US beam axis. By convention, a negative velocity is oriented towards the US transducer, while a positive one points away from it. The experimental results show a better agreement for the AC case (fig 5a), where the flow structure is simpler than for the SC one (fig 5b). The velocity in a point from the experimental profiles represents the average velocity in a volume centered in that point, which is limited by the lateral US beam divergence. Therefore, if the spatial velocity gradient is higher (associated to a more complex flow structure like in the SC case) the average velocity volume is farther away from the point value taken from the simulation. Also, the material constants may vary slightly in reality from the values considered in the simulations and this, along with the auto-induced magnetic field, can also be a cause of the differences between numerical model and experiment.

As was observed from the flow structures particle tracking in fig 4, the experimental results also show that for the AC the rotation set in motion at the electrodes level goes down all the way to the bottom, while it changes from top to bottom for the electrodes SC.

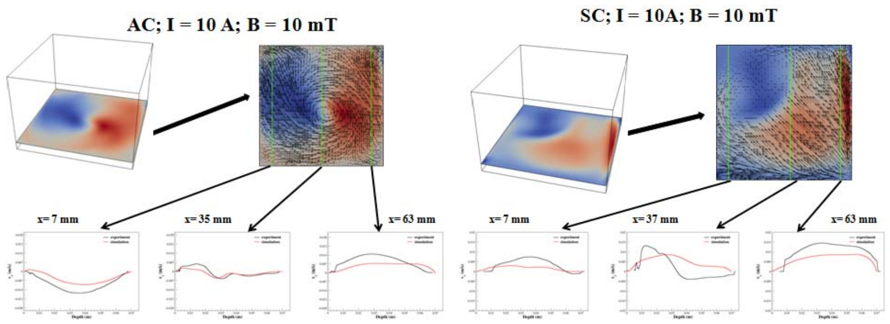

(a) (b)

Figure 5: Experimental and numerical velocity profiles at 10 A, 10 mT compared for :
(a) asymmetrical case; (b) symmetrical case.

4. Conclusions

It was found that even a small magnetic field (3-10 mT) and an electrical current in the electrodes of maximum 10 A can produce a significant stirring effect. Melt rotation develops in the whole mass of the melt, which could have a beneficial effect for the application of this technique to silicon DS for photovoltaic applications. This is important because it could be more cost effective to implement a smaller magnetic field inside a DS furnace, or maybe use the magnetic field generated by the induction coils in the cases where the furnace uses inductive heating. The numerical results for the melt convection (intensity and flow patterns) are in good agreement with the experimental findings. The results prove the potential of the proposed method to control convective flows in a rectangular crucible relevant for the silicon DS method.

5. References

[1] Reimann, C.; Trempa, M.; Jung, T.; Friedrich, J.; Müller, G.: Modeling of incorporation of O, N, C and formation of related precipitates during directional solidification of silicon under consideration of variable processing parameters. Journal of Crystal Growth 312 (2010) 878–885.

[2] Chen, X.; Nakano, S.; Kakimoto, K.: Three-dimensional global analysis of thermal stress and dislocations in a silicon ingot during a unidirectional solidification process with a square crucible. Journal of Crystal Growth 312 (2010) 3261–3266.

[3] Vizman, D.; Friedrich, J.; Müller, G.: 3D time-dependent numerical study of the influence of the melt flow on the interface shape in a silicon ingot casting process. Journal of Crystal Growth 303 (2007) 231–235.

[4] Miyazawa, H.; Liu, L.; Hisamatsu, S.; Kakimoto, S.: Numerical analysis of the influence of tilt of crucibles on interface shape and fields of temperature and velocity in the unidirectional solidification process. Journal of Crystal Growth 310 (2008) 1034–1039.

[5] Kuliev, A.T.; Durnev, N.V.; Kalaev, V.V.: Analysis of 3D unsteady melt flow and crystallization front geometry during a casting process for silicon solar cells. Journal of Crystal Growth 303 (2007) 236–240.

[6] Teng, Y.; Chen, J.; Lu, C.; Chen C.: The carbon distribution in multicrystalline silicon ingots grown using the directional solidification process. Journal of Crystal Growth 312 (2010) 1282–1290.

[7] Popescu, A.; Vizman, D.: Numerical Study of Melt Convection and Interface Shape in a Pilot Furnace for Unidirectional Solidification of Multicrystalline Silicon.Crystal Growth and Design 12 (2012) 320–325.

[8] Pihan, E. et al.: Influence of Lateral Temperature on Light Elements Precipitations during MC-SI Crystallization in a DS Furnace. 26th EU PVSEC Conference (2011), 1900 - 1903

[9] Zheng, L.; Ma, X.; Hu, D.; Zhang, H.; Zhang, T.; Wan, Y.: Mechanism and modeling of silicon carbide formation and engulfment in industrial silicon directional solidification growth. Journal of Crystal Growth 318(2011), 313–317.

[10] Rudolph, P.: Travelling magnetic fields applied to bulk crystal growth from the melt: The step from basic research to industrial scale. Journal of Crystal Growth 310 (2008) 1298–1306.

[11] Dropka, N.; Frank-Rotsch, Ch.; Miller, W.; Rudolph P.: Influence of travelling magnetic fields on S–L interface shapes of materials with different electrical conductivities. Journal of Crystal Growth 338 (2012) 208–213.

[12] Dadzis, K.; Ehrig, J.; Niemietz, K.; Patzold, O.; Wunderwald, U.; Friedrich, J.: Model experiments and numerical simulations for directional solidification of multicrystalline silicon in a traveling magnetic field. Journal of Crystal Growth 333 (2011) 7–15.

[13] Griffiths, W.D.; McCartney, D.G.: The effect of electromagnetic stirring during solidification on the structure of Al-Si alloys. Materials Science and Engineering A 216 (1996) 47–60.

[14] Willers, B.; Eckert, S.; Michel, U.; Haase, I.; Zouhar, G.: The columnar-to-equiaxed transition in Pb–Sn alloys affected by electromagnetically driven convection. Materials Science and Engineering A 402 (2005) 55–65.

[15] Willers, B.; Eckert, S.; Nikrityuk, P.A.; Räbiger, D.; Dong, J.; Eckert, K.; Gerbeth, G.: Efficient Melt Stirring Using Pulse Sequences of a Rotating Magnetic Field: Part II. Application to Solidification of Al-Si Alloys. Metallurgical and Materials Transactions B 39 (2008) 304–316.

[16] Tanasie C.; Vizman D.; Friedrich J.: Numerical study of the influence of different types of magnetic fields on the interface shape in directional solidification of multi-crystalline silicon ingots. Journal of Crystal Growth 318 (2011) 293–297.

[17] Vizman D.; Tanasie C.:Novel method for melt flow control in unidirectional solidification of multi-crystalline silicon. Journal of Crystal Growth 372 (2013) 1–8.

[18] Dumitrica, S.; Vizman, D.; Garandet, J.-P.; Popescu, A.: Numerical studies on a type of mechanical stirring in directional solidification method of multicrystalline silicon for photovoltaic applications. Journal of Crystal Growth 360 (2012) 76–80.

[19] Watanabe M.; Eguchi M.; Hibiya T.: Silicon Crystal Growth by the Electromagnetic Czochralski (EMCZ) Method. Japanese Journal of Applied Physics 38 (1999) 10-13

MODELLING OF PATTERN FORMATION DURING THE MELTING OF SILICON BY HF EM FIELD

BERGFELDS K., VIRBULIS J., KRAUZE A.
Faculty of Physics and Mathematics, University of Latvia
8 Zeļļu str., LV-1002, Riga, Latvia
E-mail: kristaps.bergfelds@lu.lv

Abstract. The present work investigate causes of inhomogeneous silicon melting during floating-zone crystal growth. It is proposed that this phenomenon is caused by the concentration of electric current in the melt which is caused by the different material properties of silicon melt and solid. Coupled model of EM, temperature and phase change field is developed and used to describe the transient melting-solidification process. *Octave/Matlab* script language is used for the implementation of this model. Calculation results demonstrate that melt structure development is related to the magnetic skin-depth in solid silicon

1. Introduction

During floating-zone (FZ) crystal growth, high-frequency electromagnetic (HF EM) field is used to melt the polycrystalline silicon feed rod. Usually inductor current with a frequency around 3 MHz is used to ensure sufficiently small penetration depth of the EM field for proper melting of the feed rod [1]. In case of lower frequencies, instable shape of feed rod melting surface can develop [2].
However, even with 3 MHz inductor current, ring-like silicon melt structures parallel to the current lines are formed during the FZ process on the surface of the feed rod with radial size of 1-2 mm (Fig. 1, left). Similar non-homogenous melting occurs when 5 mm thick silicon plate is located under the HF inductor (Fig. 1, right). Resulting melt pattern can be used to determine the asymmetry of the inductor currents [3].

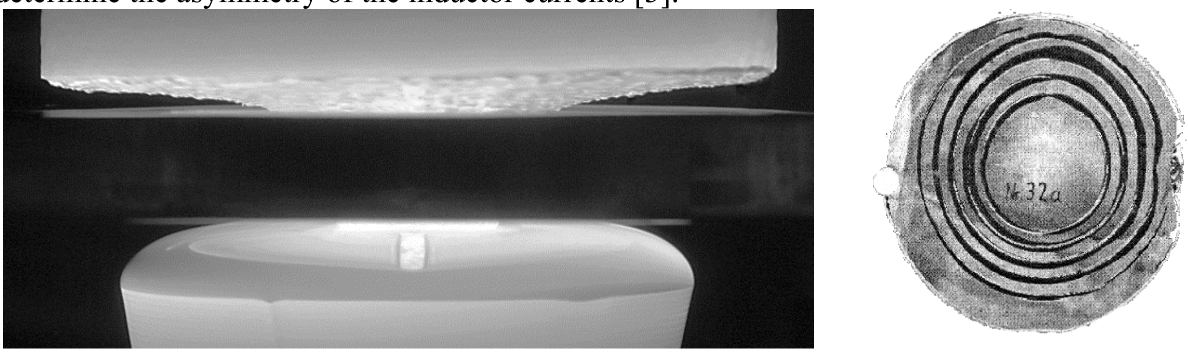

Figure 1: Left: inhomogeneous melting front on the feed-rod in a floating-zone silicon growth process [1]. Right: molten rings on a silicon plate created by HF EM inductor [3].

It is important to understand the formation of these structures as it is crucial to ensure continuous and stable melting during the FZ process. The ability to maintain stable growth at relatively low frequencies can even be regarded as key for growing larger diameter FZ crystals, i.e. larger melting powers can be achieved by lowering the frequency and thus inductor impedance [4]. Such motivation dictates that research regarding inhomogeneous melting during silicon HF EM melting is a worthwhile effort.

Melt pattern formation on silicon material has been studied previously – laser beam irradiation on a silicon surface creates ridges with size comparable to radiation wavelength and orientation determined by the beam polarization [5]. Such situation arises due to interference between incident beam and scattered radiation from surface imperfections. This example shows that periodic material structures are common result of non-linear system evolution. It is also clear that revealing the driving force of such pattern formation is a valuable contribution to the understanding of processes within such non-linear systems.

2. Mathematical model

Previously described problem is studied in a local scale. Two-dimensional domain of solid silicon with dimensions of 5×5 mm and orientation normal to direction of electric current is chosen (Fig. 2). It is believed to be small enough to assume homogenous boundary conditions, but sufficiently large for considered melt structures to develop. In this region temperature and phase change is calculated. In order to obtain EM induced heat sources, magnetic field is calculated in the silicon as well as in the air region between silicon and inductor surfaces. It is assumed that inductor is located 5 mm from the silicon surface. All calculations are carried out by using finite difference method implemented within *Octave/Matlab* environment.

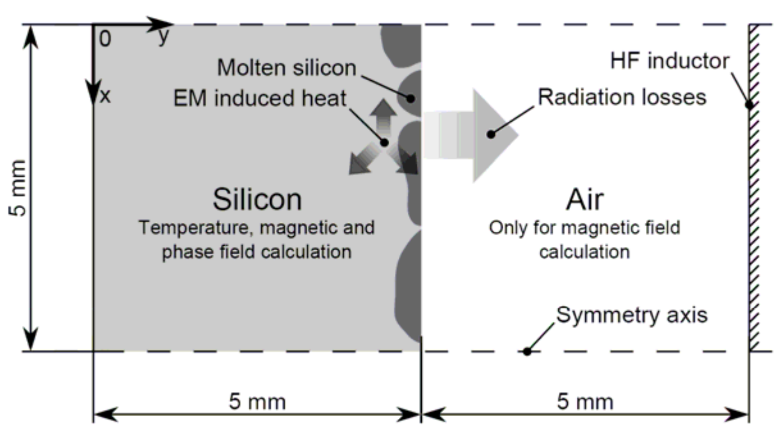

Figure 2: Schematics of the modelled system. Domain size and modelled physical processes are depicted.

Phase field model [6] is used to describe transient melting-solidification process. Assumption has been made that the phase transition happens within a narrow temperature interval ΔT_S. In such case the crystallization fraction f_c could be modeled as the temperature function (1).

$$f_c = \begin{cases} 0 & \text{if} \quad T > T_0 + {\Delta T_S}/{2} \\ \dfrac{T_0 + {\Delta T_S}/{2} - T}{\Delta T_S} & \text{if} \quad T \geq T_0 - {\Delta T_S}/{2} \text{ and } T \leq T_0 + {\Delta T_S}/{2} \\ 1 & \text{if} \quad T < T_0 - {\Delta T_S}/{2} \end{cases} \tag{1}$$

With such assumption, the transient equation of conductive heat transfer can be written as (2). Insulation boundary conditions are used on the symmetry axis, fixed temperature value on the inside of the domain, but radiation condition on the surface with air.

$$\left(\rho c_p - L\frac{\mathrm{d}f_c}{\mathrm{d}T}\right)\frac{\partial T}{\partial t} = \lambda \Delta T + q_{EM} \tag{2}$$

EM induced heat sources q_{EM} are obtained by calculating the magnetic vector potential (3) which has only one non-zero component in the chosen system geometry. Zero-value boundary condition is used on the inside of silicon domain, but fixed-value condition on inductor surface is varied to account different inductor currents and thus melting powers.

$$\frac{\partial^2 A_z}{\partial x^2} + \frac{\partial^2 A_z}{\partial y^2} - i\omega\sigma\mu A_z = 0, \qquad q_{EM} = \frac{|-i\sigma\omega A_z|^2}{\sigma} \tag{3}$$

Material properties that are relevant to the developed mathematical model are listed in [7, 8]. These values are obtained by laboratory experiments and extensively used for mathematical modelling purposes. Electrical conductivities for melt $\sigma_m = 1.2 \cdot 10^6\ {}^{S}/_{m}$ and solid

$\sigma_s = 5 \cdot 10^4\ S/m$ should be noted as important parameters regarding the investigated problem. Emissivity coefficient is modelled as temperature dependent parameter (Fig. 3, left).

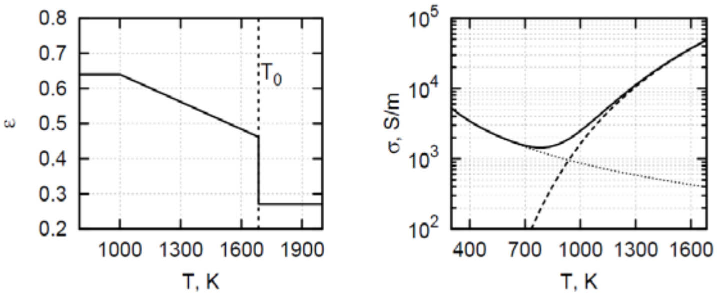

Figure 3: Left: modelled silicon emissivity coefficient temperature dependence. Right: modelled temperature dependence of solid silicon (solid line) as sum of conduction electron generation (dashed line) and conductivity due to dopants (dotted line).

When calculation studies involve large temperature intervals, temperature dependent heat conductivity of solid silicon is considered as suggested in [9]. Assumption is made that conductivity is determined of two processes – generation of conductivity electrons and presence of dopants in the material (Fig. 3, right).

3. Calculation results

Calculations were first carried out with a setup and mesh shown in Fig. 4. After 20 s stationary structure of melt regions with a size of about 1.4 mm were obtained for a certain simulated inductor current interval (Fig. 5). The magnetic field lines are bended in Si and gas and the induced heat sources are concentrated in molten regions.

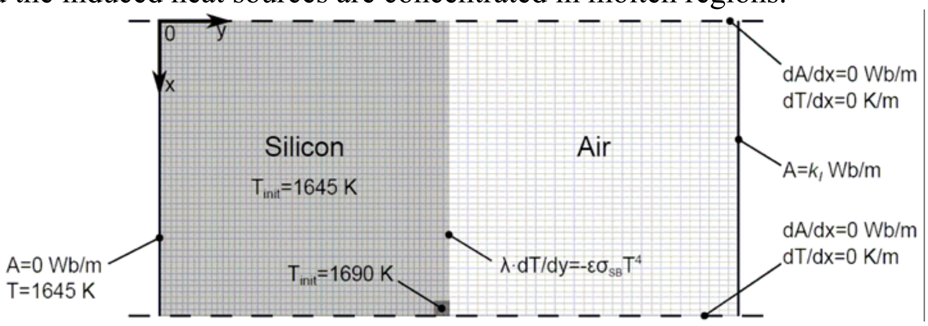

Figure 4: Schematics of the modelled system. Calculation mesh, initial and boundary conditions are displayed.

Such structures are obtained when initial temperature field perturbation is used. In case of uniform initial temperature field, completely uniform melting process occurs with no phase-field distribution variation along the direction of silicon surface. Further studies indicated that inhomogeneous vector potential boundary condition (linear distribution of 5–10% slope on 5 mm length) is also sufficient to obtain observed melt patterns.

Further studies considered different materials properties to locate the determinative parameters that ensure the melt pattern formation. Varied parameters were: solid silicon electrical conductivity, magnetic field frequency and emissivity coefficient of silicon melt.

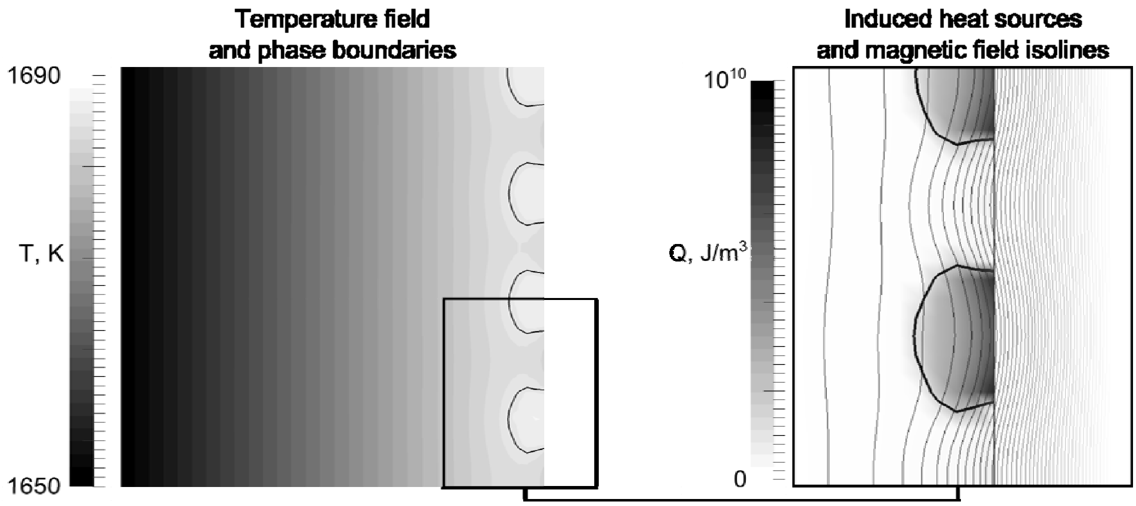

Figure 5: Calculation results for case with stationary melt structures developed during the course of 20 s treatment with HF EM field.

By applying equal and fixed value of 0.64 as emission coefficient of both melt and solid, it was observed that pattern formation still occurred. This proves that different emissivity properties of solid and liquid Si are not imperative for the observed phenomena. However, in this study solid silicon layer formed on top of melt regions due to comparatively larger radiative losses from the surface.

By varying the solid silicon conductivity, different spatial pattern distribution developed (Fig. 6, left). Additionally, EM field frequency variation causes similar effect. Such situation can be analyzed in a context of skin-depth $\delta = 1/\sqrt{\pi f \sigma \mu}$ (where f is frequency, σ is electrical conductivity, but μ is magnetic constant). Such approach illustrates the process characteristics at least qualitatively (Fig. 6, right). It must be noted that spatial pattern remained unchanged if different length of silicon surface l_x was used for calculations (blue and yellow lines in Fig. 6, right).

To simulate aforementioned practices with 5 mm thick Si plate under HF EM inductor, calculations using radiation boundary condition on both sided of silicon domain were performed. Additionally, initial temperature of 300 K were used in the domain (with 45 K perturbation at the corner) to simulate the effects of hugely varying electrical conductivity (as in Fig. 3, right). In this case non-stationary melt patterns were obtained at about 20% higher inductor powers as previous studies with fixed temperature boundary condition (Fig. 7). It must be noted that distance between observed melt regions is noticeably larger.

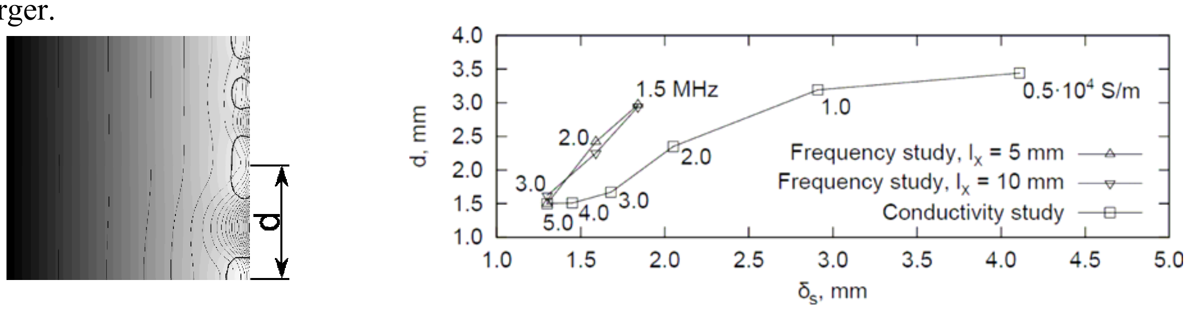

Figure 6: Left: Calculated temperature field, phase boundary (thick black line) and magnetic field at reduced electrical conductivity of $2{\cdot}10^4$ S/m. Right: melt region size as a function of skin-depth in solid silicon for calculation studies with various frequencies (triangular data points) and solid silicon electrical conductivities (rectangular data points).

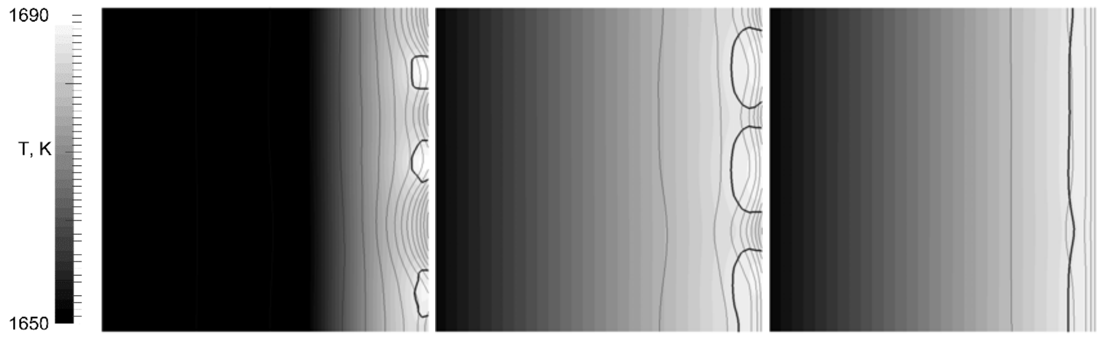

Figure 7: Calculated temperature field, phase boundary (thick black line) and magnetic field (thin black lines). From left to right: time instances of 3.5, 8.0 and 16.0 seconds.

4. Conclusions

Present work demonstrates that melt pattern formation during inductive melting of Si is determined by the EM field interaction with two-phase environment with different electrical conductivities. Characteristic size of patterns has been shown to be around 1.4 mm which corresponds well to observed situation in floating-zone furnaces. Wider structures are obtained at lower solid Si electrical conductivities which also correspond qualitatively to observations [3]. It has been shown that, in general, size of patterns is related to the skin-depth in the solid material and thermal boundary conditions.

5. Acknowledgements.

This work has been supported by the European Regional Development Fund, project Contract № 2013/0051/2DP/2.1.1.1.0/13/APIA/VIAA/009.

6. References

[1] T. Duffar, Crystal Growth Processes Based on Capillarity: Czochralski, Floating Zone, Shaping and Crucible Techniques, Wiley-Blackwell, 2010.

[2] W. Wünscher, A. Lüdge and H. Riemann, "Crucible-free pulling of germanium crystals," *Journal of Crystal Growth,* vol. 318, no. 1, pp. 1039-1042, 2011.

[3] H. Riemann, A. Ludge, K. Bottcher, H. J. Rost, B. Hallmann, W. Schroder, W. Hensel and B. Schleusener, "Silicon Floating Zone Process: Numerical Modeling of RF Field, Heat Transfer, Thermal Stress, and Experimental Proof for 4 Inch Crystals," *Journal of The Electrochemical Society,* vol. 142, no. 3, pp. 1007-1014, 1995.

[4] R. Menzel, "Growth Conditions for Large Diameter FZ Si Single Crystals," *Ph.D. Thesis at the Technische Universität Berlin,* 2013.

[5] J. F. Young, J. S. Preston, H. M. van Driel and J. E. Sipe, "Laser-induced periodic surface structure. II. Experiments on Ge, Si, Al, and brass," *Phys. Rev. B,* vol. 27, no. 2, pp. 1155-1172, 1983.

[6] I. Steinbach, M. Apel, T. Rettelbach and D. Franke, "Numerical simulations for silicon crystallization processes—examples from ingot and ribbon casting," *Solar Energy Materials and Solar Cells,* vol. 72, no. 1-4, pp. 59-68, 2002.

[7] A. Muhlbauer, A. Muiznieks, J. Virbulis, A. Ludge and H. Riemann, "Interface shape, heat transfer and fluid flow in the floating zone growth of large silicon crystals with the needle-eye technique," *Journal of Crystal Growth,* vol. 151, no. 1-2, pp. 66-79, 1995.

[8] A. Sabanskis, K. Bergfelds, A. Muiznieks, T. Schröck and A. Krauze, "Crystal shape 2D modeling for transient CZ silicon crystal growth," *Journal of Crystal Growth,* vol. 377, pp. 9-16, 2013.

[9] C. Kittel, Introduction to Solid State Physics, 8th ed., Wiley, 2005.

ANISOTROPY OF FLOW AND TRANSITION BETWEEN MIXING REGIMES IN STRATIFIED EM FORCE GENERATED FLOW

GEZA[1] V., BAAKE[1] E., NACKE[1] B., JAKOVICS[2] A.
[1]Leibniz University of Hanover, Institute of Electrotechnology, Hannover, Germany
[2]Laboratory for Mathematical Modelling of Environmental and Technological Processes, University of Latvia, 8 Zellu, Riga, Latvia
E-mail: geza@etp.uni-hannover.de

As fossil energy resources are getting exhausted, demand for alternative energy sources is growing. In 2011 in Germany the renewable energy part was 12.5%, which is almost doubled since 2005 [1]. Photovoltaic solar energy still has small fraction of the total power production – only around 2% - but it is still growing. Directional solidification (DS) is widely used for the production of photovoltaic materials for convenient and material-loss effective wafer production. The production process of the polycrystalline material influences the quality of the wafers significantly and for this reason design of DS furnaces has to be proceeded with care. One of aspects influencing the successful material production is the melt flow in the crucible during solidification stage [2]. This work is devoted to numerical and experimental investigation of the Lorentz force generated turbulent melt motion at moderate Reynolds numbers (2000-10000) in a square crucible where vertical temperature gradient is present and causing stratification of flow.

Experimental results were obtained using physical model, which consisted of square crucible, placed on aluminium plate with constant temperature and covered by heater-lid, which allowed obtaining vertical temperature gradient in melt. Wood's alloy (50% Bi, 25% Pb, 12.5% Sn, 12.5% Cd, melting temperature 72°C) was used as working liquid. Experimental set-up allows measuring velocity field in the crucible using Ultrasound Doppler Velocimetry (UDV) technique and temperature dynamics using thermocouples. Results show that there is steep transition from 3D flow to quasi two-dimensional flow near critical Richardson number Ri_{CR}~5..10. As Richardson number increases any vertical motion of fluid becomes more damped by buoyancy forces and 2D turbulence takes place. However, 2D turbulence appears at reasonably higher Richardson numbers than transition to 2D flow, $Ri \sim 10^3$, which is not possible to realize in this experimental set-up. Stratified flow is well known to possess wave-like flow character in high-Ri region, where so-called weak mixing regime with high turbulent Prandtl number takes place [3].

Numerically the melt flow in described system was investigated using Large Eddy Simulation (LES) approach. Simplified thermal boundary conditions were used – constant temperature at bottom, adiabatic walls and constant temperature or convective type boundary condition at top. OpenFOAM code was used for fluid dynamics calculations and GetDP as electromagnetic solver. LES results match well with UDV measurements and also show transition between different flow regimes at Ri_{CR}. Another issue resolved in LES is that anisotropy of flow increases with Richardson number. To quantify this effect anisotropy coefficient was used. LES results also show that in such square crucible plane of symmetry of flow field can differ from plane of symmetry of EM forces.

References

[1] Bohme, D.: Entwicklung der erneuerbaren Energien in Deutschland im Jahr 2011. http://www.erneuerbare-energien.de.
[2] Reimann, C. et al.: Journal of Crystal Growth, 2010, vol. 312. p. 878.
[3] Zilintikevich, S.S. et al.: Q. J. R. Meteorol. Soc. 134 (2008) 793–799.
[4] Smith, W.D. et al.: Phys. Fluids, 2000, vol. 12, no. 6. p. 1343-1362.

MODELING OF MELTING AND SOLIDIFICATION PROCESSES OF PHOTOVOLTAIC SILICON IN A TRAVELING MAGNETIC FIELD

DADZIS[1] Kaspars, LUKIN[2] Gleb, FÜTTERER[2] Wolfgang, BÖNISCH[1] Paul, SYLLA[1] Lamine, PÄTZOLD[1] Olf

[1]SolarWorld Innovations GmbH, Berthelsdorfer Str. 111A, 09599 Freiberg, Germany

[2]Inst. f. NE-Metallurgie und Reinststoffe, TU Bergakademie Freiberg, Leipziger Str. 34, 09599 Freiberg, Germany

E-Mail: kaspars.dadzis@sw-innovations.de

Abstract: Directional solidification of silicon is modeled using a gallium volume with a square horizontal cross-section and dimensions of 10x10x7.5 cm^3. The container with gallium is heated at the top and cooled at the bottom. It is placed in a coil system generating a traveling magnetic field. Coupled 3D numerical simulations of melt flow and phase interface are carried out and compared to first experimental measurements of temperatures in gallium and the phase interface motion. The transfer of the results to silicon melts using scaling laws is discussed.

1. Introduction

The directional solidification process is used in the photovoltaic industry to produce large silicon ingots with a weight up to 1000 kg. In a crystallization furnace, silicon raw material is first melted and then directionally solidified in a square-shaped silica crucible that is surrounded by several heaters at the side or top and a heat sink at the bottom. In the liquid silicon, a flow is usually generated by buoyancy or Marangoni forces as well as by Lorentz forces due to alternating currents in the heaters or additional inductors. It has been shown that there is a tight mutual interaction between the melt flow and the shape and velocity of the melting or solidification interface [1]. Melt flow may significantly change the temperature gradients and the phase interface shape, whereas a geometrically large deformation of the interface may lead to significant changes in the flow pattern. For example, the effect of small Lorentz force inhomogeneities on the flow pattern can be considerably increased due to this interaction [1].

Direct experimental investigations of processes in silicon melts are generally very complicated due to the high melting point of 1685 K. While numerical simulations can be a very useful tool for such investigations, the numerical models must be verified and validated. This can be achieved using model experiments in low-melting-point low-Prandtl-number metals, such as gallium. Pure gallium allows for an induction of Lorentz forces similarly to a silicon melt and can be also solidified in a controlled manner [2, 3, 4].

A new experimental setup for model experiments has been developed recently [5]. It contains a model melt with a square horizontal cross-section of 10x10 cm^2 and variable height up to 10 cm. The melt is located within a coil system that generates a traveling magnetic field (TMF). A cooling system at the bottom and a heating system at the top of the melt enable to generate a vertical temperature difference up to about 50 K. Various experiments with a GaInSn melt and ultrasonic measurements of the flow pattern as well as temperature measurements with thermocouples have been already presented in [5]. This contribution focuses on melting and solidification processes of gallium in this experimental setup. Thermal regimes of the heater and cooler to obtain a continuous phase interface movement are discussed. The coupled problem of melt flow and phase interface motion under the influence of a magnetic field is investigated by 3D numerical simulations.

2. Numerical model

The 3D time-averaged Lorentz force F_L induced by the TMF in the melt was calculated using the finite element package *GetDP* by solving the time-harmonic equations for the electric and magnetic potentials V and A:

$$\nabla \times \nabla \times \vec{A} = \mu_0 \vec{j}\,, \quad \nabla \cdot \vec{j} = 0\,, \quad \vec{B} = \nabla \times \vec{A}\,, \quad \vec{j} = \sigma\left(-i\omega\vec{A} - \nabla V\right), \quad \vec{F}_L = \left(\vec{j}^* \times \vec{B}\right)_{re}/2\,,$$

where j is the current density, B is the magnetic field, and $\omega = 2\pi f$ is the current frequency. Material properties are given in Tab. 1. See [6] for further details. The Lorentz force was imported into the finite volume package *OpenFOAM*, which was used to solve the coupled unsteady equations of melt velocity u and melt/ crystal temperature T:

$$\rho\left[\frac{\partial \vec{u}}{\partial t} + (\vec{u} \cdot \nabla)\vec{u}\right] = -\nabla p + \eta \Delta \vec{u} + \vec{F}_L - \beta(T - T_0)\rho\vec{g}\,, \quad \nabla \cdot \vec{u} = 0\,, \quad \rho c\left[\frac{\partial T}{\partial t} + (\vec{u} \cdot \nabla)T\right] = \lambda \Delta T$$

In each time step, the finite volume grid was deformed according to the interface velocity distribution v_n, which was calculated from the local heat balance on the solid (S) and liquid (L) sides: $v_n \rho_S q_0 = \lambda_S \partial T/\partial n|_S - \lambda_L \partial T/\partial n|_L$. See [1] for further details of the model.

Property	Symbol, Units	Ga: solid	Ga: liquid	Si: solid	Si: liquid
Density	ρ [kg/m^3]	5904	6116	2329	2520
Viscosity	η [Pa·s]	-	0.00213	-	0.00076
Specific heat	c [J/kg·K]	374	360	986	986
Therm. conductivity	λ [W/m·K]	40.8	34.1	22	67
Therm. expansion	β [1/K]	-	0.00013	-	0.000144
Elec. conductivity	σ [S/m]	-	3.9e6	-	1e6
Latent heat	q_0 [J/kg]	8e4 (29.76 °C)	-	1.8e6 (1412 °C)	-

Table 1: Material properties of solid and liquid gallium (e.g., [7]) and silicon [1] used in this study.

The model was tested with a benchmark [2] for the melting of gallium influenced by buoyancy forces. An initially solid volume of 64x38x89 mm^3 is considered with a prescribed temperature T_H = 38 °C on the left and T_C = 28.3 °C on the right wall. Melting starts at the left (hot) wall, with the interface moving toward the right wall. A 3D simulation was carried out with 30x43x33 fluid and 30x43x27 solid elements, with the initial melt grid compressed to 4.5 mm (this introduces a time offset of about 1 min). The interface shape for several time instants is shown in Fig. 1 and demonstrates a good agreement with both experimental and numerical literature data.

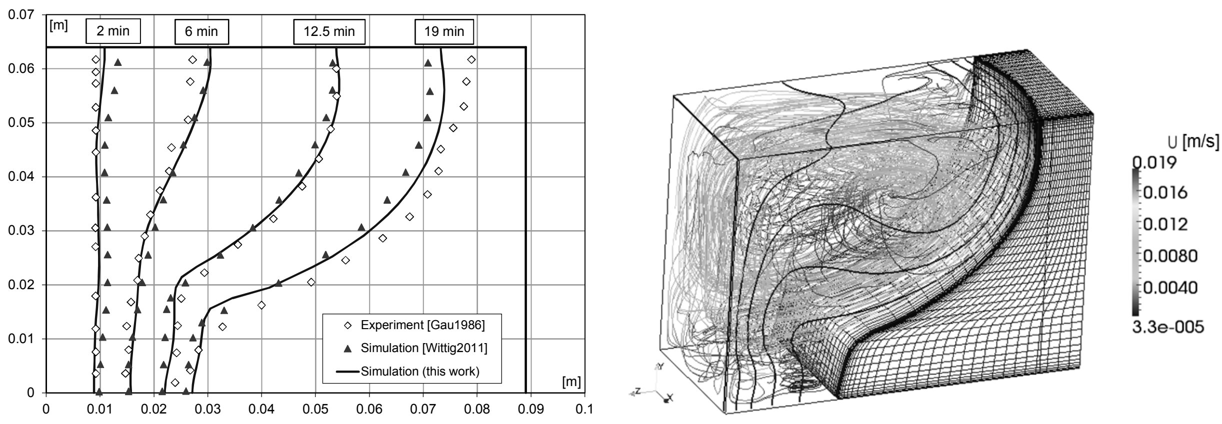

(a) (b)

Figure 1: (a) Calculated melting interface shape for several time instants in comparison with literature data [2, 8]; (b) Deformed crystal mesh, flow streamlines, and temperature isolines at the walls in the simulation after 20 min.

3. Numerical results

We consider the experimental setup from [5] but with pure gallium instead of GaInSn, with a height of 7.5 cm. The Lorentz force distribution (see Fig. 2) from [5] for GaInSn with a height of 5 cm is used here for gallium neglecting the relatively small difference in electrical conductivities. Furthermore, the force distribution is deformed in *OpenFOAM* together with the grid, without recalculation for different melt heights. The grid in *OpenFOAM* consists of 42x42x27 fluid elements and 42x42x13 solid elements, the melt height is initially compressed to 3.8 mm. No slip conditions on all melt boundaries are used for the velocity field; buoyancy and Lorentz forces are considered in the volume. Sidewalls are assumed adiabatic for the temperature calculation. At the crystal bottom and melt top, heat transfer between gallium and heater (H) or cooler (C) is described according to $\lambda_{S/L}\partial T/\partial n\big|_{S/L} = p_{C/H}(T - T_{C/H})$. The heat transfer coefficient $p_{C/H}$ = 1563 W/m^{2}K from [5] is applied.

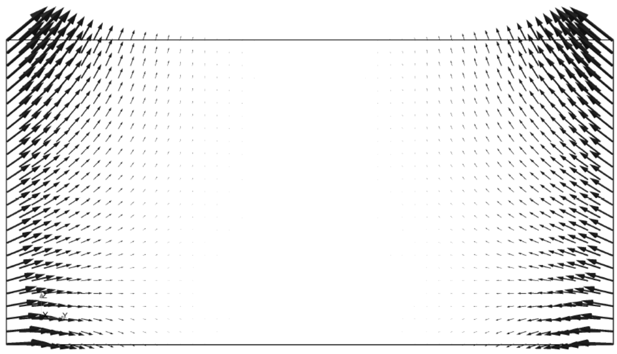

Figure 2: Lorentz force distribution in a vertical cut (F_{Lmax} = 115 N/m^3) for a melt height of 5 cm due to 6 coils generating an upward TMF with a frequency of 50 Hz [5].

Two simulations were carried out with different vertical temperature gradients (approximately 1 K/cm and 4 K/cm in the melt without flow), which were set by the cooler/ heater temperatures T_C/ T_H. Solid gallium is first melted down to approximately 1 cm thickness in the center, then the cooler/ heater temperatures are switched and the melt is solidified again. The results are summarized in Fig. 3. It can be seen that a 4 times higher temperature gradient leads to about 3 times shorter melting and solidification times in the cases without melt flow. The melt flow reaches only 8 mm/s with a high (stabilizing) temperature gradient and has practically no influence on the phase interface, see Fig. 3(a). A low temperature gradient is not able to damp the TMF-induced flow structure, the melting time is significantly reduced due to the flow, and the phase interface develops a deflection of about 1 cm.

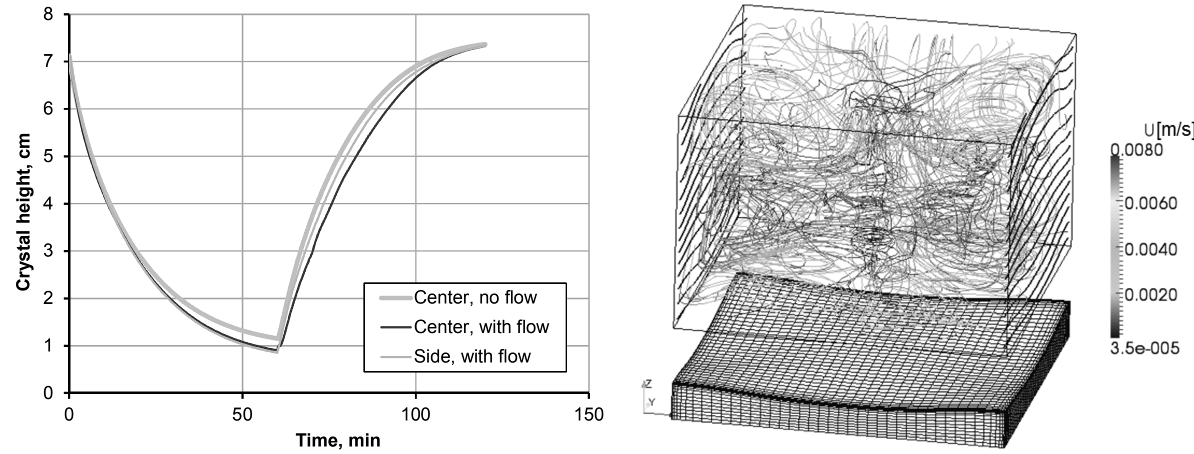

(a) Melting: T_H / T_C = 64.5/ 17.8 °C; solidification: T_H / T_C = 38.5/ −3.9 °C

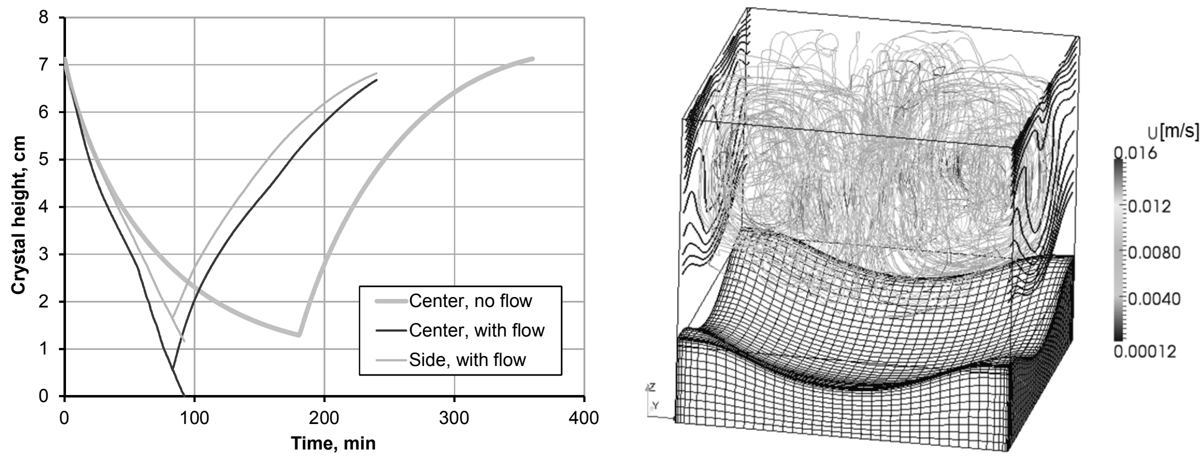

(b) Melting: T_H / T_C = 38.5/ 26.8 °C; solidification: T_H / T_C = 32.0/ 21.4 °C

Figure 3: Numerical simulations with various heater/ cooler temperatures (a,b). Phase interface motion in the center and at the side (left); deformed crystal mesh, flow streamlines, and temperature isolines at the walls after the melting phase (right).

4. Experimental results

The experimental setup as described in the previous section and in [5] was adjusted for experiments with gallium. A slightly different cooler design, stronger joints between the sidewalls, new coatings of the heater and cooler were introduced in particular. The most important changes for numerical modeling are different heat transfer coefficients of the heater (temperature T_H) and cooler (temperature T_C). They were determined from measurements of temperatures at the top (T_T) and bottom (T_B) of solid or liquid gallium of height H. With an approximate vertical heat flux density through gallium $q = \lambda_{S/L}\left(T_T - T_B\right)/H$ it was estimated $p_C = q/\left|T_C - T_B\right| = 600$ and $p_H = q/\left|T_H - T_T\right| = 450$ W/m^{2}K.

Fig. 4 summarizes the first experimental results. Solid gallium of 7.5 cm height was first melted and then solidified without TMF. In addition to the temperatures at the top and bottom, phase interface motion was measured by ultrasonic Doppler velocimetry through the heater using the equipment from [5]. While the temperatures and the melting rate agree well with numerical calculations, the solidification rate shows some deviations. These might be caused by an asymmetric phase interface, probably due to the anisotropic thermal conductivity of solid gallium [2]. Further experiments are required to evaluate the reproducibility of these results.

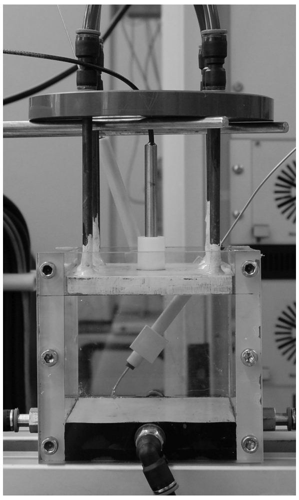

(a)

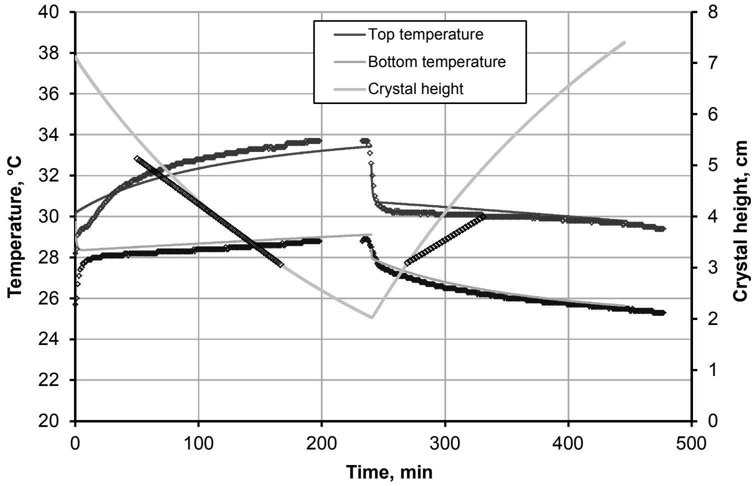

(b)

Figure 4: (a) Photo of the experimental setup (without melt); (b) measured (dots) and calculated (lines) temperatures and interface position during melting (T_H / T_C = 38.5/ 26.8 °C) and solidification (T_H / T_C = 32.0/ 21.4 °C) without TMF.

5. Scaling of results

The topic of scaling between small-scale model experiments with GaInSn and silicon processes has been discussed in [5, 6]. The same approach can be used also for gallium, with additional parameters describing the phase change. We consider scaling from gallium (the case with solidification in Fig. 3(b)) with a characteristic length L_0 = 5 cm to silicon with L_0 = 10 cm. The following dimensionless numbers can be kept constant

$$S_{EM} = \mu_0 \sigma \omega L_0^2 = 3.8\,,\; F_{EM} = F_{L0} \frac{L_0^3 \rho_L}{\eta^2} = 2 \cdot 10^7\,,\; J_{S/L} = \lambda_{S/L} \frac{\Delta T_{S/L}}{q_0 \rho_S L_0 v_0} = 2.5 / 0.5$$

by adjusting the frequency f = 50 → 48 Hz, Lorentz force density (by inductor current) F_{L0} = 115 → 4.5 N/m^3, temperature difference in the melt ΔT_L = 2 → 5 K and crystal ΔT_S = 8 → 68 K. As a consequence the flow velocity changes as u_0 = 1 → 0.4 cm/s and solidification velocity as v_0 = 2 → 0.5 cm/h. The Peclet and Grashof numbers are not kept constant:

$$Re = \frac{u_0 L_0 \rho_L}{\eta} = 10^3\,,\; Pe_V = \frac{\rho_S c_S L_0 v_0}{\lambda_S} = 0.015\,,\; Pe = \frac{\rho_L c_L L_0 u_0}{\lambda_L} = \begin{cases} 32\,(\mathrm{Ga}) \\ 16\,(\mathrm{Si}) \end{cases},$$

$$Gr = \frac{\rho_L^2 g \beta \Delta T_L L_0^3}{\eta^2} = \begin{cases} 3 \cdot 10^6\,(\mathrm{Ga}) \\ 8 \cdot 10^7\,(\mathrm{Si}) \end{cases}$$

Consequently, only phase change and melt flow with Lorentz forces dominating over buoyancy forces ($Gr \ll F_{EM}$) can be transferred to a larger silicon melt with the current scaling scheme.

6. Conclusions

Numerical simulations of the melting and solidification of gallium show that a TMF-induced flow can increase the melting rate several times but also leads to a deflected phase interface. A high stabilizing temperature gradient damps the TMF flow and reduces the role of the melt flow. First melting and solidification experiments of gallium without TMF were successfully carried out.

Acknowledgment

The authors would like to thank the Federal Ministry for the Environment (BMU) for the funding received within the grant 0325646A (project ENOWA).

References

[1] Dadzis, K.; Vizman, D.; Friedrich, J.: Unsteady coupled 3D calculations of melt flow, interface shape, and species transport for directional solidification of silicon in a traveling magnetic field, J. Cryst. Growth 367 (2013) 77–87.

[2] Gau, C.; Viskanta, R.: Melting and solidification of a pure metal on a vertical wall, J. Heat Transfer 108 (1986) 174–181.

[3] Zhang, H.; Veilleux, D.; Faghri, M.; Charmchi, M.: Numerical and experimental investigation of melting in the presence of a magnetic field: simulation of low-gravity environment, J. Heat Transfer 129 (2007) 568–576.

[4] Oborin, P.; Kolesnichenko, I.: Application of the ultrasonic Doppler velocimeter to study the flow and solidification processes in an electrically conducting fluid, Magnetohydrodynamics Vol. 49, No. 1 (2013), 231–236.

[5] Dadzis, K.; Niemietz, K.; Pätzold, O.; Wunderwald, U.; Friedrich, J.: Non-isothermal model experiments and numerical simulations for directional solidification of multicrystalline silicon in a traveling magnetic field, J. Cryst. Growth 372 (2013) 145–156.

[6] Dadzis, K.; Ehrig, J.; Niemietz, K.; Pätzold, O.; Wunderwald, U.; Friedrich, J.: Model experiments and numerical simulations for directional solidification of multicrystalline silicon in a traveling magnetic field, J. Cryst. Growth 333 (2011) 7–15.

[7] Braunsfurth, M. G.; Skeldon, A. C.; Juel, A.; Mullin, T.; Riley, D. S.: Free convection in liquid gallium, J. Fluid Mech. 342 (1997) 295–314.

[8] Wittig, K.; Nikrityuk, P. A.: Three-dimensionality of fluid flow in the benchmark experiment for a pure metal melting on a vertical wall, IOP Conf. Series: Materials Science and Engineering 27 (2011) 012054.

ON THE FLOW PATTERNS DRIVEN BY A HELICAL PERMANENT MAGNETIC STIRRER

WANG[1] X., NA[2] X.
[1] University of Chinese Academy of Sciences, Beijing, China
[2] Central Iron and Steel research Institute, Beijing, China

Magnetic fields and electromagnetic forces have long been used to control the flow of a solidifying melt. Recently, low-frequency modulated traveling or rotating magnetic fields attracted more and more attentions because they could efficiently interference solute rejection process of metallic alloy elements during solidifying process, and the study may have a potential to improve macrosegregation. In this study, we construct a helical magnetic field using permanent magnets, namely a series of small pieces permanent magnets magnetizing in their own radii's direction are piled along Archimedes's spiral.

Such helical magnetic field can be considered as the superposition of traveling and rotating magnetic field, and consequently the liquid metal flow driven by such rotating stirrer is three dimensional, to understand the physical underlying is essential for certain electromagnetic process of materials.

The azimuthal and meridian velocity profiles of liquid GaInSn alloy was quantitatively measured using an Ultrasonic Doppler Velocimetry (UDV), which exhibits different flow patterns either secondary flow or global axial vortices in the meridian direction depending on the several key experimental parameters, which include the helical magnetic structure, the ratio of radius of magnetic stirrer and radius of the liquid metal bulk etc. Figure 1 show the schematic of this Archimedes's permanent magnetic field.

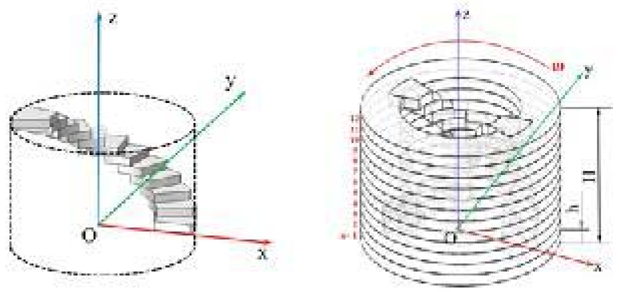

Figure: Schematic of an electromagnetic stirrer constructed on the permanent magnets along Archimedes spiral.

MHD FLOW UNDER AN IMPACT OF PERMANENT MAGNETS DRIVING SYSTEM

BEN-DAVID O., LEVY A., MIKHAILOVICH B.
Pearlstone Center for Aeronautical Engineering Studies, Department of Mechanical Engineering
Ben-Gurion University of the Negev, P.O.B. 653, Beer-Sheva 8410502, Israel
E-mail:: borismic@bgu.ac.il

Abstract: Liquid metal MHD flow initiated by a system of rotating permanent magnets in rectangular cavity has been investigated. We examine the impact of influential magnetic forcing parameters on the produced hydrodynamic structures in the cavity. The spin-up modes and steady-state flow regimes have been simulated in 3D numerical model and verified experimentally on a specially designed setup using Doppler ultrasound technique.

1. Introduction

The flow regime in the process of metal melting and solidification considerably affects the dynamics of the solid-liquid interface. The possibility of flow control should ultimately lead to the possibility of controlling temperature and concentration fields within the metal volume, phase change front shape and process duration.

Electromagnetic methods of the impact of rotating (RMF) or traveling (TMF) magnetic fields on liquid metals have been known for many years [1]-[3] However, it is hard to affect purposefully the phase change front, and the impact of the fields of moving (rotating) permanent magnets on liquid metal becomes more efficient [4], [5]. Besides, using movable permanent magnets system provides some advantages in comparison with RMF impact due to their design simplicity, relatively small overall size and low power consumption.

In the papers [4], [5] analyzing such systems, in the main, integral ("pump", pressure vs flow rate) characteristics were studied. Some hydrodynamic characteristics within limited flow volumes were investigated in [6].

Here we examine a closed container of orthogonal cross-section with liquid metal, in which it is necessary to organize a flow with specified parameters that will allow us, for example, to control the shape of phase change fronts [7]. We cannot use directly the results of some known papers, e.g., those describing MHD flow in a cavity of a similar geometric form [8] under the action of RMF, since in this case a local impact on liquid metal is limited by the electromagnetic system design. In fact, in the mentioned problems with RMF-driven flows, a well-known shape function (a function of electromagnetic body force (EMBF) distribution over the coordinates) is used, the dimensionless amplitude of EMBF being characterized by the magnetic Taylor number. In particular, for cylindrical containers, the relationship between the values of the azimuthal flow velocity and the magnetic Taylor number values and aspect ratios are established, and the conditions of the appearance of flow instability with respect to various disturbances are described.

We use a 3D computer model to examine flow regimes. Numerical results are compared with experimental ones, where the components of the flow melt velocity measured by Doppler velocimeter.

2. Formulation of the problem

In the present study we use a 3D approach to solve complicated problem of metal mixing in an orthogonal container in the presence of rotating magnetic field. The configuration under study is schematically presented in Figure 1.

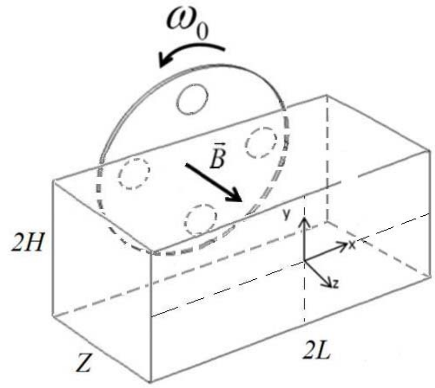

Figure 1: schematic presentation of problem statement: $2L,\ 2H,\ 2Z$ – container's dimensions; origin of coordinates is located in the center of container (cross-section in plane *x*-*y*).

The governing system of MHD equations includes a number of approximations:
Liquid metal motion under the action of electromagnetic forces are examined in the induction-free approximation (magnetic Reynolds number $\mathrm{Re}_m = \mu\sigma u_0 R_0 << 1$), which makes it possible to detach the electrodynamic part of the problem from hydrodynamic one.
Together with low-frequency approximation ($\bar{\omega} = \mu\sigma\omega_0 R_0^2 < 1$) it allows us to reduce equations of electrodynamics to the following:

$$\begin{aligned}
&\frac{\partial \vec{B}}{\partial t} = \frac{1}{\mu\sigma}\Delta\vec{B},\\
&\nabla\cdot\vec{B} = 0,\\
&\nabla\times\vec{E} = -\frac{\partial \vec{B}}{\partial t},\\
&\vec{j} = \sigma\left(\vec{E} + \vec{u}\times\vec{B}\right),\\
&\nabla\cdot\vec{j} = 0,
\end{aligned} \tag{1}$$

where $\vec{B},\ \vec{E},\ \vec{j}$ are the magnetic induction, electric field intensity and current density, $\vec{u}$ is the flow velocity, $\rho,\ \nu,\ \sigma,\ \mu$ – liquid metal density, kinematic viscosity, conductivity and magnetic permeability, respectively.
Magnetic system consists of cylindrical permanent magnets with diameter *d* and height *h* are arranged at a distance R_0 from the rotation axis in parallel to the two side walls of the container and rotate with the angular velocity ω_0. The magnetic field on the end-face of each rotating permanent magnet is $\pm B_0\vec{e}_z$.

In our problem, the magnetic field is specified on d-wide ring surfaces on the disks as $B_z \Big|_{z=\pm(Z+\delta)} = B_0 \cos(\omega_0 t - p\ arctg\,\frac{y}{x})$, where p – the number of pole pairs, which depends on magnets polarity alternation, δ – the distance between the plane of driving magnets end-faces and inner surfaces of corresponding container's lateral walls.

The cause of the conducting liquid flow in a rotating field is an EMBF, whose density is determined by

$$\vec{f}_{em} = \sigma(\vec{E} + \vec{u} \times \vec{B}) \times \vec{B}. \qquad (2)$$

Besides, in the approximation of a small magnetic interaction parameter $St = \frac{Ha^2}{\mathrm{Re}} < 1$ (where $Ha = B_0 R_0 \sqrt{\frac{\sigma}{\rho\nu}}$, $\mathrm{Re} = \frac{u_0 R_0}{\nu}$ are Hartmann and Reynolds numbers) we do not take into account the variable electromagnetic force component and examine its constant part only (here $T = 2\pi / \omega_0$ – period of disk revolution):

$$\langle f_{em} \rangle = \frac{1}{T} \int_0^T \left| \vec{f}_{em} \right| dt. \qquad (3)$$

We should note another simplification assumed in the problem, which is connected with the smallness of the magnetic Reynolds number – the effect of the term $\left(\vec{u} \times \vec{B}\right)$ of Eq. (2) on flow computation results. It was estimated before [7] for several sets of parameters and established that this term can be also neglected.

In this case, the flow is described by the following equations

$$\frac{\partial \vec{u}}{\partial t} + (\vec{u} \cdot \nabla)\vec{u} = -\frac{1}{\rho} \nabla P + \nu \cdot \Delta \vec{u} + \frac{1}{\rho} \vec{f}_{em}, \qquad (4)$$

$$\nabla \cdot \vec{u} = 0,$$

where flow velocity at the initial time: $\vec{u} \Big|_{t=0} = 0,$ and on the container inner face $\vec{u} \Big|_S = 0$ (here P is a pressure).

3. Results and discussion

Calculated values of the magnetic field and the flow velocity in the cavity of the container were compared with the experimental ones obtained by Doppler ultrasound velocimeter (description of the experiment is given in [7]). Figure 2 shows the distribution of longitudinal mean velocity component, and Figures 3 and 4 illustrate some typical hydrodynamic structures generated in the container.

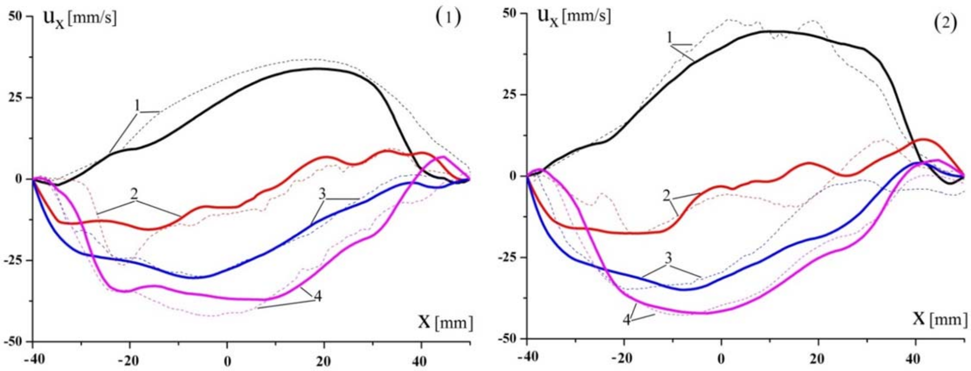

Figure 2: comparison of x-component of the flow at x-y section (z = 20mm), for different rotation velocities - 1) $\omega_0 = 10.74\, rad/\mathrm{s}\ (100 rpm)$; 2) $\omega_0 = 15.7\, rad/\mathrm{s}\ (150 rpm)$. Numbers on the curves correspond to y-coordinate: 1 – y = -23mm; 2 – y = 0; 3 – y = 11.5mm; 4 – y = 23mm; solid lines – computation, dashed lines – experiment (ultrasonic Doppler velocimeter DOP 2000).

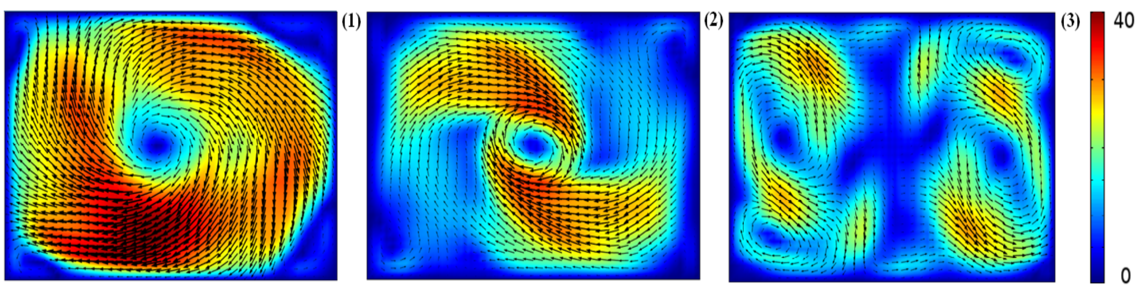

Figure 3: comparison of steady-state flow regime for different cross-sections:
1) x-y plane (z = 20mm); 2) center of x-y plane (z = 0); 3) center of x-z plane (y = 0)

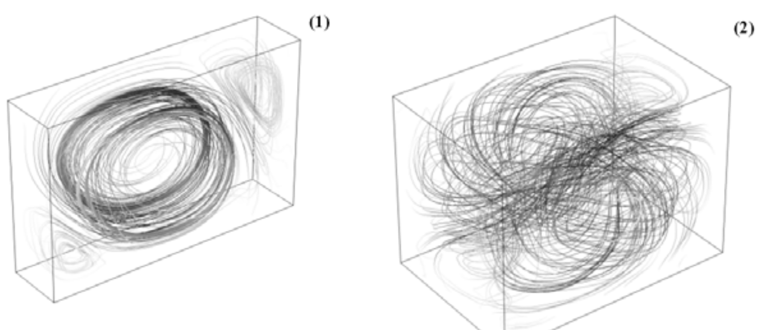

Figure 4: 3D flow patterns at $\omega_0 = 15.7 rad / s$ in containers with different width $(Z_{02} = 2Z_{01})$.

Depending on the parameters of the control of the magnetic system and the geometric relationships between the dimensions of the container we have calculated several scenarios of development and steady-state flow with characteristics, which agree satisfactorily well with experimental data. The analyzed variants indicate wide opportunities of systems with permanent magnets using, for example, for melts homogenization or for control the shape of the phase change front in the processes of solidification and melting.

4. Conclusion

3D computer simulation of MHD flow activated by rotating permanent magnets in a container of orthogonal cross-section was carried out using a laminar model, and the results were validated by experimental data obtained using Doppler ultrasound velocimetry. That allows to examine the features of the various hydrodynamic structures and even to realize the required flow regime by setting the magnetic driving system parameters.

The obtained results complement the existing findings and expand the applicability region and the potential of the used method of controlling the processes of liquid metals stirring. In the framework of this research we intend to optimize the parameters of the magnetic driving system conformably both to laminar and turbulent flow regimes.

5. References

[1] Moffatt, H.K.: On fluid flow induced by a rotating magnetic field. Journal of Fluid Mechanics. 22 (1965) 521-528.

[2] Kapusta, A.:Motion of a conducting fluid under the action of a rotating magnetic field. Magnetohydrodynamics. 4 (2) (1968) 51-53.

[3] Davidson, P.A.: Swirling flow in an axisymmetric cavity of arbitrary profile, driven by a rotating magnetic field. Journal of Fluid Mechanics. 245 (1987) 669-699.

[4] Kalnin, T.K.; Petrovicha, R.A.; Priedniek, E.V.: Study of salient-pole MHD pump with permanent magnets. Magnetohydrodynamics. 6 (1) (1970) 141-142.

[5] Bucenieks, I.; Kravalis, K.; Krishbergs, R.: Pressure-flow rate characteristics of the pumps with permanent magnets. Magnetohydrodynamics. 47 (1) (2011) 97-104.

[6] Bojarevics, A.; Beinerts, T.: Experiments on liquid metal flow induced by rotating magnetic dipole. Magnetohydrodynamics. 46 (4) (2010) 333-338.

[7] Ben-David, O.; Levy, A.; Mikhailovich, B.; Azulay, A.: 3D numerical and experimental study of gallium melting in a rectangular container. International Journal of Heat and Mass Transfer. 67 (2013) 260-271.

[8] Frana, K.; Stiller, J.: A numerical study of flows driven by a rotating magnetic field in a square container. European Journal of Mechanics B/Fluids. 27 (2007) 491-500.

INFLUENCE OF MHD STIRRING ON SOLIDIFICATION OF ALUMINUM ALLOY IN A CYLINDRICAL CRUCIBLE

DENISOV[1] S.A., DOLGIKH[1] V.M., KHRIPCHNKO[1,2] S.YU., KOLESNICHENKO[1] I.V., NIKULIN[1] L.V.
[1] Institute of Continuous Media Mechanics UB RAS (Russia)
[2] Perm National Research Polytechnic University (Russia)

Abstract: The processes taking place in a molten metal during its crystallization in the presence of MHD-stirring in a cylindrical crucible are investigated. We describe the results of physical and numerical experiments devoted to the study of directional crystallization of aluminum alloy in a cylindrical crucible in diverse MHD-stirring modes generated by travelling and rotating magnetic fields, and by their superposition. The experiments have shown that the types of magnetic (travelling or rotating) fields and their intensity determine the shape of crystallization front of ingots and the type of the grain structure of alloys (solid solutions and alloys with eutectic). They also affect the structural zone length, grain size, distribution of structural components, rigidity, and other mechanical characteristics of alloys in ingots cast using some form of MHD-stirring.

1. Introduction

MHD stirring ensures success when casting aluminum ingots (most commonly used for semi-continuous casting in metallurgy) because it provides homogeneous distribution of admixtures and alloy homogenization, produces a homogeneous fine-grain structure of solid solutions, reduces a specific fraction, and enhances the refinement and uniform distribution of second (intermetallic) phases, etc. MHD stirring can also be used for aluminum ingot casting in cylindrical moulds of finite volumes (equipment for this process is simple and cheap). It has been found that the properties of the molten metal in the presence of MHD-stirring are improved. However, MHD-stirring has some specific features, in particular, the stirring velocity during ingot solidification decreases when the volume of the liquid phase in the ingot reduces. That is why investigation of the process of crystallization of aluminum alloys in a finite volume in the presence of MHD-stirring has aroused a great deal of interest.

2. Presentation of the problem

In the numerical experiment, the process of crystallization of aluminum in a cylindrical crucible in the presence of MHD-stirring generated by travelling or rotating fields was considered. The wall and lid of the crucible were assumed to be thermally insulated, and the heat was taken away through the crucible bottom. Electromagnetic forces in a liquid metal were determined as in [1], and hydrodynamics and the process of crystallization were analyzed in terms of the k-ε model and using the enthalpy-porosity method [2]. The liquid phase was characterized by singular porosity, the solid phase – by zero porosity, and the intermediate phase – by the intermediate value of porosity. Boundary conditions used in the problem were prescribed similar to those of the physical experiment. The velocity component on solid boundaries was taken to be zero. The temperature on the upper and lower boundaries of the region was, respectively, higher and lower than the crystallization temperature of the metal. The heat flow through the side walls was absent. During calculations, the value of porosity varied, which made it possible to describe an increase in the solidified metal.

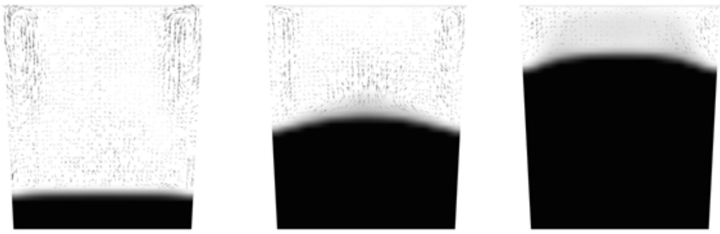

Figure 1: Evolution of the interface and velocity field during crystallization of the aluminum ingot in the rotating magnetic field, 6 A (6.09 mT; 50 Hz). Left – beginning of the process.

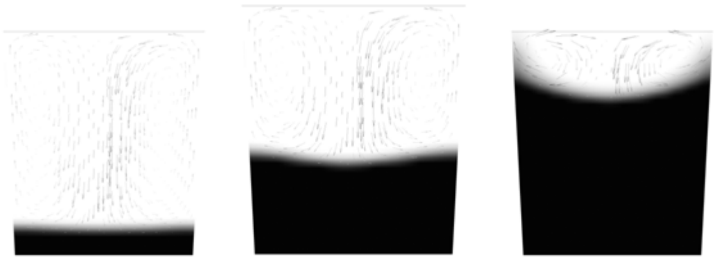

Figure 2: Evolution of the interface during crystallization of the aluminum ingot in the upward-traveling magnetic field, 3 A (3.98 mT; 50 Hz). Left – beginning of the process.

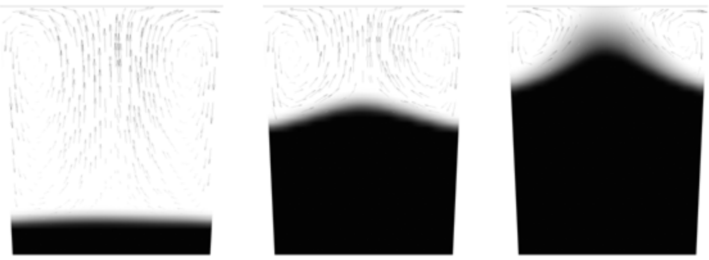

Figure3: Evolution of the interface during crystallization of the aluminum ingot in the downward-traveling magnetic field, 3 A (3.98 mT; 50 Hz). Left – beginning of the process.

The numerical experiment indicates (Fig.1) that as the solid phase volume fraction increases in the crucible in the presence of the rotating magnetic field, the interface remains flat for a long time. At the end of the process, i.e., when the liquid phase reduces sharply, the speed of rotation of metal decreases and the crystallization boundary rises in the middle of the crucible.

Under the action of the travelling magnetic field on the solidified metal, the crystallization pattern changes. When the magnetic field goes upward (Fig. 2), the interface has a small concave in the center of the crucible and rises slightly near its walls.

This depends upon the fact that the hot metal in the upper part of the crucible descends in the middle of the crucible, slowing down the process of aluminum crystallization. After cooling, the hot metal moves to the walls and solidifies there. At the end of the process, the velocity of a poloidal flow in the liquid phase of metal decreases much stronger than the velocity of a toroidal flow in the case of a travelling field. A descent of the interface in the middle of the crucible and its rise near the crucible walls become more pronounced.

When the magnetic field travels downward (Fig. 3), the hot metal descends near the walls, impeding the crystallization process. Then, it moves to the middle of the crucible and solidifies. In this case, even at the initial stages of the process, a convexity in the center of the interface occurs. The convexity becomes more marked as the crystallization proceeds. At such topology of the flow, the boundary of crystallization front in the metal is not flat, and its deformation increases in the course of the process.

We set up an experiment to determine the azimuthal velocity of liquid aluminum in the crucible (Fig.4), induced by the rotating magnetic field generated by an MHD-stirrer. The velocity was found with the aid of a turbine submerged into the liquid metal [1].

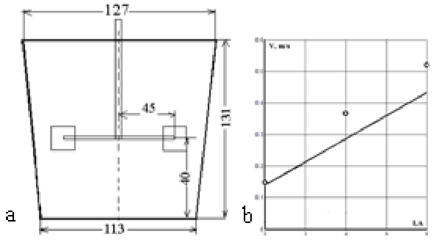

Figure 4: a - Crucible for liquid aluminum with a measuring turbine; b – maximum melt flow velocity V versus the inductor current (I, A) creating the rotating magnetic field. Solid line and points indicate, respectively, the results of numerical and physical experiments.

In the numerical experiment, the flow of aluminum in a closed cylinder was calculated. The physical experiment was conducted on silumine in the crucible with free surface, which provides an explanation for some divergence of the results of numerical and physical experiments with increasing electrical current in the inductor. Crystallization experiments were performed with Al-4.5%Zn and AK9ч alloys in the presence of MHD stirring. The alloys were poured at 680^0C into the crucible placed in the MHD-stirrer generating the travelling and rotating magnetic fields. The crucible walls were thermally insulated and could be heated, and the bottom was cooled by circulating water. After pouring the melt, the crucible was closed by an insulated lid (Fig. 5).

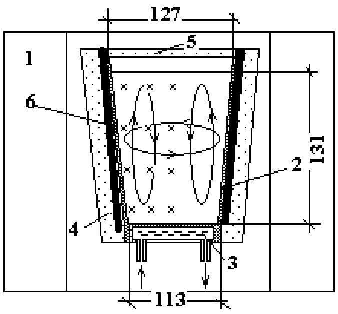

Figure 5: MHD stirrer with a crucible placed inside it:
1 – MHD-stirrer; 2 – crucible - crystallizer;
3 – water -cooled bottom; 4 – wall insulation;
5 – mullite-siliceous lid; 6 – heater.

The structure and properties of ingots solidified in magnetic fields were compared with those of ingots solidified in the absence of MHD-stirring. The influence of the rotating magnetic field on the microstructure of alloys Al-4.5%Zn and AK9ч is given in Fig .6. In the absence of MHD-action, the Al-4.5%Zn ingot consists of large dendrite crystals (Fig.6a). Application of the rotating magnetic field changes the large-dendrite structure of the ingot to the fine sub-dendrite structure (Fig. 6b). Such transformations were also observed in the eutectic alloy AK9ч. In Fig. 6c, the structure of the alloy solidified without the MHD-action is represented by dendrite crystals with the 1st order extended axis (dendrite trunk) and secondary branches, as well as by eutectic areas. Use of MHD stirring makes it possible to transform the morphology of dendrites: the dendrite axis becomes a compact grain in the center, where it is surrounded by the secondary branches of a spatial cluster (Fig. 6d).

Formation of the shape of grains in ingots depends on both the stirring flow and the intensity and directivity of heat sink cooling. At fast cooling of ingots in the zone adjacent to the water-cooled bottom of the crucible, one can observe the formation of columnar crystals oriented along the normal to the bottom surface (Fig. 7a) and slightly bent in the direction of rotation of the metal.

In the layer adjacent to the thermally insulated wall, the relatively equi-axial small crystals with arbitrary orientation are formed. Formation of such crystals takes place in the flow in a suspended state, and therefore the dynamic flow has only a minor effect on these crystals (Fig. 7b).

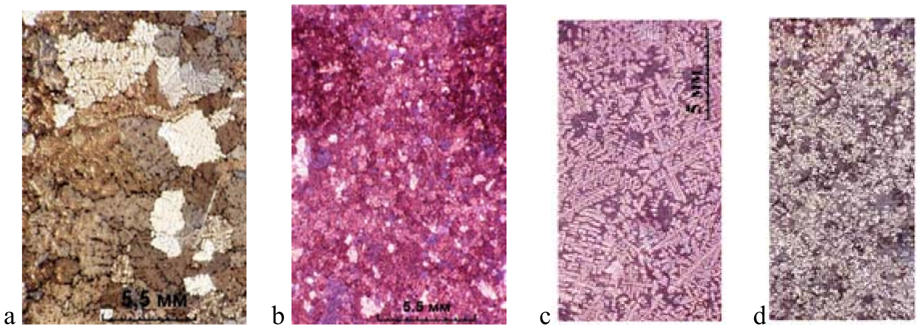

Figure 6: Macrostructure of the solid solution of Al-4.5%Zn alloy without stirring (a) and under the action of the rotating magnetic field (b); the same for the eutectic АК9ч alloy: without stirring (c) and under the action of the rotating magnetic field (d); comments are given in the text (current of 4 A and induction of 4.6 mT).

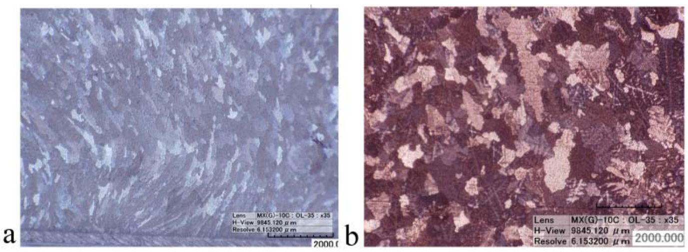

Figure 7: Macrostructure of the Al-4.5%Zn alloy solidified in the rotating magnetic field: a – in the near-bottom zone of rapid cooling; b – in the layer adjacent to the thermally insulated wall of the crucible (inductor current of 4A, magnetic field induction of 4.6 mT).

Significant changes are observed in the microstructure of АК9ч alloy solidified under the action of the rotating field (Fig. 8). Application of the rotating magnetic field transforms the silicic phase: the plate-like shape practically disappears; relatively compact fragments randomly distributed in the matrix of aluminum solid solution prevail (Fig. 8d).

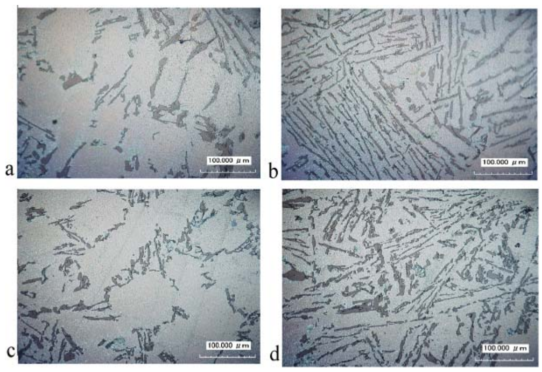

Figure 8: Macrostructure of АК9ч alloy ingots solidified in the absence of MHD fields: secondary branches of dendrite (a) and eutectic area (b); macrostructure of АК9ч alloy solidified under the action of the rotating magnetic field: grain cross-section (c) and eutectic area (d) (inductor current 4 A, magnetic field induction 4.6 mT).

Quantitative estimation of the structural parameters of the alloy solidified in the presence of the rotating magnetic field of 4.6 mT (inductor current of 4A) and without it is given in Table 2.

Table 2. Sizes of dendrites of solid solution and silicic fragments in АК9ч alloy solidified with no MHD forces and under MHD stirring.

Parameters	Sizes
Length of the dendrite trunk in ingots with no MHD forces applied	4.0 – 4.5 mm
Overall size of the dendrite with modified morphology (through the external circuit) in ingots subjected to MHD forces	1.4 – 1.6 mm
Thickness of the secondary branches of dendrites in ingots with no MHD forces applied	0.06 – 0.09 mm
Thickness of the secondary branches of dendrites in ingots with applied MHD forces	0.08 – 0.10 mm

Sizes of silicic plates in eutectic in ingots with no MHD forces; (thickness/length)	(3–9)/(45–60) mm
Sizes of silicic plates in eutectic in ingots with application of MHD-forces; (thickness/length)	(10-13)/(29-40) mm

The Al-4.5%Zn alloys were used to evaluate the length of structural zones (the near-bottom zone of large oriented columnar crystals and the upper zone of randomly oriented large dendrites), grain size and rigidity (Figs. 9 and 10).

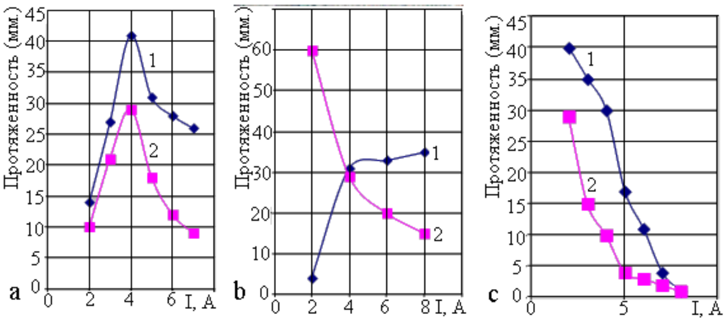

Figure 9: Structural zone length (mm) versus MHD-stirring modes: a – rotating field, b – travelling field; c- combined regime; 1 – near-bottom zone, 2 – upper zone; (Al- 4.5% Zn alloy, I, A – inductor current).

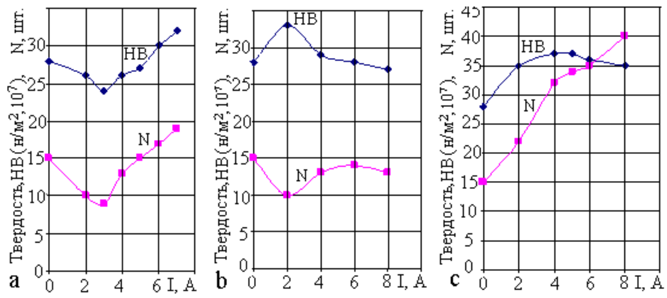

Figure 10: Influence of rotating (a) and travelling (b) fields and their joint action (c) on the HB hardness, n/m^2 and the number of grains, N, items in the Al- 4.5% Zn alloy.

3. Conclusion

Investigations showed that the crystalline structure of ingots depends on the type of MHD-stirring. Application of MHD-stirring changes significantly the structure of ingots, that is, the dendritic structure is transformed into the sub-dendritic one. The effect of transformation in many cases is defined by the rate of MHD-stirring. The rate of cooling during the solidification process influences the crystalline structure of ingots as well.

Acknowledgements. This research was supported by the project of the International Research Group “Magnetohydrodynamic Stirring of Liquid Metal and Its Influence on the Solidified Alloy Structure”.

References

[1] Kolesnichenko, I., Khalilov, R., Khripchenko, S., Pavlinov, A.: MHD-stirrer for cylindrical moulds of continuous casting machines fabricated aluminum alloy ingots, Magnetohydrodynamics, vol. 48 (2012), no.1, pp. 221-233.

[2] Voller, V. and Prakash, C.: A fixed-grid numerical modeling methodology for convection-diffusion mushy region phase-change problems. Int. J. Heat Mass Transfer, 30 (1987): 1709–1720.

NUMERICAL SIMULATION OF LOW-FREQUENCY PULSED ELECTROMAGNETIC FORCE INFLUENCE ON THE MELT FLOW IN INDUCTION CRUCIBLE FURNACE

MUSAEVA[1] D., ILIN[1] V., BAAKE[2] E., GEZA[2,3] V.
[1]Kazan State Power Engineering University, Kazan Russia
[2]Leibniz University of Hannover, Institute of Electrotechnology, Hannover, Germany
[3]University of Latvia, Faculty of Physics and Mathematics, Laboratory for Mathematical Modeling of Environmental and Technological Processes, Riga, Latvia
musaeva.d.a@gmail.com

Abstract: In the article the behavior of the melt in induction crucible furnace under the action of periodic force of electromagnetic (EM) field (f_{pulse} = [0-1] Hz) in comparison with the melt flow formed by steady EM force was observed. The melt flow in the ANSYS Fluent software package was numerically simulated. The influence of steady and pulsed EM field on the flow was compared through the change of turbulent kinetic energy in the melt. Also, the vortices decay after the different kinds of impact was calculated and compared.

1. Introduction

It is claimed that electromagnetic vibrations can significantly refine solidified microstructure. Influence of pulsed EM field might lead to more homogeneous temperature and velocity distribution, spread of grains in melt and as consequence more homogeneous structure after solidification [1, 2]. By now the most researches in that field directed on EM field vibrations with frequencies upward of 1 Hz and influence of different kinds of impulses (pneumatic, acoustic, mechanical etc.) with symmetrical periodical form. With this project is provided to investigate impact of non-steady asymmetrical low-frequency pulses of force of EM field.

2. Presentation of the problem

A conventional sinusoidal distribution of the current in the inductor in induction furnaces with relatively steady force of EM field are widely used for metal alloy, glasses melting and processing. In the considered case, a pulsating force of EM was created by interruption of the sinusoidal current in inductors with different frequencies (f_{pulse}). Each period of the impulse consists with two half-periods: the first – a period of EM force in action T_{act} (current in inductors); the second – a period without any current in inductors and no forces from EM field in the melt T_0 (Fig.1, 2). The frequency of the impulses is estimated as (1):

$$f_{puls} = 1/T, \; T = T_{act} + T_0 . \tag{1}$$

In the active period for the EM field force the commuted current force is equal to 2000 A and has the frequency f_{ac} = 400 Hz. It is expected that low-frequency pulsed magnetic field might have greater influence on fluid because due to inertia of the melt it takes a relatively long time for fluids reaction on EM field's changing.

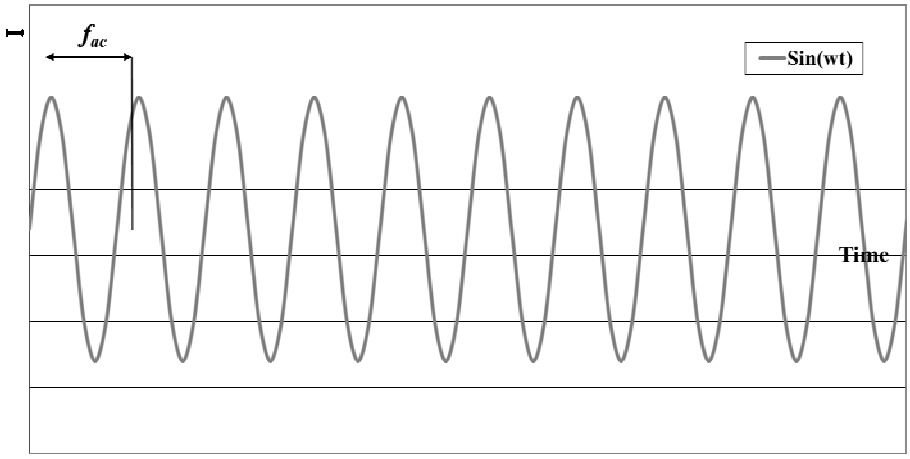

Figure1: Distribution of the current in inductors for simulation of steady EM field force.

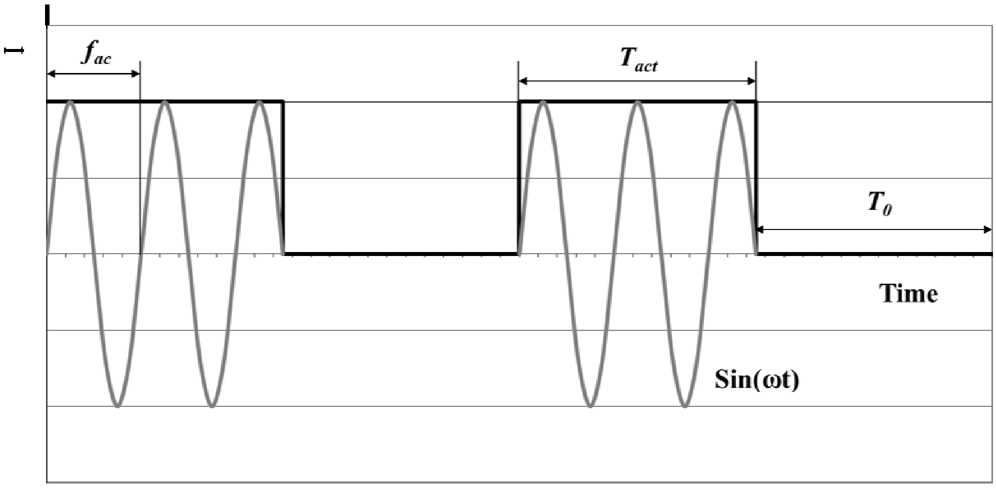

Figure 2: Distribution of the current in inductors for simulation of non-steady EM field force [6].

In the unsteady regime the influence of four frequencies were investigated: f_{pulse} = 1; 0.2; 0.1 Hz. The force causing the melt motion is the Lorenz force which can be as (2) [3]:

$$F_{EM} = j \times B \,, \tag{2}$$

where j is the electric current density, B is the EM field density.
The ratio of the action time to the time of force absence gives the coefficient of pulses asymmetry – it varies from 0 to 1, where 1 gives the symmetrical impulses and 0 corresponds to the steady process (3):

$$\Psi = T_{act} / T_0 \,. \tag{3}$$

The calculation mesh of the cylindrical crucible for 3D simulation consisted from 1.3 million elements. In the points located on the planes in different distance from the bottom of the crucible (close to the bottom, in the middle cross-plane and on the ¾ of the cylinder height) the velocity and pressure was obtained (Fig. 3).
The numerical models verification was made on the basis of the experimental research of the melt flow under condition of steady force of EM field [3].

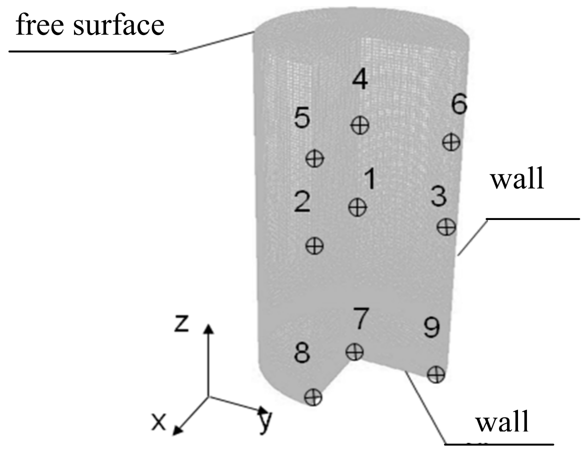

Figure 3: 3D mesh for melt flow simulation in induction crucible furnace, boundary conditions and measuring points.

3. Simulation results

The data reduction process in the CFD Post application was made. For comparison of pulsed and steady EM field force influence and frequency and asymmetry coefficient influence measuring the turbulent kinetic energy in the melt volume was integrated. The volume of the crucible on the 30 layers in the radial and axial directions was divided and in each layer the integrated value was obtained (Fig. 4).

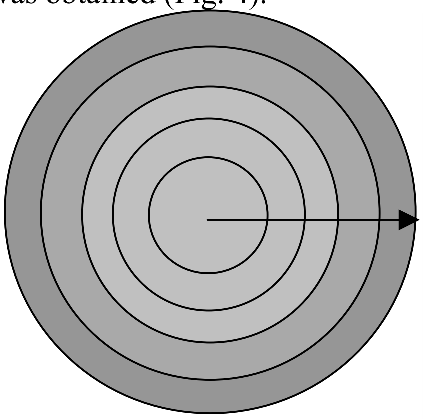

a)

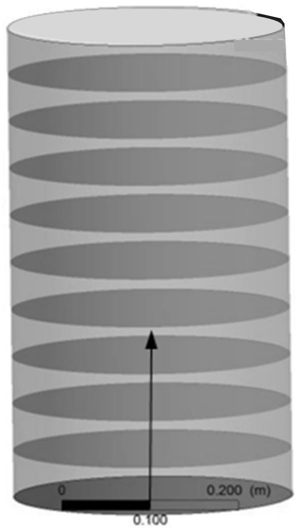

b)

Figure 4: A model of induction crucible and the direction of integrating: (a) – radial and (b) – axial direction [4].

The simulation results showed the most influence on the melt motion of the frequencies f_{pulse} = 0.2 Hz and 0.1 Hz in comparison with steady regime and impulses with higher frequency for all asymmetry coefficients as for integrating from the bottom to the top as for integrating from the center to the walls (Fig. 5).

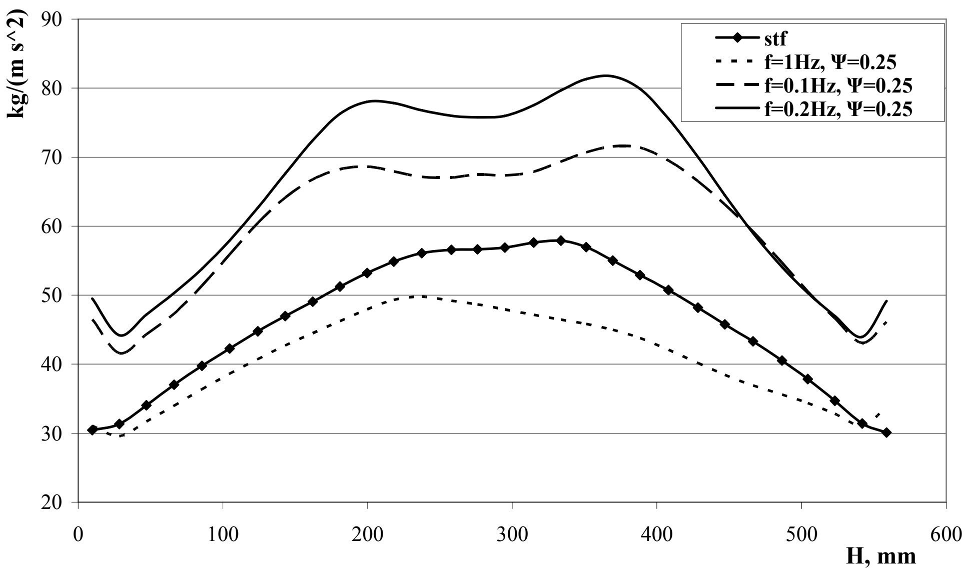

a)

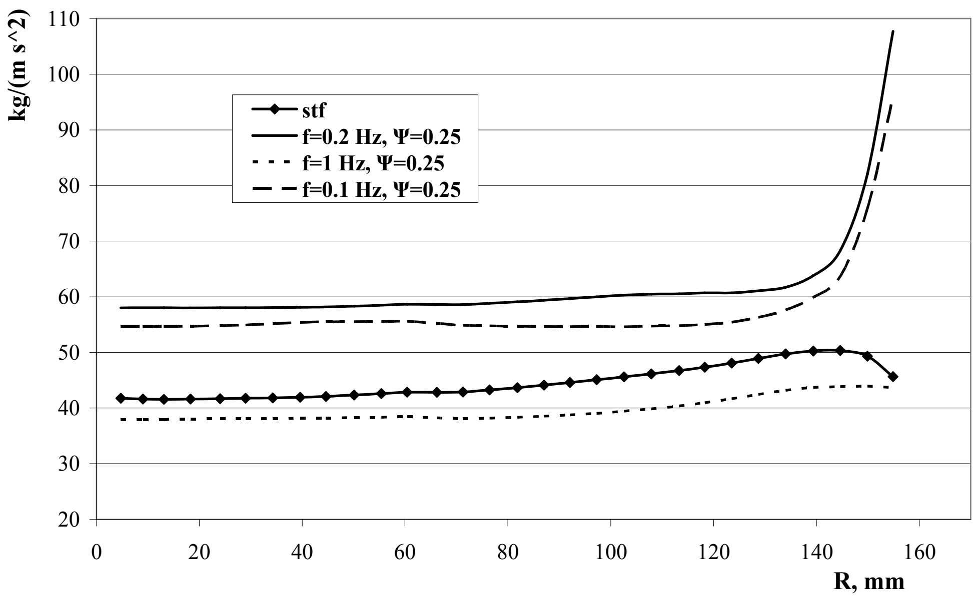

b)

Figure 5: Distribution of turbulent kinetic energy integrated in radial (a) and axial (b) directions for steady (stf) and pulsed with different frequencies force of EM field.

The mathematical modeling data do not present considerable impact of changing of asymmetry coefficients (Ψ) and the impulses with frequency f_{pulse} = 1 Hz, which probably occurs due to the fluids inertia.

It is expected that it might be the resonance frequency for pulsed force of EM field and natural frequency of turbulent vortices in the melt, which could give the maximum increase of kinetic energy of the vortices for taken geometry of the crucible. It is suggested that such pulsed regimes might improve efficiency of melting, solidification and homogenization processes of metal in induction furnace [5].

During the numerical simulation the question about the impact of crucible geometry and frequency of the impulses on the time span of vortices decay in the melt appeared. The mathematical experiment of turbulent vortices decay (quantity of energy decrease in the flow) with no force in action after 60 seconds of steady and pulsed EM force influence on the melt motion development was made.

The length of time in 60 second was taken because it is a time for stationary (in case of steady EM field force) and quasi-stationary (in case of pulsed EM field force) flow settling.
The quantity of motion decrease in the melt was measured by fixing of changing of flow velocity, integrated for the volume. The comparison of integrated velocity changing in time for steady and unsteady regimes is presented of Figure 6.

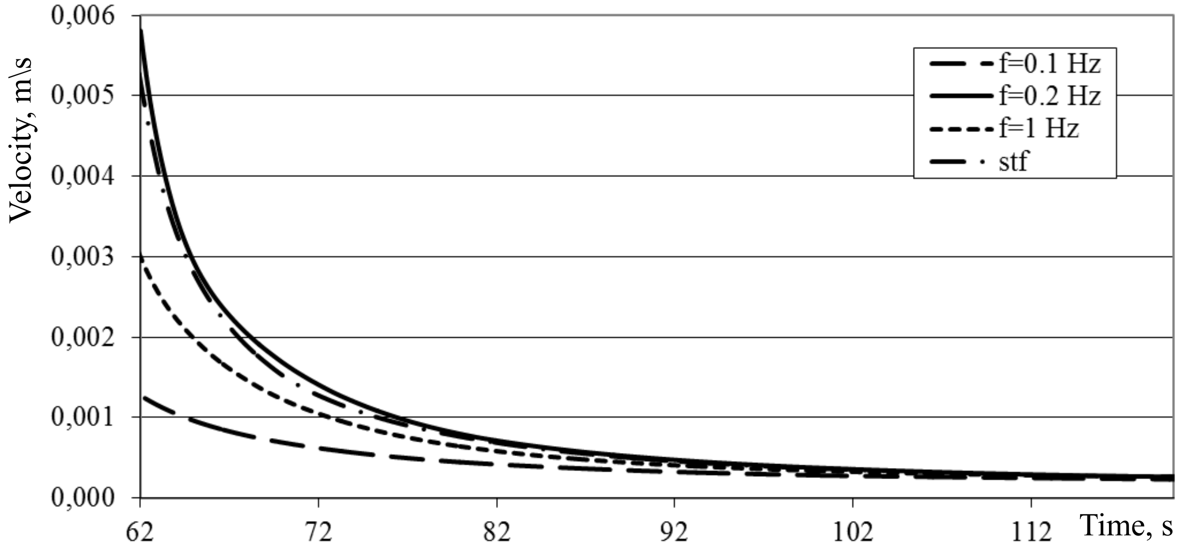

Figure 6: Velocity changing in the melt volume in consequence of the turbulent vortices decay process.

From Figure 6, one can see that for taken geometry of the induction crucible variation of the EM field force impulses does not have impact on the time length of the vortices decay. However, under condition of impulses with frequency f_{pulse} = 0.2 Hz the melt flow has the same quantity of motion as under the impact of the steady force (f_0) and it is expected the such pulsed regime might give effect of energy saving because there is no internal force spending during the time between the impulses and motion of the melt is under the action of the inertia forces.

4. References

[1] Inaba, T.; Kubo.T.: Enhanced heat transfer through oscillatory flow, J. Heat Transfer, Japanese Research. 1993. Vol.22, no 5. P. 480-92.

[2] Olayiwola B.O.; Walzel P.: Flow pulsation and modified duct surface for process heat transfer intensification. International Journal of Chemical Reactor Engineering. 2007, vol.5. P. 10.

[3] Kirpo M.: Modeling of Turbulence Properties and Particle Transport in Recirculated Flows, Thesis submitted for the PhD degree, University of Latvia, Riga, 2008, 169 p.

[4] Musaeva D.; Geza V.; Nacke B.; Sinyavin A.; Gurianov A.: Mathematical modeling of low-frequency asymmetrical impulses of EM field influence on Wood’s metal melt flow. The XV International Research and Application Conference “Technologies of Strengthening, Plating and Repair: Theory and Practice”: conference information package, Saint-Petersburg, 2013. P. 289-294.

[5] Radjai A.; Miwa K.: Effects of the intensity and frequency of electromagnetic vibrations on the microstructure refinement of hypereutectic A1–Si alloy, Melt. Mat. Mater. Trans. A 31A, 2000, 755–762 P.

EXPERIMENTAL AND MHD SIMULATION FOR GRAIN REFINEMENT OF ALLOYS UNDER LOW-VOLTAGE PULSED MAGNETIC FIELD

YANG Y., FENG X., LI Y., LUO T.
Institute of Metal Research, Chinese Academy of Sciences
E-mail: ysyang@imr.ac.cn

A new approach, low-voltage pulsed magnetic field (LVPMF) technique, to refine metal materials has been developed. The effect of the LVPMF on the solidified structure of magnesium alloys under common casting and direct casting conditions was investigated.

The results show that the grain refinement effects on AZ31, AZ91D, AZ80, AM60, AS31 and Mg-Gd-Y-Zr alloys under the LVPMF are obvious. Meanwhile, the morphology of α-Mg is transformed from developed dendrite to fine rosette with the application of LVPMF. The solute segregation in the alloys decreases obviously under the LVPMF.

The magnetic force, flow field and Joule heat with the application of LVPMF were analyzed using the ANSYS element software.

The grain refinement mechanism of magnesium alloys was discussed in terms of nucleation and growth theories.

A model for spheroidization of developed dendrite α-Mg under LVPMF was developed by analyzing the growth behavior of α-Mg dendrite.

EFFECTS OF PULSED MAGNETIC FIELD ON MICROSEGREGATION OF SOLUTE ELEMENTS IN K4169 NI-BASED SUPERALLOY

YANG Y., FENG X., LUO T., LI Y., TENG Y.
Institute of Metal Research, Chinese Academy of Sciences, China
E-mail: ysyang@imr.ac.cn

The effects of pulsed magnetic field (PMF) on microsegregation of solute elements during the solidification of K4169 Ni-based superalloy are investigated experimentally. The results show that PMF significantly affects the microsegregation of Al, Ti, Co, Cr and Nb elements in the alloy. However, the distribution behaviors are different for positive segregation elements and negative segregation elements. The microsegregation of positive segregation elements, Fe and Cr, is restrained effectively with the application of PMF. But the microsegregation of negative segregation elements, Al, Mo, Ti and Nb, is aggravated by the application of PMF.

A segregation model is established to reveal the mechanism of the distribution of elements with PMF. It is considered that, under the action of PMF, the jumping of solute atoms from the liquid phase to the solid phase is hindered, but the jumping of solute atoms from the solid phase into the liquid phase is promoted during solidification. As a result, the effective distribution coefficient of the solute atoms is reduced, which leads to reduction of the microsegregation of positive segregation elements and aggravation of microsegregation of negative segregation elements.

ON THE INFLUENCE OF MHD FLOW PARAMETERS ON THE INGOTS STRUCTURE

KAPUSTA[1] A., MIKHAILOVICH[2] B., KHRIPCHENKO[2,3] S., NIKULIN[2] L.

[1]Center for MHD Studies, Department of Mechanical Engineering
Ben-Gurion University of the Negev, P.O.B. 653, Beer-Sheva 8410502, Israel
[2]Laboratory of Hydrodynamics, Institute of Continuous Media Mechanics
Korolev 1, Perm 614013, Russia
[3]Perm National Research Polytechnic University, Russia
E-mail: borismic@bgu.ac.il

Abstract: We discuss the capabilities of the proposed method to establish the dependence between the MHD parameters of melt mixing and structure of crystallized ingot.

1. Introduction

To obtain ingots with high mechanical characteristics, MHD stirring is often used. However, the process of choosing optimal values of MHD parameters assuring a satisfactory quality of cast articles is expensive and time-consuming in each specific case, which is due to the absence of reliable basic mathematical models connecting the structure of cast articles with the melt motion in the vicinity of the crystallization front. One of the causes of such situation probably roots in an immense variety of scales used for the description of the crystal formation process and melt motion. A high practical importance of the development of such mathematical models calls for the use of alternative methods based on macroscopic processes connecting melt motion with macrostructure formation.
Since the cause of crystallization is the process of heat removal from the melt into the environment, it makes sense to examine, first, how it occurs in the absence of stirring and then take into account the influence of stirring on this process.

2. Problem statement and description of the method

As known [1], certain semi-quantitative information about the structure of ingots/castings in the absence of melt stirring can be obtained by computing thermal processes in the systems ingot/mold or casting/casting form. The final result of such computation is the establishment of a relation between the solid phase thickness and time. In fact, the following Figure 1 taken from [1] shows that the curve of the solidification velocity $dS/d\tau$ of a steel ingot of 700 mm diameter has four distinct segments. In our opinion, these segments can be interpreted, with a certain degree of reliability, as characteristic thicknesses of regions with different macrostructures. Thus, the region 1 corresponds to the structure consisting of small close-packed equiaxial crystals arising at the initial solidification stage and characterized by the maximal heat flow value as a result of maximal temperature gradient between the melt and the cold wall of the mold. The region 2 characterizes a transition from fine-grained structure to a columnar dendritic structure in the region 3. The transition point from region 1 to region 2 can be interpreted as a point of critical values of dimensionless thermal parameters characterizing the crystallization front instability at the boundary of region 1, and region 2 – as a transition region from region 1 to region 3. The region 3 is characterized by a heat flow decrease as a result of increasing thermal resistance of the solid phase and decreasing temperature difference between the crystallization temperature and the growing mold temperature. The transition point from region 3 to region 4 characterizes the moment of the appearance of coarse equiaxial crystals as a result of the melt overcooling and the establishment of thermal equilibrium between the ingot and the mold, i.e. the moment of the transition to the bulk crystallization of the melt.

Electromagnetic impact on the melt in the process of ingot/casting crystallization leads to the appearance of forced turbulent convection, which cardinally changes the fields of temperature and impurities concentration in the melt and results in the formation of narrow hydrodynamic temperature and diffusive boundary layers in the vicinity of the crystallization front.

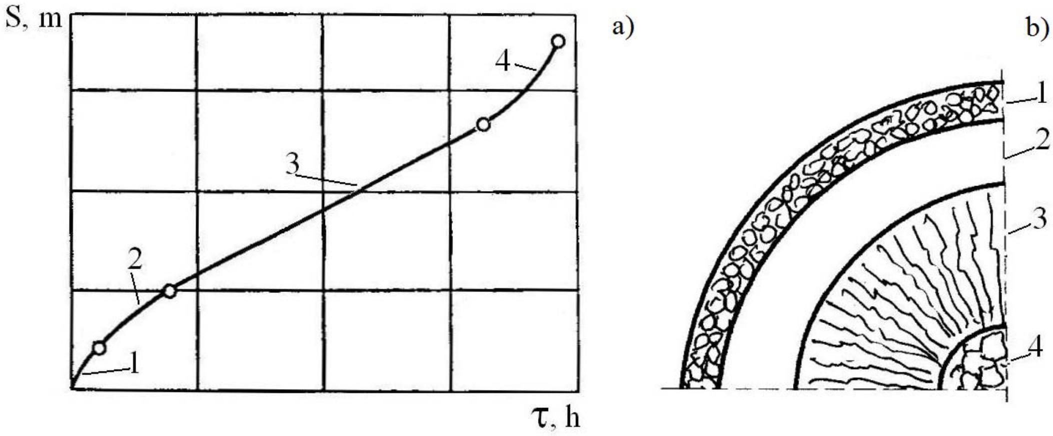

Figure1: diagram of cylindrical ingot transversal solidification in casting form (a), and corresponding ingot structure (b). See the text for additional details.

The appearance of boundary layers intensifies heat transfer from the melt into the solid phase at the expense of a large temperature gradient created in the boundary layer. This accelerates the crystallization process as a result of a decrease in the melt crystallization temperature due to an increase in the impurity concentration (if the distribution coefficient $K_0 < 1,$ where $K_0 = K_s / K_l$ is the ratio of impurity concentrations in the solid and liquid phases).

We are developing a method of creating a semi-empirical mathematical model connecting characteristic grain size of the structure in the direction of the solid phase growth with the thickness δ of the so-called mixed boundary layer [2]. This thickness is determined in the coordinates system r^*, φ, z^*:

$$\delta = \int_0^{\delta_T} \frac{u(n)}{\langle V_0 \rangle} \left[1 - \vartheta(n)\right] dn, \qquad (1)$$

where $r^* = R_0 - r;\ z^* = Z_0 - z$ are the coordinates; δ_T - the thickness of temperature boundary layer; $u(n)$ - velocity profile in the boundary layer; $\langle V_0 \rangle$ - mean velocity of the melt in the flow core; $\vartheta(n) = \dfrac{T - T_{cr}}{T_{core} - T_{cr}}$ - dimensionless temperature profile in the boundary layer; $\vec{n} = \vec{e}_r r^* + r^* \vec{e}_\varphi \varphi + \vec{e}_z z^*$ - a normal to the crystallization front. Since $u(n)$ and V_0 directly, while $\vartheta(n)$ - through a dependence on the melt velocity depend on such MHD criteria as $Ha = B_0 R_0 \sqrt{\sigma / \eta}$ and $\mathrm{Re}_\omega = \omega R_0^2 / \nu$, Eq. (1) determines the relation between the boundary layer thickness δ and MHD parameters.

We assume to evaluate the connection between the thickness of the mixed boundary layer and the ingot structure by measuring the change in the heat flow in the process of ingot crystallization and the thickness of the temperature boundary layer. At that, it is necessary to study the ingot macrostructure at various intensities of MHD stirring and to compare this information with respective estimations of MHD and thermal processes.

The method being elaborated does not refer to bulk crystallization arising at the last stage of solidification.

3. Conclusion

We have provided a possible method to reveal the correlations between parameters of MHD effect on the molten metal and the structure of crystallized ingots. The ways to implement it are identified.

Acknowledgments. The study was performed under the project MIG "Magnetohydrodynamic Stirring of Liquid Metal and Its Action on the Structure of Solidified Ingots" sponsored by the Perm Territory Government.

4. References

[1] Goldfarb, E.M.: Heat Engineering of Metallurgical Processes. Moscow: Metallurgy 1967 (in Russ.).
[2] Loitsyansky, L.G.: Mechanics of Liquids and Gases. New York: Begell House 1995.

INVESTIGATION OF HYDRODYNAMICS OF ALUMINA OXIDE MELT IN A COLD CRUCIBLE AT CONTINUOUS MELTING AND DISCHARGING

KICHIGIN[1] V., GEZA[1] V., NACKE[1] B., POZNIAK[2] I.
[1] Institute of Electrotechnology, Leibniz University Hannover,
Wilhelm-Busch-Str. 4, 30167 Hannover
[2]St. Petersburg State Electrotechnical University, Prof. Popov str., 5, 197376,
St. Petersburg, Russia
E-mail: olin24@yandex.ru

Abstract: A distinctive feature of induction furnaces with cold crucible is skull melting without introduction any impurities in the melt and overheating of the melt over 3000°C at air. Therefore the technology of induction melting in cold crucible is suitable for high temperature synthesis of oxide materials. However, the dispersion of synthesized oxide material as monolithic ingot is not always technically advantageous. Therefore, the paper proposes a new technology for continuous melting and pouring of oxide melts. In the article the results of hydrodynamics of the melt flow and the temperature field during pouring on the basis of numerical simulation with taking into account the forced and free convection are presented. Beside the melt flow inside the cold crucible special attention is paid also to the behavior of the pouring stream. The numerical results are compared with experimental data of melting and pouring experiments in the skull melting installation at the Institute of Electrotechnology in Hannover.

1. Introduction

The offer technology of continuous pouring of the oxide melt is using method of the induction melting in the cold crucible [1]. For stability condition of continuous pouring of the melt it is necessary to support required temperatures near pouring hole and on the surface of the melt. The required temperature of the melt surface provides the specified productivity of the raw melting. Technological parameters of the system are configured such a way that pouring rate of the melt and melting rate of the raw are the same. The melting process and pouring occurs in a continuous quasi- stationary mode. Maintaining equal productivities of the melting raw and pouring directly depends on the stabilization of the temperature field in the melt. On the other hand, in the temperature field influence non-stationary hydrodynamic flows in the melt, temperature dependences of the physical properties of the melt, formation the skull and crusts in the pouring hole region, occurrence of oscillations of the melt surface uneven loading raw. Therefore, for the system parameters optimization necessary to define boundaries zone of the insensitivity temperature field in the melt, depending on the above disturbing factors. Thereby, for the investigation can be selected the next tasks:

- optimization geometry of the pouring hole,
- appearing of skull layer on the pouring hole,
- instability of the melt stream.

Induction system for the continuous pouring is shown on the Figure 1, it consist from inductor, crucible, bottom and separator which are cooled down by water. The separator is installed between the pouring region and the main surface of the melt, and prevents the raw in the pouring hole.

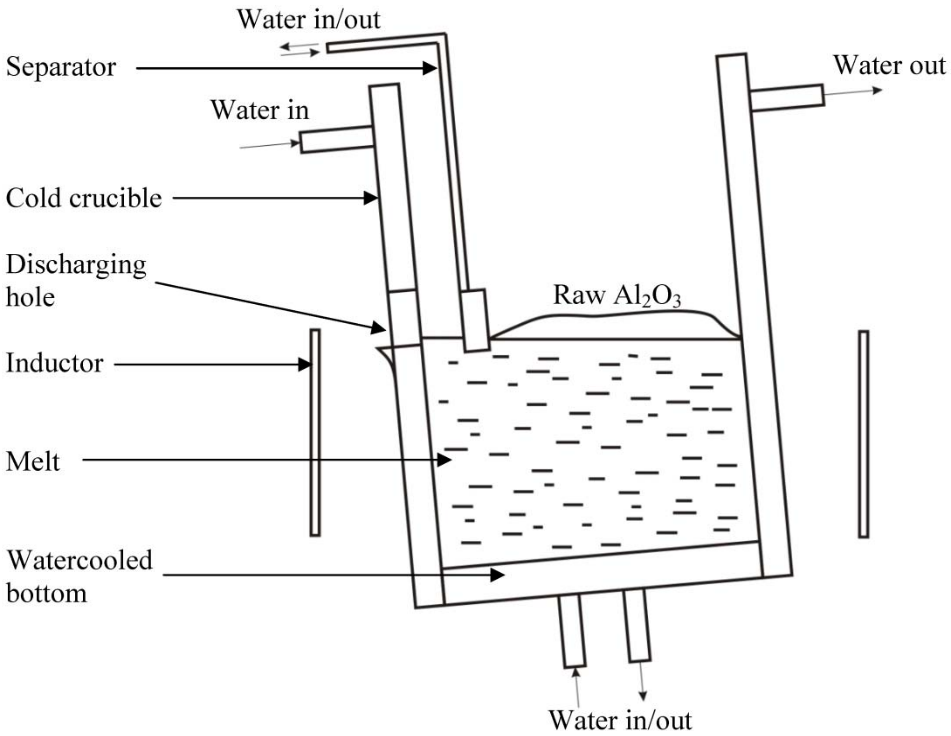

Figure 1: Induction furnace for continuous melting and discharging of oxide melt.

To prevent melt dripping on the wall of the crucible in the construction of the pouring hole nozzle is provided and also crucible is tilted to the horizon.

2. Mathematical model

Calculation of electromagnetic (EM) problem is performed using ANSYS software [2]. The obtained solution data (EM forces, Joule heat sources) are imported in fluid dynamic calculation, which is performed by CFX software [2].
The incompressible flow of melt is described by Navier-Stokes equation:

$$\frac{\partial \vec{u}}{\partial t} + \vec{u}\nabla\vec{u} = -\frac{1}{\rho}\nabla p + \nu\Delta\vec{u} + \frac{1}{\rho}\vec{f} - \beta T\vec{g}$$

Here u –velocity, p –pressure, T –temperature, f - Lorentz force density, β - thermal expansion coefficient, ν - kinematic viscosity.
Thermal processes in melt are described by heat transfer equation:

$$\frac{\partial T}{\partial t} + \vec{u}\nabla T = \frac{\lambda}{c\rho}\Delta T + q$$

Here λ - thermal conductivity, c - specific heat, q - Joule heat density. Constant temperature $T=T_{melt}$ boundary condition was used walls and bottom with no slip for flow field, which corresponds to solid-liquid interface between melt and skull (Figure 2). Top surface is treated differently in both sections. In the main part inflow with fixed temperature and flow rate Q is used - this condition represents continuous charge of new material. This condition is however idealized, because in experiment charging is not constant over whole area. In the smaller area, which is isolated by separator, radiation boundary condition with free slip is used.

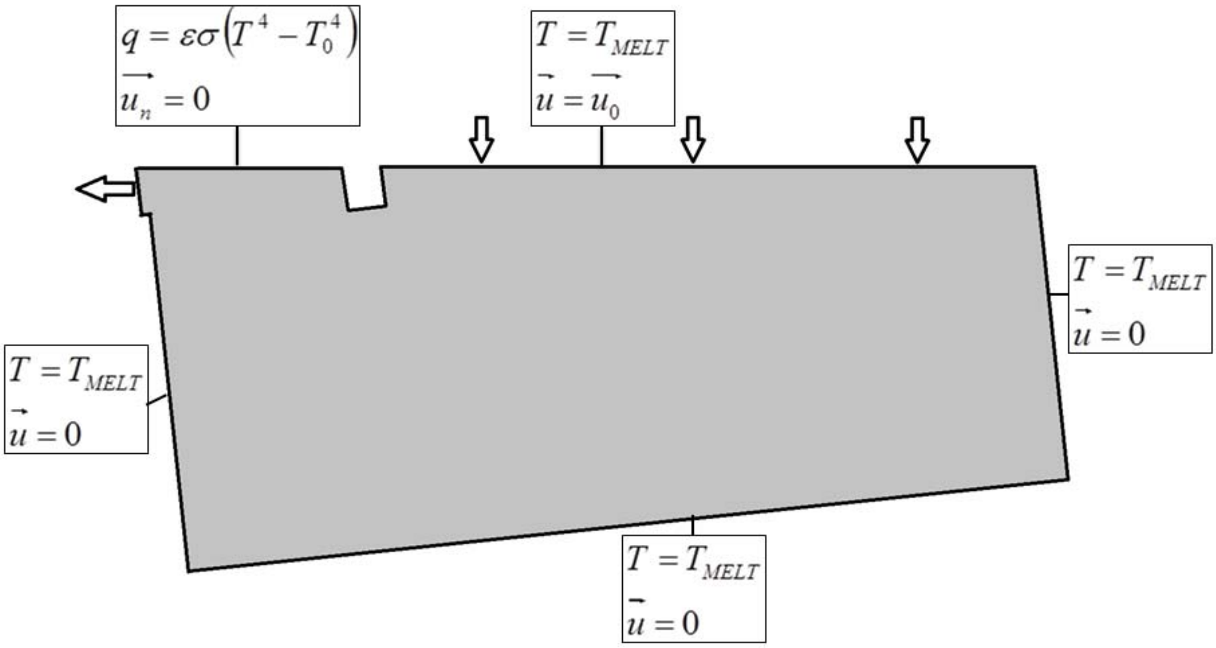

Figure 2: Calculation area and boundary conditions for hydrodynamic and thermal problem.

As in all problems with oxide melts, material properties are strictly temperature dependent [3, 4]. However, aluminum oxide data for high temperatures are limited and therefore electromagnetic conductivity temperature dependence was neglected, and decoupled problem is solved (EM sources calculated once and imported in fluid dynamic simulations). Thermal expansion coefficient is also known only for solid state of aluminum oxide and therefore influence of this value was also investigated.

3. Results

Simulations are performed for different charging rates on top surface (0.2 kg/min - 1.2 kg/min). Same flow and temperature field character is observed for all cases, certain differences are observed only in peak values. Figure 3 shows temperature distribution in vertical cross section of crucible, which also matches to symmetry plane. It is visible that in middle part of the crucible temperature iso-lines are horizontal and no vertical motion due to buoyancy forces can appear in this part. In the left bottom corner of this figure it is visible that melt temperatures here are significantly lower than in other regions of crucible. On the right side of Figure 3 near wall, steep change of temperature in radial direction is observed. This region coincides with skin-layer of EM fields, where intensive Joule heating appears. Maximal temperatures are observed in the upper right corner of the crucible, which are more almost 800°C over melting temperature. The flow field is intensive only in the zone near outflow, where it reaches several centimeters per second. In the rest part of the crucible velocities are only few mm/s (Figure 4). Along whole perimeter of crucible buoyancy vertices are observed (best seen on the right side of Figure 4), which are caused by strong radial temperature gradient. These vertices are narrow in radial direction and long (length of wall) in vertical direction. In the region of outflow this vortex is more intensive and larger in radial direction. Additionally vortex is formed directly under the surface in the charge-free zone, it has velocity vectors directed downwards at the separator due to cooling of melt. Combination of these vertices and transit flow (constant flow out of the crucible) results in complicated three dimensional flow structure near the outflow. All dominant motion structures in this crucible are established by buoyancy forces and influence of Lorentz forces is small.

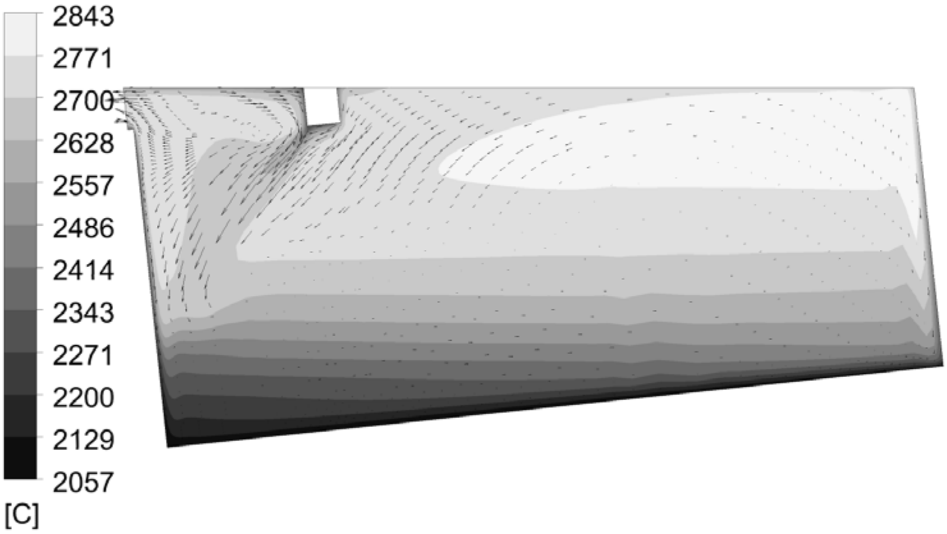

Figure 3: Distribution of temperature in vertical cross section. Arrows show velocity in this plane. Q = 800 g/min.

Figure 4: Streamlines of velocity. Q = 800 g/min.

Simulations were also performed for different flow rates and maximal and mean temperatures in the melt and at the outflow were observed. Figure 5 (left) shows this dependency. It is obvious that increased charge of cold material leads to lower melt temperatures.

Figure 5 (right) shows dependency of the melt temperatures on thermal expansion coefficient, which is not certainly known for used material. Higher thermal expansion coefficient leads to more intensive mixing and better heat fluxes through the side walls. Additionally more intensive vertical mixing leads to more heat transported through the bottom of the crucible.

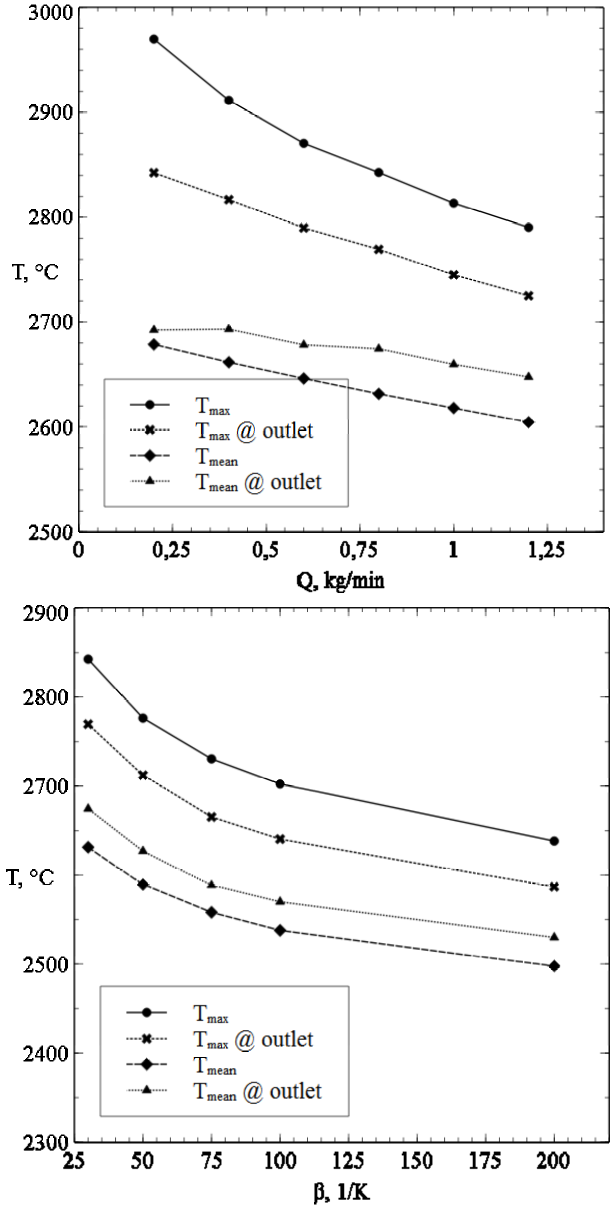

Figure 5: Dependence of temperature in melt on charge rate (left) and thermal expansion coefficient (right).

4. References

[1].Petrov, Yu.B. The Induction Melting of Oxides. Energoatomizdat, Leningrad. 1983, 104 p.
[2]. ANSYS, Inc. Theory Reference. Ansys Release 14. http://www.ansys.com
[3]. Krzyzanowski R.E., Stern Z.Yu. Thermal Properties of Non-Metallic Materials, L., "Energy", 1973.
[4]. Samsonov G.V. Physical Chemical Properties of Oxides, Publishing House "Metallurgy", 1978, 472 p.

LOCAL LORENTZ FORCE VELOCITY USING SMALL-SIZE PERMANENT MAGNET SYSTEMS

HERNÁNDEZ Daniel, KARCHER Christian, THESS André
Technische Universität Ilmenau
Institute of Thermodynamics and Fluid Mechanics
P.O.Box 100565, D-98684 Ilmenau, Germany
corresponding author: daniel.hernandez@tu-ilmenau.de

Abstract: Lorentz force velocimetry (LFV) is a contactless velocity measurement technique suited for electrical conductive fluids like liquid metals. This technique is based on the interaction of the melt flow with an externally applied magnetic field produced by a special arrangement of permanent magnets. These interactions result in the generation of a flow-breaking Lorentz force inside the melt which is proportional to the velocity of the flow. In the case of local Lorentz force velocimetry, the permanent magnet system is significantly small compared to the melt volume giving access to local velocity information.

1. Introduction

Measurement of local velocities or volumetric flow rate of liquid metals still presents a big challenge in metallurgic applications. As metal melts such as liquid steel are highly aggressive and opaque, flow measurement techniques providing mechanical contact between melt and probe as well as optical methods cannot be used. Recently, a non-contact electromagnet technique has been developed called Lorentz force velocimetry (LFV). Applying this technique, the electrically conductive moving melt interacts with an externally arranged magnetic field that is generated by a special arrangement of permanent magnets. Due to the principles of magnetohydrodynamics, eddy currents are generated within the fluid giving rise to Lorentz forces which are acting in the direction opposite to the flow. According to Newton's third law, there is a counter force of the same magnitude that acts on the magnet system. LFV is based on measuring this reaction force using a force sensor on which the arrangement of permanent magnets is mounted. The magnitude of this flow-braking Lorentz force F_L depends on the electrical conductivity σ, the volumetric flow rate Q or velocity V, and the strength of the imposed magnetic field B_0 according to the scaling relation [1]

$$F_L \sim \sigma\, Q\, B_0^2 \qquad \text{or} \qquad F_L \sim \sigma\, V\, B_0^2 \qquad (1,\ 2)$$

In case of flow rate measurement, the magnetic lines penetrate the entire cross-section of the flow (cf. Eq. (1)). On the other hand, in the case of local Lorentz force velocimetry (cf. Eq. (2)), magnets that are significantly smaller than the cross-section of the flow are of interest. It has been already demonstrated by Heinicke in [2] that by applying this technique it is possible to resolve the wake behind a small mechanical obstacle submerged in liquid metal flow. The present paper aims to extend these model experiments by using a novel arrangement of miniaturized permanent magnets resulting in both a higher resolution and a higher sensitivity of the measurement. Additionally, we provide measurement of both the streamwise force and the total moment acting on the magnet system by using a multi-degree-of-freedom sensor. Here, the force will provide information of the velocity and the torque information of the local velocity gradient. The model experiments are performed in the liquid metal loop GALINKA (fig 1) using the low-melting alloy GaInSn in eutectic composition.

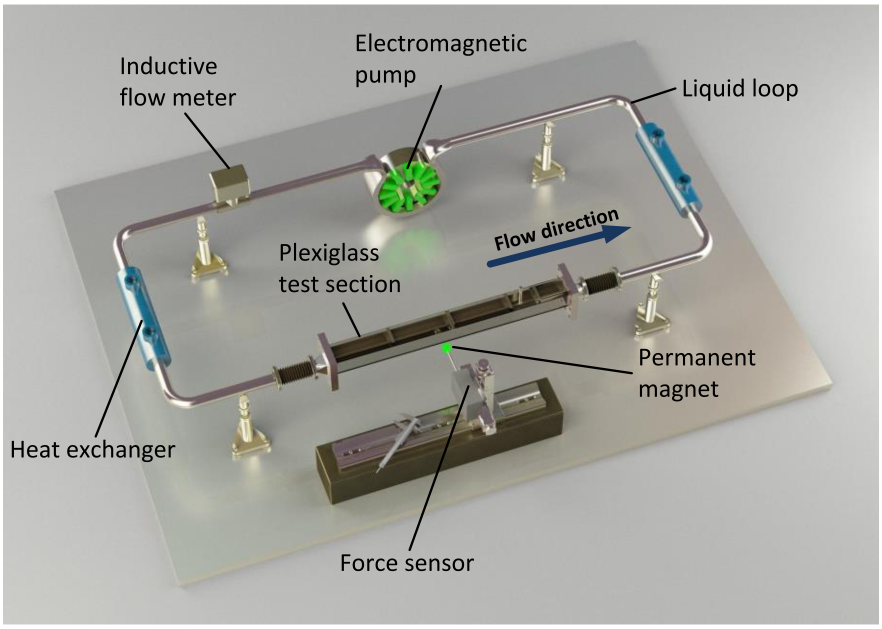

Figure 1: Experimental facility GALINKA. GaInSn in eutectic composition is pumped by a an electromagnetic pump and circulates in a loop made of stainless steel and a 50 mm x 50 mm plexiglass rectangular test section. Aside the test section, a permanent magnet is arranged and fixed to a force sensor.

2. Presentation of the problem

As explained before, LFV gives us the possibility of performing local velocity measurement in electrical conductive liquids. In order to do that, the volume of the liquid that interacts with the magnetic field has to be considerably smaller than the cross-section of the flow. This requirement is met when using miniaturized magnets characterized by a rapid decay of magnetic field strength with distance. According to this principle, in Ref. [2] a spatial resolution of 3 cm has been achieved by using a 10 mm cubic magnet. Using such set-up, detection of obstacles submerged inside the flow and the wake behind them could be achieved. However, if we decrease the size of the magnets, the measured force decreases likewise making its measurement a big challenge for currently existing force measurements devices. For example, a magnet-size parametric study has shown that clear force measurements using a 5 mm cubic magnet is not possible [3].

The current goal is not just to increase the spatial resolution of the force but also to have local information of the velocity gradient with an arrangement of small-size permanent magnet system (fig 2). For this purpose, the magnet system shall be attached to a multi-degree-of-freedom force sensor which is currently been developed in the A-2 project of the RTG Lorentz Force Velocimetry and Eddy Current Testing at Technische Universität Ilmenau [4]. In this proposal, the total streamwise force and net torque acting on the permanent magnet arrangement will be measured simultaneously having a local velocity as well as a local velocity gradient assessment respectively. Additionally and prior to validation experiments, the number, the magnetization direction and location of each magnet will be the results of an optimization procedure using the software Ansys Workbench, Fluent and Maxwell. Afterwards, the results of optimization would be validated in the experimental facility GALINKA (fig 1).

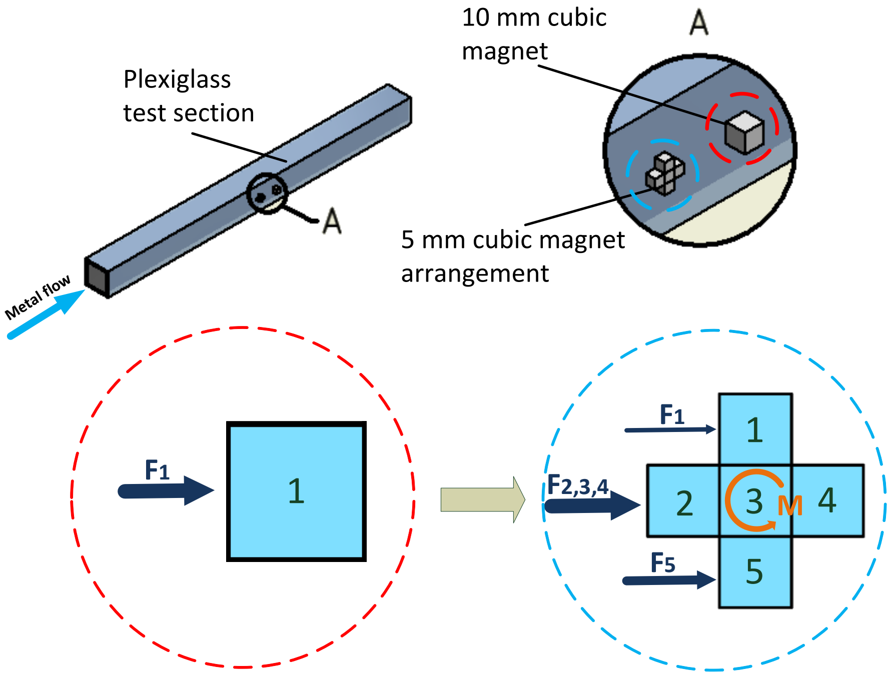

Figure 2: Proposal of replacement of a 10 mm cubic magnet with a 5 mm cubic magnet arrangement. For a better understanding, just the plexiglass test section, the old (10 mm cubic magnet) and the new (five 5 mm cubic magnet arrangement) magnet systems are shown *(top)*. In the current set-up, the force sensor is fixed to the 10 mm magnet and measures the streamwise force F_1. However, in the proposed model, the multi-degree-of-freedom force sensor is fixed to the magnet 3 which allow us to simultaneously measure the total streamwise force $\sum_{i=1}^{5} F_i$ and the net torque M, which are a local qualitative measurement of the velocity and its gradient respectively *(bottom)*. The magnet arrangement shown in this picture is for explanation purpose only. The number, the magnetization direction and location of each of the 5 mm cubic magnets will be determined by an optimization procedure.

We start our analysis on comparing the current and the proposed magnet systems by finding the imposed magnetic field that they produced on the liquid metal. As first approach, we will start with a permanent magnet system arrangement composed by three small magnets aligned to the direction to the flow. In fig 3 is shown the simulation of the magnitude of the magnetic field *Mag_B* of a 10 mm N42 cubic magnet and three 5 mm N42 cubic magnets inside a 50 mm x 50 mm rectangular duct using the electromagnetic field simulation software Maxwell 2014. The magnetization direction of each permanent magnet is constant and perpendicular to the flow and the distance between the surface of each magnet and the fluid is 5 mm. The results show that there is an increase of the spatial resolution of the magnitude of the magnetic field due to the oval-shaped magnetic field distribution. However, there is a decrease by a factor of approx. 1.8 of the maximum magnitude of the magnetic field in comparison with the 10 mm cubic magnet.

The next step is to perform validation experiments within GALINKA with the aim of comparing the spatial resolution of the force using the current and the proposed magnet systems. Additionally, we will continue with the optimization of the small-size permanent magnet system using the electromagnetic field simulation software Maxwell 2014. The magnetization direction, the number and location of 5 mm cubic magnets will be taken into account with the objective of maximizing the total Lorentz force acting on the magnet system.

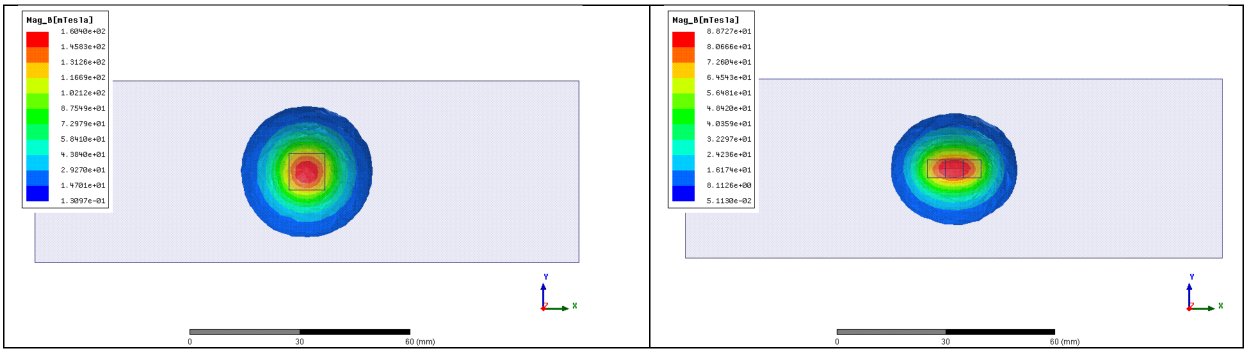

Figure 3: Magnitude of the magnetic field produced by a 10 mm N42 cubic magnet (*left*) and an arrangement of three 5 mm N42 cubic magnets (*right*) inside a 50 mm x 50 mm rectangular duct. The distance between the surface of the magnet arrangement and the liquid is 5 mm and the magnetization direction is perpendicular to the flow in each case. In this two magnetic field simulations, we can see that the magnetic field of the proposed magnetic arrangement has an oval-type distribution providing a higher spatial resolution of the force in the flow direction x with a decay of a factor 1.8 of the maximum value in comparison with the 10 mm permanent magnet. The simulations were performed using the electromagnetic field simulation software Maxwell 2014.

3. Conclusion

The oval-shaped magnetic field distribution of a 5 mm permanent magnetic system arrangement was compared with the current one of a single 10 mm cubic magnet used in local Lorentz velocimetry. The new magnet system presents the possibility of increasing the spatial distribution of the magnetic field in the streamwise direction, and therefore, an increase of the spatial resolution of the total Lorentz force. This enables us to increase the sensitivity of the local velocity measurement which is the main aim of this local velocity measurement technique for liquid metals. However, the maximum value of the magnitude of the magnetic field was 1.8 times lower. In order to reduce this difference, an optimization procedure of the 5 mm permanent magnet arrangement is proposed having as input variables the magnetization direction, the number, and the location of magnets; and as output, the total force acting on the magnet system will be considered.

4. References

[1] Thess, A.; Votyakov, E., Knaepen, E.; Zikanov, O.: Theory of the Lorentz force flow meter. New Journal of Physics. 9 (2007)

[2] Heinicke, C.: Spatially resolved measurements in a liquid metal flow with Lorentz force velocimetry. Exp Fluids. 54 (2013) 54:1560

[3] Heinicke, C.: Local Lorentz force velocimetry for liquid metal duct flows. PhD thesis, Technische Universität Ilmenau. (2012)

[4] RTG Lorentz Force Velocimetry and Lorentz force Eddy Current Testing, http://www.tu-ilmenau.de/lorentz-force/rtg-research

Model Experiment Validating the Feasibility of a Permanent-Magnet Stirrer for Large-Scale Metal Melting Furnaces

Andris Bojarevičs, Toms Beinerts, Mārtiņš Sarma, Yurii Gelfgat

Institute of Physics University of Latvia, Miera str. 32, LV-2169, Salaspils, Latvia, andrisb@sal.lv

Abstract: Model experimental set-up was built aiming to ensure achievable similitude to large scale metal melting furnaces, where electromagnetic stirring is required to reduce the melting time and to achieve thermal and compositional uniformity. The widely used three-phase AC current linear travelling magnetic field inductor is substituted by a new energy-saving concept of a Permanent-Magnet (PM) inductor, consisting of a multitude of cylindrical dipoles, which form a Halbach array and are rotated synchronously. The stirrer creates very unstable time-dependent flow pattern in the liquid metal pool. The turbulent local velocity has been measured, delivering experimental data about time-averaged flow and turbulence intensity as well. Spatial components of velocity were measured by ultrasound Doppler anemometry and by potential difference probe with an incorporated permanent magnet, delivering mutually verifying and complementary data with higher reliability. The experimental data would be used to validate the full three dimensional numerical simulations of the stirring produced in actual large scale metal melting furnaces.

1. Introduction

Electromagnetic stirrers EMS of the molten metals are widely used during light metal alloy remelting and conditioning to achieve uniform temperature and composition of the melt in large furnaces up to 70 m^3 in capacity. Most of the EMS available today are AC current travelling magnetic field inductors. Since safety, energy economy and durability of the furnaces requires the stirring to be achieved through thick refractory walls, usually enclosed in additional steel jacket up to 50 mm thick, the travelling magnetic field stirring is realized by a large size Copper coils carrying high ampere-windings of a 3-phase current. In order to deliver high integral stirring in large pools of the melt, the frequency of the AC current is kept as low as 0.2 to 1 Hz allowing to deliver electromagnetic impact with considerable penetration depth, limited by the skineffect [1,2]. Most widely used are the AC current EMS by several companies. All the AC current stirrers consume quite high electrical power and require intense water or air cooling of the inductor coils. Alternative to AC current travelling magnetic field stirring has been implemented using permanent magnet stirrers PMS, which as a rule have a multitude of alternating polarity permanent magnets in an axially symmetric array, which during rotation deliver travelling magnetic field impact in the liquid metal. In order to deliver the EM-forcing through thick walls, the magnet size should be large and usually require local reduction of the wall thickness and/or modification of the wall configuration [3,4,5]. Here we report a novel design of the PMS [6,7,8] and the model experiment validation of the efficiency of this design for stirring in a large scale Aluminium furnaces through thick walls of the bottom of the furnace.

2. Experimental model and similitude criteria

The reported PM EMS, delivering linear travelling magnetic field, consists of a multitude of the cylindrical permanent magnet dipoles with magnetization of each cylinder in direction normal to the axis. The magnet cylinders are mechanically conjugated allowing synchronous rotation of the whole array, sustaining unchanging phase shift of the magnetization directions between them. The PM assembly forms a Halbach array delivering increased magnetic field magnitude to the side of the liquid metal pool.

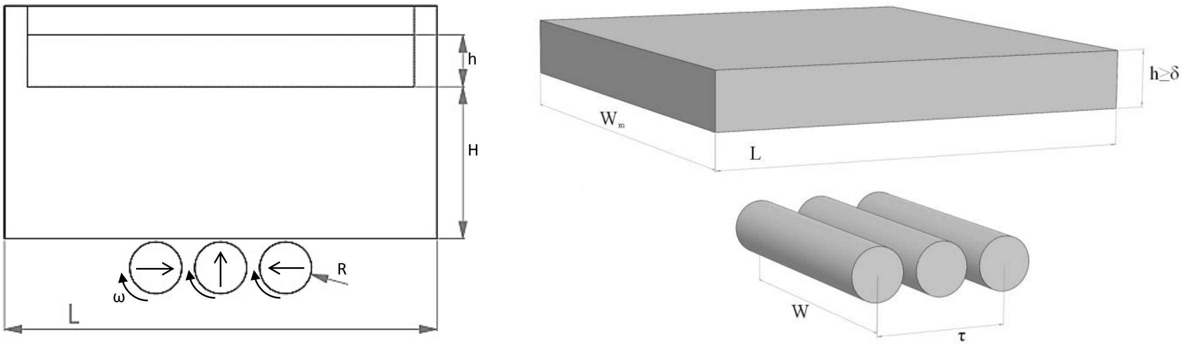

Figure 1. Experimental setup.

During synchronous rotation of the cylinders a magnetic field travelling parallel to tangent of the magnet rotation is delivered in the liquid metal region [6]. A schematic of the experimental model is shown on Fig. 1. The geometrical similarity of the experimental model to the proposed large scale Aluminium stirrer is given by a set of a dimensionless aspect ratios: $h/\tau = 0.25$; $H/\tau = 0.6$; $W/\tau = 0.93$; $L/\tau = 2.7$; $W_m/\tau = 1.9$, H – the distance from the magnets to the bottom of the liquid metal pool, W – length of the magnet cylinders, R – the radius of the magnets, and $\delta = \sqrt{\frac{2}{\sigma\omega\mu}}$ is the skin-depth in the liquid metal at angular frequency ω of the magnet rotation. The physical similitude of the model and the actual furnace requires identity of following dimensionless criteria:

$$\Omega_d = \left(\frac{\tau}{\delta}\right)^2 \text{ and } N = \frac{B}{\omega\tau\sqrt{\mu\rho}}$$

where ρ is the density of the melt, μ – magnetic permeability, B – the magnitude of magnetic field induction in the liquid metal region, Ω_d – dimensionless frequency, and N – electromagnetic interaction parameter. The model experiment was built aiming to similitude to 7.5 times larger scale liquid Aluminium pool. Since both physical similitude criteria identity could not be met on a single model, the dimensionless frequency identity was set as a priority – the skin-depth were required not to exceed the liquid metal pool depth. The unconventional electromagnetic interaction parameter both during the model experiment, and for the proposed large scale Aluminium pool would be much smaller than unity $N \ll 1$, but during the model experiment was for an order of magnitude smaller than for the large scale Aluminium pool. The N = idem (simultaneous to Ω_d = idem) could not be achieved, because of physical limitations set by achievable remanence of the permanent magnet material. A second model experiment to achieve similitude of N, but not satisfying Ω_d = idem, is considered as a next step. During experiment the liquid metal was In-Ga-Sn eutectic with density 6400 kg/m^3, electrical conductivity $3.3\cdot10^6$ S/m and kinematic viscosity $3.1\cdot10^7$ m^2/s. Reference liquid Aluminium properties were taken as for pure liquid Al.

The liquid metal velocity measurements were done by two methods, permitting to verify each other. One was the potential difference local velocity probe with an incorporated miniature permanent magnet, the other – ultrasound Doppler anemometry.

3. Experimental results

The local velocity of the flow was measured in two vertical cross-sections, normal to the travelling magnetic field direction. At a large relative distance from the PM cylinders to the liquid metal layer $H/\tau = 0.6$ or 2.5 diameters of the magnet cylinders, the amplitude of the travelling magnetic field induction did not exceed 10 mT. At 50 rev/s of the cylinder rotation the velocity magnitude above the stirrer exceeded 10 cm/s. Since the main purpose of the stirrer is too achieve high integral flow rate, the surface plot shown on Fig. 2 and 3, are most informative – at the vertical cross-section above the longitudinal midpoint of the stirrer the flow-rate was 0.47 l/s, at the cross-section downstream at 0.2 L from the end wall – 0.14 l/s. For the 7.5 times larger Aluminium pool that would be equivalent to 26 l/s or mass stirring rate 220 tons per hour at 0.3 rev/s of permanent magnet cylinders.

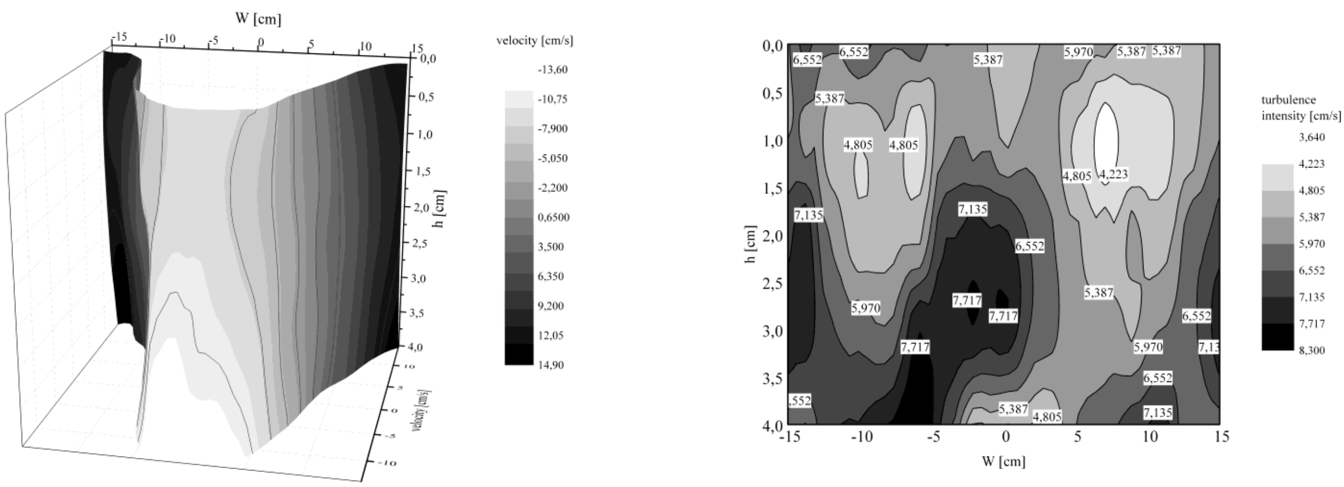

Figure 2. Velocity field above the middle magnet (left) and turbulent velocity pulsations (right).

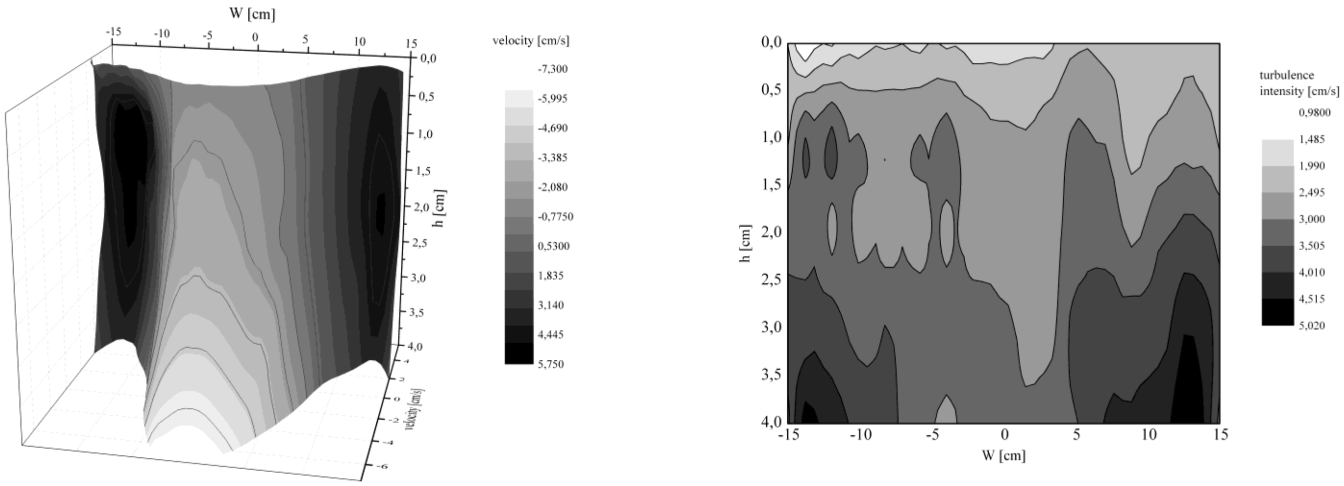

Figure 3. Velocity field between the last magnet and wall (left) and turbulent velocity pulsations (right).

The second major task of the model experiment was to demonstrate if the stirring is efficient all over the pool region. Fig. 2 and 3 show also the information on turbulence intensity, standard deviation distribution is depicted in both above mentioned cross-sections.

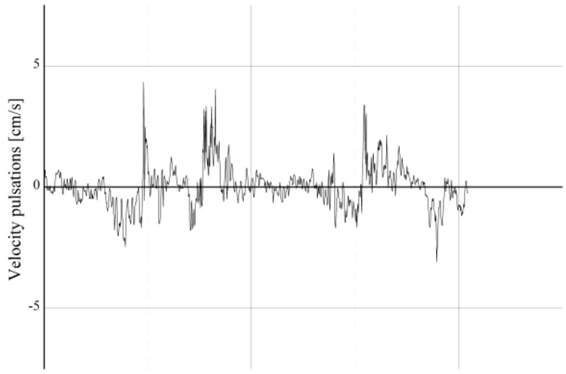

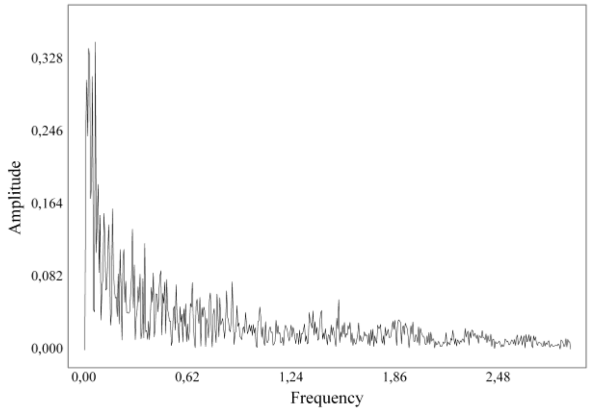

Figure 4. Time dependent velocity signal (left) and Fourier spectrum in the corner of the pool (1 cm from both walls and under liquid metal surface) (right). Average velocity is 0.9 cm/s. Peak-to-peak is 7.41 cm/s.

Besides that the most questionable region regarding the stirring – in the corner of the pool – was investigated. From general considerations the time averaged velocity in the corner region should be small, tending to zero. Fig. 4 confirm very efficient stirring even in the corner of the pool due to very unstable character of induced flow, the turbulence intensity is quite high all over the melt pool. Peak-to-peak velocity oscillations in the corner region are nearly the same as the maximum of the time-averaged velocity of the jet on the bottom of the pool just above the center of the stirrer. The turbulence spectra shown on the right side of Fig.4 confirm that the large scale vortices, corresponding to very low frequencies, are dominant in this flow. The extreme instability of the flow is shown on Fig. 5, where a photo of the momentous free surface deformations of the melt is shown.

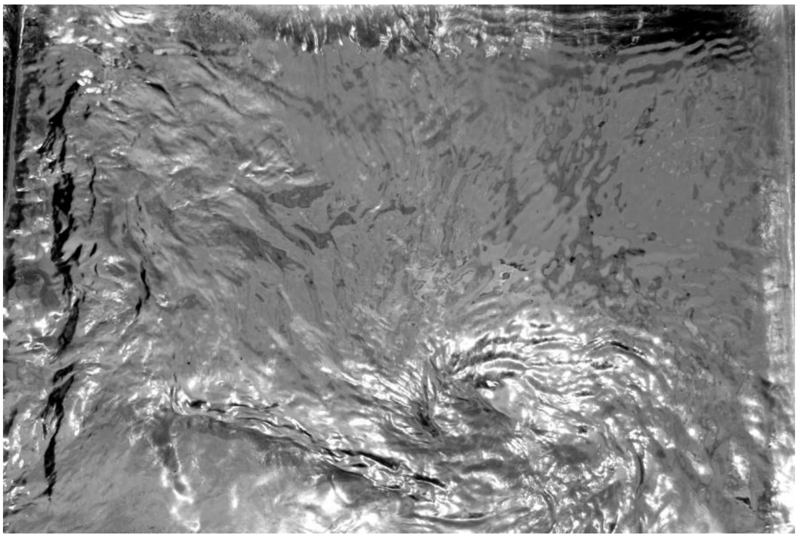

Figure 5. Snapshot of vortex in Ga-In-Sn when mixing is done with high angular frequency.

4. Conclusions

Experimental model did not achieved the full similitude with the industrial scale of stirring in a large Aluminium remelting furnace, since simultaneous identity of relevant physical dimensionless criteria could not be achieved. Nevertheless since both of the compared phenomena involve electromagnetic interaction parameter N << 1, the results may be considered sufficient to prove feasibility of the proposed linear permanent magnet inductor for the task of stirring the Aluminium pools in furnaces with bottom thickness up to 50 cm and capacity up to 50 tons. The power consumption of such a stirrer does not exceed 10 kW, there is no requirement for water cooling or intense air cooling. The results of model experiment will be used also to validate the three-dimensional numerical model, currently being developed.

Acknowledgments

The research, which is the contribution of Dr. A. Bojarevičs and Mārtiņš Sarma was financially supported by European Social Fund (project no. 2013/0018/1DP/1.1.1.2.0/13/ APIA/VIAA/061).

References

1. M.Savenas, O.Sjoden. Electromagnetics causing a stir. Aluminium Today, June 2001, pp 9-10.
2. В.Н.Тимофеев, Р.М.Христинич, С.Я.Бояков и др. Электротехнологические установки для плавильно-литейного производства алюминиевых сплавов.1-й Международный конгресс "Цветные металлы сибири - 2009" 8-10.09.2009г., Россия, г.Красноярск.
3. Т.К.Калнинь. ЯВНОПОЛЮСНЫЕ МГД – НАСОСЫ. Зинатне, Рига, 1969.
4. KENZO TAKAHASHI. „Non-ferrous metal melt pump and non-ferrous metal melting furnace using the same" Patent No: CN 101837433(A). Applicant: ZMAG LTD, May 29, 2009
5. Dr. I. Bucenieks. PERSPECTIVES OF INCREASING EFFICIENCY AND PRODUCTIVITY OF ELECTROMAGNETIC INDUCTION PUMPS FOR MERCURY BASING ON PERMANENT MAGNETS. In:14thInternational Conference in Nuclear Engineering Miami, Florida, USA, July 17-20, 2006
6. Andris Bojarevičs, Jurijs Gelfgats, Toms Beinerts, Imants Bucenieks. METĀLA SAKAUSĒJUMA SŪKNĒŠANAS UN MAISĪŠANAS PAŅĒMIENS UN IEKĀRTA TĀ REALIZĒŠANAI**.** Latvijas republikas patents LV 14404 B, 20.10.2011. Patenti un preču zīmes, 10/2011, 1453-1454 lpp.
7. A. Bojarevičs, T. Beinerts. Experiments on Liquid Metal Flow Induced by Rotating Magnetic Dipole Moment. Magnetohydrodynamics, vol. 46 (2010), no. 4, 6 lpp.
8. Toms Beinerts, Andris Bojarevičs, Jurijs Gelfgats, Imants Bucenieks, „Linear Permanent-Magnet Pump and Stirrer for Molten Aluminium". EPM 2012 conference, Pekin, October 2012.

NUMERICAL SIMULATION OF ELECTROMAGNETIC LEVITATION IN A COLD CRUCIBLE FURNACE

SPITANS[1,2] Sergejs, BAAKE[1] Egbert, JAKOVICS[2] Andris, FRANZ[3] Henrik
[1]Institute of Electrotechnology, Leibniz University of Hannover,
Wilhelm-Busch Straße 4, 30167 Hannover, Germany
[2] Laboratory for Mathematical Modelling of Environmental and Technological Processes,
University of Latvia, Zellu Street 8, LV-1013 Riga, Latvia
[3]ALD Vacuum Technologies GmbH, Wilhelm-Rohn Straße 35, 63450 Hanau, Germany
e-mail address of the corresponding author: spitans@etp.uni-hannover.de

Abstract: Design considerations of a cold crucible (CC) levitation melting furnace have been examined in the course of the literature studies. Meanwhile, by means of external coupling between electromagnetic (EM) and hydrodynamic (HD) problems a numerical model for the liquid metal flow with free surface dynamics in an alternate EM field has been developed and verified. The 3D model with a Large Eddy Simulation (LES) turbulence description is applied for the case of 1 kg of liquid titanium levitation in a CC furnace. Calculation results are compared to a simplified model of the furnace section.

1. Introduction

The conventional induction furnace with CC is a very useful technology for EM processing of a high purity materials. The application areas range from manufacturing of titanium parts for aerospace, automotive or medical industry, photovoltaic silicon purification and crystallization, up to the treating of nuclear fusion products [1].

Due to the air gaps the sectioned metallic crucible is partially transparent for EM field and acts as a secondary inductor. In this case EM pressure prominently squeezes the melt and semi-levitation is achieved. The crucible is cooled by the water and the melt is mainly abutted upon the skull - in such way interaction between the melt and crucible material is reduced. However, thermal losses through the water-cooled crucible and melt contact regions appear to be a limiting factor for reaching a higher level of overheating and efficiency.

From this point of view, a CC for complete EM levitation melting is an attractive option. In this case there is no contact between the melt and crucible and heat losses are limited only to radiation and evaporation. This ensures a higher level of superheat, permits investigation of materials at extreme temperatures and metal evaporation for coating purposes [2].

In the same time, industrial requirements must be satisfied for the scale-up potential of the CC levitation melting processes and for this purpose numerical simulation is an advantageous tool. Meanwhile, by means of external coupling between *ANSYS Classic*, *FLUENT*, *CFX-Post* and a self-written surface filtering procedure a numerical model for the liquid metal flow with free surface dynamics in an alternate EM field has been developed. Detailed verification of the model has approved accuracy of our calculation approach [3]-[4].

In this work a review of recent developments and design considerations in the field of CC construction is presented. Generalized CC design is used for simulation of EM levitation of 1 kg of liquid titanium by means of full 3D model with LES turbulence description. Calculation results are compared to the simplified k-ω SST model of a single CC section.

2. Literature studies and a cold crucible furnace design considerations

In the following articles [5, 6] it is shown that levitation in CC with a small number of segments can lead to a flower like charge shape and a contact between the molten metal and the centre of a palisade. Furthermore, a cone-shaped crucible is considered to be the best for a stable CC levitation melting [5 - 7]. Application of different AC frequencies for lower and upper inductors can be tailored specially to separate control of levitation (with several kHz) and heating (with several tens of kHz) [5], [7]. Taking into account these considerations, authors were able to levitate and melt 2.3 kg of titanium in two to three minutes [5].

In article [2] it is stressed that on a larger scale the mechanism of levitation confinement is considerably different from a small droplet case, where surface tension plays the key role. A numerical investigation led to a conclusion that the levitation of a large fluid mass requires a high AC frequency, because lower penetration depth concentrates the EM force near free surface and stabilizes it. On top of that higher intensity of a turbulent flow that perturbs free surface corresponds to a lower AC frequency and greater penetration depth. Full levitation of 2 kg of titanium melt has been achieved in a 2D k-ω numerical simulation using EM field frequency of 20 kHz. Despite the singularity of EM forces and the lack of surface tension to ensure confinement on the axis the leakage of the melt was not observed because of tangential flow along the surface away from the bottom stagnation point.

The work [6] describes the design, optimization and experimental realization of a CC levitation melting system for light alloys. By appropriate shape of a lower part of CC it was possible to compress magnetic field lines through the nozzle at the bottom of crucible and to increase the field gradient around critical null point. Moreover, stability of the levitated melt was enhanced by the null-field region introduced by a number of reverse turns. In result, few hundred grams of light metal alloy were successfully melted and solidified in levitation conditions using 10 kHz frequency [6].

Taking into account some of these considerations, authors were able to melt 0.85 kg of titanium and 0.15 kg of tantalum in levitation conditions and to produce 1 kg of uniform composite using 3 kHz and 50 kHz for levitation and heating coils accordingly [7].

Promising study [1] is devoted to a prominent enhancement of cold crucible efficiency by decreasing vertical adjacent surfaces of gaps and increasing the distance between them.

3. Numerical simulation

Two numerical models have been used for simulation of 1 kg of liquid titanium levitation: a simplified model considering a single CC section (fig. 1, a) and a full 3D model of CC furnace and titanium charge (fig. 1, b). Example of numerical mesh applied for a simplified (10^5 elem.) and full ($5\cdot10^5$ elem.) harmonic EM problem with fine resolution of magnetic field penetration depth δ_{em} = 2.1 mm is shown next to numerical mesh for the simplified ($0.8\cdot10^5$ elem.) and full ($13\cdot10^5$ elem.) transient HD calculation of two-phase turbulent flow. In the HD part of the problem k-ω SST and precise LES turbulence descriptions have been used for simulation of a single section and a full CC furnace accordingly. Lorentz force recalculation upon the new free surface shape was performed every 6 ms of the flow time. The full 3D LES simulation of 2 s of flow takes 1 month of computation time on a cluster with 14 nodes (3 GHz each).

The following temperature independent material properties of liquid titanium were used: density ρ_{Ti} = 4110 kg/m^3, surface tension γ_{Ti} = 1.557 N/m, electrical conductivity σ_{Ti} = 0.56 MS/m and dynamic viscosity η_{Ti} = 4.42 mPa·s.

The modification of a cold crucible melting apparatus described in [7] is used for numerical simulation of liquid titanium EM levitation. Our CC is composed of 20 palisades separated by the gaps of 1.5 mm. In principle, gap size can be increased, because no contact is expected between the CC and levitated melt.

The bottom tapping nozzle has inner diameter d_{noz} of 2 cm. This part of CC is responsible for squeezing EM field lines and increasing the field gradient in the critical null point region on the symmetry axis. Greater inner diameter d_{noz} will lead to a greater curvature radius of the melt at the bottom point and may cause a leakage; however, making d_{noz} too small makes it hard to install the cooling system in the palisade, as well as to drain the melt with no contact to CC. The angle α between the cone-shaped wall of palisade and a horizontal plane is 35º.

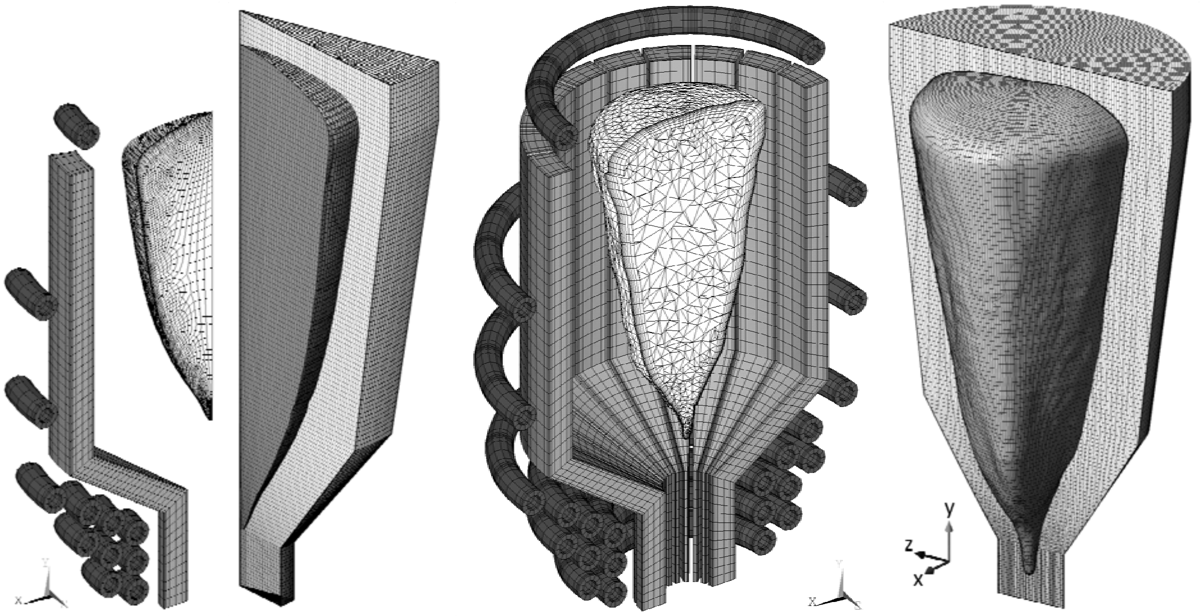

(a) (b)

Figure 1: numerical mesh for EM and two-phase HD calculation of a molten titanium levitation. Simplified model considering a single CC section (a) and complete 3D model of CC furnace and titanium charge (b).

Inner diameter of CC walls d_{wall} is 10 cm. Initially d_{wall} was chosen to be 20 cm (fig. 2, a) in order to reduce the contribution of EM forces that squeeze the melt in radial direction and results in greater height of the melt and hydrostatic pressure at the critical bottom point. However, in this case isosurface of magnetic field inside the CC have a pronounced local maximum right above the nozzle. Magnetic field distribution in the air inside the CC is shown below (fig. 2, b). Because of that position and shape of liquid metal is asymmetric, moreover, it might "jump" along this local ring-shaped EM field minimum from one palisade centre to another.

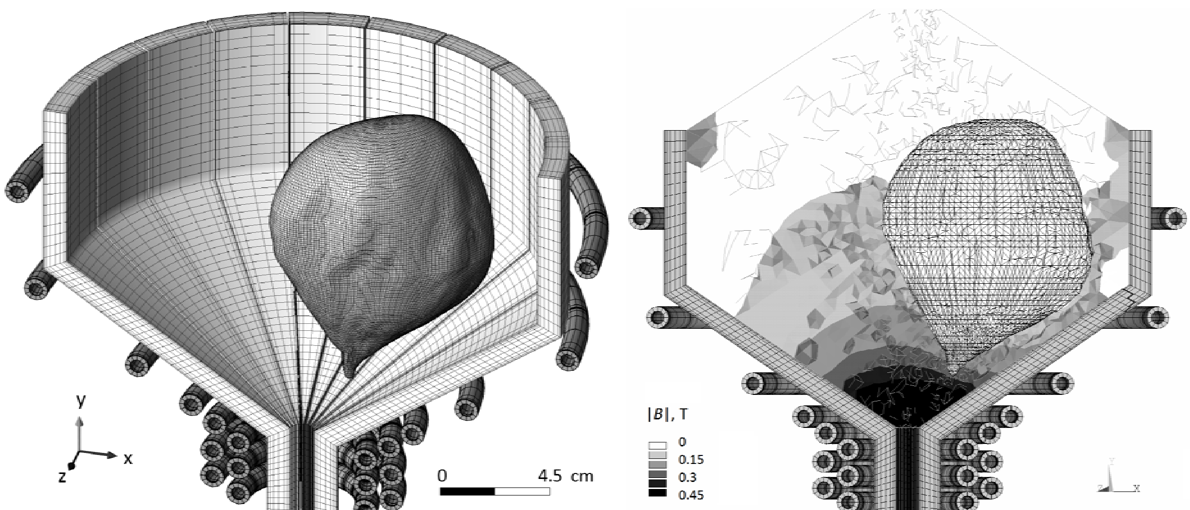

(a) (b)

Figure 2: asymmetric position of levitated titanium (1 kg) in CC furnace with d_{wall} = 20 cm obtained by 3D LES simulation (a) due to the magnetic field maximum above the nozzle (b).

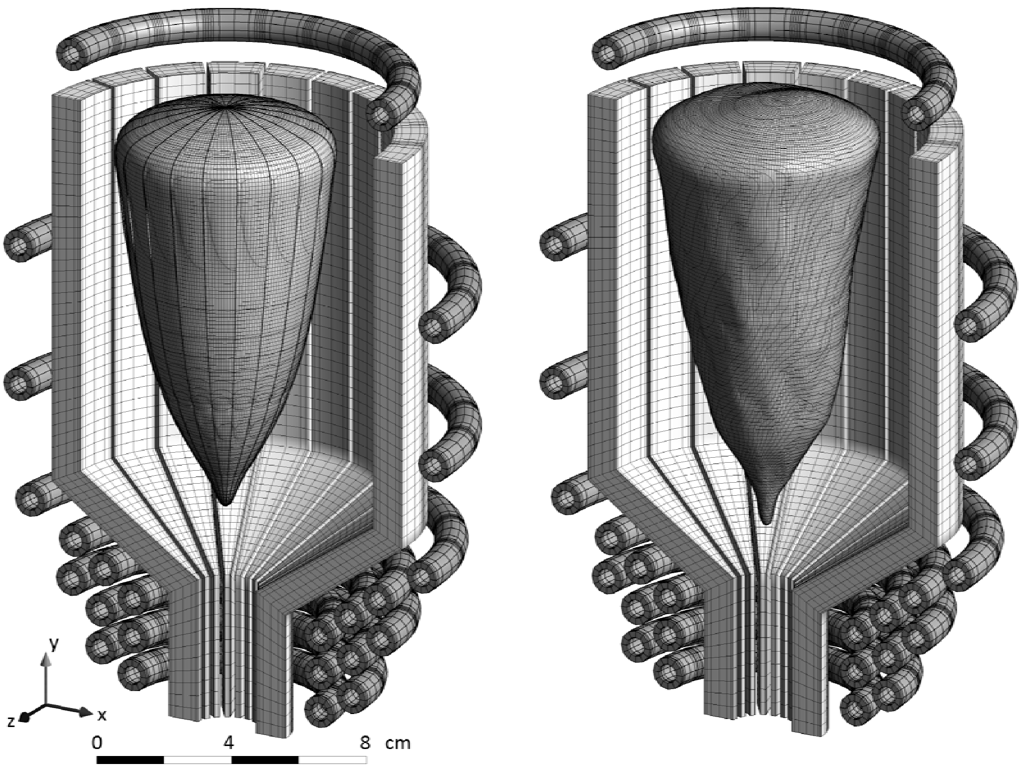

(a) (b)

Figure 3: free surface shape of liquid titanium (1 kg) obtained by simplified k-ω SST calculation of a single section (a) and full 3D LES simulation of CC levitation furnace (b).

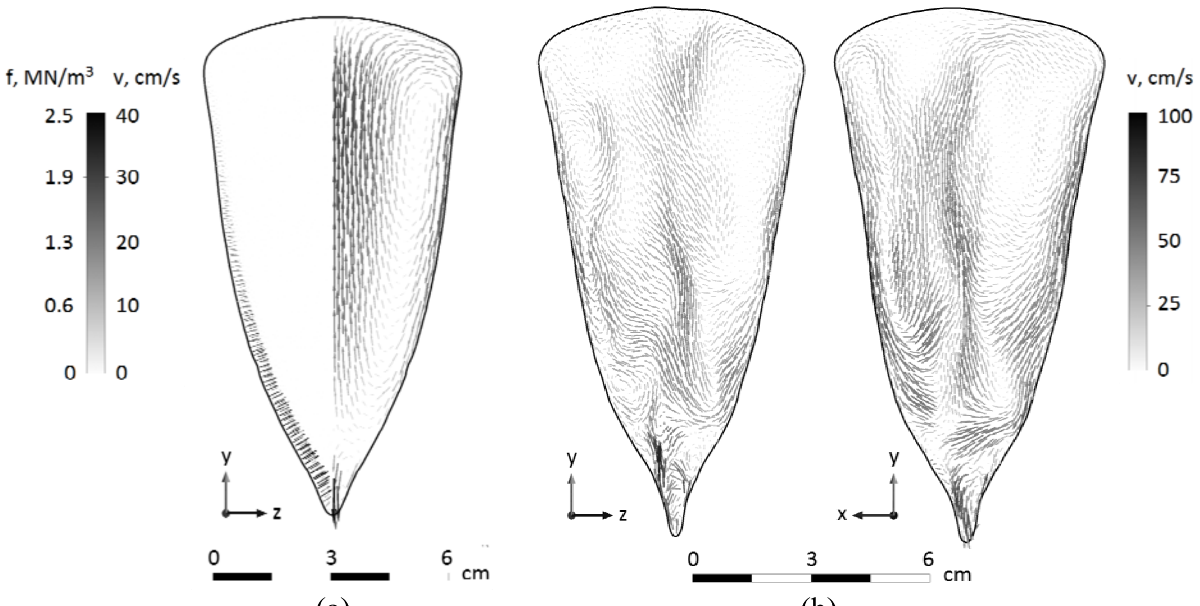

(a) (b)

Figure 4: EM force (on the left) and flow pattern (on the right) obtained by k-ω SST calculation of a single section (a) and instant velocity pattern calculated with full 3D LES model of CC levitation furnace (b).

11 turns of inductor mainly concentrated in the nozzle region and additional reverse turn above the crucible are fed with effective current I_{ef} of 3.44 kA at a frequency f of 100 kHz. Applying lower frequency causes higher flow intensity and instability of free surface, moreover, lower frequency leads to a greater δ_{em} for which the lower part of the melt with

small curvature radius of approx. 1 mm becomes transparent and results in a melt leakage predicted by our 3D LES calculation. It must be mentioned, that k-ω SST calculation of a single CC section predicts high turbulent viscosity of 1.5 Pa·s in the lower vortex region. Because of that levitation is retained even at lower EM field frequencies by k-ω SST model.

Free surface shape of liquid titanium at a quasi steady state regime obtained by simplified k-ω SST calculation of a single section and revolved for better visualization (fig. 3, a), as well as full 3D LES simulation of CC levitation furnace (fig. 3, b) is shown. According to k-ω SST Reynolds-averaged calculation the EM force, free surface shape and the flow with maximal velocity of 40 cm/s adjust themselves to a completely steady state regime with characteristic two torroidal vortex structure (fig. 4, a). Meanwhile, the finer flow structures resolved with LES reach up to 100 cm/s (fig. 4, b) and contribute to continuous free surface fluctuations, especially notable in the lower vortex region.

4. Conclusions

Important design considerations of the CC levitation furnace have been obtained in the course of literature studies. Following this experience a pilot design of CC has been proposed.

By means of recently developed and verified 3D LES numerical approach for calculation of liquid metal flow with free surface dynamics in EM field the pilot design of CC furnace has been optimized in order to meet conditions for stable levitation of 1 kg of liquid titanium.

In comparison to a simplified calculation of a single CC section the 3D model is able to predict asymmetric allocation of charge due to the specific EM field distribution. In comparison to k-ω SST calculation, 3D LES model predicts fluctuating behavior of velocity and free surface shape, much greater instant flow intensity, as well as metal leakage in case of lower EM field frequencies. Calculation of 3D EM levitation with free surface dynamics and LES turbulence model is in principle a new approach that permits more precise and detailed investigation of free surface instabilities in levitation furnaces of different kinds.

The developed 3D numerical approach with précised LES turbulence description can be used for further optimization of EM levitation melting installations.

5. Acknowledgements.

Current research was performed with financial support of the ESF project of the University of Latvia, contract No. 2009/0138/1DP/1.1.2.1.2/09/IPIA/VIAA/004. The authors wish to thank the German Research Association for supporting this study under the Grant No. BA 3565/3-1.

6. References

[1] Dumont, M.; Ernst, R.; Garnier, C.; Hasan, G.; Petitpas, P.: Innovative inductive cold crucible configurations with improved efficiency. Journal of Iron and Steel Research Int., 19/1 (2012) 669-672.

[2] Bojarevics, V.; Roy, A.; Pericleous, K.: Magnetic levitation of a large liquid volume. Magnetohydrodynamics 46/4 (2010) 317-329.

[3] Spitans, S.; Jakovics, A.; Baake, E., Nacke, B.: Numerical modelling of free surface dynamics of melt in an alternate EM field. Part I: implementation and verification of model. *Met. Mat. Trans. B*, 44/3 (2013) 593-605.

[4] Spitans, S.; Baake, E., Nacke, B.; Jakovics, A.: 3D LES two-phase simulation of conventional electromagnetic levitation experiment. In the Proc. of Int. Conf. on Fundamental and Applied MHD, Thermo acoustic and Space technologies, Riga, Latvia, 16-20 June, 2014.

[5] Tadano, H.; Fujita, M.; Take, T.; Nagamatsu, K.; Fukuzawa, A.: Levitation melting of several kilograms of metal with a cold crucible. IEEE Transactions on Magnetics. 30/6 (1994) 4740-4742.

[6] Chintarin, G.; Timelli, G.; Losco, R.; Bonollo, F.: Development and operational experience on cold crucible levitation melting apparatus for light metal casting. In: Proc. Int. Conf. on Heating by Electromag. Sources HES-13, Padua, Italy, 21-24 May, 2013, pp. 423-430.

[7] Morita, A.; Fukui, H.; Tadano, H.; Hayashi, S.; Hasegawa, J.; Niinomi, M.: Alloying titanium and tantalum by cold crucible levitation melting (CCLM) furnace. Mat. Sci. and Eng. A280 (2000) 208-213.

3D LES TWO-PHASE FLOW SIMULATION OF CONVENTIONAL ELECTRO-MAGNETIC LEVITATION MELTING EXPERIMENT

SPITANS[1,2] S., BAAKE[1] E., NACKE[1] B., JAKOVICS[2] A.
[1]Institute of Electrotechnology, Leibniz University of Hannover,
Wilhelm-Busch Straße 4, 30167 Hannover, Germany
[2] Laboratory for Mathematical Modelling of Environmental and Technological Processes,
University of Latvia, Zellu Street 8, LV-1013 Riga, Latvia
E-mail address of the corresponding author: spitans@etp.uni-hannover.de

Abstract: By means of external coupling between electromagnetic (EM) and hydrodynamic (HD) problems a numerical model for the liquid metal flow with free surface dynamics in an alternate EM field is developed. The 3D model with precise Large Eddy Simulation (LES) turbulence description is applied for the case of conventional EM levitation. Simulation results are compared to experimental measurements of the levitated molten metal free surface shape, as well as calculation results obtained with other models.

1. Introduction

Numerical simulation in the field of magnetohydrodynamics (MHD) at the present moment is the main widely available tool for investigation of EM induced flow. Advanced multiphysical processes like energy and mass transfer, crystallization and homogenization of alloying particles in induction furnaces are calculated nowadays in 3D with fixed hydrostatic steady free surface shape and précised LES turbulence description [1].

Free surface dynamics of EM levitated melt, flow and energy transfer in 2D axisymmetric consideration, as well as crystallization processes with free surface behavior in EM induction furnaces were successfully simulated using simplified two-parameter turbulence models [2]. The results of 3D numerical calculation of a liquid droplet dynamics in a high DC magnetic field were published recently [3].

However, at the present moment there is no approach developed for 3D calculation of multiphysical processes in EM induction equipment with consideration of free surface dynamics and application of LES description for turbulent flow. The previous investigations revealed that in case of Induction Crucible Furnace (ICF) with two characteristic mean flow vortexes only the LES model gives comparable results to experimental measurements [1].

Meanwhile, by means of external coupling between *ANSYS Classic*, *FLUENT*, *CFX-Post* and a self-written surface filtering procedure a numerical model for the liquid metal flow with free surface dynamics in an alternate EM field has been developed. The comparison of our k-ω SST calculation results to experimental measurements and results of other models for the molten metal free surface shape in ICF, induction furnace with cold crucible and EM levitation setup, as well as comparison of free surface small amplitude oscillation period to analytical estimation, revealed a good correlation and approved accuracy of our approach [4].

In this article the further validation of our numerical model is presented. Our two-phase flow 2D k-ω SST, 3D k-ω SST and 3D LES calculations of EM levitated molten aluminum are compared to experimentally observed free surface shape and simulation results of V. Bojarevics *et. al.* [5].

2. Conventional EM levitation melting experiment

For EM processing of metallic materials at great temperatures and high purity a contactless method of EM levitation melting is known to be appropriate since older times. In particular, melting and EM levitation of liquid aluminum sample (m = 21.5 g) in a laboratory-scale levitation furnace was investigated experimentally in the early fifties [6]. The experimental setup consisted of two coaxial inductors - upper pancake coil and a lower cone-shaped coil - that were fed with counter oriented alternate currents of I_{ef} = 600 A at a frequency of f = 9.6 kHz. The sketch of the setup with dimensions can be found in [6].

However, the article [6] did not provide any quantitative information about the dynamics and average shape of the levitated melt so it was decided to repeat the experiment ourselves. The copper water-cooled inductor we have manufactured and used in experiment is shown in fig. 1, a. Levitation melting of aluminum sample (m = 19.6 g) was successfully performed at I_{ef} = 650 A and f = 9.65 kHz. As the sample was molten completely the series of experiment photos were post-processed and a time-averaged free surface shape of the liquid aluminum charge was obtained (fig. 1, b).

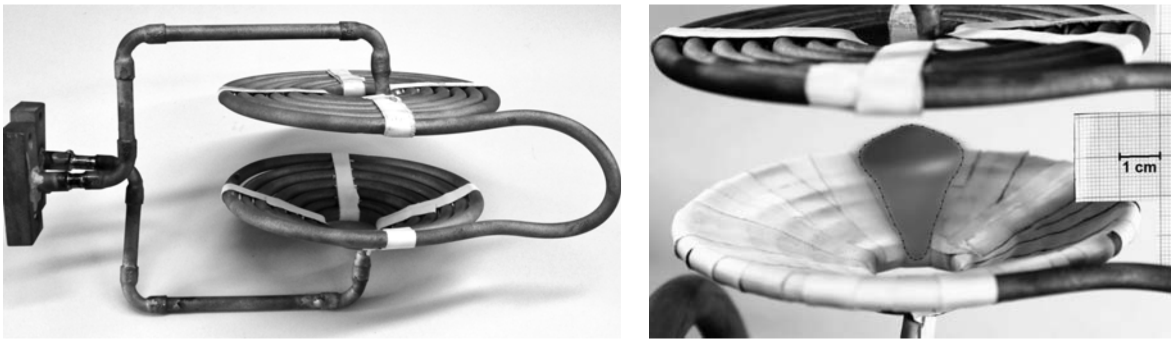

(a) (b)

Figure 1: Our experimental setup for repeating of Okress *et. al.* levitation melting experiment (a) and a post-processed time-averaged shape of the molten aluminum sample (b).

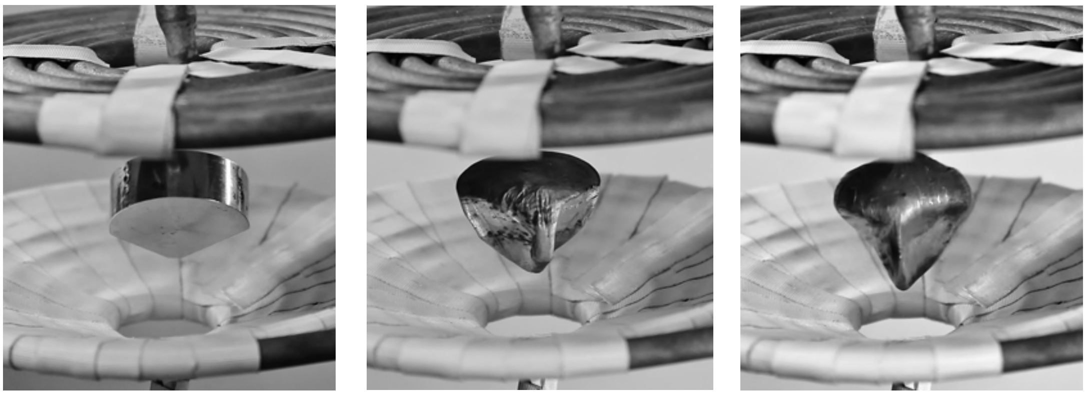

(a) (b) (c)

Figure 2: Solid (a), partially molten (b) and completely liquid (c) aluminium sample covered with oxide layer in our levitation melting experiment.

To reduce the instability of a solid sample at the beginning of experiment the specimen initial cylindrical shape was modified as shown on fig. 2, a. During the experiment not yet molten part of the sample remained above the liquid part because of a higher solid electrical conductivity, meanwhile edged shape of the solid aluminum introduced wrinkles on the free surface of the melt (fig. 2, b). The experiment was performed in an open air conditions so the surface of the sample was covered with an oxide layer. Because of oxide shell these wrinkles partially remained even after the sample was completely molten (fig. 2, c).

However, first experiments failed because of the leakage of the semi-molten sample. It could be noticed that right before the leakage the unmolten aluminum had detached from top and accelerated by the flow drag started to circulate with the flow introducing additional free surface instability that caused draining.

Nevertheless, completely molten aluminum sample was successfully levitated for 3 minutes, after that inductor current was slowly decreased down to I_{ef} = 600 A and the sample was drained into a container with sand avoiding the contact to inductor.

3. Numerical simulation and validation

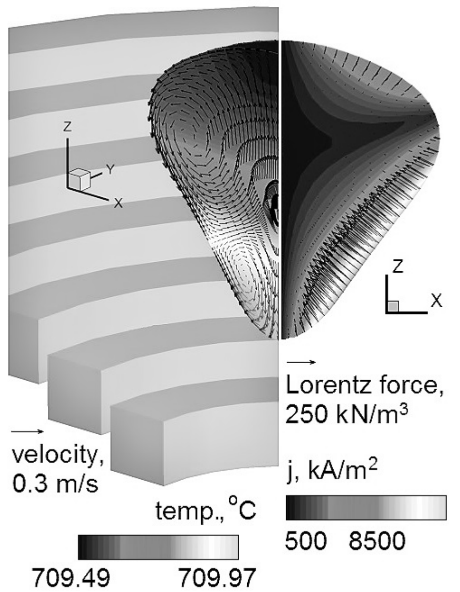

Figure 3: Velocity (on the left), EM force (on the right) and a shape of molten aluminium by V. Bojarevics *et. al.* transient 2D calculation [5].

A transient numerical simulation of the heat transfer, levitated molten metal flow and free surface shape in this original experiment [6] has already been performed by V. Bojarevics *et. al.* in 2D axisymmetric consideration using a modification of k-ω turbulence model and a self written software [2]. The results appeared to be in a good agreement with experimentally observed “spinning top” shape and indicated on a fully turbulent two torroidal vortex flow structure and nearly homogeneous temperature distribution (fig. 3).

In order to supplement the previous verification of our model [4] the particular levitation experiment was numerically calculated in 2D axisymmetric and full 3D consideration using k-ω SST and LES turbulence models. The following temperature independent material properties of liquid aluminum were used in our and V. Bojarevics *et. al.* numerical simulations: density ρ_{Al} = 2380 kg/m^3, surface tension γ_{Al} = 0.94 N/m, electrical conductivity σ_{Al} = 3.85 MS/m and dynamic viscosity η_{Al} = 2.38 mPa·s.

Example of our 3D model mesh at particular instant free surface shape for EM problem ($4 \cdot 10^5$ elements) with precise resolution of EM skin-depth δ_{em} = 2.6 mm (fig. 4, a and b) and a fine HD mesh ($7 \cdot 10^5$ elements) for LES two-phase flow calculation (fig. 4, c) is shown. Lorentz force recalculation upon the new free surface shape was performed every 5 ms of the flow time. The simulation of 3 s of flow took 1 month of computation time on a cluster with 10 nodes (3 GHz each).

According to our transient 2D (fig. 5, a) and 3D (fig. 5, b) k-ω SST calculations (black lines), as well as transient 2D k-ω calculation of V. Bojarevics (grey line), the EM field, free surface shape and the flow adjust themselves to a completely steady state regime with characteristic two torroidal vortex structure. Velocity patterns predicted by 2D and 3D k-ω SST models, as well as confining EM forces for the 2D k-ω SST case are shown below (fig. 5, a and b). The calculation of the free surface shape and position of the mass centrum by these models are nearly the same, however, our 2D and 3D k-ω SST models predict 15 % and 50 % less maximal velocity in comparison to 2D k-ω model of V. Bojarevics.

Meanwhile, these URANS models still differ from our measurements of the time-averaged droplet shape, as well as do not predict the fluctuating behavior of velocity and free surface in a quasi steady state regime observed in experiment.

Time-averaged free surface shape obtained with our 3D LES calculation (fig. 5, c) appears to be in a better agreement with time-averaged experimental measurements (fig. 1, b) and maximal velocity of the time-averaged flow pattern proves to be 67 % greater than in calculation of V. Bojarevics.

In comparison to the Reynolds-averaged flow and a smooth free surface shape obtained with transient 2D and 3D k-ω SST calculations (fig. 5, a and b) the finer flow structures resolved with LES reach up to 1 m/s in velocity maximum value (fig. 6, c) and on account of dynamic pressure contribute to free surface fluctuations. Instability of molten aluminum free surface shape at a quasi steady state regime observed in experiment (fig. 6, a) is in a good qualitative agreement with the transient 3D LES results (fig. 6, b).

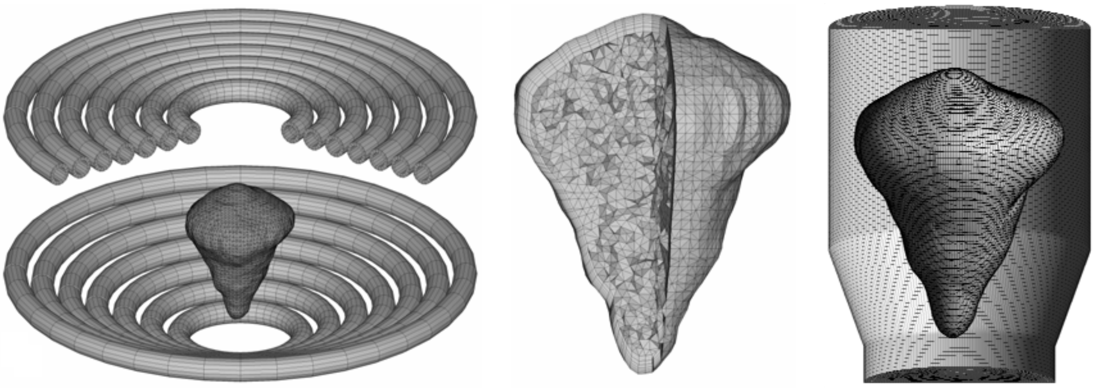

(a) (b) (c)

Figure 4: numerical mesh for 3D EM calculation (a) with a fine resolution of the molten metal skin-depth (b) and numerical mesh for 3D LES two-phase flow calculation (c).

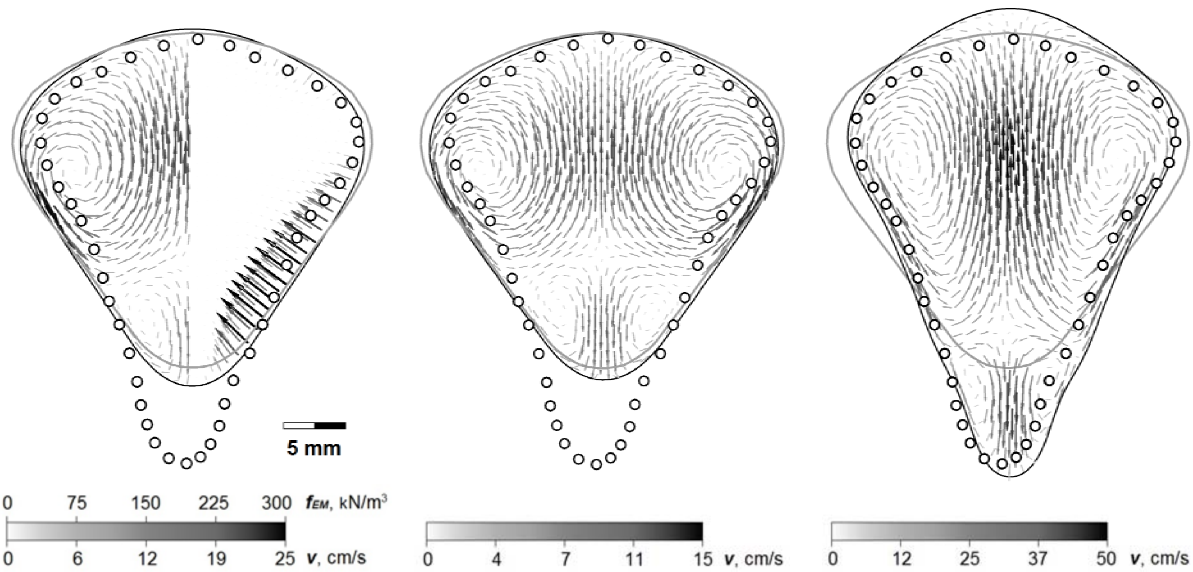

(a) (b) (c)

Figure 5: comparison of experimentally measured time-averaged free surface shape (O) and 2D k-ω calculation results of V. Bojarevics (–) to our 2D k-ω SST (a), 3D k-ω SST (b) and 3D LES (b) time-averaged solution.

5. Conclusions

3D numerical model for coupled free surface and liquid metal flow calculation in EM field is developed. The model is adjusted for the case of EM levitation and can be used with précised LES turbulence description.

In comparison to k-ω Reynolds-averaged calculation the 3D LES model is able to predict the fluctuating behavior of velocity and free surface shape at a quasi steady state regime, much greater instant flow velocity values and better agreement with time-averaged and instant free surface shapes obtained in experiment.

Using the developed model it is planned to tailor the design of the novel levitation melting setup [7] and configuration of EM field in order to meet the conditions for stable EM levitation of industrial-scale molten metal charge and reproduce it in the laboratory experiment.

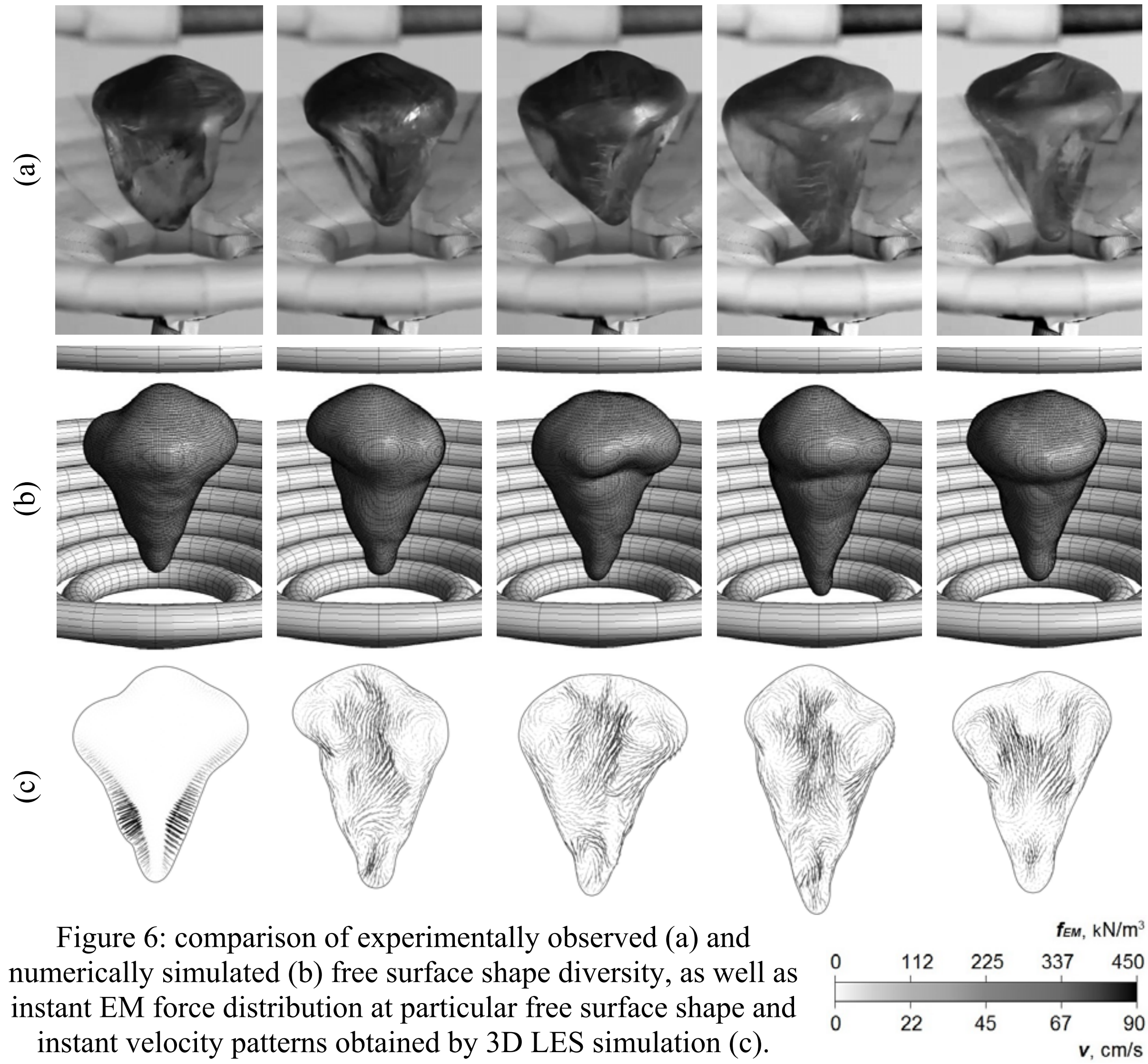

Figure 6: comparison of experimentally observed (a) and numerically simulated (b) free surface shape diversity, as well as instant EM force distribution at particular free surface shape and instant velocity patterns obtained by 3D LES simulation (c).

5. Acknowledgements.

Current research was performed with financial support of the ESF project of the University of Latvia, contract No. 2009/0138/1DP/1.1.2.1.2/09/IPIA/VIAA/004. The authors wish to thank the German Research Association (DFG) for supporting this study under the Grant No. BA 3565/3-1. The authors would like to acknowledge Dr. Valdis Bojarevics for kindly sharing his simulation data of E. C. Okress *et. al.* experiment.

6. References

[1] Kirpo, M.: Modelling of turbulence properties and particle transport in recirculated flows. Ph. D. Thesis, University of Latvia, Riga (2008).

[2] Bojarevics, V.; Harding, R.; Pericleous, K., Wickins, M.: The development and experimental validation of a numerical model of an induction skull melting furnace. *Met. Mat. Trans. B*, 35 (2004) 785-803.

[3] Easter, S., Bojarevics, V., Pericleous, K.: Numerical modelling of liquid droplet dynamics in microgravity. *J. Phys. Conf. Ser.*, (2011) 327 012027.

[4] Spitans, S.; Jakovics, A.; Baake, E., Nacke, B.: Numerical modelling of free surface dynamics of melt in an alternate EM field. Part I: implementation and verification of model. *Met. Mat. Trans. B*, 44/3 (2013) 593-605.

[5] Simulation data obtained through a personal communication with Dr. Valdis Bojarevics.

[6] Okress, E.; Wroughton, D.; Comenetz, G.; Brace, P. and Kelly, J.: Electromagnetic Levitation of Solid and Molten Metals. *J. Appl. Phys.*, 23 (1952) 545-552.

[7] Baake, E., Spitans, S., Jakovičs A.: New technology for EM levitation melting of metals. In the Proc. of Int. Conf. on Heating by Electromag. Sources HES-13, Padua, Italy, 21-24 May, 2013, pp. 1-8 (addendum).

NUMERICAL MODELING OF GAS BUBBLE DYNAMICS IN LIQUID METAL IN APPLIED DC MAGNETIC FIELD

TUCS[1] A., SPITANS[1,2] S., JAKOVICS[1] A., BAAKE[2] E.
[1] Laboratory for Mathematical Modeling of Environmental and Technological Processes, University of Latvia, Zellu Str. 8, LV-1002 Riga, Latvia
[2]Institute of Electrotechnology, Leibniz University of Hannover
Wilhelm-Busch Str. 4, 30167 Hannover, Germany

Abstract. Apart from common steam reforming process the thermal decomposition of methane is regarded as an alternate route to producing hydrogen and elemental carbon with out of CO_2 emissions. Chemical reaction of decarburation can be ensured by means of methane bubbly flow through a molten metal bath and additionally controlled by external electromagnetic field. On this stage of research model for single bubble rise in presence of external DC magnetic field, based on VOF approach is developed. Model is verified, in absence of applied field, for different liquid types (water solution, GaInSn) at different flow conditions, obtained bubble terminal shapes and velocities reveal a fine correlation with existing experimental and model results. Bubble rise dynamics is studied in GaInSn in longitudinal/transversal DC magnetic field, appropriate rise characteristics and their dependencies on field strength are in agreement with existing (experimental/model) predictions.

1. Introduction

One of the possibilities to produce H_2 without forming CO_2 is decomposition of CH_4 [1]:

$$CH_4 \rightarrow C + 2H_2, \ (\Delta h_0 = 74.85 \text{ kJ/mol}).$$

Due to fact that reaction of decarburation is endothermic the temperature must be above 600 ˚C for the reaction to proceed at a reasonable rate. The main problem for this process is the deposition of the nanocarbon particles on the reactor walls (or catalyst surface), which causes the pressure to drop and creates thermal resistance, thereby decreasing reactor life. Alternative way is realization of reaction ensuring a methane bubbly flow through a molten metal bath and for process control and increase of efficiency use applied DC/AC magnetic field.

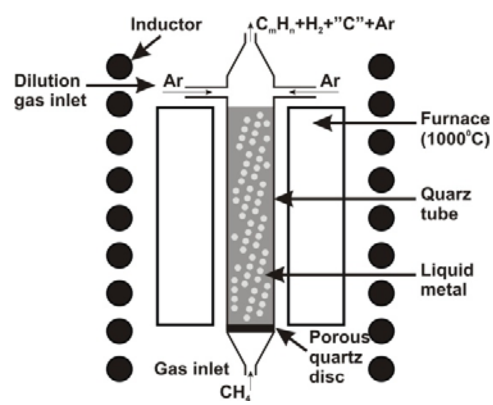

Figure 1: Liquid metal bubbly column for H_2 production without CO_2 emission.

Knowledge of single bubble rise properties (characteristic force coefficients: drag, lift, acceleration) can be used for implementation in bubble cloud behavior model like Euler-Euler, Euler-Lagrange which, in turn, can be used for description of methane thermal cracking reactor (Figure 1). In appropriate context great challenge is attributed to the tracking of sharp interface between the gas bubble and the surrounding liquid, classical difficulty causes: discontinuity of the physical properties across the fluid interface, geometric complexity caused by bubble deformation, numerical smearing of interface between the gas bubble and the surrounding liquid, effects of surfactants on the interface. Mentioned factors are dependent on the mesh quality and in majority of cases significantly increase calculation time. In the present work for appropriate problem class there was examined applicability of VOF method implemented in *ANSYS Fluent*, obtained results for different liquids (water solution, GaInSn) are compared with existing experimental approaches [2].

2. Rising bubble model

Bubble rise dynamics in electrically conductive liquid in external DC EM field can be characterized by the following set of equations:

$$\frac{\nabla^2 \boldsymbol{B}}{\mu_{mag}\sigma_{el}} + (\boldsymbol{B}\cdot\nabla)\boldsymbol{U} - (\boldsymbol{U}\cdot\nabla)\boldsymbol{B} = 0, \tag{1}$$

$$\boldsymbol{j} = \sigma_{el}(-\nabla\varphi + [\boldsymbol{U}\times\boldsymbol{B}]), \tag{2}$$

$$\nabla\cdot\boldsymbol{U} = 0, \tag{3}$$

$$\frac{\partial \boldsymbol{U}}{\partial t} + (\boldsymbol{U}\cdot\nabla)\boldsymbol{U} = -\frac{\nabla p}{\rho_l} + \nu_l\nabla^2\boldsymbol{U} + \boldsymbol{f}, \tag{4}$$

where $\boldsymbol{B}$ is magnetic field induction, $\boldsymbol{j}$ – current density, $\boldsymbol{U}$ - velocity, p - pressure, ν_l - kinematic viscosity, $\boldsymbol{f}$ - sum of volume forces, e. g. gravitational: $\boldsymbol{f}_g = \boldsymbol{g}$ and Lorentz force: $\boldsymbol{f}_L = [\boldsymbol{j}\times\boldsymbol{B}]$. First pair of equations describes EM nature of the process: Induction equation (1), where free charges/displacement currents are neglected, for process magnetic Reynolds number: $Rm \ll 1$, in turn equation (2) corresponds Ohm's law. The second pair of equations characterizes hydrodynamic processes of conductive viscous liquid that is considered as incompressible (3). Momentum balance is achieved on account of equation (4).

Because the system contains two phases a dynamics of their boundary should also be described. This can be done by means of coupling magnetohydrodynamics (MHD) module and Volume of Fluid (VOF) technique implemented in *ANSYS Fluent.*

3. Bubble free emersion in simple liquids

3.1. Analysis of numerical effects. In industrial applications density of primary phase $\rho_l \sim 10000$ kg/m^3, numerical effects in case of such systems can play significant role, thus their impact on physical results should be studied very carefully. It is known fact: to obtain accurate results appropriate momentum equation discretization should have high order of precision. However, how these results are dependent on mesh quality and time discretization is rather unclear for appropriate systems under consideration. To study this effects on rather popular for CFD applications QUICK scheme (which is based on a weighted average of second-order-upwind and central interpolations of the velocity) there was considered 2D planar circular air bubble emersion (ρ_{air} = 1.2 kg/m^3, η_{air} = 18 μPa·s, D = 4 mm) in GaInSn eutectic (ρ_{GaInSn} = 6361 kg/m^3, σ_{el} = 3.27 MS/m, σ = 2.2 mPa·s) initialized at the bottom of rectangular fluid domain ($x = 33\cdot D$ and $y = 63\cdot D$) in the beginning of calculation, obtained results for bubble trajectory and velocity are shown on Figure 2a,b. For fixed mesh in case of QUICK scheme there can be seen strong dependence on time step (dotted, dash-dotted and solid line). If time step is too large than there is not observed transition from straight rise trajectory to zig-zagging, bubble rise is initially oscillatory. With decrease of time step there is observed decrease of oscillation amplitude and increase of velocity. Very close results to most precise (QUICK with small enough time step: $dt = 10^{-6}$ s and number of quadratic

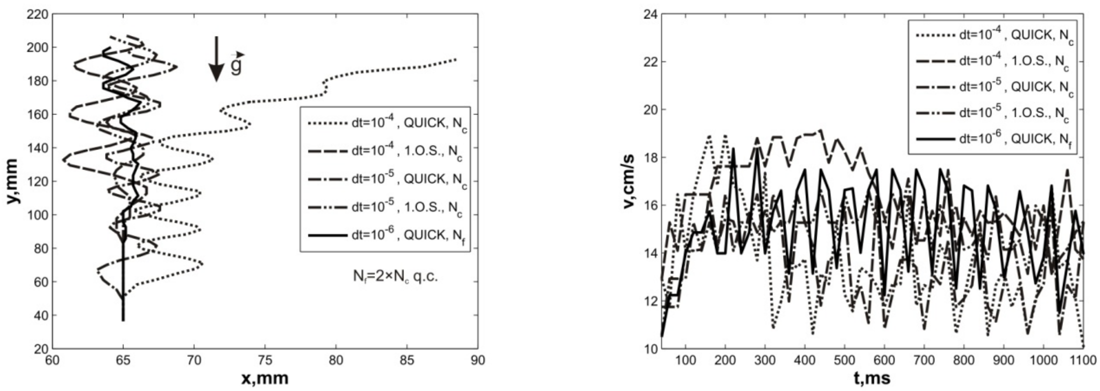

(a) (b)

Figure 2: Time step, mesh quality and momentum discretization scheme influence on 2D bubble rise dynamics in liquid metal (a) - trajectory (b) - velocity.

Cells: $N_f = 265980$, correspondent solid lines) can be obtained with 1 – order scheme (velocity quantities at cell faces are determined by assuming that the cell-center values represent a cell-average value and hold throughout the entire cell) (with $dt = 10^{-5}$ s and $N_c = 147364$, correspondent dash-dash-dotted lines), due to numerical stability of this approach. It can be concluded that 1 – order scheme have better (with lower computational costs) convergence properties than high order scheme when spatial-time discritization is not high. In general, it can be concluded that for single bubble rise in GaInSn appropriate Courant condition: $Udx/dt < C$ instead of traditional $C = 1$, in case of usage of 1 – order scheme must be $C \approx 0.05$. Recently in [3] there was considered bubble rise in aluminum ($\rho_{Al} = 2380$ kg/m^3) also in 2D approach, it was stated that for numerical simulations of such system in case of 2 – order scheme: $C < 0.2$.

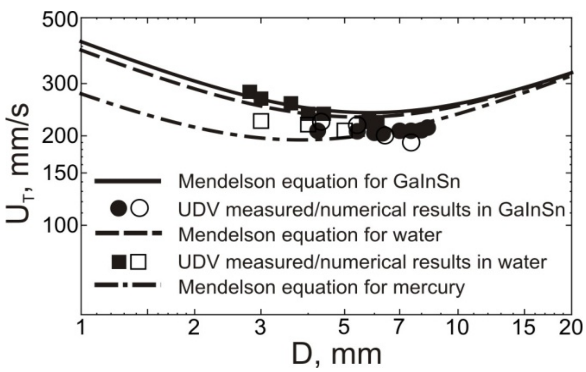

Figure 3: Termianl bubble velocity vs. equivalent bubble diameter in various liquids [2].

To check physical correctness of chosen numerical approach there was considered 3D bubble rise ($N = 2\square10^6$) in GaInSn and also in pure water due to very similar ρ_l/σ ratios (same bubble shape characteristics) of both liquids, appropriate results compared with experiment/theory [2,4] (Figure 3), there can be seen good correlation.

3.2. DC magnetic field influence on a rise dynamics. For demonstration of models ability to describe physical aspects of DC magnetic field influence on bubble rise there was considered 2D system. General mechanism of appropriate influence is shown on Figure 4. With increase of applied field induction there is observed damping of bubble induced vortex structures which is accompanied with increase of bubble rise velocity. However when field strength is enough to suppress all vorticity in bubble wake there is observed decrease in relative velocity as well as damping of oscillations in field transversal directions. Bubble rise ($D = 4$ mm) trajectories for different field orientations (longitudinal/transversal) and induction values are presented on Figure 5a,b. From simulation results for bubble trajectories there can be observed domination of parallel velocity components to appropriate field direction in moderate induction value range. When field is strong enough surprisingly in both cases observed straightening of appropriate rise trajectories, however similar straightening process is also observed in transversal field for 3D bubble rise in mercury [5].

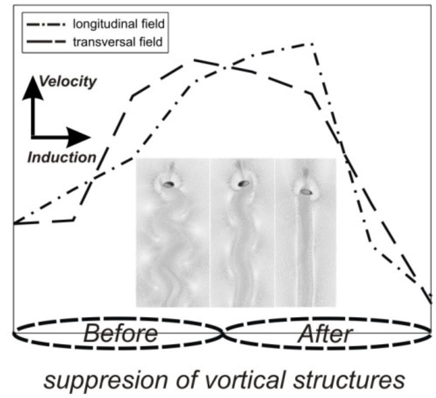

Figure 4: General mechanism of field influence on bubble rise.

There was considered 3D bubble rise in applied longitudinal field (B = 0.3 T), obtained result comparison with experiment [2] for relative drag coefficients vs. interaction parameter are shown on Figure 6. In general there is observed tendency that for smaller bubbles drag coefficient increase with increase of field value, similar tendency is also observed in case of liquid metal flow past insulating sphere. In turn, for larger bubbles is observed reverse tendency: decrease of drag coefficient with increase of interaction parameter, this is stimulated by coupling between bubble elongation in fields direction and modification of bubble wake due to applied field. There can be seen qualitative correspondence between experiment and numerical prediction in case of Bo = 2.2, however for Bo = 3.4; 4.9 there is sufficient deviation, this is due to presence of impurities in melt of appropriate experimental setup [2], in turn, occurrence of oxides in melt diminishes the surface tension significantly [6]. Thus in experiment $C_D/C_D(N\ =\ 0)$ character change (symmetry brake) is observed at smaller Bond number value comparing to corresponding numerical model result (Bo ~ 6.6), from physical point of view it can be expected, because in last case surface tension decreasing factors are not present, this mean that with increase of diameter Lorentz force influence on bubble shape will be smaller, due to increased surface tension force. Contrary in [7] using immersed boundary method symmetry brake is observed at even smaller Bond number value than in experiment [2]. In case when B = 1 T appropriate model predicts increase of relative drag experienced by bubble with increase of Bond number (Figure 7), in general such tendency could be expected, because in this case Lorentz force impact on bubble shape is balanced by surface tension force, thus impact on rise process is possible only through wake modifications, like in case of small bubbles (Figure 6). In turn, increase of Bond number in field absence indicates increase in rise velocity, in applied field this will lead to larger Lorentz force values, thus larger drag values. Similar tendency in relation between drag and Bond number like in Figure 7 is observed in case of bubble rise in transversally applied DC magnetic field [5]. In general, obtained model results

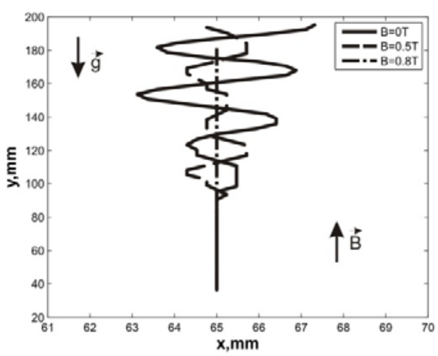

(a)

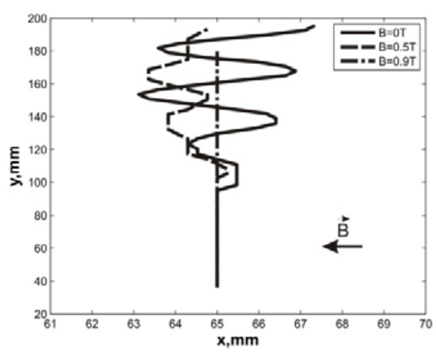

(b)

Figure 5: Stationary magnetic field influence on bubble (D = 4 mm) in 2D approach on rise trajectory (a) – longitudinal field (b) – transversal field.

are very promising also due to fact that system is considered on $2x10^6$ element mesh, in turn, appropriate results in [7] are obtained on $83.9x10^6$ element mesh, thus usage of VOF method can lead to considerable decrease of computational costs.

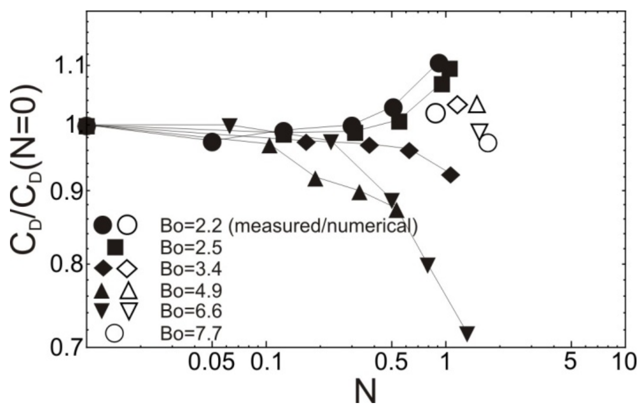

Figure 6: Relative change of drag coefficient vs. magnetic interaction parameter result comparison with experiment [2].

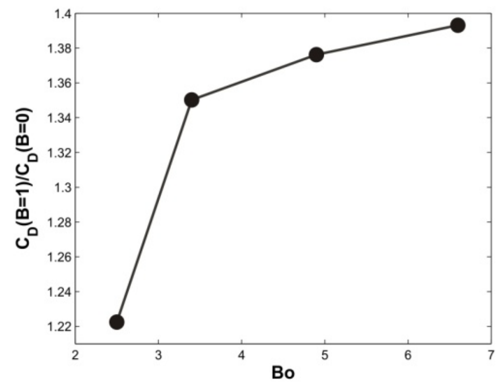

Figure 7: Drag coefficient vs. Bond number in longitudinally applied field (B = 1 T).

4. Conclusions

The obtained model results clearly show ability to describe bubble rise process for different liquid classes. It is shown that for minimization of computational costs for systems with high density ratios 1 - order scheme can be applied for momentum equation and in case of GaInSn appropriate Courant condition: $C < 0.05$ should be taken into account. In case of applied DC magnetic field model give correct physical results, which are in good agreement with experiments [2], for high magnetic field values (B ~ 1 T) model predicts increase of bubble experienced relative drag with increase of Bond number.

5. Acknowledgments.

The current research was performed with financial support of the LIMTECH project.

6. References

[1] Abanades, A.: Experimental analysis of direct methane cracking, Int. J. Hydrogen Energy 36 (2011) 12877-12886.

[2] Zhang C., Eckert S., Gerbeth G.: Experimental study of single bubble motion in a liquid metal column exposed in a DC magnetic field, Int. J. Multiphase Flow 31 (2005) 824-842.

[3] Liu H., Xie M.Z., Liu H.S., Wang D.Q.: Numerical study on bubble rising behaviour in a reciprocally stirred molten metal flow, Rev. Adv. Mater. Sci. 33 (2013) 195-201.

[4] Mendelson H.D.: The prediction of bubble terminal velocity from wave theory, AlChE J. 13 (1967) 250-253.

[5] Mori Y., Hijikata K., Kuriyama K..: Experimental study of bubble motion in mercury with and without a magnetic field, J. Heat Transfer 99 (1977) 404-410.

[6] Szekely J.: Fluid flow phenomena in metals processing, Academic Press 1979.

[7] Schwarz S., Frohlich J.: DNS of single bubble motion in liquid metal and influence of magnetic field, Proc. Symposium on Turbulent Shear Flow Phenomena, Ottawa, Canada 2011.

PORE SCALE SIMULATION OF MAGNETOSOLUTAL MICROCONVECTION IN FERROFLUID SATURATED POROUS STRUCTURES

ZABLOTSKY D., BLUMS D.
Institute of Physics of University of Latvia, 32 Miera str., Salaspils, LV-2169, Latvia
E-mail: dmitrijs.zablockis@gmail.com

Abstract: We consider an idealized model of ferrofluid saturated porous medium composed of microscale non-magnetic inclusions with simple geometry. The application of homogeneous magnetic field induces complicated pattern of internal demagnetizing fields owing to the difference in magnetic permeability. In turn, the imbalance of ferroparticle concentration is created by non-uniform heating and associated colloidal thermophoresis. Numerical simulations of magnetosolutal microconvection show significant intensification of pore-scale mixing and appearance of solvent flux in the direction of temperature gradient.

1. Introduction

Ferrofluids – colloidal solutions of magnetic nanoparticles – exhibit pronounced Soret effect, i.e. colloidal thermophoresis. The influence of magnetic field on the drift of colloidal particles attracts interest as a means of control and intensification of mass transport in these media. While theory predicts that in bulk solutions the direct dependence of molecular mass transport coefficients on homogeneous magnetic field is weak [1]-[3], specific microconvective phenomena, i.e. magnetic solutal microconvection, may appear [4]-[5] causing significant intensification of mass transfer. Recent experimental evidence [6]-[7] suggests that magnetic phenomena are also quite significant in porous environments or membranes resulting in considerable attenuation of the thermophoretic separation due to enhanced mixing. It is hypothesized that similar magnetic microconvection may be partially responsible for this effect [8].

When magnetic field is applied to a ferrofluid saturated porous medium the jump of magnetic permeability across the boundary of non-magnetic inclusions may cause the appearance of significant gradients of internal magnetic field in the vicinity of the interface. A system of such inclusions thus forms markedly nonhomogeneous internal magnetic field within the porous environment. In turn, in the conditions of non-uniform heating the strong colloidal thermophoresis induces the formation of corresponding gradients of ferroparticle concentration. Both the appearance of the spatial non-homogeneity of the distribution of dispersed magnetic phase and the internal magnetic field contribute to the formation of the associated non-potential magnetosolutal buoyant force, which may entrain the ferrofluid and create pore-scale magnetosolutal microconvection. Apart from pore-scale microconvective circulations [8]-[9], the formation of integral flow is possible in the vicinity of the inclusions [8].

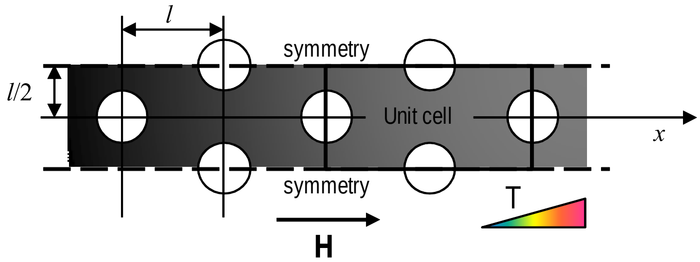

Figure 1: Scheme of the arrangement – non-magnetic cylindrical elements immersed in ferrofluid, temperature gradient and magnetic field are applied across the porous structure.

Here we report preliminary results of numerical simulations of pore-scale magnetosolutal microconvection in geometrically simple model of porous media. We create a

1D arrangement of non-magnetic microscale cylinders immersed in ferrofluid (Fig.1). The porosity of the system is $\varepsilon=1-\pi/l^2$. A temperature gradient is applied across the structure and homogeneous external magnetic field is imposed in the same direction.

2. Magnetic microconvection

The magnetic force density acting on ferrofluid due to magnetic field is expressed by Kelvin body force term $\mathbf{F}=\mu_0(\mathbf{M}\nabla)\mathbf{H}$ with **M** – magnetization of ferrofluid and **H** – magnetic field. Assuming $\mathbf{M}=\chi(c,H)\mathbf{H}$, where $\chi(c,H)$ – magnetic susceptibility at given mass concentration and magnetic field, and with linear relationship for the magnetic susceptibility $\chi(c,H)=\chi_0(1+\chi_c\Delta c)$, where $\Delta c=c-c_0$, c_0 – reference mass concentration, $\chi_c=1/c_0$ and χ_0 – susceptibility at reference parameters, the non-potential part of the force density becomes $\mathbf{F}=\mu_0\chi_0\chi_c\Delta c H_0\nabla[(\mathbf{h}+\mathbf{\Delta H}/2H_0)\mathbf{\Delta H}]$ with $\mathbf{\Delta H}=\mathbf{H}-\mathbf{H_0}$, $\mathbf{H_0}=H_0\mathbf{h}$ – reference magnetic field, **h** – unit vector. Thus variation of ferroparticle concentration and magnetic field can produce magnetic convection in ferrocolloid.

The diffusive dynamics of colloidal nanoparticles is very slow and are only relevant on submillimetre lengthscales. In turn, the Schmidt number $Sc=\eta(\rho D)^{-1}$, where η and ρ – viscosity and density of ferrocolloid, D – diffusivity of ferroparticles, expresses the ratio of momentum and mass diffusivities and is of the order 10^4-10^5. The magnetosolutal microconvection then is creeping convection. Introducing characteristic scales for length L, time L^2D^{-1}, magnetic field $\overline{\Delta H}$, concentration perturbation $\overline{\Delta c}$ the dynamics of the ferrocolloid is described by dimensionless Stokes equation

$$-\nabla p+\Delta\mathbf{u}+Rm_c c\nabla[(\mathbf{h}+r_H\boldsymbol{\delta}\mathbf{H})\boldsymbol{\delta}\mathbf{H}]=0 \tag{1}$$

and the continuity condition $\nabla\cdot\mathbf{u}=0$. Here $r_H=\overline{\Delta H}/2H_0$ typically does not exceed 5% and is disregarded. The magnetosolutal Rayleigh number is $Rm_c=\mu_0\chi_0\chi_c H_0 L^2(\eta D)^{-1}\overline{\Delta c}\,\overline{\Delta H}$.

In non-isothermal ferrocolloid the linearized mass flux due to diffusion and thermophoresis is $\mathbf{J}=\mathbf{u}c-D\nabla c-c_0(1-c_0)DS_T\nabla T$ [10], where S_T is Soret coefficient. For now we neglect magnetophoretic contributions. Introducing the thermal scale $\overline{\Delta c}=c_0(1-c_0)|S_T|\overline{\Delta T}$ the normalized concentration dynamics equation

$$\frac{\partial}{\partial t}c+\mathbf{u}\nabla c=\Delta(c-T) \tag{2}$$

The Lewis number $Le=\alpha D^{-1}$ characterizing the ratio of thermal and mass diffusivities is also very large in ferrofluids. Thus, the temperature dynamics is much faster than that of concentration and magnetosolutal microconvection does not influence the distribution of temperature. We impose the temperature gradient gradT and calculate $\overline{\Delta T}=\mathrm{gradT}\cdot L$.

A non-magnetic cylinder immersed in ferrofluid with magnetic permeability $\mu_0 = 1 + \chi_0$ and placed in homogeneous magnetic field creates around itself magnetic perturbation $\mathbf{\delta H}$. In dimensionless form (the radius of the cylinder is assumed as length scale L)

$$\mathbf{\delta H} = \mathrm{sign}(K_H)\frac{\cos(\Theta)}{r^2}\mathbf{e}_r + \mathrm{sign}(K_H)\frac{\sin(\Theta)}{r^2}\mathbf{e}_\Theta \tag{3}$$

where r and Θ, $\mathbf{e_r}$ and $\mathbf{e_\Theta}$ – cylindrical coordinates and basis vectors, $K_H = \dfrac{1-\mu_0}{1+\mu_0}$,

$\overline{\Delta H} = |K_H| H_0$. We calculate magnetic perturbation produced by an array of non-magnetic cylinders directly from Maxwell's equations, but the result corresponds to a superposition of 2D dipoles (3).

For typical ferrofluid parameters (S_T=0.1K^{-1}, η=0.001Pa s, D=2·10^{-11}m s^{-2}, c_0=0.15, particle diameter 8 nm, particle spontaneous magnetization 5·10^5 A m^{-1}), external field 0.1T and imposed temperature gradient corresponding to a temperature difference of 20K applied across a 1mm thick porous membrane the magnetosolutal Rayleigh number in the vicinity of cylindrical inclusion with radius 2μm reaches Rm_c=50. This is enough to cause significant microconvective particle transfer and we use this value in simulations.

3. Results

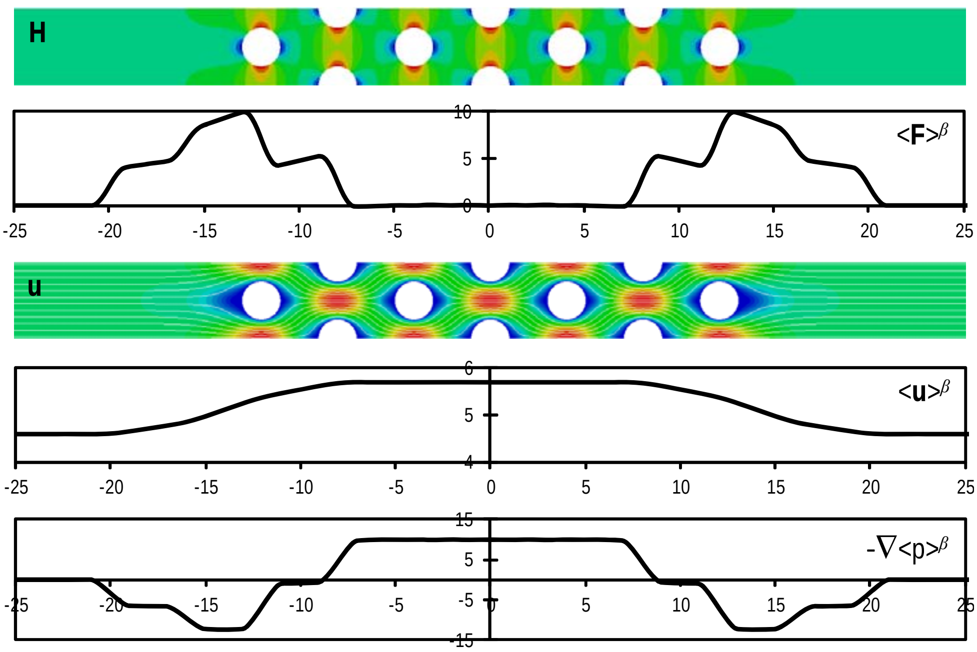

Figure 2: Case 1 simulation (ε = 0.8, fixed concentration gradient), from top to bottom – perturbation of magnetic field H, plot of averaged magnetic force <**F**>$^\beta$, streamlines of velocity **u**, plot of averaged velocity <**u**>$^\beta$, plot of the gradient of averaged pressure -∇<p>$^\beta$.

We start from initial concentration distribution c=-x, which corresponds to a stationary stratification created by temperature T=x. We have performed two series of simulations: in the first case we solve only the Stokes equation and the initial concentration distribution is not allowed to change (case 1). As expected, the calculated distribution of magnetic field perturbation H=**h·δH** is highly inhomogeneous (Fig.2) and so is the magnetic force $\mathbf{F} = Rm_c c\nabla H$. In order to reveal the macroscopic structure of the magnetic forces we perform spatial averaging. The correct average in periodic porous structures is the cellular average across a unit cell [11]. Interestingly, the averaged magnetic force density $<\mathbf{F}>^\beta$ vanishes in the bulk of the porous structure and only remains in the immediate vicinity of the membrane surface, reaching sharp maximum within approximately a single period of the porous structure at both ends of the membrane. While the averaged magnetic force is well localized, its maximum value is proportional to the value of concentration at both ends of the membrane. So, when a concentration gradient is applied across the porous membrane, the total magnetic force is proportional to the thickness of the membrane.

In the second series of calculations we solve also the concentration equation, advancing to the stationary/quasistationary state (case 2). In this case, the averaged concentration gradient decreases within the porous membrane (Fig.3) due to the change of porosity. In turn, the distribution of the averaged magnetic force becomes asymmetric with respect to the midpoint of the membrane. A component of the averaged magnetic force appears within the bulk of the membrane counteracting the pressure difference created by the forces in the vicinity of the membrane surface. These are the consequences of convective dispersion of concentration within the porous membrane. It can be expected that in 2D membranes these effects may lead to instabilities and oscillations.

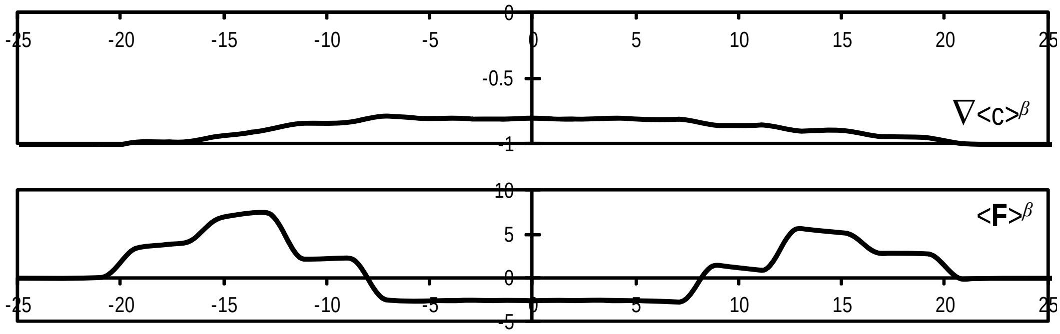

Figure 3: Case 2 simulations (ε = 0.8, concentration can change), from top to bottom – plot of the gradient of averaged pressure $-\nabla<p>^\beta$, plot of averaged magnetic force $<\mathbf{F}>^\beta$.

In the framework of Darcy theory the relationship between the averaged quantities should hold in the bulk of the porous membrane [11]

$$\langle \mathbf{u} \rangle^\beta = -\frac{K}{\varepsilon} \nabla \langle p \rangle^\beta \tag{4}$$

where K is the permeability tensor, which we calculate by solving the closure problem numerically for a unit cell [11]. In the series of calculations when the concentration gradient is fixed (case 1) the averaged magnetic force $<\mathbf{F}>^\beta$ vanishes within the porous structure. That is why it is absent from (4).

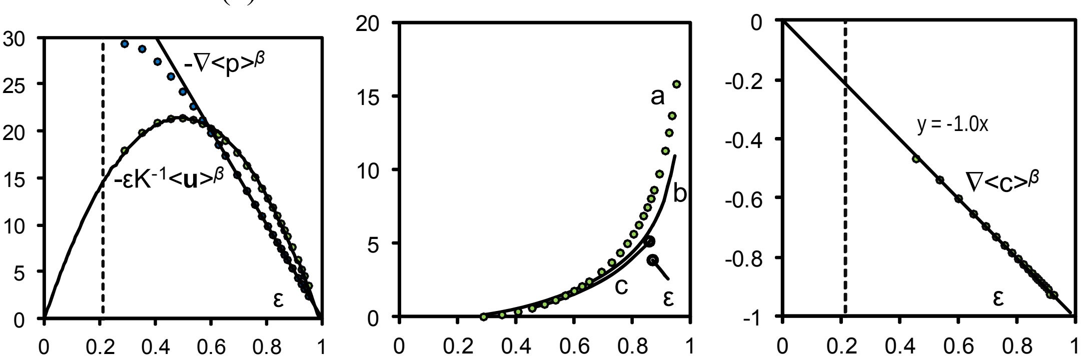

Figure 4: Results of simulations: left – plot of $-\nabla<p>^\beta$ and $\varepsilon K^{-1}<\mathbf{u}>^\beta$ for different porosities (for case 1); middle: *(a)* $<\mathbf{u}>^\beta$ (case 1), *(b)* $<\mathbf{u}>^\beta$ calculated from (4) (case 1), (c) plot of $\varepsilon^{-1}<\mathbf{u}>^\beta$ (case 2); right – plot of $\nabla<c>^\beta$ within membrane (case 2).

The calculated quantities $\widetilde{\mathbf{F}} = \varepsilon K^{-1}\langle\mathbf{u}\rangle^{\beta}$ and $-\nabla\langle p\rangle^{\beta}$ are plotted in Fig. 4 (left) with respect to the porosity ε of the membrane. While $\widetilde{\mathbf{F}}$ is closely parabolic, the dependence of the averaged pressure gradient is mostly linear. Despite the difference the Darcy law (4) acceptably captures the relationship between averaged velocity and pressure (Fig. 4, middle).

In the second series of calculations (case 2) due to the decrease of the concentration gradient within the membrane the averaged velocity decreases as compared with the unperturbed case (case 1). The magnitude of the concentration gradient within the membrane in this situation is proportional to the porosity ε (Fig.4, right). Plotting the quantity $\varepsilon^{-1}\langle\mathbf{u}\rangle^{\beta}$ (Fig.4, middle), it corresponds to the magnitude of the averaged velocity $\langle\mathbf{u}\rangle^{\beta}$ in the unperturbed case (case 1). This correspondence remains up to rather large values of porosity. The little difference can be attributed to convective dispersion within the membrane.

Starting from a certain value of porosity ($\varepsilon\approx0.85$) the dependence experiences a discontinuity and the averaged velocity begins do decrease. This happens due to the establishing of the instability of the flow. The symmetrical configuration is replaced by the asymmetrical one and further increasing the porosity ($\varepsilon>0.95$) we observed periodic oscillations.

4. Conclusions

We have performed pore-scale numerical simulations of ferrofluid magnetosolutal microconvection in 1D ordered porous membranes composed of cylindrical elements. The imbalance of concentration was created by thermophoretic separation induced by a temperature gradient. The application of external magnetic field creates highly inhomogeneous distribution of magnetic force within the membrane, which nevertheless possesses well-defined macroscopic structure. A pressure difference appears across the membrane driving the flow of ferrofluid in the direction of the temperature gradient. We show that interpretation of the results of pore-scale simulations in the framework of the Darcy theory is possible, although errors as high as 30% can take place in some cases.

Acknowledgements. The work has been supported by the Latvian Science Foundation, Project 286/2012

5. References

[1] Blums, E.Ya.: Thermomagnetophoresis of particles in a magnetic suspension. Magnetohydrodynamics 15 (1979) 18-22.

[2] Bacri, J.C.; Cebers, A.; Bourdon, A.; Demouchy, G.; Heegaard, B.M.; Perzynski, R.: Forced Rayleigh Experiment in a Magnetic Fluid. Phys. Rev. Lett. 74 (1995) 5032-5035.

[3] Morozov, K.I.: Gradient diffusion in concentrated ferrocolloids under the influence of a magnetic field. Phys. Rev. E 53 (1996) 3841-3846

[4] Maiorov, M.M.; Tsebers, A.O.: Magnetic microconvection of the diffusion front of ferroparticles. Magnetohydrodynamics 19 (1983) 360-368.

[5] Zablotsky, D.; Mezulis, A.; Blums, E.: Formation of magnetoconvection by photoabsorptive methods in ferrofluid layers. C. R. Mecanique 341 (2013) 449-454.

[6] Blums, E.; Sints, V.; Kronkalns, G.; Mezulis, A.: Non-isothermal separation of ferrofluid particles through grids: Abnormal magnetic Soret effect. C. R. Mecanique 341 (2013) 348-355.

[7] Blums, E.; Sints, V.; Mezulis, A.; Kronkalns, G.: New problems of mass transport in magnetic fluids. Magnetohydrodynamics 49 (2013) 360-367.

[8] Blums, E.: New transport properties of ferrocolloids: magnetic Soret effect and thermomagnetoosmosis. JMMM 289 (2005) 246-249.

[9] Frishfelds, V.; Blums, E.: Drift of ferrocolloids through a cylindrical grid by magnetic force. J. Phys.: Condens. Matter 20 (2008) 204130

[10] Blums, E.; Cebers, A.; Maiorov, M.: Magnetic Fluids. Walter de Gryuter, Berlin, New York, 1997.

[11] Quintard, M.; Whitaker, S.: Transport in Ordered and Disordered Porous Media I-V. Transport in Porous Media 14 (1994), 163-206, Transport in Porous Media 15 (1994), 31-196

SURFACE SHAPE OF A MAGNETIC FLUID BRIDGE BETWEEN PLATES IN THE FIELD OF AN ELECTROMAGNETIC COIL

VOLKOVA[1] T., NALETOVA[2] V., TURKOV[1] V.
[1]Institute of Mechanics, Lomonosov Moscow State University, Moscow, Russia
[2]Faculty of Mechanics and Mathematics, Lomonosov Moscow State University, Moscow, Russia
E-mail: TanyaVolkova@inbox.ru

The transfer of elastic wave energy from the source to the object of influence is a general challenge in applied acoustics. Magnetic fluid (MF) can be used for the creation of an acoustic duct in the slot gap between the surfaces of the source and the object of influence [1]. In [2], the MF bridge between two horizontal plates is studied analytically in the magnetic field of a line conductor. In [3], the surface shape of a MF volume between horizontal plates in the field of an electromagnetic coil is calculated numerically. Under an applied magnetic field, the instability of the MF can occur, which leads to a change of the surface shape of the volume and to the appearance of cavities. These effects must be considered in designing systems with MF-based acoustic contacts.

In this paper, the surface shape of a MF volume between horizontal plates is studied theoretically and experimentally. In the experiment the magnetic field of a coil, situated above the upper plate, is changed quasi-statically by varying the current. It was shown that there are different ways of creating the MF bridge between plates. It is shown that different forms of the MF can exist for the same applied current. Additionally abrupt and hysteretic behavior of the MF volume was observed. The theoretical investigation of the problem was done based on the principle of minimum energy of the system under the condition of the MF volume conservation. Sufficient conditions to determine the surface shapes, on which the energy has a local minimum, were obtained. Numerical calculations were carried out for the experimental parameters. The experimental investigations confirm the theoretical predictions, Fig.1. The obtained results of the transformation of the MF volume in non-uniform magnetic fields can be used to design systems based on MF.

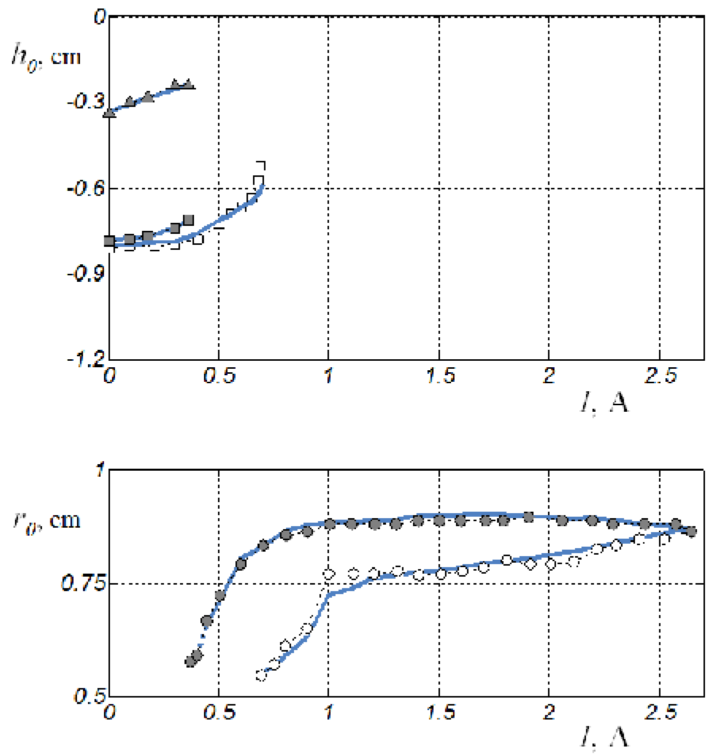

Figure: The dependencies of characteristic coordinates h_0 and r_0 on the current I obtained experimentally (markers) and numerically (solid lines) for an MF volume of 2 cm^3, when the current increases (white markers) and decreases (grey markers) quasi-statically. □ – the drop on the lower plate; Δ - the drop on the upper plate; ○ – the MF bridge between plates. h_0, 1.2 < h^0 < 0 cm, is the distance from the top of the drop to the upper plate; r^0 > 0 is the radius of the contact spot of the MF bridge with the upper plate.

References

[1] A.R. Baev, G.E. Konovalov and A.L.Maiorov. Magnetic Fluids in Technical Acoustics on Non-Destrusting Control (Technology, Minsk, 1999).

[2] V.A. Naletova, V.A. Turkov and T.I. Volkova. Physics Procedia, vol. 9 (2010), pp. 126–130.

[3] T.I. Volkova, V.A. Naletova, V.A. Turkov. Magnetohydrodynamics, vol. 49 (2013), No. 3–4, pp. 386–390.

MAGNETITE/OLEIC ACID NANOPARTICLES POSSESSING IMMOBILIZED ANTITUMOUR TETRAHYDROISOQUINOLINE DERIVATIVES

SEGAL[1] I., ZABLOTSKAYA[1] A., MAIOROV[2] M., ZABLOTSKY[2] D., BLUMS[2] E., ABELE[1] E., SHESTAKOVA[1] I.
[1]Latvian Institute of Organic Synthesis, 21 Aizkraukles, Riga, LV-1006, Latvia
[2]Institute of Physics, University of Latvia, 32 Miera, Salaspils LV-2169, Latvia
E-mail: seg@osi.lv

Abstract: Superparamagnetic magnetite/oleic acid nanoparticles bearing lipid like N-(2-hydroxyethyl)-1,2,3,4-tetrahydroisoquinoline derivatives possessing antitumour properties have been synthesized. Methods of magnetogranulometry, DLS measurements and XRD analysis have been employed to investigate their morphology and properties. *In vitro* cell cytotoxicity and itracellular NO generation caused by the water magnetic fluids of obtained nanoparticles were examined concerning tumour HT-1080 and MG-22A and normal NIH 3T3 cell lines.

1. Introduction

The progress in the field of creation and employment of different magnetic nanosystems has a large impact on biomedicine and opens new opportunities for their widespread medical application such as drug delivery [1], MRI contrast enhancement [2], antitumour therapy, which combines hyperthermia [3] and chemotherapy [4] and some others.

Our research team activity deals with targeted searching of medical remedies based on iron oxide nanoparticles, functionalized with wide spectrum of low molecular compounds possessing different kinds of biological activities and potential prolongated action. Recently water based magnetic fluids (MFs), containing model cytotoxic magnetosomes with amphiphilic trialkylsiloxyalkylamines, organosilicon choline and colamine derivatives [5], have been obtained according to the developed original approach. It has been demonstrated that resulting magnetic fluids revealed magnetic properties and affected tumour cell lines [6]. The obtained positive results make it possible to expand the research involving more complex biologically active molecules using the same principle methodology.

2. Presentation of the problem

The aim of the present investigation is synthesis, determination of morphology and biological study of magnetic nanostructures, assembling a final product composed of natural components: magnetite, the oleic acid and cytotoxic N-methyl-N-(2-trialkylsiloxyethyl)-1,2,3,4-tetrahydroisoquinolinium iodides anchored to the surface, to evaluate their efficacy as antitumour agents. The tetrahydroisoquinoline ring system is an important structural fragment, which is commonly encountered in naturally occurring alkaloids with interesting biological activities [7]. The parent alkanolamine, N-(2-hydroxyethyl)-1,2,3,4-tetrahydroisoquinoline, was modified by introduction of organosilicon group using decyldimethylsilane or hexadecyldimethylsilane into its side chain and subsequent quaternization of heterocyclic nitrogen atom with methyl iodide [8]. Thus obtained organosilicon amphiphilic heterocyclic choline analogues **1** and **2**, which we further used for the preparation of nanoparticles, can be considered as lipid like molecules: they contain lipophilic tails and are able to interact with the oleic acid shell as the first surfactant, forming cell membrane resembling structure around the magnetite core.

The desired superparamagnetic nanoparticles have been synthesized according to the recently developed synthetic procedure for linear trialkylsiloxyalkyl amines [6]. Thus created structures can provide the interaction of magnetic nanoparticles with cells via nanoparticle

shell and cell membrane fusion. Due to their original unusual magnetosome like structure, containing noncovalently linked silyl prodrugs [9] (the second surfactant) with oleic acid (the first surfactant), complex compositions of this type can be speculated as dual prodrugs; they could be able to ensure the prolongated action of the biologically active compound by the process of gradual desorption, not destroying the whole molecule immediately.
The general steps of synthesis of mixed covered magnetite samples are outlined in Scheme 1.

Fe_3O_4
Magnetite
3

OA: $CH_3(CH_2)_7CH{=}CH(CH_2)_7COOH$
$[THiQ(Me)CH_2CH_2OSiMe_2R]^+I^-$:
1, **6**, **8**, **10**, **12**: R = $C_{10}H_{21}$
2, **7**, **9**, **11**, **13**: R = $C_{16}H_{33}$

Fe_3O_4/OA
Toluene solution
4

Fe_3O_4/OA/1 or **2**
Toluene solutions
6, 7

Fe_3O_4/OA/1 or **2**
Powders
12, 13

Fe_3O_4/OA
Powder
5

Fe_3O_4/OA/1 or **2**
Water solutions
10, 11

Scheme 1. Synthesis of magnetic samples.

Magnetite particles (Fe_3O_4) **3** were obtained by wet synthesis by precipitation from an aqueous solution of Fe(II) sulfate and Fe(III) chloride with excess amount of sodium hydroxide. Initial toluene based MFs **4.1** and **4.2** were synthesized by coating of magnetic particles with OA as surfactant according to the described procedure [10] and differ by their content. The residue, which was left after the fluid **4.1** was decanted, was treated with toluene to give MF **4.2**. For determination of nanoparticles content magnetic powders **5.1** and **5.2** were prepared from initial MFs by treating them with acetone. Magnetic powders **8** and **9** were prepared by shaking of MFs **4.1** and **4.2** with corresponding tetrahydroisoquinoline derivatives and consecutive treating of obtained solutions **6** and **7** with acetone. Magnetic powders **8** and **9** were treated with water to produce water solutions **10** and **11** of nanoparticles containing **1** and **2**, correspondingly. In case of powder **9.3** shaking was replaced by US sonication to produce **11.5**. Water soluble powders **12** and **13** were obtained by solvent evaporation from the corresponding water solutions.
The method of magnetogranulometry has been applied for investigation of magnetic properties and for determination of diameter of iron oxide magnetic core. Magnetization curves were recorded at different stages of the material treatment for the monitoring magnetic material concentration and its condition as well. As a rule, measurements were done at room temperature for fields to 10 KOe. The most expected particle size at the distribution was used as a particle diameter (d). For distribution width estimation we directly use d_{min} and d_{max} at level 0.5 from distribution. Magnetic properties of colloidal solutions were studied without separating of carrier liquid. The data obtained by the method of magnetogranulometry for different powdery samples (**3**, **5** and **12**) are recorded in Table 1.
As expected, magnetite-oleic acid sample **5.2** (Fe_3O_4/OA) with a higher content of magnetite is characterized by higher magnetization value in comparison with the sample **5.1**.

Table 1. Physico-chemical properties of powdery samples **3**, **5** and **12**.

No.	Content mol/mol	Magnetization $\sigma_{10\ kOe}$, emu/g	Superparamagnetic saturation σ_s, emu/g	Magnetite concentration C, %	Magnetite core size d, nm		
					d	d^1_{min}	d^1_{max}
3	Fe_3O_4	55.8	53.8	58.5	12.4	9.9	14.3
5.1	Fe_3O_4/OA 1.95:1	29.9	29.4	32.0	6.4	4.5	8.7
5.2	Fe_3O_4/OA 5.25:1	40.7	42.9	46.6	8.4	5.9	10.8
12.1	Fe_3O_4/OA/**1** 1.95:1.0:0.65	4.84	4.78	5.20	5.2	4.7	5.9

[1] at level 0.5 from distribution density maximum

Dynamic Light Scattering (DLS) technique was used for measuring the size of colloidal particles in carrier liquid. DLS experiments were performed to determine the effective hydrodynamic diameters of the functionalized nanoparticles. Measurements were taken at 20°C. DLS gives the colloidal particles size distribution based on its translational diffusion coefficients in carrier liquid. The addition of the second biologically active surfactant, tetrahydroisoquinoline derivatives **1** or **2**, is not telling much on the obtained micelles size in the corresponding organic solutions, which ranges within 10.7–17.3 nm (Table 2).

Table 2. Size of micelles for patterns in toluene determined by DLS measurements.

Distribution mode, d (nm)		
Fe_3O_4/OA	Fe_3O_4/OA/**1**	Fe_3O_4/OA/**2**
4.1–12.5	**6.1**–10.7	**7.1**–13.1
4.2–17.3		

However, the size of micelles in water solutions in most cases is considerably bigger (Table 3). In two cases, the samples (**10.2** and **11.5**) were obtained with small micelles, which is apparently associated with a few changes in the method of preparation.

The yield of water soluble powdery samples **12** and **13** with corresponding organosilicon tetrahydroisoquinolines **1** and **2**, obtained from the initial MF **4.1**, which contained nanoparticles with a lower content of magnetite ranges within 11–16%. And just for the samples obtained from liquid **4.2** with a high content of magnetite, the yields were lower 2–4% (Table 4). It was determined by percentage to the amount of mixed covered powders, obtained from toluene solutions.

The magnitude of magnetization and magnetite concentration were calculated using the same parameters obtained for the corresponding water solutions. The calculated value of magnetization 5.08 emu/g of the powdery sample **12.1**, containing **1**, is in good agreement with the experimentally obtained data – 4.84 emu/g (see Table 1).

The compound **2**, used as the second surfactant for the immobilization, have been chosen from the compounds synthesized [8] as possessing selective cytotoxic action against human fibrosarcoma HT-1080 (IC_{50}=17 and 16 μg/ml**,** CV and MTT coloration correspondingly) and mouse hepatoma MG-22A (IC_{50}=13 and 16 μg/ml**,** CV and MTT coloration correspondingly) cell lines and as non-toxic compound (LD_{50}=1083 mg/kg).

Table 3. Size of micelles for patterns in water determined by DLS measurements.

No.	Composition	Molar ratio	d, nm
10.1	Fe_3O_4/OA/**1**	1.95 : 1.0 : 0.65	229
10.2	Fe_3O_4/OA/**1**	1.95 : 1.0 : 1.2	29
11.1	Fe_3O_4/OA/**2**	1.95 : 1.0 : 1.2	260
11.2	Fe_3O_4/OA/**2**	1.95 : 1.0 : -	215
11.3	Fe_3O_4/OA/**2**	1.95 : 1.0 : 0.95	230
11.4	Fe_3O_4/OA/**2**	5.25 : 1.0 : -	225
11.5	Fe_3O_4/OA/**2**	5.25 : 1.0 : -	44

'-' – not determined

Table 4. Physico-chemical characterization and yield of water soluble nanoparticles **12**, **13**.

No.	Composition, molar ratio	σ^a, emu/g	C^a, %	d^b, nm	Yield, %
12.1	Fe_3O_4/OA/**1** 1.95:1.0:0.65	5.08	5.0	4.8	11
12.2	Fe_3O_4/OA/**1** 1.95:1.0:1.2	-	-	5.0	-
13.1	Fe_3O_4/OA/**2** 1.95:1.0:1.2	2.78	2.78	5.1	16
13.2	Fe_3O_4/OA/**2** 1.95:1.0:-	-	-	5.5	-
13.3	Fe_3O_4/OA/**2** 1.95:1.0:0.95	9.29	10.63	6.8	13
13.4	Fe_3O_4/OA/**2** 5.25:1:-	-	-	9.2	2
13.5	Fe_3O_4/OA/**2** 5.25:1:-	19.39	18.37	9.6	4

[a]Magnetization $\sigma_{10\ kOe}$ and magnetite concentration C, calculated according to the corresponding data for **10** and **11**; [b]Magnetite core size, determined in water solutions **10** and **11**; '-' – not determined

Aqueous MF **11.3** of mixed covered magnetite nanoparticles, containing oleic acid and organosilicon derivative of tetrahydroisoquinoline **2**, was tested for cytotoxicity on monolayer human fibrosarcoma HT-1080 and mouse hepatoma MG-22A tumour cell lines and normal mouse fibroblasts NIH 3T3. It demonstrated high NO-generation ability, revealed selectivity against tumour cell lines and specificity concerning mouse hepatoma MG-22A cells, in contrast to the sample, containing its aliphatic analogue (Table 5).

The sample **11.3** influenced mouse hepatoma MG-22A cell morphology. Visible inclusions were present in cell cytoplasm, which probably accumulate the compound. The amount depends on the cell type and affects the degree of cytotoxic effect.

Table 5. *In vitro* cell cytotoxicity and itracellular NO generation caused by water MF **11.3**.

Compound	HT-1080			MG-22A			NIH 3T3
	IC_{50}[a] CV	IC_{50}[a] MTT	NO[b] CV	IC_{50}[a] CV	IC_{50}[a] MTT	NO[b] CV	IC_{50}[a] NR
11.3 Fe_3O_4/OA/**2** 1.95:1.0:0.95	0.22	0.13	400	0.09	0.08	450	0.32
Fe_3O_4/OA/*[11]	0.11	0.05	800	0.11	0.10	700	0.98

* - $[(C_{16}H_{33})Me_2SiOCH_2CH_2NMe_3]^+I^-$; [a]Concentration (mg/ml) providing 50% cell killing effect (CV, MTT or NR coloration); [b]NO concentration (CV coloration), determined according to the procedure [12]; r<0.05

3. Conclusions

Novel water soluble magnetite based nanoparticles precoated with oleic acid and bearing organosilicon heterocyclic choline derivatives have been created. Water magnetic solution of nanoparticles with immobilized cytotoxic organosilicon heterocyclic choline analogue, N-(2-dimethylhexadecylsiloxyethyl)-N-methyl-1,2,3,4-tetrahydroisoquinolinium iodide, exhibited cytotoxic effect on human fibrosarcoma HT-1080 and mouse hepatoma MG-22A cell lines, which surpassed the same against normal cells. Incorporation of the synthesized nanoparticles into cells and their strong effect on MG-22A cell morphology have been observed.

It has been demonstrated that resulting magnetic fluids revealed superparamagnetic properties and affected tumour cell lines. The data are in agreement with our earlier obtained results for aliphatic choline analogues.

4. References

[1] Chomoucka, J.; Drbohlavova, J.; Huska, D; Adam, V.; Kizek, R.; Hubalek, J.: Magnetic nanoparticles and targeted drug delivering. Pharmacol. Res. 62 (2010) 144-149

[2] Corot, C.; Robert, P.; Idee, J.M.; Port, M.: Recent advances in iron oxide nanocrystal technology for medical imaging. Adv. Drug Delivery Rev. 58 (2006) 1471-1504.

[3] Haefeli, U.; Schuett, W.; Teller, J.; Zborowski, M.: 1997, Scientific and Clinical Applications of Magnetic Carriers, New York, Plenum.

[4] Hua, M.Y.; Yang, H.W.; Liu, H.L.; Tsai, R.Y.; Pang, S.T.; Chuang, K.L.; Chang, Y.S.; Hwang, T.L.; Chang, Y.H.; Chuang, H.C.; Chuang, C.K.: Superhigh-magnetization nanocarrier as a doxorubicin delivery platform for magnetic targeting therapy. Biomaterials 32 (2011) 8999-9010.

[5] Zablotskaya, A.; Segal, I.; Popelis, Y.; Lukevics, E.; Baluja, S.; Shestakova, I.; Domracheva, I.: Silyl modification of biologically active compounds. 12. Silyl group as true incentive to antitumour and antibacterial action of choline and colamine analogues. Appl. Organometal. Chem. 20 (2006) 721-728.

[6] Zablotskaya, A.; Segal, I.; Lukevics, E.: Iron oxide based magnetic nanostructures bearing cytotoxic organosilicon molecules for drug delivery and therapy. Appl. Organometal. Chem. 24 (2010) 150-157.

[7] Scott, J.D; Williams, R.M: Tetrahydroisoquinoline antitumor antibiotics. Chem. Rev. 102 (2002) 1668-1730.

[8] Zablotskaya, A.; Segal, I.; Popelis, Y.; Grinberga, S.; Shestakova, I.; Nikolajeva, V.; Eze, D.: Silyl modification of biologically active compounds. 13. Synthesis, cytotoxicity and antibacterial action of N-methyl-N-(2-triorganylsiloxyethyl)-1,2,3,4-tetrahydro(iso)quinolinium iodides. Appl. Organometal. Chem. 27 (2013) 114-124.

[9] Parrott, M.C.; Finniss, M.; Luft, J.C.; Pandya, A.; Gullapalli, A.; Napier, M.E.; DeSimone, J.M.: Incorporation and controlled release of silyl ether prodrugs from PRINT nanoparticles. J. Am. Chem. Soc. 134 (2012) 7978-7982.

[10] Bibik, E. E: Preparation of ferrofluid. Kolloidn. Zh. 35 (1973) 1141-1142.

[11] Segal, I.; Zablotskaya, A.; Lukevics, E.; Maiorov, M.; Zablotsky, D.; Blums, E.; Shestakova, I.; Domracheva, I.: Synthesis, physico-chemical and biological study of trialkylsiloxyalkyl amine coated iron oxide/oleic acid magnetic nanoparticles for treatment of cancer. Appl. Organometal. Chem. 22 (2008) 82-88.

[12] Fast, D.J; Lynch, R.C.; Leu, R.W.: J. Leukocyt. Biol. 52 (1992) 255-261.

SEGREGATION IN THE DIPOLAR HARD SPHERE SYSTEM: NUMERICAL SIMULATION

KUZNETSOV A. A., PSHENICHNIKOV A. F.
Institute of Continuous Media Mechanics UB RAS, 1, Korolyov St., 614013, Perm, Russia
Email: pshenichnikov@icmm.ru

Abstract: A series of Monte Carlo and molecular dynamics simulations have been performed to determine equilibrium concentration profiles of dipolar hard sphere system in a wide range of coupling constant values and in the presence of the strong gravitational field. These data have been used to estimate the diffusion coefficient of colloidal particles and to determine applicability limits of the most recent analytical models for this coefficient. No signs of the first order phase transition predicted by all the models were observed in the simulation.

1. Introduction

One of the most important problems that must be handled in order to create a highly stable magnetic fluid is the problem of concentration stratification. Its essence is that in the course of time an initially homogeneous fluid becomes spatially inhomogeneous with respect to the magnetic phase concentration due to the gravitational sedimentation and magnetophoresis (the motion of particles under the action of nonuniform magnetic field). The only mechanism that prevents stratification in the absence of convective motion is the gradient diffusion of magnetic particles in fluid. Generally, to obtain the concentration profile of the fluid in a cavity one must solve a boundary-value problem including Maxwell's equation for magnetic field and the dynamic mass transfer equation with consideration for terms responsible for magnetophoresis and sedimentation. The approximation of a dilute solution (when the volume fraction of particles is small compared to unity) makes it possible to separate the magnetic and diffusion parts of the boundary-value problem and to write the diffusion equation, which is linear in terms of the particle concentration and correctly considers magnetophoresis, sedimentation and gradient diffusion [1]. But in the case of concentrated fluids a description of the segregation process is a really challenging task due to the interparticle interactions. Today, there are quite a few works on mass transfer in magnetic fluids, which take into account steric, hydrodynamic and also magnetodipole interactions. For example, a formula for the chemical potential of magnetic fluid describing the excluded volume effect was derived by Cebers [2]. A large success in the problem of taking into account steric interactions was also achieved by Buevich et al. [3]. They derived a formula for the gradient diffusion coefficient in the framework of Carnahan–Starling approximation for the hard sphere fluid equation of state. Besides, they introduced the correction, linear in concentration, for the effective attraction of spherical dipoles. The theory of diffusion processes in magnetic fluid that takes into account both steric and magnetodipole interactions was developed by Morozov [4] and Bacry with coauthors [5]. The main drawback of this theory is the geometry limitation of an infinite flat layer. Perhaps one of the most complete mass transfer equations has been proposed in Ref. [6]. This equation describes the temporal and spatial variations of the volume fraction φ of single-domain colloidal particles and, in the absence of convective flows, can be written as follows:

$$\frac{\partial\varphi}{\partial t} = -div\left\{D_0 K(\varphi)\left(\varphi L(\xi_e)\nabla\xi_e + \varphi G_\gamma e - \left[1 + \frac{2\varphi(4-\varphi)}{(1-\varphi)^4} - \varphi\frac{\partial^2(\varphi^2 G(\lambda,\varphi))}{\partial\varphi^2}\right]\nabla\varphi\right)\right\}. \quad (1)$$

Here, $K(\varphi) = b/b_0$, where b and b_0 are the particle mobility in the magnetic fluid and carrier fluid, respectively, $D_0 = b_0 kT$ is Einstein's value of the diffusion coefficient for a Brownian particle in dilute solution, $\mu_0 = 4\pi\times10^{-7}$H/m, $L(\xi) = \coth(\xi) - 1/\xi$ is the Langevin function, and

$\xi_e = \mu_0 m H_e/(kT)$ is the Langevin parameter, H_e is the effective magnetic field, which depends both on the applied field and the local concentration, $\lambda = \mu_0 m^2/(4\pi d^3 kT)$ is the coupling constant (the ratio of the magnetodipole interaction energy to the thermal energy), m and d are the magnetic moment and full diameter of the particle (including a protection shell), respectively, kT is the energy of the thermal motion, G_γ is the gravitational parameter, **e** is the unit vector in the direction of the gravitational field, and $G(\lambda,\varphi)$ is the contribution of magnetodipole interactions to the free energy density referred to the density of the thermal energy of the Brownian particle motion. The first term in the Eq. (1) represents magnetophoresis. The expression in square brackets can be considered as an effective diffusion coefficient of colloidal particles:

$$D = D_0 K(\varphi)\left[1 + \frac{2\varphi(4-\varphi)}{(1-\varphi)^4} - \varphi\frac{\partial^2(\varphi^2 G(\lambda,\varphi))}{\partial\varphi^2}\right]. \tag{2}$$

Here, the first term is responsible for the gradient diffusion, the second one – for the steric interactions (Carnahan–Starling approximation) and the last one takes into account magnetodipole interactions. The main practical difficulty associated with Eq. 1 is a need for $G(\lambda,\varphi)$ expression. Originally authors of Ref. [6] have used interpolation formula for the free energy virial expansion in terms of φ calculated up to φ^2:

$$D_1 = D_0 K(\varphi)\left[1 + \frac{2\varphi(4-\varphi)}{(1-\varphi)^4} - \varphi\frac{\partial^2(\varphi^2 G_1)}{\partial\varphi^2}\right],$$
$$G_1 = \frac{4}{3}\lambda^2 \frac{(1+0.04\lambda^2)}{(1+0.308\lambda^2\varphi)} \frac{(1+1.28972\varphi+0.72543\varphi^2)}{(1+0.83333\lambda\varphi)}. \tag{3}$$

Another, more promising expression was recently introduced in Ref. [7]. By applying it to the case of diffusion coefficient we will get:

$$D_2 = D_0 K(\varphi)\left[1 + \frac{2\varphi(4-\varphi)}{(1-\varphi)^4} - \varphi\frac{\partial^2(\varphi^2 G_2)}{\partial\varphi^2}\right],\quad \varphi G_2 = \ln\left(1 + I_1\varphi + \frac{1}{2}I_2\varphi^2 + \frac{1}{3}I_3\varphi^3\right), \tag{4}$$
$$I_1 = \frac{4}{3}\lambda^2 + \frac{4}{75}\lambda^4 + \frac{116}{55125}\lambda^6,\qquad I_3 = 2.901720\lambda^3,$$
$$I_2 = \left(4\ln 2 + \frac{2}{3}\right)\lambda^2 - \frac{20}{9}\lambda^3 + \left(\frac{661727}{9600} - \frac{1468}{15}\ln 2\right)\lambda^4 - 0.155\lambda^5 + 0.111\lambda^6 - 0.0143\lambda^7 + 0.0105\lambda^8 - 0.00$$

Finally, one more formula for D has been proposed in Ref. [8]. Instead of using free energy approach authors directly determine a magnetodipole term heuristically:

$$D_3 = D_0 K(\varphi)\left[1 + \frac{2\varphi(4-\varphi)}{(1-\varphi)^4} - \frac{8\lambda^2\varphi}{3(1+1.25\lambda\varphi)^2}\right]. \tag{5}$$

Obviously, the model is significantly less strict but it can be easily extended to the case of partially aggregated system. Eqs. (3), (4) and (5) work well in the area of moderate values of the interaction energy ($\lambda < 2$) and volume concentration ($\varphi < 0.4$). However, their extrapolation to the area of high energies and concentrations, which presents considerable interest for engineering applications, might be a risky step. The purpose of this work is to obtain reliable estimates for the diffusion coefficient of strongly coupled dipolar hard sphere system by means of the numerical simulation and to use these data in order to compare mentioned analytical models and determine their limits of applicability.

2. Simulation details

Simulated system is the finite-size circular cylinder filled with N dipolar spheres. The height of the cylinder is Z (in units of particle diameter d). Cylinder is vertically placed in the gravitational field $G_\gamma \mathbf{e}$. Cylinder axis (z-axis) is directed against $\mathbf{e}$. Applied magnetic field is absent. In our work we use Monte Carlo (MC) and molecular dynamics (MD) methods to obtain equilibrium concetration distribution profiles of particles along z-axis at given λ and φ. In the case of MC simulation we use a standard Metropolis algorithm for the *NVT* ensemble. To get the *NVT* ensemble in MD simulation we use the Langevin dynamics approach. Potential energy of the i-th particle is given by expression:

$$\frac{U_i}{kT} = G_\gamma z_i + \frac{U^{SR}_{i,boundaries}}{kT} + \sum_{\substack{j=1\\ j\neq i}}^{N} \left\{ \frac{U^{SR}_{ij}}{kT} - \lambda \left[\frac{3(\boldsymbol{\mu}_i \cdot \mathbf{r}_{ij})(\boldsymbol{\mu}_j \cdot \mathbf{r}_{ij})}{r^5_{ij}} - \frac{3(\boldsymbol{\mu}_i \cdot \boldsymbol{\mu}_j)}{r^3_{ij}} \right] \right\}, \quad (6)$$

where $\boldsymbol{\mu}_i$ is the unit vector in the direction of particle magnetic moment, r_{ij} is the distance between centers of the i-th and the j-th particles (in units of d), U_{ij}^{SR} is a short-range interparticle potential, for MC this is hard-sphere potential $U^{HS}(r_{ij}) = \infty$ if $r_{ij} < 1$ and 0 otherwise, for MD this is truncated and shifted modified Lennard-Jones potential $U^{MLJ}(r_{ij}) = 4\varepsilon(1/r_{ij}^{48} - 1/r_{ij}^{24} + 1/4)$ if $r_{ij} < 2^{1/24}$ and 0 otherwise. Interaction with a cylinder boundary is considered as a short-range interaction with an image particle placed equidistantly on the other side of a boundary. The equations of motion for the i-th particle are:

$$m_0 \dot{\mathbf{v}}_i = \mathbf{F}_i - \gamma^T \mathbf{v}_i + \boldsymbol{\zeta}^T_i, \qquad I_0 \dot{\boldsymbol{\omega}}_i = \boldsymbol{\tau}_i - \gamma^R \boldsymbol{\omega}_i + \boldsymbol{\zeta}^R_i, \quad (7)$$

where m_0 is the mass of particle, $\mathbf{v}_i$ ($\boldsymbol{\omega}_i$) is the linear (angular) velocity, $\mathbf{F}_i = -\nabla U_i$ ($\boldsymbol{\tau}_i$) is the

conservative force (torque) acting on particle, γ^T (γ^R) is the translation (rotational) friction coefficient, ζ^T_i (ζ^R_i) is the random Brownian force (torque) acting on the particle, its component are drawn independently from Gaussian distribution with moments $\langle\zeta^T_i\rangle = 0$, $\langle\zeta^R_i\rangle = 0$, $\langle\zeta^T_i(t)\zeta^T_j(t')\rangle = 6kT\gamma^T\delta_{ij}\,\delta(t - t')$, $\langle\zeta^R_i(t)\zeta^R_j(t')\rangle = 6kT\gamma^R\delta_{ij}\delta(t - t')$. We determine the concentration profile of the system by dividing cylinder into equal horizontal layers with a height equals to one particle diameter and calculating average volume fraction for each layer. To find a link between profiles and the diffusion coefficient we use the equilibrium condition derived from Eq. (1): $\partial\varphi/\partial z = -\varphi G_\gamma/(D/D_0K(\varphi))$. To ensure the system has reached equilibrium we perform every simulation with two types of initial states: 1) homogeneous particle distribution; 2) most of the particles are concentrated on the bottom of the cylinder in a thin layer four times lower than Z. Typical simulation parameters are: $N = 1000$ for MC and $N = 1024$, 8192 and 16384 for MD, $\varphi = 0.06$, $0 \le \lambda \le 8$, $Z = 20$, $G_\gamma Z = 5$, $\varepsilon/kT = 1$, MD time step $\Delta t = 0.002(m_0 d^2/\varepsilon)^{0.5}$, $\gamma^T = 10.0(m_0\varepsilon/d^2)^{0.5}$, $\gamma^R = 3.0(m_0\varepsilon d^2)^{0.5}$, number of simulation steps is 10^6 (both for MD and MC; the first 5×10^5 are rejected).

3. Results and discussion

The results achieved for the range $\lambda \le 5$ seem to be reliable. Equilibrium profiles here depend weakly on the initial state, number of particles and simulation method. Some examples of these profiles are shown in Fig. 1. To estimate the error between analytical theories and the numerical data we use the coefficient of determination R^2. If (y_i, x_i) are numerical data, $\bar{y}$ is their average and $y(x) = f(x)$ is the model function, R^2 might be written as follows:

$$R^2 = 1 - \frac{\sum_{i=1}^{n}(y_i - [f(x]_i))^2}{\sum_{i=1}^{n}(y_i - \bar{y})^2}. \quad (8)$$

$R^2 = 1$ means that the match is perfect, $R^2 = 0$ means that model function describes data no better than a straight line $y(x) = \bar{y}$. The dependences of R^2 on λ for Eqs. (3), (4) and (5) are shown in Fig. 2. For D_1 and D_2 the error starts to arise after $\lambda \approx 3$ and for D_3 after $\lambda \approx 3.5$. But for the last

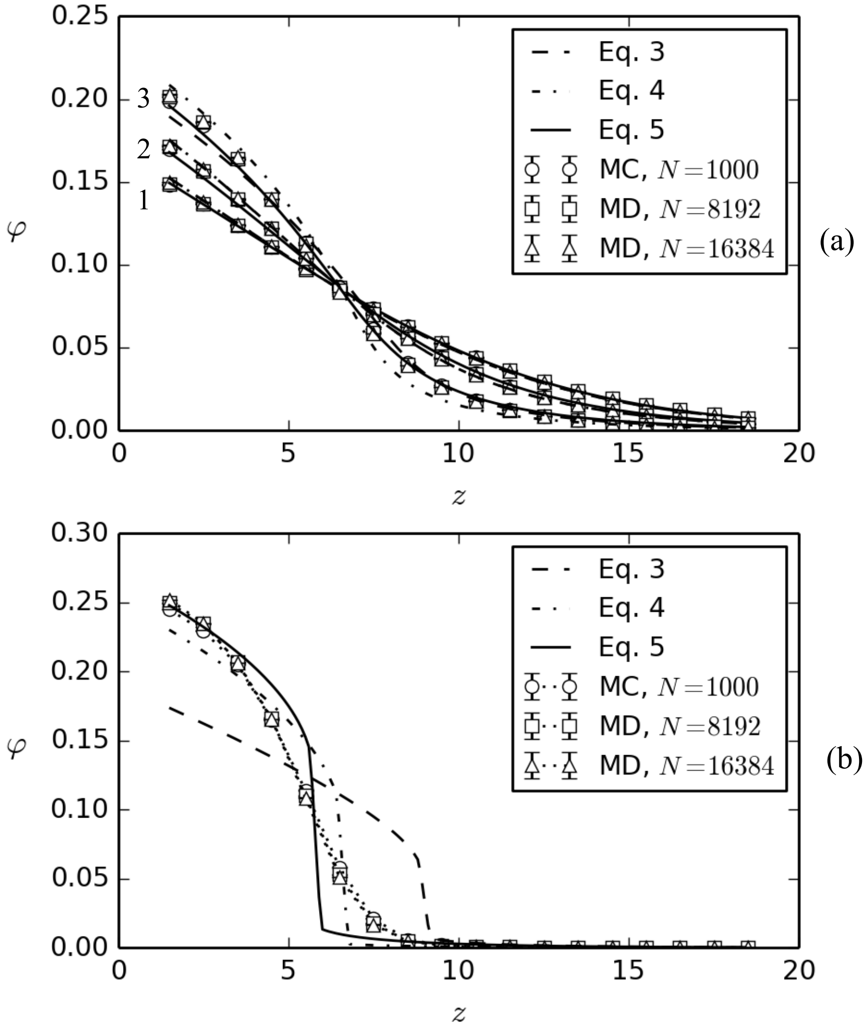

Figure 1: static concentration profiles in a vertical cylinder of finite height placed in the gravitational field. The magnetic field is absent. <φ> = 0.06. Curves correspond to analytical models and markers – to numerical results. In fig. (a): curves 1 correspond to $\lambda = 1$, curves 2 to $\lambda = 2$, curves 3 to $\lambda = 3$. In fig. (b) $\lambda = 5$.

two models the decline of R^2 is far less abrupt. Declines are obviously correlated with the critical areas where theoretical models predict the phase separation of the system. For every model there exist a critical point (λ^*, φ^*) after which the diffusion coefficient becomes negative. For Eq. (3) this is ($\lambda^* \approx 4.2$, $\varphi^* \approx 0.03$), for Eq. (4) ($\lambda^* \approx 3.5$, $\varphi^* \approx 0.05$), for Eq. (5) ($\lambda^* \approx 4.1$, $\varphi^* \approx 0.06$). After reaching this point the system becomes unstable and stratifies into two phases, weakly and strongly concentrated (phase transition "gas – liquid"). Fig. 1(b) shows examples of such a critical stratification. It also shows that at $\lambda = 5$ the agreement between D_3 and simulation results is good for sufficiently high local concentrations (outside the critical area). No signs of phase transition were observed in the numerical simulation for $6 \leq \lambda \leq 8$ as well. But it should be mentioned here that for this area of extremely strong magnetodipole interactions the equilibration time rises significantly and so does the simulation error. This issue is not so crucial in the case when initial state of the system is a concentrated layer. But still we believe that this range of coupling constant values should be investigated more accurately. Finally, we have performed some additional MC simulations for average concentrations larger than $\varphi = 0.06$ in order to directly estimate the diffusion coefficient of the colloidal particles from calculated profiles. Resulting coefficient for $\lambda = 5$ is shown in fig. 3 along with D_1, D_2 and D_3. Simulation points in figure are approximated with

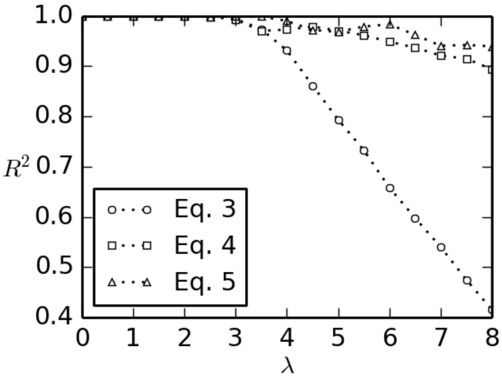

Figure 2: Coefficient of determination R^2 versus λ for different models. The closer R^2 to unity the better model approximates numerical data (MD, $\langle\varphi\rangle = 0.06$, N = 8192).

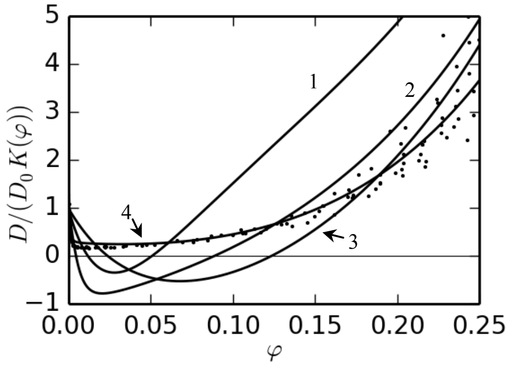

Figure 3: Diffusion coefficient versus local volume fraction for different models. $\lambda = 5$. Dots correspond to num. data (MC, N = 1000), curve 1 to Eq. (3), 2 to Eq. (4), 3 to Eq. (5), 4 to Eq. (9).

$$D_{approx} = D_0K(\varphi)\left[1 + \frac{2\varphi(4-\varphi)}{(1-\varphi)^4} - \frac{8}{3}\lambda^2\varphi\frac{1 + [\exp(3\lambda)-1]\cdot\left(0.0007\lambda\varphi + 0.002\lambda^2\varphi^2\right)}{1 + 2.5\lambda\varphi + [\exp(3\lambda)-1]\cdot\left(0.254 - 0.1711\lambda + 0.0371\lambda^2\right)\varphi^2}\right]. \quad (9)$$

4. Conclusion

In this work we have performed a series of Monte Carlo and molecular dynamics simulations to determine equilibrium concentration profiles of strongly coupled hard sphere system in the gravitational field and in the absence of magnetic field. For $\lambda \leq 5$ we have achieved sufficiently accurate results and have used them to analyze three theoretical expressions for the diffusion coefficient of interacting magnetic particles (D_1, D_2 and D_3). Model D_1 doesn't match the numerical data at $\lambda > 3$. Model D_3 works well even at $\lambda = 5$ for high local volume fractions $\varphi > 0.22$, but for the lesser concentrations, where model predicts a negative diffusion coefficient and the "gas – liquid" phase transition, the agreement is poor. Theoretical curves for D_2 are also close to numerical results for sufficiently high local concentrations. No signs of the phase transition were observed in simulations. However, the precision of results for $6 \leq \lambda \leq 8$ is lower and this area should be the object of further investigations.

5. Acknowledgements. This research was supported by the Russian Foundation of Basic Research (under Grants № 13-02-00076 and № 14-01-96007). Calculations were performed using "Uran" supercomputer of IMM UB RAS.

6. References

[1] Bashtovoi, V. G.; Polevikov, V. K.; Suprun, A. E.; Stroots, A. V.; Beresnev, S. A.: The effect of magnetophoresis and Brownian diffusion on the levitation of bodies in a magnetic fluid. Magnetohydrodynamics. 44(2) (2008) 121.

[2] Tsebers A. O.: Thermodynamic stability of magnetofluids. Magnetohydrodynamics. 18(2) (1982) 137-142.

[3] Buevich Yu. A.; Zubarev A. Yu.; Ivanov A. O.: Brownian diffusion in concentrated ferrocolloids. Magnetohydrodynamics. 25(2) (1989) 172-176.

[4] Morozov K. I.: Gradient diffusion in concentrated ferrocolloids under the influence of a magnetic field. Phys. Rev. E. 53 (1996) 3841.

[5] Bacri J.-C.; Cebers A.; Bourdon A.; Demouchy G.; Heegaard B. M.; Kashevsky B.; Perzynski R.: Transient grating in a ferrofluid under magnetic field: Effect of magnetic interactions on the diffusion coefficient of translation. Phys. Rev. E. 52 (1995) 3936.

[6] Pshenichnikov A. F.; Elfimova E. A.; Ivanov A. O.: Magnetophoresis, sedimentation, and diffusion of particles in concentrated magnetic fluids. J. Chem. Phys. 134 (2011) 184508.

[7] Elfimova E. A.; Ivanov A. O.; Camp P. J.: Thermodynamics of dipolar hard spheres with low-to-intermediate coupling constants. Phys. Rev. E. 86 (2012) 021126.

[8] Pshenichnikov A. F.; Ivanov A. S.: Magnetophoresis of particles and aggregates in concentrated magnetic fluids. Phys. Rev. E. 86 (2012) 051401.

PREPARATION AND PROPERTIES OF PLATINUM COATED MAGNETITE NANOPARTICLES

KRONKALNS[1] G., MAIOROV[1] M., SERGA[2] V., CVETKOVS[2] A., KRUMINA[2] A., KARASHANOVA[3] D.
[1]Institute of Physics, University of Latvia, 32 Miera, Salaspils, LV- 2169, Latvia
[2]Institute of Inorganic Chemistry, Riga Technical University, 34 Miera, Salaspils, LV-2169, Latvia
[3]Institute of Optical Materials and Technologies, BulgarianAcademy of Sciences, 109 Acad. G.Bonchev, 1113 Sofia, Bulgaria
Ee-mail: kron@sal.lv

Abstract: Nanoparticle compositions of noble metals Pt, Au and magnetite Fe_3O_4 were produced by the extractive-pyrolytic method (EPM). The phase composition, the size and the magnetic properties of all samples were investigated by an X-ray diffractometer, a transmission electron microscope and a vibration sample magnetometer, respectively. Formation of the nanocomposite particles was confirmed by the above-mentioned investigations.

1. Introduction

Composite nanoparticles with two or more functional phases in each particle significantly enhance the functions of nanoparticles. Composites containing nanosized particles of noble metals on oxide carriers such as Al_2O_3, MgO, TiO_2, SiO_2, Fe_2O_3 are widely used in heterogeneous catalysis [1]. Synthesis of composite magnetic nanoparticles with noble metal is a promising method to create a new type of material, which can be manipulated by an external magnetic field. Therefore, presently great attention is paid to the preparation and study of catalytic and magnetic properties of such composites [2-7]. The extractive-pyrolytic method (EPM) is a promising new method for the preparation of oxides [8] and composite materials containing nanoparticles of noble metals [9, 10]. The EPM allows quickly and simply (without the use of complex hardware design) to obtain nanoscale metal particles in various media. The aim of this work was to obtain composite Pt/F_3O_4 and Au/F_3O_4 magnetic nanoparticles by the EPM, and investigate the phase composition, morphology and magnetic properties of the composites.

2. Experimental

In order to produce Pt/Fe_3O_4, Au/Fe_3O_4 composites, at the first step a magnetite magnetic fluid (MF) was prepared by the wet chemical method [11] with toluene as a carrier liquid and with oleic acid as a surfactant. A magnetite phase powder specimen was produced by the method of vacuum evaporation of the carrier liquid of MF at 323 K. For the synthesis of noble metal–magnetite nanocomposite, some volume of n-trioctylammonium salt solution in toluene with a certain concentration of noble metal was added to the given mass of MF or nanoparticle powder. Then the mixture was stirred, dried and subjected by pyrolysis by heating from room temperature to the 673 K and cooled at room temperature. To a portion of the 3.8 wt% powder sample Fe_3O_4/Pt a mixture of oleic acid and oleylamine was added. The sample was then placed into a ball mill and subjected to grinding during 170 hours. Afterward the product was transferred to undecane. A stable magnetic fluid MF-1 was produced with the magnetization 7 emu/g and the magnetite mean sizes 18 nm and 8 nm of immobilized platinum particles on it. Magnetic properties of the colloid and of all powder samples were measured by a vibration sample magnetometer (VSM) (Lake Shore Criotronic Co., model 7404 VSM) in fields up to 1 T. The specific magnetization, the spectrum of particle magnetic moments as well as the magnetic size of nanoparticles were obtained from the magnetization curve of the MF sample. The specific magnetization and coercivity of the solid phase were determinate from the magnetization curves of relative powder specimens. The phase composition of Pt, Au-containing composites was characterized by an X-ray diffraction method using a diffractometer D8 Advance (Bruker Corporation) with CuKα radiation (λ = 1.5418Å). The mean size of platinum and gold crystallites was defined from the (111) peak width by the Scherrer method. The morphology of the composite nanoparticles and sizes of noble metal nanoparticles were observed by a transmission electron microscope (TEM) using the JEOL JEM 2100 operating at 200 kV.

3. Results and discussion

The X-ray image of the magnetic particle powder obtained from the magnetic fluid showed a perfect face-centered crystalline spinel structure. During the pyrolysis reaction with increased temperatures, some ferrous ions oxidized to ferric ones and formed hematite because the reactions were conducted in an open vessel.

Fig. 1 shows the typical XRD spectra of the composite nanoparticles F_3O_4/ Pt 3.8 wt%. In all the patterns with the concentration of noble metal > 1 wt% a significant peak due the definitely metallic phase of noble metal was observed. All curves in the pattern obviously showed two sets of strong diffraction peaks, indicating that the synthesized products were composite materials having good crystallinity and high purity. If the introduced noble metal concentration in the precursor was less than 1 wt%, in the final product after pyrolysis the noble metals were X-ray amorphous. The increasing of the Au content in the composite caused the formation of large metal crystallites (up to 60 nm). When the platinum content increased from 1.1 wt % to 7.4 wt %, the carrier phase composition did not change, and the final product contained basic phase - magnetite and hematite as an admixture. The platinum metal nanoparticles with the mean size less than d < 10 nm were immobilized on magnetite particles.

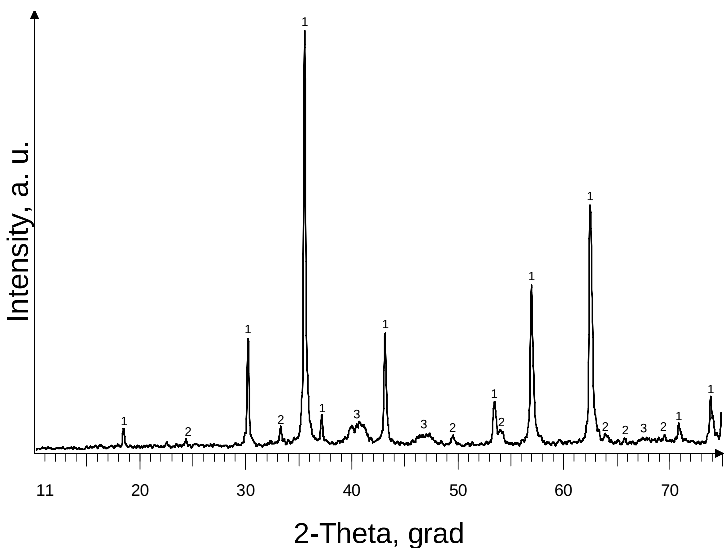

Figure 1: Typical X-ray diffraction pattern of Pt-containing composite nanoparticles: 1 – Fe_3O_4, 2 – α-Fe_2O_3, 3 – Pt.

Fig. 2 (a) displays a typical TEM micrograph of the Fe_3O_4/ Pt 7.4 wt% composite. Smaller particles' images with stronger contrast show platinum metal, indicating their good dispersion on the surface of larger magnetite nanoparticles observed with weaker contrast. Fig. 2 (b) represents the particle size distributions of platinum metal nanoparticles immobilized on magnetite particles.

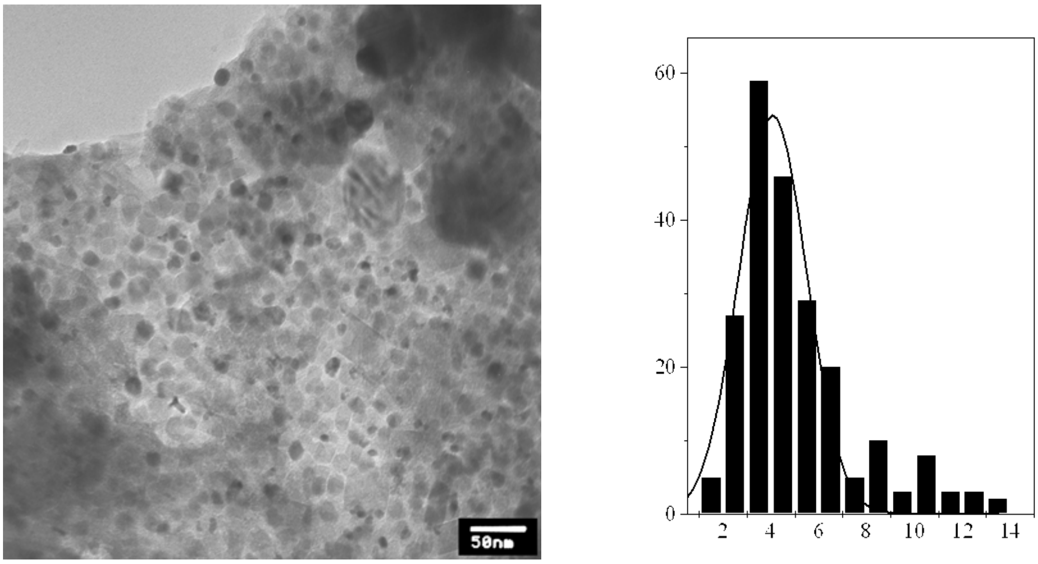

a) b)

Figure 2: The typical TEM micrograph of composite nanoparticles of Fe_3O_4/Pt 7.4 wt % (a). The size distribution of platinum nanoparticles immobilized on magnetite particles (b).

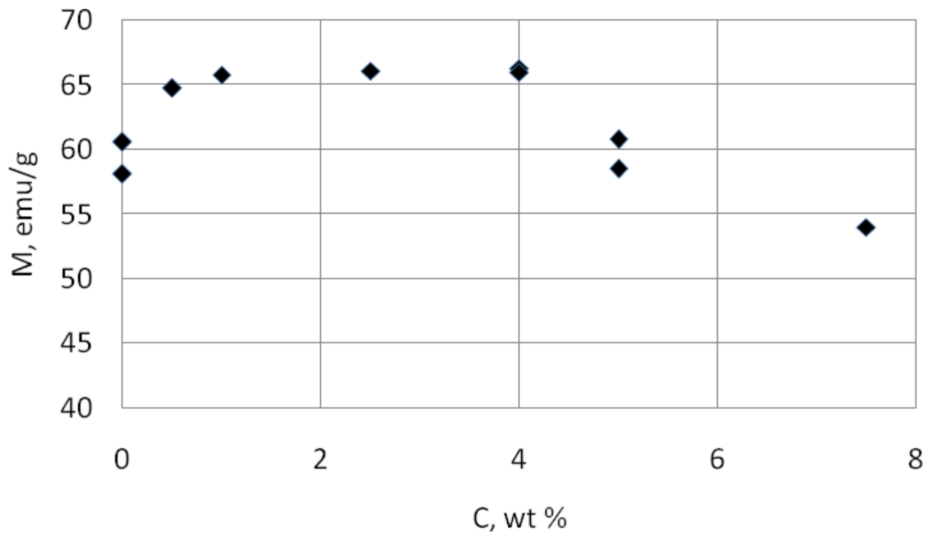

Figure 3: Specific magnetization of the composite nanoparticles.

Fig. 3 shows the dependence of specific magnetization of the composite solid phase on the concentration C of noble metal in the pattern at room temperature. The initial magnetite nanoparticles' magnetization was smaller than that of the bulk phase. This is attributed to an increase in the disorder of the magnetic moment orientation in various sites when the surface/volume ratio increased. With the noble metal concentration increase, the magnetization of the powder samples increased, reached a maximum at 4 wt % and decreased upon further increasing of the noble metal concentration. The initial increase of magnetization apparently was due to the increasing in nanoparticle sizes after thermal treatment. The further decrease in magnetization with the increasing concentration of noble metal was associated with the decrease in concentration of the magnetic phase in the nanoparticle.The summarized results of all experimental measurements are listed in Table 1.

Table 1.

Sample	Magnetization at max. field, emu/g	Coercivity Oe	Fe_3O_4 crystallite size from XRD, nm	Noble metal crystallite size from XRD, nm	Mean diameter of noble metal particles from TEM, nm
MF	11.2	0	-	-	-
MF-1	7.0	-	18	8	-
Fe_3O_4 powder	58.1	0	11	-	-
Fe_3O_4/Pt 1.1 wt %	65.8	134	39	amorphous	2.46
Fe_3O_4 /Pt 2.4 wt %	64.3	51.1	20, 55 (2 phases)	5.0	-
Fe_3O_4/Pt 3.8 wt %	63.5	100	63	10, 15 (2 phases)	-
Fe_3O_4/Pt 3.6 wt %	63.9	75	68	3	-
Fe_3O_4/Pt 3.8 wt % after grinding	43.4	284	18	~8	-
Fe_3O_4 /Pt 5.0 wt %	55.6	81	60	-	
Fe_3O_4/Pt 7.4 wt %	50	94	58	6, 20 (2 phases)	4.07
Fe_3O_4/Au 0.4 wt %	64.8	140	-	amorphous	3.47
Fe_3O_4/Au 4.9 wt %	-	-	40	60	7.85

3. Conclusions

Magnetic composite nanoparticles were produced by the extractive-pyrolytic method on the base of magnetite and with noble metals Pt and Au as the immobilized part. The formation of the composite nanoparticles was confirmed by XRD. TEM observation revealed that the noble metal nanoparticles were immobilized on the surface of magnetic iron-oxide nanoparticles. The Fe_3O_4/Pt particles dispersion in undecane was achieved by using oleylamine and oleic acid as surfactants. The Fe_3O_4/Pt and Fe_3O_4/Au composite nanoparticles can be manipulated by an external magnetic field, which is a potential for their application in various fields.

4. Acknowledgements. This work was supported by the Latvian Science Foundation, project Nr. 286/2002

5. References

[1] Heiz, U.; Landman, U.: Nanocatalysis, Springer, Berlin and Heidelberg and New York, 2007-2008.
[2] Lu, A.-H.; Salabas, E.L.; Schuth F.: Magnetic nanoparticles: synthesis, protection, functionalization, and application. Angew. Chem. Int. Ed. 2007, vol.46, no.8, pp. 1222-1244.
[3]Liu, Y.; Zhou, J.; Gong, J.; Wu, W.-P., Bao, N., Pan, Z.-Q., Gu, H.-Y.: The investigation of electrochemical properties for Fe_3O_4@Pt nanocomposites and an enhancement sensing for nitrite. Electrochimica Acta 111 (2013), 876-887.
[4] Semenova, E.M., Vorobyeva, S.A., Lesnikovich, A.I., Fedotova, Y.A., Bayev V.G.: Interphase synthesis of magnetite nanoparticles with a gold shell. BSU Reports, ser. 2 (2010), no. 2, 12-16 (in Russ.).
[5] Šmit, G.: Magnetite and maghemite as gold-supports for catalyzed CO oxidation at low temperature. CroaticaChemicaActa 76, 3 (2003), 269-271.
[6] Tzitzios, V.K.; Petridis, D.; Zafiropoulou, I.; Hadjipanayis, G.; Niarchos, D.: Synthesis and characterization of L10 FePt nanoparticles from Pt-Fe_3O_4 core-shell nanoparticles. J. Magnetism and Magnetic Materials 294 (2005), e95-e98.
[7] Seino, S.; Kinoshita, T.; Otome, Y.; Maki, T.; Nakagawa, T.; Okitsu, K.; Mizukoshi, Y.; Nakayama, T.; Sekino, T.; Niihara, K.; Yamamoto, T.A.: γ-ray synthesis of composite nanoparticles of noble metals and magnetic iron oxides. ScriptaMaterialia, 51 (2204), pp. 467-472.
[8] Kholkin, A.I.; Patrusheva, T.N.: Extractive-pyrolytic method: Production of Functional Oxide Materials, ComBook, Moscow, Russia, 2006, pp. 56-90.
[9] Serga, V.; Kulikova, L.; Cvetkov, A.; Krumina, A.: EPM fine-disperse platinum coating on powder carriers, IOP Conf. Series: Materials Science and Engineering, 38 (2012), pp.1-4. DOI:10.1088/1757-899X/38/1/012062.
[10] Ivanov, I.; Petrova, P.; Georgiev, V.; Batakliev, T.; Karakirova, Y.; Serga,V.; Kulikova, L.; Eliyas, A.; Rakovsky, S.: Comparative study of ceria supported nano-sized platinum catalysts synthesized by extractive-pyrolytic method for low-temperature WGS reaction, Catalysis Letters 143 (2013) 9, pp. 942-949.
[11] Kronkalns, G.; Maiorov, M.; Blums, E.: Preparation and properties of temperature-sensitive magnetic fluids. Magnetohydrodynamics, vol. 33 (1997), no. 1, p. 92.
[12] Grants, A.; Irbitis, A., Kronkalns, G.; Maiorov, M.M.: Rheological properties of magnetite magnetic fluid, J.Magn.Magn.Mat., 85 (1990) 129-132.

MAGNETIC FLUID NANOPARTICLE FRACTIONATION: EXPERIMENTS AND SAMPLE ANALYSIS

MAIOROV M., MEZULIS A.
Institute of Physics, University of Latvia, 32 Miera, Salaspils LV-2169, Latvia
E-mail address of corresponding author: maiorov@tesla.sal.lv

Abstract:
In the present work, fractionation is achieved by two different experiments: centrifugation and gravity sedimentation column. Three samples are obtained and compared by their particle size distribution: the fractions from the bottom and from the top of the gravity sedimentation column after 30 days of exposition, and the light fraction after centrifugation for 8 hours at acceleration 7000 g.

1. Introduction

The ferrofluid is a colloidal solution of stabilized magnetic nanoparticles in a liquid carrier. Usually it is a polydisperse system with a rather wide size distribution. Under some conditions, such as gravitation, acceleration, gradient magnetic field and temperature, redistribution of the magnetic nanoparticles occurs in the volume [1]. As a result, not only the particle concentration but also the mean particle size of the colloidal solution varies with taken part of the solution volume i.e. the fractionation takes place.

2. Experiment

The setup for gravity sedimentation is shown in fig 1. The concentration of magnetic nanoparticles at the top and at the bottom of the test-tube was obtained by measuring the inductance of the coils by a high precision LC meter Quad-Tech 7600. The sample exposition lasted for 30 days.

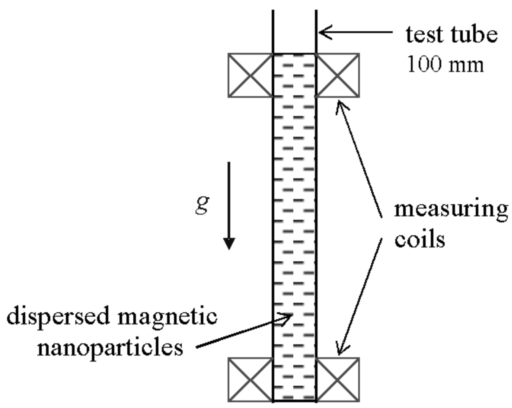

Figure 1: Setup for the gravity sedimentation.

A sketch of the centrifugation is shown in fig 2. The centrifugation time was 8 hours. After centrifugation, the upper layer of the sample was collected by a syringe.

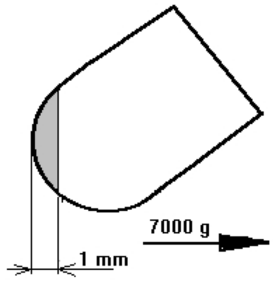

Figure 2: Centrifugation of a sample.

Three samples were obtained: S1 and S2 are fractions from the bottom and top of the gravity sedimentation column, and S3 is the light fraction after centrifugation. These samples were examined by the relaxation of the optical anisotropy setup [2, 3]. The relaxation of the optical anisotropy is studied according to the method in Ref. [2] with turnoff time for the magnetic field < 300 ns, and by a digital oscilloscope and a PC for performing measurements illustrated in fig. 3.

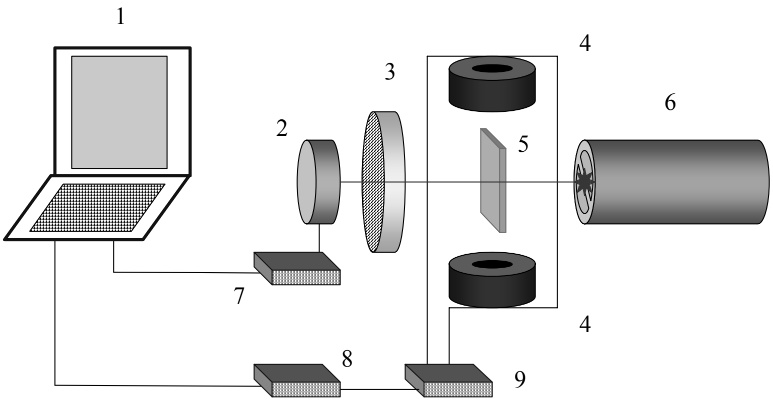

Figure 3: The experimental setup: 1 – PC, 2 – photo-detector, 3 – optical analyzer, 5 - experimental cell, 4 – pulse electromagnet, 6 – laser, 7 – digital oscilloscope, 8 – pulse generator, 9 – powerful pulse amplifier.

Polarized light beam from the laser 6 passes through the sample cell 5, which is submitted to the pulse magnetic field of the magnet 4. The polarization plane of the light makes a 45° angle with the direction of the magnetic field. Afterwards the beam passes through the optical analyzer 3, which polarization plane is normal to that of the laser beam. The setup is adjusted so that no light passes to the photo-detector 2 when the sample is isotropic. Main information was obtained by recording the relaxation process of optical anisotropy after switching off the external magnetic field. The relaxation curves of tested samples are displayed in fig 4.

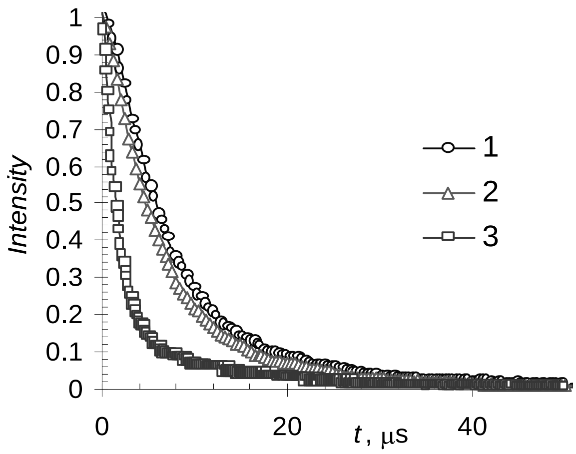

Figure 4: The relaxation of ferrofluid optical anisotropy after fractionation: 1, 2 - bottom and top of the gravity sedimentation column, 3 - top of the centrifuge cell.

As the next step, the obtained optical signal relaxation curves were analyzed by decomposition on the sum of exponents by the regularization method [4]:

$$I(t) = \sum_{i}^{N} I_i \, exp(-12 D_{ri}\, t), \tag{1}$$

where N is the number of the particle fractions, D_{ri} is the rotational diffusion coefficient of a particle from the corresponding fraction, I_i is the light intensity induced by the corresponding fraction. In this case, results were obtained by minimization of the next functional:

$$S_c = \frac{1}{t_{\max}} \int_0^{t_{\max}} \left(I(t) - \sum_{i=1}^{N} I_i \cdot e^{-12 D_{ri} t} \right)^2 dt + \alpha \cdot \Omega \tag{2}$$

where $\Omega = \sum_{i=1}^{N} I_i^2$ is the Tikhonov stabilizer of the first type, $0 < \alpha << 1$ is a regularization parameter.

The rotational diffusion coefficient D_r depends on the viscosity of the carrier, particle size and temperature. For a spherical particle it is:

$$D_r = \frac{kT}{6\eta V}, \tag{3}$$

where k is the Boltzmann constant, T is the temperature, η is the viscosity of the carrier fluid, V is the volume of a particle. The set of D_{ri} was converted to the set of diameters d_i.

3. Results

The comparison of the size distribution obtained from the optical relaxation analysis confirms the particle fractionation during sedimentation (fig 3).

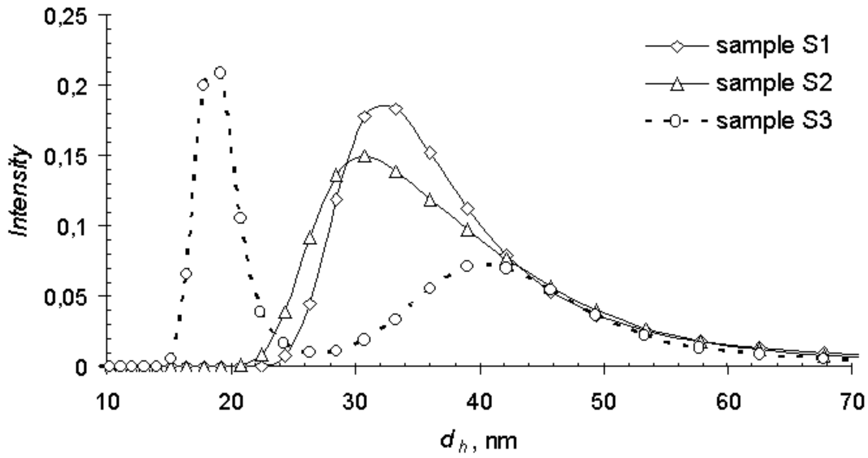

Figure 5: Particle size distribution after gravity sedimentation (S1, S2) and centrifugation (S3).

The bimodal distribution obtained with the centrifuged sample S3 may be explained by a phenomenon that particle sedimentation is dependent not only on the particle size, but also on the particle form. With this in mind, after centrifugation the sample may contain round particles of small size and some quantity of big elongated particles. The elongated particles have highly exposed optical anisotropy and thus give a significant contribution to the analysed optical signal.

So the relaxation of optical anisotropy has high sensitivity, and its analysis may be useful for the magnetic colloid fractionation monitoring under the condition of gravity.

4. References

[1] Blums E., Cebers A., Maiorov M. M., Magnetic Fluids. Berlin, New York, Walter de Gruyter & Co 1997.

[2] Maiorov M. M., Zablotsky D. Y., Measurements of rotary and translation diffusion of magnetite nanoparticles in hydrocarbon based magnetic fluid. Magnetohydrodynamics, vol. 41 (2005), no. 4, pp. 353–359.

[3] Maiorov M. M., Experimental investigation of the kinetics of magnetic birefringence and dichroism in a dilute magnetic fluid. Magnetohydrodynamics, vol. 13 (1977), no. 3, pp. 281-285.

[4] Maiorov M. M., Blums E., Raj K. Inverse task for evaluation of particle size distribution of polydisperse magnetic fluids. (12th International Conference on Magnetic Fluids). Physics Procedia 9 (2010) 74–77.

FERROFLUID BRIDGE BETWEEN TWO CONES AND A CYLINDER IN THE MAGNETIC FIELD OF A LINE CONDUCTOR

VINOGRADOVA[1] A.S., NALETOVA[1, 2] V.A.
[1]Institute of mechanics, Lomonosov Moscow State University / Michurinskij Pr. 1, 119192, Moscow, Russia
[2]Faculty of mechanics and mathematics, Lomonosov Moscow State University / Leninskie Gory, 119991, Moscow, Russia
E-mail address of corresponding author: vinogradova.msu@gmail.com

Abstract: The behaviour of a ferrofluid bridge between two cones and a cylinder in the magnetic field of a line conductor in the presence of a pressure drop is investigated. Here we consider a particular case of right circular coaxial truncated cones with different apex angles. A line conductor is also located on their axis. The cones intersect in a circle of the conductor radius. The possibility of the fluid shape hysteresis for a cyclic increase and decrease of the current and of spasmodic changes at certain values of the current is studied.

1. Introduction

The free surface of a ferrofluid changes its shape near a line conductor while the current is slowly changing. For some values of the current, hysteresis and spasmodic phenomena may be observed. For small magnetic fields in [1], the spreading of a ferrofluid drop along a wire in case of wetting was studied theoretically and observed in the experiment. In [2] the behaviour of a ferrofluid bridge between coaxial cylinders with a line conductor on their axis for both cases of wetting and non-wetting was investigated theoretically. Taking into account the results obtained in [1], the behaviour of a ferrofluid drop on a line conductor for any values of wetting angles and magnetic fields was developed in [3]. A ferrofluid drop on a line conductor with limiting conical surfaces in case of non-wetting was studied in [4]. We take into account the results obtained in [2], [4] and state the problem of a ferrofluid bridge between two cones and a cylinder in the magnetic field of a line conductor. It should be noted that the ferrofluid bridge considered in [2] cannot sustain any pressure drop in contrast to this problem where there is a pressure drop.

2. Problem statement and its solution

We consider a heavy, incompressible, homogenous, isothermal ferrofluid (V is the ferrofluid volume) between a cylindrical surface of the radius R_c and two limiting right circular truncated conical surfaces with different apex angles α_1 and α_2. All these surfaces are coaxial, and a line conductor of the radius r_0 with the current I is located on their axis. The cones intersect in a circle of the conductor radius (fig. 1). In this geometry the ferrofluid bridge can sustain a pressure drop $\Delta p = p_1 - p_2$. The pressure p_1 is maintained above the ferrofluid and the pressure p_2 is maintained beneath the ferrofluid. The ferrofluid is immersed in a non-magnetic liquid with the same density (the case of hydroimponderability). If the ferrofluid does not wet solid boundaries then $90^\circ < \theta_1, \theta_2, \theta_3 \le 180^\circ$, where θ_1 is the wetting angle of the upper conical surface, θ_2 – of the lower conical surface, θ_3 – of the outer cylinder. If the ferrofluid wets solid boundaries then $0^\circ \le \theta_1, \theta_2, \theta_3 \le 90^\circ$ (the case $\theta_i > \alpha_i$, $i = 1, 2$ is only considered). The ferrofluid has a free axially symmetric surface $z = h(r)$, $r^2 = x^2 + y^2$ (the axis z is directed along the axis of the conductor). In this geometry, the magnetic field of the conductor $|\boldsymbol{H}|$ is not deformed by the ferrofluid and $|\boldsymbol{H}| = H$, $H(r) = 2I/(cr)$, where c is the speed of light in vacuum. We consider that for a ferrofluid with small concentration of the same ferromagnetic particles its magnetization M_f can be described by the Langevin law as for paramagnetic gas: $M_f(\xi) = M_S\,L(\xi)$, $L(\xi) = cth\,\xi - 1/\xi$, $\xi = mH/(kT)$, $m = M_S/n$. Here M_S is the saturation magnetization of a ferrofluid, m is the magnetic moment of one ferromagnetic particle, n is the number of ferromagnetic particles per unit volume of a ferrofluid, T is the fluid temperature, k is the Boltzmann constant, ξ is the Langevin parameter which corresponds to the current in a line conductor.

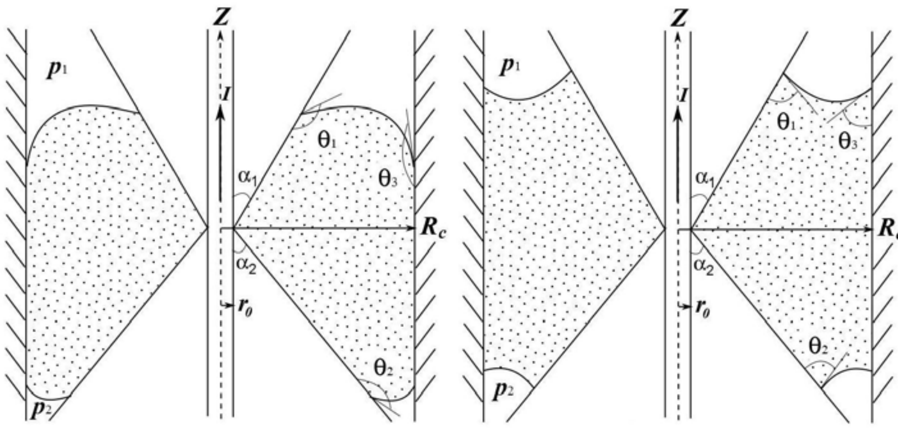

a) b)

Figure 1: Ferrofluid bridge between coaxial conical and cylindrical surfaces in the magnetic field of a line conductor under a pressure drop in case of a) non-wetting and b) wetting

We use the hydrostatic equation:

$$-\nabla p_i + M_i(H)\nabla H + \rho_i \boldsymbol{g} = \boldsymbol{0}, \quad i = f, l \quad , \tag{1}$$

where the indexes f and l designate the ferrofluid and the non-magnetic liquid surrounding the ferrofluid (the magnetization $M_l = 0$), p is the fluid pressure, ρ is the fluid density, $\boldsymbol{g}$ is the gravitational acceleration. We also use the boundary condition on the free surface $h(r)$:

$$p_l - p_f = \pm 2\sigma K, \quad 2K = (h'' + h'^3/r + h'/r)/(1 + h'^2)^{3/2}, \tag{2}$$

where σ is the coefficient of surface tension and K is the mean curvature of the surface. The sign "+"("−") should be chosen when the non-magnetic liquid is situated above (beneath) the ferrofluid.

From (1) and (2) we get the general, inhomogeneous, non-linear, second-order differential equation. In case of hydroimponderability, when $\rho_f = \rho_l$, we may reduce the order of this equation and get the general analytical solution for any axially symmetric shape of the ferrofluid free surface $h(r)$ in any axisymmetric magnetic field in the dimensionless form [2]. Here we need to describe the upper contact surface of fluids $h_1^*(r^*)$ and the lower contact surface of fluids $h_2^*(r^*)$ separately in the dimensionless form:

$$\begin{aligned} h_1^*(r^*) &= -\int_{r^*}^{R_c^*} G_1/(1-G_1^{\,2})^{1/2}\, dr^* + D_1, \quad G_1(r^*) = C_1/r^* + B_1 r^* - P_1/r^* \int_{r_1^*}^{r^*} r^* P(r^*, \xi_0)\, dr^*, \\ h_2^*(r^*) &= -\int_{r^*}^{R_c^*} G_2/(1-G_2^{\,2})^{1/2}\, dr^* + D_2, \quad G_2(r^*) = C_2/r^* + B_2 r^* + P_1/r^* \int_{r_2^*}^{r^*} r^* P(r^*, \xi_0)\, dr^*. \end{aligned} \tag{3}$$

The following dimensionless parameters are introduced: $r^* = r/r_0$, $R_c^* = R_c/r_0$, $h_i^* = h_i/r_0$, $r_i^* = r_i/r_0$, $i = 1, 2$, $H^* = H/H_0 = 1/r^*$, $H_0 = 2I/(cr_0)$, $\xi_0 = mH_0/(kT)$, $P_1 = nkTr_0/\sigma$,

$P(r^*, \xi_0) = ln\,[sh\,(\xi_0 H^*)/(\xi_0 H^*)]$. Later, the signs "*" are omitted and parameters are considered as non-dimensional, unless otherwise specifically agreed.

On contact lines of three media, for $r = r_1$ and $r = R_c$, the Jung condition should be satisfied and it gives the following boundary conditions:

$$G_1(r = r_1) = -\cos(\theta_1 - \alpha_1), \quad G_1(r = R_c) = \cos\theta_3. \tag{4}$$

From (4) the constants B_1 and C_1 may be determined as functions of r_1. On contact lines of three media, for $r = r_2$ and $r = R_c$, other boundary conditions hold true:

$$G_2(r = r_2) = \cos(\theta_2 - \alpha_2), \quad G_2(r = R_c) = -\cos\theta_3. \tag{5}$$

From (5) the constants B_2 and C_2 may be determined as functions of r_2. The constants $D_1 = h_1\,(R_c)$ and $D_2 = h_2\,(R_c)$ are determined from the following conditions:

$$h_1(r = r_1) = (r_1 - 1)\; ctg\alpha_1, \quad h_2(r = r_2) = -(r_2 - 1)\; ctg\alpha_2. \tag{6}$$

The relation between the constants B_1 and B_2 follows from the condition of fluid equilibrium:

$$B_1 + B_2 = r_0 \Delta p / (2\sigma). \tag{7}$$

In turn, the variables r_1 and r_2 have to satisfy equation (7) and the conservation law of ferrofluid volume.

It should be noted that for $p_1 > p_2$ in case of non-wetting, the ferrofluid bridge can take two different positions: to contact simultaneously the upper and the lower conical surfaces (fig. 1a) or to contact only the lower conical surface. In case of wetting, the ferrofluid bridge can take all three different positions: to contact simultaneously the upper and the lower conical surfaces (fig. 1b), to contact only the upper conical surface or to contact only the lower conical surface. If the ferrofluid contacts only the lower conical surface, then instead of (4) the following boundary conditions hold true:

$$G_1(r = r_1) = -\cos(\theta_2 + \alpha_2), \quad G_1(r = R_c) = \cos\theta_3. \tag{8}$$

If the ferrofluid contacts only the upper conical surface, then instead of (5) the following boundary conditions hold true:

$$G_2(r = r_2) = \cos(\theta_1 + \alpha_1), \quad G_2(r = R_c) = -\cos\theta_3. \tag{9}$$

3. Numerical simulation

To simulate numerically the static shapes of the ferrofluid free surface, we fix the following values of the problem parameters: $r_0 = 5{\cdot}10^{-4}$ m, $R_c = 50{\cdot}10^{-4}$ m, $T = 300^{\circ}$K, $\Delta p = 101.325$ Pa, $n = 0.19{\cdot}10^{24}$ m^{-3} ($M_S = 56.6{\cdot}10^{-4}$ T), $\sigma = 20{\cdot}10^{-3}$ N/m, $a_1 = a_2 = 5°$. In case of non-wetting $\theta_1 = \theta_2 = \theta_3 = 175°$, and in case of wetting $\theta_1 = \theta_2 = \theta_3 = 30°$.

By varying the parameter r_1, for each value of the current ξ_0 it is possible to calculate the ferrofluid shapes with the fixed volume V before we reach the value of current $\xi_0 = \xi_{break}$. At this value of current the surface $h_1(r)$ contacts the surface $h_2(r)$, the ferrofluid volume becomes minimal to bridge the gap between conical and cylindrical surfaces and the ferrofluid bridge breaks up (at the same time, in case of non-wetting the constants $D_1 = D_2$). However, at some critical value of current $\xi_0 = \xi_{cr}$ solution (3), which describes the static shape of the ferrofluid free surface, may stop existing earlier than the surface $h_1(r)$ contacts the surface $h_2(r)$. In this case, for some value of the radius r the absolute values $|G_1|$ and $|G_2|$ are equal to 1 and the ferrofluid bridge breaks up unpredictably.

4. Hysteresis and spasmodic phenomena

We consider the dependence of the value $z_1 = h_1(r_1)$ on the current ξ_0 for different values of the ferrofluid volume V in case of non-wetting (fig. 2a). For $0 < V < 2460$ (for example, line 1 for $V = 1076$ in fig. 2a) the dependence $z_1 = z_1(\xi_0)$ at first monotonically increases, and later it has a range of values with no physical sense, for which the ferrofluid tends to the conductor while the current is decreasing. For $V = 2460$ the line $z_1 = z_1(\xi_0)$ stops being simply connected: the lower part has its former state, but a new second branch of solutions appears as a dot (line 2 in fig. 2a). For $2460 < V < 9580$ (for example, line 3 in fig. 2a for $V = 7925$) the dependence $z_1 = z_1(\xi_0)$ is biconnected and multivalued, one value of the current ξ_0 may be associated with one, two or three values of z_1. For $V = 9580$ the dependence $z_1 = z_1(\xi_0)$ becomes again simply connected, the lower and the upper solutions grow together (line 4 in fig. 2a). For $9580 < V < 17770$ (for example, line 5 in fig. 2a for $V = 16772$) the dependence $z_1 = z_1(\xi_0)$ continues to be simply connected and multivalued. For $V = 17770$ the dependence $z_1 = z_1(\xi_0)$ has an inflection point and it becomes single-valued (line 6 in fig. 2a). For $17770 < V < 40720$ (for example, line 7 in fig. 2a for $V = 26828$) the dependence $z_1 = z_1(\xi_0)$ continues to be simply connected and single-valued. The volume $V = 40720$ ($5 \cdot 10^{-6}$ m^3) corresponds to the maximal ferrofluid volume, which can be placed in the gap between conical and cylindrical surfaces. The lines in fig. 2a come abruptly to an end when the ferrofluid bridge breaks up either predictably at the current $\xi_0 = \xi_{break}$, or unpredictably at the current $\xi_0 = \xi_{cr}$.

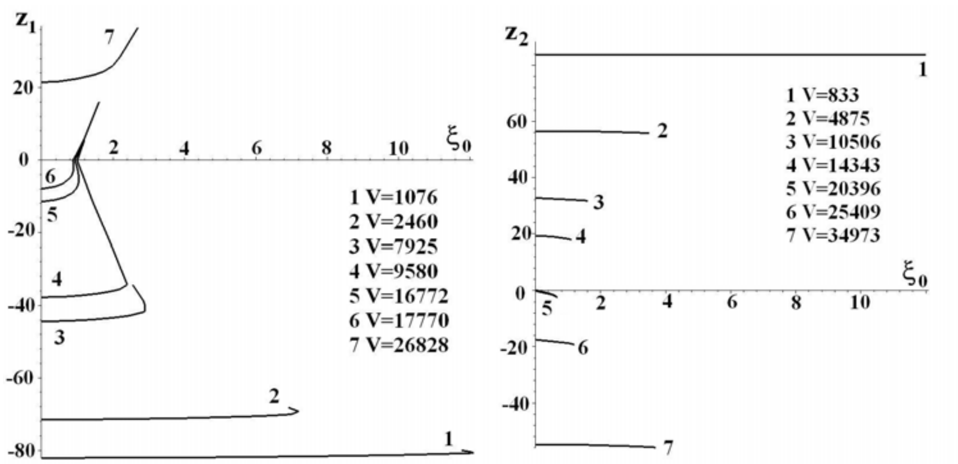

a) b)

Figure 2: Dependences a) $z_1 = z_1(\xi_0)$ in case of non-wetting and b) $z_2 = z_2(\xi_0)$ in case of wetting for different values of the volume V.

In case of wetting the dependence of the value $z_2 = h_2(r_2)$ on the current ξ_0 for different values of the ferrofluid volume V is shown in fig. 2b. We can see that for all range of the volumes $0 < V < 40720$ the dependence $z_2 = z_2(\xi_0)$ decreases monotonically. The lines in fig. 2b come abruptly to an end at the critical values of current $\xi_0 = \xi_{cr}$. Hence, in case of wetting for these parameters of the problem hysteresis and spasmodic phenomena are not observed.

In fig. 3 we consider in detail the dependence $z_1 = z_1(\xi_0)$ in case of non-wetting, namely line 5 for $V = 16772$ from fig. 2a. While the current is increasing quasistatically from $\xi_0 = 0$ to $\xi_{02} = 1.042$ (36 A), the value z_1 increases monotonically from $z_1 = -11.4$ ($-57 \cdot 10^{-4}$ m) to $z_1 = -5.7$ ($-28.5 \cdot 10^{-4}$ m), in other words the ferrofluid moves to the region of bigger magnetic fields. At the current ξ_{02} the ferrofluid jumps from the point $z_1 = -5.7$ on the lower conical surface to the point $z_1 = 2.2$ ($11 \cdot 10^{-4}$ m) on the upper conical surface. Later, while the current is increasing quasistatically from ξ_{02} to $\xi_{break} = 1.537$ (53 A), the value z_1 increases monotonically from $z_1 = 2.2$ to $z_1 = 14.3$ ($71.5 \cdot 10^{-4}$ m). At the current ξ_{break} the ferrofluid bridge breaks up and all ferrofluid volume turns into a drop on conical surfaces. However, if the current does not reach the value ξ_{break} and the ferrofluid bridge does not break up, then while the current is decreasing from some value $\xi_{02} < \xi_0 < \xi_{break}$ to the value $\xi_{01} = 0.94$ (32.4 A), then the value z_1 decreases monotonically to $z_1 = 0.1$ ($0.5 \cdot 10^{-4}$ m). At the current ξ_{01} the ferrofluid jumps from the point $z_1 = 0.1$ on the upper conical surface to the point $z_1 = -8.4$ ($-42 \cdot 10^{-4}$ m) on the lower conical surface. Later, while the current is decreasing quasistatically from the value ξ_{01} to $\xi_0 = 0$, the value z_1 decreases monotonically from $z_1 = -8.4$ to $z_1 = -11.4$. Hence, in case of non-wetting the ferrofluid free surface can change spasmodically and the shape hysteresis may be observed, that is the change of the ferrofluid shape, while the current is increasing, does not coincide with the change of the ferrofluid shape, while the current is decreasing.

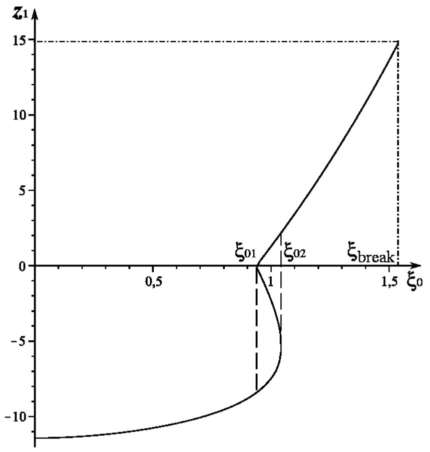

Figure 3: The dependence $z_1 = z_1(\xi_0)$ for $V = 16772$ in case of non-wetting.

5. Conclusion

It is shown that the presence of conical surfaces allows the ferrofluid bridge in the magnetic field of a line conductor to sustain a pressure drop. In case of non-wetting, spasmodic and hysteresis phenomena may be presented for some ferrofluid volumes and currents in a line conductor. In case of wetting, such phenomena are not found. The ferrofluid bridge breaks up either at the critical value of current, for which the static shape of the ferrofluid free surface stops existing, or at the value of current for which the ferrofluid volume is minimal to bridge the gap between conical and cylindrical surfaces. Presence or absence of hysteresis and spasmodic behaviour of a ferrofluid shape should be taken into account for the construction of different devices with controlled ferrofluid volumes, in which the magnetic field is changed periodically, such as seals, interrupters, valves, batchers.

Acknowledgements. This work is supported by the Russian Foundation for Basic Research (projects No. 14-01-90003, No. 14-01-31146 and No. 13-01-00703).

6. References

[1] Bacri, J.-C.; Frenois, C.; Perzynski, R.; Salin, D.: Magnetic drop-sheath wetting transition of a ferrofluid on a wire. Rev. Phys. Appl. 23 (1988) 1017-1022.

[2] Naletova, V.A.; Turkov, V.A.; Vinogradova, A.S.: A magnetic fluid bridge between coaxial cylinders with a line conductor. Physics Procedia. 9 (2010) 68-73.

[3] Vinogradova, A.S.; Naletova, V.A.; Turkov, V.A.; Reks, A.G.: Hysteresis of the shape of a finite magnetic fluid volume in axisymmetric magnetic fields. Magnetohydrodynamics. 49 (2013) 119-126.

[4] Vinogradova, A.S.; Naletova, V.A.; Turkov, V.A.; Reks, A.G.: Influence of apex angles of limiting conic surfaces on the hysteresis of the shape of a magnetic fluid drop on a line conductor. Magnetohydrodynamics. 49 (2013) 350-354.

THE EXPERIMENTAL STUDY OF THE MOTION OF ELONGATED BODIES WITH MAGNETIZABLE MATERIAL IN ROTATING MAGNETIC FIELD

PELEVINA D.A., TURKOV V.A., LUKASHEVICH M.V., KALMYKOV S.A., NALETOVA V.A.
Lomonosov Moscow State University, Leninskiye gory, 119992, Moscow, Russia
E-mail address of corresponding author: pelevina.daria@gmail.com

Abstract: The rotation and translational motion of a fixed volume made of a magnetizable material in a uniform applied rotating magnetic field are examined experimentally. We consider two magnetizable materials: a magnetic fluid and a magnetizable polymer.

1. Introduction

In [1] experimentally investigated the translational motion of magnetic fluid drop, wetting the smooth horizontal substrate, in a rotating magnetic field. Drop moving towards the solid rolling or in the opposite direction depending on the properties of the surrounding liquid. In this paper, we investigate experimentally the rolling drop of magnetic fluid, not wetting the substrate, along a rough bottom of the vessel.

In [2] theoretically and experimentally the motion of an elongated cylindrical body with a magnetizable polymer in a traveling magnetic field is considered. In this paper, we investigate experimentally the ellipsoid made of magnetizable polymer in a rotating magnetic field.

1. Experimental setup

Uniform applied magnetic field H_∞ is generated by two pairs of Helmholtz coils (a pair of coils with a common axis, the distance between the coils is equal to the coil radius; magnetic field on the axis of the coils is uniform).

Current in the coils is controlled by a software package LabView. The relationship between the current in the coils and the magnetic field on the axis was found by the Hall sensor. Field amplitude can reach 29.4 kA/m, field frequency varies from zero to 50 Hz.
Body (drop) with magnetizable material was placed in a rectangular vessel made of plexiglass (L = 7.5 cm, δ = 0.3 cm, h = 2 cm) and was immersed in a viscous non-magnetic liquid (water, glycerol, a mixture of glycerol and water). The cell was placed in a rotating homogeneous field.

Properties of the MF and polymer used in the experiment are shown in the table, see Tab. 1. Also the mixture of glycerol (ρ = 1261 kg/m^3, μ = 5.94 kg/sm) and water was used in the experiments.

Table 1. Properties of magnetizable materials.

Material	Density ρ, $10^3\cdot$kg/m^3	Saturation magnetization M_s, kA/m	Initial susceptibility χ_0	Volume V, mm^3
MF	1.21	31.8	1.89	14.2
Polymer	3.6	394	4.39	12.4

2. Behavior of the MF drop immersed in a nonmagnetic fluid in a rotating magnetic field

In the experiments the drop made of highly magnetizable MF EFH1 based on kerosene with ferrite particles was placed in the rectangular vessel made of plexiglass ($L = 7.5$ cm , $\delta = 0.3$ cm , $h = 2$ cm), filled with a mixture of glycerol and water in equal proportions by volume. The vessel was placed in a rotating homogeneous magnetic field of Helmholtz coils. The MF drop extends along the field. The drop rotation and translational motion along the bottom was observed for some magnetic field amplitudes and frequencies. The nonmonotonic dependence with one maximum of the average speed U of the drop translational motion on the frequency ω of the magnetic field was found. Average speed U is calculated as the ratio of a distance of 3 cm and a time in which the drop passes this distance. For some field values and frequencies, the drop has an ellipsoidal shape (see Fig. 1 a.) and moves toward solid rolling. Also, there are field values and frequencies in which the drop has a curved shape (see Fig. 1 b.) and moves toward the side opposite to the solid rolling.

Figure 1: The MF drop shape a. $H_\infty = 7.95$ kA/m, $\omega = 2.5$ Hz; b. $H_\infty = 7.95$ kA/m, $\omega = 5.25$ Hz; c. Separation of the MF drop $H_\infty = 9.94$ kA/m, $\omega = 4$ Hz..

When $H_\infty < 5.96$ kA/m the MF drop does not move, just oscillates and remains in the same place. When $H_\infty = 5.96$ kA/m drop has an ellipsoidal shape and rolls along the bottom of the vessel in the direction of solid rolling. Dependence of the average speed U on the field frequency ω is not monotonic and has a single maximum, see Fig. 2, point line. For some value of ω (ω=8.75 Hz for H_∞=5.96 kA/m), the MF drop stops and does not move with further increasing of the field frequency.

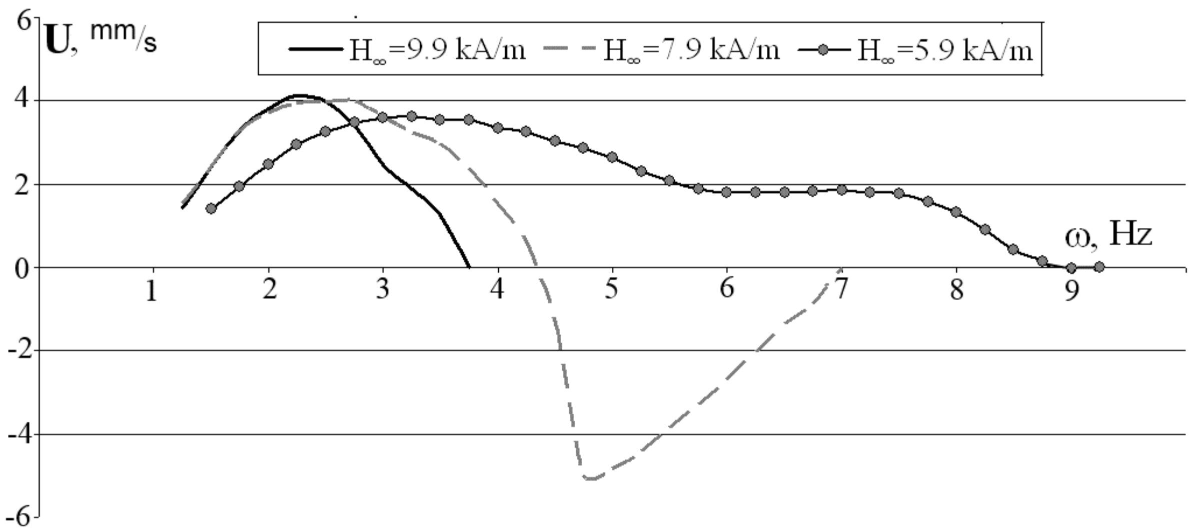

Figure 2: Dependence of the MF drop average speed U on the field frequency ω for different amplitudes H_∞.

In the larger field amplitude H_∞= 7.95 kA/m for the low frequencies ω the MF drop moves similarly to the case H_∞ = 5.96 kA/m. However, after the stop with further increasing of frequency ω the MF drop gets a curved shape and begins to move in the opposite direction to the solid rolling (see Fig. 2, dash line). At the same time drop continues to rotate in the direction of the field rotation.

In fields H_∞ = 9.94 kA/m the effect of the translational motion in the opposite direction to the solid rolling is not obtained. For H_∞ = 9.94 kA/m before the MF drop stops it's motion is similarly to the case H_∞ = 5.96 kA/m (see Fig. 2, solid line). After the stop with further increasing of frequency ω the MF drop is divided into smaller droplets, see Fig. 1. c. Each of the smaller droplets rolls in the direction of solid rolling.

When the amplitude of the applied field H_∞ increases the frequency at which the drop has the maximum average speed U, and the frequency at which the drop stops, decrease (see Fig. 2). The value of the maximum of the average speed U weakly depends on the amplitude of the applied field H_∞.

3. Behavior of magnetizable polymer in a rotating magnetic field

The behavior of the ellipsoid of magnetizable polymer in a nonmagnetic environment in a rotating homogeneous magnetic field was investigated. In experiments it was used the ellipsoidal body made of visco-elastic polymer with nickel micro-sized particles. Polymer's long axis orients along the field vector $\boldsymbol{H}_\infty$. Body rotates in the same direction as the field, and thus rolls along the bottom of the vessel.

We investigated the average speed U of the polymer body on frequency ω of the magnetic field for different field amplitudes H_∞, elongation of ellipsoid and various environments. The nonmonotonic dependence of the average speed U on ω with one maximum was received. At low frequencies ω, the frequency of the body rotation is equal to the field frequency ω, and speed U= $\omega \cdot L_p$ (L_p - circumference of the ellipsoid). At the higher frequencies ω the speed U decreases due to body inertia, and then for some value of ω the polymer stops (see Fig. 3, a.). The average speed U and frequency range, in which the body moves, reduces with decreasing of the ellipsoid elongation and field amplitude H_∞, also with increasing of the environment viscosity (see Fig. 3).

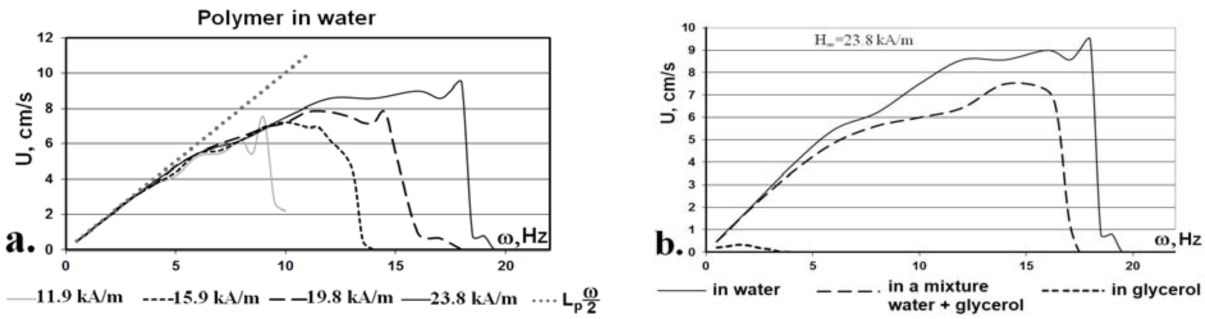

Figure 3: Dependence of the polymer average speed U on the field frequency ω a. For different field amplitudes H_∞; b. For different environments, H_∞=23.87 kA/m.

4. Comparison of droplets and polymer

A comparison of the behavior of the MF drop and ellipsoidal body with magnetizable polymer in rotating magnetic fields was done. It was shown that even at low field frequencies ω the drop speed differs significantly from the polymer speed (see Fig. 4). Thus, even at relatively slow speeds drop motion is not similar to the solid body motion, as it is initiated by the hydrodynamic flow.

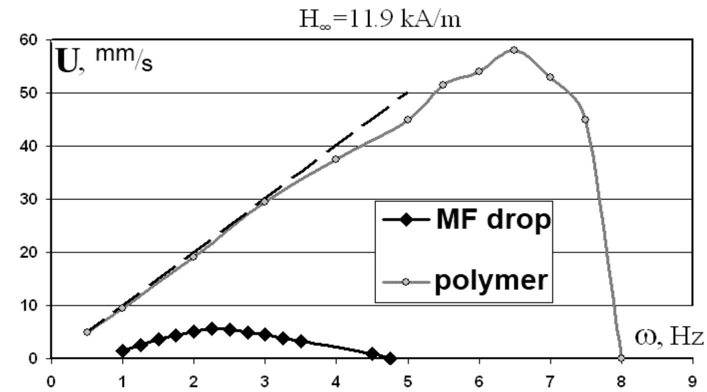

Figure 4: Dependence of the average speed U of the MF drop and the magnetizable polymer on the field frequency ω for H_∞ = 11.93 kA/m.

5. Conclusion

The magnetic fluid drop movements in a nonmagnetic environment near the bottom of the vessel in a rotating magnetic field were investigated experimentally. The drop rotation and translational motion are observed. The nonmonotonic dependence of the average velocity of the frequency of the applied magnetic field was found. For some field values and frequencies, the drop has an ellipsoidal form and moves toward solid rolling. Also, it was obtained field values and frequencies in which the drop has a curved shape and moves in the opposite direction.

The movements of ellipsoidal body with magnetizable polymer were investigated experimentally. The rotation in the direction of the field rotation and the translational motion toward solid rolling are observed. The nonmonotonic dependence of the average velocity on the frequency of the applied magnetic field was found.

The results of this work can be used to create micro robots made of magnetizable materials.

6. Acknowledgements.
This work was supported by RFBR (project No. 14-01-31146, 14-01-91330).

7. References

[1] Zakinyan A., Nechaeva O., Dikansky Yu.: Motion of a deformable drop of magnetic fluid on a solid surface in a rotating magnetic field. Experimental Thermal and Fluid Science, 39 (2012), 265–268.
[2] Kalmykov S. A., Naletova V. A., Turkov V. A. Motion of a Slender Body Made of Magnetizable Composite in a Traveling Magnetic Field. Fluid Dynamics, 48, No. 1 (2013), 4–13.

EXPERIMENTAL INVESTIGATION OF MAGNETIC NANOPARTICLE TRANSFER WITHIN A POROUS MEDIUM AND UNDER INFLUENCE OF A MAGNETIC FIELD

SINTS[1] V., BLUMS[1] E., MAIOROV[1] M., KRONKALNS[1] G., PETRICENKO[2] O.
[1]Institute of Physics, University of Latvia, Miera 8, Salaspils, LV-2169, Latvia
[2]Department of Theoretical Physics, University of Latvia , Riga, Zellu 8, LV-1002, Latvia
E-mail: viesturs.shints@gmail.com

Abstract: Diffusive and thermodiffusive transfer of magnetic nanoparticles within a porous medium is investigated in series of experiments. While observed changes in mass transfer coefficient that are associated with the medium itself are evidently significant, emphasis has been put on effects of magnetic field. Dependence of transfer coefficients on magnetic field has been investigated for a range of ferrofluids and compared with theoretical predictions, to find good correspondence.

1. Introduction

Diffusion and thermodiffusion processes of ferrofluids were investigated with the aim of understanding mass transfer coefficient changes within a porous environment and under the influence of a magnetic field. Ferrofluid is a stable colloid with solid phase made of single domain magnetic nanoparticles; liquid phase of the ferrofluid is not magnetic and is referred to as carrier fluid. As is the case of colloids in general, the thermodiffusion coefficients exceed those seen in molecular liquids by several orders of magnitude, making thermodiffusion an effect of interest. Furthermore, depending on the coating method used to prevent particle agglomeration, thermodiffusive mass transfer in ferrofluids can be directed to either hotter or colder temperatures.

Performing the experiments in a porous environment gives the advantage of suppressing convective motion at temperature gradients high enough to be of interest in thermodiffusion research. An obvious drawback of such setup, however, is the effects that the porous environment itself has upon mass transfer. Experimental results described in this article include measurements of both diffusion and thermodiffusion coefficients of the two kinds of ferrofluids – surfracted and ionic, in a magnetic field of various intensity values and orientation relative to temperature and concentration gradients. Effects of the porous environment are briefly discussed, while changes in mass transfer coefficients resulting from the magnetic field are compared to theoretical predictions.

2. Influence of magnetic field on ferrofluid mass transfer

Particle mass flow resulting from diffusion and thermodiffusion can be written as

$$\vec{j} = -D\nabla\rho_i - \rho_i(1-n_i)DS_T\nabla T \tag{1}$$

Here $\vec{j}$ is particle mass flux, ρ_i is particle mass concentration, n_i is mass fraction of particles, D is the diffusion coefficient and $S_T = D_T/D$, where D_T is thermodiffusion coefficient, is the Soret coefficient. The flux is proportional to gradients of particle mass concentration and temperature.

Theoretical model to predict changes in the Soret coefficient in the presence of magnetic field is described in detail in [1]. By introducing a flow associated with magnetic sedimentation and assuming that a uniform magnetic field is aligned with temperature gradient, as is the case in our thermodiffusion experiments, we can write the mass flow equation as

$$\vec{j} = -D\left(1+\frac{\gamma L^2(\xi)}{1+\gamma L'(\xi)}\right)\nabla\rho_i - \rho_i(1-n_i)DS_T\left(1-\frac{\gamma L^2(\xi)}{1+\gamma L'(\xi)}\cdot\frac{\alpha_T}{S_T}\right)\nabla T \qquad (2)$$

Here $\gamma = \varphi\xi M_S/H$ is a parameter of particle magnetic interaction (φ being volume concentration of particles, $\xi = \mu_0 mH/k_B T$ and M_S is saturation magnetization of particle material, m – magnetization of a single particle), $L(\xi)$ is the Langevin function and $L'(\xi)$ is the derivative of Langevin function, α_T is pyromagnetic coefficient.

Should a stationary state be attained and the mass flux become equal to zero, particle mass distribution would be described by

$$\nabla\rho_i = \rho_i(1-n_i)S_T\left[\left(1-\frac{\gamma L^2(\xi)}{1+\gamma L'(\xi)}\cdot\frac{\alpha_T}{S_T}\right)/\left(1+\frac{\gamma L^2(\xi)}{1+\gamma L'(\xi)}\right)\right]\nabla T. \qquad (3)$$

Which allows us to introduce the effective magnetic Soret coefficient

$$S_{T,M} = S_T\left[\left(1-\frac{\gamma L^2(\xi)}{1+\gamma L'(\xi)}\cdot\frac{\alpha_T}{S_T}\right)/\left(1+\frac{\gamma L^2(\xi)}{1+\gamma L'(\xi)}\right)\right]. \qquad (4)$$

On the other hand, if temperature gradient is zero and magnetic field is aligned along the concentration gradient, the effect of magnetic field on diffusion coefficient can likewise be calculated form equation (2), as

$$D_{M,parallel} = D\left(1+\frac{\gamma L^2(\xi)}{1+\gamma L'(\xi)}\right). \qquad (5)$$

However, (5) only accounts for particle transfer caused by inhomogeneity of the magnetic field due to particle distribution. Another cause of changes in diffusion coefficient is related to magnetic interaction between the particles[2]. If there is no gradient of magnetization along the magnetic field lines – that is, if the field is normal to the concentration gradient, interaction among particles is the sole mechanism of magnetic field affecting magnetic particle transfer. Then, mass diffusion coefficient in a magnetic field normal to the concentration gradient is

$$D_{M,normal} = D\left(1-\frac{\lambda\gamma L^2(\xi)}{1+\lambda\gamma L'(\xi)}\right). \qquad (6)$$

Here λ is a parameter of magnetic interaction called the effective field constant and can be calculated within the effective field model presented in[3].

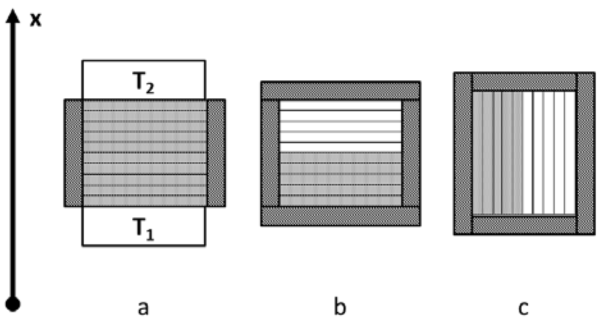

2. Experimental setup

Figure 1: layouts of porous layers in various experiments

Particle transfer is investigated in a porous environment of a flat cylindrical shape, l = 1.3 mm in height and d_{layer} = 67 mm in diameter. Porous layer itself is made of ten sheets of filter paper saturated with ferrofluid and pressed together to form a continuous porous environment. Porosity of the layers is ε = 0.8 and pore diameters of size d_{pore} = 9-20 μm.

In thermodiffusion experiments, there is no mass flux and no heat exchange at side walls, no mass flux at top and bottom walls and temperatures at top and bottom walls are fixed, with temperature at top wall being the biggest of two and temperature difference being $\Delta T = 40\ K$ (Fig.1 a). Magnetic field, when applied, is parallel to the temperature gradient.

Diffusion experiments are much like the thermodiffusion case, with the defining difference being that only lower five of the ten layers are saturated with ferrofluid, while the other five are saturated with pure carrier fluid. Obviously, there is also no temperature gradient present (Fig.1 b). A variation of the diffusion experiment includes the layers being positioned so that magnetic field is aligned parallel to the layers and perpendicular to the concentration gradient (Fig.1 c).

In all experiments, magnetic particle distribution is attained by splitting the layers apart at the end of each experiment and measuring the particle concentration in each layer by the method of vibrational magnetometry that allows us to learn the distribution of magnetic moments. Particle mass distribution can then be determined, as in single domain particles magnetic moment is proportional to size of the particle.

3. Experimental work

The two major types of ferrofluids are identified by the choice of method of stabilization – either applying a surfactant to form a layer of molecules that covers the particles and prevents them from coming too close together, or forming a double ionic layer around the particles to the same effect. A notion of the type of ferrofluid is added to results in Table 1. There, the default values of Soret coefficient are measured directly with the method of Forced Rayleigh scattering, while diffusion coefficients are either measured in magnetic grating experiments or calculated from the Stokes' formula.

Thermodiffusion experiments are conducted for 24 hours. By this time, the Fourier number $Fo = Dt/l^2$ has reached sufficient values to indicate that a stationary state has formed. Solving the mass flux equation (2) with the necessary boundary conditions yields

$$\frac{\varphi}{\varphi_0} = \frac{S_T \Delta T}{2 \cdot \sinh(\frac{S_T \Delta T}{2})} exp[-\frac{S_T \Delta T \cdot x}{l}]. \qquad (7)$$

Experimental values of effective separation (Soret) coefficient are attained by fitting (7) to experimental data. Examples of data with the respective approximation functions are presented in Figure 2. It should be pointed out that for the ferrofluid sample with $S_T = 0$, an inversion of particle flow direction has been observed.

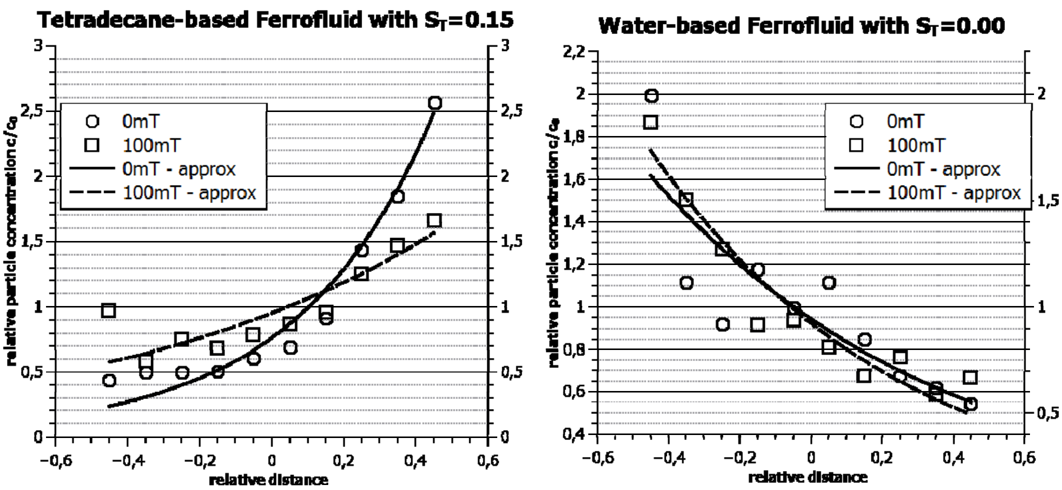

Figure 2: relative concentration profiles for surfracted (df-105) and ionic (FF 13-04) ferrofluid, along with exponential approximation curves. Temperature gradient is directed toward positive distance values.

In diffusion experiments, as no meaningful stationary state exists, measurements are performed after various intervals of time have passed, observing the decay of initial step-like concentration profile. At sufficiently small values of Fourier number, concentration profile is described by[4]

$$\frac{\varphi}{\varphi_0} = \frac{1}{2}\left[erf\left(\frac{x}{2\sqrt{Dt}}\right)+1\right]\frac{\Delta c(t=0)}{c_0}. \quad (8)$$

Equation (8) is relevant to both two and four hour experiments. From $Fo > 0.1$, however, particle distribution is described by

$$\frac{\varphi}{\varphi_0} = \frac{4}{\pi}exp(-\pi^2 Fo)\,sin\left(\frac{\pi x}{l}\right). \quad (9)$$

Data from 2 hour (equation (8) fitted to data points) and 24 hour (equation (9) fitted to data points) diffusion experiments of a surfracted ferrofluid are given in Figure 3.

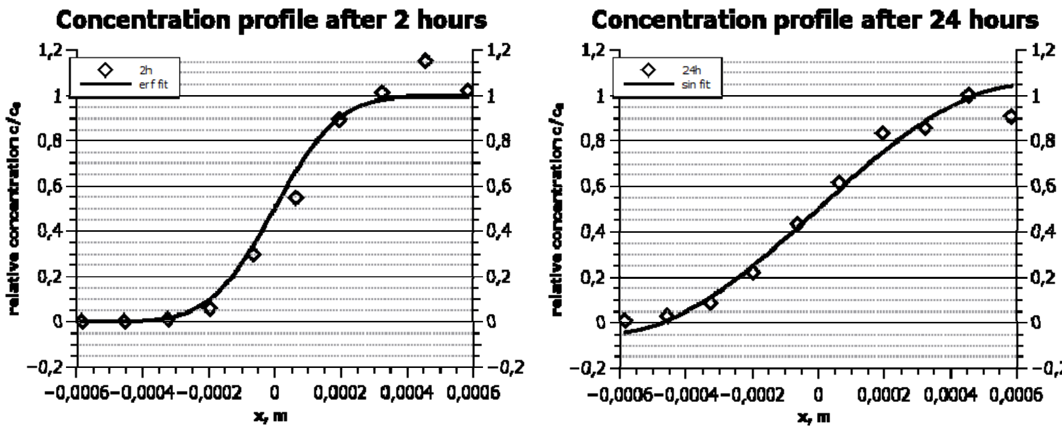

Figure 3: concentration profiles in diffusion experiments with surfracted ferrofluid df-105 after 2 and 24 hours

Results of the initial experiments, without magnetic field, have been summarized in Table 1.

Ferrofluid	S_T, 1/K	$S_{T,exp.}$ (0mT), 1/K	R^2	D, m^2/s	$D_{exp.}$ (0mT, 2h), m^2/s	R^2	$D_{exp.}$ (0mT, 4h), m^2/s	R^2
df-105 (surfracted)	1.50E-01	4.75E-02	0.99	1.86E-11	1.61E-12	0.98	1.25E-12	0.98
S-1 (surfracted)	2.00E-02	6.21E-02	0.59	2.46E-11				
U5 (surfracted)	1.50E-01	5.64E-03	0.98	3.50E-11				
FF13-04 (ionic)	0.00E+00	-3.00E-02	0.72	1.34E-11	1.36E-11	0.98	3.71E-12	0.44

Table 1: results from experiments without magnetic field. R^2 denotes the coefficient of determination

Two conclusions can immediately be drawn from these results. The first is that both Diffusion and thermoseparation (Soret) coefficients in the porous environment are significantly lower than in free fluid. One of the possible causes is being related purely to the geometry of the porous layer, namely to tortuosity that should decrease diffusion coefficient (though a decrease by an order of magnitude seems unlikely)[5], but not effective Soret coefficient, and the other to gradients of chemical potential near pore walls that could cause slip velocity directed towards higher temperatures to arise[6]; it is assumed that neither is affected by magnetic field, therefore only relative values to coefficients in the porous environment, and not free fluid, are used in result analysis. The other conclusion is that values of diffusion coefficient do not seem entirely reliable. This is associated with possible non-diffusive mass transfer occurring at very early stages of the experiment and diminishes quickly. Only 24 hour diffusion experiments are analyzed further.

6. Results

Values of relative Soret coefficient in magnetic field of $B = 100\ mT$ are summarized in Table 2. All values are relative to the experimental value of S_T at $B = 0\ mT$. Theoretical values are calculated from (4).

ferrofluid	$S_{T,\ experimental}$(100mT)/S_T(0mT)	$S_{T,\ theoretical}$(100 mT)/S_T(0mT)
df105	0.480	0.482
U-5	0.560	0.618
S1	0.035	0.034
FF1304	-0.739	-0.323

Table 2: comparison of experimental and theoretical values of relative S_T

Relative values of the diffusion coefficient are given in Table 3. As before, all values are relative to experimental value at zero magnetic field. Theoretical values in parallel and normal fields are calculated by (5) and (6), respectively.

field orientation	$D_{experimental}$(100mT)/D(0mT)	$D_{theoretical}$(100 mT)/D(0mT)
parallel	1.35	2.03
normal	0.92	0.81

Table 3: comparison of experimental and theoretical values of relative D

7. Conclusions

While it is undeniable that diffusive mass transfer of colloidal particles in a porous medium is significantly affected by the porous medium itself through mechanisms not fully understood, measurements of mass transfer coefficients undergoing changes when a ferrofluid is subjected to a magnetic field give results well comparable with theoretical values. Theoretical model presented in [1] gives reasonably accurate predictions of dependence of mass diffusion and Soret coefficients in a magnetic field.

8. References

1. Blums, E.; Sints, V.; Kronkalns, G.; Mezulis, A: Non-isothermal separation of ferrofluid particles through grids: Abnormal magnetic Soret effect. C. R. Mecanique 341 (2013) 348–355
2. Bacri, J.C. et al.: Transient grating in a ferrofluid under magnetic field: Effect of magnetic interactions on the diffusion coefficient of translation. Phys.Rev.E Vol. 52, No. 4 (1995) 3936–3942
3. Cebers A.: Thermodynamic stability of magnetofluids. Magnetohydrodynamics 18 (1982) 137-142
4. Maiorov,M.M.; Zablotsky, D.Y.: Measurements of rotary and translation diffusions of magnetite nanoparticles in a hydrocarbon-based magnetic fluid. Magnetohydrodynamics Vol. 41, No. 4 (2005) 353–359
5. Davarzani, H.; Marcoux, M.; Quintard, M.: Theoretical predictions of the effective thermodiffusion coefficients in porous media. Int. J. Heat Mass Transfer. 53 (2010) 1514–1528
6. Blums, E.et al.: Thermoosmotic transfer of sterically stabilized ferrofluid particles in non-isothermal capillary porous layer. J. Magn. Magn. Mater. 289 (2005) 275-277

100 μM THICK FERROFLUID LAYER AS A RESETTABLE MEMORY CELL

PUKINA L., MEZULIS A., ZABLOTSKY D.
Institute of Physics, University of Latvia, 32 Miera str. 32, Salaspils LV-2169, Latvia
e-mail: lasma.pukina@gmail.com

Abstract: We report an experimental work in which a 100 μm thick ferrofluid layer is exposed to Nd:Yag laser light and an external magnetic field. The ferrofluid layer is illuminated by the interference pattern of the laser light gone through the optical system. The interference fringes of the laser light induce the temperature grating in the sample. In the magnetic field the magnetostatic interaction occurs, tending to create a hexagonal pattern [1],[2]. The outcome image, whether hexagonal cells or interference pattern of the warming light, is dependent on the order of excitation applied.

1. Introduction

Ferrofluids are colloidal solutions that typically consist of magnetic nanoparticles. Each particle has a constant magnetic dipole moment proportional to its size that can align with an external magnetic field [3]. So ferrofluids are systems capable of unique pattern forming behavior spontaneous phase separation and formation of ordered and disordered patterns in layers of magnetic colloid may occur under the influence of external magnetic fields [4]. These patterns are the consequence of magnetic dipole-dipole interactions and the reversible agglomeration of the magnetic nanoparticles.

In this work, we studied the interaction between a concentration grating of colloidal nanoparticles, induced by means of a laser beam and an external magnetic field in 100 μm thick ferrofluid layer. This research demonstrates that the concentration grating of the ferrofluid layer differs by the order of external excitations that are applied to it. The external magnetic field can be applied as the first, as the last one or at the same time as the warming laser light.

2. Experimental setup

Simplified optical scheme of experimental setup is shown in Fig.1. Nd:Yag laser with a wavelength of 532 nm is used as a power laser. The work was done with the continuous laser forced scattering setup in combined scattering mode. The latter means that agglomerated particles form objects the characteristic size of which is compatible with the laser wavelength, therefore light scattering outsteps Rayleigh type. Theoretical model for that situation, which is not a subject of the present paper, becomes complicated because Rayleight scattering creates the index optical grating whereas agglomerated particles cause Tyndall scattering and absorption. In the first degree of explanation, the combined scattering results with seeing the grating picture in a correct geometry but with an excessive contrast. Due to uncertain focus plane of combined scattering image, we take the pictures from a diffusive reflecting screen, (Fig. 1). In order to exclude the thermo gravitation convection, the Nd:Yag laser beam transmits the sample layer from above. Power laser beam is expanded and entered into the prism and mirror system, where it is split into two beams. Both beams are focused in a narrow angle on the sample at the same place where they interfere. As the ferrofluid absorbs most of the green light, the interference fringes of the laser light induce a sinusoidal 1D temperature grating in the sample. The optical setup can be modified to more complicated by splitting the two narrow angle beams once again. As a result, two interfering beam pairs induce sinusoidal square-shaped 2D temperature grating. Due to the Soret effect, the temperature grating in the sample induces the corresponding particle concentration grating.

The low power reading He-Ne red laser beam has the same direction through the sample. The Rayleigh type scattering causes the appearance of diffracted intensities of the reading beam (optical index grating). Since the diffracted intensities are hundred times weaker than zero order transmitted beam, the camera lens must be focused on the optical index grating image plane. With the present geometry this plane is ca. 10 mm after the ferrofluid layer. That is close enough to the sample to see Tyndall and absortion effects rather clearly. It means, we see the optical grating of single particles (low contrast regular grating) and agglomeration of particles (high contrast structures) simultaneously. The intensity distribution of the reading laser's beam along the diameter has a shape of a Gausian. In order to avoid Gaussian distribution in presented pictures it is necessary to subtract the stationary background picture with the same Gausian intensity distribution from the recorded video. The stationary background picture is obtained by filming the screen with the grating projection before any excitation is applied to the sample.

The sample is put into a solenoid so that its magnetic field direction coincides with that of laser beams. The intensity of the external magnetic field can be applied up to 50 mT. The solenoid heats up as a current passes through it, therefore a little fan is used to cool the solenoid. Additional heat would affect the results of the experiment.

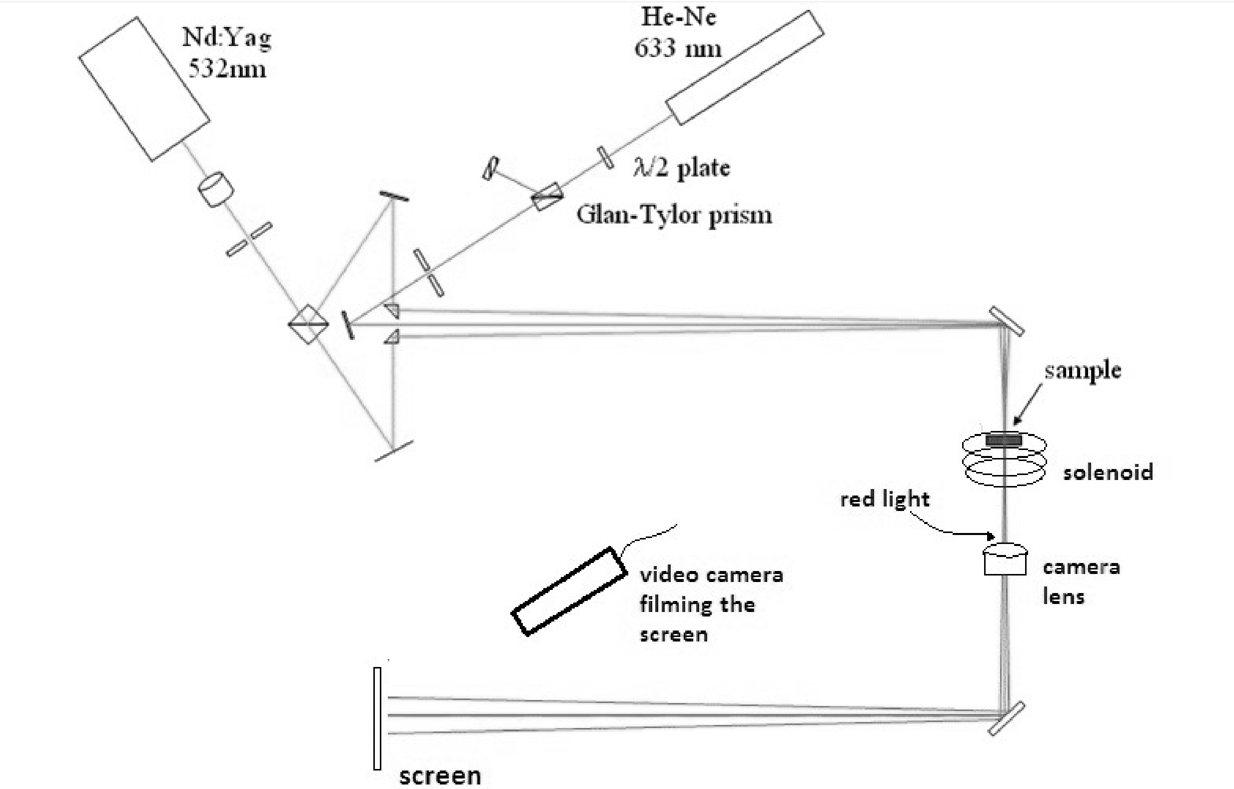

Video camera connected to a computer with the necessary video processing software.

Figure 1: Simplified scheme of the observation of concentration grating in ferrofluid layer induced by means of a laser beam and an external magnetic field.

Our ferrofluid sample contains Fe_2CoO_4 particles, the mean magnetic diameter of which is 8…10 nm. The Soret coefficient of the ferrofluid is 0.15 1/K, measured by the forced Rayleigh scattering method.

3. Discussion and results

If the sample is exposed only to the laser light the ferrofluid layer stores plain image of the interference pattern of the warming light, either parallel lines or square shaped lattice depending whether the optical setup for 1D or 2D interference was used. If the sample is exposed only to the external magnetic field, the image of hexagonal cells can be observed instead. The cells start to form from one center and the pattern evenly expands (Fig. 2. a).

In our experiment, we exposed the sample to both those excitations (warming light or magnetic field). We changed the sequence of excitation, the intensity of the external magnetic field.

We observed that the pattern mostly preserves the shape of the first excitation.

In the experiments where the magnetic field was applied first, whatever the time after which the power laser was turned on or the intensity of the magnetic field, the Soret effect is too weak to change created hexagonal structures. In some experiments we turned out the magnetic field, but did not turned out the warming laser yet. After turning out the magnetic field the pattern still remains, although only the power laser is turned on. The pattern of course fades out by switching off the power laser too (Fig. 2.b).

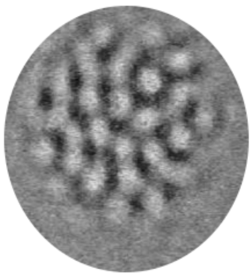

A If the magnetic field is applied, the magnetostatic interaction occurs, tending to create a hexagonal pattern. The cells start to form from one center.

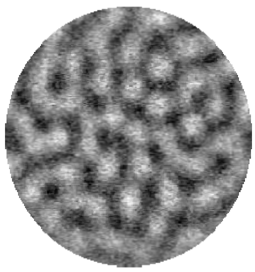

B The pattern while the external magnetic field is not applied any more, but the power laser is still turned on.

Figure 2: Patterns of concentration grating of the ferrofluid layer if the magnetic field is applied before the warming light.

In the experiments with reverse order of excitations - the temperature grid was induced first. Due to the Soret effect, during the characteristic time the particle concentration grid was created. We observed that the external magnetic field turned on afterwards does affect the image. Interference fringes (the concentration gradient) became more contrasted (Fig. 3. a, b) after the magnetic field's application. If the intensity of the magnetic field was set at its maximum (50 mT) the shape of the interference fringes was slightly deformed (Fig. 4. a, b).

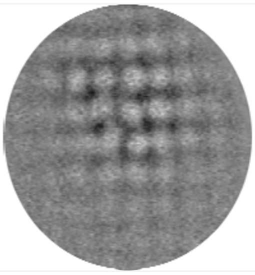

A 2D pattern short after the magnetic field is turned on. Square-shaped 2D grating starts to become more contrasted starting from one center. (The period of the structure is 100 μm)

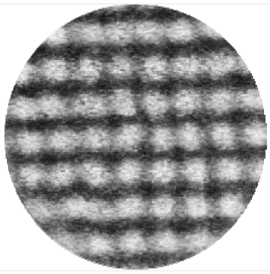

B 2D pattern after the magnetic field is turned on. (The period of the structure is 100 μm)

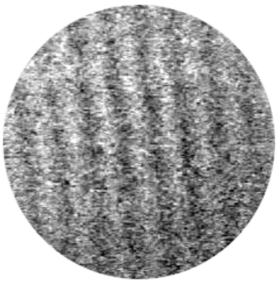

B 1D pattern before the magnetic field is turned on. (The period of the structure is 100 μm)

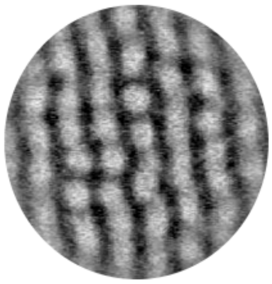

C 1D pattern after the magnetic field is turned on its maximum. (The period of the structure is 100 μm).

Figure 3: Patterns of concentration grating of the ferrofluid layer if the warming light is applied before the magnetic field.

In the experiments where both excitations were applied simultaneously the competition of the both patterns could be seen. The hexagonal cells started to appear at one spot at the same time as the interference fringes started to form (Fig. 4).

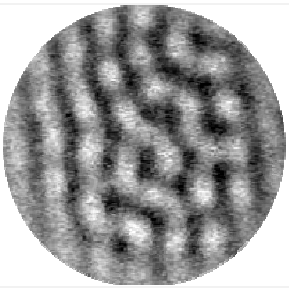

The mixing between the 1D interference fringes and the hexagonal cells as both excitations are applied at the same time. (The width of the image represents 800 μm)

Figure4: Patterns of concentration grating of the ferrofluid layer if the warming light and the magnetic field are applied simultaneously.

This effect is completely resettable – after both excitations are switched off, the aggregation disappears and the sample is ready for the next exercise.

4. Conclusions

Summing up the observed behavior of a 100 μm thick ferrofluid layer under experimental conditions, it could be pointed out:

1. If the magnetic field to the ferrofluid layer is applied first, a pattern of concentration grating preserves a hexagonal shape.
2. If the warming light to the ferrofluid layer is applied first, a pattern of concentration grating tends to preserve its shape during the experiment, but could be slightly damaged if the intensity of the magnetic field is too high.
3. If the warming light and the magnetic field to the ferrofluid layer are applied simultaneously hexagonal cells and the pattern representing interference fringes appear.

5. References

[1] Cebers, A.: Magnetohydrodynamics, vol. 35 (1999), no. 4, pp. 278-296.

[2] Bacri, J.-C., Salin, D.:. Optical scattering on ferrofluid agglomerates. J. Physique - LETTRES 43 L-771 - L-777, 1982

[3] Herng-Er Horng, Chin-Yih Hong, Wai Bong Yeung, and Hong-Chang Yang. Magnetochromatic effects in magnetic fluid thin films. Applied Optics, vol. 37 (1998), no. 13 y 1.

[4] Blums, E., Cebers, A., Maiorov, M.M.: Magnetic Fluids. Walter de Gruyter & Co., Berlin, New-York, 1997.

EXPERIMENTAL STUDY OF INITIATION OF CONVECTION IN A SPHERICAL CAVITY FILLED WITH NANOFLUID

BOZHKO[1] A.A., KRAUZINA[1] M.T., PUTIN[1] G.F., SUSLOV[2] S.A.
[1]Department of General Physics, Perm State National Research University, Perm, Russia
[2]Department of Mathematics, Swinburne University of Technology, Hawthorn, Victoria, Australia
E-mail: marina.krauzina@gmail.com

Abstract: The stability of mechanical equilibrium in a spherical cavity filled with ferro-nanofluid heated from below is investigated experimentally. It is shown that when the temperature difference between the sphere poles is increased gradually the flow arises as a result of supercritical transition provided that nanofluid is well mixed before the start of the experiment. The subcritical transition from a motionless state arises if nanofluid remains at rest for a sufficiently long time (from one day to several weeks) prior to the experiment. The evolution of convection from a finite-amplitude excitation to a steady flow is described.

1. Introduction

In the present work we study the stability of mechanical equilibrium and the evolution of convective motions in a differentially heated spherical cavity filled with a ferrocolloid. It is known [1] that the loss of mechanical equilibrium in a single component fluid can lead to a gradual increase of the convective flow amplitude that is proportional to the square root of the supercriticality (i.e. of the parametric distance from a critical point). This scenario corresponds to a supercritical transition. However it is also possible for the transition to convection to occur abruptly. This is the case if a transition is subcritical so that a hysteresis is observed when the variation path of the control parameter is reversed. However in contrast to a classical case of subcritical bifurcation when both forward and reverse transitions are abrupt, in the case of multi-component nanofluids the reverse transition from the convective state to the state of rest occurs gradually [2-4]. The reason for this peculiar behaviour is that the stability of mechanical equilibrium in magnetic colloids in a gravitational field is influenced by a large number of factors such as buoyancy, thermodiffusion of various components of a liquid phase, thermophoresis and barometric sedimentation of solid particles and their aggregates and the variation of rotational viscosity of a fluid seeded with nano-particles. In many regards convective instability in nanofluids is similar to that observed in double diffusion systems [5, 6].

2. Experimental setup

The experimental setup consisted of a spherical cavity with the diameter of 16.0 ± 0.1 mm cut inside two plates made of organic glass and glued together to form a block with overall dimensions $53\times53\times18$ mm^3, see Figure 1. The block is placed between two flat parallel water-filled heat exchangers. The temperature of water in heat exchangers was controlled using two jet thermostats.

Four copper-constantan thermocouples located in the equatorial plane of a sphere were used to detect the structure of the arising convection flows, see Figure 1. Such an equidistant

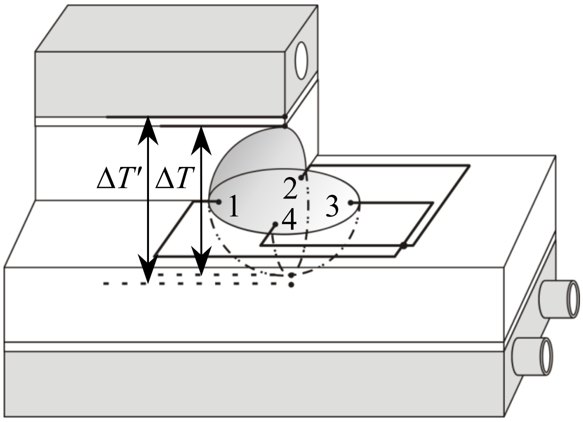

Figure 1: Schematic of the experimental setup: thermocouples 1–4 used for detecting the flow structure; $\Delta T'$ and ΔT are the temperature differences between the heat exchanger plates and poles of the sphere, respectively.

positioning of thermocouples enabled the detection of a single-vortex flow corresponding to the first instability mode in a sphere [7, 8] as well as of other structures including toroidal flows [7]. The digital data acquisition system "Thermodat T29BM1" was used for registering thermocouple readings with the accuracy of 0.01K. The data obtained in experiments lasting several days was automatically recorded on a computer hard drive via a USB port.

A single convection vortex with an arbitrarily oriented horizontal axis can be represented as a superposition of two base vortices with orthogonal axes oriented along the lines connecting thermocouples 1, 3 and 2, 4. Figure 2 shows one of such base vortices with the axis connecting thermocouples 1 and 3. The axis of a second base vortex (not shown) connecting thermocouples 2 and 4 forms the 90° angle with axis of the first (shown) vortex.

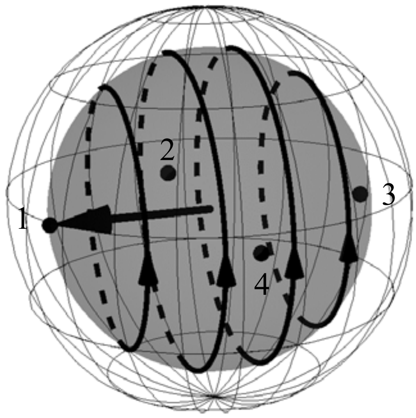

Figure 2: Schematic view of the first base vortex.

The thermal perturbations θ_{I} and θ_{II} induced by the orthogonal base vortices are given by $\theta_{\mathrm{I}} = \theta_1 - \theta_3$ and $\theta_{\mathrm{II}} = \theta_2 - \theta_4$, where θ_1, θ_2, θ_3 and θ_4 are the readings of the corresponding thermocouples. In the case of approximately linear vertical temperature profile in the central part of the sphere the orientation and intensity of a convection vortex can be described by the vector of angular velocity whose magnitude is proportional to the convective perturbation $\theta = \sqrt{\theta_I^2 + \theta_{II}^2}$.

An important characteristic of convective heat transfer is Nusselt number *Nu* that is the ratio of a full heat flux including convection and conduction components to the value of a conduction heat flux. In order to measure the heat flux organic glass plates were placed between the poles of a sphere and heat exchangers. Thermocouples were installed on both sides of the plates to register the temperature differences $\Delta T'$ between the heat exchangers and ΔT between the poles of the cavity. Nusselt number then was determined as $Nu = \Delta T_p/(k\Delta T)$, where $\Delta T_p = \Delta T' - \Delta T$ is the temperature difference across the plates and k is the empirical constant representing the ratio of thermal conductivities of a fluid and organic glass. The ferrofluid used in experiments had transformer oil base. The solid phase consisted of magnetite particles with the average size of 10 nm that were stabilised using oleic acid. The fluid density was 1.37×10^3 kg/m^3 and its dynamic viscosity was 0.069 Pa·s.

3. Results

As has been previously shown theoretically [7] and experimentally [8], a single-vortex convective motion in a spherical cavity filled with a one-component Newtonian fluid heated from below arises when the applied temperature difference exceeds the critical value ΔT_C as a result of supercritical bifurcation. A similar result was established here for a well-mixed multi-component ferrofluid. Specifically, in experiments with uniform ferrocolloid the threshold value of $\Delta T_C = 1.8 \pm 0.1$ K was reproduced in several independent runs using the method of convective pre-mixing: the experimental setup was turned sideways so that the heat exchanger plates that were maintained at the maximum possible temperature difference of $\Delta T' = 40$ K became vertical. They were kept in this position for an hour ensuring a strong convective flow inside the sphere. In contrast, when such a preliminary mixing was not performed the convection was found to establish abruptly and the hysteresis was observed when a gradual increase of the applied temperature difference was reversed.

The experiments with non-premixed fluid were performed using the fluid that remained in mechanical equilibrium for several days. After the start of heating the experiment proceeded with the incremental temperature increases of 2 K. After each temperature step the system was left to adjust to the new thermal condition for 24 hours. Once convection flow patterns were detected they were observed for a substantial time ranging from several days to several months.

Figure 3 shows the dependence of Nusselt number on the relative temperature difference $\Delta T/\Delta T_C$ between the poles of a sphere. Black squares along $\Delta T/\Delta T_C$ axis correspond to regimes where the abrupt transition was detected. Empty circles correspond to self-induced oscillations that are associated with the precession of the axis of the convection vortex in the equatorial plane. Black circles depict the regimes of stationary single-vortex convection when the orientation of the flow axis did not change with time.

The thin arrow at $\Delta T/\Delta T_C = 3.9$ in Figure 3 shows the abrupt transition to convective motion in a magnetic fluid that remained at rest in isothermal conditions for 34 days prior to the start of experiment. As seen in Figure 4, where the convective thermal perturbations θ_I и θ_{II} are presented as functions of time, 10 hours after the fixed temperature difference of $3.9\Delta T_C$ was applied quasi-harmonic oscillations with an increasing amplitude were established and existed for the next 27 hours. A similar transition was observed at $\Delta T/\Delta T_C = 2.0$ (thick arrow in Figure 3) for a fluid that remained isothermal and at rest for 3 days before the experiment. In this case the convective vortex with a precessing axis appeared 29 hours after the temperature difference was applied.

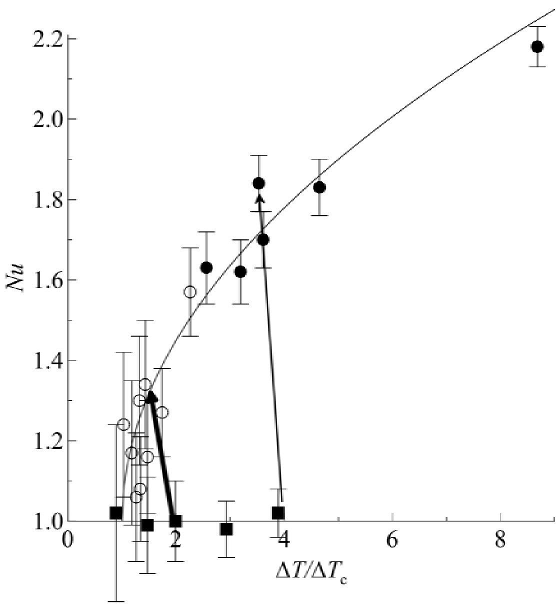

Figure 3: Nusselt number as a function of the relative temperature difference.

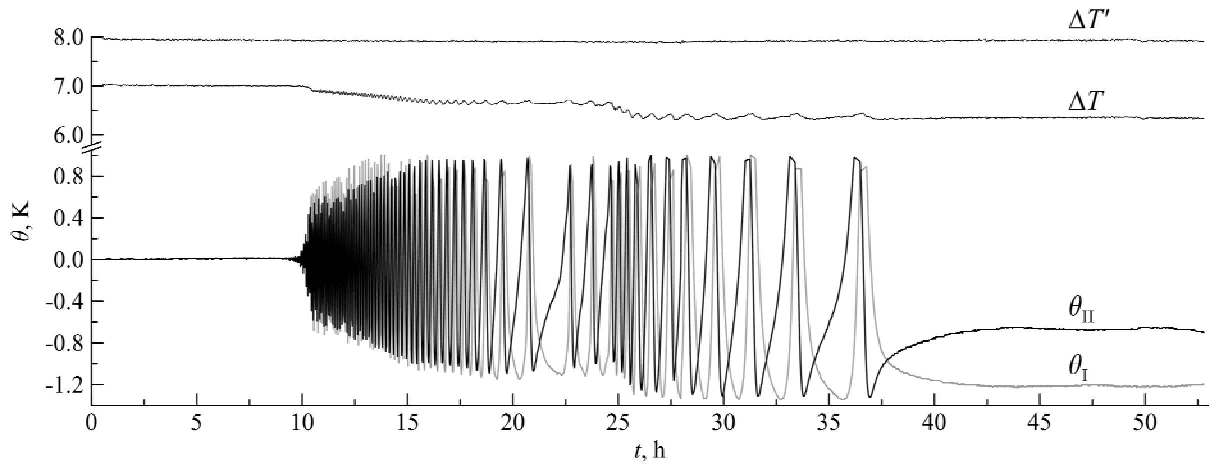

Figure 4: Thermogramm at $\Delta T/\Delta T_C = 3.9$.

The oscillations of the temperature difference between the poles of the cavity during the transient period seen in Figure 4 led to the variation of heat flux through a sphere. The corresponding variation of Nusselt number was around 5% between 15 and 24 hours after the convection flows were first detected. This increased to about 11% 15-24 hours after the start of convection, but finally died out after 53 hours so that the thermocouple readings remained unchanged for the next 10 days.

Figure 5 shows Morlet wavelet-transform of θ_I signal starting from the moment when convection flow was first detected. The horizontal axis corresponds to the observation time t and vertical the period of oscillations τ. The grey shade is used to show the amplitude of the. wavelet transform. In particular, the figure demonstrates that 7-12 hours after the start of oscillations they had the dominant period between 1 and 2, however at later times between 15 and 27 observation hours their period increased to approximately 3 hours.

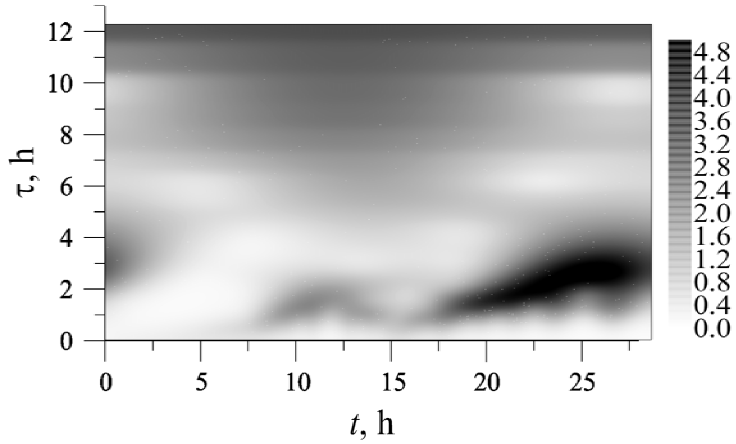

Figure 5: Morlet wavelet-transform at $\Delta T/\Delta T_C = 3.9$.

4. Conclusion

The current experimental investigation of the transition from mechanical equilibrium to convection flow in a spherical cavity filled with ferrofluid and heated from below showed that in a nanofluid that remained isothermal and at rest for several days convection flows arise abruptly and the hysteresis is observed in reverse transition to a stationary state. The depth of the hysteresis depends on the time the fluid stayed at rest before the start of the experiment: the critical temperature difference required to initiate convection increases with the duration of the period of rest prior to measurements. At the same time the reverse transition to a stationary state always occurs gradually at the same critical temperature difference. The likely explanation of such a peculiar behaviour is the presence of gravitational sedimentation of solid phase in a resting nanofluid that creates a stable density stratification that requires a stronger thermal forcing to initiate convection. At the same time convection leads to mixing of a nanofluid so that the reverse transition is not affected by the non-uniformity of solid phase concentration so that the ferrofluid behaves as a regular fluid.

The work was supported by the grant НШ-4022.2014.1 as a part of the National Program for Supporting Leading Research Organizations, Russian Federation.

5. References

1. Arnold, V.I.: Catastrophe theory. Moscow, Science 1990 (in Russian).
2. Bogatyrev, G.P., Shaidurov, G.F.: Convective stability of a horizontal layer of ferromagnetic fluid in a uniform field. Magnetohydrodynamics. 3 (1976) 137–146 (in Russian).
3. Bozhko, A.A., Putin, G.F.: Heat transfer and flow patterns in ferrofluid convection. Magnetohydrodynamics. 39 (2003) 147–168.
4. Bozhko, A.A., Bulychev, P.V., Putin, G.F., Tynjala, T.: Spatio-temporal chaos in convection of colloids. Reports of the Russian Academy of Sciences. Fluid Dynamics. 1 (2007) 29–38.
5. Ahlers, G., Lerman, K., Cannell, D. S.: Different convection dynamics in mixtures with the same separation ratio. Physical Review E. 53 (1996) 2041–2044.
6. Donzelli, G., Cerbino, R., Vailati, A.: Bistable heat transfer in a nanofluid. Physical Review Letters. 102 (2009) 104503 (4).
7. Gershuni, G. Z., Zhukhovitsky, E.M.: Convective stability of incompressible fluid. Moscow, Science 1972 (in Russian).
8. Ovchinnikov, A.P., Shaidurov, G.F.: Convective stability of uniform fluid in a spherical cavity. Hydrodynamics. Perm State University. 1 (1968) 3–21 (in Russian).

DIFFUSION COEFFICIENT OF A FERROFLUID-WATER SYSTEM IN A HELE-SHAW CELL

KITENBERGS[1,2] G., PERZYNSKI[2] R., CĒBERS[1] A., ĒRGLIS[1] K.
[1]Lab MMML, Department of Theoretical Physics, University of Latvia, Riga, Latvia
[2] Lab PECSA, UMR 7195, UPMC, Paris, France
E-mail: guntars.kitenbergs@lu.lv

Experimental studies of complex phenomena observed in ferrofluids (e.g., magnetic micro-convection [1]) require a good understanding of the intrinsic properties and behavior of the ferrofluid used. Here we examine a simple mixing of water and ferrofluid droplets that are brought to contact in a Hele-Shaw cell. With bright field microscopy, we film the diffusion process over time and obtain magnetic particle concentration fields from acquired images via Beer-Lambert law. Following a concentration profile of a sample line perpendicular to the diffusion front shows an unforeseen nonsymmetrical development (see figure). In addition, it gives much greater diffusion length augmentation than expected from Fick's law for a colloid of the average particle size of around 10nm. We reveal the causes of these differences, by using simulations of the model system, and compare results with control measurements of sample parameters that are obtained by standard techniques (Magnetization, Birefringence, Dynamic Light Scattering and Forced Rayleigh Scattering measurements). In addition, we discuss the differences in the obtained measurement results and their causes.

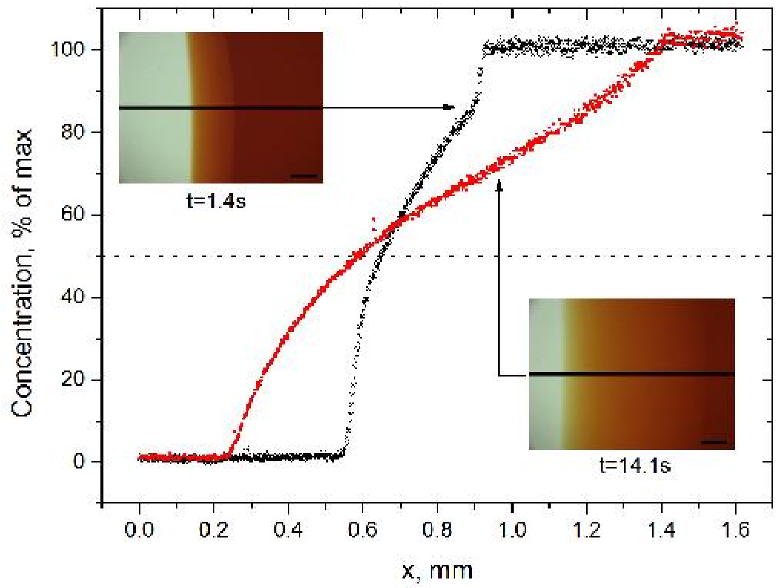

Figure: Ferrofluid concentration distribution over sample lines (long dark lines in bright field images) at two different times, during diffusion mixing. Dark short lines in images are scale bars that correspond to 0.2 mm.

Reference

[1] Erglis, K., et al.: J. Fluid Mech., 714 (2013), p. 612.

DEFORMATION OF A BODY WITH A MAGNETIZABLE POLYMER IN A UNIFORM MAGNETIC FIELD

NALETOVA V.A.[1], MERKULOV D.I.[1], ZEIDIS I.[2], ZIMMERMANN K.[2]
[1] Faculty of Mechanics and Mathematics, Lomonosov Moscow State University, Leninskiye gory, 119992, Moscow, Russia,
[2] Faculty of Mechanical Engineering, Ilmenau University of Technology, Ilmenau, D-98693, Germany
Email address of corresponding author: igor.zeidis@tu-ilmenau.de

Abstract: The deformation of a spherical body with a magnetizable polymer in the uniform applied magnetic field is studied theoretically. Elastic properties of such composite are described by Mooney-Rivlin model. The possibility of existence of more than one form of the equilibrium of such body in the applied uniform magnetic field is obtained. The theory predicts the hysteretic behavior of the body form if the applied magnetic field increases and decreases cyclically, when many-valuedness of the body form exist.

1. Introduction

The deformation of various bodies with magnetizable polymers was explored in many works (for example, in [1]). However, in these researches usually there was one solution of a problem of static only.
In the present work, the deformation of a spherical body with a magnetizable polymer in the uniform applied magnetic field is studied theoretically. Elastic properties of such composite are described by Mooney-Rivlin model [2]. The possibility of existence of more than one form of the equilibrium of such body in the applied homogeneous magnetic field is obtained.

2. Setting problem

A spherical body (R is body radius) with a magnetizable polymer in a uniform applied magnetic fields $\boldsymbol{H}_0$. Consider that magnetization of the polymer $\boldsymbol{M}$ depend on magnetic field linearly,

$$\boldsymbol{M} = \chi \boldsymbol{H}, \qquad \chi = \text{const}, \qquad \mu = 1 + 4\pi \chi = \text{const} \tag{1}$$

Consider uniform stretch of the body. The spherical body in the magnetic field $\boldsymbol{H}_0$ becomes elongated along the applied magnetic field and becomes ellipsoid of rotation with axes a and b, $b < R < a$. Introduce some parameter λ:

$$\lambda = a / R \tag{2}$$

Condition $\lambda = 1$ means an undistorted spherical body.
Introduce the demagnetization coefficient N ($H^{(i)}$ is a uniform magnetic field inside the body):

$$N = -\frac{H^{(i)} - H_0}{4\pi M}, \qquad M = \chi H^{(i)} \tag{3}$$

In the case elongated ellipsoid of rotation the well known formula for N are [3]:

$$N = \frac{1 - e^2}{e^3}(\operatorname{arctanh}(e) - e), \quad e = \sqrt{1 - b^2 / a^2} \tag{4}$$

The parameter e depends on λ because the body volume is constant:

$$e=\sqrt{1-b^2/a^2}=\sqrt{1-\lambda^{-3}} \tag{5}$$

The formula for N due to (5) may be written as:

$$N(\lambda)=\frac{\operatorname{arctanh}\sqrt{1-\lambda^{-3}}-\sqrt{1-\lambda^{-3}}}{(\lambda^3-1)\sqrt{1-\lambda^{-3}}} \tag{6}$$

From (3) a dependence $H^{(i)}$ on H_0 is obtained:

$$H^{(i)}=\frac{H_0}{1+4\pi\chi N} \tag{7}$$

3. Static form of the body

Full energy of the ellipsoid in the applied magnetic field $E(H_0, \lambda)$ equals summa of elastic and magnetic energies [1, 3]:

$$E=E_m+E_0^{(e)}, \tag{8}$$

$$E_0^{(e)}=V_b\left[C_1\left(\lambda^2+\frac{2}{\lambda}-3\right)+C_2\left(\frac{1}{\lambda^2}+2\lambda-3\right)\right], \tag{9}$$

$$E_m=-\frac{V_b}{2}\chi\frac{H_0^2}{1+4\pi\chi N} \tag{10}$$

Here the coefficient C_1 has the sense of the rubber-like elasticity modulus, and the coefficient C_2 relates with initial shear modulus of the polymer η by formula $\eta = 2(C_1 + C_2)$ [1].
Using (8), (9) and (10), full energy of unit of the volume of the ellipsoid in the applied magnetic field is determined by the following formula:

$$\frac{E(H_0,\lambda)}{V_b}=\left[C_1\left(\lambda^2+\frac{2}{\lambda}-3\right)+C_2\left(\frac{1}{\lambda^2}+2\lambda-3\right)\right]-\frac{1}{2}\chi\frac{H_0^2}{1+4\pi\chi N} \tag{11}$$

Condition of the body equilibrium is

$$\frac{\partial}{\partial\lambda}\left(\frac{E(H_0,\lambda)}{V_b}\right)\Bigg|_{H_0=const}=0 \tag{12}$$

From (12) and (11) the equation of the body equilibrium may be written as:

$$2(C_1\lambda+C_2)\left(1-\frac{1}{\lambda^3}\right)+2\pi\chi^2\frac{H_0^2}{(1+4\pi\chi N)^2}\frac{\partial N}{\partial\lambda}=0 \tag{13}$$

Let us denote left part of equation (13}) as a function $\Psi(\lambda, H_0)$:

$$\Psi(\lambda,H_0)=2(C_1\lambda+C_2)\left(1-\frac{1}{\lambda^3}\right)+2\pi\chi^2\frac{H_0^2}{(1+4\pi\chi N)^2}\frac{\partial N}{\partial\lambda} \tag{14}$$

So the equation of the body equilibrium (13) is rewritten as

$$\Psi(\lambda, H_0) = 0 \tag{15}$$

Equation (15) is implicit dependency of the parameter λ on the applied magnetic field value H_0. Introduce dimensionless parameters:

$$\Psi^* = \frac{\Psi(\lambda, H_0)}{C_1}, \tag{16}$$

$$K = \frac{C_2}{C_1}, \qquad P = \frac{\chi H_0}{\sqrt{C_1}} \tag{17}$$

The formula for $\Psi^*(\lambda, P)$ is

$$\Psi^*(\lambda, P) = 2(\lambda + K)\left(1 - \frac{1}{\lambda^3}\right) + 2\pi P^2 \frac{1}{(1 + 4\pi\chi N)^2}\frac{\partial N}{\partial \lambda} \tag{18}$$

The equation of the body equilibrium may be written in dimensionless form:

$$\Psi^*(\lambda, P, K, \chi) = 0 \tag{19}$$

Equation (19) allows us to study implicit dependence of the parameter λ on the dimensionless parameter P for different parameters χ and K.

4. Results

In Fig. 1 for $\chi = 3$ and $K = 15, 54, 82, 130$ dependences λ on P are shown. It is clear that for enough large magnetic susceptibility χ for some value of the parameter P three solutions for form of the body exist. With increasing of the parameter K, values of the parameter P, for which three equilibrium forms of the body exist, increase.

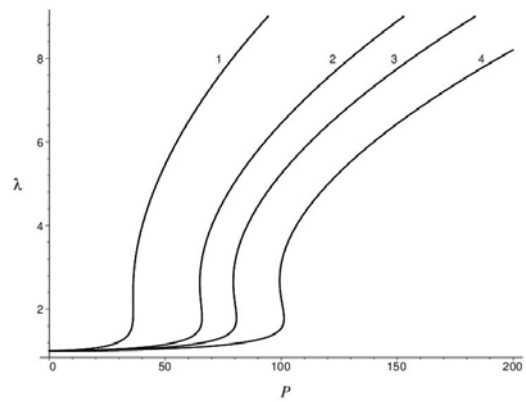

Figure 1: Dependencies λ on P for $\chi = 3$, line 1 – $K = 15$, 2 – $K = 54$, 3 – $K = 82$, 4 – $K = 130$.

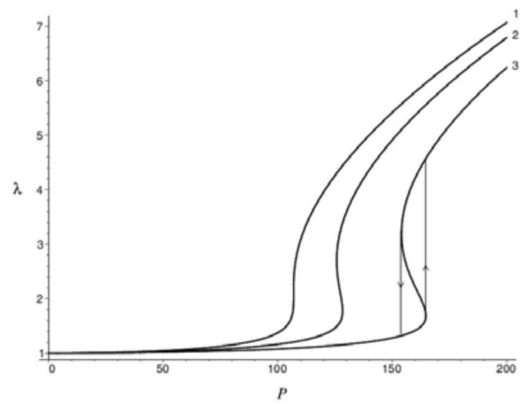

Figure 2: Dependencies λ on P for $K = 210$, line 1 – $\chi = 2.4$, 2 – $\chi = 2.5$, 3 – $\chi = 3$.

In Fig. 2 for $K = 210$ and $\chi = 2.4, 2.5, 3$ dependencies λ on P are shown. From Fig. 2 we can see that for enough small magnetic susceptibility χ many-valuedness of the solution does not exist. If solution many-valuedness exist (for example, for $K = 210$ and $\chi = 3$) the hysteretic behavior of the body form may be observed if the applied magnetic field increases and decreases cyclically, see Fig. 2.

It is shown that for $\chi < 10^{-1}$ for all value of the parameter K many-valuedness of solution does not exist (Fig. 3).

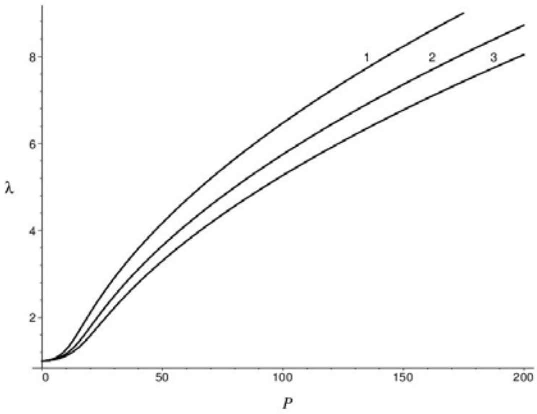

Figure 3: Dependences λ on P for $\chi = 0.1$, line 1 – K=100, 2 – K=150, 3 – K = 200.

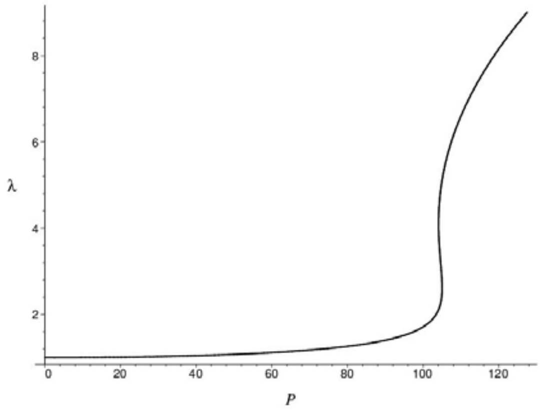

Figure 4: Dependence λ on P for $K = 0$ and $\chi = 30$.

At last, the dependence λ on P for $K = 0$ (the empirical rule for swollen rubbers [2] and $\chi = 30$ is shown on Fig. 4. When $K = 0$ it needs very large value of the magnetic susceptibility χ for existence many-valuedness of the body form.

5. Conclusion

The deformation of a spherical body with a magnetizable polymer in a uniform applied magnetic field is studied theoretically. Elastic properties of such polymer are described by Mooney-Rivlin model. The possibility of existence of more than one form of the equilibrium of such bodies in the applied uniform magnetic field is obtained. It is shown that for any values of the elasticity moduli for enough large magnetic susceptibility three equilibrium forms of the body exist for some value of the applied magnetic field. It is needed to note that for enough small magnetic susceptibility many-valuedness of the solution does not exist for any values of the elasticity moduli. The presented theory predicts the hysteretic behavior of the body form if the applied magnetic field increases and decreases cyclically.

6. Acknowledgements

This work is supported by the Russian Foundation for Basic Research (projects 14-01-91330) and Deutsche Forschungsgemeinschaft (DFG Zi 540-14/1).

7. References

[1] Raikher Yu.L.; Stolbov O.V.: Magnetodeformation effect in a ferroelastic material. Technical Physics Letters. 26(2) (2000) 156-158.
[2] Vinogradov G.V.; Malkin A.Ya.: Rheology of Polymers. Berlin-Heidelberg-New York: Springer Verlag 1980.
[3] Landau L.D.; Lifshitz E.M.: Electrodynamics of Continuous Media. Oxford: Pergamon 1960.

WAVES IN FERROFLUID CONVECTION INDUCED BY INCLINED MAGNETIC FIELD

SIDOROV[1] A., SUSLOV[2] S., RAHMAN[2] H., PUTIN[1] G., BOZHKO[1] A.
[1]Perm State University (PSU), Perm, Russia
[2]Swinburne University of Technology
E-mail: sidorovaliksandr@mail.ru

Ferrofluids are modern strongly magneto-polarisable nanofluids flows of which can be non-intrusively controlled by applying an external magnetic field. One of their prospective applications is as a heat carrier in thermal management systems operating in zero-gravity conditions. The purpose of the research that we will present in this talk was the estimation of parametric boundaries of magneto-convection regimes anticipated to occur in an arbitrarily inclined magnetic field in the lead to the corresponding experiments planned onboard Autonomous space module "OKA-T" (Russian Space Corporation) and International Space Station.

The influence of the field inclination angle on ferrofluid convection was the main purpose of the investigation. It was found that when a field is strictly perpendicular to a ferrofluid layer stationary thermomagnetic patterns develop, but an unexpected form of convection, waves propagating in the direction of concavity of magnetic field lines have been discovered for non-orthogonally applied fields. Therefore on the one hand a symmetry breaking associated with a nonlinear refraction of magnetic field lines results in the appearance of thermo-magnetic waves that propagate in the direction of concavity of field lines so that in contrast to the classical Rayleigh-Benard problem stationary convection patterns exist for sufficiently large values of magnetic Grashof number only when magnetic field is strictly perpendicular to a ferrofluid layer. One the other hand the deviation of the applied field lines from the direction normal to a ferrofluid layer in the absence of gravity leads to the stabilization of a motionless state.

The preliminary ground-based experiments were performed with chamber containing a magnetic fluid layer of the thickness 6.0 mm, length 375 mm and the width 180 mm. The maximal intensity of a magnetic field creating by Helmholtz coils was 35 kA/m. The flows were visualized using an infrared camera with an accuracy of 0.1 C.

DYNAMICAL PROPERTIES OF TRANSFORMER OIL BASED MAGNETIC FLUIDS

RAJNAK[1] M., TOTHOVA[2] J., KOVAC[1] J., KURIMSKY[2] J., DOLNIK[2] B., KOPČANSKÝ[1] P., MOLCAN[1] M., ROYER[3] F., TIMKO[1] M.
[1]Institute of Experimental Physics, Slovak Academy of Sciences, Watsonova 47, 040 01 Kosice, Slovakia, timko@saske.sk
[2]Faculty of Electrical Engineering and Informatics, Technical University, Kosice, Slovakia
[3]Laboratoire LT2C 25, rue du Dr Remy Annino 42000 Saint Etienne, France

Abstract: In this article, our experimental study of the dynamic dielectric behavior of transformer oil-based ferrofluid with magnetite nanoparticles is presented. Electro-kinetic properties of the original transformer oil MOGUL based ferrofluid sample with the magnetic volume fraction of 6.6 % were investigated by means of dielectric spectroscopy method. Frequency-dependent dielectric permittivity was measured within the frequency range from 20 Hz to 2MHz by a capacitance method. The effect of temperature on the viscosity of ferrofluid was studied using a modular compact viscosimeter. The temperature dependence of the viscosity was measured in the temperature range from 20 up to 80°C. The magnetization of different concentrations of MPs in MFs was determined by using of the vibrating sample magnetometer.

1. Introduction

Ferrofluids are colloidal suspensions of nanosized ferromagnetic particles coated with surfactants and dispersed in a carrier liquid. Since their physical properties can be easily influenced by external forces such as the magnetic field, they have found many applications in a variety of fields such as electronic packing, mechanical engineering, aerospace or bioengineering. In particular, if MFs are based on water as a carrier liquid, they can be used in such areas as magnetic drug delivery, cancer treatment by means of magnetic induced hyperthermia, or magnetic imagine [1]. One of many unique properties of ferrofluids is their tuneable viscosity by the external magnetic field. This is called the magnetoviscous effect [2]. One of the most successful applications of thermophysical property of magnetic fluid is audio speaker. In the audio speakers, magnetic fluid is filled around the voice coil. Because thermal conductivity of magnetic fluid is much larger than that of the air, the fluid provides a lower heat resistance between the coil and pole plate [3].

However, if we apply a magnetic fluid to heat transfer applications such as cooling system for power transformer or micromachine [4], it is necessary to perform the detailed investigation on the properties of heat transfer of a magnetic fluid under magnetic field. For a good understanding of this phenomenon, the knowledge of the viscous properties of MFs in the absence of magnetic fields is very important. Particularly its dependence on the amount of suspended magnetic particles (MPs) and temperature is very interesting.

Several previous studies [9-10, 14] on polarization and relaxation processes in ferrofluids were carried out using a dielectric spectroscopy method. It has been shown that the variation of both relative permittivity and dissipation factor with frequency may result from: (1) polarization due to molecular rotation either in polar liquids or in solid polar liquid mixtures, (2) polarization due to charge accumulation at the interfaces of different media in colloidal suspension, (3) polarization due to ion atmosphere displacement, and (4) polarization due to diffusion coupling between ion flows [15]. This indicates that the frequency dependence of relative permittivity and dissipation factor of ferrofluids permits identification and analysis of a number of completely different underlying mechanisms.

In our experiment we have used liquid crystal (LC) cells as capacitors to achieve more precise dielectric measurement of ferrofluids. In the LC cells, two Indium Tin Oxide (ITO) conductive, transparent, thin layers function as electrodes. With the distances between the electrodes down to a micrometer range, only a low voltage is needed to obtain a high electric field and just a droplet of ferrofluid is required to fill the LC cell. The objective of this work is to examine magnetic, viscosity and dielectric properties of transformer oil-based ferrofluid placed in a LC cell under the electric field within the frequency range from 20 Hz to 2MHz.

1. Results

The measurement of magnetization was performed at room temperature by a vibrating sample magnetometer (VSM) with the uncertainty of about 1%. The saturation magnetization of the prepared undiluted ferrofluid was 26.6 $A.m^{2}\cdot kg^{-1}$. As it was shown earlier the shear stress versus shear rate dependence for pure transformer oil MOGUL is linear what is presenting a Newtonian-like fluid behavior. Similarly prepared sample of magnetic fluid based on this oil and used in our experiment behave as Newtonian fluids, since its viscosity do not depend on the shear rate too (results are not given here). The temperature dependence of viscosity shows the classical behaviour at which increasing temperature initiates decreasing viscosity for our sample of ferrofluid. The influence on viscosity is coming from changing the viscosity of pure oil with temperature and from Brownian motion of nanoparticles. With the increasing temperature the Brownian motion of the particles in the ferrofluid was strengthened, which reduced the speed difference between the carrier liquid and the magnetic particles.

Electro-kinetic properties of the original ferrofluid sample with the magnetic volume fraction of 6.6 % were investigated by means of dielectric spectroscopy method. To obtain the frequency dependent complex permittivity of the sample we employed an LCR meter (Agilent E4980A) with the frequency range from 20 Hz up to 2 MHz. Liquid crystal cells with two parallel plate ITO electrodes, whose distance apart d = 1.6 μm and the active electrode area A = 25 mm^2, were used as capacitors (sample holders). The capacitance of the air filled cell C_0 was 148 pF. In order to investigate the influence of a static magnetic field on the electro-kinetics in the ferrofluid, the capacitor was placed between two permanent squared magnets, separated 5 cm apart. The sample was therefore exposed to the quasi homogenous magnetic field of 150 mT. In that way the capacitance $C(\omega)$ and dissipation factor $\tan\delta(\omega)$ of the sample were measured at room temperature. The related real and imaginary part of the complex permittivity was determined according to (1) and (2), respectively. The uncertainty of the acquired data is less than 0.3 %.

$$\varepsilon'(\omega) = \frac{C(\omega)}{C_0} \tag{1}$$

$$\varepsilon''(\omega) = \varepsilon'(\omega)\tan\delta(\omega) \tag{2}$$

The complex permittivity of the undiluted ferrofluid measured in the absence of magnetic field is depicted in Fig. 1. In the low frequency range, one can see the pronounced dielectric dispersion, which is related to a relaxation process [5]. Since the ferrofluids belong to the complex systems, a continuous distribution of relaxation times can be expected. To analyze the low frequency relaxation process, we start by fitting the complex permittivity data with Havriliak-Negami equation [6, 7]:

$$\varepsilon^*(\omega) = \varepsilon_\infty + \frac{\varepsilon_s - \varepsilon_\infty}{[1+(i\omega\tau_m)^{\alpha}]^{\beta}} \tag{3}$$

where α and β are empirical exponents, τ_m is the characteristic relaxation time, ω is the angular frequency of the electric field, ε_s and ε_∞ are the low and high frequency limits of the permittivity, respectively. For the low frequency relaxation process, the best fitting value of the both empirical exponents was found to be 1, what gives the famous Debye relaxation law. Following these fitting parameters we consider the relaxation maximum to be associated with a single relaxation process which can stem from a polarization of electric double layer (EDL) presented on the magnetic particles. The possible formation of the EDL, consisting of adsorbed OH^- and oleate ions on the particle surface and surrounded by hydrated NH_4^+ ions, is discussed in recent studies [8-11]. Such a relaxation is then described by Schwarz model of EDL polarization [12].

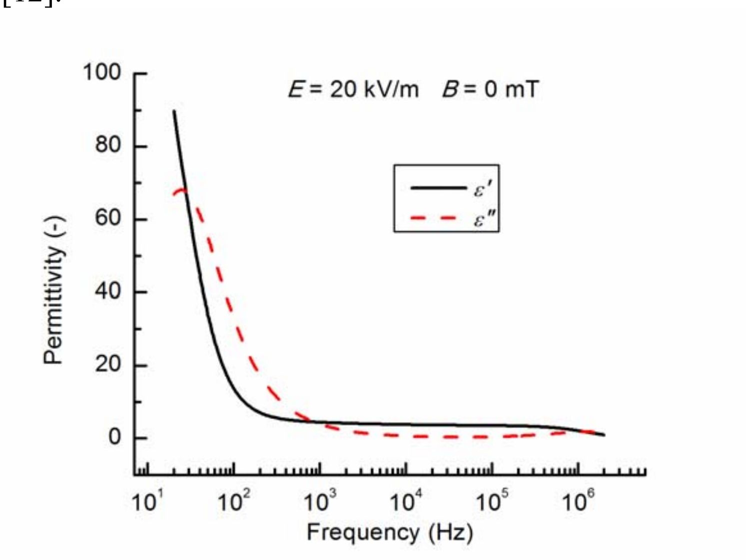

Figure 1: Frequency dependent complex dielectric permittivity.

In the measured frequency range, the real permittivity spectrum has been found as nearly independent on the magnetic field applied to the sample in parallel and perpendicular configurations in regard to the electric field (Fig. 2).

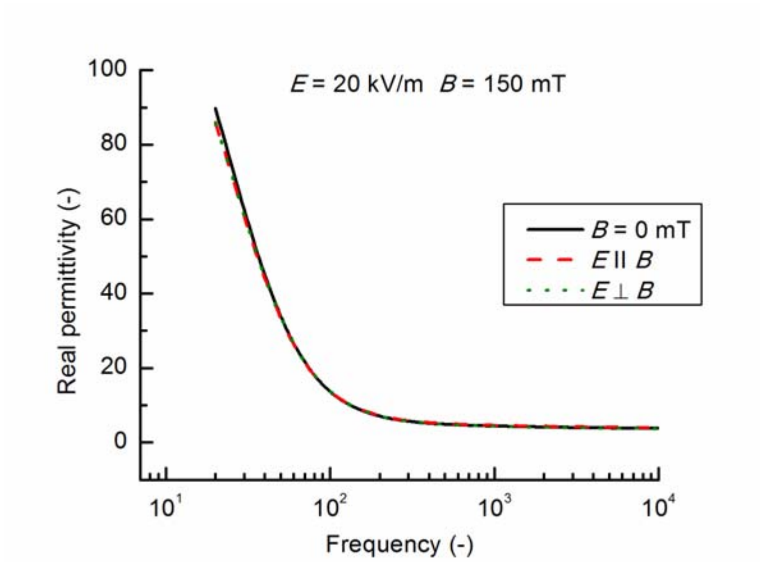

Figure 2: Influence of magnetic field on the real permittivity spectrum.

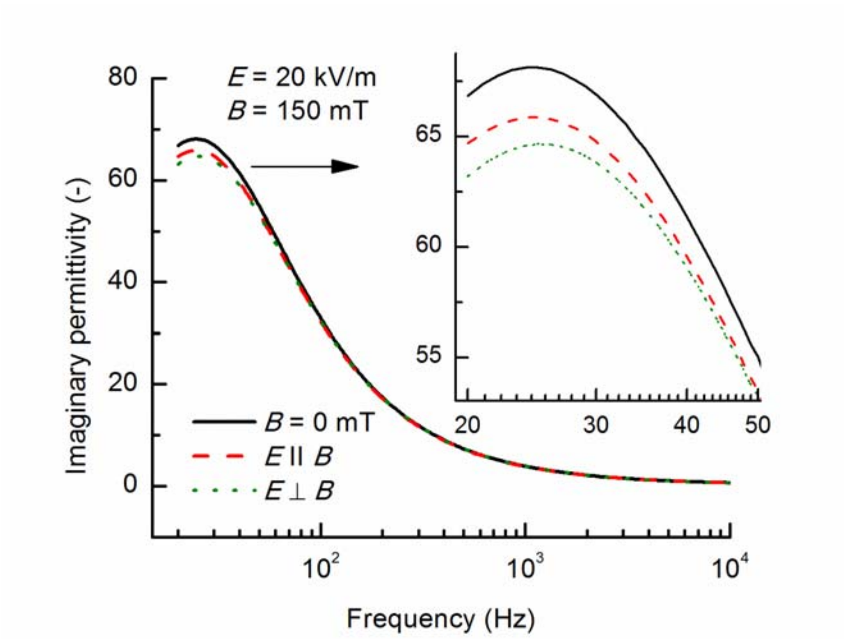

Figure 3: Magnetic field dependent imaginary permittivity spectrum.

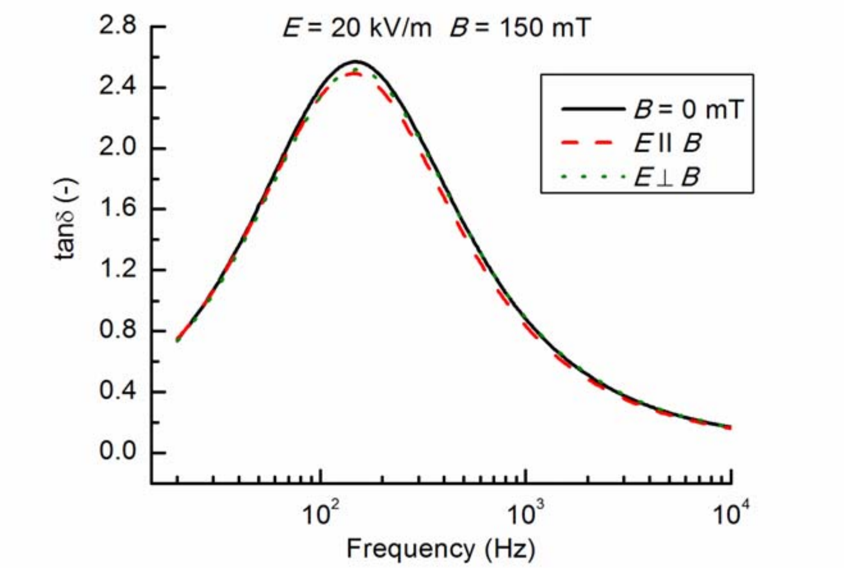

Figure 4: The influence of magnetic field on the spectrum of dissipation factor.

The well-known magneto-dielectric effect [13-14] has not been directly proven in the ferrofluid micro layer. However, looking at the loss spectra (Fig. 3, 4), one can see the decrease in both, the magnitude of the loss peak and the relaxation time, when the magnetic field is applied. As the height of the relaxation maximum is associated with the value of static permittivity, one can deduce the decrease in the static permittivity as well. This is related to reduction in the electric dipole moment values and its ordering with *E* field. Then, the reduced distance between the ions forming the electric dipoles and their reduced relaxation path, when the magnetic field induces formation of chain like particle clusters, can account for the observed lower relaxation maxima. Nevertheless, better experimental statistics and more quantitative analysis is necessary to understand the non-typical magneto-dielectric phenomenon.

3. Conclusion

We have shown, that the temperature dependence of viscosity shows the classical behaviour at which increasing temperature initiates decreasing viscosity coming from changing the viscosity of pure oil with temperature and from Brownian motion of nanoparticles. With the increasing temperature the Brownian motion of the particles in the ferrofluid was strengthened, which reduced the speed difference between the carrier liquid and the magnetic particles. It was shown that the height of the relaxation maximum is associated with the value of static permittivity what can be assigned to the decreasing in the static permittivity. This fact is connected with reduction in the electric dipole moment values and its ordering with *E* field and formation of chain like particle cluster in *E* field too.

Acknowledgements.

This work was supported by the project VEGA 0043, 2/0045/13, 1/0487/12, the Slovak Research and Development Agency under the contract Nos. APVV-0171-10 and 20-006005, Ministry of Education Agency for Structural Funds of EU in frame of projects 26110230061, 26220120046 and M-era.Net – MACOSYS.

4. References

[1] Q.A. Pankhurst, N.K.T. Thanh, S.K. Jones, J. Dobson, J. Phys. D: Appl. Phys. **42**, 224001 (2009). DOI:10.1088/0022-3727/42/22/224001

[2] S. Odenbach, Magnetoviscous Effects in Ferrofluids ISBN 3-540-43068-7, Springer-Verlag, Berlin, 2002.

[3] D.B. Hathaway, Sound Eng. Mag., **13** 42 (1979).

[4] K. Nakatsuka, B. Jeyadevan, S. Neveu, H. Koganezawa, J. Magn. Mag. Mat., **252**, 360 (2002)

[5] Y. Feldman, A. Puzenko, and Y. Ryabov, Dielectric Relaxation Phenomena in Complex Materials, Fractals, Diffusion, and Relaxation in Disordered Complex Systems, W. T. Coffey and Y. P. Kalmykov, Eds. John Wiley & Sons, Inc., 2005, pp. 1–125.

[6] N. Axelrod, E. Axelrod, A. Gutina, A. Puzenko, P. B. Ishai, and Y. Feldman, Dielectric spectroscopy data treatment: I. Frequency domain, Meas. Sci. Technol., vol. 15, no. 4, p. 755, Apr. 2004.

[7] M. Wübbenhorst and J. van Turnhout, Analysis of complex dielectric spectra. I. One-dimensional derivative techniques and three-dimensional modelling, J. Non-Cryst. Solids, vol. 305, no. 1–3, pp. 40–49, Jul. 2002.

[8] I. Malaescu and C. N. Marin, Dielectric behavior of some ferrofluids in low-frequency fields, J. Colloid Interface Sci., vol. 251, no. 1, pp. 73–77, Jul. 2002.

[9] M. M. Rădulescu, Low-frequency dielectric losses in ferrofluids containing magnetite particles in kerosene, J. Magn. Magn. Mater., vol. 85, no. 1–3, pp. 144–146, Apr. 1990.

[10] P. C. Fannin, C. N. Marin, I. Malaescu, and N. Stefu, Microwave dielectric properties of magnetite colloidal particles in magnetic fluids, J. Phys. Condens. Matter, vol. 19, no. 3, p. 036104, Jan. 2007.

[11]M. Rajnak, J. Kurimsky, B. Dolnik, K. Marton, L. Tomco, A. Taculescu, L. Vekas, J. Kovac, I. Vavra, J. Tothova, P. Kopcansky, and M. Timko, Dielectric response of transformer oil based ferrofluid in low frequency range, J. Appl. Phys., vol. 114, no. 3, p. 034313, Jul. 2013.

[12] G. Schwarz, "A theory of the low-frequency dielectric dispersion of colloidal particles in electrolyte solution1,2" J. Phys. Chem., vol. 66, no. 12, pp. 2636–2642, Dec. 1962.

[13] A. Espurz, J. M. Alameda, and A. Espurz-Nieto, Magnetically induced dielectric anisotropy in concentrated ferrofluids, J. Phys. Appl. Phys., vol. 22, no. 8, p. 1174, Aug. 1989.

[14] A. Spanoudaki and R. Pelster, Frequency dependence of dielectric anisotropy in ferrofluids, J. Magn. Magn. Mater., vol. 252, pp. 71–73, Nov. 2002.

[15] K. Arulanandan, Low frequency dielectric dispersion of clay-water-electrolyte systems, Clays Clay Miner. 16, 337–351 (1968).

EXPERIMENTAL TESTING OF THE MASS EXCHANGE ON THE FERROFLUID SURFACE

LICKRASTINA A., MAIOROV M., BLUMS E.
Institute of Physics, University of Latvia, 32 Miera, Salaspils LV-2169, Latvia
E-mail address of corresponding author: agnese.lickrastina@inbox.lv

Abstract: The experimental investigation is carried out to evaluate the effect of the gradient magnetic field on the mass exchange during the bubbles run through the ferrofluid. The results show the influence of the magnetic field on the volume of the mass exchange cell.

1. Introduction

The border between gas and ferrofluid is sensitive to applied magnetic field - it warps the free surface of ferrofluid very strongly. The gradient magnetic field increases the floatation of nonmagnetic bodies in the ferrofluid that has an influence on the size of the bubbles in the ferrofluid. The external magnetic field determines also the shape and the movement of the bubbles [1]. Consequently, it gives the opportunity to impact the mass exchange between gas and fluid as it is determined by the surface area and movement intensity.

Due to these properties the utilization of the ferrofluids is a promising technology in the mass exchange techniques. For example: it may be effective for purification of air or other gases from impurities, gas enrichment and processing, as well as gas transport inside ferrofluid, gas recovery for analysis, etc. Usage of the magnetic fluid gives a possibility to control listed processes by the magnetic field.

2. Experiment

The ferrofluid consist of ferromagnetic particles suspended in the liquid carrier. For reported experiments the liquid carrier is composed by two components. One of the components easily evaporates as the boiling temperature is low, while another component has high boiling temperature and therefore remains longer in the liquid carrier. The concentration of the volatile liquid carrier component in the air passing through the ferrofluid is measured during the experiment. The data are collected by the IR spectrometer. Subject of the present work is experimental examination of the influence of a magnetic field on the removing volatile components from the higher-boiling magnetic fluid.

The experimental setup is shown in fig. 1. The permanent airflow was supplied by the peristaltic pump. Tetradecane is used as a high-boiling carrier for the ferrofluid, and the small quantity of hexane composes a low-boiling addition to the ferrofluid. IR spectrum of the gas at the output has a stripe of hexane, which intensity depends on the experiment duration or quantity of the air passing through. The obtained data presents the information about hexane concentration in the measured air. The influence of the magnetic field on the mass exchange may be tested as the change of hexane concentration in the measured airflow with or without the magnet .

The magnetic field is formed by two joined permanent rectangle magnets with vertical magnetization in opposite directions, see fig.1. At the horizontal side the magnetic field induction of the above described system reaches its maximum value in the point above the central area. Due to the symmetry of the magnetic system the induction vector at that point is headed horizontally. The correlation between the maximum values of the magnetic field induction and the distance to the surface of the magnetic system is displayed in fig. 2.

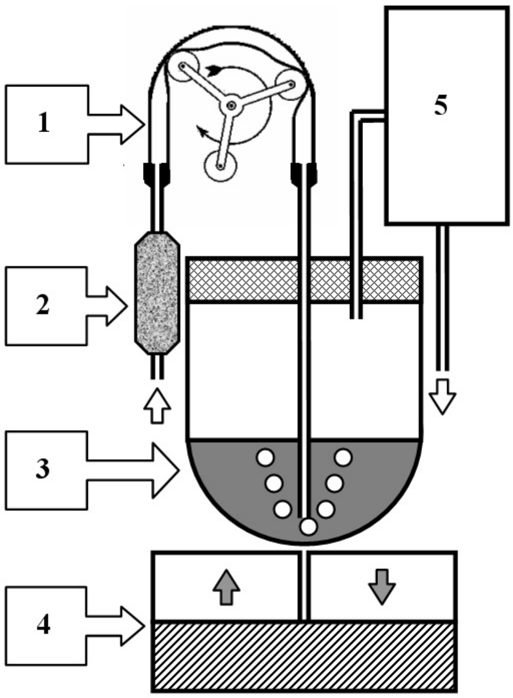

Figure 1: Experimental setup. 1 – peristaltic pump, 2 – dehumidifier, 3 – ferrofluid, 4 – magnet system, 5 – IR analyzer.

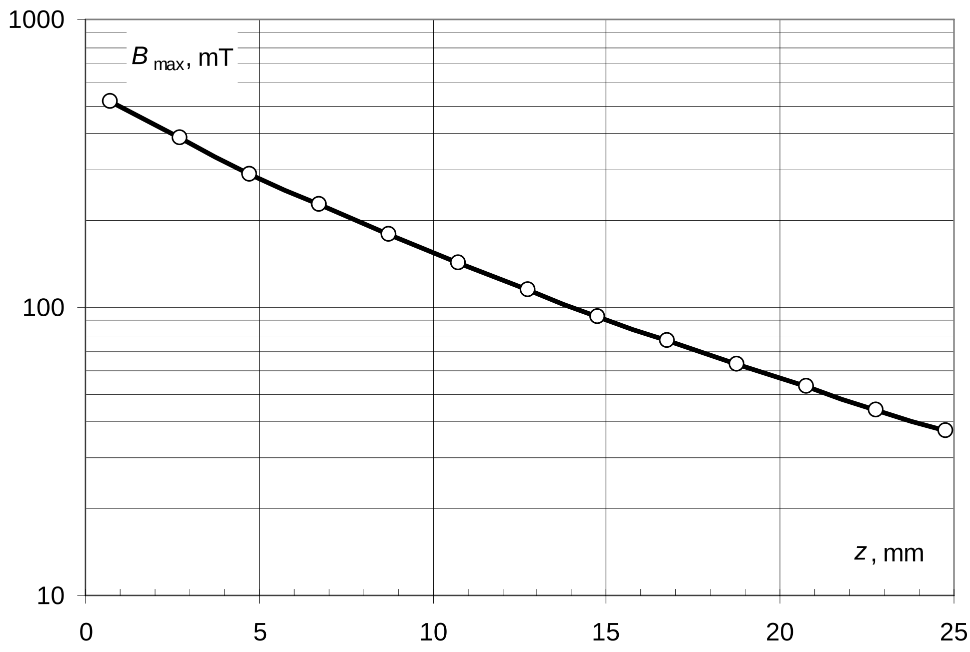

Figure 2: The maximum magnetic field induction from the distance to the magnet surface.

The initial ferrofluid is composed by magnetite particles dispersed in tetradecane, stabilized by the oleic acid. The particle size of magnetite varies from 5 to 13 nm (the sample

DF-105 is produced at the Institute of Physics of Latvia University), the density of the ferrofluid is 1070 kg/m^3. The curve of the ferrofluid magnetization is displayed in fig. 3.

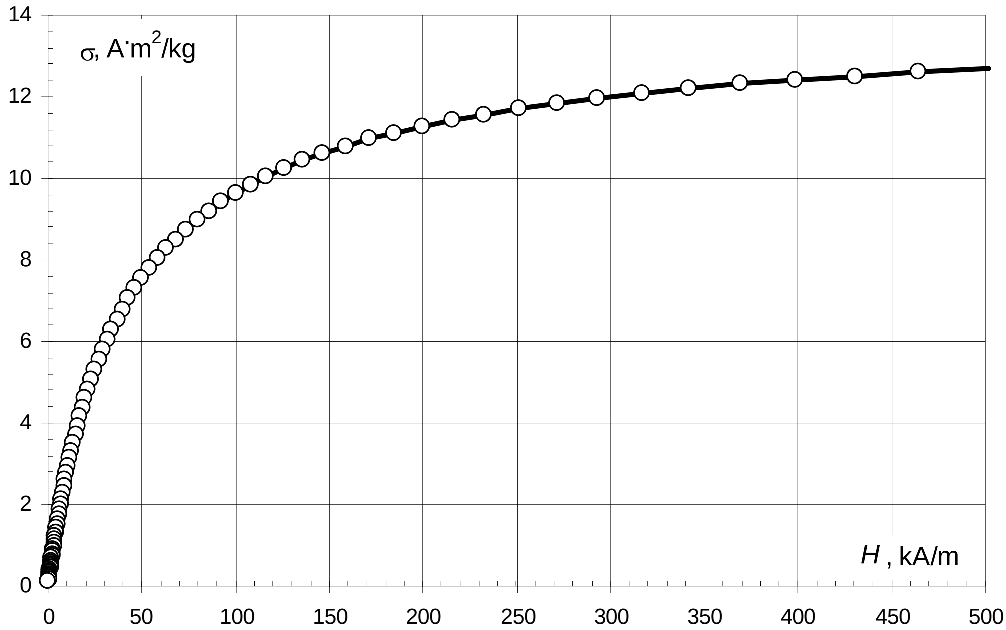

Figure 3: Magnetization curve of ferrofluid.

Before the experiments an amount of 0.2 ml of ferrofluid is located into the test-tube with a diameter 12 mm. 0.01 ml of hexane is added and the liquid is stirred. Afterwards the copper capillary tube with a diameter 1 mm is put into the test-tube down to the bottom. The air is blown through the capillary tube into the ferrofluid at velocity 0.23 ml/s. The air flow upwards through the ferrofluid, then being collected into the IR spectrometer gas probe. Absorption spectra are measured by the IR spectrometer every 2 minutes. Duration of the experiment is about 2 hours. The experiment with the magnetic field is carried out similarly, in this case the bottom of the test tube is located in the central surface area of the magnet set.

3. Results

The IR spectral analysis showed that of the tetradecane stripe increases at the beginning of the experiment and afterwards remains constant. The intensity of the hexane stripe shows an increase at the beginning of the experiment that is followed by decreasing of the spectral lines down to complete disappearance. Fig. 4 shows the change of the IR hexane stripe in the outflowing air during the experiment. The relative concentration of hexane in the air passing through the ferrofluid is calculated from the spectral area. Fig. 5 shows the relative concentration of the hexane vapor in the gas probe of IR spectrometer. The increase of the concentration at the beginning of the experiment is caused by the filling of the gas probe with the test gas, while the subsequent decrease of the concentration is determined by hexane separation from the ferrofluid.

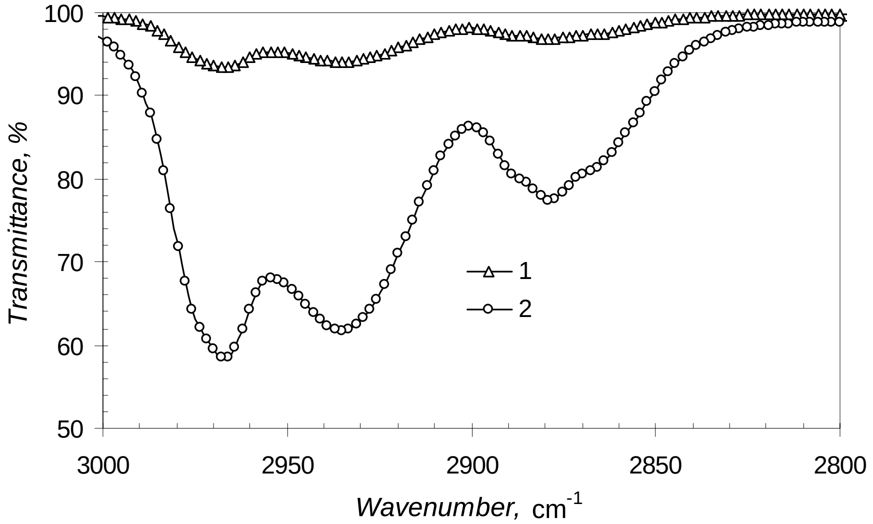

Figure 4: The stripe of hexane in the IR spectrum of the air at the set output. 1 - 48 min., 2 – 24 min. after flow beginning.

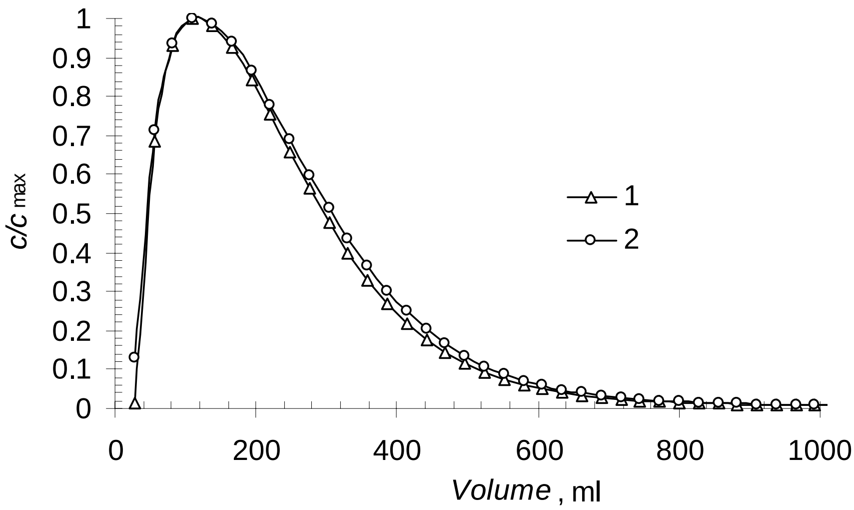

Figure 5: Dependence of hexane vapor concentration in the output air from its quantity with magnet and without magnet. 1 - without magnet, 2 - with magnet.

Fig. 6 shows the condition of ferrofluid cell during the air bubbles run with and without gradient magnetic field.

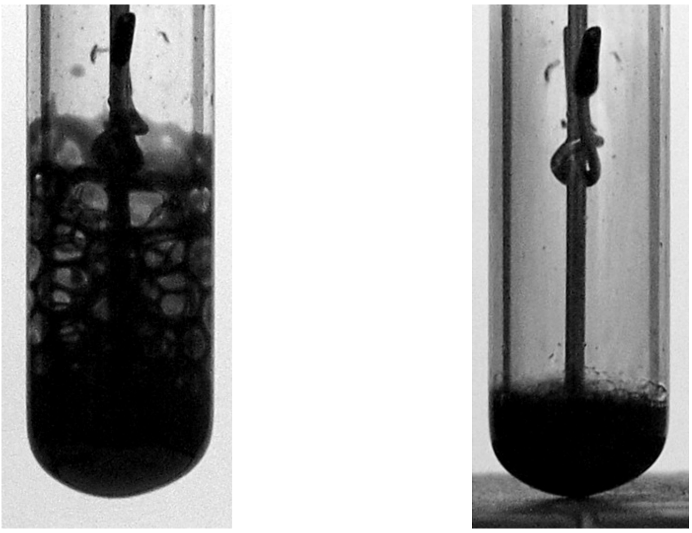

a b

Figure 6: The view of the mass exchange cell: *a* – without magnet, *b*-with magnet.

4. Conclusion

The impact of the Archimedes principle on the bubble formation can be evaluated by considering the magnetic field effect, its gradient and the ferrofluid magnetization curve. According to the formula for calculation of the ferrofluid effective density in the gradient magnetic field [1]:

$$\frac{\rho_{eff}}{\rho} = 1 + \frac{M\left|\nabla H\right|}{\rho g}$$

According to data from fig. 2 and fig. 3 the lifting force at the distance of 1 mm from the magnet surface increases about 85 times than that one without field. If assuming that the bubble volume is inversely proportional to the lifting force, while the surface area to maintain the spherical shape is proportional to the volume in the degree of 2/3 and simultaneously not considering the bubble deformation and gas compression, the amplification coefficient of the relative surface area to the gas mass reaches app. 19 times. It should make an impact on the mass exchange process.

However, under these physical conditions the magnet does not have an influence on the result of the mass exchange (fig. 5). One of the eventual reasons may be the achievement of the equilibrium concentration of the hexane vapor in the airflow in both cases. Nevertheless, the impact of the magnet on the volume of the two phase system of the mass exchange cell is very significant (fig. 6) as the two phase system volume is many times smaller when the magnet is set.

5. References

[1] Blums E., Cebers A., Maiorov M. M., Magnetic Fluids. Berlin, New York, Walter de Gruyter & Co 1997

INCREASE OF THE SENSITIVITY OF LIQUID CRYSTALS TO MAGNETIC FIELD DUE TO DOPING WITH MAGNETIC NANOPARTICLES

KOPČANSKÝ[1] P., TOMAŠOVIČOVÁ[1] N., TIMKO[1] M., GDOVINOVÁ[1] V., TÓTH-KATONA[2] T., ÉBER[2] N., HU[3] C.-K., HAYRYAN[3] S., CHAUD[4] X.
[1]Institute of Experimental Physics, Slovak Academy of Sciences, Watsonova 47, 040 01 Kosice, Slovakia, kopcan@saske.sk
[2]Research Institute for Solid State Physics and Optics, Wigner Research Centre for Physics Hungarian Academy of Sciences, H-1525 Budapest, P.O.Box 49, Hungary
[3]Institute of Physics, Academia Sinica, 128 Sec.2, Academia Rd., Nankang, Taipei 11529, Taiwan
[4]High Magnetic Field Laboratory, CNRS, 25 Avenue des Martyrs, Grenoble, France

Abstract: The contribution is an overview of the observations regarding the structural transitions in ferronematics based on thermotropic nematics doped with magnetic nanoparticles of different shape, and the magnetic field induced shift of the isotropic to nematic phase transition temperature. Due to presence of magnetic particles an increase of the isotropic-nematic phase transition temperature was observed as a function of applied magnetic field. The response of ferronematics to very low magnetic fields is also presented which is important for the construction of various magneto-optical devices.

1. Introduction

Liquid crystals can be oriented by electric or magnetic fields due to the anisotropy of the dielectric permittivity or the diamagnetic susceptibility [1]. As the former is in the order of unity, in conventional devices the driving voltages are in the order of a few volts. However, because of the small value of the anisotropy of the diamagnetic susceptibility (~ 10^{-7}), the magnetic field necessary to realign liquid crystals have to reach rather large values ($\boldsymbol{B}$ ~ 10T depending on the thickness of the liquid crystal layer). In an effort to enhance the magnetic susceptibility of liquid crystals, the idea of doping them with small amount of tiny magnetic particles was theoretically introduced by Brochard and de Gennes [2]. They have developed the continuum theory of magnetic suspensions in nematic liquid crystals (ferronematics). In their theoretical work rod-like magnetic particles with the length $L >> a$ (where a is the molecular size of the nematic liquid crystal) and with a diameter of d ~ L/10 were considered. The volume concentration of magnetic particles was supposed to be sufficiently small (□ ~ 10^{-4}) in order to be able to ignore the inter-particle magnetic dipole-dipole interaction. They predicted that a rigid anchoring with $\boldsymbol{m} \parallel \boldsymbol{n}$ would result in the ferromagnetic behaviour of the mixture. Here the unit vector $\boldsymbol{n}$ (the director) describes the preferential direction of the nematic molecules and the unit vector $\boldsymbol{m}$ denotes the orientation of the magnetic moment of the magnetic particles. In the first experimental paper, Rault et al. [3] reported about the basic magnetic properties of a suspension of rod-like γ-Fe_2O_3 particles in the liquid crystal MBBA. In order to stabilize the suspension, the particles were first coated with a surfactant and then mixed with the nematic liquid crystal. The obtained results confirmed the existence of a ferromagnetic state in such suspension. Additionally they have found that the temperature of the nematic-isotropic transition decreases with increasing volume concentration of particles. Later, based on the estimations given in [2], first lyotropic [4,5] and then thermotropic [6] ferronematics have been prepared and studied. These experiments confirmed the existence of considerable orientational and concentrational effects in liquid crystals doped with magnetic particles, but raised a lot of questions as well.

One of the most important questions solved in the theory of ferronematics is the problem of the equilibrium orientation of magnetic particle, i.e. the direction of its magnetic moment $\boldsymbol{m}$, in the nematic matrix. The Brochard and de Gennes theory [2] considers the rigid anchoring with ***m*** parallel with ***n***. Based on later experiments, which excluded the co-alignment of ***m*** and ***n*** in some thermotropic ferronematics, the Burylov and Raikher's theory was constructed [7-9]. This theory considers the finite value of the surface density of the anchoring energy W at the magnetic particle - nematic boundary. The finite value of W, as well as the parameter $\omega = Wd/K \leq 1$, characterize the soft anchoring of nematic molecules on the surfaces of magnetic particles (d - typical size of magnetic particle, K - corresponding Frank orientation-elastic modulus of liquid crystal). The soft anchoring, unlike the rigid one, permits both types of boundary conditions ($\boldsymbol{m} \perp \boldsymbol{n}$ and $\boldsymbol{m} \parallel \boldsymbol{n}$), thus the Burylov and Raikher's theory could explain the experimental findings. In the frame of this theory the instabilities of the uniform texture in ferronematics exposed to external magnetic or electric field (Fréedericksz transitions) were analysed and the expressions for their critical fields in different geometries were derived.

2. Results

The studied ferronematic samples were based on the thermotropic nematic 4-(trans-4'-n-hexylcyclohexyl)-isothiocyanatobenzene (6CHBT). 6CHBT is an enantiotropic liquid crystal with high chemical stability [10]. The temperature of the nematic-to-isotropic transition (the clearing point) of the studied nematic is $T_{NI} = 42.8$°C. The nematic samples were doped with different kind of magnetic particles in volume concentration of $2\text{x}10^{-4}$. The synthesis of magnetic particles of various shape was described in [11]. The size of spherical particles was 11.6nm; the diameter and the length of rod-like particles were 25nm and 1200nm, respectively. The length of chain-like particles was approximately 400nm; the size of a single particle in the chain was 34nm.

The structural transitions in ferronematic samples were monitored by capacitance measurements in a capacitor made of ITO-coated glass electrodes (LINCAM Co.). The capacitor with an electrode area of approximately 1cmx1cm was connected to a regulated thermostat system; the temperature was stabilized with the accuracy of 0.05°C . The distance between the electrodes (sample thickness) was D = 5µm. The capacitance was measured at the frequency of 1kHz by a high precision capacitance bridge Andeen Hagerling. The stability of the samples in the strong magnetic fields was verified by repeating the capacitance measurements after 5 months on the same samples, with reproducible results.

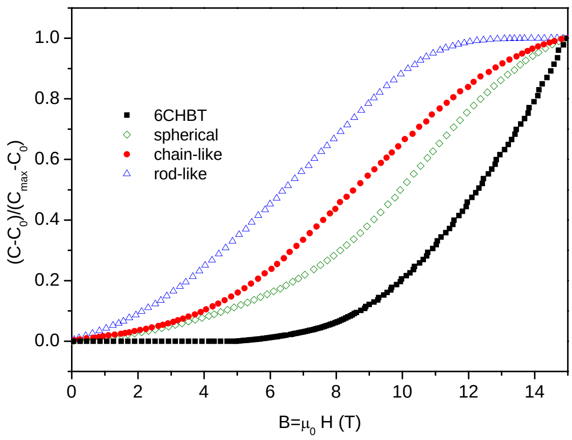

Figure 1: Reduced capacitance dependence of undoped 6CHBT and 6CHBT doped with spherical particles, chain-like particles and rod-like particles on external magnetic field measured at U_B = 10V (C_0 and C_{max} are the capacitance at B=0 and at B which restores the planar alignment, respectively).

The ferronematics based on the magnetic particles of various shape [11] were subjected to the combined action of electric and magnetic fields at the temperature of 35 °C. The magnetic field was applied perpendicular to *E*. Fig. 1 exhibits the dependence of the dimensionless reduced capacitance on the magnetic field at a bias voltage of 10V for undoped 6CHBT as well as for 6CHBT doped with magnetite particles of different shape. Doping with magnetic nanoparticles evidently reduces the critical field, confirming that the coupling between the director and the magnetic moment favours $\boldsymbol{m} \parallel \boldsymbol{n}$. The reduction is the smallest for spherical particles and the largest for rod-like particles. It has been concluded [11] that the larger shape anisotropy of the particles changes the character of the anchoring at the liquid crystal – particle interface from soft to rigid. The presented results show that doping with magnetic particles shaped similarly to the molecules of the host liquid crystal is more effective and thus offer better perspectives for ferronematics in applications where the magnetic field is necessary to control the orientation of the liquid crystal.

Another interesting phenomenon in liquid crystals is the possibility to alter the isotropic to nematic phase transition with external field [12-14]. However, the effect could not be induced by magnetic-field [15] until recently [16]. The principal reason is that the estimated critical fields are well over 100 T for traditional liquid crystal materials [15]. The first experimental observation of the predicted magnetic-field dependence of the nematic-isotropic phase transition temperature has been recently carried out [16] on a powerful electromagnet (*B* up to 30T). To demonstrate the effect, besides the powerful electromagnet, the proper choice of a „non-conventional” (bent-core) nematic liquid crystal material was also necessary. The „non-conventional” nematic material chosen in Ref. [16], has considerably different physical properties compared to „conventional” calamitic nematics; the first-order character of the nematic-isotropic transition at the „clearing point” is substantially weaker than that for „conventional” nematics. These properties, combined with the high magnetic field have contributed to the observation of the phase transition temperature shift of ~0.8°C at the magnetic field of 30T.

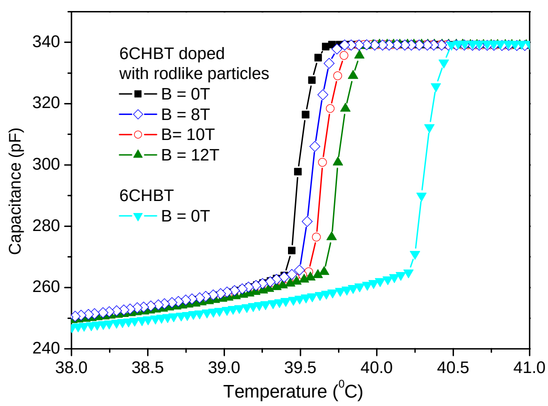

Fig.ure 2: Capacitance vs. temperature for undoped 6CHBT and 6CHBT doped with rodlike magnetic particles measured at different magnetic fields.

The influence of the magnetic particles on the magnetic field induced isotropic-nematic phase transition was also studied in a “conventional” calamitic liquid crystal 6CHBT by capacitance measurements [17]. The used magnetic particles were either spherical or rod-like. In both cases the size of the magnetic particles was much greater than the dimensions of the liquid crystal molecules, i.e. the magnetic particles can be regarded as macroscopic objects floating in the liquid crystal. The surface of the magnetic particles is able to orient the adjacent liquid crystal molecules. During the measurements the magnetic field was applied parallel with the capacitor electrodes.

Our results have confirmed that the shape of the magnetic particles affects the phase transition from the isotropic phase. In the pure 6CHBT as well as in 6CHBT doped with spherical magnetic particles no measurable field induced shift of the isotropic-nematic phase transition temperature was observed in magnetic fields up to 12T. On the contrary, in 6CHBT doped with rodlike magnetic particles (diameter size 10 nm, length 50 nm and volume concentration $2x10^{-4}$) a shift of 0.25°C was found in the phase transition temperature at 12T (Fig. 2). Therefore, our results have proven that ferronematics composed of calamitic liquid crystals and rod-like magnetic nanoparticles can be just as effective in demonstrating the magnetic field induced isotropic-nematic phase transition as bent-core nematics [16].

In recent works by Podoliak et al. [18], and Buluy et al. [19] both experimental and theoretical investigations have been reported about the optical response of suspensions of ferromagnetic nanoparticles in nematic liquid crystals on the imposed magnetic field. The authors have measured a linear optical response in ferronematics at very low magnetic fields (far below the threshold of the Freedericksz transition). A similar effect was also observed in our dielectric measurements in samples doped with spherical [20] or rod-like [21] magnetic particles as it is demonstrated in Fig.3. The figure provides a clear evidence for a nearly linear magnetic field dependence of the capacitance in the low magnetic field region.

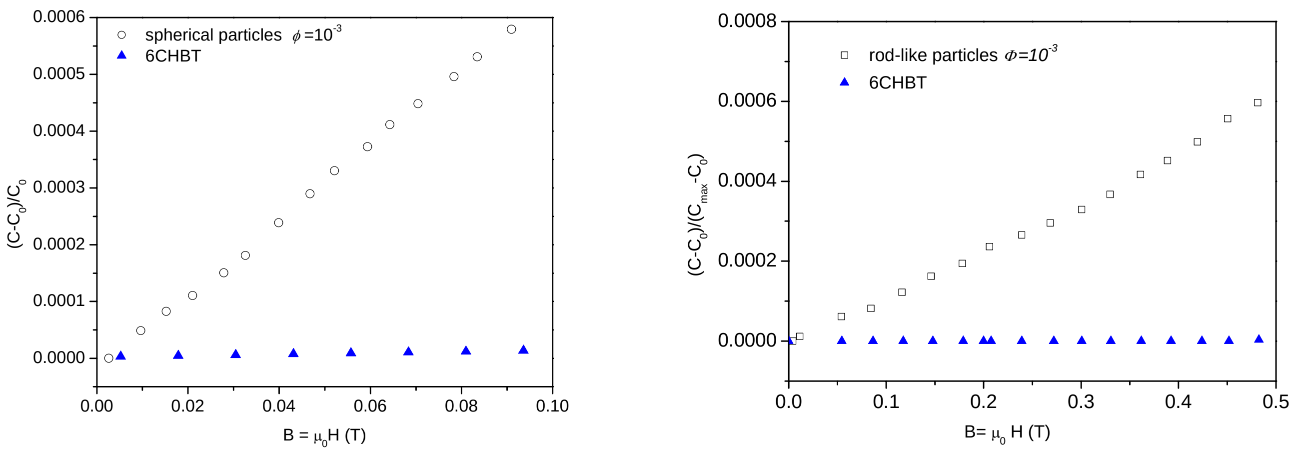

Figure 3: Reduced capacitance versus magnetic field for undoped 6CHBT and for 6CHBT doped with spherical particles and rod-like particles.

3. Conclusion

We have shown, that doping liquid crystals with magnetic nanoparticles increases the sensitivity to external magnetic field. The shape and the size of the magnetic nanoparticles play significant role in structural transitions. We have observed an increase of the isotropic-nematic phase transition temperature in ferronematics based on the calamitic liquid crystals doped with magnetic nanoparticles in magnetic field of ~ 10T. Moreover, the magnetic particles can influence the response of liquid crystals also in the low magnetic field region, far below Fréedericksz transition.

Acknowledgements.
This work was supported by the project VEGA 0045, the Slovak Research and Development Agency under the contract No. APVV-0171-10, Ministry of Education Agency for Structural Funds of EU in frame of projects 26220120021, 26220120033 and 26110230097, the GHMFL (CRETA), the Hungarian Research Fund OTKA K81250, and M-era.Net – MACOSYS (OTKA NN110672).

4. References

[1] de Gennes, P.G.; The Physics of Liquid Crystals, (Clarendon Press, Oxford 1974)
[2] Brochard, F.; de Gennes, P.G.; (1970) Theory of magnetic suspensions in liquid crystals, J.Phys. (Paris) 31, 691
[3] Rault, J.; Cladis, P.E.; Burger, J.P.; (1970) Ferronematics, Phys.Lett. A 32, 199
[4] J. Liebert, A. Martinet, (1979) Coupling between nematic lyomesophases and ferrofluids, J.Phys.Lett. 40, 363
[5] A.M. Figueiredo Neto, L. Liebert, A.M. Levelut, (1984) Study of ferrocholesteric discotic and calamitic lyotropics by optical microscopy and X-ray diffraction, J.Phys. (Paris) 45, 1505
[6] S.H. Chen, N.M. Amer, (1983) Observation of macroscopic collective behaviour and new texture in magnetically doped liquid crystals, Phys.Rev.Lett. 51, 2298
[7] S.V.Burylov, Y.L.Raikher, (1990) On the orientation of an anisometric particle suspended in a bulk uniform nematic, J.Phys.Lett. A 149, 279
[8] S.V.Burylov, Y.L.Raikher, (1993) Magnetic Fredericksz transition in a ferronematic, J.Magn.Magn.Mater. 122, 62
[9] S.V.Burylov, Y.L.Raikher, (1995) Macroscopic properties of ferronematics caused by orientational interactions on the particle surfaces. 1.Extended continuum model, Mol.Cryst.Liq.Cryst. 258, 107
[10] Dabrowski, R.; Dziaduszek, J.; Szczucinski, T.; (1984) 4-(Trans-4-n-Alkylcyclohexyl)Isothiocyanatobenzenes a new class of low-melting stable nematics, Mol.Cryst.Liq.Cryst.Lett. 102, 155
[11] Kopčanský, P.; Tomašovičová, N.; Koneracká, M.; Závišová, V.; Timko, M.; Džarová, A.; Šprincová, A.; Éber, N.; Fodor-Csorba, K.; Tóth-Katona, T.; Vajda, A.; Jadzyn, J.; (2008) Structural changes in the 6CHBT liquid crystal doped with spherical, rodlike, and chainlike magnetic particles, Phys Rev E 78, 011702
[12] Helfrich, W.; (1970) Effect of electric fields on the temperature of phase transition of liquid crystals, Phys. Rev. Lett. 24, 201
[13] Lelidis, I.; Durand, G.; (1993) Electric-field-induced isotropic-nematic phase transition, Phys. Rev. E 48, 3822
[14] Stanley, H.; Introduction to Phase Transitions and Critical Phenomena, Oxford Science, New York, 1971
[15] Rosenblatt, C.; (1981) Magnetic field dependence of nematic-isotropic transition temperature, Phys. Rev. A.24, 2236
[16] Ostapenko, T.; Wiant, D.B.; Sprunt, S.N.; Jákli, A.; Gleeson, J.T.; (2008) Magnetic- field induced isotropic to nematic liquid crystal phase transition, Phys. Rev. Lett. 101, 247801/1-4
[17] Kopčanský, P.; Tomašovičová, N.; Koneracká, M.; Závišová, V.; Timko, M.; Hnatič, M.; Éber, N.; Tóth-Katona, T.; Jadzyn, J.; Honkonen, J.; Beaugnon, E.; Chaud, X.; (2011) Magnetic-field induced isotropic to nematic phase transition in ferronematics, IEEE Transactions on Magnetics 47, 4409.
[18] Podoliak, N.; Buchnev, O.; Buluy, O.; D'Alessandro, G.; Kaczmarek, M.; Reznikov, Y.; Sluckin, T.J.; (2011) Macroscopic optical effect in low concentration ferronematics, Soft Matter 7, 4742-4749.
[19] Buluy, O.; Nepijko, S.; Reshetnyak, V.; Ouskova, E.; Zadorozhnii, V.; Leonhardt, A.; Ritschel, M.; Schonhense, G.; Reznikov, Y.; (2011) Magnetic sensitivity of a dispersion of aggregated ferromagnetic carbon nanotubes in liquid crystals, Soft Matter 7, 644-649.
[20] Tomašovičová, N.; Timko, M.; Mitróová, Z.; Koneracká, M.; Rajňak, M.; Éber, N.; Tóth-Katona, T.; Cahud, X.;
Jadzyn, J.; Kopčanský, P.; (2013) Capacitance changes in ferronematic liquid crystals induced by low magnetic fields, Phys. Rev E 87, 014501
[21] Kopčanský, P.; Tomašovičová, N.; Tóth-Katona, T.; Éber, N.; Timko, M.; Závišová, V.; Majorošová, J.; Rajňak, M.; Jadzyn, J.; Chaud, X.; (2013) Increasing the magnetic sensitivity of liquid crystals by rod-like magnetic nanoparticles, Magnetohydrodynamics 48, 407–413

Numerical study of magnetic field driven micro-convection in the Hele-Shaw cell

A.Tatulcenkovs,* G.Kitenbergs,† K.Ērglis,‡ and A.Cebers§

University of Latvia, Riga, Zellu 8, LV-1002, Latvia

The interfacial instability of miscible magnetic fluids in a horizontal Hele-Shaw cell under the action of a vertical magnetic field is studied numerically. The fingering at the interface between the magnetic and non-magnetic fluids is induced by a uniform external magnetic field greater than a critical value. The numerical results of the simulation are compared with the experimental results.

I. INTRODUCTION

The studies on interfacial phenomenon between miscible magnetic fluids have been started more than thirty years ago [1] extending the previous work on magnetostatic instabilities of magnetic liquids in the Hele-Shaw cell for miscible fluids. Due to the dipolar interactions between the nanoparticles, a demagnetizing field appears in the volume of the magnetic fluid. As a result, the magnetic field is larger outside than inside. The ponderomotive force on the magnetizable fluid is proportional to the concentration of magnetic particles and the local gradient of the magnetic field strength. A gradient of magnetic field appears at the frontier: this gradient is the origin of the destabilizing magnetic force. Hence, the theoretical model of the magnetic micro-convection considers the Hele-Shaw flow in the Darcy approximation [2] under the action of the ponderomotive forces due to the self-magnetic field of the fluid, the equations for the magnetostatic field, and the diffusion equation for the concentration of the magnetic nanoparticles.

$$-\nabla p - \frac{12\eta}{h^2}\mathbf{u} - \frac{2M(c)}{h}\nabla\psi_{\mathrm{m}} = 0,\ \nabla\cdot\mathbf{u} = 0\ , \tag{1}$$

*Electronic address: andrejs.tatulcenkovs@lu.lv
†Electronic address: guntars.kitenbergs@lu.lv
‡Electronic address: kaspars.erglis@lu.lv
§Electronic address: aceb@tesla.sal.lv

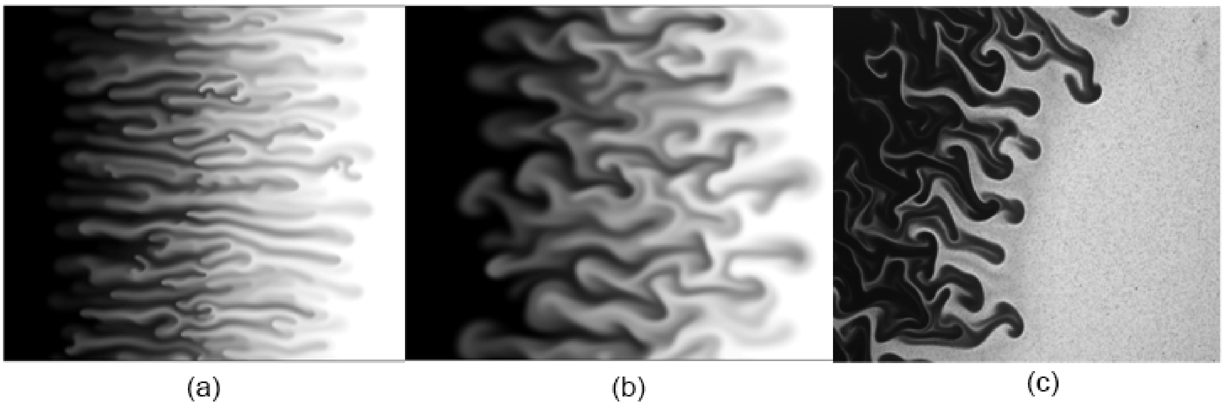

FIG. 1: Concentration snapshots of miscible magnetic and non-magnetic fluids in a Hele-Shaw cell (a) Darcy model for Rayleigh number $Ra_m = 1250$, (b) Darcy model with viscous part for Rayleigh number $Ra_m = 1250$, (c) experimental data for magnetic field strength $B = 28$ Oe, which corresponds to $Ra_m = 168$

$$\frac{\partial c}{\partial t} + (\mathbf{u} \cdot \nabla)c = D\Delta_2 c \ . \tag{2}$$

The magnetostatic potential ψ_{m} is given by [3, 4]

$$\psi_{\mathrm{m}}(\mathbf{r}, t) = M_0 \int c(\mathbf{r}', t) K(\mathbf{r} - \mathbf{r}', h) \mathrm{d}S' \ , \tag{3}$$

where $K(\mathbf{r}, h) = 1/ \mid \mathbf{r} \mid -1/\sqrt{\mid \mathbf{r} \mid^2 + h^2}$ and the magnetization $M(c)$ is proportional to the concentration of the magnetic fluid c ($M = M_0 c$)

II. NUMERICAL SIMULATIONS

The equations Eq.(1)-(3) are put in dimensionless form by introducing the following scales: length h, time h^2/D, velocity D/h and magnetostatic potential $M_0 h$ are solved numerically in the vorticity-stream function formulation. The stream function ψ is defined as $u_x = \partial\psi/\partial y$ and $u_y = -\partial\psi/\partial x$ and the vorticity ω as $\omega = -\nabla^2\psi$. The growth increment of perturbation of quiescent state depends on the magnetic Rayleigh number $Ra_{\mathrm{m}} = M_0^2 h^2/12\eta D$ and the smearing of the interface between the magnetic and non-magnetic liquids. A Fourier spectral method is used as the basic scheme for numerical

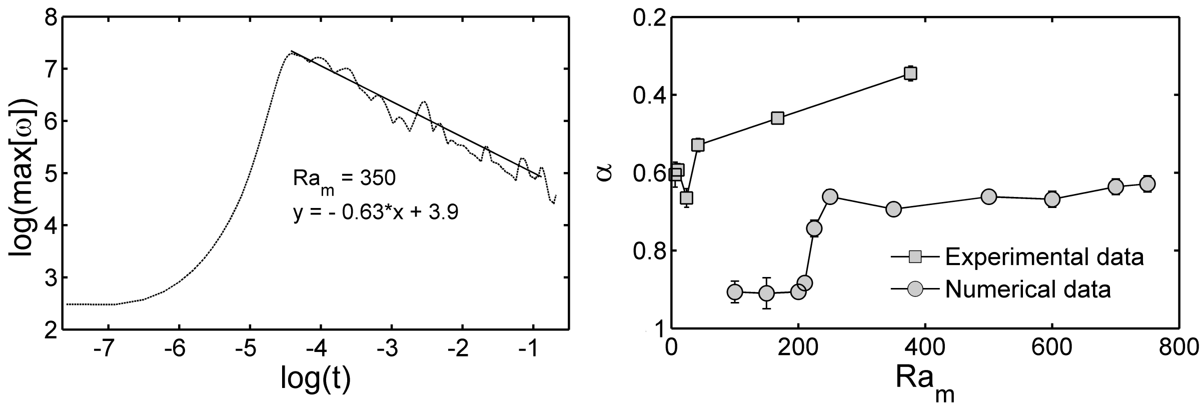

FIG. 2: (a) Maximal value of vorticity as a function of time for a magnetic Rayleigh number $Ra_m = 350$ on a logarithmic scale. (b) The exponent of the power law α for the experimental data given by (square) and numerical data (circle) for the magnetic Rayleigh numbers Ra_m.

simulations, the problem can be reduced to two algebraic equations for flow quantities and a first-order ordinary differential equation in time for the concentration and is solved by applying the linear propagator method and three-step Adams-Bashforth method.

In Fig.1 the qualitative comparison of characteristic concentration images between Darcy (a), Darcy with viscous part (b) and experiment bright field intensity image (c) are shown. A much better agreement of Darcy model and experimental results is reached when viscous stress, tangential to the boundary velocity gradients, is taken into account.

The time dependence of the maximal vorticity for several values of the magnetic Rayleigh number Ra_m is calculated to make a comparison with the experimental data. This dependence allows us to obtain the evolution of the vorticity field during the development of the magnetic micro-convection and its decay due to the diffusion of particles. It corresponds to a rapid increase of the vorticity followed by its slow decay Fig.2(a). Experimental and numerical data for the vorticity decay may be fitted with a power law $\omega_{max} \sim t^{\ \alpha}$. The obtained values of the exponent α are shown in Fig.2(b). The experimental and the numerically obtained exponent α values correlate. Although, having a noticeable displacement, both have small values for Ra_m close to the critical field and become clearly higher for greater Ra_m values. The magnetic Rayleigh number $Ra_{\mathrm{m}} = M_0^2 h^2/12\eta D$ of experimental data is calculated with a diffusion coefficient $D = 2.1 \cdot 10^{\ 5}$ cm^{2}s$^{\ 1}$, which is estimated from the critical field ($H_c = 5.3$ Oe [2]), and is close to a diffusion coefficient $D = 2.8 \cdot 10^{\ 5}$ cm^{2}s$^{\ 1}$ calculated from a magnetic fluid and water diffusion experiment measurements. This imprecision together with the resolution limitations of the experimental vorticity measurements play the main role for the differences of the comparison.

III. CONCLUSIONS

The proposed model of the magnetic micro-convection qualitatively describes the experimental data on the development and decay of the magnetic micro-convection. The theoretical analysis for the Darcy model shows that a non-potential magnetic force at magnetic Rayleigh numbers Ra_m greater than a critical value causes fingering at the interface between the miscible magnetic and nonmagnetic fluids. Fingering with its subsequent decay due to diffusion of particles significantly increases the mixing at the interface. The vorticity decay rate dependence on Ra_m show a similar behavior for simulations and experiments. To verify the differences, a more precise experimental study on vorticity formation must be carried out.

[1] M. Maiorov and A. Cebers, Magnetohydrodynamics **19**, 376 (1983).

[2] K.Erglis, A.Tatulchenkov, G.Kitenbergs, O.Petrichenko, F.G.Ergin, B.B.Watz, and A. Cebers, J. Fluid Mech. **714**, 612 (2013).

[3] A. Cebers, Magnetohydrodynamics **17**, 113 (1981).

[4] D. P. Jackson, R. E. Goldstein, and A. O. Cebers, Phys. Rev. E. **50**, 298 (1994).

EXPERIMENTAL STUDY ON FORCED CONVECTIVE HEAT TRANSFER AND FLOW RESISTANCE OF MAGNETIC FLUID FLOW UNDER NON-UNIFORM MAGNETIC FIELD

MOTOZAWA*[1] M., TATSUNO[2] S., SAWADA[3] T., KAWAGUCHI[2] Y., FUKUTA[1] M.
[1]Shizuoka University, 3-5-1 Johoku Naka-ku Hamamatsu 432-8561, Japan,
[2]Tokyo University of Science, 2641 Yamazaki, Noda 278-8510, Japan,
[3]Keio University, 3-14-1 Hiyoshi Kohoku-ku Yokohama 223-8522, Japan
*E-mail address of corresponding author: tmmotoz@ipc.shizuoka.ac.jp

Abstract : Forced convective heat transfer and flow resistance of rectangular duct flow of a magnetic fluid by applying non-uniform magnetic field was investigated experimentally. One characteristic result shows that heat transfer is largely enhanced by applying non-uniform magnetic field in the laminar flow regime. Comparing with the result with applying uniform magnetic field, heat transfer enhancement is larger than that with applying uniform magnetic field. This seems that thermal convection excited by applying non-uniform magnetic field strongly affects the heat transfer.

1. Introduction

A magnetic fluid is a kind of typical magnetic functional fluid which has the function of changing physical properties by applying magnetic field. This fluid is a colloidal suspension which is composed of surfactant-coated ultrafine ferromagnetic particles and liquid carrier such as water. The diameter of inner magnetic particles of mangnetic fluid are about 10 nm and these particles are well dispersed due to the effect of surfactant. On the other hand, a nanofluid, which is the fluid conteains nano-order size pirticles in a liquid carrier, has been attracted attentions in the last two decades [1]. Because of its composition, magnetic fluid can be consieded a kind of nanofluid. Actually, magnetic nanofluid which has similar feature and composition to matnetic fluid was developed by nanofluid researchers [2]. In the recent, several studies of heat transfer characteristics of magnetic fluid have been performed by not only magnetic fluid researchers but also nanofluid researchers. Particularly, some of them including our previous study [3] reported enhancement of forced convective heat transfer by the effect of magnetic field in laminar flow regime [4, 5]. However, it still remains unclear why and how much heat transfer is enhanced by applying magnetic field.

In our previous studies [6], we investigated the forced convective heat transfer of magnetic fluid flow in a rectangular duct by applying uniform magnetic field. Furthermore, in order to discuss this heat transfer characteristics, we measured the velocity distribution by ultrasonic velocity profiling (UVP) method. However, since magnetic field gradient does not exist in the case of uniform magnetic field, it is also important to investigate heat transfer characteristics by applying non-uniform magnetic field and compare with the results with applying uniform magnetic field for discussion of the effect of magnetic field gradient. Based on this background, we investigated the forced convective heat transfer of magnetic fluid flow in same rectangular duct by applying non-uniform magnetic field, and also measured velocity distribution by UVP and flow resistance in this study.

2. Experiment

The schematic diagram of the experimental apparatus used in this study is shown in Fig. 1. The upper figure shows the flow system. The flow system consists of storage tank, pump and rectangular duct which is the test section. Two thermocouples are set at inlet and outlet of the test section. The lower figure in Fig.1 shows the structure of the rectangular duct. The heater

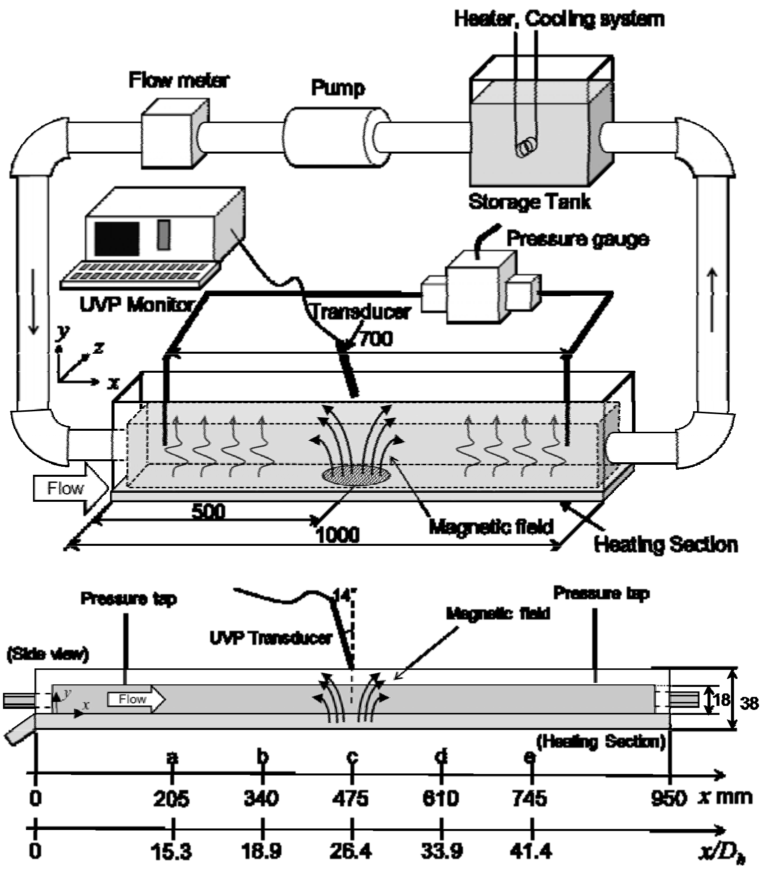

Figure 1 : Experimental apparatus.

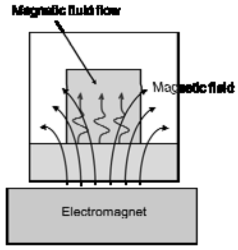

(a) Magnetic field situation

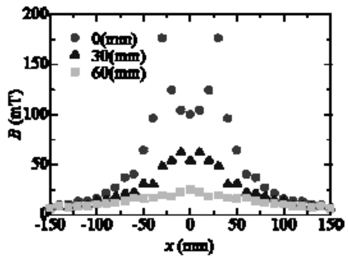

(b)Magnetic field distribution

Figure 2 : Non-uniform magnetic field

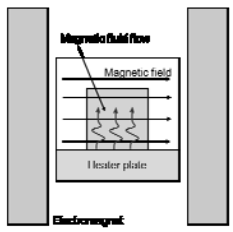

Figure 3 Uniform magnetic field

plate which is made of copper plate and heater attached to one-side of rectangular duct. The cross sectional area and the length of this duct are 18 mm×18 mm and 950 mm, respectively. Five thermocouples are installed in this heater plate and the position of these thermocouples are shown in the lower figure of Fig. 1. UVP transducer was set on the test section at the position (c) and we can measure the streamwise velocity distribution normal to the heater plate. We reported previously the measurement details and results of the velocity distribution of magnetic fluid flow by applying non-uniform magnetic field in [7].

Magnetic field is applied at the center of the rectangular duct, that is, at position (c). The electromagnet which is composed of a solenoid and an iron core was installed under the test section as shown in Fig. 2 (a) and the diameter of this iron core was 60 mm. The magnetic field distribution in a radial direction at each height from the top surface of iron core is also shown in Fig. 2(b). This figure is the magnetic field distribution when the magnetic field intensity is 100 mT near the center of the top surface of the iron core. In this study, magnetic field intensity was varied from 50 mT to 100 mT. In order to compare with our previous study in which was applied uniform magnetic field [6], Fig. 3 shows the situation of applying uniform magnetic field. The diameter of electromagnet was 150 mm.

Magnetic fluid used in this study is water-based magnetic fluid named as W-40 produced by Taiho Industries Co., Ltd. We diluted this magnetic fluid with water. The density and viscosity of this magnetic fluid without magnetic field are 1.3×10^3 kg/m^3 and 8.0 mPa·s, respectively. Experiments were carried out in both laminar flow and turbulent flow. Reynolds number based on the hydraulic diameter and bulk mean velocity are around 950 in the laminar flow case and around 2800 in the turbulent flow case. Moreover, we measured heat transfer and flow resistance with applying uniform magnetic field again for comparison in this study and almost similar results were obtained.

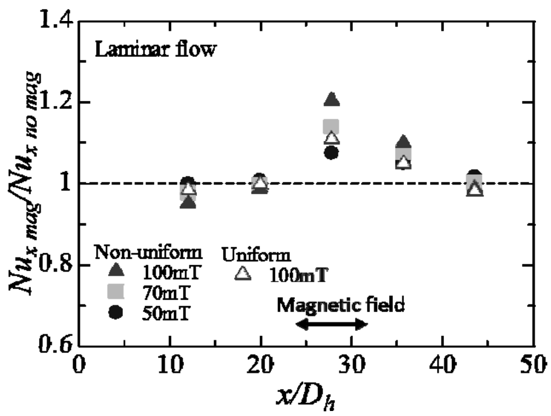

Figure 4 : Heat transfer result in laminar flow.

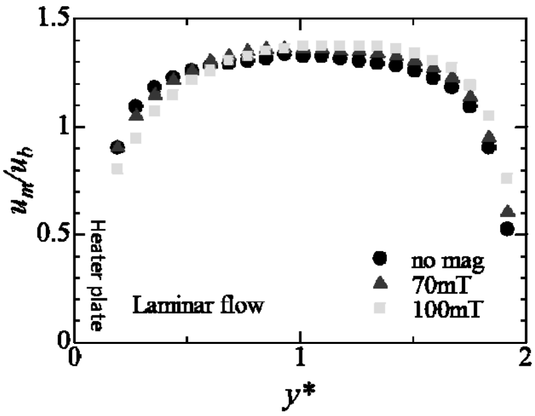

Figure 5 : Velocity distribution in laminar flow.

3. Results and discussion

3.1. Laminar flow case. Figure 4 shows the changes in heat transfer of a rectangular duct flow of a magnetic fluid with applying non-uniform magnetic field in a laminar flow. For comparison, the heat transfer characteristic by applying uniform magnetic field at 100 mT is also shown in this figure. This figure indicates that heat transfer increases with increasing magnetic field intensity at the position of applying magnetic field. This tendency is the same as the heat transfer by applying uniform magnetic field. Furthermore, the increment level of heat transfer by applying non-uniform magnetic field is much larger than that by applying uniform magnetic field. We discuss this difference of heat transfer enhancement. In the case of laminar flow, the following three changes by applying magnetic field affect the heat transfer; (1) change in thermal conductivity of magnetic fluid, (2) change in the velocity distribution and (3) convection occurs by the effect of magnetic field.

Regarding (1), some researchers reported that the increment of thermal conductivity of magnetic fluid in the direction of magnetic field [8, 9]. The increment of thermal conductivity should lead to the heat transfer enhancement. When the magnetic field is applied to magnetic fluid, the inner particles coagulate and form chain-like structure along the magnetic field. This clustering structure seems to have close relationship with thermal conductivity of magnetic fluid. However, in accordance of previous study [10], it takes time to grow the chain-like cluster. Considering this study, because the region where magnetic field exists is short, it is difficult to form the clustering structure and it seems that thermal conductivity of magnetic fluid hardly changes in this short region. Therefore, we consider that the change in the thermal conductivity hardly affects this heat transfer.

Next, we consider the change in the velocity distribution by applying magnetic field. Figure 5 shows the velocity distribution of a laminar rectangular duct flow with and without non-uniform magnetic field. In this figure, the vertical axis is the velocity at each *y*-position u_m normalized by the bulk mean velocity u_b. The heater plate is $y^*=0$. This figure indicates that the velocity of magnetic fluid flow decreases near the heater plate and velocity gradient also decreases. In contrast, the flow velocity in the upper side from the duct center (i.e. y^* is around 1.5) increases to follow the continuity equation. The decrement of velocity gradient does not lead to heat transfer enhancement. Therefore, we think that the change in the velocity distribution also hardly affects heat transfer. The detailed results of the velocity distribution by applying non-uniform magnetic field and discussion can be found in [7]. On the contrary, in the situation of applying uniform magnetic field [6], the velocity gradient increases near the heater plate by applying magnetic field and this increment of velocity gradient leads to heat transfer enhancement.

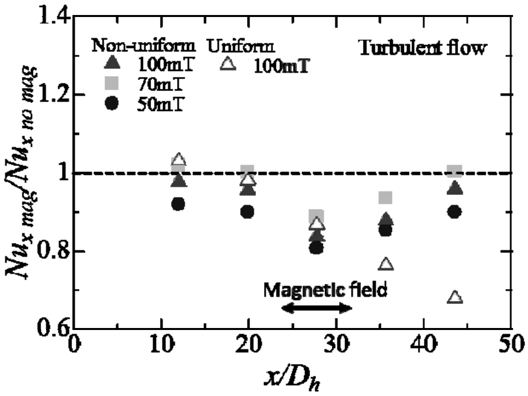

Figure 6 : Heat transfer result in turbulet flow.

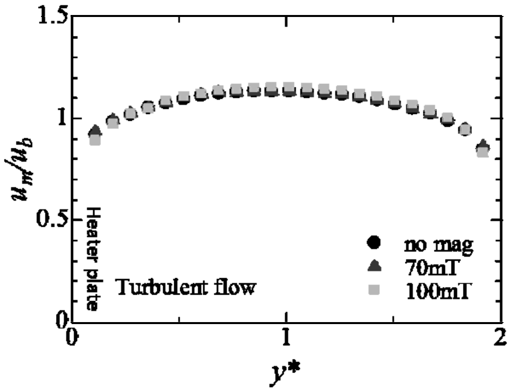

Figure 7 : Velocity distribution in turbulent flow.

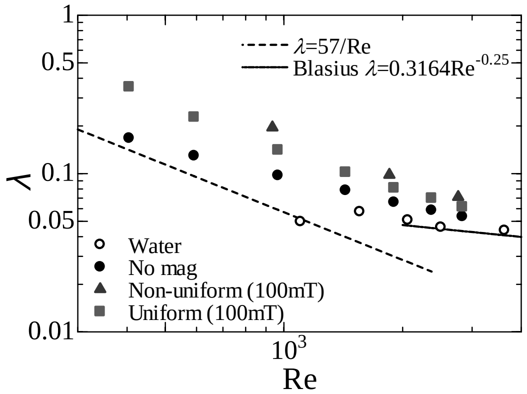

Figure 8 : Pipe frictional coefficient.

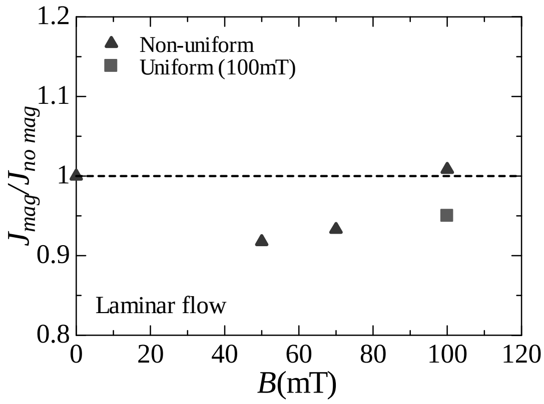

Figure 9 : Evaluation of flow resistance and heat transfer.

Finally, when the non-uniform magnetic field is applied to magnetic fluid flow, thermomagnetic convection occurs by the effect of magnetic body force. This convection strongly affects the forced convective heat transfer. Ganguly et al. [11] investigated the influence of thermomagnetic convection on forced convective heat transfer of magnetic fluid flow by numerical simulation, and reported forced convective heat transfer was largely enhanced by the effect of the thermal convection induced by the non-uniform magnetic field. Therefore, the heat transfer enhancement by applying non-uniform magnetic field in this study is caused by the convection induced by the magnetic body force. However, in the case of applying uniform magnetic field, because magnetic gradient does not exist, magnetic body force is zero theoretically. Therefore, the effect of convection is weak, and the enhancement level is smaller than that by applying non-uniform magnetic field.

3.2. Turbulent flow case. Figure 6 shows the effect of magnetic field on forced convective heat transfer of magnetic fluid flow in turbulent flow regime. This figure indicates that the heat transfer was suppressed at the position where magnetic field exists and this is the similar tendency by applying uniform magnetic field. However, considering the tendency of suppression of heat transfer, the result by applying 50 mT is relatively strange and so we need to check again in the future. The suppression level of heat transfer by applying non-uniform magnetic field is similar value by applying uniform magnetic field. As already discussed in our previous study [6], this suppression of heat transfer is caused by suppression of turbulent diffusion. Although the result is not shown in this paper, we also measured velocity fluctuation by UVP method and we confirmed streamwise velocity fluctuation is also suppressed by applying non-uniform magnetic field.

The velocity distribution in turbulent flow is shown in Fig. 7. This figure indicates that velocity near the heater plate slightly decreases but the velocity at the center of the duct increases. However, because this change in the velocity distribution is very small, the change in the velocity distribution hardly affect the heat transfer suppression. Moreover, in our previous study [7], we obtained characteristic change in the velocity distribution by applying stronger uniform magnetic field. Therefore, it seems that magnetic field is not so strong that the velocity distribution changes.

3.3. Relationship between flow resistance and heat transfer. Figure 8 shows the Reynolds number dependence of pipe frictional coefficient (λ).When the magnetic field is applied to magnetic fluid flow, flow resistance increases in both laminar flow and turbulent flow. The increment of flow resistance by applying magnetic field is relatively larger in the laminar flow. However, comparing applying non-uniform magnetic field with uniform magnetic field, the increment level is comparable in both flow cases.

As mentioned above, when a non-uniform magnetic field is applied to magnetic fluid flow, heat transfer is largely enhanced in laminar flow regime but flow resistance also increased. Same as our previous study [6], we evaluate this relationship by using Colburn's *J*-factor which is defined by $J = \mathrm{St} \cdot \mathrm{Pr}^{2/3} / (C_f / 2)$. Figure 9 shows the magnetic field dependence of the change ratio of J by applying magnetic field. This figure indicates that when 100 mT of non-uniform magnetic field is applied to magnetic fluid flow, the change ratio slightly exceeds 1. This means that heat transfer enhancement relatively exceeds the increase of flow resistance. In the case of applying uniform magnetic field, this ratio did not exceed 1. Therefore, thermal convection induced by magnetic field gradient by applying non-uniform magnetic field works effectively. However, as the exceeded value is just a small, we will continue to consider the way for how heat transfer enhances without increasing flow resistance in the future.

4. Conclusion

We investigated the forced convective heat transfer and flow resistance of rectangular duct flow of a magnetic fluid by applying non-uniform magnetic field in this study. Experiment was performed in both laminar flow and turbulent flow. In the case of laminar flow, heat transfer is largely enhanced in the region where magnetic field exists. Comparing with the results with applying uniform magnetic field, the enhancement level is larger. This is because of the effect of convection induced by non-uniform magnetic field. In contrast, heat transfer is suppressed by applying non-uniform magnetic field in turbulent flow. The suppression level is similar to that with applying uniform magnetic field.

Acknowledgements. This study was partly supported by a Grant-in-Aid for Young Scientists (B) Number 25820049 of the Japan Society for Promotion of Science.

References

[1] Das, S. K. et al.: Nanofluids; Science and Technology. John Wiley and Sons. Inc. (2008)
[2] Sundar, L.S. et al.: Experimental Thermal and Fluid Science. 37 (2012) 65-71.
[3] Motozawa, M. et al.: Physics Procedia. 9 (2010) 190-193.
[4] Fumoto, K. et al.: Journal of Thermal Science and Technology. 4 (2009) 332-339.
[5] Azizian, R. et al.: International Journal of Heat and Mass Transfer. 68 (2014) 94-109.
[6] Motozawa, M. et al.: Journal of Physics: Conference Series. 412(2013) 012025.
[7] Tatsuno, S. et al.: Proc. 12th Int. Symp. Fluid Control, Measurement and Visualization, Nara, (2013).
[8] Li, Q. et al.: Experimental Thermal and Fluid Science. 30(2005) 109-116.
[9] Krichler, M. et al.: Proc. 8th World Conf. Exp. Heat Transfer, Fluid Mech., and Therm. Lisbon (2013).
[10] Motozawa, M. et al.: Journal of Physics: Condensed Matter. 20(2008) 204117.
[11] Ganguly, R. et al.: Journal of Magnetism and Magnetic Materials. 271(2004) 63–73.

STABILITY ANALYSIS OF A PARTICLE WITH A FINITE ENERGY OF MAGNETIC ANISOTROPY IN A ROTATEING AND PRECESSING MAGNETIC FIELD

CĪMURS[1] Jānis, CĒBERS[1] Andrejs
Affiliation: [1]*University of Latvia*, Zeļļu 8, Rīga, LV-1002, Latvia
e-mail address of corresponding author: janis.cimurs@lu.lv

Abstract : A model of a single ferromagnetic particle with a finite coupling energy of the magnetic moment with a body of particle is formulated and regimes of its motion in liquid in a rotating magnetic field are investigated. As the special case, when the field strength H are large compared to anisotropy field H_a, the stability of synchronous with the field regime of superparamagnetic particle in precessing magnetic field is studied.

1. Introduction

The dynamics of magnetic particle in AC magnetic field plays an important role in different phenomena and applications. The technique of magnetic hyperthermia uses energy dissipated by the motion of magnetic particles in an AC field for cancer therapy [1-3]. It was predicted that magnetotactic bacteria in a rotating magnetic field should follow complex trajectories [4], which were also found in experiment [5]. It was demonstrated that a suspension of the magnetic Janus particles, which possess anisotropic magnetic susceptibility, forms different structures in a precessing field depending on the field's precession frequency and angle [6]. Chain formation of superparamagnetic particles in a precessing magnetic field was studied in [7]. Precessing magnetic field are used for driving magnetic swimmers, for example, magnetic dipoles with attached flexible tail [8,9].

Here we formulate model for single ferromagnetic particle with a finite coupling energy of the magnetic moment with the body of the particle in a magnetic field. The regimes of particle dynamics in the rotating magnetic field are investigated. As special case a superparamagnetic particle in the precessing magnetic field is studied.

2. Model

We introduce single domain ferromagnetic particle with magnetic moment **m**=m**e** and easy axis of magnetization **n**. Energy in external magnetic field **H**=H**h** reads:

$$E=-mH\,\boldsymbol{e}\cdot\boldsymbol{h}-\tfrac{1}{2}KV\left(\boldsymbol{n}\cdot\boldsymbol{h}\right)^2\,, \tag{1}$$

where K is a constant of magnetic anisotropy and V is volume of the particle. We assume that magnetic relaxation time is much smaller than the characteristic time of the particle motion, so the magnetic moment is in equilibrium state determined by ($\boldsymbol{K}_e=\boldsymbol{e}\times\partial/\partial\boldsymbol{e}$) $\mathbf{K_e}$E=0. It gives

$$\boldsymbol{e}\times\boldsymbol{h}=\frac{2H_a}{H}(\boldsymbol{e}\cdot\boldsymbol{n})\boldsymbol{n}\times\boldsymbol{e}\,, \tag{2}$$

where H_a=KV/2m. The dynamics of the easy axis is determined by the balance of viscous and mechanical torques and reads ($\boldsymbol{K}_n=\boldsymbol{n}\times\partial/\partial\boldsymbol{n}$)

$$-\zeta\boldsymbol{\Omega}-\boldsymbol{K}_n E=0\,;\ \ \frac{d\boldsymbol{n}}{dt}=\boldsymbol{\Omega}\times\boldsymbol{n}\,, \tag{3}$$

where ζ is the rotational drag coefficient of the particle. We assume that particle is spherical. Eq. (3) is the particular case of more general "egg-yolk" model proposed in [10,11], where it reads $\zeta\boldsymbol{\Omega}=-\boldsymbol{K}_n E-\boldsymbol{K}_e E$. In Eq. (3) internal magnetic relaxation is neglected ($\mathbf{K_e}$E=0).

From Eq. (2) it can be seen that **e** is in the plane defined by the vectors **n** and **h** and reads:

$$\boldsymbol{e}=\frac{H/H_a\boldsymbol{h}+2(\boldsymbol{e}\cdot\boldsymbol{n})\boldsymbol{n}}{H/H_a(\boldsymbol{e}\cdot\boldsymbol{h})+2(\boldsymbol{e}\cdot\boldsymbol{n})^2}\,, \tag{4}$$

where $(\boldsymbol{e}\cdot\boldsymbol{n})^2=1-(2H_a/H)^2[1-(\boldsymbol{e}\cdot\boldsymbol{n})^2](\boldsymbol{e}\cdot\boldsymbol{n})^2$. From [12] we know that in the range $H/H_a<1$ magnetic moment **e** has one stable states, in the range $H/H_a>2$ **e** has two stable states, but in the range $1<H/H_a<2$ number of stable states (one or two) are determined by angle between **n** and **h**. In this range of magnetic field strength irreversible jumps of the magnetic moment can take place and should be taken into account, when the motion of the particle is considered. The orientation of the magnetic moment of the particle is found minimizing dimensionless equation of energy (1):

$$\hat{E}=-(H/H_a)\boldsymbol{e}\cdot\boldsymbol{h}-(\boldsymbol{n}\cdot\boldsymbol{h})^2\,, \tag{5}$$

with has one or two minimums for **e** for fixed **n·h**.

We introduce dimensionless time $\tilde{t}=\omega_H t$, where ω_H is angular frequency of rotating magnetic field. Using Eq. (4) the equation of motion of particle (2), can now be written in the form (tilde is omitted henceforth):

$$\frac{d\boldsymbol{n}}{dt}=\frac{\omega_a}{\omega_H}C(\boldsymbol{n}\cdot\boldsymbol{h}\,,H/H_a,\xi)[\boldsymbol{h}-\boldsymbol{n}(\boldsymbol{n}\cdot\boldsymbol{h})]\,, \tag{6}$$

where $\omega_a=KV/2\zeta$. The function

$$C(\boldsymbol{n}\cdot\boldsymbol{h}\,,H/H_a,\xi)=\frac{H/H_a(\boldsymbol{e}\cdot\boldsymbol{n})_\xi^2}{H/H_a(\boldsymbol{n}\cdot\boldsymbol{h})+2(\boldsymbol{e}\cdot\boldsymbol{n})_\xi}\,, \tag{7}$$

in general depends on history due to hysteresis of vector **e**. Here history dependence is introduced by variable ξ, which has two values (e.g. 1 and 2) and changes its value in jumps of **e**.

3. Rotating field

In a rotating magnetic field $\boldsymbol{h}=(\cos t\,,\sin t\,,0)$ synchronous with field regimes, when particle rotates with angular velocity $\boldsymbol{\omega}=(0,0,1)$, $d\boldsymbol{n}/dt=\boldsymbol{\omega}\times\boldsymbol{n}$, can be calculated from Eq. (6):

$$\frac{H/H_a(\boldsymbol{e}\cdot\boldsymbol{n})^2(\boldsymbol{e}_z\cdot\boldsymbol{n})(\boldsymbol{n}\cdot\boldsymbol{h})}{H/H_a(\boldsymbol{n}\cdot\boldsymbol{h})+2(\boldsymbol{e}\cdot\boldsymbol{n})}=0\,, \tag{8}$$

We see that three types of synchronous regimes are possible:

- Planar regime, where $\mathbf{e_z}$·**n**=0
- Precession regime, where **n·h**=0
- Unstable stationary regime, where **e·n**=0

The existence intervals and stability analysis of these regimes can be found in [13]. It can be found that besides synchronous regimes there exists asynchronous planar regime. The analysis of this regime can also be found in [13]. In Table 1-2 and Fig. 1 the results of [13] is reviewed.

Regime	Existence interval
Synchronous planar regime ($\mathbf{e_z}\cdot\mathbf{n}$=0)	$\frac{\omega_H}{\omega_a}<1 \wedge \frac{\omega_H}{\omega_a}<\frac{H}{H_a}$
Precession regime ($\mathbf{n}\cdot\mathbf{h}$=0)	$\left(\frac{\omega_H}{\omega_a}\right)^2>\left(\frac{H}{H_a}\right)^2-\left(\frac{H}{2\mathrm{H}_a}\right)^4 \wedge \frac{H}{H_a}<2$
Asynchronous planar regime ($\mathbf{e_z}\cdot\mathbf{n}$=0)	$\frac{\omega_H}{\omega_a}>1 \vee \frac{\omega_H}{\omega_a}>\frac{H}{H_a}$

Table 1: Existence intervals of regimes of single domain ferromagnetic particle dynamics in rotating magnetic field

Regime	Stability interval
Synchronous planar regime ($\mathbf{e_z}\cdot\mathbf{n}$=0)	$\left(\frac{\omega_H}{\omega_a}\right)^2>\left(\frac{H}{H_a}\right)^2-\left(\frac{H}{2\mathrm{H}_a}\right)^4 \vee \frac{H}{H_a}<\sqrt{2}$
Precession regime ($\mathbf{n}\cdot\mathbf{h}$=0)	$\frac{H}{H_a}<\sqrt{2}$
Asynchronous planar regime ($\mathbf{e_z}\cdot\mathbf{n}$=0)	$\int_0^{2\pi}\frac{C(\cos\beta, H/H_a, \xi(\beta))}{\omega_H/\omega_a-C(\cos\beta, H/H_a, \xi(\beta))}d\beta>0$

Table 2: Stability intervals of regimes of single domain ferromagnetic particle dynamics in rotating magnetic field

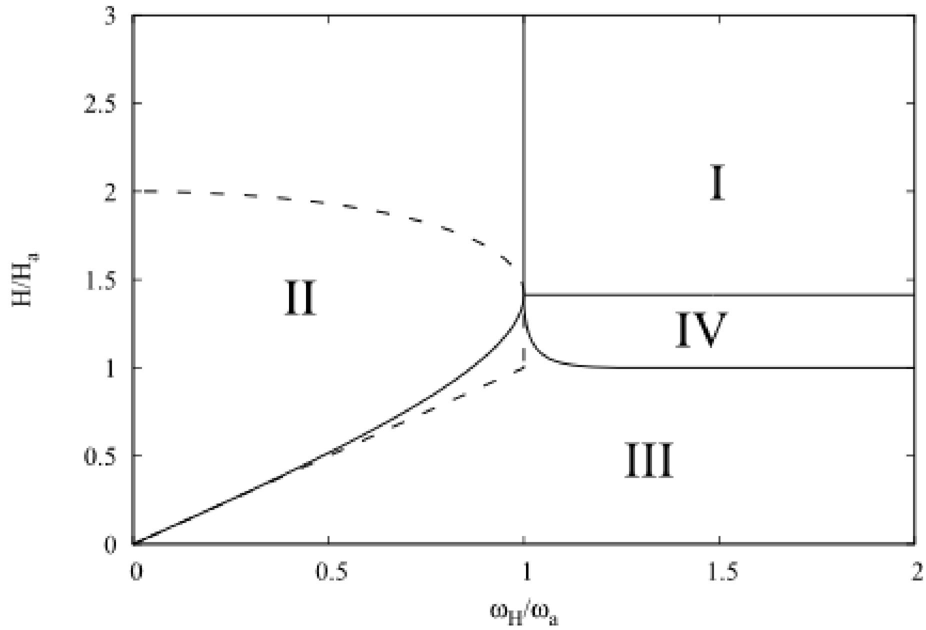

Figure 1: Phase diagram. The solid line indicates boundary between regions where stability of regime changes. In region I only asynchronous planar regime is stable. In region II only synchronous planar regime is stable and dashed line in this region is boundary of existence of

unstable precession regime. In region III only precession regime is stable and dashed line in this region is boundary of existence of unstable synchronous planar regime. In region IV precession and asynchronous planar regimes are stable.

4. Precessing field

As a special case, when magnetic field strength H is large compared to anisotropy field H_a, the particle can be modelled as superparamagnetic ($H \gg H_a$). In this case **e**=**h** and $C(\boldsymbol{n}\cdot\boldsymbol{h}, H/H_a, \xi)=\boldsymbol{n}\cdot\boldsymbol{h}$.

It is found in [14] that in a precessing magnetic field $\boldsymbol{h}=(\sin\vartheta\cos t, \sin\vartheta\sin t, \cos\vartheta)$ synchronous and asynchronous with the field regimes are possible for superparamagnetic particle. If we choose magnetically oblate particles (particles with negative ω_a) than analysis is the same as for prolate particle, but with negative time. That makes stable states unstable and vice versa. The results of [14] is reviewed in Fig. 2

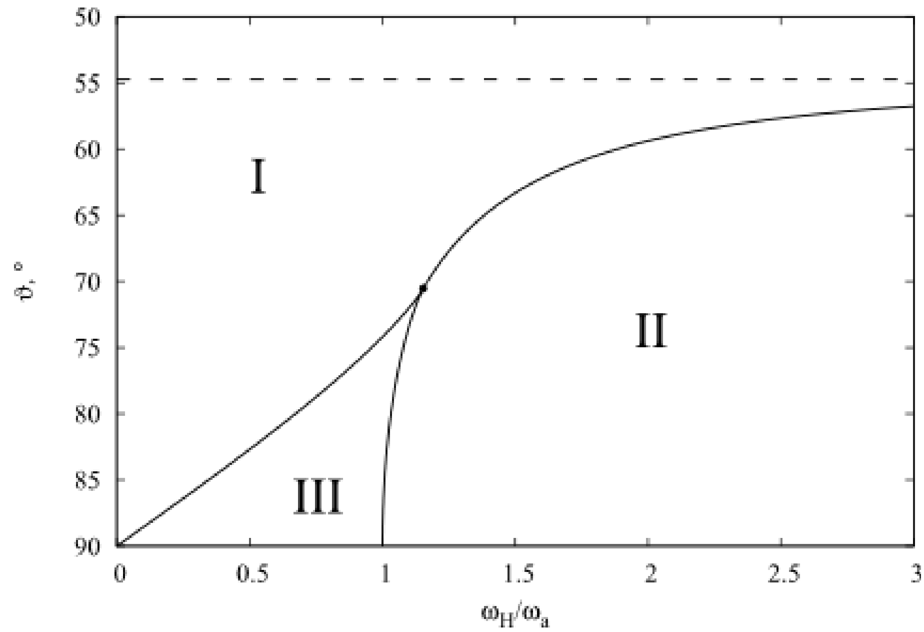

Figure 2: Phase diagram. The prolate superparamagnetic particle has a stable synchronous regime in region I∪III, and the oblate superparamagnetic particle in region II∪III. The point shows a codimension-2 bifurcation point with coordinates (2/√3,arccos(1/3)). The dashed line is asymptote $\vartheta=\arccos(1/\sqrt{3})$ of the solid line.

5. Conclusion

It shows that synchronous and asynchronous regimes are possible for a particle with a finite energy of the magnetic anisotropy in a rotating magnetic field. In the synchronous regime the easy axis of the particle is in the plane of a rotating field at low frequencies (a planar regime) and on the cone at high frequencies (precession regime). The stability of both regimes is investigated and it is shown that precession regime is stable for the magnetic field strength below the critical value. Taking into account irreversible jumps of the magnetic moment it is shown that the planar asynchronous regime is unstable for the field strength below the critical value. In addition the bifurcation diagram for the prolate and oblate superparamagnetic particles in precessing magnetic field has been shown. It generalizes results for the case of rotating field. In spite differences in behaivior of prolate and oblate particles in the precessing field, their bifurcation diagrams are identical expect for interchanged stable and unstable fixed points.

6. References

[1] Fortin, J. P.; Wilhelm, C.; Servais, J.; Menager, C.; Bacri, J. C.; Gazeau, F.: Size-Sorted Anionic Iron Oxide Nanomagnets as Colloidal Mediators for Magnetic Hyperthermia, J. Am. Chem. Soc., 129 (2007) 2628–2635

[2] Wilhelm, C.; Gezeau, J. C.: Magnetic nanoparticles: internal probes and heaters within living cells, J. Mag. Mag. Mat. 321 (2009) 671-674

[3] Rosensweig, R. E.: Heating magnetic fluid with alternating magnetic field, J. Magn. Magn. Mater. 252 (2002), 370-374

[4] Tanaka, H.; Isobe, M.; Miyazawa, H.: Shear-induced discontinuous and continuous topological transitions in a hyperswollen membrane system, Phys. Rev. E 73 (2006) 021503

[5] Erglis, K.; Wen, Q.; Ose, V.; Zeltins, A.; Sharipo, A.; Janmey, P. A.; Cebers, A.: Dynamics of Magnetotactic Bacteria in a Rotating Magnetic Field, Biophys J. 93 (2007) 1402–1412

[6] Yan, J.; Bloom, M.; Bac, S. C.; Luijten, E.; Granick, S.: Linking synchronization to self-assembly using magnetic Janus colloids, Nature 491 (2012) 578–581

[7] Martin, J. E.: Theory of strong intrinsic mixing of particle suspensions in vortex magnetic fields, Phys. Rev. E 79 (2009) 011503

[8] Gao, W.; Kagan, D.; Pak, O. S.; Clawson, C.; Campuzano, S.; Chulun-Erdene, E.; Shipton, E.; Fullerton, E. E.; Zhang, L.; Lauga, E.; Wang, J.: Cargo-Towing Fuel-Free Magnetic Nanoswimmers for Targeted Drug Delivery Small 8 (2012) 460-467

[9] Livanovičs, R.; Cēbers, A.: Magnetic dipole with a flexible tail as a self-propelling microdevice Phys. Rev. E 85 (2012) 041502

[10] Shliomis, M. I.; Stepanov, V. I.: Rotational viscosity of magnetic fluids: contribution of the Brownian and Néel relaxational processes, J. Magn. Magn. Mater. 122 (1993) 196-199

[11] Shliomis, M. I.; Stepanov, V. I.: Frequency dependence and long time relaxation of the susceptibility of the magnetic fluids, J. Magn. Magn. Mater. 122 (1993) 176-181

[12] Landau, L. D.; Lifshitz, E. M.: Electrodynamics of Continuos Media, Oxford: Pergamon 1960

[13] Cīmurs, J., Cēbers, A.: Three-dimensional dynamics of a particle with a finite energy of magnetic anisotropy in a rotating magnetic field, Phys. Rev. E 88 (2013) 062315

[14] Cīmurs, J., Cēbers, A.: Dynamics of anisotropic superparamagnetic particles in a precessing magnetic field, Phys. Rev. E 87 (2013) 062318

DEFORMATION OF A DOUBLE-LAYER DROP IN AN ALTERNATING ELECTRIC FIELD

KVASOV D.I., NALETOVA V.A.
Lomonosov Moscow State University, GSP-1, Leninskie Gory, Moscow, 119991, Russian Federation
E-mail address of corresponding author: naletova@imec.msu.ru

Abstract: In the present work, the problem of deformation of a double-layer drop, which is surrounded by other fluid, in an alternating electric field is solved. Permittivity and conductivity of all fluids are considered as constants. Fluids are assumed to be incompressible and viscous. The problem is solved by the method of expansion on small parameter which is proportional to the amplitude of an electric field squared. At the solution capillary forces are taken into account, the gravity is not taken into account. Average shape of the surface of the double-layer drop is found.

1. Introduction

The deformation of a simple liquid drop, immersed in other conducting fluid, which is subjected to an electric field, was investigated by many authors [1-5]. The most interesting researches deal with the form's dependency on the frequency of the harmonic electric field [2, 3, 5]. But there is one common thing in these papers: it is not possible for a prolate drop to become oblate while the frequency of electric field increases. In [5] the convective transport of a surface charge was taken into account, but it makes drops only more prolate. The purpose of this work is to investigate the form in the framework of double-layer liquid drop, and compare results with well-known ones in the framework of simple drop [2].

2. Presentation of the problem

To describe the task, an electrohydrodynamic model is used. Electrohydrodynamics is a branch of fluid mechanics concerning electrical force effects, at the same time neglecting magnetic force effects. More specifically this model is described in [1].

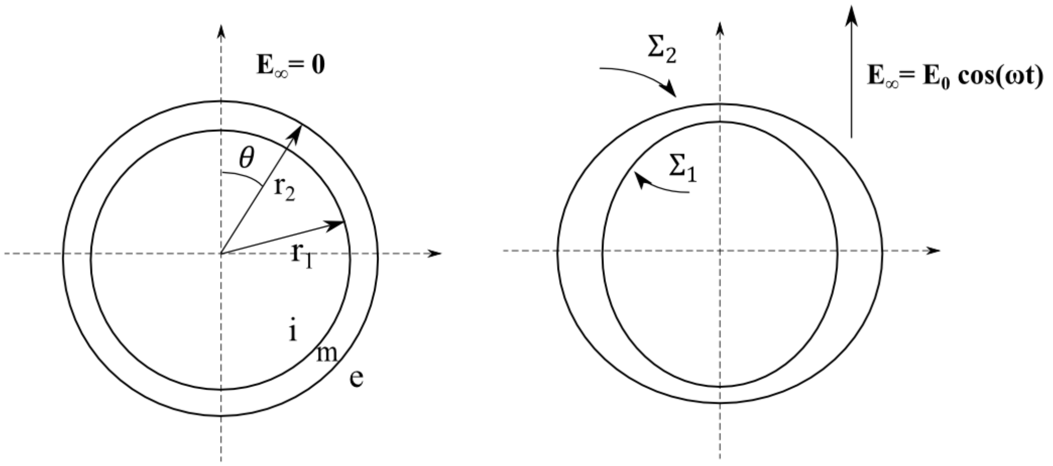

Figure 1: Double-layered drop in the harmonic electric field

Now let us consider an axisymmetric double-layer liquid drop, immersed in another liquid, and subject it to a harmonic electric field E_∞ (Fig. 1). If the intensity of the field equals zero, surfaces of the double-layer drop are spherical with radii $r=r_1$, $r=r_2$. Liquids are assumed to be dielectric with small electric conductivity. The dielectric permeability ε and conductivity λ of the liquids are considered as constants. Also, all liquids are incompressible and significantly viscous (μ = const). Moreover, the velocity is expected to be small, so it leads to a small Reynolds number. Because of it, the Stokes approximation can be used. Considering all these assumptions, fluid motion equations can be written as follows:

$$\Delta\phi = 0, \qquad E = -\nabla\phi,$$

$$\rho\frac{\partial v}{\partial t} = -\nabla p + \mu\Delta v, \qquad \operatorname{div} v = 0$$

Boundary conditions at all the interfaces $r = f_i(\theta, t), i = 1,2$:

$$[\phi] = 0, \qquad n \cdot (\varepsilon_0 \varepsilon E) = \sigma,$$

$$n \cdot [J] + \nabla_\Sigma \cdot j_\Sigma + \frac{\partial(\sigma\sqrt{g})}{\sqrt{g}\partial t} = 0,$$

$$[p_{ij}n^j e^i] = \pm 2TKn,$$

$$[v] = 0, \qquad {}^{df}/_{dt} = v_n$$

and the boundary conditions at the infinity:

$$v \to \infty, \qquad \phi \to \phi_\infty, \qquad E_\infty = -\nabla\phi_\infty, \qquad (r \to \infty).$$

There g is a determinant of metrical tensor, K is a mean curvature, T is an interfacial tension, σ is a charge on the surface, $r = f_j(\theta, t), j = 1,2$ is a form of the interfaces Σ_1 and Σ_2, ∇_Σ is a surface Nabla. All the parameters of liquids inside, in the middle, and outside the droplet hereinafter will be marked "i", "m" and "e" consequently. Also the properties of interfaces Σ_1 and Σ_2 will be marked "1" and "2" consequently. [A] is a jump of A across the interface.

3. Solution of the problem

Before solving the problem, let us introduce some dimensionless parameters:

$$\alpha = \frac{\varepsilon_0\varepsilon E_0^2 r_2}{T_2}, v_c = \frac{\varepsilon_0\varepsilon E_0^2 r_2}{\mu_e}, \gamma = \frac{\varepsilon_0\varepsilon T_2}{\lambda_e\mu_e r_2}, R = \frac{\rho v_c r_2}{\mu_e}, l_0 = \frac{r_1}{r_2},$$

$$\Lambda_i = \frac{\lambda_i}{\lambda_e}, \Lambda_m = \frac{\lambda_m}{\lambda_e}, \Lambda_e = \frac{\lambda_e}{\lambda_e} = 1, \Lambda_{S1} = \frac{\lambda_{\Sigma 1}}{\lambda_e r_2}, \Lambda_{S2} = \frac{\lambda_{\Sigma 2}}{\lambda_e r_2},$$

$$\varepsilon_i^* = \frac{\varepsilon_i}{\varepsilon_e}, \varepsilon_m^* = \frac{\varepsilon_m}{\varepsilon_e}, \varepsilon_e^* = \frac{\varepsilon_e}{\varepsilon_e} = 1, M_i = \frac{\mu_i}{\mu_e}, M_m = \frac{\mu_m}{\mu_e}, M_e = \frac{\mu_e}{\mu_e} = 1.$$

and some dimensionless variables:

$$r^* = \frac{r}{r_2}, p^* = \frac{p r_2}{T}, v^* = \frac{v}{v_c}, E^* = \frac{E}{E_0}, \phi^* = \frac{\phi}{E_0 r_2}, \sigma^* = \frac{\sigma}{\varepsilon_0\varepsilon_e E_0}, t^* = \frac{t v_c}{r_2}$$

From this moment all calculations will be performed in a dimensionless way. So, to simplify the notation we will not write asterisks anymore. The equations dimensionless form can be written as follows (hereinafter k takes values {i, m, e}):

$$\Delta\phi_k = 0,$$

$$\alpha R\frac{\partial v_k}{\partial t} = -\nabla p_k + \alpha M_k \Delta v_k, \qquad \operatorname{div} v_k = 0$$

The boundary conditions on the inside surface Σ_1 for $r = f_1(\theta, t)$:

$$[\phi]_i^m = 0, \qquad \varepsilon_m E_{nm} - \varepsilon_i E_{ni} = \sigma_1,$$

$$\Lambda_m E_{nm} - \Lambda_i E_{ni} + \Lambda_{S1}\frac{\partial\left(E_\theta\sqrt{g_{1\varphi\varphi}}\right)}{\sqrt{g_1}\partial\theta} + \frac{\alpha\gamma}{\sqrt{g_1}}\left(\frac{\partial(\sigma_1\sqrt{g_1})}{\partial t} + \frac{\partial\left(\sigma_1 v_\theta\sqrt{g_{1\varphi\varphi}}\right)}{\partial\theta}\right) = 0,$$

$$[p]_i^m n - \alpha[M\Pi_1]_i^m = -2\frac{T_1}{T_2}K_1 n + \alpha F_1,$$

$$F_1 = \left(\varepsilon_m\left(E_{nm}E_m - \frac{1}{2}E_m^2 n\right) - \varepsilon_i\left(E_{ni}E_i - \frac{1}{2}E_i^2 n\right)\right),$$

$$v_{\tau i} = v_{\tau m}, \qquad v_{ni} = v_{nm} = D_1$$

The boundary conditions on the outside surface Σ_2 for $r = f_2(\theta, t)$ look the same:

$$[\phi]_m^e = 0, \qquad \varepsilon_e E_{ne} - \varepsilon_m E_{nm} = \sigma_2,$$

$$\Lambda_e E_{ne} - \Lambda_m E_{nm} + \Lambda_{S2}\frac{\partial\left(E_\theta\sqrt{g_{2\varphi\varphi}}\right)}{\sqrt{g_2}\,\partial\theta} + \frac{\alpha\gamma}{\sqrt{g_2}}\left(\frac{\partial\left(\sigma_2\sqrt{g_2}\right)}{\partial t} + \frac{\partial\left(\sigma_2 v_\theta\sqrt{g_{2\varphi\varphi}}\right)}{\partial\theta}\right) = 0,$$

$$[p]_m^e n - \alpha[M\Pi_2]_m^e = -2K_2 n + \alpha F_2,$$

$$F_2 = \left(\varepsilon_e\left(E_{ne}E_e - \frac{1}{2}E_e^2 n\right) - \varepsilon_m\left(E_{nm}E_m - \frac{1}{2}E_m^2 n\right)\right),$$

$$v_{\tau m} = v_{\tau e}, \qquad v_{nm} = v_{ne} = D_2$$

and, finally, the boundary conditions at the infinity:

$$v \to \infty, \qquad \phi \to -r\cos\theta\, e^{i\omega t}, \qquad (r \to \infty).$$

In should be noted that: $g_{j\varphi\varphi} = f_j^2 \sin^2\theta,\ g_{j\theta\theta} = f_j^2 + \left(\frac{\partial f_j}{\partial\theta}\right)^2,\ g_j = g_{j\varphi\varphi}\, g_{j\theta\theta},\ j = 1, 2$.

Let us assume that α parameter is small, and use the asymptotic method - expand all functions (for example, ***v***, *p*, σ) by this small parameter in the following way:

$\Phi(r,\theta,t) = \Phi^{(0)}(r,\theta,t) + \alpha\Phi^{(1)}(r,\theta,t) + \alpha^2\Phi^{(2)}(r,\theta,t) + \cdots$

The zero approximation of the small parameter corresponds to the absence of electric field. So, in this case, the drop's form remains spherical, no flows appear. But there is a pressure jump on the interfaces because of interfacial tension.

$$p_e^{(0)} = 0, \qquad p_m^{(0)} = 2, \qquad p_i^{(0)} = 2 + 2\,{}^{T_1}\!/_{T_2}$$

The first approximation by α for simple drop theory was presented in papers [2-5], and according to them, in this paper the same method is used. The whole system of equations splits into two parts. The first part is Laplace equation for electrodynamic potential and its boundary conditions, and the second part is the hydrodynamic equations and boundary conditions. As the first part does not depend on the second part, it is possible to solve it separately, and then substitute the variables found to the second part.

The solution for electric potential:

$$\phi_i^{(0)} = \frac{9}{(L_1+2)(L_2+2) + 2(L_1-1)(L_3-1)l_0^3}\, r\cos\theta\, e^{i\omega t},$$

$$\phi_m^{(0)} = 3\frac{(L_1+2)r + (L_1-1)l_0^3 r^{-2}}{(L_1+2)(L_2+2) + 2(L_1-1)(L_3-1)l_0^3}\cos\theta\, e^{i\omega t},$$

$$\phi_m^{(0)} = \left(-r + \frac{(L_1+2)(L_2-1) + (L_1-1)(2L_3+1)l_0^3}{(L_1+2)(L_2+2) + 2(L_1-1)(L_3-1)l_0^3}\, r^{-2}\right)\cos\theta\, e^{i\omega t},$$

$$L_1 = \frac{\Lambda_i + i\alpha\gamma\omega\varepsilon_i + 2\Lambda_{S1}}{\Lambda_m + i\alpha\gamma\omega\varepsilon_m}, \qquad L_2 = \frac{\Lambda_m + i\alpha\gamma\omega\varepsilon_m + 2\Lambda_{S2}}{\Lambda_e + i\alpha\gamma\omega\varepsilon_e}, \qquad L_3 = \frac{\Lambda_m + i\alpha\gamma\omega\varepsilon_m - \Lambda_{S2}}{\Lambda_e + i\alpha\gamma\omega\varepsilon_e}$$

Knowing these formulas, it is possible to find the surface charge distribution.

To find velocities and pressure let us introduce a stream function as follows, k = e, m, i:

$$\psi^k = \left(K_1^k r^{-2} + K_2^k r^3 + K_3^k + K_4^k r^5\right)\sin^2\theta\cos\theta$$

There K_j^k are constants, which can be found from boundary conditions. There are no formulas for K_j^k in this article because of their big size. So, velocities and pressure expressed in terms of these constants can be written in the following way:

$$v_i^{(0)} = \left[2\left(K_2^i r + K_4^i r^3\right)P_2, -\left(3K_2^i r + 5K_4^i r^3\right)\sin\theta\cos\theta, 0\right],$$

$$v_m^{(0)} = \left[2\left(K_1^m r^{-4} + K_2^m r + K_3^m r^{-2} + K_4^m r^3\right)P_2, \left(2K_1^m r^{-4} - 3K_2^m r - 5K_4^m r^3\right)\sin\theta\cos\theta, 0\right],$$

$$v_e^{(0)} = \left[2\left(K_1^e r^{-4} + K_3^e r^{-2}\right)P_2, 2K_1^e \sin\theta\cos\theta, 0\right],$$

$$p_i^{(1)} = 14M_i P_2 K_4^i r^2 + C_1,$$

$$p_m^{(1)} = 4M_m P_2\left(K_3^m r^{-3} + \frac{7}{2}K_4^m r^2\right) + C_2,$$

$$p_e^{(1)} = 4M_e P_2 K_3^e r^{-3} + C_3$$

The main purpose of this work is to find deformation, so here are some formulas, which allow finding the form or the drop.

$$f_2^{(1)} = 2XP_2, \qquad P_2 = \frac{1}{2}(3\cos^2\theta + 1),$$

$$X = \frac{1}{4}\left((8K_1^m - 2K_2^m + 6K_3^m + K_4^m)M_m - 2(4K_1^e + 3K_2^e)M_e + [\![F]\!]_2 \cdot n\right)$$

Let us define a new parameter as:

$$D = \frac{f_2(\theta = 0) - f_2\left(\theta = \frac{\pi}{2}\right)}{2} = \frac{3\alpha}{2}X$$

In the next section, we will show the dependence of parameter *D* on properties of liquids.

4. Results

In this section, the dependence of drop deformation *D* on the frequency of electric field *ω* is shown. The parameters of liquids are in the Table 1.

	μ, Pa*s	ε	λ, 1/(Om*m)	T, N/m	$l_0=r_1/r_2$
Magnetic fluid	0.015	5.2	10^(-6)	0.028	0.9
Oil	0.03	2.2	1.4*10^(-12)	0.027	
Liquid X	0.003	2.46	10^(-16)	0.00325	

Table 1. Parameters of the liquids.

Let us consider the case where the magnetic fluid is inside the drop, the oil is outside the drop, and the “liquid X” is in the middle. This liquid is almost like oleic acid, but with much smaller viscosity.

In Fig. 2, you can see the difference between simple drop of magnetic fluid in oil and double-layer drop, including “liquid X” in the middle. As you can see the double-layer drop can change the prolate form *(D>0)* to oblate form (*D<0*) while the frequency increases, instead of the simple drop.

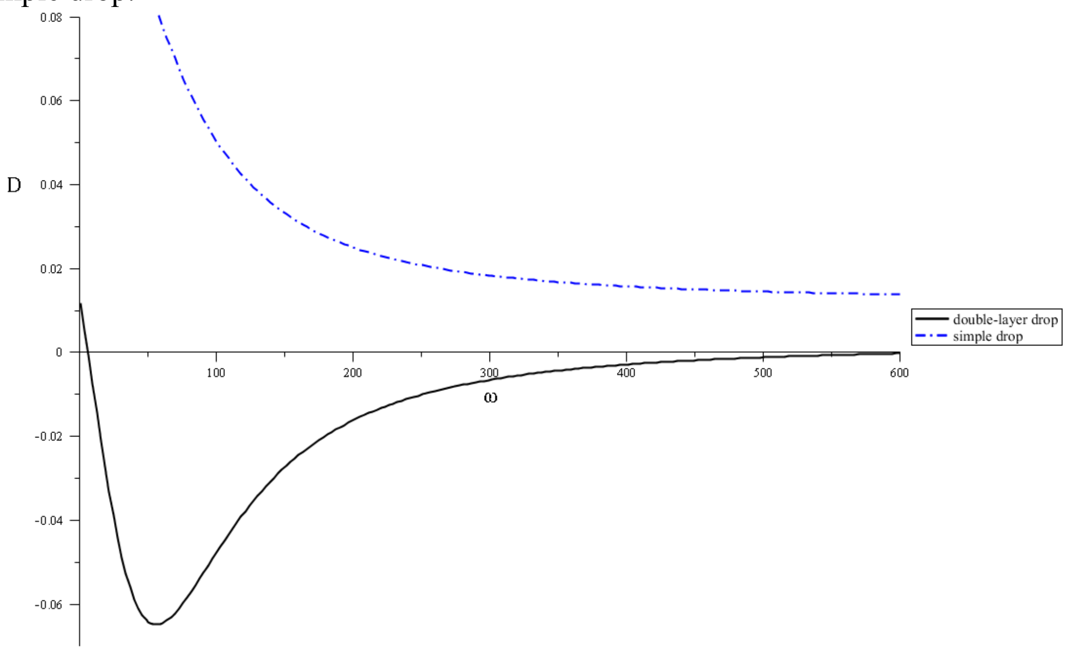

Figure 2: Deformation of magnetic drops in oil.

Now let us consider another case (Fig. 3) where the magnetic fluid and oil changes their places, and “liquid X” remains in the middle. Dependencies of *D* on the frequency *ω* for the double-layer drop and the simple drop of oil in magnetic fluid are also different.

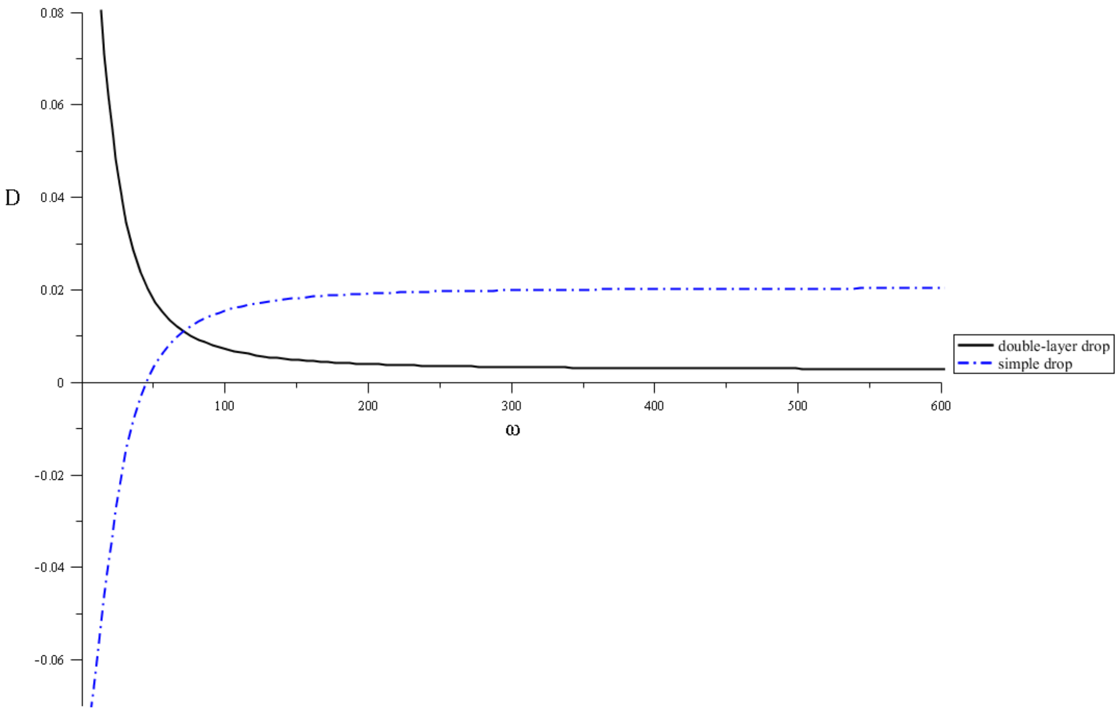

Figure 3: Deformation of oil drops in magnetic fluid.

5. Conclusion

So, in this work the double-layer liquid drop in harmonic electric field is considered. Many calculations are made to find the parameters of liquid “X” where the double-layer drop deformation differs considerably from simple drop deformation. It is possible due to the thin middle-layer of liquid “X” with very small viscosity and conductivity.

Acknowledgements. This work is supported by the Russian Foundation for Basic Research (project 14-01-90003).

6. References

[1] Melcher J.R., Taylor G.I. Electrohydrodynamics: a review of the role of interfacial shear stresses // Annual Rev. Fluid Mech. Palo Alto: California 1969 V.1, P.111-146.
[2] Torza S., Cox R.G. & Mason S.G. Electrohydrodynamic deformation and burst of liquid drops. Phil. Trans. R. Soc. Lond. A 1971 V.269, №1198, P.295-319.
[3] Sozou C. Electrohydrodynamics of a liquid drop: the time-dependent problem. Proc. R. Soc. Lond. A 1972, V.331, P.263.
[4] V.Ya. Shkadov, A.A Shutov. Drop and Bubble Deformation in an Electric Field. Fluid Dynamics. 2002, vol. 37, no. 5, c. 713-724.
[5]. Yu.I. Dikanskii, D.I. Kvasov, V.A. Naletova and E.S. Tkacheva. Deformation of a magnetic fluid drop in an alternating electric field. In: Proceeding of IV Russian Scientific Conference “Physical, chemical and application problems of magnetic disperse nanosystems”. Stavropol, 2013, pp. 58-64 (in Russian).

DIFFUSION OF MAGNETOTACTIC BACTERIA IN ROTATING MAGNETIC FIELD

TAUKULIS[1] R., CĒBERS[1] A.
Affiliation: [1]University of Latvia, Zeļļu 8, Riga, Latvia
e-mail address of corresponding author: reinis.taukulis@gmail.com

Abstract: Various kinds of so-called circle swimmers that operate in low-Reynolds number environments garner a lot of interest and are being studied extensively. Magnetotactic bacteria are examples of such swimmers. When placed in a rotating magnetic field these bacteria move in circles if the field frequency is less than a critical value. Here an expression for diffusion coefficients of magnetotactic bacteria in rotating field with random switching of swimming direction are derived and compared to a numerical simulation.

1. Introduction

Various kinds of so-called circle swimmers have been studied by various groups of researchers [1,2,3,4,5]. Effective diffusion coefficients of circle swimmers subjected to thermal noise are calculated in [1,2]. A specific example of circle swimmers is magnetotactic bacteria. If these bacteria are subjected to a rotating magnetic field they move in circles provided that the field frequency is less than a critical value and that thermal noise can be neglected [6]. A random walk of the centers of circular trajectory is observed due to random switching of the direction of rotation of their flagella [6,7]. Here the properties of this random walk are studied using the Fokker-Planck equation for the position and the direction of swimming of the bacteria.

2. Diffusion of circle swimmers

When the field frequency ω is less than a critical value (synchronous regime) the magnetotactic bacteria rotate synchronously with the field. Suppose that the bacterium moves with speed v in direction $\vec{n}$ of it's magnetic moment and consider the probability density function $f(\vec{x}, \vec{n}, t)$ of the position of the bacterium $\vec{x}$ and the direction of motion $\vec{n}$. Using the operator of infinitesimal rotations $\vec{K}_{\vec{n}} = \vec{n} \times \partial/\partial\vec{n}$ the Fokker-Planck equation accounting for a random switching rate λ of the direction of a rotary motor rotation reads

$$\frac{\partial f}{\partial t} = -\frac{\partial(v\vec{n}f)}{\partial\vec{x}} - \vec{\omega}\vec{K}_{\vec{n}}f - \lambda f + \lambda\hat{f} + D_B\frac{\partial^2 f}{\partial\vec{x}^2} + D_R\vec{K}_{\vec{n}}^2 f \ , \tag{1}$$

where $f = f(\vec{x}, \vec{n}, t)$, $\hat{f} = f(\vec{x}, -\vec{n}, t)$ and D_B and D_R are translational and rotational diffusion coefficients respectively.

A simple approach to analysis is based on calculation of time-evolution for several moments of the distribution from equation (1) [8]. The obtained set of equations is closed and reads

$$\begin{aligned} \frac{d}{dt}\langle\vec{x}^2\rangle &= 2v\langle\vec{x}\vec{n}\rangle + 6D_B \ , \\ \frac{d}{dt}\langle x_z^2\rangle &= 2v\langle x_z n_z\rangle + 2D_B \ , \\ \frac{d}{dt}\langle\vec{x}\vec{n}\rangle &= v + \omega\langle(\vec{n}\times\vec{x})_z\rangle - 2(D_R+\lambda)\langle\vec{x}\vec{n}\rangle \ , \\ \frac{d}{dt}\langle(\vec{n}\times\vec{x})_z\rangle &= -2(D_R+\lambda)\langle(\vec{n}\times\vec{x})_z\rangle - \omega\langle\vec{x}\vec{n}\rangle + \omega\langle x_z n_z\rangle \ , \end{aligned} \tag{2}$$

$$\frac{d}{dt}\langle x_z n_z\rangle = v\langle n_z^2\rangle - 2(D_R+\lambda)\langle x_z n_z\rangle \ ,$$
$$\frac{d}{dt}\langle n_z^2\rangle = 2D_R - 6D_R\langle n_z^2\rangle \ .$$

In order to derive the set of equations (2) the condition of normalization $\int f(\vec{x},\vec{n},t)d\vec{x}d^2\vec{n} = 1$ and the anti-hermitian property of the operator $\vec{K}_{\vec{n}}$ are used. Since the set is closed it is possible to obtain an analytical solution for $\langle\vec{x}^2\rangle$ and $\langle x_z^2\rangle$which characterize the random process of the particle diffusion. In the stationary case where all other moments considered are constant the solution is

$$\begin{aligned}\frac{d}{dt}\langle x_z^2\rangle &= 2D_B + \frac{v^2}{3(D_R+\lambda)} \ ,\\ \frac{d}{dt}\langle \vec{x}^2 - x_z^2\rangle &= 4D_B + \frac{2v^2}{3(D_R+\lambda)(1+[\frac{\omega}{2(D_R+\lambda)}]^2)} \ .\end{aligned} \tag{3}$$

Therefore there are two distinct effective diffusion coefficients $D_{\parallel}$ (along the angular velocity $\vec{\omega} = \omega\hat{e}_z$) and $D_{\perp}$ (in the plane of rotation) and they read

$$\begin{aligned}D_{\parallel} &= D_B + \frac{v^2}{6(D_R+\lambda)} \ ,\\ D_{\perp} &= D_B + \frac{v^2}{6(D_R+\lambda)(1+[\frac{\omega}{2(D_R+\lambda)}]^2)} \ .\end{aligned} \tag{4}$$

In the limit $\lambda \to 0$ these expressions reduce to those found in [2] using correlation functions.

It is seen that in absence of rotating external field ($\omega = 0$) the rate of swimming direction reversal λ plays the role of rotational diffusion coefficient and constricts motion of the bacterium. External field further restricts motion in the plane of rotation but there exists a maximum of the transversal diffusion coefficient $D_{\perp}$ at $\lambda_{max} = \omega/2 - D_R$ if $\omega > 2D_R$. Thus in this case a bacterium has a possibility to increase its diffusion coefficient for seeking more favorable conditions by adapting the switching rate of the rotary motor. If $\omega < 2D_R$ it is not advantageous for the bacterium to employ the switching mechanism.

3. Numerical simulation algorithm

In the synchronous regime the tangent vector to the trajectory $\vec{n}$, which we choose along the magnetic moment of the bacterium, rotates with the angular velocity of the field:

$$\frac{d\vec{n}}{dt} = \vec{\omega}\times\vec{n} \ . \tag{5}$$

Using the fluctuation-dissipation theorem equations for the change of $\vec{x}$ and $\vec{n}$ in a time interval Δt can be obtained and read

$$\begin{aligned}\Delta\vec{x} &= v\vec{n}\Delta t + \sqrt{2D_B\Delta t}\ \vec{G},\\ \Delta\vec{n} &= (\vec{\omega}\Delta t + \sqrt{2D_R\Delta t}\ \vec{H}\ )\times\vec{n},\end{aligned} \tag{6}$$

where components of vectors $\vec{G}$ and $\vec{H}$ are standard normal random variables. A set of switching times τ_i $(i = 1, ...N)$ distributed according to the Poisson law $p_i = \exp(-\lambda\tau_i)$ are introduced and at time moments $T_i = \sum_{j=1}^{i-1} \tau_j + \tau_i$ the tangent vector $\vec{n}$ reverses it's direction.

The generated trajectory is used to calculate autocorrelation of the bacterium position $\vec{x}$, which in turn is used to obtain diffusion coefficients $D_{\parallel}$ and $D_{\perp}$ using regression analysis in the region where the autocorrelation becomes linear. The estimated diffusion coefficients for a range of λ values and different field frequencies are shown in Fig.1. The results are in excellent agreement with (4) and shows the maximum in transversal diffusion at $\lambda_{max} = D_R/2$ when $\omega = 3D_R$.

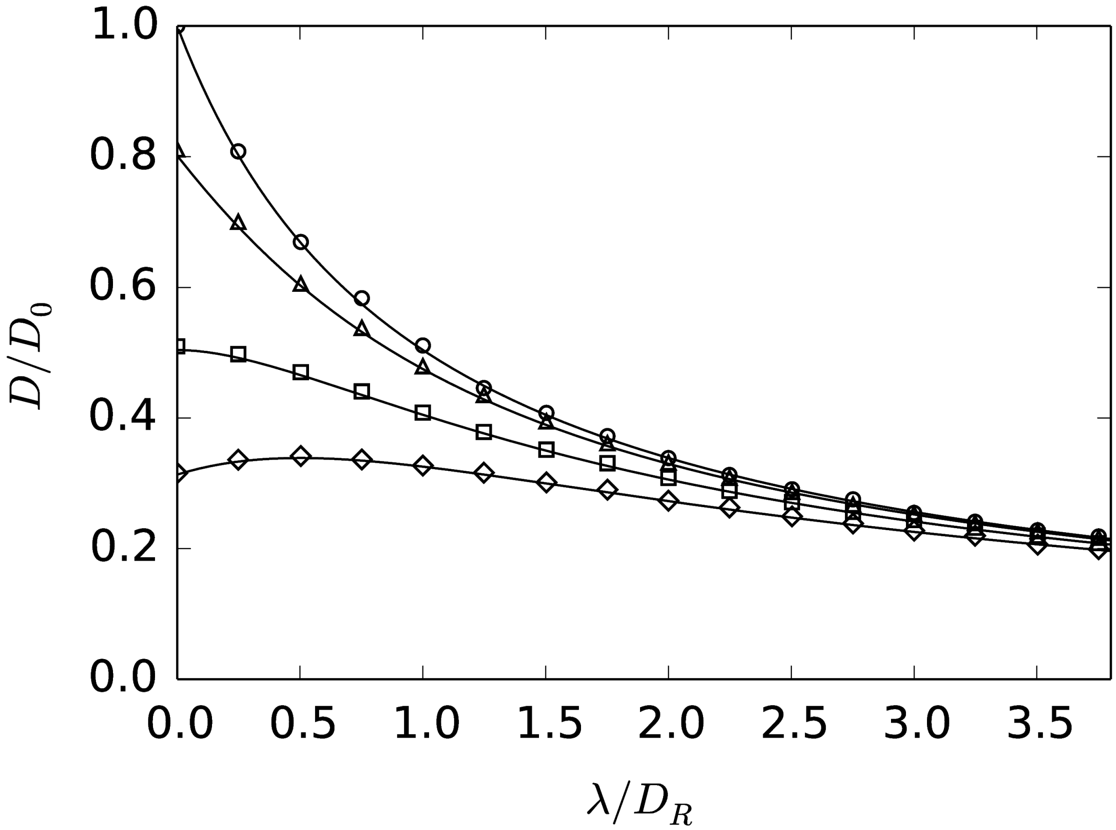

Figure 1: Diffusion coefficients as functions of switching rate λ. Here $D_0 = D_B + v^2/6D_R$. Numerically computed diffusion coefficients shown are $D_{\parallel}$ (circles) and $D_{\perp}$ at $\omega = D_R$ (triangles), $\omega = 2D_R$ (squares) and at $\omega = 3D_R$ (diamonds). Respective theoretical curves according to equations (4) are shown. Common parameters of simulations: bacterium size $r = 1\mu m$, speed $v = 5\mu m/s$, $D_B = 0.214\mu m^2/s$, $D_R = 0.161 s^{-1}$ (assuming spherical bacteria in water at room temperature) and trajectory length $2.5 \times 10^6 s$.

4. Conclusion

In [8] it was noted that previous experimentally observed random trajectories of bacteria are caused by the switching of rotary motors and not due to thermal fluctuations. Here we provide a theory for the interaction between ordinary rotational diffusion and random reversal of swimming direction of bacteria. It is seen that maximum of the diffusion coefficient in the plane of the rotating field, already noted in [8], exists only when the field frequency is sufficiently large so the bacterium can increase it's diffusion by switching the swimming direction with an appropriate rate.

5. References

1. Ebbens, S.; Jones, R.A.L.; Ryan, A.J.; Golestanian, R. and Howse, J.R.: Self-assembled autonomous runners and tumblers. Phys.Rev.E. 82 (2010) 015304(R)
2. Sandoval, M.: Anisotropic effective diffusion of torqued swimmers. Phys.Rev.E. 87 (2013) 032708
3. Kummel, F.; ten Hagen, B.; Witkowski, R.; Buttinoni, I.; Volpe, G.; Lowen, H. and Bechniger, C.: Circular motion of asymmetric self-propelling particles. arXiv:1302.5787v (2013)
4. Friedrich, B.M.; Julicher, F.: The stochastic dance of circling sperm cells: sperm chemotaxis in the plane. New Journal of Physics. 10 (2008) 123025
5. Takagi, D.; Braunschweig, A.B.; Zhang, J. and Shelley, M.J.: Dispersion of self-propelled rods undergoing fluctuation-driven flips. Phys.Rev.Lett. 110 (2013) 038301
6. Erglis, K.; Wen, Qi; Ose, V.; Zeltins, A.; Sharipo, A.; Janmey, P.A. and Cebers, A. Dynamics of magnetotactic bacteria in a rotating field. Biophysical Journal. 93 (2007) 1402
7. Cebers, A. Diffusion of magnetotactic bacterium in rotating magnetic field. JMMM 323 (2011) 279-282
8. Taukulis, R.; Cebers, A. (in press) Diffusion in active magnetic colloids. JMMM

AUTHOR INDEX TO VOLUME 2